frontiers | Research Topics

# Frontiers in multi-source positioning, navigation and timing (PNT)

**Edited by**
Zukun Lu, Zhu Xiao and David Plets

**Published in**
Frontiers in Physics
Frontiers in Astronomy and Space Sciences

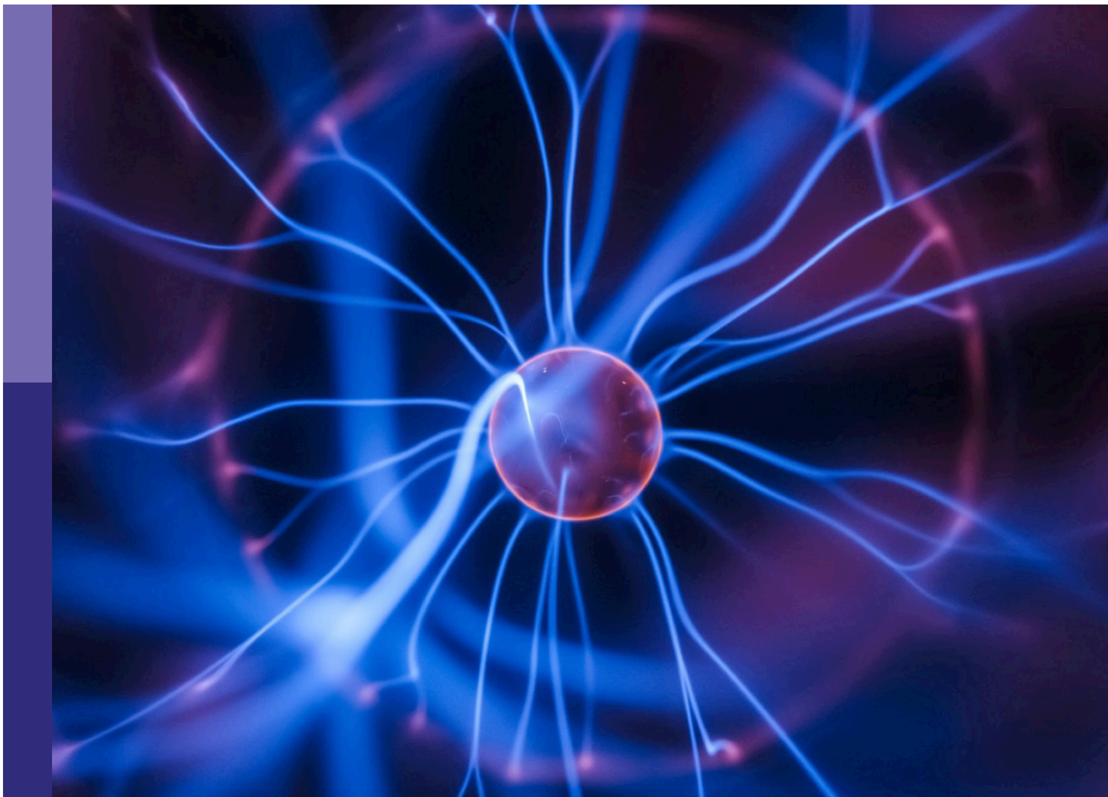

ISSN 1664-8714
ISBN 978-2-8325-7038-8
DOI 10.3389/978-2-8325-7038-8

**Generative AI statement**
Any alternative text (Alt text) provided alongside figures in the articles in this ebook has been generated by Frontiers with the support of artificial intelligence and reasonable efforts have been made to ensure accuracy, including review by the authors wherever possible. If you identify any issues, please contact us.

## About Frontiers

Frontiers is more than just an open access publisher of scholarly articles: it is a pioneering approach to the world of academia, radically improving the way scholarly research is managed. The grand vision of Frontiers is a world where all people have an equal opportunity to seek, share and generate knowledge. Frontiers provides immediate and permanent online open access to all its publications, but this alone is not enough to realize our grand goals.

## Frontiers journal series

The Frontiers journal series is a multi-tier and interdisciplinary set of open-access, online journals, promising a paradigm shift from the current review, selection and dissemination processes in academic publishing. All Frontiers journals are driven by researchers for researchers; therefore, they constitute a service to the scholarly community. At the same time, the *Frontiers journal series* operates on a revolutionary invention, the tiered publishing system, initially addressing specific communities of scholars, and gradually climbing up to broader public understanding, thus serving the interests of the lay society, too.

## Dedication to quality

Each Frontiers article is a landmark of the highest quality, thanks to genuinely collaborative interactions between authors and review editors, who include some of the world's best academicians. Research must be certified by peers before entering a stream of knowledge that may eventually reach the public - and shape society; therefore, Frontiers only applies the most rigorous and unbiased reviews. Frontiers revolutionizes research publishing by freely delivering the most outstanding research, evaluated with no bias from both the academic and social point of view. By applying the most advanced information technologies, Frontiers is catapulting scholarly publishing into a new generation.

## What are Frontiers Research Topics?

Frontiers Research Topics are very popular trademarks of the *Frontiers journals series*: they are collections of at least ten articles, all centered on a particular subject. With their unique mix of varied contributions from Original Research to Review Articles, Frontiers Research Topics unify the most influential researchers, the latest key findings and historical advances in a hot research area.

Find out more on how to host your own Frontiers Research Topic or contribute to one as an author by contacting the Frontiers editorial office: frontiersin.org/about/contact

# Frontiers in multi-source positioning, navigation and timing (PNT)

**Topic editors**
Zukun Lu — National University of Defense Technology, China
Zhu Xiao — Hunan University, China
David Plets — Ghent University, Belgium

**Citation**
Lu, Z., Xiao, Z., Plets, D., eds. (2025). *Frontiers in multi-source positioning, navigation and timing (PNT)*. Lausanne: Frontiers Media SA.
doi: 10.3389/978-2-8325-7038-8

# Table of contents

Frontiers in Physics

TYPE Original Research
PUBLISHED 03 July 2024
DOI 10.3389/fphy.2024.1404236

# Cascaded multiplier-free implementation of adaptive anti-jamming filter based on GNSS receiver

Jie Song[1,2†], Lei Chen[1,2†], Zukun Lu[1,2*], Baiyu Li[3], Zhe Liu[1,2*], Zhihao Xue[1,2], Guangfu Sun[1,2] and Wenhong Liu[3]

[1]College of Electronic Science and Technology, National University of Defense Technology, Changsha, China, [2]Key Laboratory of Satellite Navigation Technology, Changsha, China, [3]Scientific Research Office, National University of Defense Technology, Changsha, China

EDITED BY
Jiansen He,
Peking University, China

REVIEWED BY
Zhaowen Yan,
Beihang University, China
Ying-Ren Chien,
National Ilan University, Taiwan

*CORRESPONDENCE
Zukun Lu,
✉ luzukun@nudt.edu.cn
Zhe Liu,
✉ l_z@nudt.edu.cn

[†]These authors have contributed equally to this work

RECEIVED 20 March 2024
ACCEPTED 28 May 2024
PUBLISHED 03 July 2024

CITATION
Song J, Chen L, Lu Z, Li B, Liu Z, Xue Z, Sun G and Liu W (2024), Cascaded multiplier-free implementation of adaptive anti-jamming filter based on GNSS receiver.
*Front. Phys.* 12:1404236.
doi: 10.3389/fphy.2024.1404236

Evaluating the computational complexity is critical for assessing the time-domain anti-jamming performance of GNSS receivers. The multiplier is the core component that contributes to the computational complexity in time-domain anti-jamming. However, current algorithms aimed at reducing the complexity of time-domain anti-jamming typically concentrate on shortening the filter length, which fails to address the high computational complexity introduced by the use of multipliers. This paper introduces a cascaded multiplier-free approach for implementing time-domain anti-jamming in navigation receivers. We propose a numerical power decomposition technique based on optimal Canonical Signed Digit coding and coefficient decomposition. By substituting the multiplier with minimal adder and shift operations, the computational complexity of the anti-jamming filter with a high quantization bit-width can be considerably decreased. An optimization strategy is presented, and the low-complexity multiplier-free technique is applied to the time-domain anti-jamming filter. Compared to the traditional Canonical Signed Digit multiplier-free technique, our method can reduce the components required for a 12-bit quantization anti-interference filter by one adder, 20 shift operations, and five coded word lengths, while maintaining a pseudo-range measurement deviation below 0.27 ns.

KEYWORDS

**GNSS receiver, time domain anti-interference, optimal CSD coding, numerical power decomposition, cascaded multiplier-free implementation**

## 1 Introduction

The Global Navigation Satellite System (GNSS) offers precise spatial and temporal reference data, including three-dimensional positioning, velocity, and timing [1]. Due to the substantial distance between the satellites and the ground, and the limited satellite resources, the navigation signal is susceptible to being overwhelmed by jamming [2]. As various electronic systems have advanced, competition for electromagnetic frequency bands has become intense, leading to severe jamming [3]. Ensuring anti-jamming capabilities for GNSS receivers is crucial to navigate through complex electromagnetic and electronic warfare environments, ensuring the accuracy of positioning, navigation, and timing for navigational terminals [4].

Given the spectrum overlap, mutual interference occurs between satellite navigation, radar, and 5G systems [5]. The low cost of time-domain anti-jamming makes it a prevalent solution for fixed-band narrowband jamming suppression, and is crucial for assessing GNSS receiver performance. Researchers are developing cost-effective navigation receivers to keep pace with the evolving GNSS systems and the development of new features. Chien [6] presents a cost-effective cascaded IIR adaptive notch filter for interference suppression that significantly reduces complex computations resulting from Fourier Transforms (FFT), inverse FFT, or wavelet transformations. Ren et al. [7] proposes a subspace projection algorithm with a brief projection length for continuous wave and linear frequency-sweep interference, thereby reducing computational complexity. Wang et al. [8] introduces an adaptive narrowband interference (NBI) suppression technique utilizing coded-aid technology that obviates the need for FFT or matrix inversion. Additionally, variable tap-length LMS and sparse algorithms have seen extensive development [9–11]. Nonetheless, the multiplier continues to impact complexity. The multiplier is a pivotal component of DSP calculations within the navigation receiver [12]. Its complexity scales quadratically with the quantization bit width, thus necessitating considerable computational resources. Because multiplication operations influence the jamming suppression performance in hardware, a multiplier-less implementation has been adopted to reduce costs and accelerate convergence [13, 14].

Multiplier-less implementation replaces multipliers with other operations, such as the read-only memory (ROM) lookup table, distributed arithmetic (DA) algorithm, binary complement, Coordinate Rotation Digital Computer (CORDIC), multiple constant multiplication (MCM), and canonic signed digit (CSD) coding [15–17]. CSD coding components the filter coefficient as the sum or difference of the power of 2, replacing the multiplier by shift operation and adder [18]. The coefficient decomposition decomposes the coefficient into the product of several numbers by the lookup table, reducing the adder number by cascading. Methods can be used in conjunction to reduce the adder number and sampling bit width. There have been optimization studies on the implementation methods of various filters without multipliers [19–21].

However, the above multiplier-less implementation methods are limited in the practical GNSS receiver applications, which are usually used in fixed-coefficient filters. The anti-jamming filter coefficient of GNSS receivers is usually considerable, while the existing multiplication-less implementation scheme is limited by the quantization bit width, resulting in significant quantization errors. The anti-jamming filter multiplication-less implementation method should be further optimized to minimal adders and shift operations with easy implementation.

Building on previous work, this paper proposes a cascaded multiplier-free implementation method for GNSS receiver time-domain anti-jamming filters. This method is applied to the static time-domain anti-jamming of satellite navigation receivers, optimizing the design of high-gain filter coefficients without multipliers. It reduces the number of adders, shift operations, and the coding word length of filter coefficients, thereby decreasing the computational complexity of the anti-jamming filters.

# 2 System model

## 2.1 GNSS receiver model

The GNSS system consists of the space segment, ground segment, and user segment. Figure 1 illustrates the GNSS receiver structure. The user terminals process the received radio frequency (RF) signals in RF front-end (RFFE). The baseband digital signal processing (DSP) suppresses the unexpected interference after the digital down conversion (DDC), and applies the multiplier-free anti-jamming filter based on the LMS adaptive algorithm. After the anti-jamming data is captured and tracked, it finally enters terminal's back-end (BE) for realizing positioning, navigation and timing (PNT) functions [22].

Satellite navigation signals include the carrier, pseudo-random (PRN) code, and message data. The satellite navigation signal can be expressed by the carrier modulated with the spread spectrum signal of PRN code and data in Eq. 1:

$$s(t) = \sum \sqrt{2P_t}\,(x(t)D(t))\sin(2\pi f t + \theta) \tag{1}$$

where, $P_t$ is the average power of navigation signal, $x(t)$ is the PRN code level, $D(t)$ is the satellite broadcast message data, $f$ is the central frequency of RF signal, $\theta$ is the initial phase of the carrier.

Suppose that the receiver thermal noise is $u[n]$, the interference signal is $j[n]$, such as continuous wave interference or narrowband Gaussian noise interference. Continuous wave interference (CWI) aims at the central frequency of satellite navigation signals by the continuous high-power single-frequency signal [23]. Narrowband interference (NBI) is generated by band-limited Gaussian white noise [24]. The CWI and NBI can be expressed as Eqs 2, 3 respectively:

$$J_{\mathrm{CWI}} = \sqrt{2P_J}\cos(2\pi f_J t + \varphi_0) \tag{2}$$

$$J_{\mathrm{NBI}} = A_n G(t) * Sa(t) \tag{3}$$

where, $P_J$ is the interference power, $f_J$ is the interference frequency, $\varphi_0$ is the initial phase, $A_n$ is the narrowband interference amplitude, $G(t)$ is the Gaussian white noise, $G(t)$ is convoluted with the finite band-pass gate function $Sa(t)$ to generate narrowband interference.

The resultant input signal before the anti-jamming module can be expressed in Eq. 4 [25]:

$$x[n] = s[n] + j[n] + u[n] \tag{4}$$

## 2.2 Multiplier-free time-domain adaptive anti-jamming model

The time-domain anti-jamming algorithm utilizes the adaptive filter to suppress interference. The iterated filter coefficients should be implemented to be multiplier-free and then assigned to the weight storage module. Figure 2 illustrates the flow chart of the multiplier-free time-domain adaptive anti-jamming algorithm.

Suppose that the input vector of the $N$-long filter at time $n$ is as Eq. 5:

$$\mathbf{x} = [x(n), x(n-1), \cdots, x(n-N+1)]^{\mathrm{T}} \tag{5}$$

Suppose the filter quantization bit width is L. The filter weight vector is as Eq. 6:

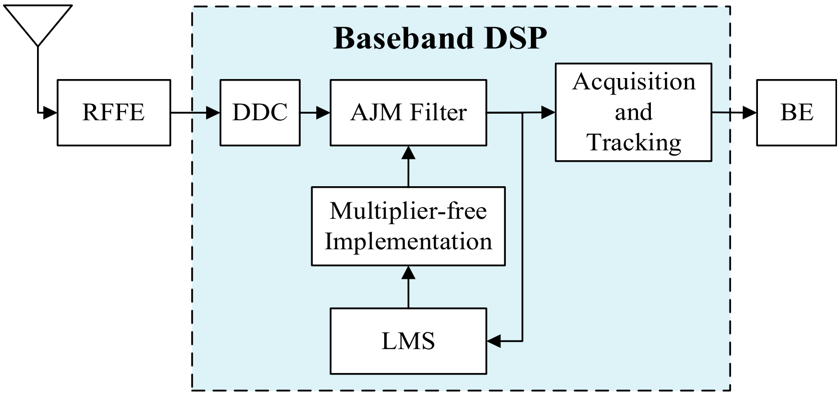

FIGURE 1
GNSS receiver structure.

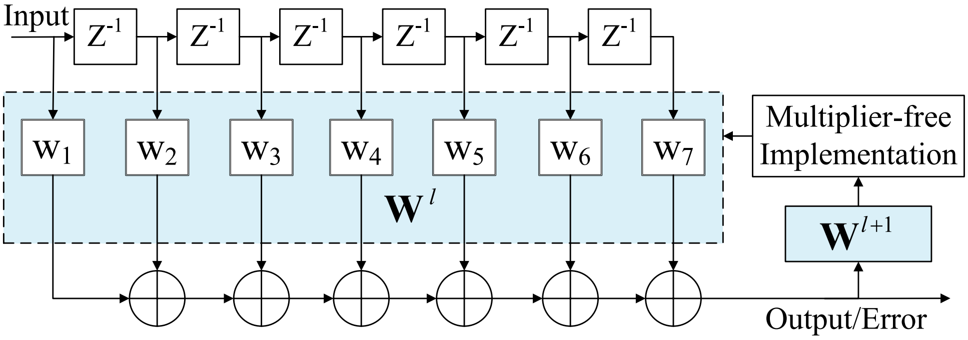

FIGURE 2
Anti-jamming flow chart with multiplier-free implementation.

$$\mathbf{W} = \text{fix}\left[\text{Norm}\left[\omega_1, \omega_2, ..., \omega_N\right] \cdot 2^L\right] = \left[w_1, w_2, ..., w_N\right] \tag{6}$$

where, $\text{fix}[\cdot]$ is the rounding function to round off the input signal, $\text{Norm}[\cdot]$ is the normalized function.

Define the multiplier-free implementation method as $\Phi[\cdot]$. With the iterated coefficients implemented multiplier-free, the anti-jamming output signal can be expressed as:

$$y(n) = \mathbf{x} \cdot \mathbf{W} = \sum_{k=1}^{N} x(n-k+1)\Phi[w_k] \tag{7}$$

The error signal $e(n)$ is defined as the difference between the anti-jamming output signal $y(n)$ and the desired signal $d(n)$, where the desired signal is generally considered to be navigational signal, as shown in Eq. 8:

$$e(n) = d(n) - y(n) \approx s(n) - y(n) \tag{8}$$

The iterative formula of LMS algorithm can be expressed as Eq. 9 [26]:

$$\begin{aligned} \mathbf{W}_M^{n+1} &= \mathbf{W}_M^n + \mu \mathbf{x}^*(n) e(n) \\ &= \mathbf{W}_M^n + \mu \mathbf{x}^*(n)\left[s(n) - y(n)\right] \approx \mathbf{W}_M^n - \mu \mathbf{x}^*(n) y(n) \end{aligned} \tag{9}$$

where $[\cdot]^*$ represent the conjugation.

The multiplier-free implementation of GNSS time-domain anti-jamming is applicable to satellite navigation receivers with limited hardware resources. For instance, mobile phones require the development of miniaturization capabilities and maintaining anti-interference capabilities, and spaceborne receivers' functionality is expanded within the constraints of limited resources. Figure 3 depicts a ground-test module of a satellite-borne receiver in its practical application.

## 3 Problem formulation

### 3.1 CSD coding

The signed number is one of the essential non-standard fixed-point number in computer algorithm implementation, and its digital range is $\{1, 0\}$. Since it is not unique, the system with the least nonzero elements is called the regular signed digit system.

The CSD coding expresses the filter coefficients as the sum or difference of the power of 2, which is realized by shift operation and adder. The optimal CSD coding can also reduce the adder number and the maximum encoding lord length [27].

The mathematical expression of the FIR-filter anti-jamming can be simplified as shown in Eq. 10 [28]:

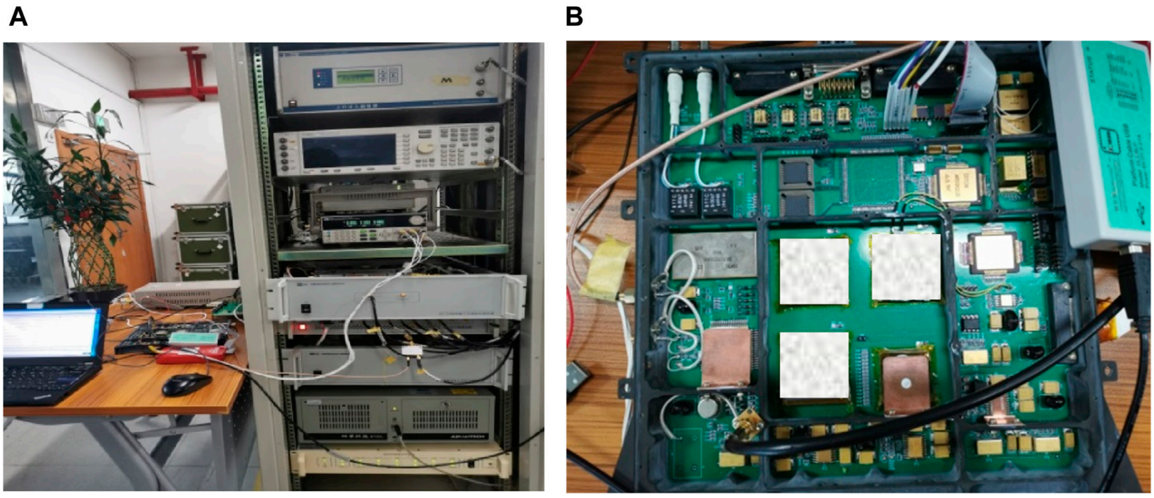

FIGURE 3
Practical application: ground-test module of spaceborne receiver. **(A)** Ground testing architecture. **(B)** Hardware development board.

$$y_i = \sum_{i=0}^{N-1} h_i x_i = \sum_{i=0}^{N-1} x_i \sum_{j=0}^{M-1} h_i(j)$$
$$= \sum_{i=0}^{N-1} x_i \left(2^{M-1} h_i(M-1) + 2^{M-1} h_i(M-1) + \cdots + 2^1 h_i(1) + 2^0 h_i(0)\right) \tag{10}$$

where, $h_i$ represents the $i-th$ weight of the filter, $x_i$ is the input data to the $i-th$ weight, $h_i(j) = 0, 1, -1$ represents the binary representation of the $i-th$ weight, $M$ is the binary bit length.

CSD coding replaces all 1 sequences greater than 2 with $10...0\bar{1}$ from the lowest bit, where $\bar{1}$ represents the negative 1 bit. The best CSD coding has minor nonzero elements and the least subtraction times. Starting from the highest significant bit, replace $10\bar{1}$ with 011 [29].

Suppose that the word length of the binary complement-on-two of value $\omega$ is $L_{\text{bin}}$ then the Binary expression is as Eq. 11:

$$A_{\text{bin}} = a''_{L_{\text{bin}}-1} a''_{L_{\text{bin}}-2} \cdots a''_1 a''_0 \tag{11}$$

where, $a_i = 0, 1, i = 0, 1, ..., L_{\text{bin}} - 1$

The word length of CSD encoding of value A is $L_{\text{CSD}}$ then the CSD expression is as Eq. 12:

$$A_{\text{CSD}} = a'_{L_{\text{CSD}}-1} a'_{L_{\text{CSD}}-2} \cdots a'_1 a'_0 \tag{12}$$

where, $a'_j = -1, 0, 1, j = 0, 1, ..., L_{\text{CSD}} - 1$. Usually, the relationship between CSD code word length and binary complement word length is as shown in Eq. 13:

$$L_{\text{CSD}} = L_{\text{bin}}(+1) \tag{13}$$

The binary complement is updated to CSD coding as shown from Eqs 14–16:

$$\theta_i = a_i \wedge a_{i-1} \tag{14}$$

$$\zeta_i = \bar{\zeta}_{i-1} \theta_i \tag{15}$$

$$a'_j = (1 - 2a_{i+1}) \zeta_i \tag{16}$$

where, $[\cdot]^\wedge$ is the exclusive OR operation, the initial value can be expressed as $a_{i-1} = 0, \zeta_{i-1} = 0, a_n = a_{n-1}$.

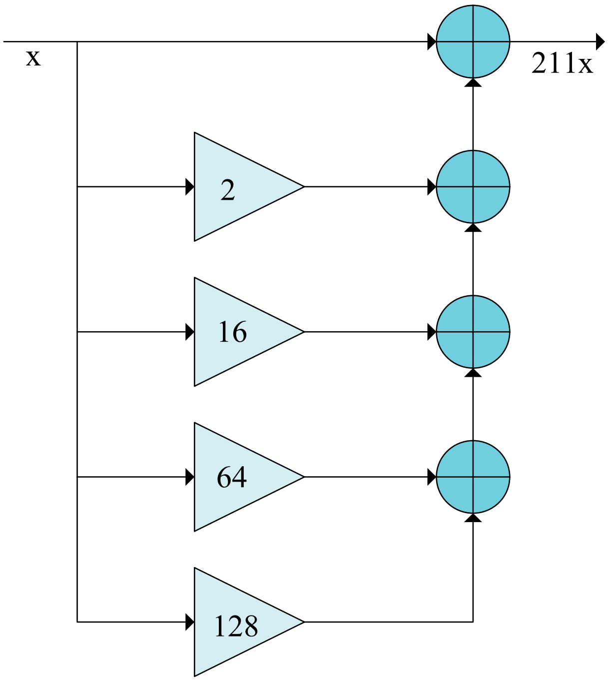

FIGURE 4
Optimal CSD coding schematic.

Then optimize the CSD coding that may have storage waste by Eq. 17:

$$A = a_{L-1} a_{L-2} \cdots a_1 a_0 \tag{17}$$

where, $a_k = -1, 0, 1, k = 0, 1, ..., L - 1$. Usually, the relationship between CSD code word length and binary complement word length is as shown in Eq. 18:

$$L = L_{\text{CSD}}(-1) \tag{18}$$

Its update process can be expressed from Eqs 19–21:

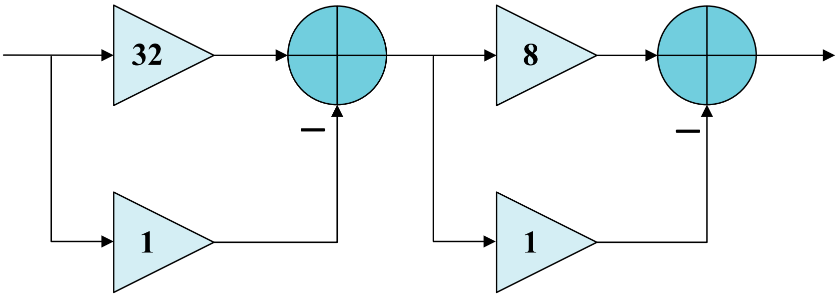

FIGURE 5
Numerical power decomposition schematic.

$$a_k = \mathrm{ceil}\left(\frac{a_j' + a_{j-2}'}{2}\right) \tag{19}$$

$$a_{k-1} = a_j' \oplus a_k \tag{20}$$

$$a_{k-2} = \left[1 - 2\left(a_{j-1}' \oplus a_{k-1}\right)\right] a_{j-2}' \tag{21}$$

where, $\oplus$ is the logical AND operation.

The number of adders is expressed as Eq. 22:

$$S_{\text{add}} = \sum_{k=0}^{n-1} |a_k| - 1 \tag{22}$$

The number of shift operations is expressed as Eq. 23:

$$S_{\text{shift}} = \sum_{k=0}^{n-1} k\big|_{|a_k|=1} \tag{23}$$

The figure shows the best CSD coding schematic. The value 211 is taken as an example in Figure 4, the multiplier-free design based on the optimal CSD coding is composed of 5 values of the power of 2, and the multiplication operation is realized by four adders and 18 shift operations.

## 3.2 Numerical power decomposition

Numerical power decomposition is achieved by cascading several values to reduce the hardware cost of multiplier-less implementation [30]. For example, the traditional binary encoding of the value 231 is $11100111_{\text{bin}}$, the best CSD encoding is $100\bar{1}0100\bar{1}$, and the original multiplier implementation can be reduced from 5 adders to 3. If 231 is factorized into the 7 × 33 cascade, the adders' number can be reduced to 2. Figure 5 is the example diagram of numerical power decomposition.

The value $\omega$ can be decomposed into the product of $\Theta$ values and realized by cascading [31] as shown in Eq. 24:

$$\omega = \Omega_1 \Omega_2 \cdots \Omega_\Theta \tag{24}$$

where, $\Omega_p$ is the $p$-th power factor, which consists of the addition and subtraction of the power of 2 as shown in Eq. 25:

$$\Omega_p = 2^{k_1} \pm \cdots \pm 2^{k_2} \tag{25}$$

The numerical value will affect the device cost of the filter. The total adder number can be expressed as the sum of the number of adders required for different decomposition factors, as shown from Eqs 26–28:

$$N_{\text{add}} = \sum_{p=1}^{\Theta} S_{\text{add}}^p \tag{26}$$

$$N_{\text{shift}} = \sum_{p=1}^{\Theta} S_{\text{shift}}^p \tag{27}$$

$$N_{\text{bit}} = \max L_p \tag{28}$$

where, $S_{\text{add}}^p$, $S_{\text{shift}}^p$, $L_p$ are the number of adders, the number of shift operations, and the maximum word length required for the optimal CSD encoding of the decomposition factor $\Omega_p$, respectively.

## 3.3 Motivations and optimization object

Static anti-jamming filters are usually used in power-sensitive terminals, and computational complexity is one of the most critical design elements. The effect of CSD optimal coding to reduce complexity is limited, and the existing numerical power decomposition is mainly the lookup table method. The accessible decomposition results are limited, creating difficulties for the multiplier-less implementation of large values.

Based on the disadvantages of optimal CSD coding and coefficient decomposition, in order to solve the problem of high gain in the actual filter coefficients, this paper proposes a cascaded multiplier-less implementation. The multiplier-less filter is implemented with minimum adders, reducing the shift operation and memory word length. The optimization objective is shown in Eq. 29:

$$\text{minimize } N_{\text{add}} \qquad \text{subject to} \begin{cases} N_{\text{add}} \le S_{\text{add}} \\ N_{\text{shift}} \le S_{\text{shift}} \\ N_{\text{bit}} \le L \end{cases} \tag{29}$$

# 4 Proposed approach

To design a multiplier-less anti-jamming filter, the numerical power decomposition of the filter coefficients is first performed to obtain each decomposition factor. The multiplier-less coding of all

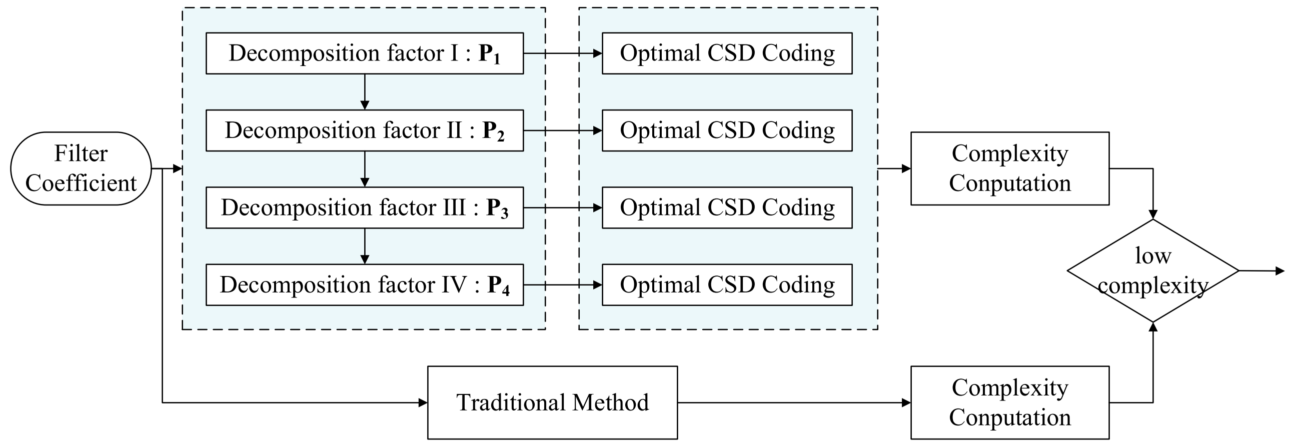

FIGURE 6
Cascaded multiplier-free implementation method flowchart.

decomposition factors is designed according to the optimal CSD coding method. The flowchart is shown in Figure 6.

Firstly, the numerical power decomposition of the filter coefficient $w_i$ is carried out, and four kinds of decomposition factors are obtained. The decomposition matrix can be expressed as is shown in Eq. 30:

$$\mathrm{P} = [\,\mathrm{P}_1 \;\; \mathrm{P}_2 \;\; \mathrm{P}_3 \;\; \mathrm{P}_4\,] \tag{30}$$

where, $\mathrm{P}_i$ is the i-th decomposition factor:

Assume that $2^j$ is a zero-order power factor $\Upsilon_0^j$, and the first type of decomposition factor $\mathrm{P}_1$ is the divisor $\Upsilon_0^j$ that can divide $w_i$ at most. Divide $w_i$ by $\mathrm{P}_1$ to get $w_i^1$, as shown in Eqs 31, 32:

$$\mathrm{P}_1 = \max\left(\Upsilon_0^j \,\middle|\, \mathrm{mod}\left(w_i, \Upsilon_0^j\right) = 0\right), \quad j = 1, 2, \ldots, \mathrm{floor}\left(\frac{B}{2}\right) \tag{31}$$

$$w_i^1 = w_i / \mathrm{P}_1 \tag{32}$$

where, $\mathrm{mod}(\cdot)$ is the residue function, $B$ is the binary length of $w_i$, and $\mathrm{floor}(\cdot)$ is the down-integer function. The cascade of the first type of decomposition factor is realized by a $j$-th forward shift operation.

Assume that $2^l + 1$ or $2^l - 1$ is a one-order power factor $\Upsilon_1^j$, the second decomposition factor $\mathrm{P}_2$ is the divisor $\Upsilon_1^j$ that can divide $w_i{}'$ at most. Divide $w_i^1$ by $\mathrm{P}_2$ to get $w_i^2$ as shown in Eqs 33, 34:

$$\mathrm{P}_2 = \max\left(\Upsilon_1^j \,\middle|\, \mathrm{mod}\left(w_i^1, \Upsilon_1^j\right) = 0\right), \quad j = 1, 2, \ldots, \mathrm{floor}\left(\frac{B'}{2}\right) \tag{33}$$

$$w_i^2 = w_i^1 / \Pi \Upsilon_1^j \tag{34}$$

where, $B'$ is the binary length of $w_i^1$. The second decomposition factor $\mathrm{P}_2$ is realized by an l-bit forward shift operation and an adder.

Assume that $2^m + 2^n + 1$ or $2^m + 2^n - 1$ or $2^m - 2^n + 1$ or $2^m - 2^n - 1$ is the second-order power factor $\Upsilon_2^j$, The third decomposition factor $\mathrm{P}_3$ is the divisor $\Upsilon_2^j$ that can divide $w_i^2$ at most. Devide $w_i^2$ by $\mathrm{P}_3$ to get $\Upsilon_2^j$, as shown in Eqs 35, 36:

$$\mathrm{P}_3 = \max\left(\Upsilon_2^j \,\middle|\, \mathrm{mod}\left(w_i^2, \Upsilon_2^j\right) = 0\right), \quad m, n = 1, 2, \ldots, \mathrm{floor}\left(\frac{B''}{2}\right) \tag{35}$$

$$w_i^3 = w_i^2 / \Pi \Upsilon_2^j \tag{36}$$

where, $B''$ is the binary length of $w_i^2$. The third type of decomposition factor is realized by 1 m displacement bit operation, 1 n displacement bit operation and 2 adders.

The fourth decomposition factor $\mathrm{P}_4$ is the remainder $w_i^3$ divided by the third decomposition factor as shown in Eq. 37:

$$\mathrm{P}_4 = w_i^3 \tag{37}$$

Define the multiplier-free implementation matrix is a cellular matrix as Eq. 38:

$$\Theta = \left\{ \begin{bmatrix} a_{1,B_1} \\ a_{1,B_2} \\ \vdots \\ a_{1,B_{M_1}} \end{bmatrix} \begin{bmatrix} a_{2,B_1} \\ a_{2,B_2} \\ \vdots \\ a_{2,B_{M_2}} \end{bmatrix} \begin{bmatrix} a_{3,B_1} \\ a_{3,B_2} \\ \vdots \\ a_{3,B_{M_3}} \end{bmatrix} \begin{bmatrix} a_{4,B_1} \\ a_{4,B_2} \\ \vdots \\ a_{4,B_{M_4}} \end{bmatrix} \right\} \tag{38}$$

Based on complexity, a better multiplier-free implementation method is selected. In the decomposition process of any power factor $\mathrm{P}_p$, it should be ensured that the cumulative number of adders and the cumulative number of shift operations do not exceed the total number of CSD codes, as shown in Eqs 39, 40:

$$\sum_{p=1}^{\Lambda} S_{\mathrm{add}}^p \le S_{\mathrm{add}} \tag{39}$$

$$\sum_{p=1}^{\Lambda} S_{\mathrm{shift}}^p \le S_{\mathrm{shift}} \tag{40}$$

When Eqs 39, 40 is violated in any numerical power decomposition process, the numerical decomposition should be stopped. The decomposition process takes the last decomposition factor as the penultimate factor, and the remainder divided by the penultimate factor is recorded as the last factor. When the complexity of the cascaded multiplier-less implementation is higher than that of the traditional optimal CSD coding, the optimal CSD coding method is still used to achieve multiplication-free coefficients.

According to Eqs 7, 38, the logic circuit flow of anti-jamming output signal is derived in Eq. 41:

**TABLE 1** Algorithm complexity comparison.

| Coefficient | Traditional method | | | Proposed method | | | |
|---|---|---|---|---|---|---|---|
| | Adder | Shift operation | Maximum code length | Decomposition structure | Adder | Shift operation | Maximum code length |
| 14 | 1 | 5 | 5 | 2*7 | 1 | 4 | 4 |
| 27 | 2 | 7 | 6 | 3*9 | 2 | 4 | 4 |
| 38 | 2 | 8 | 6 | 2*19 | 2 | 6 | 5 |
| 85 | 3 | 12 | 7 | 5*17 | 2 | 6 | 5 |
| 90 | 3 | 14 | 7 | 2*3*15 | 2 | 6 | 5 |
| 153 | 3 | 14 | 8 | 9*17 | 2 | 7 | 5 |
| 170 | 3 | 16 | 8 | 2*5*17 | 2 | 7 | 5 |
| 231 | 3 | 16 | 9 | 7*33 | 2 | 8 | 6 |
| 372 | 3 | 21 | 9 | 3*4*31 | 2 | 8 | 6 |
| 524 | 2 | 14 | 10 | 4*131 | 2 | 10 | 8 |

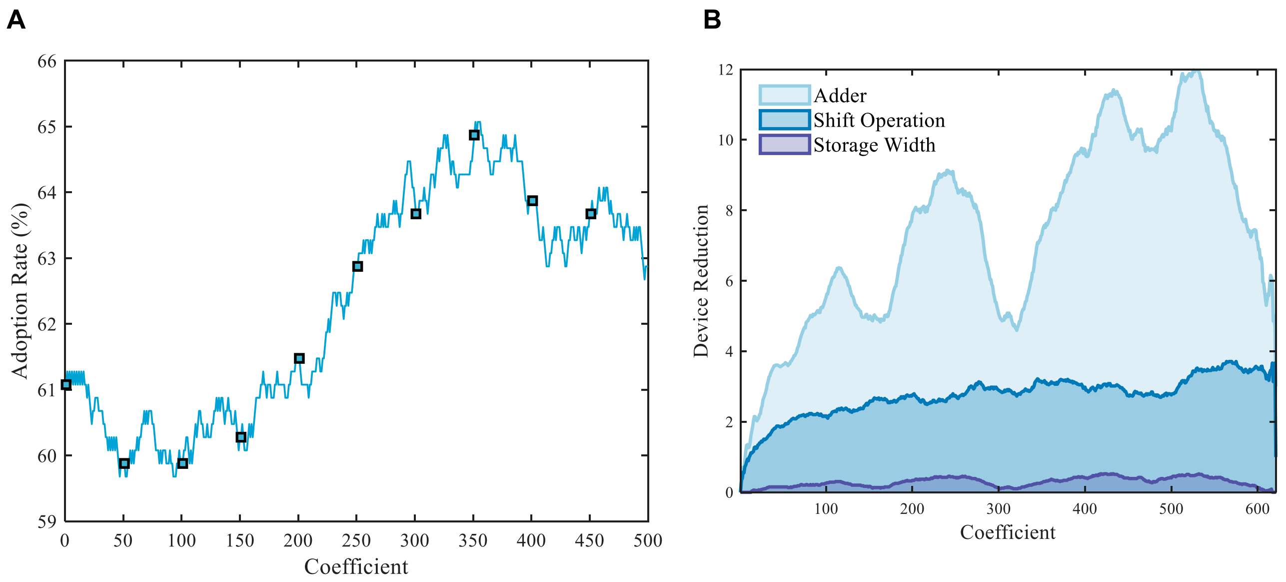

FIGURE 7
Universal adaptability analysis. **(A)** Usage proportion of the proposed method. **(B)** Complexity optimization performance.

$$y(n) = \sum_{k=1}^{N} \prod_{i=1}^{4} \sum_{j=1}^{M_i} x(n-k+1) \cdot 2^{B_j} \tag{41}$$

# 5 Performance analysis

## 5.1 Algorithm complexity comparison

Table 1 presents the complexity comparison between the proposed method and the traditional multiplier-free implementation method, considering the number of adders, shift operations, and maximum word length. The table displays the number of devices for various values under both multiplier-free implementation methods, highlighting the less complex approach. Compared to the traditional optimal CSD coding, the proposed method significantly reduces complexity in multiplier-free implementation. The number of adders is reduced by 0 or 1, while the number of shift operations and the maximum word length are reduced significantly by 13 and 2, respectively.

In order to verify the universal adaptability of the cascaded multiplier-less algorithm, the application rate and complexity optimization performance of the new algorithm with 1~1,000 values is analyzed, respectively. Figure 7A shows the usage proportion of the proposed method. The total integer value of the coefficient is 1~1,000, the smoothing point is set to 500, and the percentage of the cascade multiplier-less implementation is selected for each 400-point data

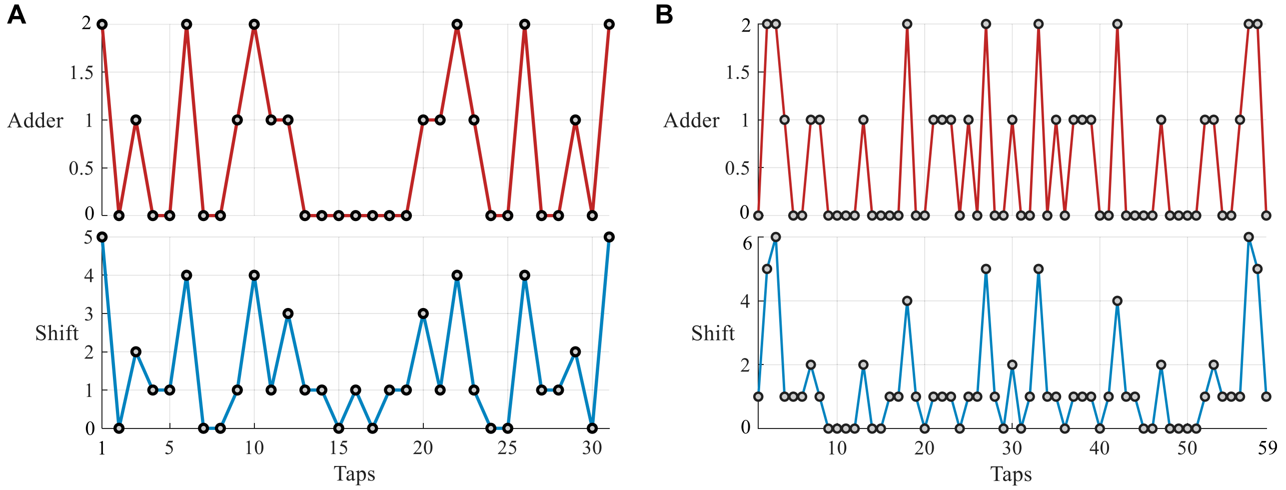

FIGURE 8
Complexity optimization comparison of different CSD codes based on factor cascade. **(A)** 30-order filter. **(B)** 58-order filter.

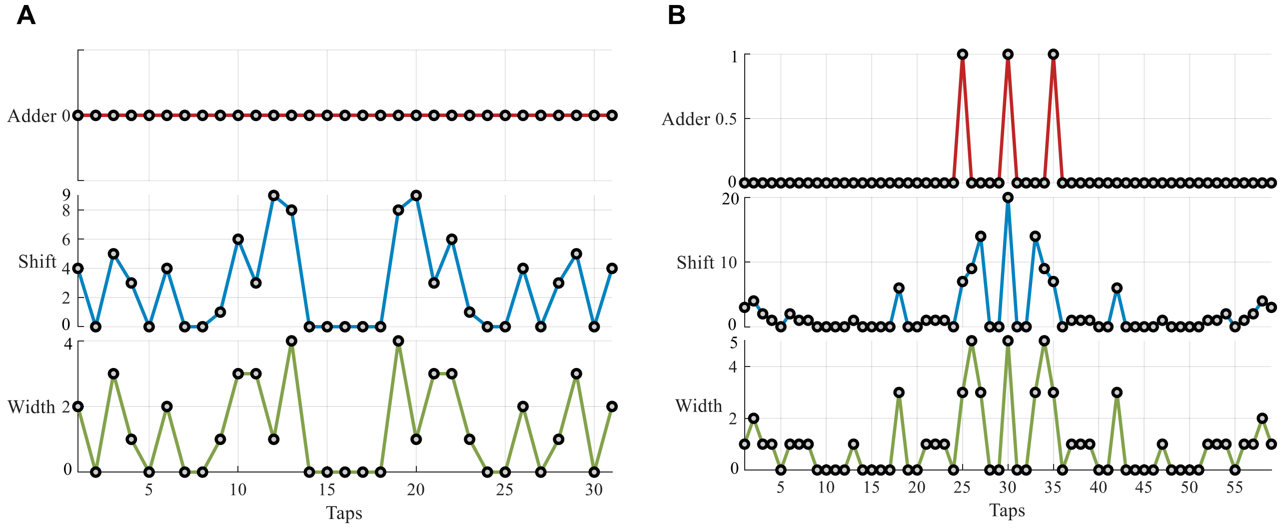

FIGURE 9
Comparison of device count between the proposed and traditional multiplier-free method. **(A)** 30-order filter. **(B)** 58-order filter.

calculation optimization method. The results show that as the coefficient increases, the optimization effect of the cascaded multiplier-less implementation method is better. Figure 7B demonstrates the smoothing result of the device reduction after using the proposed algorithm. Since the device complexity optimization results are relatively scattered, 59 is used as the smoothing unit to smooth the optimization data of adder, shift operation, and maximum coding word length, respectively. The results show that the cascade multiplier-free implementation method significantly reduces the number of the three devices on the graph. Among them, the number of shift operations decreases the most, and the maximum reduction reaches 19.

The digital filters with lengths of 31 and 59 are designed by software. The filter quantization bit width is 12, and the initially designed filter is quantized. The optimization effect of the proposed method on the device complexity is verified based on the designed anti-jamming filter to ensure the effectiveness of the cascaded multiplier-free method in the GNSS receiver. Figure 8 shows that the optimal CSD coding method based on cascaded multiplier-free implementation reduces the multiplier and shift operations compared with CSD coding. After filter coefficient decomposition, the number of adders optimized by CSD coding is reduced by 0–2, and the shift operation is reduced by 0–5.

Figure 9 compares the anti-jamming filter complexity based on the cascaded multiplier-free implementation and the traditional method to verify the method availability. The results show that the adder reduction of the proposed method is greater than 0 compared with the traditional method, and the complexity reduction of the shift operation and the maximum code length is more pronounced. When the middle tap coefficient of the 58-order

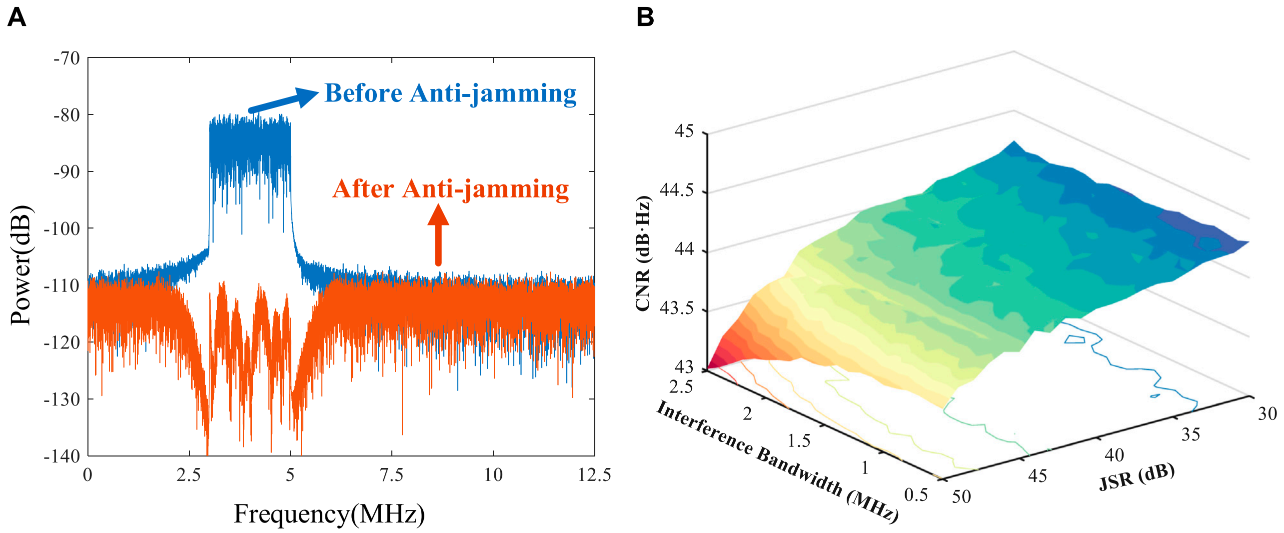

FIGURE 10
Interference suppression performance. **(A)** Spectrum diagram before and after anti-jamming. **(B)** Anti-jamming output CNR.

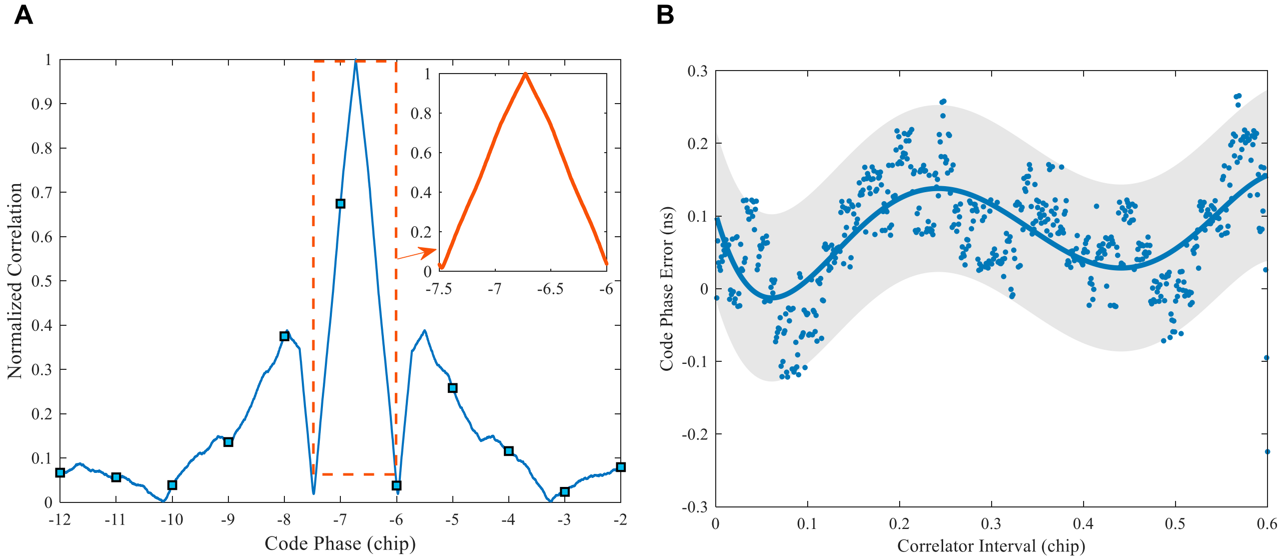

FIGURE 11
Measurement accuracy analysis. **(A)** The correlation function of the output and local signals. **(B)** SCB curve bias.

filter is 1,024, the number of shift operations is reduced by 20, and the maximum code length is reduced by 5.

Debugging and verification were performed on the test platform illustrated in Figure 3. By minimizing the number of effective operations, cascading multiplication-free processing was applied to the constant multiplier. The anti-jamming module achieved a 52% reduction in its effective circuit area.

## 5.2 Anti-jamming performance

The carrier-to-noise ratio (CNR) after interference mitigation is a quantitative assessment metric for evaluating time-domain interference resistance [32]. It is defined as the ratio of the carrier power to the power spectral density of the baseband signal noise. A too low carrier-to-noise ratio can severely affect the receiver's ability to correctly capture and track. Carrier-to-noise ratio loss is the difference between the carrier-to-noise ratio under no-interference conditions and the carrier-to-noise ratio after interference mitigation defiened as Eq. 42.

$$\begin{aligned}\Delta CNR &= [C/N]_0 - [C/N]_{\text{ajm}}\\ &= 10\lg\left\{\frac{B_n\cdot\int_{-\infty}^{\infty}S_s(f)df\cdot\left(\int_{-\infty}^{\infty}S_y(f)df-\int_{-\infty}^{\infty}|H(f)|^2S_s(f)df\right)}{\int_{-\infty}^{\infty}S_n(f)df\cdot\int_{-\infty}^{\infty}|H(f)|^2S_s(f)df}\right\}\end{aligned} \tag{42}$$

Where, $S_s(f)$, $S_n(f)$ and $S_y(f)$ are the power spectral densities of navigation signal, noise signal and anti-interference signal respectively, $H(f)$ is the filter frequency response, and $B_n$ is the noise bandwidth.

A static filter with the navigation signal frequency as the stopband center frequency is designed, and the filter quantization bit width is set to 12. The carrier-to-noise ratio (CNR) of the BD3 signal is set to 50 dB·Hz, the interference bandwidth is 2MHz, the jamming-to-signal ratio (JSR) is 40dB, and the sampling rate of the software receiver is 25 MHz. The narrowband interference suppression performance based on the BD3 signal is shown in Figure 10. Figure 10A shows the spectrum before and after anti-jamming. The results show that the cascaded multiplier-free method can achieve anti-interference. The adaptive filter forms a null at least 30 dB in the interference frequency band. Figure 10B shows the navigation signal CNR after suppressing interference. The maximum CNR loss is less than 2 dB·Hz.

Figure 11 analyzes the ranging accuracy of the cascaded multiplication-free anti-interference method. Figure 11A displays the correlation function between the anti-interference output and the local signals. By observing the 10 chips surrounding the correlation peak, the correlation function of the output signal remains symmetric with the local signal, and the correlation peak position shows no obvious distortion. Figure 11B measures the symmetry of the correlation peak by the SCB curve bias and quantitatively analyzes the ranging deviation of the receiver [30]. Control the convergence step to reduce the influence of the time-varying filter on the ranging accuracy. Under a 31-order anti-interference filter, the pseudo-range measurement deviation is kept within 0.27 ns, which can ensure the ranging accuracy.

## 6 Conclusion

This paper introduces a cascaded multiplier-free implementation method and enhances the corresponding implementation scheme. This method is applied to the static time domain anti-jamming of GNSS receivers by replacing multipliers with a minimal number of adders and shift operations, utilizing optimal CSD coding and numerical power decomposition. Simulation results demonstrate that interference occupying 20% of the navigation signal bandwidth can be effectively suppressed, optimizing the anti-jamming filter structure. The number of adders, shift operations, and maximum code length are significantly reduced, with the maximum number of shift operations decreased by 20. The pseudo-range measurement accuracy has been verified to be within 0.27 ns, ensuring adequate ranging performance.

## Data availability statement

The raw data supporting the conclusion of this article will be made available by the authors, without undue reservation.

## Author contributions

JS: Writing–review and editing, Writing–original draft, Software, Methodology, Data curation. LC: Writing–review and editing, Writing–original draft, Methodology, Conceptualization. ZuL: Writing–review and editing, Methodology, Investigation, Funding acquisition, Conceptualization. BL: Writing–review and editing, Supervision, Investigation. ZhL: Writing–review and editing, Supervision, Formal Analysis, Data curation. ZX: Writing–review and editing, Visualization, Supervision, Software. GS: Writing–review and editing, Supervision, Resources, Project administration. WL: Writing–review and editing, Supervision, Resources, Investigation.

## Funding

The authors declare that financial support was received for the research, authorship, and/or publication of this article. This research was funded by the National Natural Science Foundation of China (No. 62003354).

## Acknowledgments

The authors would like to thank the editors and reviewers for their efforts to help the publication of this paper.

## Conflict of interest

The authors declare that the research was conducted in the absence of any commercial or financial relationships that could be construed as a potential conflict of interest.

## Publisher's note

## References

1. Ferrara NG, Bhuiyan MZH, Söderholm S, Ruotsalainen L, Kuusniemi H. A new implementation of narrowband interference detection, characterization, and mitigation technique for a software-defined multi-gnss receiver. *GPS Solutions* (2018) 22(4):106. doi:10.1007/s10291-018-0769-z

2. Wang B, Sun Y, Liu Y, Zhang Y, Li S. Experimental research on narrowband interference suppression of gnss signals. *Wireless Commun Mobile Comput* (2021) 2021:3410741–12. doi:10.1155/2021/3410741

3. Zhao HZ, Wei GH, Pan XD. Evaluation method of noise electromagnetic radiation interference effect. *IEEE Trans Electromagn Compatibility* (2023) 65(1):69–78. doi:10.1109/TEMC.2022.3224791

4. Falletti E, Gamba MT, Pini M. Design and analysis of activation strategies for adaptive notch filters to suppress gnss jamming. *IEEE Trans Aerospace Electron Syst* (2020) 56(5):3718–34. doi:10.1109/TAES.2020.2982301

5. Ying L, Wei T, Zhixiong W. The frequency spectrum management for aerospace tt&C system. In: 2013 5th IEEE International Symposium on Microwave, Antenna, Propagation and EMC Technologies for Wireless Communications; 29-31 October 2013; Chengdu, China (2013).

6. Chien Y-R. Design of GPS anti-jamming systems using adaptive notch filters. *IEEE Syst J* (2015) 9(9):451–60. doi:10.1109/JSYST.2013.2283753

7. Ren Y, Zhi Y, Gao H, Zhang J. Performance analysis of subspace projection algorithm with respect to projection length for GNSS jamming mitigation. *Digit Signal Process* (2023) 142:104212. doi:10.1016/j.dsp.2023.104212

8. Wang H, Chang Q, Xu Y, Li X. Adaptive narrow-band interference suppression and performance evaluation based on code-aided in GNSS inter-satellite links. *IEEE Syst J* (2020) 14:538–47. doi:10.1109/JSYST.2019.2918055

9. Xu D, Yin B, Wang W, Zhu W. Variable tap-length lms algorithm based on adaptive parameters for tdl structure adaption. *IEEE Signal Process. Lett* (2014) 21(7): 809–13. doi:10.1109/LSP.2014.2317752

10. Liu J, Grant SL. Proportionate adaptive filtering for block-sparse system identification. *IEEE/ACM Trans Audio, Speech, Lang Process* (2016) 24(4):623–30. doi:10.1109/TASLP.2015.2499602

11. Chen W, Huang M, Lou X. Design of sparse fir filters with reduced effective length. *IEEE Trans Circuits Syst Regular Pap* (2019) 66(4):1496–506. doi:10.1109/TCSI.2018.2883965

12. Garcia R, Volkova A. Toward the multiple constant multiplication at minimal hardware cost. *IEEE Trans Circuits Syst Regular Pap* (2023) 70(5):1976–88. doi:10.1109/TCSI.2023.3241859

13. Lakshmi V, Pudi V, Reuben J. Inner product computation in-memory using distributed arithmetic. *IEEE Trans Circuits Syst Regular Pap* (2022) 69(11):4546–57. doi:10.1109/TCSI.2022.3193678

14. Aksoy L, Roy DB, Imran M, Karl P, Pagliarini S. Multiplierless design of very large constant multiplications in cryptography. *IEEE Trans Circuits Syst Express Briefs* (2022) 69(11):4503–7. doi:10.1109/TCSII.2022.3191662

15. Mohamed SM, Sayed WS, Radwan AG, Said LA. Fpga implementation of reconfigurable cordic algorithm and a memristive chaotic system with transcendental nonlinearities. *IEEE Trans Circuits Syst Regular Pap* (2022) 69(7): 2885–92. doi:10.1109/TCSI.2022.3165469

16. Ye WB, Yu YJ. Bit-level multiplierless fir filter optimization incorporating sparse filter technique. *IEEE Trans Circuits Syst Regular Pap* (2014) 61(11):3206–15. doi:10.1109/TCSI.2014.2327287

17. Kumm M, Volkova A, Filip SI. Design of optimal multiplierless fir filters with minimal number of adders. *IEEE Trans Computer-Aided Des Integrated Circuits Syst* (2023) 42(2):658–71. doi:10.1109/TCAD.2022.3179221

18. Samueli H. An improved search algorithm for the design of multiplierless fir filters with powers-of-two coefficients. *IEEE Trans Circuits Syst* (1989) 36(7):1044–7. doi:10.1109/31.31347

19. Thong J, Nicolici N *Combined optimal and heuristic approaches for multiple constant multiplication* (2010). p. 266–73.

20. Aktan M, Yurdakul A, Dundar G. An algorithm for the design of low-power hardware-efficient fir filters. *IEEE Trans Circuits Syst Regular Pap* (2008) 55(6):1536–45. doi:10.1109/TCSI.2008.917997

21. Shahein A, Zhang Q, Lotze N, Manoli Y. A novel hybrid monotonic local search algorithm for fir filter coefficients optimization. *IEEE Trans Circuits Syst Regular Pap* (2012) 59(3):616–27. doi:10.1109/TCSI.2011.2165409

22. Song J, Lu Z, Xiao Z, Li B, Sun G. Optimal order of time-domain adaptive filter for anti-jamming navigation receiver. *Remote Sensing* (2022) 14(1):48. doi:10.3390/rs14010048

23. Lv Q, Qin H. General method to mitigate the continuous wave interference and narrowband interference for gnss receivers. *IET Radar, Sonar & Navigation* (2020) 14(9):1430–5. doi:10.1049/iet-rsn.2020.0115

24. Mosavi MR, Shafiee F. Narrowband interference suppression for gps navigation using neural networks. *GPS Solutions* (2016) 20(3):341–51. doi:10.1007/s10291-015-0442-8

25. Elghamrawy H, Karaim M, Tamazin M, Noureldin A. Experimental evaluation of the impact of different types of jamming signals on commercial gnss receivers. *Appl Sci* (2020) 10(12):4240. (2076-3417). doi:10.3390/app10124240

26. Li B, Qiao J, Lu Z, Yu X, Song J, Lin B, et al. Influence of sweep interference on satellite navigation time-domain anti-jamming. *Front Phys* (2023) 10. doi:10.3389/fphy.2022.1063474

27. He Y, Zhang Z, Ma B, Li J, Zhen S, Luo P, et al. A fast and energy efficient binary-to-pseudo csd converter. In: 2015 IEEE International Symposium on Circuits and Systems (ISCAS); 24-27 May 2015 (2015). doi:10.1109/iscas.2015.7168764

28. Saneei M, Afzali-Kusha A, Navabi Z. A low power technique based on sign bit reduction. In: Proceedings The 16th International Conference on Microelectronics, 2004 ICM 2004; 6-8 Dec. 2004 (2004).

29. Cai L, Qian Y, He Y, Feng W. Design of approximate multiplierless dct with csd encoding for image processing. In: 2021 IEEE International Symposium on Circuits and Systems (ISCAS); 22-28 May 2021 (2021). doi:10.1109/iscas51556.2021.9401200

30. Erdogan AT, Arslan T. A coefficient segmentation algorithm for low power implementation of fir filters. In: 1999 IEEE International Symposium on Circuits and Systems (ISCAS); 30 May-2 June 1999 (1999).

31. Saneei M, Afzali-Kusha A, Navabi Z. Sign bit reduction encoding for low power applications. In: Proceedings 42nd Design Automation Conference; 13-17 June 2005 (2005).

32. Li X, Lu Z, Yuan M, Liu W, Wang F, Yu Y, et al. Tradeoff of code estimation error rate and terminal gain in SCER attack. *IEEE Trans. Instrum. Meas*. (2024). doi:10.1109/TIM.2024.3406807

frontiers | Frontiers in Physics

TYPE Review
PUBLISHED 08 October 2024
DOI 10.3389/fphy.2024.1425084

OPEN ACCESS

EDITED BY
Jay R. Johnson,
Andrews University, United States

REVIEWED BY
Zhu Xiao,
Hunan University, China
Sampad Kumar Panda,
K L University, India

*CORRESPONDENCE
Baiyu Li,
✉ libaiyu@nudt.edu.cn

†These authors have contributed equally to this work and share first authorship

RECEIVED 29 April 2024
ACCEPTED 23 September 2024
PUBLISHED 08 October 2024

CITATION
Wang L, Chen L, Li B, Liu Z, Li Z and Lu Z (2024) Development status and challenges of anti-spoofing technology of GNSS/INS integrated navigation.
*Front. Phys.* 12:1425084.
doi: 10.3389/fphy.2024.1425084

# Development status and challenges of anti-spoofing technology of GNSS/INS integrated navigation

Lei Wang[1,2†], Lei Chen[1,2†], Baiyu Li[1,2*], Zhe Liu[1,2], Zongnan Li[1,2] and Zukun Lu[1,2]

[1]College of Electronic Science and Technology, National University of Defense Technology, Changsha, China, [2]Key Laboratory of Satellite Navigation Technology, Changsha, China

The threat of spoofing interference has posed a severe challenge to the security application of Global Navigation Satellite System (GNSS). It is particularly urgent and critical to carry out in-depth defense research on spoofing interference. When combined with the inertial navigation system (INS), the GNSS/INS integrated navigation system offers distinct advantages in the field of anti-spoofing technology research, which has garnered significant attention in recent years. To summarize the current research achievements of GNSS/INS integrated navigation anti-spoofing technology, it is necessary to provide an overview of the three core technical aspects of spoofing attack principles and implementation strategies, spoofing detection, and spoofing mitigation. First, the principles and implementation strategies of spoofing interference attacks are introduced, and different classifications of spoofing interference attacks are given. Then, the performance characteristics and technical points of different spoofing detection and spoofing mitigation methods are compared and analyzed, and the shortcomings and challenges in the current development of GNSS/INS anti-spoofing technology are pointed out. Finally, based on the summary and shortcomings of the existing technology, a prospect for the future development of GNSS/INS integrated navigation anti-spoofing technology is discussed.

KEYWORDS

**anti-spoofing, GNSS/INS integrated navigation, spoofing interference, spoofing detection, spoofing mitigation**

## 1 Introduction

With the continuous development of the Global Navigation Satellite System (GNSS), more and more military weapons equipment, critical civil facilities, location forensic application and life safety services rely on the high-precision location, velocity and time information provided by GNSS [1–4]. However, due to the weak landing level and open civil

---

**Abbreviations:** GNSS, Global Navigation Satellite System; GPS, Global Positioning System; INS, Inertial Navigation System; RAIM, Receiver Autonomous Integrity Monitoring; PRN, Pseudo-Random Noise; IMU, Inertial Measurement Unit; AIME, Autonomous Integrity Monitoring Extrapolation; SPRT, Adaptive sequential probability ratio detection; AI, Artificial intelligence; PNN, Probabilistic Neural Network; GAN, Generative Adversarial Network; VO, Visual Odometry; MEDLL, Multipath Estimation Delay Locked Loop.

signal structure, satellite signals are vulnerable to intentional and unintentional electromagnetic interference during transmission, which makes it a severe challenge to the application of GNSS [5]. Compared with unintentional interference, intentional interference causes more harm to GNSS and mainly includes suppression jamming and spoofing interference [6]. Suppression jamming suppresses the GNSS navigation and positioning services by transmitting high-power noise to cover the satellite signal. There are already many mature anti-jamming technologies [7]. Different from suppression jamming, spoofing interference involves transmitting false satellite signals to target users, leading them to receive inaccurate navigation information. Notably, in December 2011, the Iranian military exploited falsified the Global Positioning System (GPS) signals in a UAV navigation system and successfully trapped a United States stealth reconnaissance drone RQ-170 [8]. Furthermore, between 22 and 24 June 2017, over 20 ships in the Black Sea fell victim to extensive deceptive jamming attacks [9]. The escalation of GPS jamming/spoofing incidents in the Israeli-Palestinian conflict of 2023 underscores the rising trend of such attacks, with spoofing assaults on satellite navigation systems now emblematic of modern warfare. Consequently, research into anti-spoofing technologies for satellite navigation assumes paramount importance in fortifying the security and dependability of GNSS.

Since the 1990s, with the establishment and deployment of GPS, international scholars have initiated research into electronic protection and anti-jamming techniques [10]. Following a comprehensive assessment by the United States Department of Transportation in 2001 [11], which highlighted the vulnerabilities and risks associated with GPS and identified the looming threat of spoofing attacks in satellite navigation, the pursuit of GNSS anti-spoofing technologies gained momentum. Subsequently, scholars have introduced a range of innovative anti-spoofing solutions, encompassing spoofing detection and spoofing mitigation techniques. These anti-spoofing methodologies can be categorized based on distinct technical principles:

- Anti-spoofing methodologies reliant on navigation signal attributes, such as signal power [12], carrier-to-noise ratio [13], direction of arrival [14], and Doppler frequency [15]. While conceptually straightforward and independent of auxiliary data, these approaches may struggle to counter sophisticated spoofing tactics effectively.
- Anti-spoofing methodologies grounded in signal encryption and authentication mechanisms. This category includes spread spectrum code authentication [16, 17], navigation data authentication [18, 19], and combined authentication techniques [20]. However, implementing encryption-based anti-spoofing measures necessitates modifications to satellite signals or navigation messages, which is a challenge in practical application.
- Anti-spoofing methodologies leveraging auxiliary information [21]. Autonomous navigation systems like inertial navigation and visual navigation remain impervious to spoofing attacks, allowing for integration with GNSS to thwart spoofing attempts through the redundancy of auxiliary navigation data.

In recent years, scholars have focused extensively on the research and development of anti-spoofing technology based on GNSS/INS integrated Navigation System, supported by the Inertial Navigation System (INS). This heightened interest can be attributed to several key advantages of this approach compared to other technologies:

- The seamless integration of INS and GNSS results in a highly complementary system, significantly enhancing navigation accuracy. As evidenced by the widespread adoption of GNSS/INS integrated navigation systems, these systems are capable of operating with local resources, ensuring operational flexibility.
- INS brings information redundancy. The redundancy provided by INS augments GNSS in Receiver autonomous integrity monitoring (RAIM), while also facilitating compatibility with other detection technologies.
- INS can serve as an independent navigation system that operates autonomously, offering rapid and precise positioning without reliance on external information. In the event of GNSS failure, it can transition to pure INS mode, thereby demonstrating inherent resilience against interference.
- The residual data constructed for the relevant variables of the information fusion algorithm of the integrated navigation system is relatively diversified, which can be comprehensively utilized to improve the detection probability.

To leverage the anti-spoofing benefits offered by the GNSS/INS integrated navigation system and enhance its resilience against jamming attacks, this paper summarizes GNSS spoofing attacks and anti-spoofing measures. The remaining organization of this paper is as follows: in Section 2, the principal of spoofing attacks is introduced and the spoofing scenario of GNSS is analyzed; in Section 3, anti-spoofing technologies based on GNSS/INS integrated navigation system is described via two types of methods–spoofing detection and spoofing mitigation—and then the development status is introduced and analyzed respectively; in Section 4, the challenges and prospects of anti-spoofing based on GNSS/INS integrated navigation system are summarized. Finally, Section 5 summarizes the above discussion.

## 2 Spoofing scenario analysis

Spoofing and anti-spoofing are in a adversarial relationship. A profound comprehension of spoofing is pivotal for effective research in anti-spoofing measures. With the aim to better study anti-spoofing technologies in integrated navigation, it is necessary to elucidate the basic principles, implementation strategies, and classification of deception interference based on available literature.

### 2.1 Spoofing modeling

The fundamental principle underlying spoofing involves the transmission of a deceptive signal by the spoofer, characterized by a slightly amplified power level compared to the authentic navigation signal, directed towards the targeted receiver. This act disrupts the receiver's ability to accurately capture and track the authentic satellite signal, leading it to erroneously lock onto the false

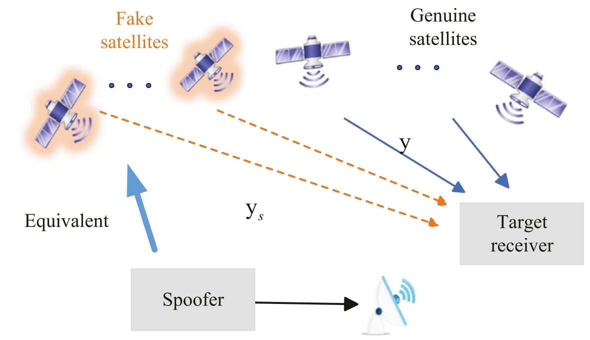

FIGURE 1
Spoofing attack model. The fake satellites are imaginary. The spoofed signals $y_s$ emitted by the spoofing source and the real satellite signals $y$ are simultaneously received by the target receiver.

satellite signal instead. Therefore, the spoofer must accurately replicate the carrier, PRN/spread spectrum, data code, and Doppler range of the real navigation signal. The conventional satellite navigation signal as perceived by the receiver can be represented by the expression Equation 1:

$$y(t) = \mathrm{Re}\left\{\sum_{i=1}^{N} A_i D_i(t-\tau_i(t))C_i(t-\tau_i(t))e^{j[(\omega_c-\omega_d)(t-\tau_i(t))+\theta_i]}\right\} \tag{1}$$

where $N$ is the number of visible satellites, the subscript $i$ indicates the $i$-th satellite, $A$ is the carrier amplitude of the satellite signal, $D$ is the data code, $C$ is the spread spectrum code, $\tau(t)$ is the code phase, $\omega_c$ is the carrier frequency, $\omega_d$ is the Doppler frequency, $\theta$ is the initial carrier phase. Therefore, a set of spoofing signals sent by the spoofer should be similar to the form shown in Equation 2:

$$y_s(t) = \mathrm{Re}\left\{\sum_{i=1}^{N_s} A_{si}\hat{D}_i(t-\tau_{si}(t))C_i(t-\tau_{si}(t))e^{j[(\omega_c-\omega_{si})(t-\tau_{si}(t))-\theta_{si}]}\right\} \tag{2}$$

where $N_s$ indicates the number of spoofing signals, $A_{si}$, $\tau_{si}$, $\omega_{si}$ and $\theta_{si}$ respectively correspond to the amplitude, code phase, Doppler frequency and initial carrier phase of the spoofing signal; $\hat{D}_i(t)$ represents the best estimate of the spoofed data code $D_i$. The carrier phase of the spoofing signal is determined by the initial phase and the Doppler frequency. Typically, to circumvent the autonomous integrity monitoring capabilities of the receiver, the spoofer would generate a number of spoofing signals equivalent to the quantity of authentic signals transmitted by the visible satellite. Under the attack of spoofing interference, the target receiver will receive both authentic navigation signal and spoofing signal, which can be expressed as Equation 3:

$$y_{tot}(t) = y(t) + y_s(t) + n(t) \tag{3}$$

where, $n(t)$ denotes noise. The noise may also be affected by spoofing attacks. Thus, a simple model of a spoofing attacks is shown in Figure 1.

The analysis above is based on the level of satellite navigation signals. When spoofing attack is directed towards the target receiver, its effects are most readily discernible at the information layer. Specifically, the influence on the pseudo-range information layer can be effectively modeled with Equation 4. Suppose that the true pseudo-range measurement model of the $i$-th satellite at time $t$ is:

$$\rho^{(i)}(t) = c\tau^{(i)} + c\left((t+\delta t_u) - (t-\delta t^{(i)})\right) = c\left(\tau^{(i)} + \delta t_u + \delta t^{(i)}\right) \tag{4}$$

where $\rho^{(i)}$ is the true pseudo-range, $c$ is the speed of light, $\tau^{(i)}$ is the signal propagation delay, $\delta t_u$ and $\delta t^{(i)}$ is the receiver clock error and satellite clock error. Supposing $\Delta\tau^{(i)}$ represents the additional signal delay imposed by the spoofer at the target receiver, the formulation for the spoofed pseudo-range can be articulated by Equation 5:

$$\rho_s^{(i)} = \rho^{(i)} + \Delta\rho = \rho^{(i)} + c\Delta\tau_s^{(i)} \tag{5}$$

where $\Delta\rho$ is the additional pseudo-range. Supposing that the spoofing signal can be expressed as an M-order polynomial of $(t - t_{\mathrm{Lock}})$ after being captured and tracked, the following expression is given:

$$\Delta\tau_s^{(i)} = \begin{cases} \sum_{n=1}^{M} a_n(t-t_{\mathrm{Lock}})^n + b, & t \geq t_{\mathrm{Lock}} \\ 0, & t < t_{\mathrm{Lock}} \end{cases} \tag{6}$$

where $t_{\mathrm{Lock}}$ is the moment when the spoofing signal is captured and tracked, $a_n$ is the polynomial coefficient, $b$ is the polynomial intercept. Generally, the polynomial order M is usually 1. Thus, based on Equation 6, the spoofing attack model at the measurement level can be derived as Equation 7.

$$\Delta\rho = c\Delta\tau_s^{(i)} = \begin{cases} c[a(t-t_{\mathrm{Lock}})+b], & t \geq t_{\mathrm{Lock}} \\ 0, & t < t_{\mathrm{Lock}} \end{cases} \tag{7}$$

Here, when $a = 0$ and $b \neq 0$, it is step spoofing. When $a \neq 0$ and $b = 0$, it is slowly varying spoofing.

## 2.2 Spoofing attack classification

There are two methods for spoofer to generate spoofing signals in the form of Equation 2, namely generative spoofing attack methods and forwarding spoofing attack methods [22, 23]. These two methods are discussed in detail below.

### 2.2.1 Generative spoofing attack

Generative spoofing attack device directly generates spoofing signals on the premise of known signal pseudo-code and navigation message parameters. Consequently, in the context of Generative spoofing attack, the spoofer can generate deceptive signals independently of the GNSS system. Besides, it is possible for a spoofer to allow for flexible adjustment of various parameters according to their own requirements. However, the implementation of this method entails relatively high costs and complexity. Generative spoofing attacks pose a significant threat to civilian receivers lacking anti-spoofing capabilities. Conversely, for military signals with undisclosed signal structures, the feasibility of generative spoofing attack is limited, thereby restricting its application scope. The general model generative spoofing attack is illustrated in Figure 2.

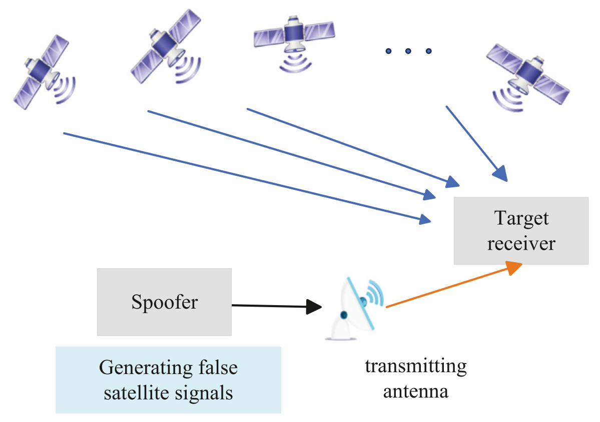

FIGURE 2
The schematic of generative spoofing attack. Generative spoofing sources do not need to receive real satellite signals and can directly generate spoofed signals based on known signal structures.

### 2.2.2 Forwarding spoofing attack

In response to the inability of generative spoofing attack to tackle encrypted navigation signals like military codes, forwarding spoofing attack has emerged. Forwarding spoofing attack involves the deceptive jamming source receiving genuine satellite navigation signals through its own antenna and then, after appropriate delay and power amplification, transmitting them to the target receiver to achieve the spoofing effect. Therefore, a prominent feature of forwarding spoofing attack is that the time delay of the spoofing signal reaching the target receiver must be greater than that of the authentic signal. Obviously, this kind of spoofer do not needs to parse navigation signals but only requires power amplification and time delay. Consequently, compared to generative spoofer, forwarding spoofer has a simpler construction, mainly comprising receiving antennas, amplifiers, and transmitting antennas.

According to the different methods of receiving and processing satellite signals, forwarding spoofing attacks can be divided into two types as shown in Figure 3. The first type spoofer involves a single antenna, which is used to receive all available genuine satellite navigation signals within the area. These signals are then uniformly delayed and power-amplified before being retransmitted using a transmitting antenna. While the second type spoofer involves multi-antenna array, which utilizes lots of high-gain narrow-beam array antennas, with each receiving antenna corresponding to a specific satellite signal within the area. Different delays are applied to the various satellite signals before retransmission. Obviously, the first type of forwarding spoofing attack, due to the uniform delay, is more easily detectable by the receiver. The second type offers higher concealment and can deceive the receiver to a designated location, but it presents greater practical operational difficulty.

To sum up, the classification characteristics of spoofing attack based on signal generation mode are summarized in Table 1.

## 2.3 Spoofing attack implementation policy

In the spoofing process, once the spoofing source successfully generates spoofing signals, it encounters the challenge of subtly injecting these signals into the tracking loop of the target receiver without detection.

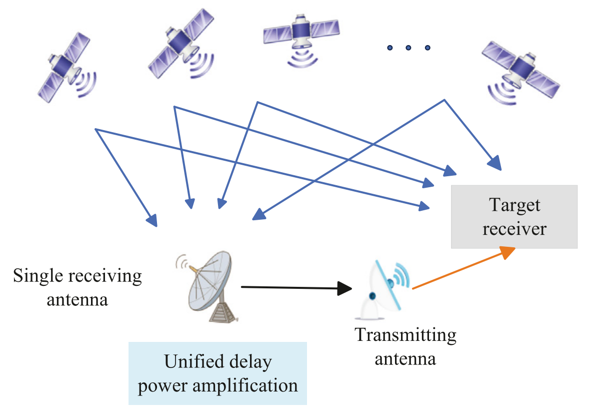

a. The forwarding spoofing based on single antenna.

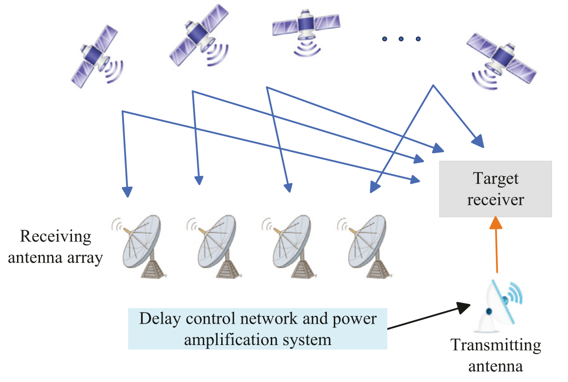

b. The forwarding spoofing based on multi-antenna array.

FIGURE 3
The diagram of forwarding spoofing attack, which is drawn with reference to the literature [65]. **(A)** The forwarding spoofing based on single antenna. **(B)** The forwarding spoofing based on multi-antenna array.

Two strategies are employed to address the challenge: synchronous spoofing and asynchronous spoofing. Synchronous spoofing involves generating false signals that align with the real signal in terms of code phase and Doppler shift. Initially, the power of the spoofing signal is kept low to evade detection before entering the tracking loop. Subsequently, the power gradually increases upon entering the loop, prompting the receiver to lock onto the spoofing signal. The desired spoofing effect is achieved by adjusting the code phase and carrier phase. This strategy facilitates incremental spoofing and is depicted in Figure 4. Synchronous spoofing offers high concealment but presents technical complexities.

On the other hand, asynchronous spoofing disrupts the target receiver by employing high-power interference to cause it to lose lock. Subsequently, spoofing signals are transmitted to allow the target receiver to capture them during reacquisition. Unlike synchronous spoofing, asynchronous spoofing does not require the interference source to generate false signals mirroring the real

TABLE 1 The summary for forwarding spoofing and generative spoofing.

| Spoofing types | Advantages | Shortcomings |
|---|---|---|
| Generative spoofing attack | Highly covert; Freely adjustable | Difficult and costly to realize; Invalid for encrypted signals |
| Forwarding spoofing attack | Easy to realize; Not restricted by encryption | Single spoofing effect; Single target for implementation |

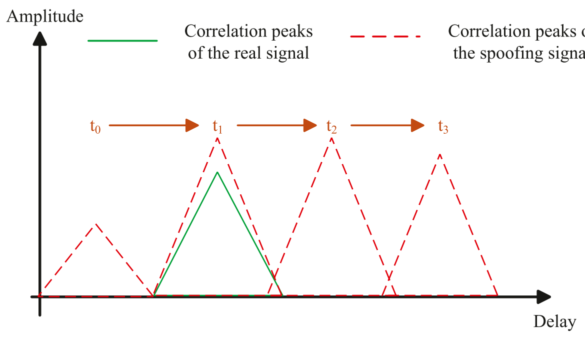

FIGURE 4
The schematic diagram of Synchronous spoofing implementation process.The spoofer captures each receiver channel by aligning the spoofed signal with the true signal from each visible satellite. It starts with low power and then gradually increases the power until it captures the receiver's tracking loop. Finally the receiver is slowly lured to a false localization result.

signal in code phase and Doppler shift. While asynchronous spoofing incurs lower technical costs, it lacks effective concealment compared to synchronous spoofing.

## 3 Development status

From the perspective of the published literature, research on anti-spoofing technology for GNSS/INS-based integrated navigation systems primarily focuses on two key areas: spoofing detection and spoofing mitigation. Spoofing detection aims to identify the presence of spoofing interference, while spoofing mitigation works to mitigate or eliminate the impact of spoofing interference. According to the difference of processing layers, spoofing detection technology for satellite navigation systems can be categorized into signal layer-based and information layer-based approaches. Currently, the predominant focus in the research area is on enhancing GNSS resilience against spoofing at the information layer by leveraging auxiliary data provided by the INS. There is comparatively less emphasis on research related to anti-spoofing efforts at the signal layer.

### 3.1 Spoofing detection based on the integrated navigation

Spoofing detection is to determine whether there is a spoofing signal in the signal from the receiver. In addition to realizing the goal of detecting the spoofed signal, spoofing detection also hopes to achieve high detection accuracy and short detection time through algorithm design and setting the appropriate test statistics, with the purpose of reducing the effect of spoofed signals on the navigation system during the detection process. Based on existing literature, the spoofing detection algorithms based on the combined GNSS/INS navigation system can be further categorized according to the different test statistics: detection algorithms based on the measured values, detection algorithms based on the filtered innovation, and other spoofing detection algorithms.

#### 3.1.1 Detection algorithms based on the measured values

The system measurement value refers to the direct measurement information resolved by the integrated navigation system and its subsystems such as position, velocity, acceleration, attitude, etc. Residual consistency detection method, which detect spoofing by utilizing the high positioning accuracy in a short period of time and independent characteristics of INS, is a typical example of this type of algorithm, e.g., position/velocity based residual consistency detection. The detection domain of literature [24] is position, and literature [25] investigates vehicle speed based spoofing detection. Figure 5 is the flow of the position/velocity consistency detection algorithm referring to [26].

In addition, literature [27] describes a method for detecting GNSS spoofing signals using accelerometers. The method performs spoofing detection by comparing the acceleration estimated from the GNSS output with the acceleration output from the INS accelerometer. Literature [28] improves the detection performance by using both the residual acceleration and the north (or east) accelerometer error component as decision variables. Literature [29] detects the spoofing using pseudo-range rate, through comparing the constructed pseudo-range rate from INS and the pseudo-range rate solved by GNSS. Different from the pseudo-range detection, the pseudo-range rate detection is more sensitive to the slowly varying spoofing interference. For scenarios of spoofed attacks on selected satellites, literature [30] takes advantage of GNSS/INS tightly coupled integration that its navigation solving is possible even with only one visible satellite for spoofing detection. The traversal method is adopted to solve all visible satellites one by one, and then the results are compared with the receiver clock difference/clock drift equivalent distance deviation to detect spoofing. By this method, the influence of spoofed stars can be eliminated to ensure the positioning accuracy of the combination navigation system.

In the case of airborne vehicles, attitude can also play a role in spoofing detection. [31] conducted experimental tests using UAV platforms and discovered that spoofing attacks significantly impact pitch and roll angles, while minimally affecting heading angle. Additionally, [32] employed carrier phase double-difference observables for spoofing signal detection and integrated this with attitude data from the INS to successfully identify and counter forward spoofing interference.

However, the above-mentioned spoofing detection methods, focusing on a single dimension, may only address specific

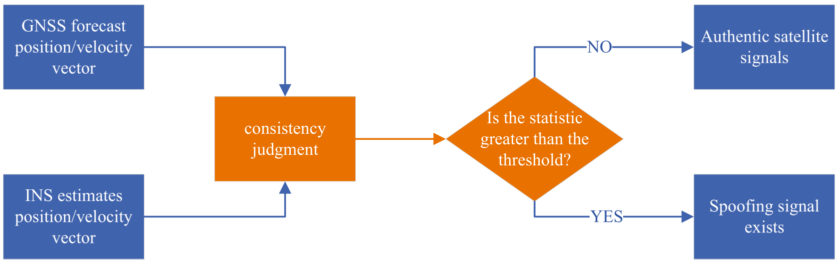

FIGURE 5
The flow chart of position or velocity consistency detection algorithm. The consistency detection algorithm achieves spoofing detection by comparing the solved data from GNSS with the solved data from INS.

spoofing interferences and are susceptible to failure when attackers alter their tactics. By expanding the dimensionality of comparison information, these limitations can be overcome while enhancing detection performance. For instance, [33] employed a short-term pure inertial error propagation model to utilize position and velocity data from inertial guidance for predicting and estimating the guard's pseudo-range and pseudo-range rate. They integrated actual system measurements to create pseudo-range and pseudo-range rate time series and conducted spoofing detection by parameter fitting of these time series. In another study referenced as [34], the impact of spoofing attacks on the navigation receiver's time was leveraged, incorporating a consistent spoofing detection model in the time dimension alongside the position dimension.

Taken together, this type of detection algorithm is simple in principle and the test statistics are easy to obtain. However, this type of detection method is greatly affected by the accuracy of the inertial device, the higher the IMU accuracy, the better the detection performance. At the same time, it is affected by the cumulative effect of the inertial navigation device error. When the spoofing attacks exist for a longer period, this type of algorithm will no longer be applicable. Besides it cannot satisfy the detection requirement of induced slowly varying spoofing interference.

### 3.1.2 Detection algorithms based on filter innovation

Filter innovation is defined as the difference between the actual observed value of a system state variable and the predicted value of the Kalman filter algorithm, which is the new information added to the observed value at the current moment. The spoofing attack directly affect the system measurement information, which in turn will cause the filter innovation to be affected. Therefore, test statistic constructed by the statistical characteristics of the normalized filter innovation can be used for spoofing detection. [35] analyzed the impact of spoofing attack on the Kalman filtering process, and the summary of the conclusions can be obtained as follows:

- the spoofing attack has a direct effect on the innovation of the current moment, and a cumulative effect on the innovation of the future moment;
- the spoofing attack has a large effect on the expectation of the innovation and the error estimation of INS, and has no significant effect on the filtering error covariance array;
- the innovation is most affected in the initial stage of spoofing introduction; and
- due to the effect of the feedback correction mechanism of the filter, the innovation is dynamically adjusted towards the expectation of zero.

Currently, spoofing detection with filter innovation can be categorized into snapshot and sequential methods [36]. Snapshot method is to construct the test statistic only with the current moment of the innovation, while sequential method is to construct the test statistic using the innovation sequences and their covariance matrices within a time window. Typical snapshot methods include the chi-square test based on innovation [37, 38], and the multiple solution separation [39]. The chi-square detection method based on innovation is only effective for step spoofing with large amplitude fluctuations. The multiple solution separation method can effectively detect slowly varying spoofing, but not for the full satellite spoofing scenario. One of the typical sequential methods is Autonomous Integrity Monitoring Extrapolation (AIME) [40], which utilizes the sequence of Kalman filtering innovation to construct a test statistic. Literature [41] states that, compared to the snapshot method of detection, the extrapolation method is more suitable for satellite slowly varying spoofing detection. Spoofing offsets of position and velocity are very small during the filtering period when facing slowly varying spoofing signal attack, leading to the filter slowly correcting the output of the inertial navigation with a small correction amount. This property gives the snapshot method a long detection time and a high rate of missed alarms [42]. Meanwhile, the error tracking and closed-loop correction mechanism of Kalman filter are also the reasons for long detection delay problem of AIME when detecting slowly varying spoofing [43].

To enhance the detection performance and reduce the detection delay associated with slowly varying spoofing detection methods, literature [44] introduced a spoofing detection algorithm based on adaptive sequential probability ratio detection (SPRT). Combined with Bayes parameter estimation theory, SPRT can adaptively adjust the test statistic by modifying the risk parameter, thereby enhancing both the detection speed and performance of the algorithm. In addition to optimizing the innovation sequence algorithm, [45] proposed the detection algorithm that utilizing the changing rate of innovation to construct the test statistic. Integration of SPRT with AIME has

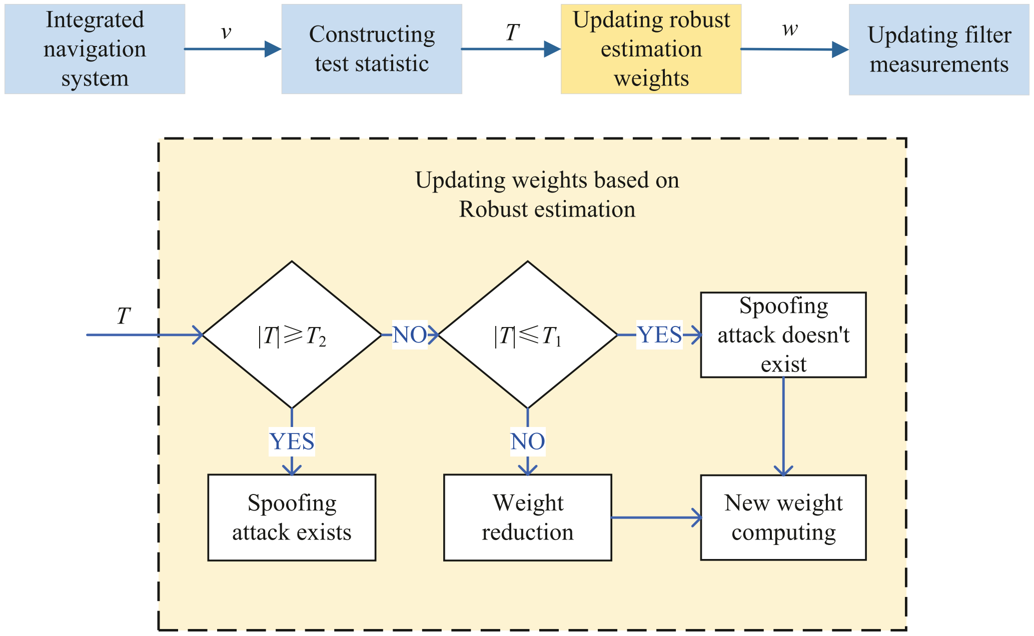

FIGURE 6
The flowchart of spoofing detection algorithm based on robust estimation. The algorithm constructs the test statistic *T* via filter innovation *v*, which is used to compare against the judgment thresholds *T*1 and *T*2. The corresponding weights *w* are then adjusted according to the comparison results.

significantly improved the detection efficiency of slowly varying spoofing detection. Additionally, [46] put forward a spoofing detection algorithm based on innovation skewness. It is experimentally demonstrated that the algorithm can improve the detection delay performance of induced retardation spoofing attacks by more than 35% compared to the general continuous method.

Robust estimation is a class of estimation methods that minimize the influence of observations in the presence of anomalous observations [47]. Therefore, robust estimation can not only be used to solve the problem of residual influence of fake calendar elements in the past for deception suppression, but also can solve the problem of error tracking and closed-loop correction feedback mechanism to improve the performance of spoofing detection algorithms. The spoofing detection algorithm based on robust estimation are designed to attenuate the effect of spoofing interference by selecting a suitable equivalent weight function to compute the weights [48–52]. The model of the detection method is shown in Figure 6, where $v$ refers to the innovation sequence, $T$ is the test statistic and $w$ denotes weight vector. Based on the robust estimation and detection window, [49] proposed an improved detection algorithm. To improve the detection performance and navigation accuracy, the algorithm calculated the weight factors by two suitable thresholds and could adaptively adjust the gain matrix to reduce the weight of the spoofed satellite measurements. [50] proposed a GNSS/INS tightly combined innovation optimized robust estimation spoofing detection algorithm, which further improved the detection efficiency and detection performance of induced retardation spoofing interference.

For the problem of high false alarm rate of the traditional innovation detection algorithms after the deception disappears, [53] established a mode adjustment criterion based on GNSS/INS tightly coupled system. Its core idea was employing sliding window detection to downgrade the innovation when the measurement value may be anomalous while other time remaining unchanged. By switching between the two modes, the computational burden of past observations and the detection delay were shortened. When subjected to intermittent spoofing attacks, the improved algorithm had higher detection sensitivity and could recover immediately after the spoofing disappeared. In addition, the response speed to the next spoofing attack was faster.

In order to avoid the effects of closed-loop correction mechanisms, other scholars have equivalently implemented closed-loop correction using an open-loop correction structure with cumulative error valuations [54]. Particularly, [55] combined the sliding window accumulation of chi-square detection based on innovation with the open-loop correction structure for spoofing detection of GNSS/INS tightly coupled system. Compared with the traditional chi-square detection method, this algorithm reduced the detection time for trap spoofing interference by 25% and improved the detection sensitivity for slowly varying spoofing interference.

Overall, the use of spoofing detection methods based on innovation can effectively identify trap spoofing. However, the detection time for slowly varying spoofing attacks may be prolonged due to error tracking and the negative feedback effect of Kalman filter. In some cases, the combined navigation system may already have been deceived by the spoofing attack before successful detection, allowing the spoofing to achieve its intended purpose. Additionally, many detection algorithms for slowly varying spoofing attacks may struggle to effectively detect when the deception disappears, potentially leading to harmful consequences.

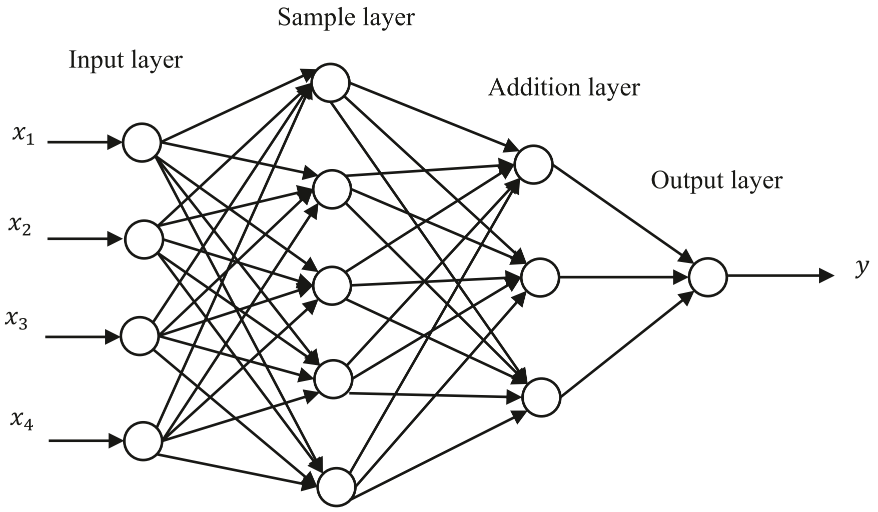

FIGURE 7
The model structure of PNN. PNN consists of input layer, sample layer, addition layer and output layer. The core of PNN is the sample layer. The sampple layer is used to calculate the pattern distance of the samples to be recognized and then the radial basis function is used as the activation function.

### 3.1.3 Other detection algorithms based on integrated navigation

With the rapid development of artificial intelligence (AI) in recent years, many scholars explore the use of neural networks for deception detection problems. The Probabilistic Neural Network (PNN), whose model structure is shown in Figure 7, stands out for its rapid convergence, high classification accuracy, and effectiveness in pattern recognition and fault detection [56]. For instance, [57] developed a PNN model for detecting forwarding spoofing, ensuring real-time detection of such interference. Additionally, researchers have leveraged innovative approaches such as generative adversarial networks (GANs) to combat GNSS spoofing by learning and analyzing spoofed signal features [58]. Furthermore, in literature [59], spoofing attacks were detected by creating a feature vector that captures the differences in velocity estimates from GNSS receivers and IMUs on genuine and spoofed trajectories, followed by training a neural network for detection. These methods have yielded good detection results. However, it is evident that AI-based spoofing detection methods require the collection of data related to spoofed and real signals in advance, and the detection model is poorly migratable, which constrains the widespread use of the algorithms.

In addition to AI-based approaches, some researchers have tapped into redundant information from alternative navigation augmentation systems like visual odometry (VO) to assist spoofing detection [60]. VO can serve as a good supplement to GNSS positioning. This article first used an optimized coupling framework to fuse the measurement results of VO and INS, and then monitored the deviation between the fusion results and GNSS. After successfully detecting deception, the optimized estimation algorithm is modified to prevent the system from being affected by deceptive GNSS data and enable it to continue localization. However, it is important to note that this detection method may necessitate adjustments to the hardware system and is typically applicable only to combined navigation systems that already include visual odometry.

## 3.2 Spoofing mitigation based on the integrated navigation

Anti-spoofing technology not only needs to detect and identify the spoofing signals, but also needs to mitigate the effects of spoofing attacks as much as possible after spoofing detection.

Some scholars have proposed borrowing deception suppression methods from multipath suppression techniques. While the characteristics of multipath effects and deception attacks share similarities, there are key distinctions: (1) Signal delay difference: The multipath signal tends to lag behind the real satellite signals, while the deception signal may be ahead of the real signals; (2) Receiver Tracking Loop Impact: Multipath signals distort the correlation peaks of the tracking loop, affecting tracking accuracy. In contrast, deception signals can be separated from the correlation peaks of the spoofed signal using correlation strategies. This separation can lead the tracking loop to lock onto the spoofed signal, preventing the estimation of parameters for the genuine satellite signal by the Multipath Estimation Delay Locked Loop (MEDLL). Therefore, the spoofing suppression algorithm needs to control the receiver tracking loop according to the spoofing signal identification results to ensure that the receiver always locks on the real satellite signal. To deal with these distinctions, a spoofing mitigation algorithm must tailor the control of the receiver tracking loop based on the identified spoofing signals. This approach ensures that the receiver consistently locks onto the authentic satellite signal, mitigating the impact of deception attacks.

The utilization of MEDLL in a GNSS/INS integrated navigation system, as described in literature [61], represents a typical approach for spoofing mitigation. By leveraging INS information, this method can effectively identify and suppress spoofed signals. Furthermore, literature [62, 63] introduced the multi-correlator structure of MEDLL for the GNSS/INS integrated navigation system. When combined with the robust Kalman filtering algorithm, this structure resulted in an effective anti-spoofing algorithm. The algorithm reduced the position error under spoofing attacks from 600 m to 10.0 m [63]. However, it is important to note that while algorithms based on multipath suppression demonstrate strong spoofing detection and suppression capabilities, they are reliant on the presence of genuine satellite signals for their operation. In scenarios where genuine satellite signals are absent, these algorithms may not be effective. Therefore, further research and development may be necessary to address this limitation and ensure robust anti-spoofing capabilities in all operational conditions.

It is indeed well-recognized that integrating robust factor into filtering algorithms can effectively suppress the impact of spoofing attacks in combined navigation systems. Many contemporary research efforts focusing on spoofing mitigation algorithms within combined navigation systems have centered their improvements on the robust estimation algorithm. For instance, [64] analyzed the impact of spoofing attacks on GNSS/INS integration and explored an anti-spoofing method based on Adaptively Robust Kalman Filter. By this way, they succeeded in bolstering the system's anti-spoofing interference capability and adaptive capacity.

Overall, current research on deception mitigation algorithms can be categorized into the following three types: a) Utilizing the MEDLL algorithm to recover genuine positioning results by distinguishing between authentic and spoofed signals; b) Incorporating the robust factor into filtering algorithms to mitigate the impact of spoofing on measurement information; c). The spoofing mitigation based on the relevant algorithms of AI. Generally speaking, the research on spoofing suppression algorithms is relatively small, and spoofing mitigation algorithms based on integrated navigation need to be studied deeper.

# 4 Challenges and future development trends

Anti-spoofing technology based on GNSS/INS integrated navigation system has become increasingly important for navigation security. Although some research progress has been made in this area, there are still many problems and challenges that need to be further explored and investigated. The following section will analyze the problems encountered and provide an outlook on future development trends for the research area.

## 4.1 Focusing on technical research in spoofing mitigation

Currently, anti-spoofing techniques for combined navigation systems mainly focus on spoofing detection and identification. But it is indeed crucial to not only focus on spoofing detection and identification but also on spoofing mitigation to enhance the safety and reliability of integrated navigation systems. By developing effective spoofing mitigation algorithms, the normal operation of the navigation system and the maintenance of high accuracy under spoofing attacks will be ensured. Research that delves deeper into the characteristics of spoofing signals and their propagation mechanisms will be essential for the advancement of anti-spoofing technologies. This will ultimately contribute to the development of more robust and secure integrated navigation systems in the future.

## 4.2 Enhancing resilience to complex and volatile spoofing techniques

Existing anti-spoofing techniques often can only address a single type of spoofing attack and lack sufficient resistance to complex and variable spoofing methods. Therefore, future research will likely focus on improving the system's ability to resist such attacks. With the continuous maturation of AI and machine learning algorithms, the GNSS/INS combined navigation system can integrate various anti-spoofing techniques, together with AI models to adaptively identify and cope with various spoofing attacks, thus achieving intelligent and adaptive anti-spoofing techniques. On the other hand, it is also necessary to strengthen research on spoofing interference techniques to provide support for feasibility testing of anti-spoofing techniques.

## 4.3 Optimize real-time performance and accuracy in highly dynamic environments

Under the dynamic environment, such as high-speed motion or complex terrain, anti-spoofing techniques are put to the test in terms of real-time and accuracy. The system must quickly and accurately distinguish between the real and spoofed signals, which places greater demands on the technique's performance. To address this challenge, future research will focus on optimizing algorithms and data processing methods to improve the system's real-time and accuracy. For instance, to reduce data processing time, one can use more efficient signal processing techniques. Additionally, to improve the system's computational power and response speed, advanced hardware platforms and parallel computing techniques can be utilized.

## 4.4 Conduct anti-spoofing techniques based on deep GNSS/INS navigation system

Depending on the depth of information, the GNSS/INS integrated navigation system has three types of combined modes: loose integration, tight integration and deep integration. The performance and impact of these modes differ significantly when dealing with spoofing interference. There are few studies analyze the impact of spoofing and anti-spoofing research for deeply coupled systems. The existing literature primarily focuses more on anti-spoofing technology based on loosely coupled systems and tightly coupled systems. In recent years, with the continuous development of theoretical research and engineering practice in deeply coupled systems, the anti-spoofing need for deeply coupled systems has become increasingly prominent. Therefore, analyzing the impact of spoofing interference on the deep GNSS/INS integration system and developing appropriate anti-spoofing studies holds great theoretical significance and practical value.

## 5 Conclusion

This paper focuses on the anti-spoofing technology of GNSS/INS integrated navigation systems for enhancing the safety of integrated system. Firstly, the paper introduces the principle of spoofing interference technology and attack strategies, which have different classifications based on their generating modes, attack strategies, and manifestations. Secondly, the paper sorts out and summarizes the current research status of anti-spoofing technology of GNSS/INS combined navigation systems. This paper compares and analyzes the performance characteristics and technical aspects of detection methods based on the measured values, filter innovation, and other detection methods based on integrated navigation systems. Then, the paper sorts out the spoofing mitigation methods based on multipath suppression and robust estimation. Finally, with the purpose of providing solid technical support for the safe application of satellite navigation systems, this paper points out the difficulties faced by the development of GNSS/INS anti-spoofing technology and the future development direction.

## Author contributions

LW: Conceptualization, Investigation, Methodology, Writing–original draft, Writing–review and editing. LC: Conceptualization, Investigation, Methodology, Writing–original draft, Writing–review and editing. BL: Funding acquisition, Supervision, Validation, Writing–review and editing. ZhL: Supervision, Writing–review and editing. ZoL: Validation, Writing–review and editing. ZuL: Funding acquisition, Methodology, Supervision, Writing–original draft, Writing–review and editing.

## Funding

The author(s) declare that financial support was received for the research, authorship, and/or publication of this article. National Natural Science Foundation of China under Grant U20A0193.

## Conflict of interest

The authors declare that the research was conducted in the absence of any commercial or financial relationships that could be construed as a potential conflict of interest.

## Publisher's note

## References

1. Zhang H, Yang X, Liang J, Xu X, Sun X. Gps path tracking control of military unmanned vehicle based on preview variable universe fuzzy sliding mode control. *Machines* (2021) 9:304. doi:10.3390/machines9120304

2. Wang X, Zhao Q, Xi R, Li C, Li G, Li LA. Review of bridge structural health monitoring based on gnss: from displacement monitoring to dynamic characteristic identification. *IEEE Access* (2021) 9:80043–65. doi:10.1109/ACCESS.2021.3083749

3. Zhu H, Chen K, Chai H, Ye Y, Liu W. Characterizing extreme drought and wetness in guangdong, China using global navigation satellite system and precipitation data. *Satellite Navigation* (2024) 5:1. doi:10.1186/s43020-023-00121-6

4. Chen Q, Zhang Q, Niu X, Liu J. Semi-analytical assessment of the relative accuracy of the gnss/ins in railway track irregularity measurements. *Satellite Navigation* (2021) 2:25. doi:10.1186/s43020-021-00057-9

5. Li X, Chen L, Lu Z, Wang F, Liu W, Xiao W, et al. Overview of jamming technology for satellite navigation. *Machines* (2023) 11:768. doi:10.3390/machines11070768

6. Gao Y, Li G, Lv Z. Current situation and prospect of satellite navigation interference technology. *Geomatics and Spat Inf Technol* (2022) 45:13–8. doi:10.3969/j.issn.1672-5867.2022.06.005

7. Song J, Lu Z, Liu Z, Xiao Z, Dang C, Wang Z, et al. Review on the time-domain interference suppression of navigation receiver. *Syst Eng and Electron* (2023) 45:1164–76. doi:10.12305/i.issn.1001-506X.2023.04.25

8. Zhang L, Zhang C, Gao Y. Gnss spoofing and detection (i): typical events and development of spoofing technology. *J Navigation Positioning* (2021) 9:1–7. doi:10.16547/j.cnki.10-1096.20210301

9. Jones M. *Spoofing in the black sea: what really happened?* (2017). p. 11. GPS World.

10. Tang B, Zheng C, Zhang L, Wang Z. New progress and implication of United States navigation warfare. *Navigation Positioning and Timing* (2020) 7:110–6. doi:10.19306/i.cnki.2095-8110.2020.04.014

11. Volpe JA. *Vulnerability assessment of the transportation infrastructure relying on the global positioning system* (2001).

12. Dehghanian V, Nielsen J, Lachapelle G. Gnss spoofing detection based on signal power measurements: statistical analysis. *Int J Navigation Observation* (2012) 2012:1–8. doi:10.1155/2012/313527

13. Nielsen J, Dehghanian V, Lachapelle G. Effectiveness of gnss spoofing countermeasure based on receiver cnr measurements. *Int J Navigation Observation* (2012) 2012:1–9. doi:10.1155/2012/501679

14. Zhang X, Ding C, Chen S. Spoofing detection technique using carrier phase double difference of spin dual-antenna. *Navigation Positioning and Timing* (2023) 10:32–8. doi:10.19306/i.cnki.2095-8110.2023.02.005

15. Li J, Zhu X, Ouyang M, Shen D, Chen Z, Dai Z. Gnss spoofing detection technology based on Doppler frequency shift difference correlation. *Meas Sci Technol* (2022) 33:095109. doi:10.1088/1361-6501/ac672a

16. Wang S, Liu H, Tang Z, Ye B. Binary phase hopping based spreading code authentication technique. *Satellite Navigation* (2021) 2:4–9. doi:10.1186/s43020-021-00037-z

17. Kuhn MG. An asymmetric security mechanism for navigation signals. In: International workshop on information hiding; 23-25 May 2004; Toronto, ON, Canada. Springer (2004). p. 239–52.

18. Kerns AJ, Wesson KD, Humphreys TE. A blueprint for civil gps navigation message authentication. In: 2014 IEEE/ION Position, Location and Navigation Symposium-PLANS 2014; 05-08 May 2014; Monterey, CA, USA. IEEE (2014). p. 262–9.

19. Ghorbani K, Orouji N, Mosavi MR. Navigation message authentication based on one-way hash chain to mitigate spoofing attacks for gps l1. *Wireless Personal Commun* (2020) 113:1743–54. doi:10.1007/s11277-020-07289-z

20. Wu Z, Zhang Y, Liu R. Bd-ii nma&ssi: an scheme of anti-spoofing and open beidou ii d2 navigation message authentication. *IEEE Access* (2020) 8:23759–75. doi:10.1109/ACCESS.2020.2970203

21. Zhang L, Zhang C, Gao Y. Gnss spoofing and detection (iii): spoofing detection technology based on auxiliary information. *J Navigation Positioning* (2021) 9:13–9. doi:10.16547/j.cnki.10-1096.20210502

22. Li X, Lu Z, Yuan M, Liu W, Wang F, Yu y., et al. Tradeoff of code estimation error rate and terminal gain in scer attack. *IEEE Trans Instrumentation Meas* (2024) 73:1–12. doi:10.1109/TIM.2024.3406807

23. Gao Y, Lv Z, Zhou P, Jia Z, Zhang L, Cong D. Current status and prospects of satellite navigation deception interference technology. *Geomatics and Spat Inf Technol* (2019) 42:116–20. doi:10.3969/j.issn.1672-5867.2019.10.034

24. Broumandan A, Lachapelle G. Spoofing detection using gnss/ins/odometer coupling for vehicular navigation. *Sensors* (2018) 18:1305. doi:10.3390/s18051305

25. Curran JT, Broumendan A. On the use of low-cost imus for gnss spoofing detection in vehicular applications. In: International Technical Symposium on Navigation and Timing (ITSNT 2017); 14-17 Nov 2017; Toulouse, France (2017). p. 1–8.

26. Wu Z. Research on inertial assisted detection algorithm for induced GNSS deception. Master's thesis. Changsha: National University of Defense Technology (2018).

27. Lee JH, Kwon KC, An DS, Shim DS. Gps spoofing detection using accelerometers and performance analysis with probability of detection. *Int J Control Automation Syst* (2015) 13:951–9. doi:10.1007/s12555-014-0347-2

28. Kwon K-C, Shim D-S. Performance analysis of direct gps spoofing detection method with ahrs/accelerometer. *Sensors* (2020) 20:954. doi:10.3390/s20040954

29. Chang H, Pang C, Zhang L, Guo Z, Lv M, Wu Q. An ins-assisted bds pseudorange rate consistency deception signal detection method. *J Air Force Eng Univ* (2022) 23: 51–7. doi:10.3969/i.issn.2097-1915.2022.04.008

30. Liu K. Research on GNSS spoofing detection algorithm and experimental verification methods. Ph.D. thesis. Changsha: National University of Defense Technology (2019).

31. Guo Y. Research on covert spoofing algorithm of UAV based on INS/GNSS integrated navigation. Ph.D. thesis. Changsha: National University of Defense Technology (2019).

32. Li S, Liu y., Zhang H, Zhang X. Inertial measurements aided gnss spoofing detection technique. *J Chin Inertial Technol* (2013) 21:336–40+353. doi:10.13695/j.cnki.12-1222/o3.2013.03.006

33. Wu Z, Wu W, Liu K. Research on algorithm of gradually induced spoofing detection based on tightly coupled ins/gnss integration. *Navigation Positioning and Timing* (2019) 6:7–13. doi:10.19306/j.cnki.2095-8110.2019.01.002

34. Liu Y, Li S, Fu Q, Zhou Q. Chip-scale atomic clock aided ins/gnss integrated navigation system spoofing detection method. *J Chin Inertial Technol* (2019) 27:654–60. doi:10.13695/j.cnki.12-1222/o3.2019.05.014

35. Liu Y, Li S, Fu Q, Liu Z. Impact assessment of gnss spoofing attacks on ins/gnss integrated navigation system. *Sensors* (2018) 18:1433. doi:10.3390/s18051433

36. Liu Y, Li S, Fu Q, Liu Z, Zhou Q. Analysis of kalman filter innovation-based gnss spoofing detection method for ins/gnss integrated navigation system. *IEEE Sensors J* (2019) 19:5167–78. doi:10.1109/JSEN.2019.2902178

37. Abuhashim TS, Abdel-Hafez MF, Al-Jarrah MA. Building a robust integrity monitoring algorithm for a low cost gps-aided-ins system. *Int J Control Automation Syst* (2010) 8:1108–22. doi:10.1007/s12555-010-0520-1

38. Yang C, Mohammadi A, Chen Q-W. Multi-sensor fusion with interaction multiple model and chi-square test tolerant filter. *Sensors* (2016) 16:1835. doi:10.3390/s16111835

39. Liu H, Yue Y, Yang Y, Jiang D. Integrity monitoring for gnss/inertial based on multiple solution separation. *J Chin Inertial Technol* (2012) 20:63–8. doi:10.13695/j.cnki.12-1222/o3.2012.01.007

40. Ye Q, Gu Y, Li L, Du F, Li R. Integrity monitoring for gnss/ins integrated navigation based on improved aime. In: *China satellite navigation conference*. Springer (2023). p. 533–44. doi:10.1007/978-981-99-6944-9_46

41. Bhatti UI, Ochieng WY, Feng S. Integrity of an integrated gps/ins system in the presence of slowly growing errors. part i: a critical review. *Gps Solutions* (2007) 11: 173–81. doi:10.1007/s10291-006-0048-2

42. Zhong L, Liu J, Li R, Wang R. Approach for detecting soft faults in gps/ins integrated navigation based on ls-svm and aime. *The J Navigation* (2017) 70:561–79. doi:10.1017/S037346331600076X

43. Wang S, Zhan X, Pan W, et al. Gnss/ins tightly coupling system integrity monitoring by robust estimation. *J Aeronautics, Astronautics Aviation* (2018) 50: 61–80. doi:10.6125/JoAAA.201803_50(1).06

44. Zhong L, Liu J, Yu L, Zhang Z. Slowly varying spoofing interference detection algorithm based on adaptive sprt. *J Signal Process* (2022) 38:2144–54. doi:10.16798/j.issn.1003-0530.2022.10.015

45. Bhatti UI, Ochieng WY, Feng S. Performance of rate detector algorithms for an integrated gps/ins system in the presence of slowly growing error. *GPS solutions* (2012) 16:293–301. doi:10.1007/s10291-011-0231-y

46. Xie F, Lin H, Yu J, Mou W. Research on spoofing detection of gnss/ins tightly coupled system based on skewness test. In: 2023 5th International Conference on Electronic Engineering and Informatics (EEI); 30 June 2023 - 02 July 2023; Wuhan, China. IEEE (2023). p. 254–61. doi:10.1109/EEI59236.2023.10212511

47. Zhou J. Classical error theory and robust estimation. *Acta Geodaetica et Cartographica Sinica* (1989) 18:115–20.

48. Jiang Y, Pan S, Ye F, Gao W, Ma C, Wang H. Approach for detection of slowly growing fault based on robust estimation and improved alme. *Syst Eng Electron* (2022) 44:2894–902. doi:10.12305/i.issn.1001-506x.2022.09.24

49. Zhang C, Zhao X, Pang C, Wang Y, Zhang L, Feng B. Improved fault detection method based on robust estimation and sliding window test for ins/gnss integration. *J Navigation* (2020) 73:776–96. doi:10.1017/S0373463319000778

50. Ke Y, Lv Z, Zhou M, Deng X, Zhou S, Ai H. Innovation optimal robust estimation spoofing detection algorithm of tightly coupled gnss/ins integration. *J Chin Inertial Technol* (2022) 30:272–80. doi:10.13695/j.cnki.12-1222/o3.2022.02.020

51. Zhang C, Lv Z, Zhang L, Gao Y. A spoofing detection algorithm for ins/gnss integrated navigation system based on innovation rate and robust estimation. *J Chin Inertial Technol* (2021) 29:328–33. doi:10.13695/j.cnki.12-1222/o3.2021.03.008

52. Ke Y, Lv Z, Zhang C, Deng X, Zhou W, Song D. Tightly coupled gnss/ins integration spoofing detection algorithm based on innovation rate optimization and robust estimation. *IEEE Access* (2022) 10:72444–57. doi:10.1109/ACCESS.2022.3186305

53. Ren L, Zhao X, Pang C, Zhang C, Zhang L. Improved integrity monitoring method based on robust estimation of gnss/ins integrated navigation. *Aerospace Control* (2021) 39:21–6. doi:10.16804/j.cnki.issn1006-3242.2021.05.004

54. Zou S, Zhang Q, Ding Z. Using accumulated errors to realize close-loop rectification of integrated navigation system. *Acta Electronica Sinica* (2001) 29: 1221–4.

55. Zhong L, Liu J. Research on spoofing attacks detection technology based on tightly integrated navigationt. In: *The 5th Chinese aeronautics science and technology conference*. Jiaxing, China: Beihang University Press (2021). p. 418–23. doi:10.26914/c.cnkihy.2021.064888

56. Zhang Y, Jia Y, Wu W, Su X, Shi X. Application of probabilistic neural network to typical fault diagnosis of vehicle gearbox. *Automotive Eng* (2020) 42:972–7. doi:10.19562/j.chinasae.qegc.2020.07.018

57. Pang C, Guo Z, Lv M, Zhang L, Zhai D, Zhang C. Bds against repeater deception iamming detection algorithm based on pnn. *J Chin Inertial Technol* (2021) 29:554–60. doi:10.13695/j.cnki.12-1222/o3.2021.04.021

58. Li J, Zhu X, Ouyang M, Li W, Chen Z, Fu Q. Gnss spoofing jamming detection based on generative adversarial network. *IEEE Sensors J* (2021) 21:22823–32. doi:10.1109/JSEN.2021.3105404

59. Guizzaro C, Formaggio F, Tomasin S. Gnss spoofing attack detection by imu measurements through a neural network. In: 2022 10th Workshop on Satellite Navigation Technology (NAVITEC); 05-07 April 2022; Noordwijk, Netherlands. IEEE (2022). p. 1–6. doi:10.1109/NAVITEC53682.2022.9847562

60. Gu N, Xing F, You Z. Gnss spoofing detection based on coupled visual/inertial/gnss navigation system. *Sensors* (2021) 21:6769–90. doi:10.3390/s21206769

61. Xu R, Ding M, Meng Q, Liu J. Spoofing interference identification technique of medll aided gnss/ins system. *J Chin Inertial Technol* (2018) 26:223–30. doi:10.13695/j.cnki.12-1222/o3.2018.02.013

62. Shang X, Sun F, Zhang L, Wang D, Ke Y. Ins aided gnss spoofing identification and suppression method. *J Chin Inertial Technol* (2022) 30:181–7. doi:10.13695/j.cnki.12-1222/o3.2022.02.007

63. Shang X, Sun F, Zhang L, Cui J, Zhang Y. Detection and mitigation of gnss spoofing via the pseudorange difference between epochs in a multicorrelator receiver. *GPS solutions* (2022) 26:37. doi:10.1007/s10291-022-01224-4

64. Hao Y, Shi C, Xu A, Sui X, Xia M. Revealing methods of gnss spoofing mitigation through analyzing the spoofing impacts on adaptively robust estimation-based rtk/ins tightly coupled integration. *IEEE Sensors J* (2023) 23:25165–78. doi:10.1109/JSEN.2023.3303199

65. Wang J, Guo Y, Tang K, He X. Development trend of spoofing jamming technology for satellite navigation. *Navigation and Control* (2022) 21:13–24. doi:10.3969/i.issn.1674-5558.2022.01.002

Frontiers in Physics

TYPE Review
PUBLISHED 12 December 2024
DOI 10.3389/fphy.2024.1487384

EDITED BY
David Ruffolo,
Mahidol University, Thailand

REVIEWED BY
Sampad Kumar Panda,
K L University, India
Zhu Xiao,
Hunan University, China

*CORRESPONDENCE
Zukun Lu,
luzukun@nudt.edu.cn

RECEIVED 28 August 2024
ACCEPTED 25 November 2024
PUBLISHED 12 December 2024

CITATION
He Y, Li B, Chen J, Wang Z, Xiao W and Lu Z (2024) Overview of the development of satellite navigation blanket interference monitoring.
*Front. Phys.* 12:1487384.
doi: 10.3389/fphy.2024.1487384

# Overview of the development of satellite navigation blanket interference monitoring

Yinhui He[1,2], Baiyu Li[1,2], Jinping Chen[3], Zhi Wang[4], Wei Xiao[1,2] and Zukun Lu[1,2]*

[1]College of Electronic Science and Technology, National University of Defense, Changsha, China, [2]Key Laboratory of Satellite Navigation Technology, Changsha, China, [3]Beijing Satellite Navigation Center, Beijing, China, [4]Transcom (Shanghai) Technology Co., Ltd., Shanghai, China

Satellite navigation interference monitoring is an important means to effectively evaluate interference and ensure the normal operation of global navigation satellite system (GNSS). Once interference is detected, this monitoring can identify the type of it, perform direction-finding and localization, evaluate its impact on GNSS, and guide the implementation of effective countermeasures. With the continuous progress of interference technology, the power required to cause the same jamming effect to the navigation system is getting smaller and smaller. Traditional radio monitoring system has been unable to meet the needs of the current satellite navigation monitoring in terms of sensitivity and accuracy. It is of great significance to develop and improve the dedicated satellite navigation monitoring system. This paper introduces the basic concept of satellite navigation interference monitoring and the composition of the system, analyzes the key technologies and finally gives an outlook on the development trends in this field.

KEYWORDS

**global navigation satellite system, interference monitoring system, interference detection, interference identification, interference direction finding**

## 1 Introduction

The Global Navigation Satellite System (GNSS) is a generic term for satellite navigation systems that provide all-weather, continuous, global coverage for positioning, navigation, and timing services. Currently, the world has seen the formation of four major global satellite navigation systems: the United States' Global Positioning System (GPS) [1–3], the European Union's Galileo Satellite Navigation System (Galileo) [1–3], Russia's Global Navigation Satellite System (GLONASS) [1, 3], and China's BeiDou Navigation Satellite System (BDS) [3, 4]. In addition, India and Japan have respectively constructed the Indian Regional Navigation Satellite System (IRNSS) [1, 3, 5] and the Quasi-Zenith Satellite System (QZSS) [1, 3, 6].

Satellite navigation systems have become fundamental spatiotemporal reference infrastructures. The development of navigation technology profoundly impacts various sectors of society including economy, surveying, power, transportation, and military affairs. An increasing number of infrastructures have developed a strong reliance on satellite navigation systems. Should these systems suffer a breakdown, it could lead to severe consequences, thereby making the enhancement of GNSS system stability increasingly critical.

TABLE 1 Some malicious interference incidents [10].

| Time | Location | Interference incidents |
|---|---|---|
| 1990 | Persian Gulf | In the Gulf War, the US, Iraq and other adversaries electronic countermeasure |
| 1999 | Yugoslavia | In the Kosovo War, the two sides send out jamming signals to reduce navigation accuracy or to mislead the enemy |
| 2011 | Iran | Iranian forces have beamed a decoy signal to capture a US RQ-170 Sentinel drone |
| 2017 | The Black Sea | The GPS systems of ships operating in the Black Sea were attacked with spoofing and jamming, and the ship was located at an airport several miles away |
| 2020 | Point Reyes | GPS crop circles in Point Reyes are deliberately GPS spoofed |

However, the GNSS system is inherently vulnerable [7] and is highly susceptible to various types of interference [8]. Interference can be broadly categorized into natural and anthropogenic types. Anthropogenic interference can be further subdivided into unintentional and intentional categories. Given the finite nature of the electromagnetic spectrum, GNSS systems are particularly susceptible to out-of-band interference from harmonics and inter-modulation products, as well as in-band interference from co-channel operations [9]. A notable example occurred at a U.S. port where GPS receivers were disrupted for several hours each evening following the workday, eventually traced back to unintentional interference from active TV antennas atop nearby residents' homes after months of investigation [3].Satellite navigation signals, originating from satellites orbiting approximately 20,000 km above the Earth's surface, arrive at ground level with powers as low as −130 dBm which is over a billion times weaker than typical broadcast television signals. Civilian signal formats used in navigation systems are publicly known, with information modulated onto fixed frequencies, rendering GNSS highly vulnerable to intentional malicious interference. Table 1 gives a brief description of some of the interference events that have occurred globally over the past period.

From the past to the present, interference and anti-interference in satellite navigation systems have been focal points of electronic warfare worldwide, particularly evident in military confrontations. Therefore, the necessity of anti-interference and interference monitoring is self-evident. This review primarily addresses malicious jamming interference. As long as the emitted interference targets the GNSS frequency bands or covers the entire system frequency spectrum with sufficient power, it can achieve significant disruptive effects, posing the greatest threat to user-end navigation receivers. The principle of interference is that as the interference power increases, the equivalent carrier-to-noise ratio (C/N0) at the receiver output degrades, leading to prolonged acquisition times or even loss of lock during signal capture, and reduced pseudo-range accuracy during tracking [11]. This results in a decline in the reliability of the GNSS system, manifesting as significant positioning errors.

Anti-interference refers to the adoption of various technologies and measures [12–17] to reduce or eliminate the impact of interference on system performance. Interference monitoring, on the other hand, involves the detection, identification, and analysis of interference signals in the electromagnetic environment. Specifically, it encompasses the localization of interference sources, the identification of interference signal types and characteristics, and the assessment of their impact. Anti-interference and interference monitoring are complementary; interference monitoring provides detailed information about the interference [18], which is the foundation for implementing anti-interference techniques. Only through effective interference monitoring can the sources and characteristics of interference be accurately identified, enabling targeted anti-interference measures to be taken. For instance, if the interference is identified as frequency sweeping or continuous wave interference, Infinite Impulse Response (IIR) adaptive notch filters can be directly employed to suppress it [19]. When interference is detected in the transform domain, adaptive filters can be directly designed in that domain to suppress the interference, after which the signal can be transformed back to the time domain to accurately recover the original GNSS signal [20–23].

In response to the challenges currently faced in interference monitoring, this paper reviews the development process of GNSS interference monitoring, focusing on the recent advancements in key monitoring technologies. It summarizes and analyzes the existing issues and identifies future research directions in this field.

# 2 Interference monitoring system

## 2.1 General situation

The development of GPS by the United States in the 1970s was primarily for military purposes, with early satellite interference monitoring relying on military electronic equipment to ensure the precision of weapon strikes. The Gulf War and the Kosovo War in the 1990s highlighted the importance of satellite navigation interference monitoring in electronic warfare environments, prompting researchers to design specialized equipment for this purpose. As GPS expanded into civilian use and became more globalized, fixed ground-based satellite navigation interference monitoring systems began to emerge. The development of digital signal processing (DSP) technology and software-defined radio (SDR) enabled these systems to identify various types of interference in complex signal environments. In the 21st century, as satellite navigation systems diversified into a quadripartite structure, there arose a need for compatibility in interference monitoring systems. Monitoring platforms have evolved from fixed ground-based systems towards mobile air- and space-based systems, with nations working to establish comprehensive, three-dimensional maritime, land, air, and space interference monitoring systems. Table 2 provides an analysis and comparison of the three types of interference monitoring platforms.

TABLE 2 Comparison of interference monitoring platforms.

| Type of platform | Function | Characterization | Typical monitoring system |
|---|---|---|---|
| Ground-based | Establishing fixed or mobile radio monitoring stations on the ground to achieve surveillance of various signals in the electromagnetic spectrum | Low cost, strong opera ability, easy maintenance, high data quality, and flexible equipment configuration<br>Limited coverage range, susceptible to obstructions, poor mobility, and strong dependence on ground infrastructure | The U.S. National RF monitoring Network and the European Space Agency's ground-based GNSS receiver network |
| Air-based | Radio monitoring systems installed on aircraft such as airplanes, drones, and airships | Strong mobility, wide coverage range, high efficiency, strong adaptability, and high positioning accuracy<br>High cost, poor continuous surveillance capability, low survive ability, complex deployment and retrieval, and strict limitations on the weight and size of monitoring equipment | The U.S. EP-3E ARIES II electronic reconnaissance aircraft, the Russian Tu-214R reconnaissance aircraft, and the Russian Luch/Blits series of satellites |
| Space-based | Relying on artificial Earth satellites to conduct global electromagnetic spectrum monitoring activities from orbit | Global coverage, high real-time performance, sustainable and stable operation, and high strategic value<br>High cost, complex technology, limited resources, and weak survive ability | The U.S. Space-Based Space Surveillance (SBSS) system, the Russian Luch/Blits series of satellites, and the U.S. HawkEye 360 |

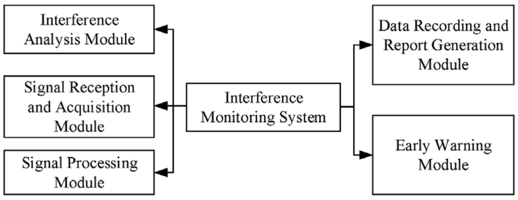

FIGURE 1
Interference monitoring system.

## 2.2 The development status

### 2.2.1 General interference monitoring System

Before the advent of satellite navigation systems, many non-navigation systems experienced disruptions due to radio interference that prevented them from operating normally. This was particularly evident in civil aviation systems, where radio interference posed a significant threat to air traffic systems, causing flight delays and even endangering personal safety. To effectively address incidents of electromagnetic interference, the U.S. Federal Aviation Administration (FAA) began constructing a nationwide radio interference monitoring system at the end of the 20th century. This system consists of multiple airborne, mobile, portable, and fixed interference monitoring systems, ensuring the takeoff and landing of flights at key airports and minimizing the impact of radio interference [24]. The primary hardware for this system is manufactured by Cubic Corporation in the United States and has been adopted by many countries, playing a significant role in civil aviation radio interference monitoring. The main modules included in the FAA's interference monitoring system are shown in Figure 1.

After years of development, in addition to the United States and other countries have also been mature radio monitoring technology. For instance, most provinces can now achieve comprehensive monitoring of critical areas such as airports within their jurisdictions. A large number of fixed monitoring stations, mobile monitoring stations, and portable interference detection devices have been established, forming a relatively complete radio interference monitoring network [25]. Figure 2 [26] shows some of the interference monitoring equipment in our country.

### 2.2.2 Dedicated GNSS interference monitoring system

General-purpose radio interference monitoring networks monitor the electromagnetic environment across the entire frequency spectrum. In contrast, the frequency bands used by GNSS systems are fixed, and the navigation signals reaching the ground are extremely weak, often buried below the noise floor. With the evolution of interference technology, the variety of interference methods has increased, and different interference techniques can produce varying effects [27]. Consequently, the power required to achieve the same level of interference on GNSS systems is decreasing. Traditional general-purpose radio interference monitoring networks are no longer sufficient in terms of sensitivity, accuracy, and speed to meet the monitoring requirements of GNSS systems. Recognizing the challenges faced by GNSS interference monitoring, countries led by the United States began constructing dedicated monitoring networks from the last century.

In 1994, the U.S. National Geodetic Survey began establishing a national network of continuously operating reference stations (CORS) for GPS, which later expanded globally. These CORS receive GPS signals and provide high-precision positioning data for applications such as geodesy and meteorological observations.any GPS CORS are equipped with anti-interference devices and can also assess the quality of received GPS signals. They utilize various techniques, including radio monitoring and noise level

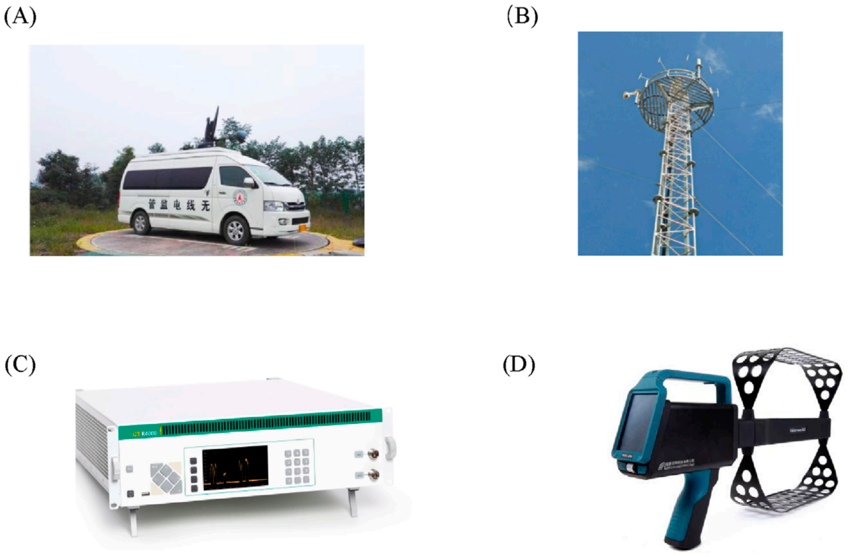

FIGURE 2
Interference monitoring equipment. **(A)** Radio monitoring vehicle. **(B)** Radio monitoring direction finding system. **(C)** Radio monitoring direction finding receiver. **(D)** Radio monitoring direction finding system.

measurements, to monitor and locate interference near the base stations.

In 1997, the U.S. Congress directed a project involving Spawar and Falon companies, which developed and demonstrated a prototype system called "LOCO GPSI." The demonstration results showed that the system was effective and practical, with the ability to locate interference sources. The entire system utilized a short baseline interferometry approach, determining the source of interference through triangulation methods [28].

The JLOC system (Joint Landaster Oriented Coordinate System) is a system commissioned by the Joint Space Operations Center under the U.S. Department of Defense and developed by NAVSYS Corporation. The system was established in 2002 and primarily provides precise geographical location information and time standards. It can monitor abnormal changes in satellite navigation signals and quickly locate the position of interference sources, conducting comprehensive performance testing and evaluation of satellite navigation systems to ensure their normal operation.

In 2009, CHRONO Technologies in the UK developed a handheld interference monitoring device capable of monitoring GPS signals and interference signals in the L1 frequency band [29]. In addition, the U.S. FAA established a GPS interference source monitoring and localization experimental system, which includes a large number of interference sources and localization systems, employing almost all interference source localization technologies [30].

Currently, the American company HawkEye 360 is building the world's first commercial radio frequency (RF) signal mapping system based on a low-orbit satellite constellation, with plans to launch a total of 60 small satellites into low-earth orbit by 2025. Its products include RFGeo, RFIQ, and SEAker. RFGeo is used to detect and locate RF signals on the Earth's surface, with Figure 3 [31] showing a precisely mapped image of Earth's RF signals. RFIQ is dedicated to space-based radio frequency spectrum data collection, providing visualization of the spectrum data gathered by the HawkEye 360 RF sensor satellite constellation, as depicted in Figure 4 [31]. SEAker leverages sophisticated algorithms to integrate automatic identification systems with HawkEye 360 sensors, enhancing maritime awareness capabilities. The entire system primarily focuses on spectrum mapping and signal source localization, offering comprehensive and timely interference detection and early warning services [32].

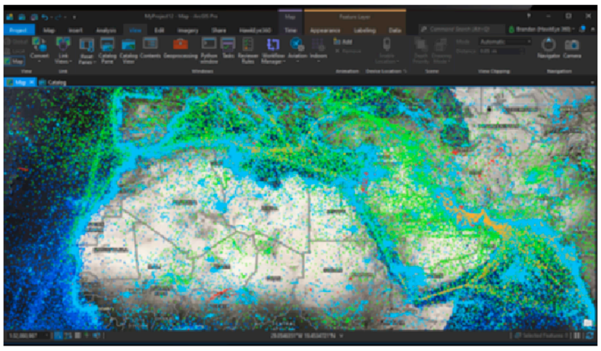

FIGURE 3
Radio-frequency signal pattern.

## 2.3 Summary

Currently, the development of interference monitoring systems faces numerous challenges: 1) Technical challenges. The electromagnetic environment is becoming increasingly complex,

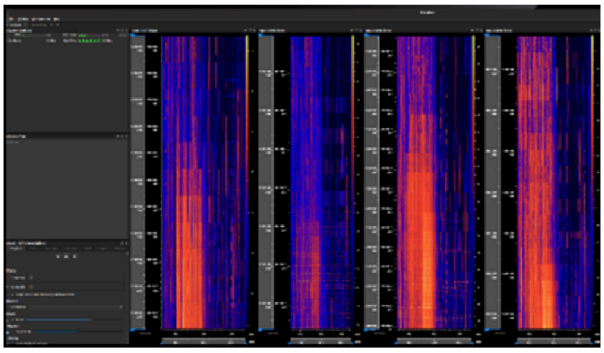

FIGURE 4
Visual spectral data.

and the accuracy, sensitivity, and speed of traditional radio interference monitoring systems are no longer sufficient for satellite navigation system interference monitoring. Efforts to overcome key technical bottlenecks within the system and promote technological innovation and advancement are essential trends. 2) Construction challenges. There are few dedicated satellite navigation interference monitoring networks, and the coverage areas of these networks are limited. Developing new systems and equipment for GNSS interference monitoring, increasing the number of monitoring stations, and expanding coverage areas are crucial for ensuring reliable GNSS services globally. 3) International Cooperation challenges. Satellite navigation monitoring involves the interests of multiple countries. Strengthening international cooperation and exchange, encouraging active participation in international organizations and activities, and promoting the establishment of multilateral cooperation mechanisms to jointly maintain space security and stability remain challenging.

# 3 Key technologies for interference monitoring

Interference monitoring refers to the process of detecting, identifying, direction-finding, locating, and assessing interference in the electromagnetic environment. Its purpose is to promptly discover and identify interference sources, evaluate the nature and intensity of the interference, and assess its impact on communication and navigation systems, thereby enabling the implementation of appropriate measures to mitigate or eliminate these interference. Figure 5 illustrates the complete interference monitoring process. Initially, specialized equipment and techniques are used to continuously collect signal data from the electromagnetic environment to detect the presence of interference. Subsequently, the detected interference is analyzed to identify its type and characteristics. Next, the impact of the interference on the system is evaluated, and direction-finding is performed to locate the position of the interference source. A monitoring report is then generated and submitted to relevant departments to assist them in making decisions regarding interference suppression [33].

Considering the importance of interference monitoring technology in interference monitoring systems, this section will detail three key technologies for suppression interference monitoring: interference detection technology, interference identification technology, and interference direction finding technology. Simulations will be used to verify the implementation of some of the algorithms involved, and the issues associated with each technology will be pointed out. Based on recent technological trends, the section will also summarize the research directions that warrant further investigation.

## 3.1 Interference detection technology

### 3.1.1 Time-domain detection algorithms

The time-domain energy detection algorithm is suitable for detecting high-power blanket interference. It does not require prior information about the signal; it only needs to compare the energy of the signal with a preset energy threshold to determine the presence or absence of interference, regardless of the type of interference. However, it cannot determine the specific frequency points of the interference. The time-domain energy detection method is simple to implement and uses the binary hypothesis testing theory from the field of mathematical statistics.

The signal received by a satellite navigation receiver can be modeled as Equation 1 [34]:

$$\boldsymbol{r}(t) = s(t) + j(t) + n(t) \tag{1}$$

In the model, $s(t)$ denotes the true satellite navigation signal; $j(t)$ represents the interference in the GNSS; and $n(t)$ is the additive white Gaussian noise with power $\sigma^2$.

The energy of the received signal can be expressed as Equation 2 [35]:

$$\boldsymbol{e}(n) = \sum_{k=0}^{K-1} r(n-k)r^*(n-k) \tag{2}$$

In the equation, $r(n)$ represents the digital signal obtained after analog-to-digital conversion, and $(\cdot)^*$ denotes the conjugation operation applied to the signal.

The hypothesis testing problem can be simply expressed as Equation 3:

$$\begin{cases} H_0{:}e(n) < \lambda, j(n) = 0 \\ H_1{:}e(n) \geq \lambda, j(n) \neq 0 \end{cases} \tag{3}$$

In the equation, $\lambda$ is the threshold value for energy detection; $H_0$ is the null hypothesis, indicating that the useful signal is not interfered with, and at this point, the signal energy value is less than the threshold value; $H_1$ is the alternative hypothesis, indicating that the useful signal is being interfered with, and at this point, the signal energy is greater than the threshold value. According to the above analysis, the key to the energy detection algorithm is how to determine an appropriate detection threshold $\lambda$ in a constantly changing noise environment.

The energy detection algorithm is significantly affected by noise uncertainty and has a low probability of detecting interference in low SNR conditions. In practical environments, noise is time-varying, and to improve detection probability, multi-node cooperative detection algorithms have been developed. Reference [29] proposes

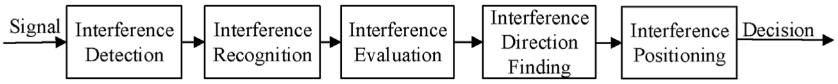

FIGURE 5
Interference monitoring flow chart.

an adaptive multi-threshold energy detection method under time-varying conditions by estimating the noise range. This method offers better detection performance compared to single-threshold energy detection algorithms. Reference [10] suggests using a hard decision strategy for dual-threshold energy detection at individual nodes. The credibility weights are assigned based on the quality of the channel environment at each node, and the final decision is made at the fusion center. This approach achieves good detection performance even under low interference-to-noise ratio (INR) conditions. Wu Jin [36] derived the expression for the error probability in energy detection algorithms and determined the optimal threshold value to minimize this probability, thereby improving detection performance to some extent. Wang Jing [37] adopted a segmented detection method for interference detection in Beidou civilian signals. This method is highly efficient and effective because it focuses on the noise within each sub-band during detection, thereby reducing the influence of noise from other bands and effectively improving the INR during detection.

### 3.1.2 Frequency-domain detection algorithms

The principle of frequency-domain interference detection is similar, although it may be slightly more complex in terms of computation compared to the time-domain energy detection method. However, it can not only detect the presence of interference but also determine the specific frequency points of the interference [38].

Frequency-domain interference detection often uses the Consecutiveean Excision (CME) algorithm proposed by P. Henttu and S. Aromaa [39]. This algorithm assumes that the initial signal samples do not contain interference signals, and thus the signal spectrum envelope follows a Rayleigh distribution with an expected value as Equation 4:

$$E(A) = \sqrt{2\sigma^2}\Gamma(1.5) \tag{4}$$

In the equation, $\sigma^2$ is the power of the Gaussian noise; and $\Gamma(x)$ is the Gamma function, which is also known as Euler's second integral. The distribution function of a Rayleigh random variable $F(A)$ is given by:

$$F(A) = 1 - \exp\left(-\frac{A^2}{2\sigma^2}\right) \tag{5}$$

Based on Equation 5, we can get Equation 6:

$$A_{th} = \sqrt{2\sigma^2} - \ln(\sqrt{1 - F(A_{th})}) \tag{6}$$

$A_{th}$ is the detection threshold for interference frequency points under the false alarm probability $P_{fa}$ (the probability of erroneously detecting interference frequency points when no interference signal exists) which is defined as Equation 7.

The threshold factor is defined as Equation 8:

$$P_{fa} = 1 - F(A_{th}) \tag{7}$$

$$T = \frac{A_{th}}{E(A)} = \frac{\sqrt{-\ln(1 - F(A_{th}))}}{\Gamma(1.5)} = \frac{2}{\sqrt{\pi}}\sqrt{-\ln\left(P_{fa}\right)} \tag{8}$$

The CME (Consecutiveean Excision) algorithm sets the size of the false alarm probability in advance and obtains the corresponding threshold factor. In each iteration, it calculates the spectral power of the signal set for frequency points that do not contain interference, multiplies this by the threshold factor to update the detection threshold, and then compares the spectral envelope at each frequency point with the detection threshold to classify them into frequency points with and without interference.

Subsequently, P. Henttu et al. [40] proposed the forward sequential mean excision algorithm, also known as the forward consecutive mean excision (FCME) method, to address the problem of impulse interference detection in radio systems. The algorithm first reorders the signal spectra in ascending order according to their energy values, selects a portion of the spectra to form a set of interference-free signals, calculates their energy, and sets a threshold value. If the energy value of the next frequency line is less than the threshold value, this spectrum line is added to the initial signal set to form a new signal set, and its energy is recalculated and a new threshold value is set. Otherwise, the algorithm ends, and the process continues iteratively. Yang Chao et al. [41] proposed an improved CME interference detection algorithm, which sorts the spectrum lines in descending order and considers the mean of the latter half of the spectrum lines as the mean in the absence of interference. This mean is used to initialize the detection threshold, reducing the number of iterations and accelerating the convergence rate of the CME algorithm without decreasing the probability of interference detection. Setting a single threshold has certain issues, such as the possibility of an interference signal with a certain bandwidth having energy below the threshold at a particular frequency point, leading to the misidentification of a single interference signal as two separate ones. Vartiainen et al. [42] addressed this issue by proposing a dual-threshold-based interference frequency point localization algorithm. The main principle of the algorithm is to set high and low detection thresholds. First, the adjacent frequency points of signal samples exceeding the low threshold are clustered, and then the maximum value of the signal spectra in each cluster is compared with the high threshold. If it is greater than the high threshold value, the frequency points belonging to that cluster are determined to correspond to the same interference signal. Otherwise, they are not. Based on this, the algorithm can estimate the bandwidth of the interference.

In frequency-domain interference detection algorithms, traditional Fourier transforms are used. Essentially, these transforms convert one-dimensional time functions into one-dimensional frequency functions, which is a relatively simple transformation method. Its disadvantages are quite apparent: it can only analyze the time-domain characteristics and frequency-domain characteristics of signals independently as a whole, and it cannot analyze the frequency characteristics of signals at specific moments or the time characteristics of signals at specific frequencies. Therefore, it is only suitable for analyzing stationary signals.

### 3.1.3 Time-frequency detection algorithms

Indeed, when GNSS signals mixed with interference are received by the receiver, they become non-stationary signals. Therefore, time-frequency analysis methods are more suitable for interference detection and analysis. The purpose of time-frequency analysis is to transform one-dimensional time signal functions into two-dimensional joint distribution functions of time and frequency, which can reflect the time-varying characteristics of non-stationary signals [43]. Linear time-frequency analysis is typified by the Short-Time Fourier Transform (STFT), proposed by Dennis Gabor in 1946. The STFT is obtained by multiplying the signal by a sliding time window and then performing a Fourier transform. Due to its linearity and low complexity, the STFT has been used in the development of interference mitigation algorithms, such as those developed by Daniele Borio et al. [44], to estimate the instantaneous frequency of interference. Wang Pai et al. [45] have combined the time-frequency characteristics and statistical properties of received GNSS signals to propose an interference detection algorithm based on the STFT, improving the detection performance of broadband and narrowband interference in low signal-to-noise ratio environments. However, the STFT also has limitations. Because of the windowing process, it is constrained by the Heisenberg uncertainty principle, meaning that the time resolution and frequency resolution cannot be simultaneously optimized.

Comparing different time-frequency analysis methods, quadratic time-frequency analysis based on the Fourier transform of the instantaneous autocorrelation function provides almost the best resolution [8]. Among these, the most commonly used is the Wigner-Ville distribution (WVD), introduced to signal processing in 1948. The WVD can achieve the lower bound of the Heisenberg uncertainty principle and can address some of the issues present in the STFT. However, when analyzing signals with multiple components, the WVD produces cross-term interference, causing the signal energy to spread over areas of the time-frequency plane where there should be no energy, making it difficult to accurately capture the signal features. Choosing appropriate time-frequency analysis methods, such as adaptive kernel time-frequency distributions or linear time-frequency distributions, can suppress cross-terms, but this leads to a degradation in the clustering property of the signal's time-frequency distribution and increases computational complexity [46]. To address these issues, Sun Kewen et al. [47] analyzed the principles and problems of STFT and WVD, proposing a new time-frequency analysis method based on a reassigned spectrogram for detecting frequency-sweeping interference. This method strikes a good balance between suppressing cross-terms and maintaining time-frequency resolution. Later, he [48] proposed using the Fractional Fourier Transform (FRFT) for detecting satellite navigation interference. The FRFT has excellent detection capabilities for linear frequency modulation (LFM) interference. Xu Huifa [49] and colleagues similarly proposed a new method based on the FRFT to solve the detection and estimation problems of strong and weak LFM signals, improving detection efficiency.

For the common frequency-sweeping interference in satellite navigation systems, many scholars in Professor Sun Kewen's team have conducted extensive and in-depth research on its detection [22, 50–52]. Their main work involves combining various time-frequency transformation methods to leverage the strengths of each method while compensating for their respective weaknesses. Chen Yuanyuan [50] used the Radon-Wigner transform to detect frequency-sweeping interference and estimate interference parameters. By combining the smoothed pseudo Wigner-Ville distribution based on time-frequency reassignment with the Radon transform, she validated the effectiveness of combining the Radon transform with time-frequency analysis methods for interference detection. Zhao Huizi [51] combined reassignment techniques and wavelet transforms to effectively address issues related to energy concentration, cross-terms, and resolution, thereby improving the accuracy of interference detection. Sun Kewen [52] combined the Hough transform with the Wigner-Ville distribution (WVD) to eliminate cross-term interference and enhance detection sensitivity. The detection performance remains excellent even at an INR of −10 dB.

The FrFT uses a set of orthogonal chirp signals as basis functions. By selecting an appropriate order, the FrFT transforms the chirp signal into the transform domain, where the energy of the chirp signal becomes concentrated, forming a peak. This allows for accurate estimation of interference parameters. Zhang Jun [22] improved the traditional method for determining the optimal order of the FrFT by proposing a combination of the bisection method and discrete polynomial algorithms. This approach reduces the computational complexity of searching for the optimal order while improving search accuracy, enabling the detection of multi-component chirp signals. Zheng Yifei [23] combined the FrFT with traditional time-frequency methods such as the short-time Fourier transform (STFT) and WVD. Compared to these traditional methods, the energy concentration of frequency-sweeping interference is enhanced in the transform domain. At an INR of −8 dB, the accuracy of parameter estimation for frequency-sweeping interference is improved by two orders of magnitude.

In interference detection, time-domain energy detection, frequency-domain energy detection, and time-frequency domain detection primarily utilize the energy distribution characteristics of interference signals in the time domain, frequency domain, and time-frequency domain, respectively. Table 3 summarizes the advantages and disadvantages of these three detection algorithms.

### 3.1.4 Full blind detection algorithms

In practical interference detection scenarios, the problem is often non-cooperative, making it difficult to obtain sufficient prior information. Therefore, researching fully blind interference detection algorithms holds greater practical significance.

Blind interference detection algorithms based on random matrix theory have been proposed. Two typical algorithms are the Covarianceatrix-based All-Blind Detection (CAV) [53] and the Eigenvalue-based All-Blind Detection (BDA) [54]. The CAV

TABLE 3 Comparison of advantages and disadvantages of interference detection algorithms.

| Interference detection algorithms | Advantages | Disadvantages |
|---|---|---|
| Time-domain Detection | Simple implementation, intuitive principle, good real-time performance, sensitive to impulsive signals, no prior information required | Lack of frequency information, inability to handle non-stationary interference, susceptibility to noise |
| Frequency-domain Detection | Determination of interference frequency points, strong noise suppression capability, suitable for analyzing simple non-stationary interference signals | High computational complexity, transient response lag, and high requirements for synchronization |
| Time-Frequency Detection | Suitable for detecting complex non-stationary interferences, capable of analyzing the local time-frequency characteristics of interferences | High computational load, cross-term issues with some methods, difficulty in interpreting time-frequency graphs, and high sensitivity to parameters |

algorithm constructs a test statistic as the ratio of the sum of the absolute values of all elements in the covariance matrix of the received signal to the sum of the absolute values of the diagonal elements. The BDA algorithm constructs a test statistic as the ratio of the maximum eigenvalue to the minimum eigenvalue. These algorithms have detection thresholds that are independent of noise information, thus completely overcoming the limitation of energy detection algorithms being sensitive to noise uncertainty. They also exhibit good detection performance even at low SNR. Based on these foundations, many researchers have conducted more in-depth studies on all-blind detection algorithms [55–61]. Their work includes developing new covariance-based decision statistics to address the computational complexity of decision metrics and thresholds, or combining these algorithms with cooperative sensing to further improve detection performance and optimize network overhead.GNSS interference detection can benefit from spectrum sensing techniques. Wu Jin [36] has introduced all-blind detection algorithms into the interference detection of the Beidou system and proposed a weighted fusion detection (WFD) algorithm, which enhances detection performance.

In recent years, with the rise of artificial intelligence, machine learning has been increasingly applied in various fields due to its excellent classification performance. In the context of all-blind detection algorithms, interference detection is essentially a binary classification problem, which aligns well with machine learning algorithms. Based on this, many scholars have introduced machine learning into full-blind detection. Reference [62] combines the traditional K-Nearest Neighbors (KNN) algorithm to achieve the detection task. Yao Di [63] combines the Support Vectorachine (SVM) to perform binary classification tasks for spectrum sensing. These algorithms effectively address the issue of low detection probability under low signal-to-noise ratio (SNR) conditions and offer high detection efficiency. However, they require manual construction of feature vectors, which can significantly impact the classification results. Shi Haodong [64] uses a Convolutional Neural Network (CNN) to achieve collaborative spectrum sensing. Lu Huachao [65] directly inputs the normalized covariance matrices of the combined I and Q signals from each node into the neural network, allowing the network to automatically extract useful features for detection. This approach yields good detection performance.

### 3.1.5 Summary

Time-domain energy detection algorithms fall into the category of semi-blind detection algorithms, as they require prior information related to the noise. Due to this requirement, their detection performance is poor at low INR and they are highly susceptible to noise uncertainty. However, they are easy to implement and do not require sophisticated detection equipment. Improvements through multi-node cooperative energy detection can somewhat alleviate these issues, but the enhancement is limited and increases the overhead of the detection network.

Full-blind detection algorithms do not require any prior information about the received signals and are independent of the noise environment. They maintain good detection performance even at low SNR. However, these algorithms are based on covariance matrix decomposition, which involves significant computational complexity. As a result, they may not meet the real-time interference detection requirements in practical applications.

The limitations of the aforementioned methods are evident; they can only detect the presence of interference but provide no information about the interference parameters, making interference suppression challenging. Time-frequency detection methods and frequency-domain detection methods, on the other hand, can not only detect the presence of interference but also estimate the interference parameters, thereby facilitating interference suppression. Time-frequency detection methods are particularly suitable for detecting non-stationary interference. Combining various time-frequency transformation methods can reduce parameter estimation errors. However, these methods are computationally complex and the interpretation of the transformation results is challenging.

## 3.2 Interference identification technology

Blanket interference can be classified in various ways. Based on the time-domain characteristics of the interference, it can be divided into pulse interference and continuous wave interference. According to the stationarity of the interference, it can be categorized into stationary interference and non-stationary interference. Furthermore, it can be classified into broadband interference and narrowband interference according to the spectral width. Narrowband interference has a bandwidth narrower than the

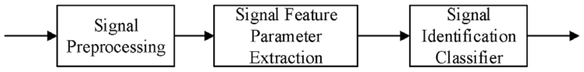

FIGURE 6
Pattern identification method flow chart.

GNSS signal, while broadband interference has a bandwidth wider than the GNSS signal [66]. Taking the GPS L1 frequency band with a spread spectrum code of CA as an example, common interferences include matched spectrum interference [67], Gaussian noise interference, linear frequency modulation (LFM) interference [68], pulse interference [69], continuous wave interference [70], etc.

### 3.2.1 Traditional pattern recognition methods

Radio communication has a relatively long history, with initial reliance on manual methods for identifying modulation schemes of radio signals. However, these manual identifications were significantly influenced by subjective factors and were both time-consuming and labor-intensive. As communication technology advanced, the advantages of automatic modulation recognition became increasingly apparent, eventually evolving into the mainstream approach for identification. Traditional modulation recognition methods can be broadly categorized into two types: decision-theoretic methods and statistical pattern recognition methods [71]. While decision-theoretic methods require substantial computational power and extensive prior information, the relevant parameters associated with the signals to be identified are often unknown. As a result, statistical pattern recognition methods have gained wider acceptance and are more commonly applied.

The pattern identification method includes three modules: signal preprocessing, signal feature parameter extraction, and signal identification classifier design, as shown in Figure 6. Firstly, the received signal is preprocessed, including noise removal, data normalization, unknown parameter estimation, etc. Then, the signal set to be classified is analyzed in different signal domains such as time domain and frequency domain, and the features that can clearly distinguish the signal types in the set are extracted to form feature vectors. This module mainly relies on machine learning methods [72] and pattern identification theory [73], and finally the signal samples to be tested are input into the classifier to realize signal identification.

A good feature parameter should easily highlight the differences between signals, significantly reducing the burden on subsequent classifiers and facilitating the identification of different signals. Azzouz, EE, and Nandi, Ak [74–76] published several papers between 1995 and 1998 on extracting time-domain feature parameters for analog and digital signals. Their work included various typical algorithms for extracting signal instantaneous features. Later scholars built upon this foundation to conduct more research on automatic modulation identification. A good identification classifier should achieve high signal identification rates. Commonly used identification classifiers are based on machine learning and include: decision tree (DT) classifier [77], support vector machine (SVM) classifier [78] and neural network (NN) classifier.

Some scholars in the field of satellite navigation interference identification have drawn on the method of automatic signal modulation identification to identify typical interference types in satellite navigation systems. Huang Ting [30] analyzed the characteristics of pulse interference and continuous wave interference, and provided the results of typical suppression interference characteristic analysis, which provided ideas for selecting appropriate characteristic parameters. Lei Liang [79] did similar work, and Li Jian et al. [80] extracted pulse width estimates, bandwidth ratios, and frequency modulation slopes to conduct identification simulation experiments on six typical interferences. When the signal to noise ratio (SNR) is 3dB, the identification rate reaches 90%. Zhu Pengcheng [10] analyzed the typical interference of GPS and Beidou systems from the time domain, frequency domain, time-frequency domain, and high-order cumulants, extracted feature values composed of high-order cumulants, normalized spectral bandwidth, and other parameters, and used decision tree classifiers for identification. The simulation results show that the identification effect is very good when the INR is large. Some of the selected features are greatly affected by noise, and when selecting a decision tree classifier, the classification threshold is generally not changed once selected, which is not adaptive. Therefore, when the INR is small, the identification effect is not ideal.

Ye Rui [81] also did interference identification work, but he used the KNN (K Nearest Neighbors) algorithm based on the traditional decision tree to calculate the distance between the test samples and the training sample eigenvalues for classification, eliminating the subjective factors brought about by manually setting thresholds, and the identification rate has been improved to a certain extent. However, when the number of samples is large, the calculation of this method is very large. Combining DTs and SVMs and directly bringing test sample data into the maximum classification interval function trained by the support vector machine can solve this problem. The amount of computation and identification effect are the best among these three methods.

The use of neural network classifiers is becoming more and more common. Lu Dongsheng et al. [82] analyzed six types of interference, extracted 13 characteristic parameters to obtain feature vectors, and constructed a CNN (Convolutional Neural Network) + LSTM (Long Short Termemory) double-layer network model for training. Compared with the LSTM network in two scenarios of strong signal interference and interference with similar power, the accuracy, mean square error, and truthfulness are all better.

Based on the research of previous scholars, the characteristics of three commonly used identification classifiers are summarized in Table 4.

In statistical pattern identification methods, the selection of feature parameters and classifiers lacks a theoretical basis. Generally, for a specific identification task to be completed, the selection can only be made based on existing experience and through multiple trials and errors. This leads to the method being exceptionally sensitive to the selection of feature parameters, where choosing different feature parameters may ultimately result in different identification effects. This lack of flexibility results in poor identification rates for interference signals.

TABLE 4 Comparison of identification classifiers.

| Identification Classifiers | Advantages | Disadvantages |
|---|---|---|
| DT | Simple idea, easy to understand, small amount of calculation, low complexity, real-time identification | Fixed threshold value, greatly influenced by human factors, cascade structure, with more levels leading to poorer identification accuracy |
| SVM | Small sample size required, easy to handle nonlinear and high-dimensional problems, can avoid local minimum problems | Reduced identification efficiency when the sample size is large, supports binary classification but is not good at solving multi-class classification problems. |
| NN | Can solve any complex high-dimensional nonlinear problems, good identification performance | Requires a large number of training samples; high computational complexity, and poor real-time performance. |

### 3.2.2 Interference recognition method based on deep learning

In 2006, the concept of deep learning was officially proposed [83]. Deep learning networks are composed of multiple layers of neurons, each layer serving different functions and purposes. Common types of layers include convolutional layers, pooling layers, and fully connected layers. Convolutional layers are used to extract local information features from the input data. Pooling layers are used to down-sample the input feature maps, retaining the most important features while reducing the computational load. Fully connected layers learn high-level abstract features from the input data and are typically used as the output layer to perform classification tasks. During the training process of a deep learning network, forward propagation and back-propagation algorithms are utilized. Non-linear activation functions are used in each layer to introduce non-linearity, enabling the network to learn complex patterns and features. The trained model ultimately achieves excellent performance in various tasks. Since then, Deep Neural Networks (DNNs) have been increasingly used by scholars as end-to-end systems for identification tasks. These networks can receive raw data, automatically learn from it, and optimize themselves to ultimately complete the identification task [84], thereby avoiding the complex feature parameter extraction issues present in traditional pattern identification methods.

In the field of recognition, converting one-dimensional interference data into two-dimensional image data and combining it with deep learning for classification has become a mainstream approach in recent years. Li Xiangjun et al. [85] proposed an interference type identification method relying on the SqueezeNet CNN model and the smoothed WVT, aiming to address the problem of low interference identification rates. Iman Ebrahimiehr et al. [86] used the WVT and spectrogram to perform time-frequency analysis on different types of chirp signals, utilizing the analysis results to create an image dataset, part of which was used for training the model and part for identification testing. Chen Xin et al. [87] proposed an interference fingerprint spectrum (FPS) consisting of time-frequency and time-power characteristics of signals, and selected the GoogLeNet DNN architecture as the training model to design the FPS-DNN interference classifier. This classifier significantly improves the identification rate under low interference power conditions and can be extended to solve more complex interference classification problems. Reference [88] uses the power spectral density (PSD) of the received signal as the input feature for the network. Compared to algorithms such as Random Forest and SVM, this approach improves recognition accuracy.

To improve recognition performance, new deep neural network models have been continuously proposed [89]. established two CNN networks that can share parameters, adding the Kullback-Leibler (KL) divergence and Euclidean distance of extracted features as new loss functions. This enables the network to learn the relationships between interference signal categories, enhancing generalization capability and recognition performance at low interference-to-noise ratios (INRs) without increasing network complexity [90]. constructed images from one-dimensional signals and used residual networks to extract multi-semantic features, followed by multi-semantic feature fusion. This approach helps the deep learning network extract more distinctive signal features, thereby improving interference recognition performance [91]. used spectrograms as the training dataset and introduced multi-head attention modules and residual convolutional modules to address the different effects of varying window lengths on Short-Time Fourier Transform (STFT) results. This resulted in improved recognition performance [92]. proposed a new method based on graph models, introducing graph signals and graph neural networks to identify the modulation categories of unknown interference signals. Their method enhances channel information interaction and extracts both local and global features, significantly improving recognition performance.

Deep learning-based recognition methods have several advantages. They can automatically learn features from data, reducing the dependence on expert knowledge. As the amount of training data increases, the performance of the model often improves significantly, demonstrating good generalization capabilities and the ability to identify interference signals in different environments and conditions. However, deep neural network models are often very complex, requiring long training times and consuming substantial network resources during recognition tasks, which can sometimes lead to resource wastage. To address these issues [93]: focused on the challenges of GNSS interference recognition in low-resource environments, emphasizing preprocessing. They proposed a method that combines traditional statistical signal processing with machine learning, effectively reducing model complexity and resource consumption [94]. Introduced a time-frequency component-aware convolutional neural network (TFC-CNN) that can determine the positions of time-frequency components in time-frequency images and perform convolution operations at these positions. During network training, an adaptive forward propagation algorithm is used to dynamically decide the depth of forward propagation based on the samples, improving the computational efficiency of interference classification and reducing resource wastage [95]. Proposed a neural network classification method that combines federated learning and transfer learning. Federated learning is used to distribute data, enhancing resource efficiency and privacy protection, while transfer learning accelerates the model learning process. Compared to traditional CNN models, this method improves classification accuracy by 8%.

### 3.2.3 Summary

Traditional pattern recognition methods have advantages in computational efficiency and interpretability, but they have limitations in feature engineering and data adaptability. In contrast, deep learning-based recognition methods excel in automatic feature extraction, generalization capabilities, and handling complex data, but they face challenges in computational resource requirements and interpretability.

Deep learning-based recognition adopts an end-to-end learning approach, where raw data is fed into the network model to directly obtain classification results. However, there is a wide variety of deep learning network models, and no theoretical method has been provided to guide the selection of models based on specific recognition problems. Additionally, there is no quantitative explanation for why the output results of a model are good or bad. Instead, people rely on their experience to try different network models iteratively to achieve better results. Improving the interpretability of models to make the decision-making process more transparent, understandable, and trustworthy is an area worthy of further research in deep learning models.

Currently, most classifiers use supervised learning, which can only recognize a few specific types of interference. When new types of interference appear, the overall recognition performance may deteriorate. This is a drawback of feature learning with labeled data. Research on feature learning from unlabeled data and techniques for automatically adding classification labels to unlabeled data [79] is necessary.

## 3.3 Interference direction finding technology

Accurately determining the direction of interference sources in satellite navigation systems can help people quickly locate them. Although the construction of satellite navigation systems started relatively late and has had a shorter development time compared to the advancement of radio technology, there are numerous methods for radio direction finding. The principles of satellite navigation interference direction finding and ordinary radio direction finding techniques are consistent, with the difference lying in the specific application scenarios. To address the issue of interference direction finding in satellite navigation systems, inspiration can be drawn from radio direction finding techniques.

### 3.3.1 Traditional direction finding algorithms

The main interference direction finding methods include amplitude comparison direction finding, phase comparison direction finding, and spatial spectrum estimation. The specific algorithms are shown in Figure 7. Among them, the first two are traditional direction finding methods, which are based on the amplitude information or phase information of the interference received by the antenna, respectively. These are the direction finding methods adopted by scalar direction finding systems. The latter benefits from the development of spatial spectrum estimation technology, which is based on both the phase and amplitude information of the interference received by the antenna. It is the direction finding method adopted by vector direction finding systems [96].

Interference direction finding can be performed using either a single antenna or an antenna array. Figure 8 showcases three commonly utilized antenna array models: linear arrays, circular arrays, and planar arrays.

Amplitude comparison direction finding relies on differences in signal amplitude, making it susceptible to noise and resulting in suboptimal direction finding outcomes. Phase comparison direction finding, also known as interferometer direction finding, relies on phase variations that contain more precise directional information. Due to its high accuracy and speed, it is widely used, including in phase interferometer methods and correlative interferometer methods. Phase interferometer-based direction finding utilizes the phase difference of interference signals received by antenna elements on a baseline. Taking single-baseline interferometer direction finding as an example, its schematic diagram is shown in Figure 9.

Assuming there are two antennas with a baseline length of $d$, they receive a far-field electromagnetic wave signal with an angle of $\theta$ with respect to the line of sight, and the wavelength of the wave is $\lambda$. The true phase difference of the signals received by the two antennas is:

$$\varphi = \frac{2\pi}{\lambda} d \sin\theta \tag{10}$$

When the signals received by the two receivers from the antennas are fed as inputs to the phase discriminator, the output of the phase discriminator is the phase difference $\phi$ between the two signals. Since the phase discrimination range of the phase discriminator is limited to $[-\pi, \pi]$, it follows that:

$$\varphi = \phi + 2k\pi, k = 0, \pm 1, \pm 2, \ldots \tag{11}$$

After undergoing an angle transformation, we can obtain Equation 12:

$$\theta = \sin^{-1}\left(\frac{\lambda}{2\pi d}\varphi\right) = \sin^{-1}\left(\frac{\lambda}{2\pi d}(\phi + 2k\pi)\right) \tag{12}$$

Upon observing Equations 10, 11, if we want to ensure that for any angle $\theta$, the true phase difference and the phase difference measured by the phase discriminator are equal, the signal wavelength $\lambda$ and baseline length $d$ must satisfy the following condition as Equation 13:

$$d \le \frac{\lambda}{2} \tag{13}$$

Otherwise, there will be an integer multiple difference between the two, which is known as the phase ambiguity problem in phase-based direction finding methods. To obtain the correct angle of arrival (AOA) of the signal, it is necessary to solve for the ambiguity

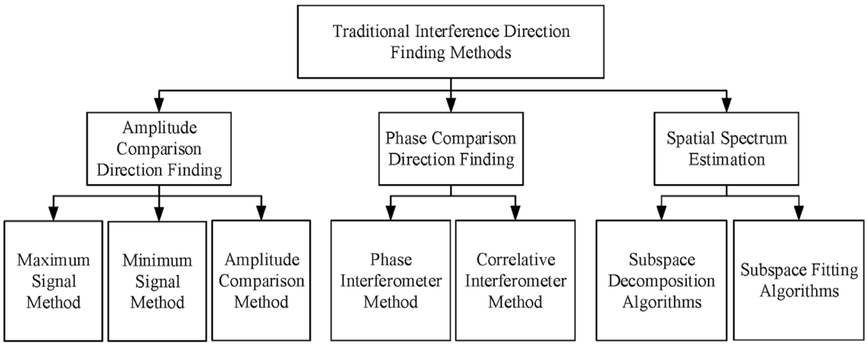

FIGURE 7
Classification of direction finding algorithms.

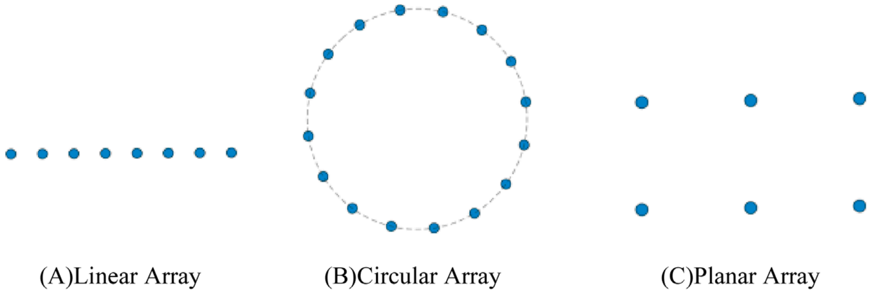

FIGURE 8
Antenna array model. **(A)** Linear array. **(B)** Circular array. **(C)** Planar array.

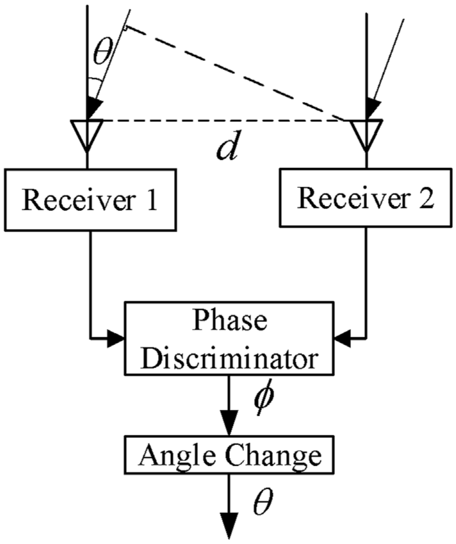

FIGURE 9
Single baseline interferometer.

number. There are already many methods to resolve this ambiguity, such as the long-short baseline method, the Chinese Remainder Theorem method [97], and so on.

It is evident that the direction finding performance is influenced by the baseline length. A longer baseline results in higher direction finding accuracy but also introduces the issue of phase ambiguity. On the other hand, a shorter baseline eliminates the phase ambiguity problem, but it can lead to mutual coupling between antenna elements, which reduces the direction finding accuracy and limits the signal bandwidth.

The correlative interferometer direction finding method can overcome the phase ambiguity problem. Its principle involves selecting several antenna pairs to obtain the phase differences of known incoming wave signals from all directions and frequencies as the original phase samples. For an unknown incoming wave signal to be measured, only the phase difference measured by the antenna pair is required, and this is then correlated and interpolated with the phase samples. The angle corresponding to the maximum correlation value is determined as the angle of arrival [98].

### 3.3.2 Direction finding algorithms based on spatial spectrum estimation

Although traditional direction finding technologies are mature, they are constrained by factors such as array size, beamwidth, and the direction finding environment. In practical applications, their direction finding accuracy and spatial resolution sometimes fail to meet requirements, especially in multipath environments where direction finding performance is poor. Spatial spectrum estimation techniques, developed in the 1960s and 1970s based on minimum variance spectral estimation, can address some of the issues with traditional direction finding methods to a certain extent.

Spatial spectrum estimation can be categorized into subspace fitting algorithms and subspace decomposition algorithms. The former category is typically represented by the maximum likelihood (ML) method, which constructs a logarithmic likelihood function based on the signal model and solves for unknown parameters to obtain the direction of arrival (DOA) of signals. This method remains effective for coherent signal direction finding and performs well even at low SNR, but its processing efficiency needs to be improved [99]. The latter category is predominantly represented by the MUSIC (Multiple Signal Classification) algorithm [100], which works by performing an eigen decomposition on the array output signals. The resulting noise eigenvectors and signal eigenvectors span the noise subspace and signal subspace, respectively. The spatial spectrum is estimated by utilizing the orthogonality between these subspaces, and the DOA is estimated by searching for spectral peaks. The MUSIC algorithm offers relatively lower complexity and computational requirements while achieving high direction finding accuracy. However, the actual electromagnetic environment is much more complex than the theoretical assumptions, leading to suboptimal direction finding results in some electromagnetic conditions. For example, under the influence of multipath effects, the presence of coherent signals can cause the array manifold matrix to become rank-deficient, resulting in poor direction finding performance. In such cases, decorrelation algorithms such as spatial smoothing algorithms are first applied to restore the array manifold matrix to a full-rank state [101]. The ESPRIT (Estimating Signal Parameter via Rotational Invariance Techniques) algorithm, proposed by Roy and Kailath [102], does not require spectral peak searching and has a lower computational burden but may exhibit reduced measurement accuracy compared to MUSIC.

We select an 8-element linear array and set up 3 incoming wave signals with different DOA. These signals have similar powers, and the INR is set to 10 dB for all of them. Among these signals, two are coherent. We conduct simulations using the MUSIC algorithm directly and after applying spatial smoothing to the signals, respectively. The purpose of these simulations is to verify the correctness of the analysis on the direction finding performance of the MUSIC algorithm. The simulation results are presented in Figure 10.

Table 5 summarizes the characteristics of the aforementioned radio direction-finding techniques, which are currently being applied in interference direction-finding for satellite navigation systems. Interferometer-based direction finding methods offer fast speed and high accuracy, and some researchers have specifically designed GNSS interference direction finding antennas to address issues such as phase ambiguity and reduce mutual coupling effects between array elements [103]. A significant number of satellite navigation interference direction finding and localization equipment employ correlative interferometer direction finding methods to achieve precise direction finding of interference signals [104]. Scholars from Beijing Jiaotong University have conducted simulations under ideal conditions, using a four-element rectangular array and MUSIC and its improved algorithms to estimate the DOA of typical incoherent narrowband interference, coherent narrowband interference, and broadband interference signals in BDS. Their results show good direction finding performance [29, 104, 105].

In practical engineering applications, however, direction finding of interference signals must take into account the impact of adverse factors such as mutual coupling between array elements and boundary effects, which can lead to amplitude and phase errors in the array elements that affect the accuracy of spatial spectrum estimation-based direction finding. To achieve direction finding results comparable to those under ideal conditions, active calibration methods can be employed, where the gain patterns of the antenna array elements are calibrated using specialized equipment to estimate the amplitude-phase error matrix and mutual impedance matrix, which are then used to correct the obtained spatial spectrum [105]. Alternatively, an error cost function can be constructed to estimate the amplitude-phase error matrix, which is then incorporated into a DOA error estimation model to achieve real-time correction [106]. With the popularity of neural network models, methods have gradually emerged that use CNN to perform phase correction on direction-finding channels [107].

As the electromagnetic environment becomes increasingly complex, it is essential to select the appropriate direction finding algorithm for different scenarios. To fully leverage the advantages of various direction finding methods and improve the results, a trend is emerging towards combining multiple direction finding techniques for interference direction finding. For instance, the maximum signal method employs high-gain directional antennas, offering high sensitivity but relatively low accuracy. In contrast, the correlative interferometer uses omnidirectional antennas, providing low sensitivity but high accuracy. By combining these two methods, it is possible to simultaneously achieve high accuracy and sensitivity in direction finding [108]. Additionally, the correlative interferometer boasts fast direction finding speeds, while the MUSIC algorithm excels in accuracy. By first using the correlative interferometer to quickly determine the direction of the interference signal, the search range of the MUSIC spatial spectrum can be narrowed, significantly reducing the computational load. The combination of these two techniques enables fast and high-precision direction finding [109, 110].

### 3.3.3 Direction finding algorithms based on timeodulated array

Although traditional direction-finding techniques have demonstrated good performance in relatively simple scenarios, they are increasingly showing limitations as the electromagnetic environment becomes more complex. For example, traditional methods struggle to address direction-finding issues in complex situations such as weak signal strength, wide bandwidth, high frequency bands, and the simultaneous presence of multiple interference sources. As a result, their application scope in modern complex electromagnetic environments is limited. Consequently, researchers have begun exploring new direction-finding techniques to overcome these challenges. In recent years, direction-finding methods based on Time modulated Arrays (TMAs) have emerged, offering new approaches to solving these problems.

A TMA is a novel type of antenna array that introduces switches at the RF front-end of a traditional antenna array to periodically time-modulate the incoming wave signals received by each antenna element. The modulated signals are then processed

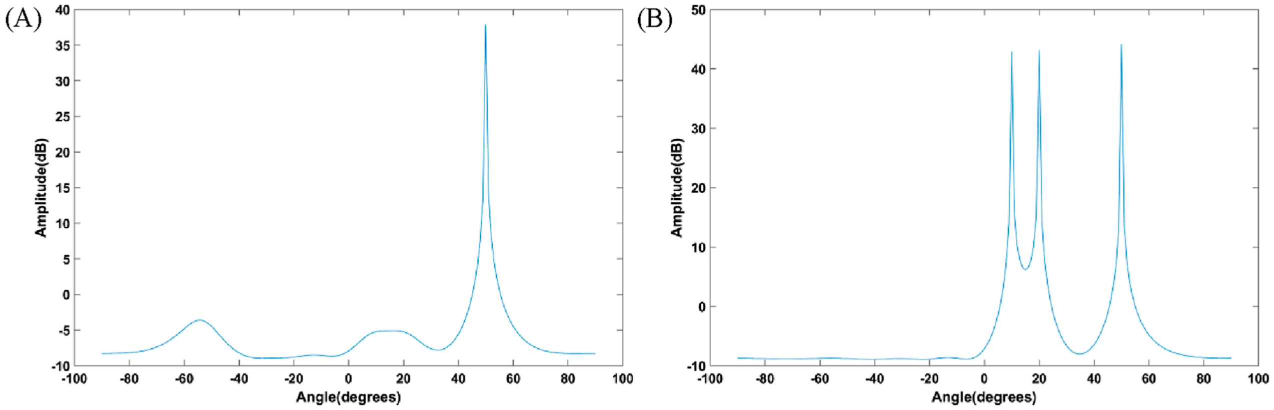

FIGURE 10
Simulation of Direction Finding by MUSIC Algorithm. **(A)** Direct MUSIC Direction Finding. **(B)** MUSIC Direction Finding after Spatial Smoothing.

TABLE 5 Performance comparison of direction finding algorithms.

| Direction finding algorithms | Direction finding sensitivity | Direction finding accuracy | Direction finding speed | Equipment complexity |
|---|---|---|---|---|
| Amplitude comparisonethod | Low | Low | Fast | Low |
| Phase comparisonethod | Relatively high | Relatively high | Relatively fast | Relatively high |
| Spatial spectrum estimationethod | High | High | Slow | High |

through a single channel by the signal processing module, extracting harmonic components that contain DOA information. By analyzing the relationships between these harmonic components, DOA estimation can be achieved. Because it introduces the time variable into the antenna array, TMA is also referred to as a four-dimensional antenna array [111]. He Chong [112] used a binary TMA to calculate the fundamental and first harmonic components of the TMA output signals. The incident angle of the incoming wave was estimated using the ratio of the harmonic component to the fundamental component. Chen Jingfeng [113] proposed a direction-finding technique based on multi-harmonic analysis, fully utilizing the angle information contained in each harmonic component. The generalized least squares estimation method was used to estimate the direction of the incoming wave signal, and selecting an appropriate number of harmonics significantly improved direction-finding performance even at low SNR. Compared to traditional algorithms that rely on multiple channels to complete direction-finding tasks, TMA uses a single channel, avoiding direction-finding errors caused by inconsistencies between channels [114]. By integrating techniques such as multi-beam arrays and spectrum feature analysis, TMA can achieve precise DOA estimation while reducing system complexity and cost [115–117]. To address direction-finding for broadband signals and potential phase ambiguity issues during the direction-finding process [118], proposed applying different periodic time modulation to different array elements. This approach independently maps the amplitude information of each antenna unit to different harmonic frequencies, avoiding phase ambiguity caused by carrier frequency variations over a wide band, thus extending the direction-finding bandwidth [119]. used channelization to divide broadband signals into multiple sub-bands, converting the broadband direction-finding problem into multiple narrowband direction-finding problems. The DOA of the broadband signal was then estimated through weighted integration [120]. introduced virtual baseline technology into TMA, further enhancing its direction-finding capabilities.

## 3.4 Summary

After years of development, traditional direction-finding methods have been extensively studied and applied in various fields such as communications, radar, and navigation. They have a solid theoretical foundation and technical accumulation, and for most conventional direction-finding tasks, their accuracy and stability meet the requirements. However, their performance in complex electromagnetic environments is not ideal. Direction-finding algorithms based on TMA offer several advantages through time modulation and spatial synthesis, including high angular resolution, strong interference resistance, low hardware complexity, and robustness. These features make TMA-based methods particularly suitable for direction-finding in complex electromagnetic environments.

Currently, TMA-based direction-finding methods, as a new technology, are still not fully mature and are primarily focused on theoretical research. Translating these methods into practical applications requires overcoming many technical barriers, such as high-precision clock sources, complex control circuits, and high-performance digital signal processing units. With advancements in technology and cost reductions, TMA-based methods are expected to see widespread application in complex electromagnetic environments, representing an important direction for the development of direction-finding technology. Meanwhile, traditional direction-finding methods will continue to play an irreplaceable role in mature fields.

## 4 Future development trends in interference monitoring

Currently, the transmission of information is generally achieved through the propagation of electromagnetic waves, where various useful signals overlap with useless interference and noise present in the space, posing significant challenges for interference monitoring. Through the analysis of key technologies for satellite navigation system interference monitoring, it can be anticipated that future interference monitoring will face even more severe challenges, with a focus on the development of interference monitoring technologies that offer high precision, high sensitivity, and high real-time performance.

### 4.1 Highly sensitive real-time interference detection

As interference technology advances, the power required to generate the same interference effect on GNSS receivers is decreasing. Moreover, when multiple interferences with significantly different power levels coexist, the lower-power interference can be overwhelmed by the higher-power interference, leading to a high probability of missed detections during interference monitoring and posing potential assessment risks. Detection equipment monitors interference within its vicinity. Enhancing the sensitivity of interference detection equipment can effectively detect low-power interferences, expand the range of interference detection, reduce the number of devices required for full-area monitoring, and lower the cost of the monitoring system.

Furthermore, if interference detection equipment can quickly identify interference, people can promptly take interference suppression measures to reduce its harmful effects. This requires the detection equipment to adopt low-complexity detection algorithms while ensuring sensitivity. This requires the detection equipment to ensure sensitivity while also maintaining real-time performance.

### 4.2 Intelligent automatic interference identification

GNSS receivers are sometimes subjected to more than one type of interference simultaneously, and the impacts of different types of interference on them are generally different. Separating and identifying these mixed interferences individually allows for an analysis of the effects of each on the terminal equipment, facilitating more informed decision-making. To achieve better interference effects, new types of interference continue to emerge. For previously identified interference types, rapid identification of their types should be possible upon re-interference, which can be achieved by establishing an interference library. For new types of interference that have never been identified before, the monitoring system's identification should also possess a certain degree of generalization ability, correctly identifying the new type of interference and adding it to the interference library.

With technological advancements, satellite navigation interference monitoring can integrate artificial intelligence, machine learning, and other technologies. Through self-learning and evolution, intelligent algorithms can continuously adapt to changing interference characteristics, achieving automatic identification and classification of interference signals with high accuracy. Furthermore, they can even predict the occurrence of interference. This deep integration of technologies can save significant human resources and greatly enhance efficiency and accuracy.

### 4.3 High-precision interference direction finding under complex conditions

Typically, the interference monitoring equipment and the interfered terminals are not located at the same geographical position, making the direction of interference arbitrary for the monitoring equipment. In complex terrain conditions such as "urban canyons," mountainous regions, jungles, or in the presence of moving obstructions or drastic meteorological changes, the interference signals are prone to various physical phenomena during propagation, including reflection and refraction, which can lead to multipath effects. These effects can reduce the accuracy of direction finding, cause ambiguity in direction finding, and result in unstable direction finding outcomes. The precision of interference direction finding directly impacts the results of interference source localization. If the interference source is located far from the monitoring equipment, even a slight deviation in the direction finding angle can result in a significant discrepancy between the localized position of the interference source and its actual location.

The premise of direction finding for multipath signals is to extract the direct interference from the detected interference signals. Improvements and optimizations to multipath resolution algorithms can be made in terms of real-time performance, implementation difficulty, and complexity. By integrating direction finding with generative AI (Artificial Intelligence) technologies, an adaptable direction finding model can be constructed that automatically adapts to complex and dynamic propagation environments, enhancing the intelligence level of the direction finding system. Furthermore, the direction finding system can introduce multi-modality and perform data fusion to address multipath interference issues.

### 4.4 Comprehensive and large-scale interference monitoring

Currently, the development of the GNSS interference monitoring network in China is still incomplete, and the capability for comprehensive interference monitoring across the entire region remains inadequate. The evolution of the monitoring network should target intelligence and automation, fully leveraging artificial intelligence, big data, and cloud computing technologies to enable real-time analysis of vast amounts of monitoring data.

Joint monitoring is a necessary means for interference monitoring. On one hand, emphasizing multinational joint monitoring on a global scale and strategically deploying interference monitoring stations worldwide can ensure comprehensive coverage. On the other hand, it is crucial to develop and integrate various interference monitoring platforms, including ground-based, air-based, space-based, and sea-based systems, to effectively tackle complex monitoring environments.

## 5 Conclusion

Interference monitoring serves as an indispensable cornerstone for maintaining the robust operation of various systems, playing a crucial role in ensuring their performance. Focusing on the domain of GNSS interference monitoring, the current system faces unprecedented challenges in multiple aspects, including technological iteration, infrastructure construction, and international collaboration. To gain a profound understanding of the essence of these challenges and explore effective strategies to address them, this paper systematically traces the developmental history of interference monitoring systems since their inception. It provides a comprehensive and in-depth analysis of the intrinsic mechanisms and unique characteristics of several core interference monitoring technologies. Building on this foundation, the paper reviews the breakthrough advancements in these key technologies over recent years. It delves deeply into the enhanced understanding of technical principles and broadly explores the continuous expansion and innovation in application domains. Through detailed examination and analysis, we gain insights into the significant potential of these technologies in improving monitoring accuracy, enhancing system robustness, and driving technological innovation. Through the review and analysis presented in this paper, we aim to provide scholars in the relevant fields with a comprehensive and in-depth report on interference monitoring technologies. We hope to inspire their innovative thinking and research enthusiasm, contributing valuable wisdom and strength to the continuous advancement and widespread application of interference monitoring technologies.

## Author contributions

YH: Writing–original draft, Writing–review and editing. BL: Writing–review and editing. JC: Writing–review and editing. ZW: Writing–review and editing. WX: Writing–review and editing. ZL: Writing–review and editing.

## Funding

The author(s) declare that financial support was received for the research, authorship, and/or publication of this article. National Natural Science Foundation of China under Grant U20A20193 and Independent scientific research project of key military scientific research laboratory of satellite navigation technology under Grant WXDHS2023110.

## Conflict of interest

Author ZW was employed by Transcom (Shanghai) Technology Co., Ltd.

The remaining authors declare that the research was conducted in the absence of any commercial or financial relationships that could be construed as a potential conflict of interest

## Publisher's note

## References

1. Hegarty CJ, Chatre E. Evolution of the global navigation satellite system (GNSS). *Proc IEEE* (2008) 96(12):1902–17. doi:10.1109/jproc.2008.2006090

2. Yalvac S. Investigating the historical development of accuracy and precision of Galileo by means of relative GNSS analysis technique. *Earth Sci Inform* (2021) 14(1):193–200. doi:10.1007/s12145-020-00560-8

3. Bonnor N. A brief history of global navigation satellite systems. *The J Navigation* (2012) 65(1):1–14. doi:10.1017/s0373463311000506

4. Xie J, Kang CB. Engineering innovation and the development of the BDS-3 navigation constellation. *Engineering* (2021) 7(5):558–63. doi:10.1016/j.eng.2021.04.002

5. Santra A, ahato S, andal S, Dan S, Verma P, Banerjee P, et al. Augmentation of GNSS utility by IRNSS/NavIC constellation over the Indian region. *Adv Space Res* (2019) 63(9):2995–3008. doi:10.1016/j.asr.2018.04.020

6. Li XP, Pan L, Yu WK. Assessment and analysis of the Four-Satellite QZSS precise point positioning and the integrated data processing with GPS. *IEEE Access* (2021) 9:116376–94. doi:10.1109/access.2021.3106050

7. Yan K. *Research on GNSS vulnerability simulation and assessment platform technology*. Shanghai: Shanghai Jiaotong University (2013) p. 1–6.

8. Li XJ, Lu ZK, Yuan MZ, Liu WX, Wang FX, Yu Y, et al. Tradeoff of code estimation error rate and terminal gain in SCER attack. *IEEE Trans Instrum Meas* (2024). doi:10.1109/TIM.2024.3406807

9. Ioannides RT, Pany T, Gibbons G. Known vulnerabilities of Global Navigation Satellite Systems, status, and potential mitigation techniques. *Proc IEEE* (2016) 104(6):1174–94. doi:10.1109/jproc.2016.2535898

10. ROIIT. Top 10 GPS spoofing events in history (2024) Available from: https://threat.te-chnology/top-10-gps-spoofing-events-in-history/ (Accessed March 15, 2024).

11. Zhu PC. *Research on GNSS interference detection and identification technologies*. Chongqing: Chongqing University (2018) p. 41–57.

12. Wu RB, Wang WY, Lu D, Wang L, Jia Q. *Adaptive interference suppression technology of GNSS*. Beijing: First Edition (2015).

13. Lv DK, Zhang YJ. A space-time-frequency domain combined anti-jamming technique for GPS. *Electron Des Eng* (2019) 27(01):94–8. doi:10.14022/j.cnki.dzsjgc.2019.01.019

14. Song J, Lu ZK, Liu Z, Xiao ZB, Dang C, Wang ZY, et al. Review on the time domain interference suppression of navigation receiver. *Syst Eng Electronics* (2023) 45(04):1164–76. doi:10.12305/j.issn.1001-506X.2023.04.25

15. Zhang Z, Deng K, Zhang Y, Liu YL, Zhu LD. Research on radio frequeney domain interference cancellation technology for non-cooperative signals. *Radio Commun Technology* (2024) 1–10.

16. Li G. Analysis ofultidimensional domain anti-interference technology in satellite communication. *Electron Technology* (2024) 53(05):248–9. doi:10.3969/j.issn.1000-0755.2024.05.111

17. Zheng BW, Liu H, Zhai GW, Meng MZ, Li HP. Research on airspace anti-jamming technology based on variable step size LMS algorithm. *J Telemetry,Tracking Command* (2024) 45(04):75–80. doi:10.12347/j.ycyk.20240228001

18. Qiao J, Lu ZK, Lin BJ, Song J, Xiao ZB, Wang Z A survey of GNSS interference monitoring technologies. *Front Phys* (2023) 11. doi:10.3389/fphy.2023.1133316

19. Borio D, O'Driscoll C, Fortuny J. GNSS jammers: effects and countermeasures. In: *6th ESA workshop on satellite navigation technologies (navitec 2012) and European workshop on GNSS signalsand signal processing*. Noordwijk, Netherlands: IEEE (2012) p. 1–7.

20. Zhao HZ. *Research on interference detection technology based ontime-frequency analysis in GNSS receiver*. Anhui: Hefei University of Technology (2017) p. 26–40.

21. Wang P. *Detection anditigation of chirp-style jammer for global navigation satellite systems receivers*. Beijing: Beijing Institute of Technology (2018) p. 80–90.

22. Zhang J. Research on fractional time-frequency analysis based anti-interference techniques for GNSS receivers. *Anhui: Hefei Univ Technology* (2020) 28-30:44–5. doi:10.27101/d.cnki.ghfgu.2020.001935

23. Zheng YF. *Satellite navigation interference detectionethod based on fractional time-frequency transform*. Anhui: Hefei University of Technology (2022) p. 36–7. doi:10.27101/d.cnki.ghfgu.2022.000842

24. Chen G. American civil aviation radio interference monitoring system. *China Radio* 2004 (4):62–3. doi:10.3969/j.issn.1672-7797.2004.04.022

25. Fan J, Li HY, Fei W, Li JC. The construction of an integrated platform to achieve a new leap in radio monitoring. *China Radio* (2016) (4) 26–9. doi:10.3969/j.issn.1672-7797.2016.04.010

26. *Picture of disturbance monitoring direction finding machine*. (2024). Available from: https://cn.bing.com/images/search?q=%E5%B9%B2%E6%89%B0%E7%9B%91%E7%9B%91%E6%B5%8B%E6%B5%8B%E5%90%91%E6%9C%BA%E5%9B%BE%E7%89%87&form=IQFRML&first=1. [Accessed, March 15, 2024].

27. Wang SL, Luo JS, Wei P, Hu L, Lai PH, Wang H, et al. *Cognitive communication anti-jamming*. Beijing: First Edition (2023).

28. Simonsen K, Suycott M, Crumplar R, Wohlfiel J. LOCO GPSI: preserve the GPS advantage for defense and security. *IEEE Aerospace Electron Systemsagazine* (2004) 19(12):3–7. doi:10.1109/maes.2004.1374060

29. Guo XQ. *Study on interference detection and identification technology of Beidou satellite navigation*. Beijing: Beijing Jiaotong University (2018).

30. Huang T *The key technology research on blanketing jamming monitoring of satellite navigation system*, 2-5. Hunan: Hunan University (2014) p. 15–9.

31. HawkEye 360. (2024). Available from: https://www.he360.com/our-products/. [Accessed, March 15, 2024].

32. Hao CY. Overview of Hawkeye 360space-based radio monitoring system. *China Radio* (2023)(1) 52–4, 62. doi:10.3969/j.issn.1672-7797.2023.01.041

33. Fan GW, Chao L, Liu L. Overview of GNSS interference monitoring techniques. In: *Proc. Of the 13th national annual conference on remote sensing, telemetry and remote control* (2012) p. 617–20.

34. ao WL, Wang WM, Sheen J, Chen P. The UKF-based RNN predictor for GPS narrowband interference suppression. In: *2012 Australian communications theory workshop (AusCTW)*. New Zealand: IEEE (2012) p. 7–12.

35. Van Dererwe JR, Franco DC, Jdidi D, Feigl T, Rugamer A, Felber W. *Low-cost COTS GNSS interference detection and classification platform: initial results//2022 Internation-al Conference on Localization and GNSS (ICL-GNSS)*. IEEE (2022) p. 1–8.

36. Wu J, Liao YP. An improved algorithm for energy detection andfull blind detection of eigenvalue. *Appl Sci Technology* (2023) 50(04):66–70. doi:10.11991/yykj.202211008

37. Wang J. *Research on Beidou civil signal interference detection technology*. Tianjin: Civil Aviation University of China (2019) p. 36–9.

38. Fan GW, Deng JN, Wang ZH, Cao L. Study of GNSS interference detection technology based on energy detection. *Radio Eng* (2013) 43(3):33–5. 39. doi:10.3969/j.issn.1003-3106.2013.03.010

39. Henttu P, Aromaa S. Consecutive mean excision algorithm. *IEEE Seventh Int Symp Spread Spectr Tech Appl* (2002) 2:450–4. doi:10.1155/2010/459623

40. Saamisaari H, Henttu P. Impulse detection and rejection methods for radio systems. In: *IEEEilitary communications conference*, 2. Boston,A, USA (2003) p. 1126–31.

41. Yang C, Xu K, Yang HL. Study on detection for interference signals in satellite communication. *Command Control and Simulation* (2016) 38(06):125–8. doi:10.3969/j.issn.1673-3819.2016.06.026

42. Vartiainen J, Lehtomaki JJ, Saarnisaari H *Double-Threshold based narrowband signal extraction//2005 IEEE 61st Vehicular Technology Conference*, 2. Stockholm, Sweden: IEEE (2005) p. 1288–92.

43. Liu W. *Satellite navigation receiver interference detection technology research*. Anhui: Hefei University of Technology (2014).

44. Borio D, Camoriano L, Savasta S, Presti L. Time-Frequency excision for GNSS applications. *IEEE Syst J* (2008) 2(1):27–37. doi:10.1109/jsyst.2007.914914

45. Wang P, Cetin E, Dempster AG, Wang YQ, Wu SL. GNSS interference detection using statistical analysis in the Time-Frequency domain. *IEEE Trans Aerospace Electron Syst* (2018) 54(1):416–28. doi:10.1109/taes.2017.2760658

46. Zhou HX, Dai QH, Li YD, Lu XG. Non-existence of time-frequency distributions without cross-term interference and with WVD clustering. *Sci China (Series E)* (2001) (4) 348–54. doi:10.3969/j.issn.1674-7259.2001.04.008

47. Sun KW, Jin T, Yang D. A new reassigned spectrogram method in interference detection for GNSS Receivers. *Sensors* (2015) 15(9):22167–91. doi:10.3390/s150922167

48. Sun KW, Zhang J. A GNSS interference detection method based on fractional order Time-Frequency analysis. In: *Proc. Of the 10th China satellite navigation academic conference* (2019) p. 1–5.

49. Xu HF, Liu F, Zhang X. Detection and parameter estimation of strong and weak LFM signals in the Fractional Fourier domain. *Joural Signal Process.* (2011) 27(7):1063–8. doi:10.3969/j.issn.1003-0530.2011.07.016

50. Chen YY. *Satellite navigation interference detection technology based on transform domain analysis*. Anhui: Hefei University of Technology (2022).

51. Zhao HZ, Sun KW. GNSS receiver interference detection based on rearranged wavelet transform. *Technology Innovation Appl* (2017) 11:13–5.

52. Sun KW, Zhang L. *A novel interference detection based on wigner-hough transform for GNSS receivers//proc. Of the 10th China satellite navigation academic conference* (2019) p. 1–7.

53. Zeng YH, Liang YC. Spectrum-sensing algorithms for cognitive radio based on statistical covariances. *IEEE Trans Vehicular Technology* (2009) 58(4):1804–15. doi:10.1109/TVT.2008.2005267

54. Zeng YH, Liang YC. Eigenvalue-based spectrum sensing algorithms for cognitive radio. *IEEE Trans Commun* (2009) 57(6):1784–93. doi:10.1109/TCOMM.2009.06.070402

55. Liu HH, Deng XH, Chen W. Blind sensing algorithm based on eigenvalue in multiple antennas cognitive radio. *Appl Res Comput* (2015) 32(01):191–3. doi:10.3969/j.issn.1001-3695.2015.01.043

56. Lei KJ, Yang X, Xiang CQ, Wang XM, Tian K, Tan ZW. A total blindulti-antenna spectrum sensing algorithm based on difference of extreme eigenvalues. *J Hunan Univ (Natural Sciences)* (2023) 50(12):76–85. doi:10.16339/j.cnki.hdxbzkb.2023300

57. Li YX, Lei J, Zhong SY, Huang CM, Huang C. Covariance blind detectionethod based on eigenvector in cognitive radio network. *Telecommunications Sci* (2015) 31(11):104–8.

58. Jiao CH, Wang KR, Feng H. Cooperative blind sensing based on autocorrelation matrix in cognitive radios. *J Circuits Syst* (2011) 16(01):12–9. doi:10.3969/j.issn.1007-0249.2011.01.003

59. Liu HH. *Multi-user cooperative spectrum sensing in cognitive radio*. Hubei: Wuhan University of Technology (2014).

60. Li PJ. *Research of cooperative spectrum sensing technology based on adaptive double thresholds in cognitive radio network*. Chongqing: Chongqing University of Posts and Telecommunications (2013).

61. Wu J. *Research on interference detection and recognition technology in BDS. Heilongjiang*. Harbin Engineering University (2023).

62. Qu YT. *Research on intelligence spectrum sensing algorithm based on signal energy distribution*. Jiangsu: Nanjing University of Posts and Telecommunications (2021).

63. Yao D, Liu HJ, Liu J, Xie ZC. Support vector machine based spectrum sensing algorithm in cognitive radio. *Electron Des Eng* (2018) 26(21):1–5. doi:10.14022/j.cnki.dzsjgc.2018.21.001

64. Shi HD, Jiang B, Bao JR, Liu C. Cooperative spectrum sensing with Covarianceatrix decomposition and CNN. *J Hangzhou Dianzi Univ (Natural Sciences)* (2024) 44(01):1–5. doi:10.13954/j.cnki.hdu.2024.01.001

65. Lu HC, Zhao ZJ, Shang JN, Dai SG. Cooperative spectrum sensing algorithm using convolutional neural networks and covariance. *J Signal Process* (2019) 35(10):1700–7. doi:10.16798/j.issn.1003-0530.2019.10.010

66. Lorraine KJS, Ramarakula M. A comprehensive survey on GNSS interferences and the application of neural networks for anti-interference. *IETE J Res* (2023) 69(7):4286–305. doi:10.1080/03772063.2021.1953407

67. Li J, Huang YB, Nie J, Wang FX. Parameter selection analysis of matched spectrum interference. In: *2015 4th international conference on computer science and network technology (ICCSNT)*. Harbin, China: IEEE (2015) p. 1340–4.

68. Qin W, Dovis F. Situational awareness of chirp interference threats to GNSS based on supervised machine learning. *IEEE Trans Aerospace Electron Syst* (2022) 58(3):1707–20. doi:10.1109/TAES.2021.3135014

69. Ma PC, Tang XM, Lou SQ, Liu KX, Ou G. Code tracking performance analysis of GNSS receivers with blanking model under periodic pulse interference. *Radio Eng* (2021) 30(1):184–95. doi:10.13164/re.2021.0184

70. Borio D. GNSS Acquisition in the presence of continuous wave interference. *IEEE Trans Aerospace Electron Syst* (2010) 46(1):47–60. doi:10.1109/taes.2010.5417147

71. Zeng CZ, Jia X, Zhu WG. Odulation classification of communication signals. *Commun Technology* (2015) 48(3):252–7. doi:10.3969/j.issn.1002-0802.2015.03.002

72. ahadevkar SV, Khemani B, Patil S, Kotecha K, Vora D, Abraham A. A review on machine learning styles in computer vision-techniques and future directions. *IEEE Access* (2022) 10:107293–329. doi:10.1109/ACCESS.2022.3209825

73. Zhang XY, Liu CL, Suen CY. Towards robust pattern recognition: a review. *Proc IEEE* (2020) 108(6):894–922. doi:10.1109/jproc.2020.2989782

74. Nandi AK, Azzouz EE. Algorithms for automatic modulation recognition of communication signals. *IEEE Trans Commun* (1998) 46(4):431–6. doi:10.1109/26.664294

75. Nandi AK, Azzouz EE. Odulation recognition using artificial neural networks. *Signal Process.* (1997) 56(2):165–75. doi:10.1016/S0165-1684(96)00165-X

76. Azzouz EE, Nandi AK. Automatic modulation recognition-I. *J Franklin Inst* (1997) 334B(2):241–73. doi:10.1016/s0016-0032(96)00069-5

77. Safavian SR, Landgrebe D. A survey of decision tree classifier methodology. *IEEE Trans Systems,an, Cybernetics* (1991) 21(3):660–74. doi:10.1109/21.97458

78. Cortes C, Vapnik V. Support-vector networks. *achine Learn* (1995) 20(3):273–97. doi:10.1007/bf00994018

79. Lei L. *GNSS satellite navigation system interference monitoring technology research*. Lanzhou: Lanzhou Jiaotong University (2017) p. 30–5.

80. Li J, Wang FX, Li BY, Li CH. An automatic modulation type interference recognition method. In: *Proc. Of the 5th China satellite navigation academic conference* (2014) p. 5.

81. Ye R. Research on satellite navigation interference feature recognition technology. In: *Sichuan*. University of Electronic Science and Technology of China (2019) p. 49–59.

82. Lu DS, Huang L, Long H. A civil aviation GPS interference recognition method based on deep learning. *Commun Technology* (2022) 55(3):330–8.

83. Hinton GE, Salakhutdnov RR. Reducing the dimensionality of data with neural networks. *Science (New York, N.Y.)* (2006) 313(5786):504–7. doi:10.1126/science.1127647

84. Lecun Y, Bengio Y, Hinton G. Deep learning. *Nature* (2015) 521(7553):436–44. doi:10.1038/nature14539

85. Li XJ, Fu D, ou WH, Liu WX, Wang FX. An identification method of navigation signal interference type based on SqueezeNet model. In: *2020 IEEE 9th joint international information technology and artificial intelligence conference (ITAIC)*. Chongqing, China: IEEE (2020) p. 875–80.

86. ehr IE, Dovis F. Detection and classification of GNSS jammers using convolutional neural networks. In: *2022 international conference on localizatio and GNSS (ICL-GNSS). Tampere*. Finland: IEEE (2022).

87. Chen X, He D, Yan XY, Yu WX, Truong TK. GNSS interference type recognition with fingerprint spectrum DNN method. *IEEE Trans Aerospace Electron Syst* (2022) 58(5):4745–60. doi:10.1109/taes.2022.3167985

88. Yu J, Alhassoun M, Buehrer RM. Interference classification using deep neural networks. In: *2020 IEEE 92nd vehicular technology conference (VTC2020-Fall)*. IEEE (2020) p. 1–6.

89. Wang P, Cheng YF, Dong BH, Xu H. Convolutional neural network-based interference recognition. In: *2020 IEEE 20th international conference on communication technology (ICCT)*. IEEE (2020) p. 1296–300.

90. Ge HF. *Detection and identification of SatelliteInterference signals*. Zhejiang: Hangzhou Dianzi University (2022) p. 35–41.

91. Zhang T. *Research on jamming detection and recognition techniques of satellite navigation system*. Shandong: Shandong University (2023) p. 48–53.

92. Zhang QC, Ji HB, Li L, Zhu ZG. A graph-based ABS-assisted TBS sleep scheme. *IEEE Wireless Commun Lett* (2024) 13(9):1. doi:10.1109/lwc.2024.3481467

93. Van Dererwe JR, Franco DC, Feigl T, Rugamer A. A deep neural network approach for classification of GNSS interference and jammer. *IEEE Trans Aerospace Electron Syst* (2024) 60(3):1–18. doi:10.1109/taes.2024.3462662

94. Wang PY, Cheng YF, Shang GY, Wang J, Li S. Time-frequency component-aware convolutional neural network for wireless interference classification. *IEEE Wireless Commun Lett* (2022) 11(12):2487–91. doi:10.1109/lwc.2022.3204756

95. Jiang M, Ye ZQ, Xiao Y, Gou XG. Federated transfer learning aided interference classification in GNSS signals. *2024 Ieee/cic Int Conf Commun China (Iccc) IEEE* (2024) 1988–93. doi:10.1109/ICCC62479.2024.10681801

96. Xu ZJ, Han JY. Overview of radio direction finding system. *China Radioanagement* (2002) (3) 29–35. doi:10.3969/j.issn.1672-7797.2002.03.013

97. Zhou YQ, Chen Z, Huangfu K, Sun ZK. Algorithm of solving multi-baseline interfer-ometer phase difference ambiguity in noisy circumstance. *J Electronics and Inf Technology* (2005) 27(2):259–61.

98. Li P. *Research on direction finding system of two-channel correlation interferometer*. Xian: Xi'an University of Electronic Science and Technology (2009).

99. Yu B, Song Z. Survey of spatial spectrum estimation techniques. *China Radar* (2004) (4) 21–5.

100. Schmidt R. Ultiple emitter location and signal parameter estimation. *IEEE Trans Antennas Propagation* (1986) 34(3):276–80. doi:10.1109/TAP.1986.1143830

101. Han QQ. *The Technology Research of multi-signal recognition and suppress interference direction finding. Heilongjiang*. Harbin Engineering University (2013) p. 16–7.

102. Roy R, Paulraj A, Kailath T. ESPRIT-A subspace rotation approach to estimation of parameters of cisoids in noise. *IEEE Trans.on Acoustics, Speech, Signal Process.* (1986) 34(5):1340–2. doi:10.1109/tassp.1986.1164935

103. Song HT, Zheng XD, Fan GW. Design of GNSS interference direction finding antenna. *Digital Commun World* (2017) (8) 5–7, 18. doi:10.3969/J.ISSN.1672-7274.2017.08.002

104. Zhu L. *Research and implementation of in-terference recognition and direction finding technology in BeiDou navigation satellite system*. Beijing: Beijing Jiaotong University (2019).

105. Li XX. *Research and implementation of anti-jamming antenna direction finding technology for BeiDou navigation*. Beijing: Beijing Jiaotong University (2019).

106. Fan GW, Yu BG, Deng ZX, Chen PL. Research on adaptive array elements calibration algorithm in GNSS interference direction detection. *Computer Simulation* (2012) 29(11):141–4. doi:10.3969/j.issn.1006-9348.2012.11.033

107. Jiang YL, Zhang W, Chen T, Zhang YX. A phase calibrationethod of passive direction-finding channel based on convolutional neural network. *Res Exploration Lab* (2023) 42(07):54–7. doi:10.19927/j.cnki.syyt.2023.07.011

108. Zou YF, Yang JP, Wang HC, Liu P. GNSS complex electromagnetic environment integrated monitoring direction finding and analysis assessment technology. *Navigation Positioning and Timing* (2001) 8(5):88–95. doi:10.19306/j.cnki.2095-8110.2021.05.012

109. Yin Z, Zhen WM, Jin RM, Lin ZY, Wang RZ, Che L. ulti-interference source direction finding and positioning technology for satellite navigation and its application. *GNSS World of China* (2023) 48(1):111–6. doi:10.12265/j.gnss.2023006

110. Yao ZC, Xu JN, Yang J, Wang HY. An improved interferometer-MUSIC joint direction finding algorithm. *J Ordnance Equipment Eng* (2023) 44(11):240–7. doi:10.11809/bqzbgcxb2023.11.030

111. Jin RH. Wireless direction finding technology based on TMA//national conference of antenna - NCANT,2023.

112. He C. *Theory and application research for timeodulated array*. Shanghai: Shanghai Jiao Tong University (2015) p. 50–2.

113. Chen JF. *Research on timeodulated array: theory and its application in direction finding*. Shanghai: Shanghai Jiao Tong University (2018) p. 84–93.

114. Du HM, Fu CN. A single channel DOA estimationethod based on timeodulated array. *J Detect and Control* (2017) 39(1):111–5.

115. Wang MQ, He C, Xiang D, Cao AJ, Yang Y, You YH. A full-angle direction finding method with a single channel based on time modulated multi-beam array. *Chin J Radio Sci* (2024) 39(2):296–304. doi:10.12265/j.cjors.2023079

116. Liu H, Chen JF, Yang L, Ni G, He C, Jin RH. ulti-harmonic direction-finding method in time-modulated array based on frequency spectrum property analysis. *Chin J Radio Sci* (2023) 38(1):123–9. doi:10.12265/j.cjors.2021275

117. Lin YL, Wang WJ, Wu JW, Cheng Q. High-precision direction finding based on timeodulation array with single radio frequency channel and composite baselines. *J Electronics and Inf Technology* (2024) 46:5. doi:10.11999/JEIT231137

118. Bian DP, Zhao XN, Liu ZJ, Chen JF, Jin RH. Single-channel amplitude-comparison wideband direction finding method with nonuniform time modulation. *Chin J Ship Res* (2024) 19(4):282–9. doi:10.19693/j.issn.1673-3185.03367

119. Jiang Y, Li HH, Shuai YM. Broadband DOA estimation based on timeodulated array. *Ship Electron Eng* (2019) 39(7):60–2. 91. doi:10.3969/j.issn.1672-9730.2019.07.015

120. Yang L, Xia Y, Liu DP, He C, Chen JF, Jin HR. Omnidirectional broadband direction-finding method based on time-modulated array. *Chin J Radio Sci* (2023) 38(1):130–6. doi:10.12265/j.cjors.2002097

frontiers | Frontiers in Physics

TYPE Review
PUBLISHED 17 December 2024
DOI 10.3389/fphy.2024.1428544

OPEN ACCESS

EDITED BY
Zhu Xiao,
Hunan University, China

REVIEWED BY
Mandeep Singh,
National Institute of Technology, India
Jan M. Kelner,
Military University of Technology (WAT), Poland

*CORRESPONDENCE
Zukun Lu,
luzukun@nudt.edu.cn

RECEIVED 06 May 2024
ACCEPTED 23 September 2024
PUBLISHED 17 December 2024

CITATION
Lu C, Lu Z, Liu Z, Huang L and Chen F (2024) Overview of satellite nav spoofing and anti-spoofing techniques.
*Front. Phys.* 12:1428544.
doi: 10.3389/fphy.2024.1428544

# Overview of satellite nav spoofing and anti-spoofing techniques

Cheng Lu[1], Zukun Lu[1,2]*, Zhe Liu[1,2], Long Huang[1,2] and Feiqiang Chen[1,2]

[1]College of Electronic and Technology, National University of Defense Technology, Changsha, China, [2]Key Laboratory of Satellite Navigation Technology, Changsha, China

In recent years, satellite navigation systems have witnessed widespread adoption across diverse fields, including military surveillance, precision agriculture, traffic monitoring, resource exploration, and disaster assessment. However, navigation signals are susceptible to interference, with deceptive interference posing the most significant threat to navigation systems. This paper provides a comprehensive overview of satellite navigation spoofing and anti-spoofing techniques. It reviews the current state of spoofing and anti-spoofing technologies, analyzing advancements in spoofing techniques and the evolution of countermeasures. Furthermore, the paper elaborates on the impact of spoofing interference on receiver performance, examining its effects on positioning, timing, and velocity estimations. A detailed analysis of various anti-spoofing methods is presented, categorizing them into detection, identification, suppression, and localization techniques. This review aims to provide a thorough understanding of the evolving landscape of satellite navigation spoofing and anti-spoofing technologies, fostering further research and development efforts to ensure the integrity and resilience of satellite navigation systems in the face of sophisticated threats.

KEYWORDS

**satellite navigation, generative spoofing jamming, induced deceptive jamming, induced deceptive jamming monitoring, induced spoofing interference suppression**

## 1 Introduction

Global navigation satellite systems (GNSSs) provide ground users with continuous, all-weather, high-precision positioning, timing, and velocity information through navigation signals transmitted from artificial satellites [1]. The remarkable performance of GNSSs has led to their widespread adoption across civilian and military domains [2].

As shown in Figure 1, in the military domain, modern warfare increasingly relies on high-precision positioning and velocity data for the precise control of precision-guided weapons, aircraft, ships, and various vehicular equipment. Satellite navigation systems are thus a critical enabler for land, sea, and air weapon systems, facilitating the construction of fully digitized battlefields.

GNSS technology has permeated many industries in the civilian domain, including providing precise timing for power systems, navigation for civil aviation and vehicles, and high-precision positioning and timing services for ship navigation. It plays a crucial role in disaster relief efforts and numerous aspects of daily life, becoming an indispensable component of modern society's infrastructure.

Navigation signals, typically transmitted from satellites to ground receivers, are susceptible to various intentional and unintentional disruptions due to long-distance propagation and low signal power at ground reception [3, 4]. Moreover, the

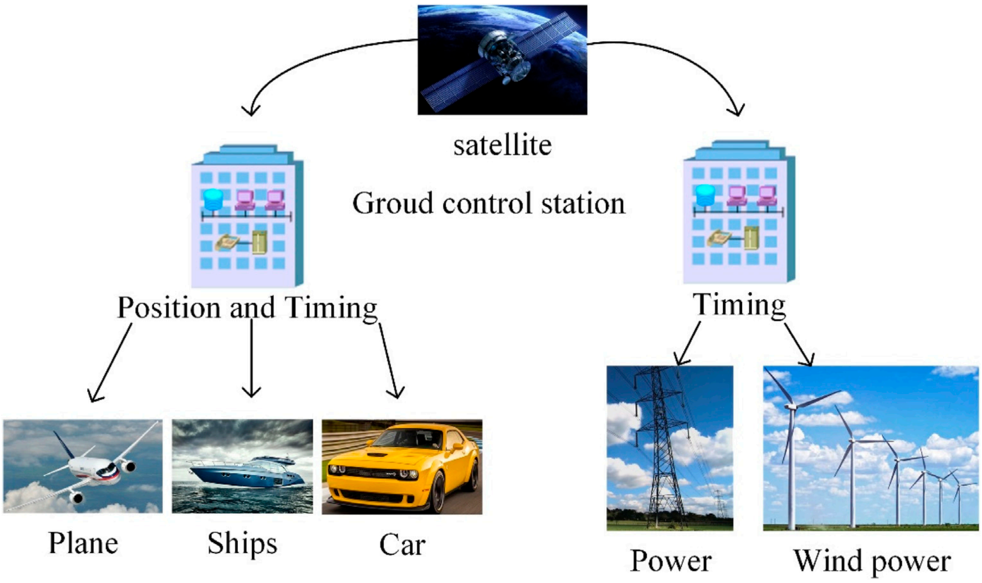

FIGURE 1
Role of satellites in civil navigation.

information transparency and open signal characteristics of navigation systems [5, 6], particularly the detailed specifications and descriptions of civilian GNSS control interface documents (ICDs) regarding carrier frequency, modulation schemes, and navigation messages [7], make them highly vulnerable to information tampering and deceptive spoofing attacks, posing significant threats to navigation systems. Spoofing signals, with power levels comparable to genuine navigation signals, exhibit high stealthiness and efficiently disrupt navigation receivers, resulting in inaccurate positioning and timing information and potentially catastrophic consequences [8]. This is particularly concerning in the case of drones, where spoofing interference can manipulate the drone's navigation system through pseudo-range spoofing, leading to erroneous positioning results [9, 10].

This paper delves into the mechanisms of GNSS spoofing attacks and explores a range of countermeasures. The paper begins by examining the vulnerabilities of GNSS receivers to spoofing attacks, highlighting the security threats they pose. It then analyzes the strategies and mechanisms employed in spoofing attacks, providing a comprehensive overview of different attack methodologies. The paper further examines the impact of spoofing signals on targeted receivers, delving into the underlying principles of induced spoofing attacks and their rapid evolution in recent years. Subsequently, the paper explores various anti-spoofing technologies tailored to counter different spoofing attacks. This includes an analysis of five signal-level spoofing detection techniques, examining advancements in deep learning-based spoofing identification techniques and providing a summary of the application scenarios and performance characteristics of various anti-spoofing technologies. Finally, the paper concludes by presenting methods for locating the source of spoofing interference.

To make it easier for readers to understand this survey, Table 1 lists some important abbreviations and their meanings. These abbreviations apply only to this survey. Specific explanations are given in Table 1.

## 2 Current status and case studies of spoofing

The concept of spoofing interference in satellite navigation systems, first detailed in 2003 by British researchers D.J. Shepherd and M.G. Bitterlin [11], has transitioned from a theoretical possibility to a demonstrable reality [12]. Early research outlined the potential for such attacks and proposed basic countermeasures, but advancements in technology and increasing threats have spurred further investigation and a deeper understanding of spoofing interference. The danger has manifested in real-world scenarios, with notable examples including the capture of American unmanned reconnaissance aircraft, "RQ-170" and "Scan Eagle," by Iranian forces in 2011 and 2012, respectively [13, 14]. These operations reportedly employed spoofing techniques to disrupt communication between the drones and their satellites, transmitting deceptive signals that lured them to land. Further experiments conducted by Professor Todd Humphreys' team in 2012 demonstrated the feasibility of hijacking GPS-guided drones and manipulating their navigation systems using spoofing signals [15]. Later that year, the team successfully hijacked a civilian drone at the U.S. Army's White Sands Missile Range, highlighting the vulnerability of civilian drones to spoofing attacks [16]. In 2013, the team demonstrated the potential for spoofing attacks at sea by successfully diverting an $80 million yacht from its course using a compact GPS spoofing jammer [16]. These experiments, along with others conducted by M.L. Psiakiand and T.E. Humphreys in 2017 [17], underscore the susceptibility of GNSS receivers to spoofing attacks and the challenge for users in detecting such interference.

In April 2013, at the Hack in the Box security conference in Amsterdam, Hugo Teso, a commercial pilot and engineer from a German cybersecurity company, unveiled the PlaneSploit application, a tool capable of bypassing aircraft security systems

TABLE 1 Abbreviations table.

| Abbreviation | Meaning | Abbreviation | Meaning |
|---|---|---|---|
| AOA | Angle of arrival | BPNN | Backpropagation neural network |
| CDMA | Code division multiple access | CNN | Convolutional neural network |
| CNR | Carrier-to-noise ratio | CRPD | Carrier-phase single difference |
| CSI | Channel state information | DLLS | Delay-locked loops |
| FDOA | Frequency difference of arrival | FLLS | Frequency-locked loops |
| FWHM | Full width half maxima | GNSS | Global navigation satellite system |
| GSI | Generative spoofing interference | ICD | Interface control document |
| IF | Intermediate frequency | INS | Inertial navigation units |
| MIMO | Multiple-input multiple-output | PLLS | Phase-locked loops |
| PRN | Pseudo-random noise code | PRDD | Pseudo-range double differences |
| RAIM | Receiver autonomous integrity monitoring | RF | Radio frequency |
| SNR | Signal-to-noise ratio | SQM | Signal quality monitoring |
| SVM | Support vector machines | TDOA | Time difference of arrival |
| TOA | Time of arrival | UAV | Unmanned aerial vehicle |

and gaining control of the aircraft's computer systems [18]. Teso successfully demonstrated PlaneSploit's capabilities by altering the flight path, adjusting air conditioning settings, and even simulating a crash landing, highlighting the significant risks posed by such attacks. In 2017, the Unicorn Team, a hacking group affiliated with 360 company, further demonstrated the feasibility of spoofing civilian GPS devices at the Def Con hacking conference in the United States. Later that year, they showcased their ability to spoof the BeiDou navigation system at the POC hacking conference, demonstrating the global reach of spoofing capabilities. In 2018, the U.S. Navy conducted a real-world spoofing attack simulation exercise named "Sea Lion Father" in the Pacific Ocean. The exercise involved using false GPS signals to disrupt the electronic equipment of their vessels, effectively counteracting the real positioning capabilities of their location and navigation systems. This exercise highlighted the potential for spoofing to disrupt critical maritime operations, emphasizing the urgent need for robust countermeasures.

## 3 Analysis of spoofing interferes

Satellite navigation signals employ direct sequence spread spectrum modulation composed of three components: carrier, pseudo-random code, and navigation message data code. The carrier, residing at the bottom layer of the satellite navigation signal, carries the pseudocode and navigation message. The pseudo-random code is used primarily for spreading the data code, and the data code stores the satellite ephemeris. The specific signal can be represented by the following Equation 1:

$$S(t) = \mathrm{A} \times C(t) \times D(t) \times \cos(\omega t + \varphi). \tag{1}$$

A represents the amplitude, $C(t)$ represents pseudocode, $D(t)$ represents the data code, $\omega$ represents the carrier frequency, and $\varphi$ represents the carrier phase.

Spoofing operates by transmitting signals that mimic the format of authentic satellite navigation signals with altered parameters, targeting the receiver. The receiver, unaware of the manipulation, captures and tracks these spoofed signals, resulting in erroneous positioning and timing data. There are two primary categories of spoofing interference: generative spoofing and forwarding spoofing.

### 3.1 Relay-based spoofing interference

Relay-based spoofing interference operates by forwarding intercepted genuine satellite navigation signals, effectively extending their propagation time and introducing inaccuracies into positioning results [19, 20]. To ensure that the relayed spoofed signal is captured and tracked by the receiver, it is typically transmitted with a power approximately 2 dB higher than the genuine satellite signal [21]. Relay-based spoofing interference can be categorized into two types: single-antenna and multi-antenna. Single-antenna relay-based spoofing utilizes a single omnidirectional antenna to receive, amplify, delay, and forward signals from all satellites within its field of view. As the interference device introduces the same additional delay to all visible satellite signals, this method can induce deviations in the target receiver's positioning but cannot precisely control or set the final position. Multi-antenna relay-based spoofing interference, however, employs multiple omnidirectional antennas, each corresponding to a visible satellite in its field of view. This allows for the introduction of distinct delays and Doppler shifts to each visible satellite signal, enabling precise control over the target receiver's positioning and even directing it to a predetermined false location. In terms of effectiveness and covertness, multi-antenna relay-based spoofing interference aligns better with the requirements of future information warfare, such as navigation warfare and time warfare. Its potential applications in these domains make it a valuable area of ongoing research.

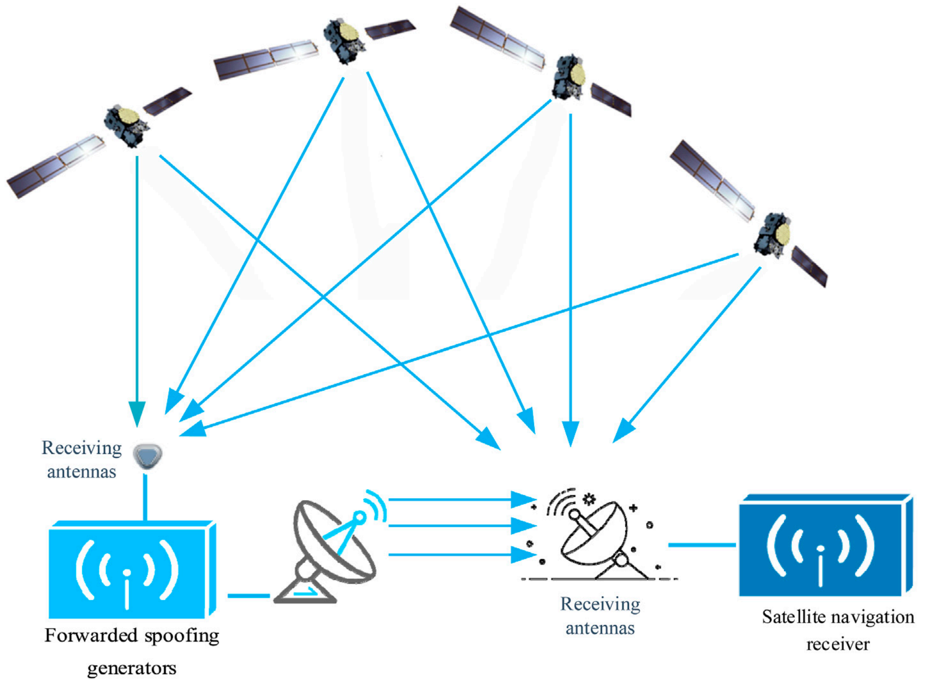

FIGURE 2
Schematic diagram of relay-based spoofing interference.

Despite its advantages, current research has identified a significant drawback of multi-antenna relay-based spoofing interference. When the distance between the interference device and the target receiver exceeds a certain range, it can cause abrupt jumps in the clock bias calculated by the target receiver. The receiver can successfully identify this type of spoofing by performing integrity monitoring and analysis on the calculated clock bias data. This limitation significantly restricts the operational range of multi-antenna relay-based spoofing interference. The primary solution proposed for this issue involves demodulating the satellite signal and manipulating the code phase of the pseudo-random noise code (PRN) sequence to compensate for the additional clock bias introduced at the target receiver. However, demodulating the satellite signal requires knowledge of the signal structure and PRN sequence, making it unsuitable for military signals [22]. Figure 2 illustrates the architecture of a relay-based spoofing interference system. Distributed relay-based spoofing interference leverages natural or controllable propagation delays during signal forwarding to disrupt receiver operations. Due to the confidential nature of the M-code, relay-based spoofing has become a key focus for targeting military codes.

Simultaneously, regional augmentation techniques based on pseudo-satellites have matured [23]. Building upon this foundation, literature [24] proposes a regional navigation and spoofing interference integrated system based on pseudo-satellites. This system consists of three components: a relay-based interferer, a carrier platform, and a ground control station. The relay-based interferer, positioned approximately 20 km above ground, generates interference signals. The ground control station controls the carrier platform's location and transmits instructions to the interferer, controlling the magnitude of the introduced delay in the forwarded signal. This system utilizes controlled forwarding delays to achieve regional mapping spoofing interference. Concurrently, code division multiple access (CDMA) technology is employed to superimpose the platform's location information and the introduced delay information onto the forwarded signal. As the friendly spread spectrum signal is orthogonal to the forwarded signal, the two signals act as noise to each other without mutual interference. Enemy GPS receivers acquire erroneous delay information, mapping the true location (R) to a virtual location (F), achieving spoofing interference. Simultaneously, friendly receivers obtain the carrier platform's location information and compensate for the delay, allowing for their navigation and positioning. The system principle is illustrated in Figure 3.

## 3.2 Generative spoofing interference

Generative spoofing interference is created by a satellite signal simulator that autonomously generates signals that mimic real satellite navigation signals based on known signal characteristics, including carrier frequency, C/A code, code phase, and modulation scheme [25]. These spoofed signals are synchronized with genuine signals to create a deceptive effect. Figure 4 illustrates the architecture of a generative spoofing interference system.

Generative spoofing interference (GSI) can be categorized into three levels based on its implementation complexity: primary, intermediate, and advanced [26–28]. Primary GSI relies on satellite signal simulators to generate spoofing signals without synchronizing parameters with the genuine signal, resulting in weak spoofing capabilities. Intermediate GSI, on the other hand, estimates the genuine satellite signal parameters, such as power,

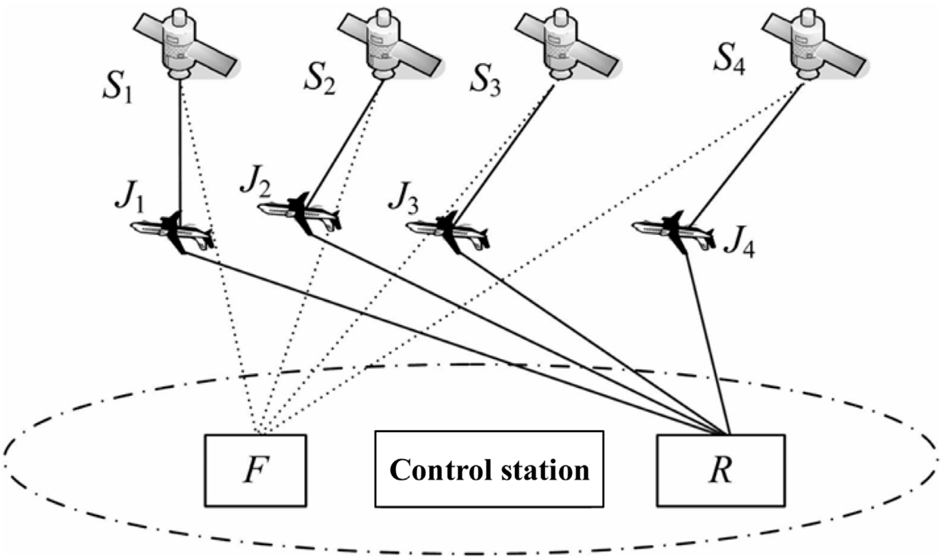

FIGURE 3
Schematic diagram of a GPS decoy jamming and regional navigation-integrated system [24].

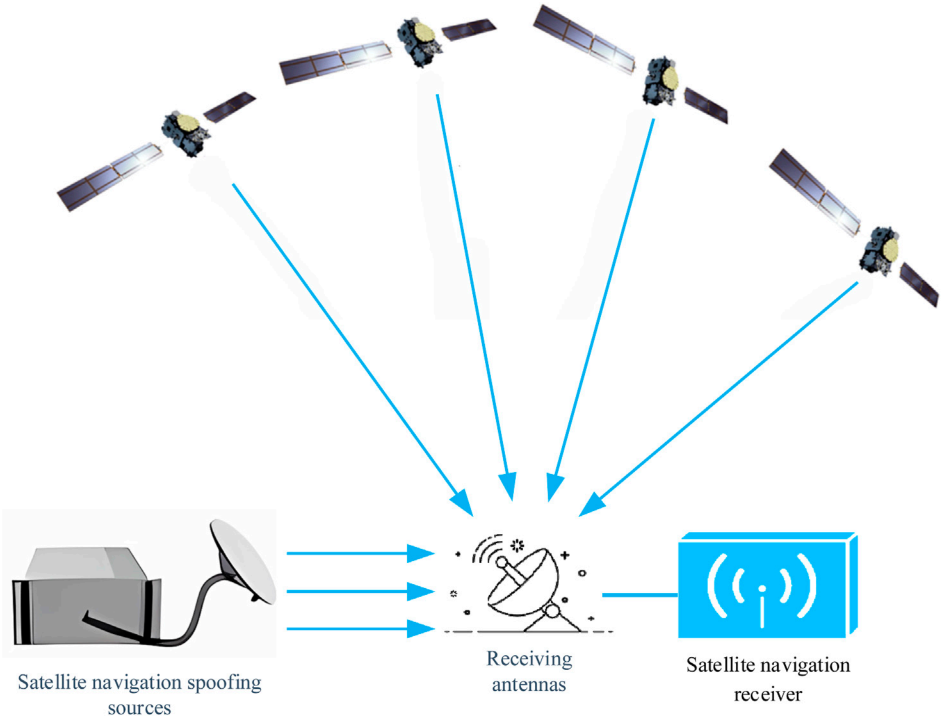

FIGURE 4
Schematic diagram of generative spoofing interference.

code phase, carrier frequency, navigation message, and modulation scheme. This enables the spoofing signal to mimic the genuine signal in terms of signal structure, thus increasing the likelihood of deceiving target receivers [29]. Advanced GSI builds upon intermediate GSI by employing multiple intermediate GSI sources for joint spoofing, overcoming the limitations of single-antenna transmission. It further integrates beamforming techniques to perfectly synchronize spoofing signals in parameters such as arrival angle. Intermediate GSI is the most widely adopted and successful technique, with the highest intrusion success rate. This paper focuses on intermediate GSI. The core principle of intermediate GSI lies in parameter synchronization with the

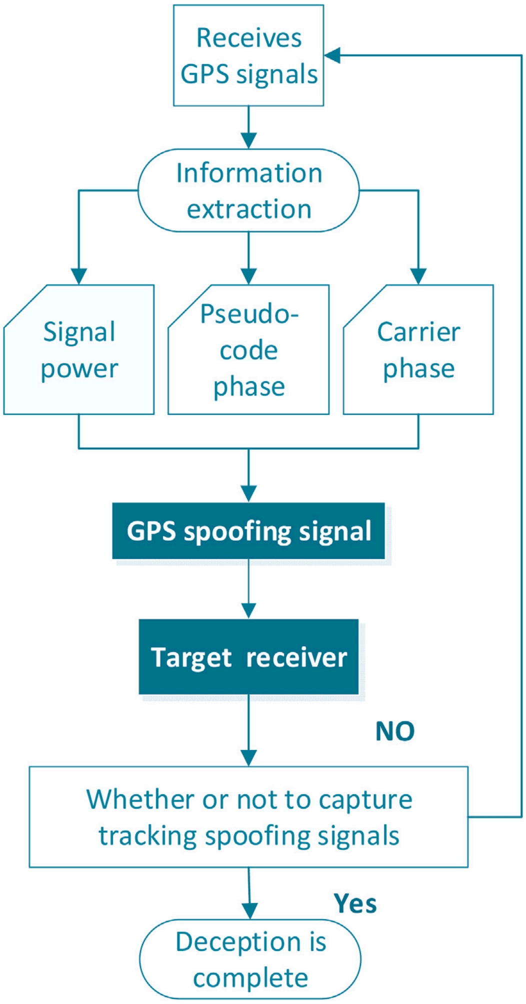

FIGURE 5
Intermediate generative deception interference flowchart.

genuine signal, including power, carrier frequency, code phase, modulation scheme, and navigation message synchronization. This ensures the spoofing signal can successfully decouple the genuine signal within the tracking loop of the satellite navigation receiver, thus facilitating the receiver to track the spoofing signal and achieve the spoofing effect. Figure 5 illustrates the general workflow of intermediate GSI.

As illustrated in Figure 5, the implementation process of intermediate generative spoofing interference can be described as follows: Initially, the satellite signal receiver in the spoofing interference module captures, tracks, and decodes the authentic signal, obtaining the code phase, carrier phase, received power, and navigation message of the authentic signal. Subsequently, the obtained parameters are utilized to adjust the parameters of the spoofed signal. Finally, the spoofed signal is modulated and transmitted.

The spoofed signal arrives at the receiver alongside the authentic signal. Generally, the power of the spoofed signal exceeds the power of the authentic signal by 3 dB. Under the power advantage of the spoofed signal, the receiver will abandon tracking the authentic signal and switch to tracking the spoofed signal, effectively completing the spoofing of the satellite navigation receiver. For receivers already tracking the genuine signal, capturing other search units will not affect the channel. Therefore, a corresponding phase induction model is required to execute spoofing interference against a receiver already in tracking mode while maintaining the lock. This model employs phase induction to perform covert spoofing against the receiver. This can be further categorized into synchronous induction and asynchronous induction [30] based on the different induction methods.

### 3.2.1 Induced spoofing interference analysis

The GPS radio frequency (RF) signal received by the antenna cannot be directly processed at the user receiver. It first needs to undergo down conversion by the RF front-end, followed by necessary filtering and gain control to obtain the GPS intermediate frequency (IF) signal. Finally, the IF signal is fed into the receiver for signal processing and position calculation.

The signal structure of an induced spoofing signal is identical to that of a genuine satellite signal. Therefore, the IF signal entering the receiver can be represented by Equations 2, 3, respectively [31]:

$$x_a(t) = \sum_{i=1}^{N_a} \sqrt{P_a^i(t)} D^i(t-\tau_a^i) C^i(t-\tau_a^i) \cos\left(2\pi\left(f_0 + f_{d,a}^i\right)t + \phi_a^i\right), \tag{2}$$

$$x_s(t) = \sum_{i=1}^{N_s} \sqrt{P_s^i(t)} D^i(t-\tau_s^i) C^i(t-\tau_s^i) \cos\left(2\pi\left(f_0 + f_{d,s}^i\right)t + \phi_s^i\right). \tag{3}$$

In this formula, $x_a(t)$ and $x_s(t)$ represent the real satellite signal and the spoofing signal, $N_a$ and $N_s$ represent the number of satellites included, $P_a^i$ and $P_s^i$ represent the signal power, $D^i(t)$ represents the navigation data message, $C^i(t)$ represents the C/A code, $\tau_a^i$ and $\tau_s^i$ represent the code phase of each signal, $f_0$ represents the intermediate frequency (IF), $f_{d,a}^i$ and $f_{d,s}^i$ represent the Doppler shift of the signals, and $\phi_a^i$ and $\phi_s^i$ represent the initial phase of the carrier of the signals, respectively. Therefore, when induced spoofing interference is present, the receiver mixed IF signal would have both a real satellite signal and a spoofing signal:

$$x(t) = x_a(t) + x_s(t) + n(t), \tag{4}$$

where $n(t)$ represents Gaussian white noise with a mean value of 0.

The satellite signal must be captured before the receiver performs the signal processing part. This process is a rough estimate of the carrier frequency and code phase of the satellite signal. The principle is to use the local end of the receiver to generate a signal with a certain carrier frequency and code phase and then correlate and mix the received signal with the local replication signal to detect the correlation degree between the two. When the correlation between the received signal and the local signal exceeds the preset capture threshold, the carrier phase and code phase of the local replicated signal can be roughly assumed to be the same as that of the real satellite signal. However, the signal acquisition is only a rough estimation of the parameters of the received satellite signal, which is not enough to meet the requirements of positioning and solving. Accurate estimation of the satellite signal parameters also needs the receiver to enter the tracking loop to be realized. Induced spoofing jamming is a kind of covert spoofing jamming, which usually implements spoofing after

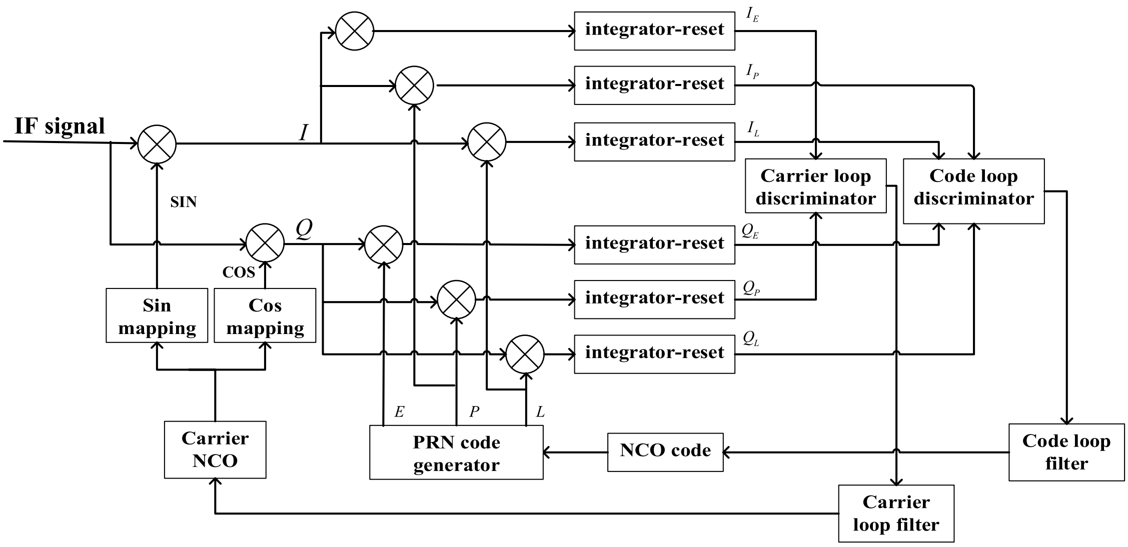

FIGURE 6
General schematic diagram of the receiver tracking loop.

the receiver enters the tracking stage and cannot interrupt the tracking state of the receiver's tracking loop, so the impact of induced spoofing jamming on the receiver is mainly reflected in the tracking loop. Due to the continuous relative motion between the receiver and the satellite, the pseudocode phase, carrier phase, and carrier frequency of the receiver-received signal all change from time to time. Signal tracking means that the receiver should accurately always track these signal parameters. As shown in the figure, the tracking loop of the receiver includes a code tracking loop and a carrier tracking loop. Carrier tracking loops often include frequency-locked loops (FLLs) and phase-locked loops (PLLs), and delay-locked loops (DLLs) are often used in code tracking loops. FLLs, PLLs, and DLLs are characterized by a feedback adjustment mechanism that continuously corrects the carrier frequency, phase, or code phase generated within it according to the input signal to track the input GPS signal.

As shown in Figure 6, when the GPS IF signal enters the tracking loop, the received IF signal is first mixed with the carrier copied by the receiver's carrier tracking loop, and the carrier stripping is carried out to produce two data, in-phase (I) and quadrature (Q). Then, the code tracking loop will generate three C/A codes with a phase interval of d/2 in the lead (E), instant (P), and lag (L), which are correlated with the I/Q signal to obtain a six-way integration output. Among them, the recurrence codes generated by the leading branch, the immediate branch, and the lagging branch can be called the early code, the instant code, and the late code, respectively. Subsequently, the correlation integral values of the leading and lagging branches will be input to the code ring discriminator, and the correlation values of the instant branches will be input to the carrier ring discriminator. The phase and frequency errors are then calculated by different discrimination algorithms so that the carrier frequency, phase, and code phase reproduced in the tracking loop are corrected. The following is a detailed analysis of the impact of spoofing signals on PLLs and DLLs.

When there is no spoofing, the received signal contains a real satellite signal, and the correlation function between the real signal pseudocode and the locally reproduced pseudocode can be expressed as Equation 5 [31]:

$$R_a(t,\tau) = 1 - |\tau|, |\tau| \le 1\,(0, \text{others}), \tag{5}$$

where $\tau$ represents the code phase difference between the real signal t and the locally reproduced signal. After the signal enters the tracking loop, the real signal received after the carrier stripping and correlation operation will obtain the output result of the six-way correlator, which can be expressed as Equations 6–11 [31]:

$$I_E(t) = \sqrt{P_{\mathrm{a}}}R_a\left(\Delta\tau - \frac{d}{2}\right)\cos(\phi_a), \tag{6}$$

$$Q_E(t) = \sqrt{P_{\mathrm{a}}}R_a\left(\Delta\tau - \frac{d}{2}\right)\sin(\phi_a), \tag{7}$$

$$I_P(t) = \sqrt{P_{\mathrm{a}}}R_a(\Delta\tau)\cos(\phi_a), \tag{8}$$

$$Q_P(t) = \sqrt{P_{\mathrm{a}}}R_a(\Delta\tau)\sin(\phi_a), \tag{9}$$

$$I_L(t) = \sqrt{P_{\mathrm{a}}}R_a\left(\Delta\tau + \frac{d}{2}\right)\cos(\phi_a), \tag{10}$$

$$Q_L(t) = \sqrt{P_{\mathrm{a}}}R_a\left(\Delta\tau + \frac{d}{2}\right)\sin(\phi_a), \tag{11}$$

where $P_{\mathrm{a}}$ indicates signal power, $R_{\mathrm{a}}(\cdot)$ represents a correlation function, $\Delta\tau$ represents the code phase difference between the received signal and the locally copied signal, and $\varphi_a$ represents the carrier-phase difference between the received signal and the locally copied signal. When there is induced spoofing interference, the received signal contains a real signal and a spoofing signal, and after the real signal pseudocode is correlated with the local reproduction pseudocode, taking the real-time code as an example, the outputs of the I and Q correlators are as follows Equations 12, 13 [31, 32]:

$$I_p(t) = \sqrt{P_a(t)}R_a(t,\tau)\sin c\left(\Delta f_{d,a}T\right)\cos\left(\varphi_a\right) + \sqrt{P_s(t)}R_s(t,\tau)\sin c\left(\Delta f_{d,s}T\right)\cos\left(\varphi_s\right), \tag{12}$$

$$Q_p(t) = \sqrt{P_a(t)}R_a(t,\tau)\sin c\left(\Delta f_{d,a}T\right)\sin\left(\varphi_a\right) + \sqrt{P_s(t)}R_s(t,\tau)\sin c\left(\Delta f_{d,s}T\right)\sin\left(\varphi_s\right), \tag{13}$$

where $P_a(t)$ and $P_s(t)$ represent the power of the real signal and the spoofing signal, and $R_a(t,\tau)$ and $R_s(t,\tau)$ represent the correlation functions between the real signal pseudocode and the spoofed signal and the local pseudocode. $\Delta f_{d,a}$ and $\Delta f_{d,s}$ represent the carrier frequency difference between the real and spoofed signals and the local signal, respectively; $\varphi_a$ and $\varphi_s$ are the carrier-phase difference between the real and spoofed signals and the local signal, respectively. First, the output result of the instant branch correlator is sent to the PLL discriminator, assuming that the arctangent function phase discriminator is used, as shown in the formula $\Delta\hat{\varphi} = \arctan(Q_p/I_p)$. If there is no spoofing signal, the output of the phase detector is Equation 14 [31]:

$$\Delta\hat{\varphi} = \arctan\left(\frac{\sqrt{P}\,R_a(\Delta\tau)\sin\left(\Delta\varphi_a\right)}{\sqrt{P}\,R_a(\Delta\tau)\cos\left(\Delta\varphi_a\right)}\right) = \Delta\varphi_a. \tag{14}$$

At this time, the output result of the phase detector is that the phase deviation between the real signal and the local signal is $\Delta\varphi_a$. The PLL can then correct the local signal accordingly so that the carrier phase of the received signal can be continuously tracked.

However, when a spoofing signal is present, the output of the phase detector is Equation 15 [32]:

$$\Delta\hat{\varphi} = \arctan\left(\frac{\sqrt{P_a(t)}\,R_a(t,\tau)\sin c\left(\Delta f_{d,a}T\right)\sin\left(\varphi_a\right) + \sqrt{P_s(t)}\,R_s(t,\tau)\sin c\left(\Delta f_{d,s}T\right)\sin\left(\varphi_s\right)}{\sqrt{P_a(t)}\,R_a(t,\tau)\sin c\left(\Delta f_{d,a}T\right)\cos\left(\varphi_a\right) + \sqrt{P_s(t)}\,R_s(t,\tau)\sin c\left(\Delta f_{d,s}T\right)\cos\left(\varphi_s\right)}\right). \tag{15}$$

From this formula, when there is a spoofed signal, the phase identification result of the phase detector will be incorrect, and the PLL will not be able to correct the carrier phase of the local signal according to the phase identification result so that the carrier phase of the real signal cannot be tracked. Similarly, in the case of DLL, it is assumed that the DLL uses an incoherent leading hysteresis power phase detector. When there is no spoofing signal, the phase detector result is Equation 16 [32]:

$$\varepsilon = \frac{1}{2}\left[\left(I_E^2 + Q_E^2\right) - \left(I_E^2 + Q_E^2\right)\right] = \frac{p_a}{2}\left[R^2\left(\Delta\tau - \frac{d}{2}\right) - R^2\left(\Delta\tau + \frac{d}{2}\right)\right]. \tag{16}$$

Because the autocorrelation function of the pseudocode is symmetrical, $R(\Delta\tau - \frac{d}{2}) = R(\Delta\tau + \frac{d}{2})$. So, when the DLL keeps track of the received signal, $\varepsilon = 0$.

When there is a spoofing signal, it is not difficult to conclude that the correlation function between the received signal and the local copy code will be distorted to different degrees, and the code phase deviation of the spoofed signal relative to the real signal will lead to the asymmetry of the relevant peaks, thus causing the phase discrimination error of the DLL phase discriminator. For the sake of simplicity, if the PLL has tracked the carrier phase of the received signal at this time, the output result of this DLL phase detector is Equation 17 [32]:

$$\varepsilon = \frac{p_s}{2}\left[R\left(\Delta\tau - \frac{d}{2}\right) - R\left(\Delta\tau + \frac{d}{2}\right)\right] + \frac{P\cdot P_s}{4}\left[R\left(\Delta\tau_s - \frac{d}{2}\right) - R\left(\Delta\tau_s + \frac{d}{2}\right)\right], \tag{17}$$

where $\Delta\tau_s$ is the phase difference between the spoofed signal and the real signal number.

In conjunction with GNSS positioning principles, errors in the DLL and PLL discriminator tracking results can lead to inaccurate estimations of the code phase, carrier Doppler, and carrier phase of the received signal. This, in turn, introduces bias in the subsequent user position calculation, resulting in erroneous position and/or time information. However, the tracking loop also incorporates protective mechanisms. When the tracking loop is in a locked state and stably tracks the received satellite signal, it is in a tracking state. When the received signal fails to meet the tracking conditions, the tracking loop will cease operation, indicating a tracking loop loss of lock. This can lead to the receiver ceasing operation or attempting to reacquire the satellite. Such a scenario would be easily detectable and not conducive to covert spoofing. Therefore, spoofed signals must strive to avoid triggering a tracking loop loss of lock while gradually gaining control over the tracking loop to ensure it continuously tracks the spoofed signal. Ultimately, this will result in the receiver being misled by the spoofed signal.

### 3.2.2 Synchronous-induced spoofing model

Leveraging the receiver's inherent inclination to prioritize signals with greater power levels, the synchronous-induced spoofing model operates as follows: Once the receiver has acquired the authentic signal, the spoofing jamming platform utilizes the decoded code phase of the authentic signal to generate a spoofed signal with an identical code phase. This ensures that the authentic signal and the spoofed signal align at their correlation peaks. Subsequently, the spoofing jamming platform increases its transmission power to achieve a power advantage over the authentic signal, thereby causing the receiver to switch its tracking to the spoofed signal. The code phase of the spoofed signal is then gradually shifted away from the code phase of the authentic signal, effectively decoupling the receiver from the authentic signal.

Based on the correlation peak shown in Figure 7A, the general steps involved in the synchronous-induced spoofing model can be outlined [33].

(1) Initialization: The navigation receiver initially tracks the genuine signal. The spoofing jamming platform accurately estimates the parameters of the genuine signal upon its arrival at the receiver, including its code phase, carrier frequency, and signal power. Subsequently, a spoofed signal with a code phase aligned with the genuine signal is transmitted. At this stage, the power of the spoofed signal is lower than that of the genuine signal.

(2) Power enhancement: The power of the spoofed signal is gradually increased until it surpasses the power of the genuine signal. Upon achieving a power advantage, the target receiver loses lock on the genuine signal and re-locks onto the spoofed signal. The code loop and carrier loop begin to track the spoofed signal.

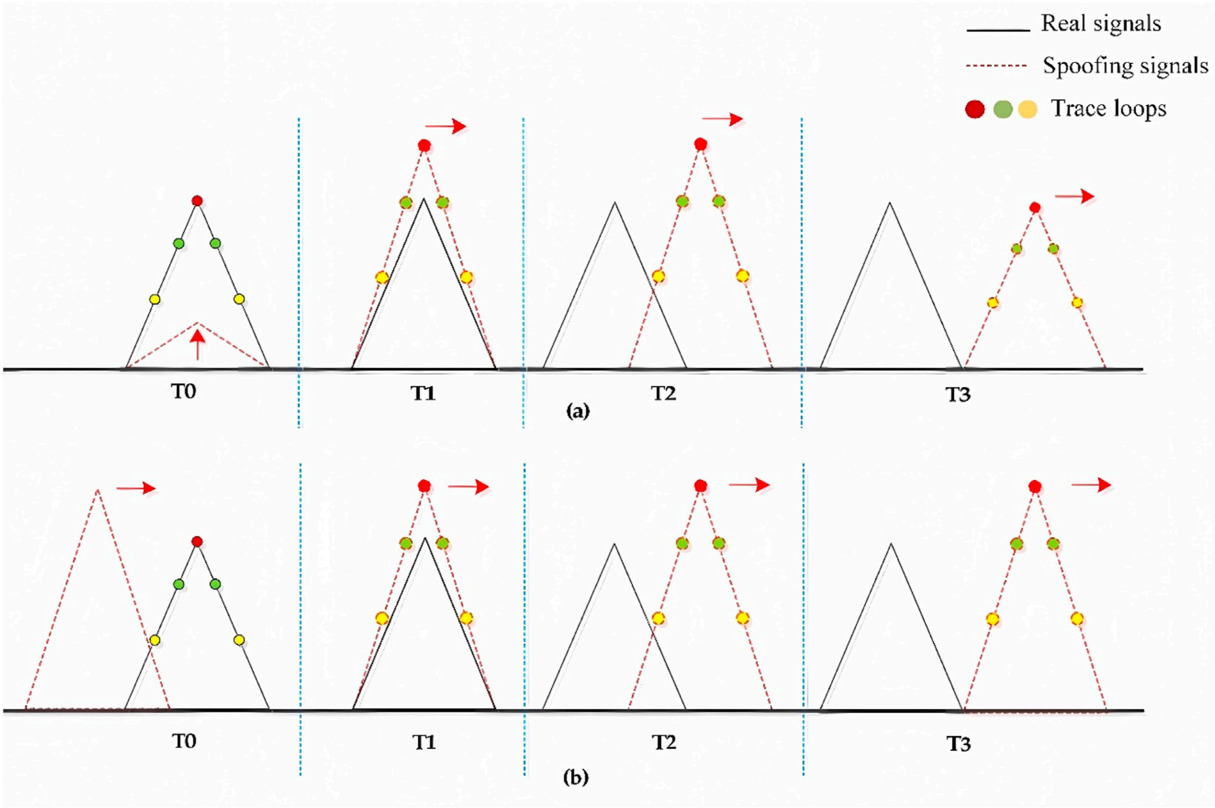

FIGURE 7
Schematic diagram of the changes of related peaks in the synchronous induction model and the asynchronous induction model.

(3) Code phase shift: Once the receiver is tracking the spoofed signal, its pseudo-random code rate is gradually adjusted, causing a shift in its code phase away from the code phase of the genuine signal. The target receiver then completely loses lock on the genuine signal, and the spoofed signal gradually replaces it entirely, effectively deceiving the receiver.
(4) Power reduction and completion: The transmission power of the spoofed signal is reduced to match the power level of the genuine signal, minimizing detection while completing the synchronous-induced spoofing process.

### 3.2.3 Asynchronous-induced spoofing model

While synchronous-induced spoofing models require precise alignment of the spoofed signal's code phase with that of the genuine signal, practical implementation faces challenges due to inherent inaccuracies in range and velocity measurements by the target receiver. The precision of parameter estimation, particularly for code phase, carrier frequency, and their respective compensations, often falls short of the requirements for synchronous induction. This presents significant hurdles in achieving synchronous spoofing. An asynchronous-induced spoofing model can be built on the synchronous-induced model. This model only necessitates a rough alignment between the code phase of the spoofed signal and the genuine signal. The spoofed signal then employs variable code rates to match the code phase of the genuine signal, enabling the tracking loop to lock onto the spoofed signal. The asynchronous-induced spoofing model presents a less challenging implementation than its synchronous counterpart. The correlation peak shown in Figure 7B illustrates the process.

Based on the correlation peak variations, the asynchronous-induced spoofing model can be divided into four steps [33].

(1) Initialization: The navigation receiver initially tracks the genuine signal. The spoofing jamming platform accurately estimates the parameters of the genuine signal upon its arrival at the receiver, including its code phase, carrier frequency, and signal power. Subsequently, a spoofed signal with a code phase slightly lagging the genuine signal is transmitted. Meanwhile, the spoofed signal maintains a power advantage over the genuine signal.
(2) Code phase matching: The code rate of the spoofed signal is gradually adjusted to bring its code phase closer to that of the genuine signal. When the two code phases align, the code loop, relying on the power advantage of the spoofed signal, tracks the spoofed signal, thus successfully disrupting the target receiver.
(3) Code phase shift: Once the receiver is tracking the spoofed signal, its pseudo-random code rate is gradually adjusted again, causing a shift in its code phase away from the code phase of the genuine signal. The target receiver then completely loses its lock on the genuine signal, and the spoofed signal gradually replaces it entirely, effectively deceiving the receiver.

**TABLE 2** Characteristics of different methods of deception.

| Types of spoofing | Forwarding spoofing attack | Generating spoofing attack | |
|---|---|---|---|
| | | Synchronous-induced spoofing | Asynchronous-induced spoofing |
| How it works | Relays real satellite signals to increase latency and appropriate power for spoofing attacks | Imitate a satellite signal, increase the power from the same code phase, and then slowly change the code phase so that the receiver tracks the spoofing signal | Imitate the satellite signal, gradually approach the real signal number phase from the place where the code phase is different, and when the signal overlaps, increase the power and gradually increase the code phase so that the receiver tracks the deceptive signal |
| Merit | There is no need to know the specific parameters of the signal, and the implementation is simple | It is highly concealed, has a good deception effect, and is not easily detected by the receiver | It is highly concealed, has a good deception effect, and does not need to know the exact phase of the real letter number |
| Limitations | Latency alone is easy to detect. | The implementation is complex and also requires a relatively accurate analysis of the real signal. Because the military code data are not public, it is impossible to replicate the military signal | The implementation is complex and also requires a more accurate analysis of the real signal. Because the military code data are not public, it is impossible to replicate the military signal |

(4) Power reduction and completion: The transmission power of the spoofed signal is reduced to match the power level of the genuine signal, along with adjustments to other parameters, minimizing detection while completing the asynchronous-induced spoofing process.

### 3.3 Summary

All the deception models mentioned above, as well as their applicable scenarios, advantages, disadvantages, and limitations, are shown in Table 2.

## 4 GNSS anti-spoofing jamming technology

In recent years, significant progress has been made in the development of spoofing interference countermeasure techniques, with numerous constructive solutions proposed by researchers from various countries. Current mainstream methods include signal power detection [34–37], time-of-arrival analysis [38], carrier and code phase consistency [39], carrier Doppler analysis [40], clock difference and stability analysis [41], signal arrival angle [42, 43], message verification [44], correlator output statistical characteristics [45], signal quality detection [46], signal spatial correlation [47], positioning results [48, 49], inertial navigation assistance [50, 51], and array antenna nulling techniques [52]. With the rapid development of machine learning, spoofing interference countermeasure methods can also be integrated with machine learning. Machine learning-based spoofing interference detection methods utilize the receiver to generate different types of feature values for spoofing identification. The type of signal can be detected by extracting these features, especially when the correlation peak of the spoofing signal is close to the original signal's correlation peak. Based on the implementation objectives, spoofing interference countermeasures can be broadly classified into four categories: spoofing interference detection and identification, spoofing interference suppression, and spoofing interference source localization.

### 4.1 Spoofing interference detection and identification

Spoofing interference detection and identification primarily focus on the detection of spoofed signals. Upon detecting the presence of such signals, the receiver's normal operation is halted, preventing it from being misled and mitigating potentially severe consequences. In a battlefield scenario, for instance, this would involve suspending the use of the receiver to prevent accidental weapon activation. However, spoofing interference detection alone is insufficient to effectively eliminate the spoofing interference and restore the receiver system to its normal operating state; further actions are required. The detection of spoofed signals is typically performed at the signal level without requiring modifications to the signal architecture, resulting in a straightforward implementation. Based on the implementation approach, various methods can be employed: (1) signal power detection, (2) correlation peak detection, (3) antenna array detection, (4) signal Doppler detection, (5) signal quality monitoring (SQM), (6) deep learning-based interference monitoring and identification, and (7) other methods of anti-spoofing interference.

#### 4.1.1 Signal power detection

Satellite signals arriving at the ground typically exhibit very low power levels due to atmospheric attenuation caused by the troposphere and ionosphere, as well as multipath propagation. These signals are often masked by noise. Consequently, received navigation signals have relatively low power. The introduction of spoofing signals further exacerbates this issue, leading to a significant change in the receiver's signal-to-noise ratio, as illustrated in Figure 8. However, to effectively achieve their interference objectives, spoofing signal perpetrators typically transmit spoofed signals with slightly higher power than authentic signals. The signal power detection technique exploits this principle by establishing a reasonable detection threshold to identify the presence of spoofed signals within the receiver channel [53]. In 2012, Dehghanian V [36] proposed an effective detection method based on signal power. This method utilizes the output signal power of the correlator following signal acquisition and tracking to detect spoofing interference. It leverages the principle

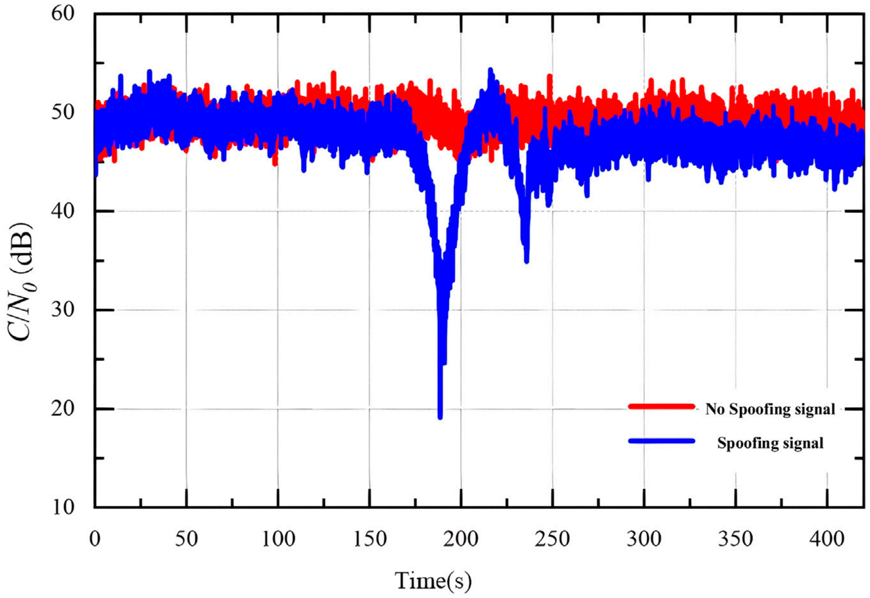

FIGURE 8
Noise floor change before and after adding the spoofing signal.

that spoofed signals typically exhibit higher power levels than genuine signals. A power threshold is established, and signals exceeding this threshold are classified as spoofed signals, while those below are considered legitimate. However, determining the appropriate spoofing interference judgment threshold for this method poses a challenge, particularly for induced spoofing interference, which can autonomously adjust its power level. This poses a significant risk of misclassification and potentially severe consequences. This algorithm requires no modifications to the receiver structure, rendering it simple to implement. However, its detection performance is compromised when the spoofed signal power is close to that of the BeiDou signal.

In 2016, [54] proposed a spoofing interference detection algorithm based on signal-to-noise ratio (SNR) measurement. This algorithm exploits the high SNR anomaly generated during spoofing signal intrusion to identify spoofed signals based on correlator peak values. While simple to implement, this method demonstrates limited effectiveness against highly concealed induced spoofing interference. In 2018, Wesson K. D. et al. [55] proposed a spoofing interference detection technique called the power distortion detector. This technique categorizes received signals as interference-free, multipath interference, or spoofing interference based on observations of received signal power and correlator function distortions. This technique effectively differentiates low-power spoofed signals from multipath signals and requires no modifications to the receiver hardware, making it straightforward to implement.

In 2019, [56] investigated the detection statistics of power detection methods based on the principles of power detection techniques and provided specific detection thresholds. In the same year, [57], recognizing the limitations of the carrier-to-noise ratio (CNR) detection algorithm, proposed a spoofing interference detection algorithm that combines the CNR algorithm with the Doppler detection algorithm during the signal tracking phase. This approach overcomes the shortcomings of relying solely on the CNR algorithm for spoofing detection. In 2020, [58], acknowledging the limitations of using solely signal power to detect spoofing interference, proposed a spoofing interference detection algorithm based on power changes for mobile terminals. This algorithm leverages the distinct power variations exhibited by spoofed and genuine signals at the same distance when the terminal is in motion to make spoofing interference judgments. This algorithm demonstrates superior performance when the interference source is less than 2000 m from the terminal, and the terminal's movement distance exceeds 200 m, but it also possesses certain limitations.

### 4.1.2 Correlation peak detection

Correlation peak detection techniques have demonstrated remarkable effectiveness in detecting forwarding-based spoofing interference. This effectiveness stems from the inherent time delay present in forwarded spoofing signals compared to genuine signals. This time delay inevitably results in a greater transmission distance and time for the spoofing signal to reach the target receiver than the genuine signal. Consequently, the received signal exhibits anomalous correlation peaks during the acquisition or tracking stages. The associated peak anomalies are shown in Figure 9.

In 2016, [59] proposed a detection algorithm that combines correlation peak and power analysis for forwarding-based spoofing interference. This algorithm determines the presence of spoofing interference by analyzing the number of correlation peaks exceeding the acquisition threshold and setting appropriate power detection thresholds. While simple and effective, it suffers from detection blind zones. Building upon Wang Zhiying's work, [60] introduced the full width half maxima (FWHM) algorithm as a supplementary approach to the multi-peak algorithm for detecting short-delay forwarding-based spoofing interference. This algorithm, which requires no modification to the receiver structure, offers

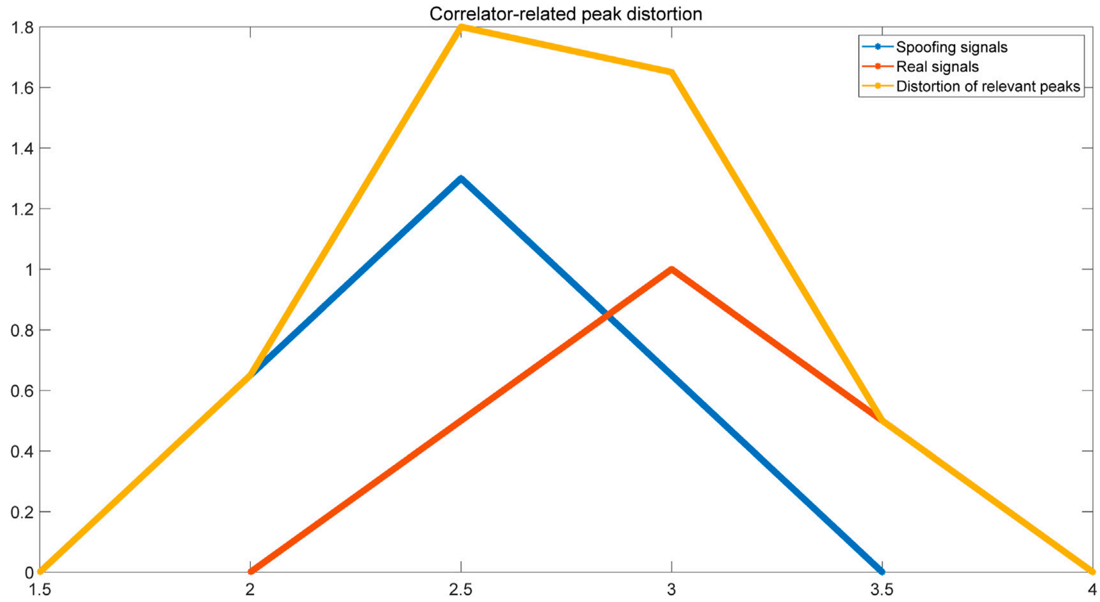

FIGURE 9
Schematic diagram of peak changes related to ultra-low delay.

simplicity in implementation. However, it cannot effectively distinguish between spoofing signals and multipath signals. To address the shortcomings of the algorithms, [61] proposed a novel joint detection algorithm for the acquisition stage in 2021. This algorithm extends the previous two approaches by incorporating a code phase difference consistency method, effectively mitigating the influence of multipath signals. It further refines the correlation function width threshold method [62], thereby addressing the limitations of the previous algorithms. This enhanced algorithm exhibits robust detection capabilities, successfully detecting forwarding-based spoofing interference with varying time delays.

The analysis presented above clearly demonstrates the efficacy of correlation peak detection techniques in detecting forwarding-based spoofing interference during the signal acquisition stage. Consequently, this research will delve into signal correlation peak detection techniques, exploring their integration with signal power detection techniques to detect forwarding-based spoofing interference. In 2022, [63] designed a receiver scheme incorporating interference identification capabilities. This scheme leverages the distinct correlation peak shapes generated by different types of interference, employing deep learning to recognize and classify these feature maps.

### 4.1.3 Antenna array detection

Array antenna detection techniques leverage the spatial characteristics of spoofing signals and BeiDou signals to identify the presence of interference. Due to implementation constraints, spoofing signals currently received by array antennas typically originate from a single direction [64, 65], while satellite signals arrive from multiple directions. These detection techniques demonstrate excellent performance but often require additional hardware implementation, resulting in high algorithmic costs.

In 2016, [66] proposed an algorithm for spoofing signal detection using the carrier-phase difference between two antennas. This algorithm utilizes the precise location of the tracked satellite as prior information to determine the carrier-phase difference of the true signal on the known antenna array. It further analyzes various error sources in the carrier-phase difference calculation to detect spoofing signals. This algorithm exhibits superior detection performance when the baseline of the antenna array is longer and the incident azimuth angle is smaller. However, it has limitations, as it is suitable for navigation receivers with fixed antenna installations. In 2018, [67] proposed a blind adaptive array signal processing method based on array antennas. This method not only adaptively forms deep nulls in non-periodic, periodic, and generative spoofing interference direction of arrival (DOA) estimation but also mitigates in-band spoofing signals and enhances the useful signal. In the same year, [68] proposed a spoofing interference detection method based on baseline data statistical analysis. This method considers three scenarios: single fixed baseline, fixed independent baseline, and dual independent baseline models. It analyzes the impact of baseline values on detection performance. However, this method may fail when the two antennas are not synchronized. Addressing this issue, [69] proposed a pseudo-range and carrier-phase measurement asynchronous model and spoofing interference detection method based on dual antenna power measurements. This method can detect spoofing interference under asynchronous conditions. Furthermore, many researchers [70, 71] have proposed corresponding multi-antenna spoofing interference detection techniques. In 2019, [72] proposed a blind detection method for spoofing signals using antenna array spatial diversity. This method is implemented in a snapshot receiver and evaluated using open data recorded by a six-element array. It exhibits a high detection rate but has high complexity. To address the challenge of detecting spoofing

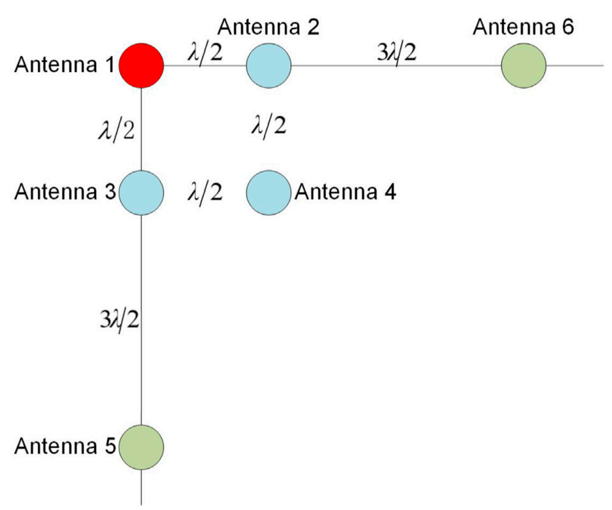

FIGURE 10
Schematic diagram of the arrangement of six array elements antenna elements [77].

signals from different emitters, [73] proposed an anti-spoofing method. This method uses pseudo-range double differences (PRDD) measurements from two receivers to detect this type of spoofing interference. Spoofing signals are identified by analyzing the difference between PRDD measurements and estimated PRDD values. This algorithm exhibits good detection performance when the two receivers are placed at an appropriate distance. However, it may fail if the platform is too small. In 2020, [74] proposed an algorithm for detecting spoofing interference using carrier-phase single difference (CPSD) measurements from a linear array. Compared to the method in [73], this algorithm has less stringent platform size requirements and can be applied to a wider range of scenarios.

In 2021, [75] addressed the limitation of traditional spoofing interference detection algorithms, which are unable to locate spoofing interference. They proposed a spoofing interference detection method based on carrier-phase difference measurement using array multi-antenna received signals. This method can estimate the arrival direction of the received signal using the direction-finding principle of the correlation interferometer without requiring prior knowledge. Spoofing interference can be determined by comparing this estimate with the satellite direction obtained from ephemeris calculations. This algorithm exhibits excellent detection performance and can identify the arrival direction of multiple spoofing signals from different satellites. However, it has high algorithmic complexity. In 2022, Wang Xiaoyu [76] utilized the difference between real satellite navigation signals, which arrive at the array antenna from multiple directions in the upper hemisphere space, and spoofing interference signals, which arrive from a single direction. The MUSIC algorithm is used to estimate the incident direction of each satellite, and spatial consistency is employed for spoofing interference determination. This algorithm has good detection performance but has high computational complexity due to the need to measure the arrival direction of each satellite.

In 2023, [77] proposed a novel six-element array spoofing interference detection array antenna, as shown in Figure 10. Spoofing interference can be detected and identified by monitoring the relevant peak values and combining spatial capture algorithms. Additionally, they used the long and short baseline algorithm to quickly search the entire cycle ambiguity, enabling high-precision detection of spoofing interference sources. This method exhibits high detection accuracy but requires many antenna elements, leading to higher costs.

### 4.1.4 Signal Doppler detection technology

For single-antenna spoofing interference, the Doppler data dispersion between two real satellite signals exhibits non-linearity in the time domain when the receiver is moving randomly. Conversely, the Doppler data dispersion between two single-antenna spoofing signals displays linearity. Additionally, the Doppler frequency shift range of the satellite signals received by the target receiver expands when spoofing interference is present. Therefore, monitoring Doppler frequency shift variations can effectively identify the presence of spoofing interference. Figure 11 shows the nominal recorded carrier frequency error for the four space vehicles (SVs) used in this article. As expected, the carrier frequency of each SV varies approximately linearly with time. The longer the transmission time, the greater the offset of the SV from the original carrier frequency. The slope of the line correlates with the expected Doppler shift of approximately ±5 kHz modeled in this study.

In 2014, [78] proposed an adaptive tracking algorithm for forwarding-based spoofing interference, combining a power threshold detector with a Doppler frequency shift detector. This algorithm is suitable for forwarding-based spoofing interference but less effective against other types. In 2018, [79] presented a GNSS anti-spoofing algorithm based on Doppler frequency shift. This algorithm derives a Doppler frequency difference model and transforms the spoofing interference detection problem into a sequence linear detection problem. While simple, effective, and demonstrating good detection performance, this algorithm may exhibit reduced effectiveness against more sophisticated spoofing interference. [82] proposed a joint detection of code and carrier Doppler that can detect and identify spoofing signals. This method is implemented on the GNSS acquisition module and requires no additional hardware. It exhibits good detection performance in static and uniform motion scenarios, but the detection effect is inferior when the receiver's acceleration is significant. In the same year, [83] proposed a spoofing interference detection algorithm based on the consistency of Doppler positioning repair and pseudo-range positioning repair. The algorithm effectively improves the performance of Doppler positioning methods and detection methods through an improved Doppler smoothing technique based on alpha filtering. In 2019, [80] proposed a spoofing interference detection algorithm for medium-level spoofing interference based on frequency-domain double peaks and relative velocity residuals. This technique employs a fast Fourier transform (FFT)-based approach to detect double peaks and extract their Doppler difference. It then calculates the relative velocity residuals based on the Doppler difference. This algorithm not only detects spoofing signals but also distinguishes them from multipath signals. In the same year, [81] proposed a detection

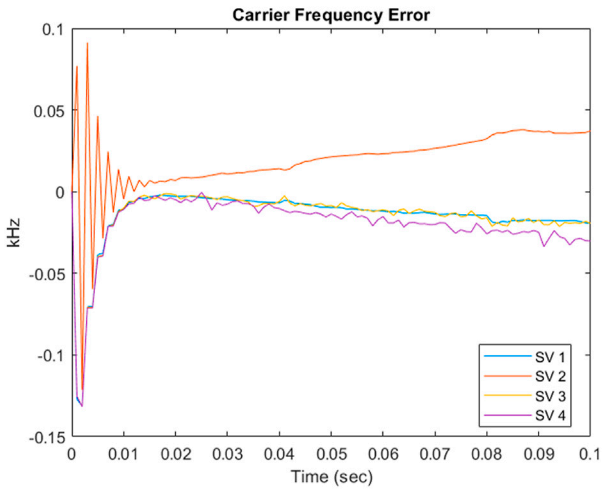

FIGURE 11
Carrier frequency error due to Doppler shift [85].

method that jointly utilizes the carrier Doppler frequency shift caused by the vertical reciprocating motion of the receiving antenna and the navigation information conveyed by the received signal. [84] proposed a spoofing detection method that utilizes the amplitude difference and frequency difference between the superposition composite signal containing interference and the normal signal unaffected by spoofing in the tracking loop as the basis for interference detection. This method can effectively detect spoofing signals in BeiDou satellite navigation signals by setting signal power anomaly thresholds and Doppler frequency shift detection thresholds. In 2022, [85] proposed a spoofing interference detection technique based on Doppler frequency difference correlation. This method calculates the Fréchet distance between two satellites by using the least-squares fitting of Doppler measurements within a window when the receiver is moving. After obtaining the similarity evaluation value between them, it is used to detect spoofing interference. This method has low computational complexity and requires less additional information, but its application scenarios are limited. In 2024, [86] proposed an unmanned aerial vehicle (UAV) GNSS spoofing detection method based on signal characteristics: Doppler frequency shift carrier-to-noise ratio density and deep learning. After training, the detection probability can reach 95%.

### 4.1.5 Signal quality monitoring (SQM)

Signal quality monitoring (SQM) technology is widely employed in satellite navigation systems. The advantage of SQM lies in its simple structure, enabling the detection of spoofing interference without altering the receiver's original design. This is achieved by analyzing the correlator output peaks of the satellite navigation receiver. Typically, the GNSS receiver correlator output exhibits a characteristic red inverted triangle shape, as depicted in Figure 7. The early code correlator output and the late code correlator output are always symmetrical with respect to the prompt code correlator output. When the correlator spacing is 0.5 chips, the prompt code correlator output is twice the sum of the early code correlator output and the late code correlator output at the same time. In the presence of interference, the outputs of the early code, prompt code, and late code correlators become abnormal, and their symmetry is disrupted. For example, under normal circumstances, the output power of the early code and the late code should be equal, ideally zero, but after the injection of deception, the output power difference between the early code and the late code will exhibit a significant abnormal change, as shown in Figure 12.

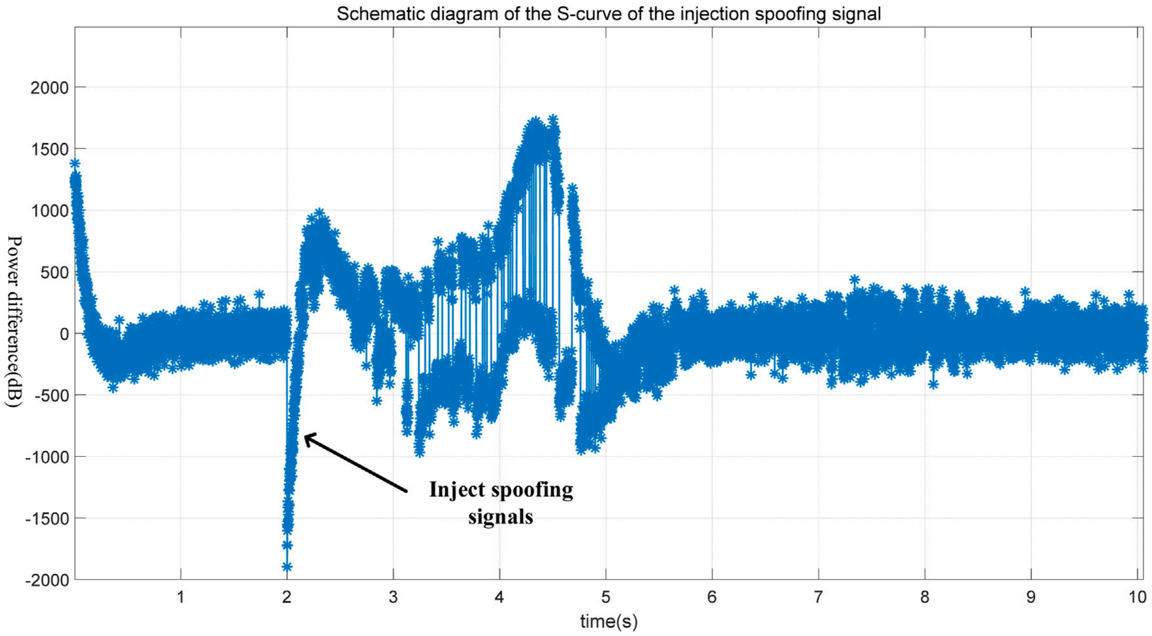

FIGURE 12
Schematic diagram of the change of early code power and late code power.

Numerous algorithms have emerged from SQM. [87] introduced the delta metric (detecting correlation peak distortion by comparing the in-phase outputs of the early and late code) and the ratio metric (detecting correlation peak distortion by observing the ratio of early and late codes to the prompt code in-phase outputs). Subsequently, [88] proposed the S-curve-bias (SCB) algorithm. Induced spoofing interference can affect the correlator output. This algorithm utilizes the difference between the outputs of the early code correlator and the late code correlator to detect induced spoofing interference. [89] introduced a joint metric approach for SQM, constructing a joint detection metric based on code delay and carrier phase to enhance detection algorithm performance. Prisiavash et al. [90] presented a two-dimensional SQM detection algorithm based on code delay and Doppler frequency. While this algorithm improves detection performance, it significantly increases computational complexity. [91] applied sliding window variance and sliding window averaging to existing SQM methods, significantly improving detection performance in static spoofing interference environments. [92] applied sliding window variance processing to the SCB method and proposed a detection algorithm based on SCB variance.

The target receiver obtains the corresponding code phase value through the zero-crossing point of the code discriminator curve (i.e., the S-curve) in the code tracking loop. In the absence of interference and noise, the code phase value corresponding to the zero-crossing point of the S-curve is zero. However, due to the channel transmission distortion and non-linear effects of power amplifiers, the code phase value fluctuates near zero. The SCB value, which measures the code tracking error, serves as a criterion for detecting spoofing attacks.

[93] proposed a method based on weighted second-order moments (WSCM) to detect induced spoofing interference, targeting the gradual dynamic adjustment process where spoofing and genuine signals interact during the tracking stage, leading to correlation peak symmetry distortion. Specifically, a weighted criterion for the time-domain transient response values of multiple correlators is established by expanding the second-order central moment (SCM) [94] of the navigation signal waveform. A WSCM test statistic is then constructed, accurately quantifying correlation peak symmetry. [95] combined radio power detection metrics with automatic gain control and C/N0 measurements, along with the multi-correlation of signal distortion, to construct new SQM thresholds for detecting and identifying spoofing interference. This method introduces a novel metric to SQM. This SQM metric requires additional correlators, which expands the investigation area but accurately identifies spoofing interference among various interference attacks.

[96] proposed a robust spoofing interference detection method for GNSS instruments using the Q-channel signal quality monitoring metric. This method utilizes and measures the abnormal energy in the Q-channel of the tracking loop for spoofing interference detection. This SQM metric overcomes the challenge of constantly changing relative carrier phases between real and spoofing signals, achieving higher detection probability while being cost-effective and highly practical. It only requires minimal modifications to the traditional receiver's baseband correlator and firmware. [97] proposed a spoofing detection algorithm based on a combination of SQM and tracking parameters. This method leverages the complementarity between different SQM metrics, proposing an “OR” rule that combines various SQM parameters and determines the corresponding optimal detection threshold. Compared to a single SQM measure, SQM measure fusion based on the “OR” principle exhibits significant performance improvements in detection. [98] proposed a spoofing detection algorithm based on a vector tracking structure using SQM. This method overcomes the limitation of traditional SQM algorithms, which become ineffective when correlation peaks do not overlap. It utilizes existing observations in tracking to detect spoofing attacks on the pseudocode and carrier. [99] addressed the low detection accuracy and susceptibility to the power advantage and carrier phase drift of spoofing signals in traditional SQM techniques. They proposed an innovative SQM method that employs the Kolmogorov–Smirnov (KS) test for detecting receiver correlator output. This method overcomes the performance limitations of traditional SQM techniques, effectively detecting subtle symmetry distortion of the correlation function and signal power changes caused by spoofing signals. It serves as a potential reliable application solution for spoofing attacks with different frequency locking modes and power consumption advantages. It also avoids changes to the receiver hardware structure and has low computational complexity.

### 4.1.6 Deep learning-based spoofing interference detection and identification

Given the rapid advancement of deep learning, its application in spoofing interference detection and identification has become inevitable. Deep learning approaches for interference signal detection and identification involve processing and analyzing received signals to isolate interference signals and determine their types and parameters. Interference signal identification typically involves analyzing signal characteristics such as feature parameters, time-domain characteristics, frequency-domain characteristics, and phase characteristics. Deep learning methods utilize signal feature parameters when spoofing is present and absent as network inputs for training, resulting in a network capable of rapidly distinguishing spoofing based on different features.

Preprocessing is usually required to identify the type of interference in the received signal. One such method is normalization or zero-mean normalization [100], transforming the signal into a standard form to minimize differences. Signal feature parameters, such as power spectral density, frequency, amplitude, and phase, are extracted by analyzing the time-domain, frequency-domain, and phase characteristics of the signal. The type of interference signal can be determined by further analyzing these feature parameters, such as narrowband interference, broadband interference, or pulsed interference [101]. Common classification algorithms include decision trees (DT) [102, 103], support vector machines (SVM), and backpropagation (BP) neural networks [104, 105].

[106] investigated the types and methods of interference signals in satellite navigation systems. Time-domain cross-correlation features of the received signal were extracted, considering the localization and identification of multiple interference signals. The SVM was then used to classify and identify the interference signals. To enhance the system's noise resistance, a convolutional neural network (CNN) was used for interference signal recognition,

significantly improving recognition performance at low interference-to-noise ratios. A backpropagation neural network (BPNN) is a neural network model trained using the error backpropagation algorithm. It consists of an input layer, hidden layers, and an output layer, where hidden layers can have multiple layers. The BPNN algorithm computes the network's output value through forward propagation and then compares the output value with the actual value to calculate the error value. Next, the error value is backpropagated to the network, adjusting the weights of each layer to minimize the error. The key to the BPNN algorithm is the error backpropagation algorithm, which utilizes the chain rule to propagate errors from the output layer to the input layer, calculating the error of each layer and then adjusting the weights of each layer to minimize the error.

[107] investigated BPNN identification algorithms, but BPNN algorithms have issues, such as becoming stuck in local optima and slow training speed. In classification and recognition problems, decision trees classify input variables into a predefined category through a series of decision nodes. In regression problems, decision trees use a series of decision nodes to ultimately produce a continuous output value. The basic principle of decision tree classification algorithms is to construct a tree-like structure based on different values of input features, assigning different input samples to different categories. The process of constructing a decision tree can use recursive partitioning, and [108] designed a stable classifier using the decision tree approach. It was implemented and tested on a hardware platform. Residual networks (ResNet) are a type of deep neural network architecture that addresses the problem of training deep neural networks by introducing residual blocks. Residual networks allow information to propagate directly across layers, enabling deep networks to better capture the relationship between input and output, thus improving the efficiency and accuracy of training deep networks. [109] simulated and analyzed deep learning-based recognition algorithms by constructing real and complex residual networks with CNNs. The study found that the main advantage of a ResNet is that it can further improve the network performance by adding more layers while maintaining model accuracy. The gravitational search algorithm (GSA) is an optimization algorithm based on Newton's law of universal gravitation and Newton's second law, simulating the interaction between celestial bodies. It searches for the optimal solution by simulating parameters such as gravity, mass, and velocity. The basic idea of the algorithm is to view the optimization problem as a celestial system, where each solution is considered a celestial body, its mass being proportional to the fitness value and its position representing the parameters of the solution. During the search process, each solution is affected by the universal gravitational force and centripetal force of other solutions. The centripetal force moves the solution toward the direction of the historical optimal position, while gravity moves the solution toward a better position.

Based on the GSA algorithm, [110] optimized the parameters of SVM for identifying audio interference in terrestrial-to-space communication. Simulation results show that GSA has advantages such as being simple to implement, having a strong global search capability, and fast convergence speed. SVM is a binary classification algorithm, but it can be used for multi-class recognition through various methods. [111] used the one-vs.-all method for multi-class recognition. This algorithm has high recognition efficiency and high classification accuracy. [112] proposed a deep learning spoofing detection method based on representation learning. This method addresses the problem of deep learning methods being limited by training data and can be trained using a single dataset. This lightweight critic-model-based score detector can be seamlessly integrated into GNSS receivers through firmware updates once trained offline, thus reducing additional overhead.

### 4.1.7 Other methods of anti-spoofing interference

Beyond signal-level detection and identification of spoofing interference, techniques involving modification of signal structures, such as spread spectrum code encryption and message encryption, can also be employed for spoofing interference monitoring and identification. However, these approaches alter the GNSS signal structure, limiting their practical applicability. Simultaneously, anti-spoofing technologies combined with external auxiliary techniques are also emerging, such as integration with inertial navigation units, other radio navigation systems, and other sensors. Among these, the combination of a GNSS with inertial navigation units (INS) is the most widely used anti-spoofing approach. INS positioning solutions are unaffected by external interference, providing auxiliary information for the detection and suppression of GNSS spoofing interference. Existing INS/GNSS integrated navigation anti-spoofing techniques mainly include spoofing detection algorithms based on Kalman filter innovations and innovation rate [113, 114], spoofing detection algorithms based on the comparison of INS and GNSS raw measurements [115], and INS-assisted GNSS carrier-phase spoofing detection [116].

## 4.2 Spoofing interference suppression

Spoofing interference suppression aims to eliminate spoofed signals after detection and identification, thereby restoring the normal operation of the navigation system. The most prevalent approach for spoofing interference suppression is the use of array antenna nulling. This technique encompasses two methods: spatial [117] and spatiotemporal [118] processing. The core principle involves generating nulls in the direction of the interfering signal to suppress the interference. Array antenna nulling can be categorized into pre-despreading and post-despreading spoofing interference suppression. Pre-despreading methods have a smaller computational load and leverage the characteristic of spoofing interference power superposition in the spatial domain. They estimate the spoofing signal steering vector or signal subspace to achieve spoofing interference suppression. However, the suppression performance of this method is significantly affected by the spoofing signal power. Higher spoofing signal power generally leads to better interference suppression performance. Conversely, post-despreading spoofing interference suppression techniques first identify the spoofing interference signal and then calculate the steering vector and weights specifically for the spoofing signal.

Pre-despreading spoofing interference suppression methods typically leverage the power advantage of spoofing interference to

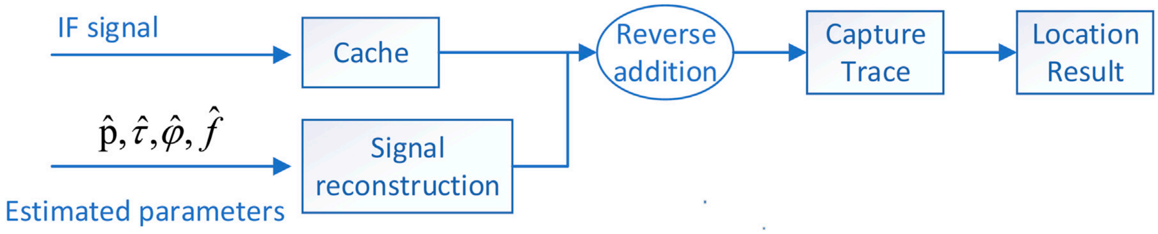

**FIGURE 13**
Block diagram of the signal reconstruction deception jamming suppression method.

estimate the steering vector and spatial information. Based on this information, weights are calculated for weighting, achieving spoofing interference suppression. However, the accuracy of spoofing interference spatial information estimation is significantly influenced by the power level due to the lower signal-to-noise ratio before despreading. The suppression performance deteriorates under low spoofing interference power conditions. Nonetheless, because despreading is not required, the computational load is smaller than post-despread interference suppression methods. Despreading improves the signal-to-noise ratio for post-despreading spoofing interference suppression methods, leading to more accurate signal spatial characteristics. It also allows for obtaining carrier phase information that can be used to identify spoofing signals based on other characteristics, further enabling interference suppression. In addition to these methods, signal reconstruction can be employed for spoofing interference suppression in single-antenna receivers, as illustrated in Figure 13. This approach involves detecting spoofing interference and extracting its code delay, Doppler frequency, carrier phase, and signal amplitude to reconstruct the spoofing signal. The reconstructed signal is then subtracted from the original intermediate frequency (IF) navigation signal, effectively eliminating the spoofing interference and yielding a spoofing-free navigation signal.

[119] proposed a spoofing signal classification module to distinguish between spoofed and genuine signals, reconstructing and eliminating the spoofed signal based on its characteristics. The processed signal is then re-examined, and if spoofing interference is detected, the process of reconstruction and elimination is repeated. [120] estimated the amplitude and phase of the spoofing signal to reconstruct it, subtracting the reconstructed signal from the delayed original signal. The performance was evaluated using the interference cancellation ratio (ICR). Simulation results from these studies indicate that signal reconstruction exhibits excellent suppression performance, but it necessitates continuous and accurate acquisition of spoofing signal information, leading to significant complexity and implementation challenges.

The difficulty and computational complexity of accurately estimating all parameters of spoofed signals significantly limit the application of signal reconstruction methods [121]. HANS et al. [122] proposed a subspace projection method that estimates the carrier frequency and code phase of spoofed signals through capture tracking. A signal subspace of the forged signal is constructed by exploiting the near orthogonality of their PRN codes. The received signal is then orthogonally projected onto this subspace, suppressing the spoofed signal and enabling the capture and tracking of the true signal. Compared with signal reconstruction methods, this method requires less information about the spoofed signal and exhibits better robustness. However, if the phase difference between the spoofed and true signals is less than one chip, the suppression function will be lost, indicating that this method cannot detect spoofed signals with small deviations.

[123] proposed an adaptive beamforming algorithm for spoofing interference suppression in GNSS receivers. Adaptive beamforming can control the radiation pattern of the antenna array, suppressing spoofed signals from the direction of the spoofing interference source and enhancing the true navigation signals from the direction of navigation satellites. Beamforming technology is used simultaneously with spoofing interference detection technology based on antenna arrays. First, baseband signals are acquired through the antenna array, and a circulant matrix is established. Spoofing interference detection is achieved based on eigenvalue testing. Subsequently, spoofing interference is suppressed, and the true signal is enhanced through beamforming technology. Adaptive beamforming has many applications in the suppression of jamming interference, and the algorithm is relatively mature. It can be directly applied to spoofing interference suppression and can simultaneously suppress both jamming and spoofing interference. However, with the increase in the number of interference directions, the antenna array needs to further increase the number of antenna elements, making the complexity and high cost of the equipment the main reasons limiting its widespread application. Introducing a multi-correlator structure in the receiver allows for simultaneous capture and tracking of both the true signal and spoofed signals. Subsequently, a decision method confirms the true signal and eliminates spoofed signals, enabling the detection and suppression of spoofing signals. When multiple signals exist in the received signal, multi-signal tracking is performed using multiple correlators without prior knowledge of the spoofed signal. The multipath estimating delay lock loop (MEDLL) technique is used to process the baseband signal, obtaining the signal's amplitude, propagation delay, and carrier phase, denoted as [124]. Subsequently, based on the estimated amplitude, propagation delay, and carrier phase of the signal, one set of signals is removed from the original baseband signal and tracked separately, thereby obtaining the tracking results of the other set of signals.

In combined navigation-based spoofing interference detection methods, if the satellite navigation receiver is determined to be

**TABLE 3** Summary table of different spoofing interference suppression methods.

| Method | Complexity | Performance | Limitations |
|---|---|---|---|
| Signal reconstruction | High | Medium | It is necessary to obtain spoofing signal information continuously and accurately |
| Subspace projection | Medium | High | Fails when the phase difference between the deception signal and the real signal is less than one chip |
| Beamforming | Medium | High | Requires array antennas with element spacing less than half the wavelength |
| Multi-correlator method | Low | Medium | It will fail when the amount of computation is large, and the power of the spoofing signal is large |
| Integrated navigation method | Medium | Medium | Requires additional hardware or sensors |
| Direct positioning method | Medium | Medium | Has poor performance at medium to low signal-to-noise ratios |
| Receiver autonomous integrity monitoring | Medium | Medium | Spoofing signal power is required, and there are multiple satellites |

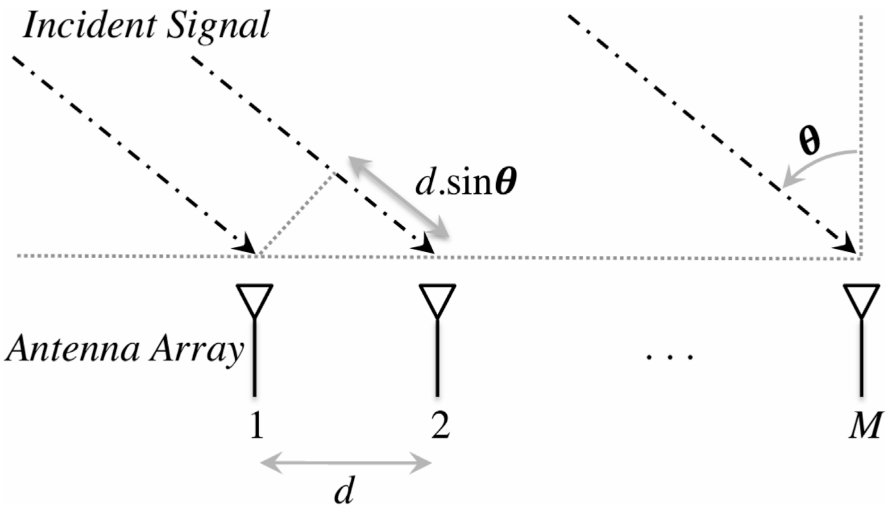

FIGURE 14
Schematic diagram of the signal angle of arrival measurement [125].

spoofed, non-satellite navigation systems are used for navigation, achieving spoofing interference suppression. The essence of this method is to discard untrustworthy satellite navigation results and select other reliable navigation results. The disadvantage of this method is that it requires multiple navigation systems, which increases costs. Moreover, the positioning accuracy after suppression depends on the performance of the other navigation methods.

Receiver autonomous integrity monitoring (RAIM) is also an effective spoofing interference suppression method. This method can effectively eliminate faulty satellites. In cases with fewer spoofing interference signals, they can be eliminated from the received signals, ensuring the authenticity and validity of the navigation positioning results. However, in general, to obtain reliable positioning solutions from the receiver, spoofing interference often requires the simultaneous transmission of false signals from multiple satellites with a higher power level than the true signal. This may lead to the receiver completely capturing and tracking the spoofed signal, rendering the RAIM algorithm ineffective. Table 3 below summarizes the complexity, performance, and limitations of various methods.

## 4.3 Spoofing interferer location

Detecting, identifying, and suppressing spoofing signals are challenging tasks, often requiring the addition and upgrade of receiving equipment, significantly increasing the cost of spoofing interference suppression. Another approach to spoofing interference suppression is to focus on high-precision strikes against the spoofing interference source, eliminating its impact by destroying it. Existing methods for locating satellite navigation spoofing sources employ a two-step localization approach. In the first step, the receiver intercepts the spoofing interference signals and performs initial signal processing to estimate parameters such as time of arrival (TOA), time difference of arrival (TDOA), frequency difference of arrival (FDOA), and angle of arrival (AOA). The second step establishes an equation relating these intermediate parameters to the spoofing source location, and solving this equation yields the location information. Angle of arrival (AOA) analysis based on antenna arrays is currently the most practical method for locating spoofing sources. The algorithm principle is illustrated in Figure 14. Given that spoofing sources are typically fixed, the direction of

**TABLE 4** Positioning methods and receiver requirements.

| Targeting method | Spoofing interference feature | Receiver requirements |
|---|---|---|
| Multi-receiver detection | Spoofing jamming is emitted by the same interferer | Multiple satellite nav receivers in different locations |
| Integrated navigation detection | Only one GNSS system is spoofed | Inertial navigation and satellite navigation combined |
| Clock error detection | The deception jamming clock is inconsistent with the real clock difference | —— |
| Signal reconstruction (residual signal detection) | Real signals can be detected. | Multiple signal reception channels |
| Spoofing interferer location | Multiple spoofing signals come from the same interferer. | Multiple receivers in different locations |
| Message verification | Unencrypted | Encryption verification |
| Power detection | Absolute power detection | The receiver has a power detection function that can distinguish higher signal amplitudes |
| | Relative power detection | |
| | Automatic gain control (AGC) detection | The receiver is equipped with a carrier-to-noise ratio detection function |
| | Power rate of change detection | |
| Arrival time detection | There is a delay in spoofing signals | Arrival time analysis |
| Correlation detection | Multiple spoofing signals come from the same direction | Measure the correlation coefficient of the output of different tracking channels |
| Signal quality checking | The true signal-related peaks are distorted | Multiple correlators |
| Airspace/space-time detection | The on-road signal is coming from the same direction | Multiple receiving antennas |

arrival of the spoofing signals remains constant. Therefore, the AOA can be determined by measuring the different phases of the same spoofing signal arriving at different antennas in a uniform linear array. [125, 126] were the first to achieve sub-meter localization accuracy, reaching 0.7 m. Subsequently, University College London leveraged multiple-input multiple-output (MIMO) technology and channel state information (CSI) to measure AOA, achieving a remarkable localization accuracy of 23 cm [127].

The accuracy of the two-step localization method is highly dependent on the accuracy of the parameter estimation. The location calculation and parameter estimation are inseparable, limiting the effective utilization of correlations between signals received at different stations, leading to information loss, difficulties correlating localization parameters, and high system sensitivity requirements. Clock offset, however, contains information about the location of the spoofing interference source relative to the receiver. Utilizing the clock offset measured at different receiver locations under both genuine and spoofing interference signal conditions allows for calculating the distance difference between the spoofing interference source and the two receivers. The location of the spoofing interference source can be estimated using hyperbolic intersection localization by employing multiple sets of receivers to measure these distance differences.

## 4.4 Summary

This article summarizes the scenarios to which the commonly used anti-spoofing methods of various receivers are applicable, what kind of spoofing signal characteristics apply, and what functions the receiver needs to have, as shown in Table 4 below.

# 5 Opportunities and challenges

As satellite navigation systems continue to evolve, dependence on these systems will inevitably increase, making the threat of satellite navigation spoofing interference increasingly prominent. Consequently, intensifying research and preventative measures, along with developing more intelligent and advanced anti-interference technologies, are crucial. Several challenges persist in the field of anti-spoofing interference:

First, the quality of spoofed signals continues to improve, resulting in enhanced concealment, increased positional and velocity accuracy, higher generation frequencies, and a closer resemblance to genuine signals. This allows spoofed signals to seamlessly and covertly integrate into receivers, posing significant challenges for anti-spoofing measures. Second, the maturation of multi-spoofing interference platform technologies has introduced a paradigm shift from single-platform spoofed signals. These multi-platform systems generate interference signals from multiple directions and utilize diverse interference types simultaneously, demanding higher anti-interference capabilities from receivers. Third, current experimental conditions for spoofing interference are overly idealized, primarily conducted in open, sparsely populated areas with minimal radio signal interference. Limited research has been conducted in complex terrain, such as mountainous regions and urban areas. The lack of experimental materials for such scenarios significantly hinders the development of effective anti-spoofing interference technologies. Meanwhile, spoofing techniques are constantly evolving. Attack methods such as security code estimation and replay (SCER), which differ from traditional spoofing methods, are becoming increasingly cost-effective [128]. With multiple spoofing methods working in tandem, receivers face a significant challenge in handling scenarios where multiple spoofing attacks coexist.

To address these challenges, future satellite navigation receivers must adopt a combined approach to anti-interference detection. This approach should leverage machine learning, consistency checks, and array testing to enable more effective and robust spoofing interference detection [129]. Additionally, by combining the performance advantages of multiple research projects, a multi-faceted aerial defense system could be developed using unmanned aerial vehicle (UAV) clusters, ships, and aircraft. This system would encompass target identification and tracking, radio countermeasures, and multi-target strikes. Finally, compact anti-interference platforms should be developed to enhance the stability of anti-spoofing measures by making anti-interference receivers portable, miniaturized, and cost-effective.

## Author contributions

CL: Writing–review and editing. ZLu: Supervision, Resources, Project administration, writing–review and editing. Zli: Supervision, Resources, Writing–review and editing. LH: Supervision, Resources, Writing–review and editing. FC: Supervision, Resources, Writing–review and editing.

## Funding

The author(s) declare that financial support was received for the research, authorship, and/or publication of this article from the National Natural Science Foundation of China under Grant U20A0193.

## Conflict of interest

The authors declare that the research was conducted in the absence of any commercial or financial relationships that could be construed as a potential conflict of interest.

## Publisher's note

## References

1. Margaria D, Motella B, Anghileri M, Floch J-J, Fernández-Hernández I, Paonni M. Signal structure-based authentication for civil GNSSs: recent solutions and perspectives. *IEEE Signal Process. Mag* (2017) 34(5):27–37. doi:10.1109/msp.2017.2715898

2. Kaplan ED. GPS principles and applications. In: *Translated by kou yan-hong*. 2nd ed. Beijing: Electronic Industry Press (2007).

3. Chen Y, Zhan X.GNSS vulnerability reliable assessment and its substitution with visual-inertial navigation[J]. *Aerospace Syst*, 2021, Vol.4(3): 179–89. doi:10.1007/s42401-021-00099-6

4. Jovanovic A, Botteron C, Fariné P-A. Multi-test detection and protection algorithm against spoofing attacks on GNSS receivers. In: *Proc. IEEE/ION position, location navigat. Symp. (PLANS)*. Monterey, CA, USA (2014).12581271

5. Psiaki ML, Humphreys TE, Stauffer B. Attackers can spoof navigation signals without our knowledge. Here's how to get back GPS lies. *IEEE Spectr* (2016) 53(8): 26–53. doi:10.1109/MSPEC.2016.7524168

6. Heng L, Work DB, Gao GX. GPS signal authentication from cooperative peers. *IEEE Trans Intell Transp Syst* (2015) 16(4):1794–805. doi:10.1109/tits.2014.2372000

7. Jiang C, Chen S, Chen Y, Bo Y, Xia Q, Zhang B. Analysis of the baseline data based GPS spoofing detection algorithm. In: *Proc. IEEE/ION position, location navigat*. Monterey, CA, USA (2018). Symp. (PLANS).397403

8. Xie X, Lu M, Zeng D. Research on GNSS generating spoofing jamming technology. In: *Proc. IET int. Radar conf.* Hangzhou, China (2015). p. 5. doi:10.1049/cp.2015.0999

9. He L, Li W, Guo C, Niu R. Civilian unmanned aerial vehicle vulnerability to GPS spoofing attacks. In: *2014 seventh international symposium on computational intelligence and design*. Hangzhou, China (2014). p. 212–5. doi:10.1109/ISCID.2014.131

10. Kugler LOGAN. Why GPS spoofing is a threat to companies, countries. *Commun ACM* (2017) 60(9):18–9. doi:10.1145/3121436

11. Jon S, Warner PD, Roger P, Johnston G. "GPS spoofing countermeasures." (2003).

12. Humphreys TE, Ledvina BM, Psiaki ML, O'Hanlon BW, Kintner PM, Jr. Assessing the spoofing threat: development of a portable GPS civilian spoofer. In: *Proceedings of the 21st international technical meeting of the satellite division of the Institute of navigation (ION GNSS 2008)*. Savannah, GA (2008). p. 2314–25.

13. Hu Y, Bian S, Li B, Zhou L. A novel array-based spoofing and jamming suppression method for GNSS receiver. *IEEE Sensors J* (2018) 18(7):2952–2958. doi:10.1109/JSEN.2018.2797309

14. Zhang N. A case study on the application of GPS forward spoofing jamming in UAV. *Aerosp China* (2015) 7:4042.

15. Shepard DP, Bhatti JA, Humphreys TE, Fansler AA. "Evaluation of smart grid and civilian UAV vulnerability to GPS spoofing attacks," in Proceedings of the 25th international technical meeting of the satellite division of The Institute of Navigation (ION GNSS 2012), Nashville, TN (2012). 3591–3605.

16. Humphreys TE. UT austin researchers spoof supery acht at sea (2013). Austin: The University of Texas at Austin. Available from: http://www.engr.utexas.edu/features/superyacht-gps-spoofing.

17. Psiaki ML, Humphreys TE. GNSS spoofing and detection. *Proc IEEE* (2016) 104(6):1258–70. doi:10.1109/JPROC.2016.2526658

18. Bian S, Hu Y, Ji B. Research status and prospect of GNSS anti-spoofing technology. *Scientia Sinica Informationis* (2017) 47(3):275–287. doi:10.1360/N112016-00073

19. Dai SG, Zhou HJ. GNSS repeater detection based on channel difference. *J Comput Methods Sci Eng* (2018) 18(2):491–8. doi:10.3233/jcm-180804

20. Bian SF, Hu YF, Chen C, Li ZM, Ji B, et al. Research on GNSS repeater spoofing technique for fake position, fake time and fake velocity [C]. In: *IEEE international conference on advanced intelligent mechatronics* (Munich, Germany: AIM) (2017). p. 1430–1434. doi:10.1109/AIM.2017.8014219

21. Jun WANG, Yan GUO, Tang K, He X. Navigation and control,2022, Vol.21(1): 13–24.

22. He T. Improvement of GNSS transponder deception jamming method. *Bull Surv Mapp* (2019) 0 (4) 71–74,83. doi:10.13474/j.cnki.11-2246.2019.0115

23. Farley MG, Carlson SG. "A new pseudolite battlefield navigation system," in *IEEE 1998 Position Location and Navigation Symposium (Cat. No.98CH36153)* (Palm Springs, CA, United States) (1998):208–217. doi:10.1109/PLANS.1998.670043

24. Zhang S, Yang J, Gaofeng P, Jiabao J. GPS area-mapping deceiving unites region navigation integrative system. In: *2010 3rd international conference on computer science and information technology*. Chengdu (2010). p. 189–91. doi:10.1109/ICCSIT.2010.5564940

25. Jafarnia-Jahromi A, Broumandan A, Nielsen J, Lachapelle G. GPS spoofer countermeasure effectiveness based on signal strength, noise power, and C/N0 measurements. *Int J Satellite Commun Networking* (2012) 30(4):181–91. doi:10.1002/sat.1012

26. Humphreys TE, Brent ML, Mark LP, Brady WO'H, Paul MK. Assessing the spoofing threat: development of a portable GPS civilian spoofer. In: *Proceedings of the ION GNSS meeting* (2008). p. 16–9.

27. Gao Y, Lv Z, Zhang L. Asynchronous lift-off spoofing on satellite navigation receivers in the signal tracking stage. *IEEE Sens J* (2020) 20(15):8604–13. doi:10.1109/jsen.2020.2984525

28. Wang J, Zhou M, Li H, Cui X, Lu M. "On the requirements of GNSS intermediate spoofing," in China satellite navigation conference (CSNC) 2014 proceedings: volume I, New Delhi, India. Editor Sun J., Jiao W., Wu H., Lu M. (Springer, Berlin, Heidelberg:

Lecture Notes in Electrical Engineering) (2014) 303. doi:10.1007/978-3-642-54737-9_47

29. Geng Z. *Research on GNSS spoofing jamming detection and suppression technology*. Ph.D. Dissertation, National University of Defense Technology (2019). doi:10.27052/d.cnki.gzjgu.2019.000344

30. Ioannides RT, Pany T, Gibbons G. Known vulnerabilities of global navigation satellite systems, status, and potential mitigation techniques. *Proc IEEE* (2016) 104(6): 1174–94. doi:10.1109/jproc.2016.2535898

31. Gang X. *GPS principle and receiver design[M]*. Electronics Industry Press (2017).

32. Yang Q. *Research on anti-jamming technology of satellite navigation receiver[D]*. Northwestern Polytechnical University (2019).

33. Fan G, Huang Y, Zhang G, Nie J, The GPS spoofing detection based on the joint WSSE of DOA and pseudorange[C].

34. Akos DM. Who's afraid of the spoofer? GPS/GNSS spoofing detection via automatic gain control (AGC). *J Navigation* (2012) 59(4):281–90. doi:10.1002/navi.19

35. Dehghanian V, Nielsen J, Lachapelle G. GNSS spoofing detection based on signal power measurements: statistical analysis. *Int J Navigation and Observation* (2012) 2012(7):1–8. doi:10.1155/2012/313527

36. Dehghanian V, Nielsen J, Lachapelle G. GNSS spoofing detection based on receiver C/N0 estimates[J]. *Proceedings of international technical meeting of the satellite division of the Institute of navigation*, 2012:2878–84.

37. Nielsen J, Dehghanian V, Lachapelle G. Effectiveness of GNSS spoofing countermeasure based on receiver CNR measurements. *Int J Navig Observations* (2012) 2012(9):1–9. doi:10.1155/2012/501679

38. Long H, Tang X, Feixue W. Research on anti-spoofing jamming method of satellite navigation receiver[C]. In: *China satellite navigation academic annual conference* (2011). p. 1344–7.

39. Gao Y, Li H, Lu M, Feng Z. Intermediate spoofing strategies and countermeasures [J], *Tsinghua Science and Technology*, 2013.18(6), 599–605. doi:10.1109/TST.2013.6678905

40. Tu JX, Zhan XQ, Zhang X, Zhang ZJ, Jing S. Low-complexity GNSS anti-spoofing technique based on Doppler frequency difference monitoring. *IET Radar, Sonar and Navigation* (2018) 12(9):1058–65. doi:10.1049/iet-rsn.2018.5151

41. Wullems CJ. A spoofing detection method for civilian L1 GPS and the E1-B galileo safety of life service. *IEEE Trans Aerospace Electron Syst* (2012) 48(4):2849–64. doi:10.1109/taes.2012.6324665

42. Motella B, Pini M, Fantino M, Mulassano P, Nicola M, Fortuny Guasch J, et al. Performance assessment of low cost GPS receivers under civilian spoofing attacks[C]. Noordwijk, Netherlands: 2010 5th ESA Workshop on satellite navigation technologies and European workshop on GNSS signals and signal processing (NAVITEC) (2010) 1–8. doi:10.1109/NAVITEC.2010.5708018

43. Psiaki ML, Ohanlon BW, Powell SP, Bhatti JA, Wesson KD, Schofield TE. Humphreys andrew, GNSS spoofing detection using two-antenna differential carrier phase. In: *Proceedings of the 27th international technical meeting of the satellite division of the Institute of navigation (ION GNSS+ 2014)*. Florida: Tampa (2014). p. 2776–800.

44. Savasta S, Presti LL, Dovis F, Margaria D. Trustworthiness GNSS signal validation by a time-frequency approach[C]. In: *Proceedings of the 22nd international technical meeting of the satellite division of the Institute of navigation (ION GNSS 2009)* (2009). p. 66–75.

45. Jafarnia-Jahromi A, Lin T, Broumandan A, Nielsen J, Lachapelle G. Detection and mitigation of spoofing attacks on a vector based tracking GPS receiver[C]. In: *Proceedings of international technical meeting of the Institute of navigation (ION ITM 2012)*. Newport Beach, CA. p. 790–800. 30 January-1 February.

46. Cavaleri A, Motella B, Pini M, Fantino M. *Detection of spoofed GPS signals at code and carrier tracking level*. Noordwijk, Netherlands: 2010 5th ESA Workshop on satellite navigation technologies and European workshop on GNSS signals and signal processing (NAVITEC) (2010). p. 1–6. doi:10.1109/NAVITEC.2010.5708016

47. Broumandan A, Jafarnia-Jahromi A, Dehghanian V, Nielsen J, Lachapelle G. GNSS spoofing detection in handheld receivers based on signal spatial correlation[C]. In: *Proceedings of IEEE/ION PLANS 2012*. p. 479–87. April 24-26, Myrtle Beach, South Carolina.

48. Shen C, Guo C. Simulation of optimal detection of spoofing signals in global navigation satellite system[J]. *Computer Simulation*, 2019, 36(6):109–113, 119. doi:10.3969/j.issn.1006-9348.2019.06.022

49. He H. Research on anti-spoofing jamming method of satellite navigation based on array[D]. In: *Heilongjiang*. Harbin Engineering University, MA thesis (2019).

50. Rui X, Mengyu D, Qian M. MEDLL-assisted spoofing signal identification method for GNSS/INS system[J]. *Chin J Inertial Technology*, 2018, v.26(02):89–96. doi:10.13695/j.cnki.12-1222/o3.2018.02.013

51. Yin W, Yang GG, Fu J. Interference identification for inertial assisted GNSS receivers[J]. *J Navigation Positioning*, 2018, v.6;No. 22(02):45–49. doi:10.16547/j.cnki.10-1096.20180208

52. Yabin L, Guo C, Zhong T. Research on GPS anti-spoofing jamming based on zeroing technology. *Electro-Optics and Control*, 2017(01):41–44. doi:10.3969/j.issn.1671-637X.2017.01.009

53. Liu D, Lv J, Rui M, et al. Research and prospect of spoofing and anti-spoofing technology of satellite navigation system[J]. *Res Beidou Satellite Navigation Signal Spoofing Jamming Detect Technology*, 2017, 50(05):837–843. doi:10.3969/j.issn.1002-0802.2017.05.001

54. Cao K, Peng X, Bao LI, et al. Spoofing jamming detection method based on signal-to-noise ratio measurement[J]. *Computer Meas and Control*, 2016, 24(04):29–32+35. doi:10.16526/j.cnki.11-4762/tp.2016.04.009

55. Wesson KD, Gross JN, Humphreys TE, Evans BL. GNSS signal authentication via power and distortion monitoring. *IEEE Trans Aerospace Electron Syst* (2018) 54(2): 739–54. doi:10.1109/TAES.2017.2765258

56. Shuli D, Taotao Z, Min L. A GNSS anti-spoofing technology based on power detection. In: *2019 IEEE 8th joint international information technology and artificial intelligence conference (ITAIC)*. Chongqing, China (2019). p. 1134–7. doi:10.1109/ITAIC.2019.8785690

57. Zhang G, Zhang Y, Ye TIAN. Research on Beidou deceptive jamming detection technology based on DOD and PTD. *Appl Sci Technology* (2019) 46(2):35–41. doi:10.11991/yykj.201807010

58. Fan G, Ran D, Zhang F, Zhouhui TUO.*Glob Positioning Syst*, 2020, 45(1):66–70. doi:10.13442/j.gnss.1008-9268.2020.01.011

59. Wang Z, Nie J, Zhengrong L. Forwarded spoofing signal detection algorithm for BOC receiver capture stage [J]. *Glob Positioning Syst*, 2016, 41(05):13–17. doi:10.13442/j.gnss.1008-9268.2016.05.003

60. Zhang G, Ding J, Zhang Y. Relay spoofing jamming detection algorithm based on GNSS signal delay feature [J]. *Radio Eng*, 2019, 49(07):626–630. doi:10.3969/j.issn.1003-3106.2019.07.015

61. Wang W, Wang P. GNSS spoofing jamming detection based on capture results [J]. *J Signal Process*, 2021, 37(08):1460–1469. doi:10.16798/j.issn.1003-0530.2021.08.013

62. Jian W, Hong L, Cui X, et al. "A new method in acquisition to detect GNSS spoofing signal [C]," in Proceedings 2013 International Conference on Mechatronic Sciences, Electric Engineering and Computer, Shenyang, China (2014). p. 2913–2917.

63. Yang B, Mei T, Ji Y, Cheng J, Xie Z, Shao S. Research on GNSS spoofing mitigation technology based on spoofing correlation peak cancellation. *IEEE Commun Lett* (2022) 3024–8. doi:10.1109/LCOMM.2022.3204944

64. Daneshmand S, Jafarnia-Jahromi A, Broumandan A. A GNSS structural interference mitigation technique using antenna array processing [C]. *IEEE 8th sensor array multichannel signal process workshop*, Coruna, Spain, 2014: 109–12.

65. Da-Jiang GE, Zhou GB, Da-Chuan XU. GPS receiver anti-deceptive jamming method based on space-time multi-antenna null [J]. *J Sichuan Ordnance*, 2015, 36(8): 41–45.

66. Long H, Ling Y, Bo X, et al. Anti-spoofing method for satellite navigation receiver using dual-antenna carrier phase difference technology[J]. *J Natl Univ Defense Technology*, 2016, 38(04): 103–106. doi:10.11887/j.cn.201604016

67. Hu Y, Bian S, Li B, Zhou L. A novel array-based spoofing and jamming suppression method for GNSS receiver. *IEEE Sensors J* (2018) 18(7):2952–8. doi:10.1109/jsen.2018.2797309

68. Jiang C, Chen S, Chen Y. Analysis of the baseline data based GPS spoofing detection algorithm [C]//IEEE/ION Position. In: *Location and navigation symposium*. Monterey, USA (2018). p. 397–403.

69. Wang F, Li H, Lu M. GNSS spoofing detection based on unsynchronized double-antenna measurements. *IEEE Access* (2018) 6:31203–12. doi:10.1109/access.2018.2845365

70. Nguyen VH, Falco G, Nicola M, Falletti E. *A dual antenna GNSS spoofing detector based on the dispersion of double difference measurements [C]//2018 9th ESA Workshop on Satellite Navigation Technologies and European Workshop on GNSS Signals and Signal Processing*. Noordwijk, Netherlands: 2018 9th ESA workshop on satellite navigation technologies and European workshop on GNSS signals and signal processing (NAVITEC) (2018). p. 1–8. doi:10.1109/NAVITEC.2018.8642705

71. Xu G, Shen F, Amin M, Wang C. DOA classification and CCPM-PC based GNSS spoofing detection technique [C]. In: *2018 IEEE/ION position, location and navigation symposium (PLANS)*. Monterey, CA, USA (2018). p. 389–396. doi:10.1109/PLANS.2018.8373405

72. van der Merwe JR, Rügamer A, Goicoechea AFD, Felber W. "Blind spoofing detection using a multi-antenna snapshot receiver," in *2019 international conference on localization and GNSS (ICL-GNSS)*. Nuremberg, Germany (2019). p. 1–7. doi:10.1109/ICL-GNSS.2019.8752840

73. Xiao L, Li X, Wang G. GNSS spoofing detection using pseudo-range double differences between two receivers [C]. In: *2019 IEEE 7th international conference on computer science and network technology*. Dalian, China (2019). p. 498–502.

74. Xiao L, Li X, Liao Z. GNSS spoofing detection with using linear array [C]. In: *2020 IEEE 8th international conference on computer science and network technology*. Dalian, China (2020). p. 181–5.

75. Mingfeng Q, Lige H, Kexin L. A deception interference detection method based on multi-baseline carrier phase difference measurement[J]. *Navigation, Positioning and Timing*, 2021, 8(03): 68–74. doi:10.19306/j.cnki.2095-8110.2021.03.009

76. Wang X, Wu S, Wang Y, et al. A method for detecting and suppressing spoofing jamming in satellite navigation based on array antenna[J]. *Mod Navigation*, 2022, 13(03):163–169. doi:10.3969/j.issn.1674-7976.2022.03.002

77. Yang H, Jin R, Xu W, Che L, Weimin Z. Satellite navigation spoofing interference detection and direction finding based on array antenna. *Sensors* (2023) 23(3):1604. doi:10.3390/s23031604

78. Jovanovic A, Botteron C, Fariné PA. Multi-test detection and protection algorithm against spoofing attacks on GNSS receivers [C]//IEEE/ION Position. In: *Location and navigation symposium*. Monterey, CA, USA (2014). p. 1258–71.

79. Tu J, Zhan X, Zhang X, Zhang Z, Jing S. Low-complexity GNSS anti-spoofing technique based on Doppler frequency difference monitoring. *IET Radar, Sonar and Navigation* (2018) 12(9):1058–65. doi:10.1049/iet-rsn.2018.5151

80. Tu J, Zhan X, Chen M, Gao H, Chen Y. GNSS intermediate spoofing detection via dual-peak infrequency domain and relative velocity residuals. *IET Radar, Sonar and Navigation* (2020) 14(3):439–47. doi:10.1049/iet-rsn.2019.0366

81. Li H, Hong L, Mingquan L. Global navigation satellite system spoofing-detection technique based on the Doppler ripple caused by vertical reciprocating motion. *Radar, Sonar and Navigation, IET* (2019) 13(10):1655–64. doi:10.1049/iet-rsn.2019.0058

82. Yuan D, Li H, Wang F, Lu M. A GNSS acquisition method with the capability of spoofing detection and mitigation, 27. *Chin J of Electronics* (2018). p. 213–22. doi:10.1049/cje.2017.11.001

83. Chu F, Li H, Wen J, Lu M. Statistical model and performance evaluation of a GNSS spoofing detection method based on the consistency of Doppler and pseudorange positioning results. *J Navigation* (2019) 72(2):447–66. doi:10.1017/S0373463318000747

84. Zhang G, Zhang Y, Tian Y. Research of Beidou navigation satellite system (BDS) spoofing detection based on DOD and PTD. *Appl Sci Technol* (2019) 46(2):3541. doi:10.11991/yykj.201807010

85. Li J, Zhu X, Ouyang M, Shen D, Chen Z, Dai Z. GNSS spoofing detection technology based on Doppler frequency shift difference correlation. *Meas Sci Technol* (2022) 33:095109. doi:10.1088/1361-6501/ac672a

86. Wei X, Sun C, Li X, Ma J. GNSS spoofing detection for UAVs using Doppler frequency and Carrier-to-Noise Density Ratio. *J Syst Archit* (2024) 153:103212. doi:10.1016/j.sysarc.2024.103212

87. Phelts R, Eric. *Multicorrelator techniques for robust mitigation of threats to GPS signal quality[D]*. California: Stanford University (2001).

88. Wang W, Li N, Wu R, Closas P. Detection of induced GNSS spoofing using S-curve-bias. *Sensors(Basel Switzerland)* (2019) 19(4):922. doi:10.3390/s19040922

89. Sun C, Cheong JW, Dempster AG, Zhao H, Feng W. GNSS spoofing detection by means of signal quality monitoring(SQM)metric combinations. *IEEE Access* (2018) 6:66428–41. doi:10.1109/access.2018.2875948

90. Pirsiavash A, Broumandan A, Lachapelle G. Two-dimensional signal quality monitoring for spoofing detection. *NAVITEC* (2016).

91. Sun C, Cheong JW, Dempster AG, Demicheli L, Cetin E, Zhao H, et al. Moving variance-based signal quality monitoring method for spoofing detection. *GPS Solut* (2018) 22:83. doi:10.1007/s10291-018-0745-7

92. Wang W, Gong J, Wang J. GNSS spoofing jamming detection algorithm based on SCB variance[J]. *Syst Eng Electronics*, 2021, 43(8):2254–2262. doi:10.12305/j.issn.1001-506X.2021.08.27

93. Zhou W, Lv Z, Deng X, Ke Y. A new induced GNSS spoofing detection method based on weighted second-order central moment. *IEEE Sensors J* (2022) 22(12):12064–78. doi:10.1109/JSEN.2022.3174019

94. Benachenhou K, Bencheikh ML. Detection of global positioning system spoofing using fusion of signal quality monitoring metrics. *Comput Electr Eng* (2021) 92:107159. doi:10.1016/j.compeleceng.2021.107159

95. Miralles D, Bornot A, Rouquette P, Levigne N, Akos DM, Chen YH, et al. An assessment of GPS spoofing detection via radio power and signal quality monitoring for aviation safety operations. *IEEE Intell Transportation Syst Mag* (2020) 12(3):136–46. Fall. doi:10.1109/MITS.2020.2994117

96. Sun C, Cheong JW, Dempster AG, Zhao H, Bai L, Feng W. Robust spoofing detection for GNSS instrumentation using Q-channel signal quality monitoring metric. *IEEE Trans Instrumentation Meas* (2021) 70:1–15. Art no. 8504115. doi:10.1109/TIM.2021.3102753

97. Blum R, Pany T. *Spoofing defense concept based on the combination of SQM and tracking parameters, tested against 100 simulated spoofer settings for GPS L1 C/A*. The International Technical Meeting of the The Institute of Navigation (2022). n. pag. doi:10.33012/2022.18184

98. Zhang X, Li H, Yang C, Lu M. Signal quality monitoring-based spoofing detection method for Global Navigation Satellite System vector tracking structure. *IET Radar, Sonar and Navigation* (2020) 14:944–53. doi:10.1049/iet-rsn.2020.0021

99. Zhou W, Lv Z, Li G, Jiao B, Wu W. Detection of spoofing attacks on global navigation satellite systems using Kolmogorov–smirnov test-based signal quality monitoring method. *IEEE Sensors J* (2024) 24(7):10474–90. doi:10.1109/JSEN.2024.3354110

100. Shen J. *Research on jamming recognition technology in communication countermeasures[D]*. University of Electronic Science and Technology of China, MA thesis (2011). p. 7–9.

101. Cohen WW, Richman J. Learning to match and cluster large high-dimensional data sets for data integration[C]. In: *Proceedings of the eighth ACM SIGKDD international conference on Knowledge discovery and data mining* (2002). p. 475–80.

102. Yu Y, Zhong-liang F, Xiang-hui Z, Wen-fang C. *Combining Classifier Based on Decision Tree*. Taiyuan, China: 2009 WASE International Conference on Information Engineering (2009) 2:37–40. doi:10.1109/ICIE.2009.12

103. Yue L. *Research on communication interference pattern recognition and parameter estimation algorithm[D]*. Xidian University, MA thesis (2019). p. 31–3. doi:10.27389/d.cnki.gxadu.2019.001061

104. Xun L, Lu N, Qiang W Communication signal modulation mechanism recognition technology based on BP neural network[J]. *Telecommunications Technology*, 2006, 46(1):143–146. doi:10.3969/j.issn.1001-893X.2006.01.031

105. Ruoran F. Compound jamming signal recognition based on neural networks[C]. In: *Sixth international conference on instrumentation and measurement*. IEEE (2016). p. 737–40.

106. Jiang M. *Identification and localization of multiple interference sources for satellite navigation[D]*. Xi'an University of Technology, MA thesis (2020) doi:10.27398/d.cnki.gxalu.2020.000518

107. Wu Y. Research on classification algorithm based on decision tree[J]. *Digital Commun World*, 2017, No. 156(12):268–269). doi:10.3969/J.ISSN.1672-7274.2017.12.232

108. Zhu L. *Research and implementation of interference identification and direction finding technology of Beidou satellite navigation satellite system[D]*. Beijing Jiaotong University, MA thesis (2019). p. 35–57. doi:10.26944/d.cnki.gbfju.2019.000581

109. Dang Z. *Research on wireless communication interference signal recognition and processing technology based on deep learning[D]*. University of Electronic Science and Technology of China, MA thesis (2020). p. 13–38. doi:10.27005/d.cnki.gdzku.2020.004101

110. Kong M, Liu J, Zhang Z, Qiao Y. Radio ground-to-air interference signals recognition based on support vector machine[C]. Singapore: 2015 IEEE International Conference on Digital Signal Processing (DSP) (2015). p. 987–990. doi:10.1109/ICDSP.2015.7252025

111. Wang G -S, Ren Q -H, Su Y -Z. The interference classification and recognition based on SF-SVM algorithm. In: *2017 IEEE 9th international conference on communication software and networks (ICCSN)*. Guangzhou, China (2017). p. 835–41. doi:10.1109/ICCSN.2017.8230229

112. Iqbal A, Aman MN, Sikdar B, "A deep learning based induced GNSS spoof detection framework," in *IEEE transactions on machine learning in communications and networking*, vol. 2, pp. 457–78. 2024. doi:10.1109/TMLCN.2024.3386649

113. Liu Y, Li S, Fu Q, Liu Z, Zhou Q. Analysis of Kalman filter innovation-based GNSS spoofing detection method for INS/GNSS integrated navigation system. *IEEE Sensors J* (2019) 19(13):5167–78. doi:10.1109/jsen.2019.2902178

114. Zhang C, Lyv Z, Zhang L. A spoofing detection algorithm for INS/GNSS integrated navigation system based on innovation rate and robust estimation [J]. *J Chin Inertial Technology*, 2021, 29(3): 328–333. doi:10.13695/j.cnki.12-1222/o3.2021.03.008

115. Ceccato M, Formaggio F, Laurenti N, Tomasin S. Generalized likelihood ratio test for GNSS spoofing detection in devices with IMU. *IEEE Trans Inf Forensics Security* (2021) 16:3496–509. doi:10.1109/tifs.2021.3083414

116. Clements Z, Yoder J E, Humphreys T. Carrier-phase and IMU based GNSS spoofing detection for ground vehicles. In: *Proceedings of the 2022 international technical meeting of the Institute of navigation*. Long Beach, California, USA (2022). p. 83–95.

117. Cui J, Cheng N, Ni S. Research on suppression method of spoofed navigation jamming signal by array antenna [J]. *Acta Electronica Sinica*, 2018, 46(2):365–71. doi:10.3969/j.issn.0372-2112.2018.02.015

118. Guo Y, Fan M, Kong M. Spoofing interference suppression using space-time process for GNSS receiver. *Int Congress Image Signal Process* (2012) 1537–1541. doi:10.3969/j.issn.1003-0530.2007.04.018

119. Broumandan A, Jafarnia-Jahromi A, Lachapelle G. Spoofing detection, classification and cancelation (SDCC) receiver architecture for a moving GNSS receiver. *GPS Solut* (2015) 19:475–87. doi:10.1007/s10291-014-0407-3

120. Sun X, Wu Z, Nie Y. A new satellite navigation spoofing jamming suppression method. In: *Proceedings of the 9th China satellite navigation academic annual conference S03 satellite navigation signal and anti-jamming technology* (2018). p. 28–32.

121. Zhang J, Gui L, Yuan Y, et al. Array anti-spoofing method based on GNSS multi-channel tracking receiver[J]. *Telecommunication Technology*, 2023, 63(6):817–825). doi:10.20079/j.issn.1001-893x.230106004

122. Hans S, Chen L, Meng W, Li C, et al. Improve the security of GNSS receivers through spoofing mitigation[J]. *IEEE Access*, 2017, 5:21057–21069. doi:10.1109/ACCESS.2017.2754414

123. Zhao H, Lian B, Feng J. ADAPTIVE BEAMFORMING ALGORITHM FOR INTERFERENCE SUPPRESSION IN GNSS RECEIVERS. *Int J Computer Sci Inf Technology* (2011) 3:17–28. doi:10.5121/ijcsit.2011.3502

124. Shang X, Sun F, Zhang L, Cui J, Zhang Y. Detection and mitigation of GNSS spoofing via the pseudorange difference between epochs in a multicorrelator receiver. *GPS Solut* (2022) 26:37. doi:10.1007/s10291-022-01224-4

125. Kotaru M, Joshi KR, Bharadia D, Katti S. SpotFi: decimeter level localization using WiFi. In: *Proceedings of the 2015 ACM conference on special interest group on data communication* (2015). n. pag.

126. Tian Z, Li Z, Zhou M, Jin Y, Wu Z. PILA: sub-meter localization using CSI from commodity wi-fi devices. *Sensors* (2016) 16(10):1664. doi:10.3390/s16101664

127. Sen S, Radunovic B, Choudhury RR, Minka T. You are facing the Mona Lisa: spot localization using PHY layer information. In: *Proceedings of the 10th international conference on Mobile systems, applications, and services (MobiSys,12)*. New York, NY, USA: Association for Computing Machinery (2012). p. 183–96. doi:10.1145/2307636.2307654

128. Li X, Lu Z, Yuan M, Liu W, Wang F, Yu Y, et al. Tradeoff of code estimation error rate and terminal gain in SCER attack. *IEEE Trans Instrumentation Meas* (2024) 73: 1–12. doi:10.1109/tim.2024.3406807

129. Zhang X. A review of satellite navigation spoofing jamming signal detection technology. *Glob Positioning Syst* (2018) 43(6):1–7. doi:10.13442/j.gnss.1008-9268.2018.06.001

frontiers | Frontiers in Physics

TYPE Original Research
PUBLISHED 27 January 2025
DOI 10.3389/fphy.2025.1533951

OPEN ACCESS

EDITED BY
Zhu Xiao,
Hunan University, China

REVIEWED BY
Jian Kuang,
Wuhan University, China
Yq Hei,
Xidian University, China

*CORRESPONDENCE
Chunjiang Ma,
✉ machunjiang13@nudt.edu.cn

RECEIVED 25 November 2024
ACCEPTED 06 January 2025
PUBLISHED 27 January 2025

CITATION
Gao S, Ma C, Tang X and Wang F (2025) Single-epoch power positioning method for multi-beam LEO communication satellites. *Front. Phys.* 13:1533951.
doi: 10.3389/fphy.2025.1533951

# Single-epoch power positioning method for multi-beam LEO communication satellites

Sibo Gao[1,2], Chunjiang Ma[1,2]*, Xiaomei Tang[1,2] and Feixue Wang[1,2]

[1]College of Electronic Science and Technology, National University of Defense Technology, Changsha, China, [2]Key Laboratory of Satellite Navigation Technology, Changsha, China

Low Earth Orbit (LEO) communication satellites offer reduced signal loss, fast movement, multi-beam, typically providing single coverage. This paper introduces a novel multi-beam power positioning method for low-orbit single-satellite, addressing the slow convergence and low accuracy of Doppler positioning. It establishes a power observation equation system, initializes with the nearest neighbor algorithm, and refines with the least squares method. Monte Carlo simulations indicate that with good initial values, the method converges in under 10 iterations, achieving 88.06% availability at 20° elevation with errors of 5,331 m (vertical) and 8,798 m (horizontal), and a timing error of 205 μs. At 70° elevation, all users converge with errors of 1,614 m and 1,088 m, and a timing error of 31.3 μs, demonstrating high power positioning availability. The statistical results show that power positioning users can obtain the positioning accuracy of kilometers and the timing accuracy of microseconds, which meets initial timing needs under strong confrontation, enhancing the medium and high orbit satellite navigation.

KEYWORDS

**LEO satellites, multi-beam, power positioning, positioning accuracy, positioning availability**

## 1 Introduction

Low Earth Orbit (LEO) communication satellites, as an emerging navigation enhancement method, possess many unique advantages. Their orbital altitude is relatively low, and the signal power is high, with the ground power being about 30 dB higher than that of Global Navigation Satellite System (GNSS), resulting in high signal quality and strong anti-interference capabilities, enabling services to be provided indoors and in obstructed areas [1, 2]. The greatest advantage of LEO satellites is their fast movement speed, which can greatly reduce the correlation between adjacent observation epochs, achieving rapid convergence in positioning [3], and the large Doppler shift, which offers good Doppler observation [4].

Based on the characteristics of LEO satellites, with a sufficient number of satellites, LEO navigation constellations can perform independent positioning and timing, or combined positioning and timing with GNSS, using traditional positioning algorithms such as pseudorange positioning and carrier phase positioning to achieve navigation enhancement [5–7]. The analysis of the combined positioning effects of LEO satellites with different orbital heights and GNSS constellations [8] shows that LEO satellites have low orbits and fast geometric motion speeds, with the geometric dilution of precision (GDOP) value changing rapidly, effectively shortening the convergence time for GPS/BDS positioning. The enhancement effect of different numbers of LEO satellites on GNSS is significantly different, with more satellites leading to more noticeable enhancement effects.

However, for LEO satellite constellations, if the GNSS pseudorange-based time difference positioning method is still used, the system's requirement for time synchronization is very high, which will greatly increase the system construction cost [9]. When the number of visible satellites is insufficient, and users do not meet the conditions for multiple coverage, both pseudorange positioning and carrier phase positioning are not available. In this case, single-satellite Doppler positioning requires a relatively long observation time for the satellite, using integrated Doppler for positioning solution, which is not real-time [10], has a long convergence time, and low precision, and has certain application limitations. In LEO-based Doppler positioning, the pioneering TRANSIT navigation system was the first satellite-based Doppler positioning system [11]. Launched in 1964 for military applications, it was later released for public use in 1968 to provide positioning and navigation services [12]. The system operated with over 10 satellites in polar orbits at an altitude of approximately 1,100 km. Typically, a receiver could only track one satellite at a time. Using about 2 min of Doppler shift observations, the point positioning accuracy was about 100–200 m. With the advent of the Global Positioning System (GPS) and its superior performance, TRANSIT was decommissioned in 1996.

To meet the rapid positioning needs of LEO users, the power measurements of multi-beam signals can be utilized to calculate the user's approximate location. Due to the beam scanning broadcast method used by LEO communication satellites [13], there are variations in received power for receivers at different locations on the Earth's surface at various times during the satellite's motion. The magnitude of these variations is related to the beamwidth and the antenna pattern. Current research on power matching positioning is focused on indoor positioning, where multiple WiFi access points can be detected indoors and their signals are easily measured, making WiFi received signal strength indication based fingerprint positioning one of the most popular positioning technologies today [14]. This method typically consists of two stages: offline and online [15, 16]. In the offline stage, reference points in the positioning area are surveyed to collect received signal strength as a fingerprint database [17, 18]; in the online stage, real-time positioning data are matched with the fingerprint database to obtain the estimated location [19].

For the first time in the context of LEO satellite scenarios, this paper proposes the use of multi-beam signal power measurements for positioning and timing. Based on traditional satellite navigation system algorithms, the nearest neighbor algorithm [20, 21] is used to solve for initial values, and the least squares method [22] is used for iterative solution, including the linearization of nonlinear equation systems, solution of linear equation systems, updating the roots of nonlinear equation systems, and judging the convergence of iterations. It is possible to use power measurements for single-point rapid positioning of users under a single LEO satellite scenario, with the expectation that some users will achieve better positioning and timing performance.

# 2 Materials and methods

## 2.1 Multi-beam signal power observation model

According to the classic Friis transmission equation, the power measurement of the multi-beam satellite signal received by the satellite azimuth angle $\beta$, the satellite elevation angle $\gamma$ and the distance between the user and the satellite $d$, which can be expressed as:

$$P_k(\gamma,\beta,d) = E_k(\gamma,\beta) - L(d) + G(\gamma) \tag{1}$$

Among them, the multi-beam number $k = 1,\cdots,M$ representing the signal transmitted by the satellite. $E_k(\gamma,\beta)$ represents the EIRP value of the satellite transmitted signal, $L(d)$ represents the spatial transmission loss of the satellite signal, and $G(\alpha)$ represents the gain value of the user's receiving antenna, which is solely related to the user's elevation angle $\alpha$ and can be calculated using the satellite elevation angle $\gamma$.

The EIRP value of the satellite transmitted beam signal and the gain value of the user's received antenna $E_k(\gamma,\beta)$, $G(\gamma)$ can usually be obtained by antenna simulation or actual measurement, and it is assumed that the accurate modeling of both has been completed, and the modeling error is ignored.

When the satellite position is known, the user's position can be determined by the satellite elevation angle $\gamma$, the satellite azimuth angle $\beta$ and the distance $d$ between the user and the satellite, and when the three-dimensional position of the satellite in the ECEF coordinate system is known, the three-dimensional position of the user in the ECEF coordinate system can be obtained by using the geometric relation. Figure 1 below shows the geometric relationship between the user and the satellite, where $R$ is the radius of the earth, $H$ is the orbital height of the satellite, $h$ is the geodetic height of the user, and $d$ is the distance between the user and the satellite. Firstly, the relationship between the elevation angle of the user and the expansion angle of the satellite beam is derived.

The geometric relationship shown in the figure above, according to the sinusoidal theorem, can be obtained:

$$(R+H)\sin\gamma = (R+h)\sin\left(\alpha + \frac{\pi}{2}\right) \tag{2}$$

Therefore, it is possible to derive the satellite beam tension angle $\gamma$ as Equation 3:

$$\gamma = \sin^{-1}\left(\frac{R+h}{R+H}\cos\alpha\right) \tag{3}$$

When the elevation angle of the user is valued between 0° and 90°, it is not difficult to conclude that the elevation angle of the user corresponds to the value of the satellite elevation angle from the function relationship.

The space transmission loss of satellite signals $L(\alpha,h)$ is deduced below, and the distance from the satellite to the user is calculated first. According to the geometric relationship shown in Figure 1, and according to the cosine theorem, we can get:

$$(R+H)^2 = (R+h)^2 + d^2 - 2d(R+h)\cos\left(\alpha + \frac{\pi}{2}\right) \tag{4}$$

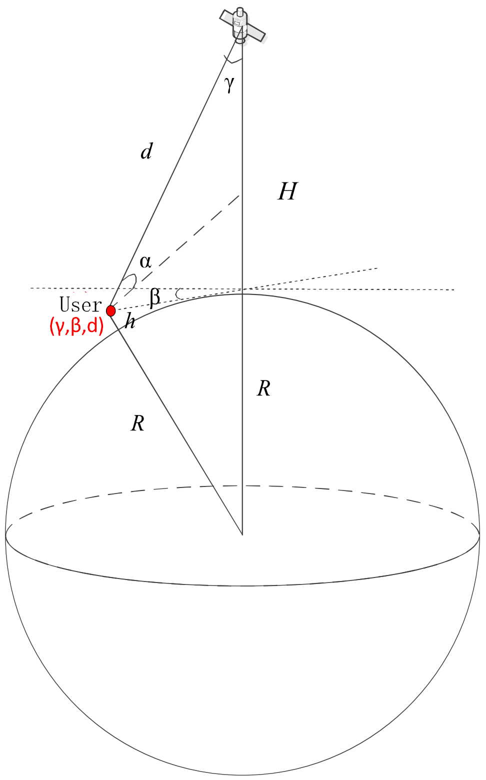

FIGURE 1
Geometry of the user's received satellite signal.

Further, the distance from the user to the satellite $d$ can be calculated as:

$$d = \sqrt{(R+H)^2 - (R+h)^2 \cos^2 \alpha} - (R+h)\sin\alpha \tag{5}$$

According to Friis transmission equation, the power in the fixed solid angle remains the same. Therefore, the spatial transmission loss of signal power at a point on the spherical surface with a radial of the transmitting antenna is Equation 6:

$$L(\alpha,h) = L(d) = 20\lg(4\pi d) - 20\lg(\lambda) \tag{6}$$

where $\lambda$ refers to the wavelength.

Thus, Equation 1 can be written in a more detailed form as Equation 7:

$$P_k(\alpha,\gamma,\beta,h) = E_k(\gamma,\beta) - L(\alpha,h) + G(\alpha) \tag{7}$$

## 2.2 Power perception measurement error model

After receiving the signal from the satellite, the user usually measures the power of the received signal by matching the reception. Assuming that the user has completed the time and frequency synchronization of the satellite signal, and stripped away the possible pseudo-random codes and Doppler frequencies that may be modulated on the signal, while ignoring the influence of the transmitted message symbol, the user's received signal can be expressed as Equation 8:

$$s(t) = A + n(t) \tag{8}$$

where the amplitude of the received signal is denoted by $A = \sqrt{2P_k(\alpha,\gamma,\beta,h)}$, the thermal noise error of the power is denoted by $n(t)$ which generally obeys a normal distribution [23].

Considering that the thermal motion of charged particles in a circuit forms thermal noise, the noise power $N$ is usually expressed as the noise temperature $T$ corresponding to the thermal noise power of the same magnitude, and the relationship between them is as Equation 9:

$$N = kTB_n \tag{9}$$

The unit of $N$ is Watts(W), the unit of $T$ is Kelvin (K) and the unit of noise bandwidth $B_n$ is Hertz (Hz). The Boltzmann constant $k$ is equal to $1.38 \times 10^{-23}$ J/K, which $T$ is taken as 290 K at room temperature.

When the duration of the signal power measurement is $T_P$, it is advisable to assume that the user takes the coherent integration method to estimate the signal amplitude, then there are:

$$\hat{A} = \frac{1}{T_P}\int_0^{T_P} s(t)dt = A + n'(t) \tag{10}$$

where $\hat{A}$ is the measured value of the amplitude of the received signal. $n'(t)$ is the coherent integrated noise, and its equivalent noise bandwidth $B_n$ is taken $1/T_P$. Before and after coherent integration, the signal power, amplitude, and noise power spectral density do not change, but because the noise bandwidth before the correlator is $B_{pd}$, and the filtering bandwidth of the coherent integrator can be regarded as $B_n$ , the narrowing of the noise bandwidth must cause a decrease in the noise power, so the noise power after coherent integration is reduced to $N/B_{pd}T_P$.

## 2.3 A system of equations for power observations

When the user receives multiple beamed satellite signals and measures the signal power, the equation is as follows:

$$\begin{cases} E_1(\gamma,\beta) + L(d) + G(\alpha) + N_1^T = \hat{P}_1 \\ E_2(\gamma,\beta) + L(d) + G(\alpha) + N_2^T = \hat{P}_2 \\ \vdots \\ E_M(\gamma,\beta) + L(d) + G(\alpha) + N_M^T = \hat{P}_M \end{cases} \tag{11}$$

Among them, $\hat{P}_1, \hat{P}_2, \cdots, \hat{P}_M$ are the power measurement of different beams, and $N_1^T, N_2^T, \cdots, N_M^T$ are the power observation noise of different beams.

The power observation equation for the other beams is different from the observation equation for beam 1, the difference between other beams and beam 1 is calculated by:

$$\begin{cases} \Delta E_2(\gamma,\beta) + N_2^T - N_1^T = \Delta\hat{P}_2 \\ \Delta E_3(\gamma,\beta) + N_3^T - N_1^T = \Delta\hat{P}_3 \\ \vdots \\ \Delta E_M(\gamma,\beta) + N_M^T - N_1^T = \Delta\hat{P}_M \end{cases} \tag{12}$$

where, take $\Delta E_k(\alpha,\beta)=E_k(\alpha,\beta)-E_1(\alpha,\beta)$, $\Delta\hat{P}_k=\hat{P}_k-\hat{P}_1$.

Assuming that the initial values of $\gamma$ and $\beta$ are $\gamma_0$ and $\beta_0$ ,where the system of equations is linearized and expanded, then there is:

$$\begin{cases} \Delta E_2(\gamma_0,\beta_0)+(\gamma-\gamma_0)\left.\dfrac{\partial\Delta E_2}{\partial\gamma}\right|_{(\gamma_0,\beta_0)}+(\beta-\beta_0)\left.\dfrac{\partial\Delta E_2}{\partial\beta}\right|_{(\gamma_0,\beta_0)}+\Delta N_2^T=\Delta\hat{P}_2\\ \Delta E_3(\gamma_0,\beta_0)+(\gamma-\gamma_0)\left.\dfrac{\partial\Delta E_3}{\partial\gamma}\right|_{(\gamma_0,\beta_0)}+(\beta-\beta_0)\left.\dfrac{\partial\Delta E_3}{\partial\beta}\right|_{(\gamma_0,\beta_0)}+\Delta N_3^T=\Delta\hat{P}_3\\ \vdots\\ \Delta E_M(\gamma_0,\beta_0)+(\gamma-\gamma_0)\left.\dfrac{\partial\Delta E_M}{\partial\gamma}\right|_{(\gamma_0,\beta_0)}+(\beta-\beta_0)\left.\dfrac{\partial\Delta E_M}{\partial\beta}\right|_{(\gamma_0,\beta_0)}+\Delta N_M^T=\Delta\hat{P}_M \end{cases} \tag{13}$$

where $\Delta N_k^T=N_k^T-N_1^T$, and cause:

$$\boldsymbol{X}=\begin{bmatrix} \left.\dfrac{\partial\Delta E_2}{\partial\gamma}\right|_{(\gamma_0,\beta_0)} & \left.\dfrac{\partial\Delta E_3}{\partial\gamma}\right|_{(\gamma_0,\beta_0)} & \cdots & \left.\dfrac{\partial\Delta E_M}{\partial\gamma}\right|_{(\gamma_0,\beta_0)}\\ \left.\dfrac{\partial\Delta E_2}{\partial\beta}\right|_{(\gamma_0,\beta_0)} & \left.\dfrac{\partial\Delta E_3}{\partial\beta}\right|_{(\gamma_0,\beta_0)} & \cdots & \left.\dfrac{\partial\Delta E_M}{\partial\beta}\right|_{(\gamma_0,\beta_0)} \end{bmatrix}^T \tag{14}$$

$$\boldsymbol{y}=\left[\Delta\hat{P}_2-\Delta E_2(\gamma_0,\beta_0),\Delta\hat{P}_3-\Delta E_3(\gamma_0,\beta_0),\cdots,\Delta\hat{P}_M-\Delta E_M(\gamma_0,\beta_0)\right]^T \tag{15}$$

$$\boldsymbol{n}=\left[N_1^T-N_2^T,N_1^T-N_3^T,\cdots,N_1^T-N_M^T\right]^T \tag{16}$$

Then the above equation can be rewritten as:

$$\boldsymbol{X}\cdot[\gamma-\gamma_0,\beta-\beta_0]^T=\boldsymbol{y}+\boldsymbol{n} \tag{17}$$

Further, it can be solved that:

$$[\gamma,\beta]^T=[\gamma_0,\beta_0]^T+\boldsymbol{X}^{-1}\cdot(\boldsymbol{y}+\boldsymbol{n}) \tag{18}$$

Equations 11–18 are the derivation process of the least squares algorithm for power positioning. According to the properties of the least squares solution for linear systems of equations, the number of equations should be greater than or equal to the number of unknowns. Considering the unknowns are the satellite elevation angle $\gamma$ and the satellite azimuth angle $\beta$, the number of equations should be at least 2. Furthermore, since the linear system of equations is derived from the differentiation of different beams, the minimum number of satellite beams required by the algorithm is 3.

## 2.4 Power positioning algorithm solution process

Since multi-beam power positioning is applied to low-orbit satellite scenarios, the quality of the received signal is poor when the user's elevation angle is too low, thus eliminating the data with low user elevation angles. In addition, according to the general specification for BeiDou/Global Navigation Satellite Systems (GNSS) geodetic receivers [24], typical values for navigation receiver acquisition and tracking sensitivities are generally below −130 dB m, thus the simulation parameters are set as Table 1:

TABLE 1 Simulation parameters.

| Parameter type | Parameter value |
|---|---|
| Earth radius $R$ | 6371 km |
| Satellite orbital altitude $H$ | 1,200 km |
| User elevation angle $\alpha$ | [10°,90°] |
| Satellite elevation angle $\gamma$ | can be calculated by $\alpha$ |
| satellite azimuth angle $\beta$ | [1°,360°] |
| Total number of satellite beams | 52 |
| User geodetic height $h$ | 0 m |
| User receive gain $G(\alpha)$ | 0 dB |
| Noise bandwidth $B_n$ | 1,000 Hz |
| Noise temperature $T$ | 290 K |
| Least squares iterations $N$ | 10 |
| Receiver sensitivity | −160 dB W, −190 dB W |

The input required for the power positioning least squares algorithm is the initial value of the satellite elevation angle $\gamma_0$, the initial value of the azimuth angle $\beta_0$, the ERIP value of k beams of prior information $E_k(\gamma,\beta)$ , and the user gain $G(\alpha)$.Figure 2 gives the flowchart of the algorithm.

The least-squares algorithm itself outputs the satellite tension angle and azimuth angle, however, we need to obtain the user's vertical and horizontal information. It is worth noticing that in the process of calculating the elevation angle of the user, $h=0$ is first assumed, which is due to the negligible altitude of the user's geodetic altitude in relation to the radius of the Earth and the orbital height of the satellite. The h after the least squares solution is obtained by a series of calculations such as link loss, and the two values are not contradictory, and the analysis of the error in the following is based on the h of the least squares solution.

Substituting Equation 2, we can get the elevation angle from the user to the satellite as Equation 19:

$$\alpha=\cos^{-1}\left\{\frac{R+H}{R+h}\sin\gamma\right\} \tag{19}$$

According to Equation 4, the user's geodetic height can be calculated as Equation 20:

$$h=-R-d\sin\alpha+\sqrt{(R+H)^2-d^2\cos^2\alpha} \tag{20}$$

where $d$ can be calculated by Equation 5, and the user vertical information is Equation 21:

$$x=d\frac{\sin\gamma}{\sin(\alpha+\gamma)} \tag{21}$$

In order to facilitate the subsequent analysis of the power positioning and timing performance, the evaluation index of the positioning and timing result error is defined here, assuming that the true value of the satellite elevation angle is $\gamma_r$ and the solution value is $\gamma$ ,then the elevation angle error is $\Delta\gamma=\gamma-\gamma_r$.

If there are $n$ users in different locations, the statistical positioning performance of these users can be given by the error deviation and the standard deviation, which is defined as Equations 22, 23:

$$E(|\Delta\gamma|)=\frac{1}{n}\sum_n|\gamma-\gamma_r| \tag{22}$$

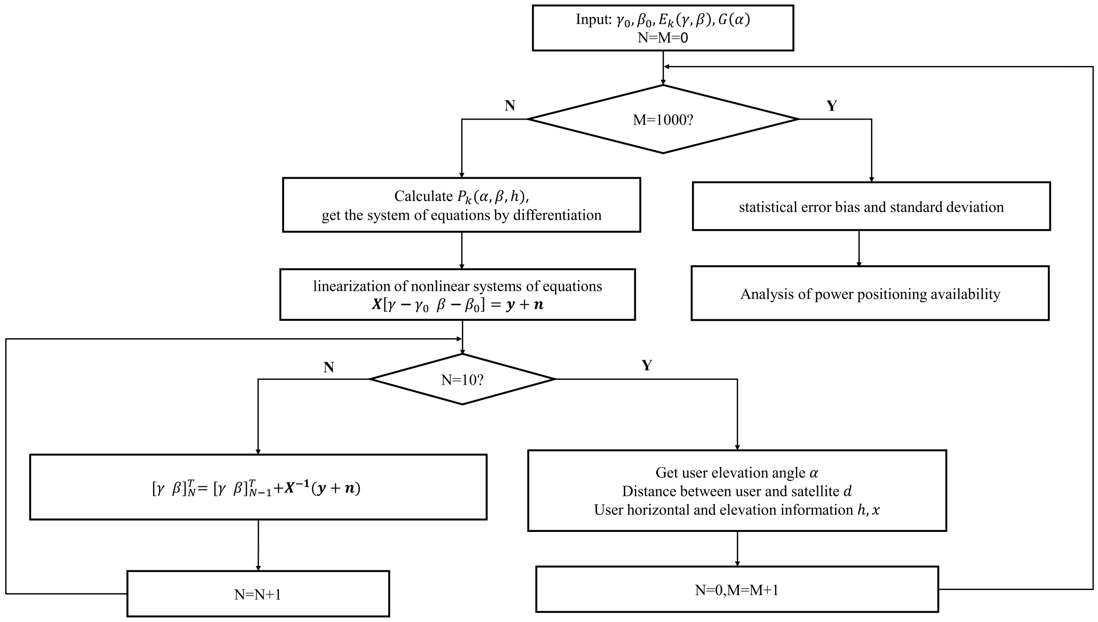

FIGURE 2
Flowchart of the power positioning least squares algorithm.

$$std(\Delta\gamma)=\sqrt{D(\Delta\gamma)}=\sqrt{\frac{1}{n-1}\sum_n(\Delta\gamma-E(\Delta\gamma))^2} \tag{23}$$

Satellite azimuth error, user horizontal error, user vertical error and their deviation are defined as above.

Assuming the true distance between the user and the satellite is $d_r$, and the distance calculated by the power positioning algorithm between the user and the satellite is d, then the timing error is defined as Equation 24:

$$\Delta t=\left|\frac{d_r-d}{c}\right| \tag{24}$$

where $c$ is the speed of light, which is approximately taken as $3\times 10^8\, m\cdot s^{-1}$.

# 3 Results

## 3.1 The requirements and acquisition of initial values in the least squares method

In the process of power positioning solution, the initial conditions have a great influence on the results, and the better initial conditions can make the iteration converge quickly, and the poor initial conditions will greatly reduce the iteration speed, and even the convergence results cannot be obtained in the end. Due to the characteristics of planar phased array antennas, ground users may have the same receiving power in different areas, and if the gap between the initial position and the user's position is too large, the solution is easy to fall into the local optimal solution, resulting in a large positioning error.

### 3.1.1 Requirements for initial values in the least squares method

When the initial values are set close to the true values, the iteration tends to converge; when the initial values are set far from the true values, the least squares iteration diverges. Consequently, the power positioning least squares scheme has certain requirements for initial values.

To determine these requirements, it is assumed that the true elevation and azimuth angles of the satellite are $\begin{bmatrix}\gamma_r\\ \beta_r\end{bmatrix}$, the initial value $\begin{bmatrix}\gamma_r\pm a\\ \beta_r\pm b\end{bmatrix}$ is set to a certain value below the true value, and the positioning results $\begin{bmatrix}\gamma\\ \beta\end{bmatrix}$ of multiple Monte Carlo simulations are required to converge to within the range of the true value of 1°, that is $\begin{bmatrix}\gamma_r\pm 0.5^\circ\\ \beta_r\pm 0.5^\circ\end{bmatrix}$, the initial value requirements of the least squares method at this time are required a and b, where a is the initial value requirement of the satellite elevation angle, and b is the initial value requirement of the satellite azimuth angle.

In the simulation, users with poor observation quality due to low elevation angles are excluded. By iterating over user elevation angles $\alpha$ in the range [10°, 90°] (which corresponds to satellite elevation angles $\gamma$ in the range [0°, 55.8°]), and satellite azimuth angles $\beta$ in the range [1°, 360°], we can statistically determine the initial value requirements a and b for the power matching least squares method.

The statistical results of the initial value of least squares solution requirements are shown in Figure 3:

It is not difficult to see that when the initial values of elevation angle and azimuth angle are below the true value of 2°, it can be

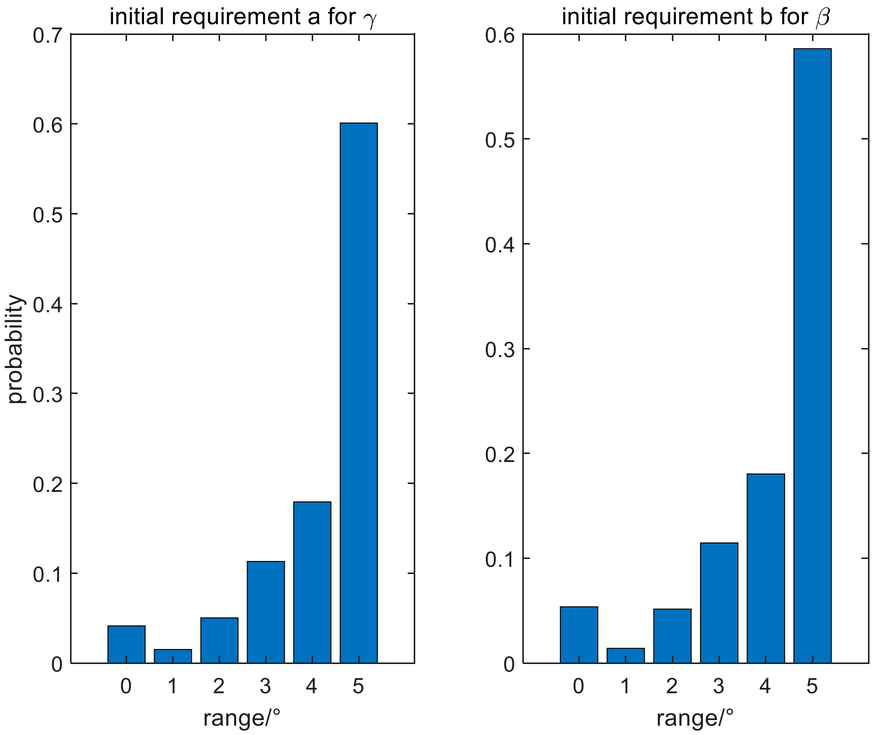

FIGURE 3
The proportion of users with different initial values required by the least squares algorithm.

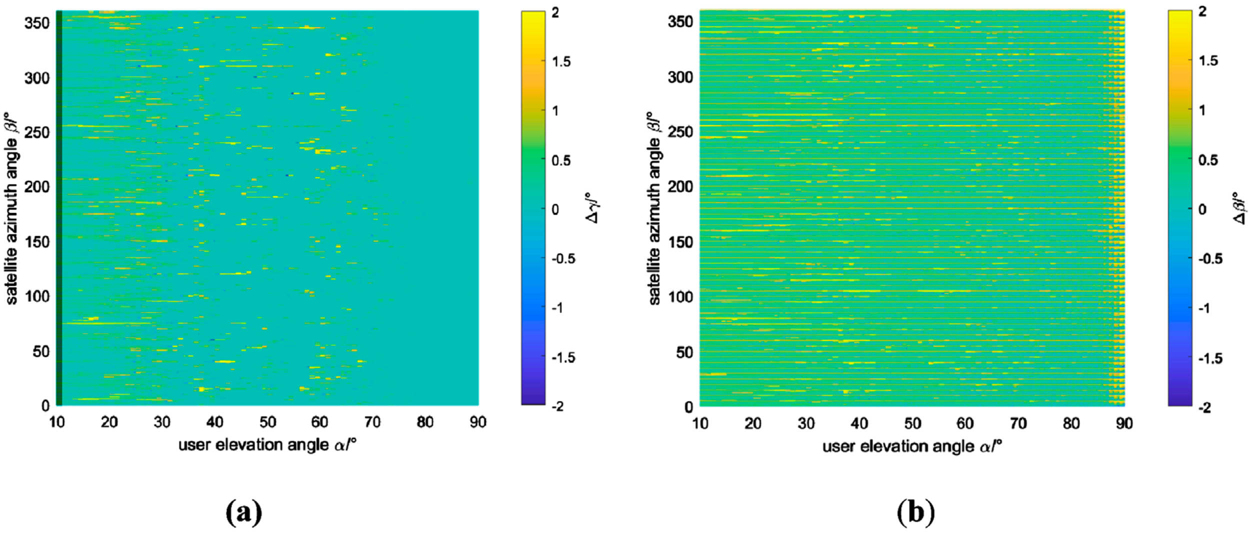

FIGURE 4
The Nearest Neighbor algorithm: **(A)** Satellite elevation angle errors **(B)** Satellite azimuth angle errors.

considered that the vast majority of users (94.5% and 93.2%) can use power matching positioning to perform least squares solution and obtain a convergence solution. The solution to meet the initial value requirements can be obtained by using user prior information or other algorithms.

### 3.1.2 Acquisition of initial values by the nearest neighbor algorithm

This section introduces the method of obtaining the initial value that satisfies the convergence condition of least squares solution, and briefly explains the nearest neighbor algorithm (K value takes

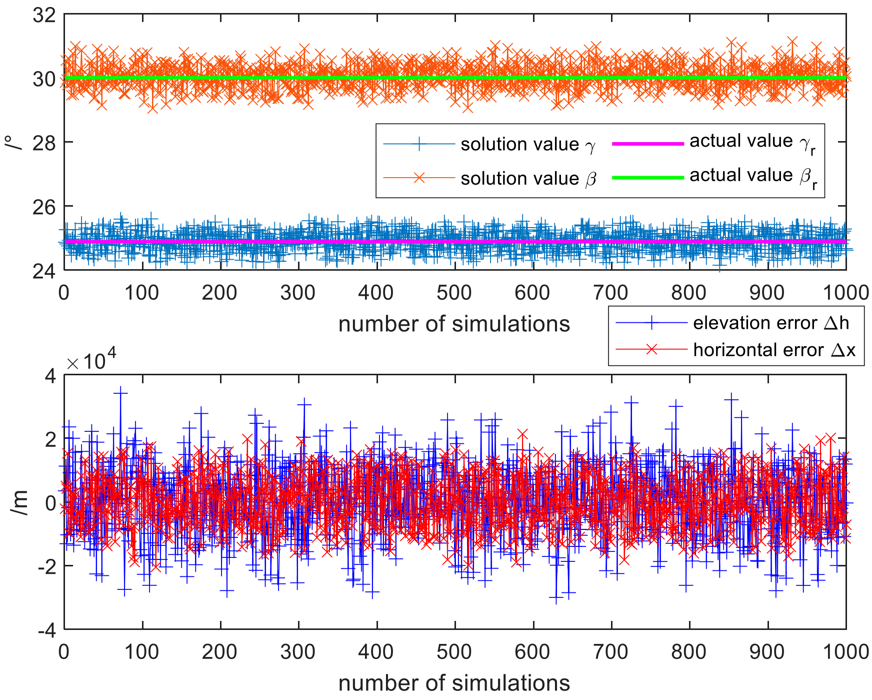

FIGURE 5
Monte Carlo results of $\gamma, \beta, \Delta h, \Delta x$.

1 in KNN) as an example, and then considers different fingerprint database frameworks and parameters.

According to the system of power measurement Equation 10, based on the EIRP information of each beam $(E_1, E_2, \cdots, E_M)$ known on the satellite side, the theoretical received power values of users at different locations $(P_1, P_2, \cdots, P_M)$ can be solved through the link budget, and in fact, for a single user, the received power of up to M beams $(\hat{P}_1, \hat{P}_2, \cdots, \hat{P}_M)$ can be obtained. When the user's fingerprint location information is the real user location, there will only be one noise deviation between the theoretical received power value of M and the actual received power value of a single user, which is very small and negligible in most cases, which is called positioning matching. However, when the user location fingerprint is different from the real user location, there will always be a large difference between the theoretical received power value and the actual received power value of some beams of a single user, which is called mismatch.

Considering the processing time of the nearest neighbor algorithm and the actual user situation, the power fingerprint database in this paper traverses the elevation angles of different users and takes a certain azimuth interval to establish it. In the matching process, the azimuth interval can be initialized by *a priori* known information, and then the azimuth search interval can be gradually narrowed to achieve more accurate and robust matching results.

In the simulation, we traverse the user's elevation angle $\alpha\epsilon[10°, 90°]$ (converted to a satellite elevation angle of $\gamma\epsilon[0, 55.8°]$), the satellite azimuth angle $\beta\epsilon[1°, 360°]$, and the user's ground height are all set to 0 m. Assuming that the user's elevation angle is unknown and the azimuth uncertainty is 5°, there are 72 different fingerprint databases, each of which contains all the user's elevation angle information and a certain azimuth information. In order to reduce the influence of noise on the nearest neighbor algorithm, the width of the fingerprint library is taken as 10 beams, which are the 10 largest beam points among the M received power obtained by each user.

The simulation results of the nearest neighbor algorithm power matching localization are as Figure 4.

The colorbar depth of the above two graphs represents the azimuth and vertical error of the satellite, and the darker the color, the smaller the error. It can be seen that the error of satellite elevation angle is small, generally below 0.5°, while the azimuth error of satellite is large, generally above 0.5°, and the error under the condition of high user elevation angle is significantly increased, which is mainly due to the fact that the beam receiving power of users with high elevation angle is generally large, and it is difficult to distinguish the difference of beam between different users, resulting in some misjudgments in the algorithm. In general, the power matching positioning of the nearest neighbor algorithm can meet the requirements of the least-squares algorithm for the initial value of convergence.

## 3.2 Analysis of the single user positioning error

Assumed the satellite angle errors are $\begin{bmatrix} \Delta\gamma \\ \Delta\beta \end{bmatrix}$, the power calculation error is $\Delta p$,if error terms are taken into

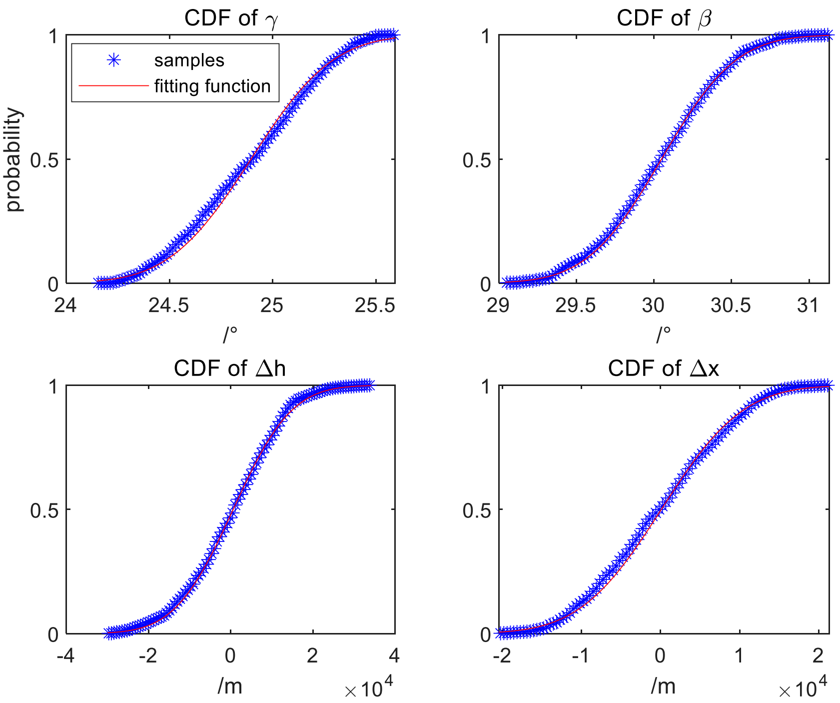

FIGURE 6
Normal distribution fits of Monte Carlo results.

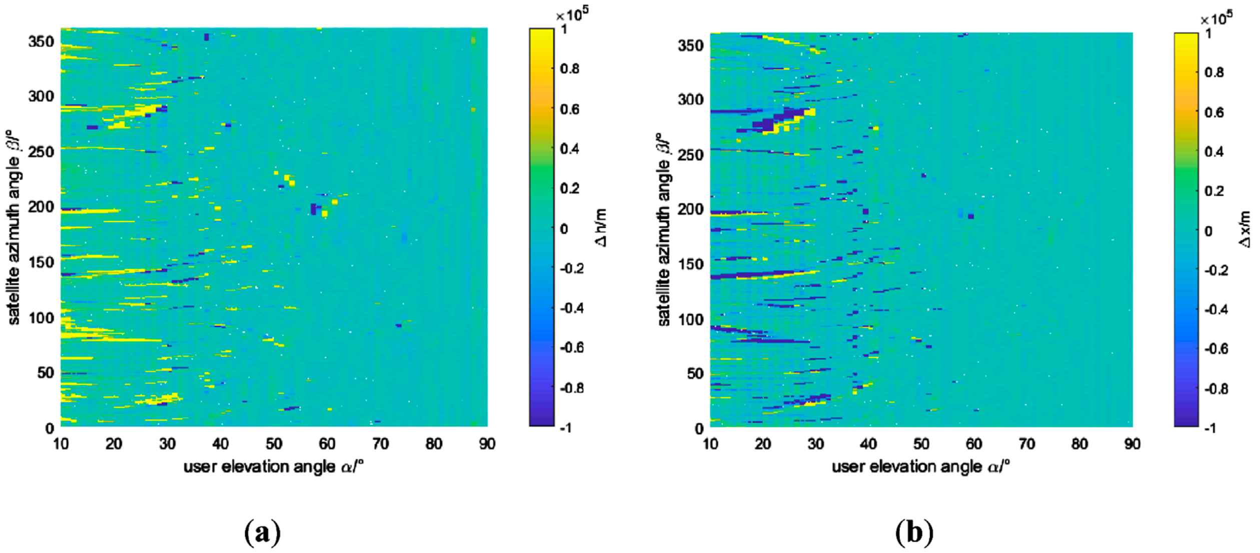

FIGURE 7
When receiver sensitivity is –160 dB W: **(A)** User vertical errors in different locations. **(B)** User horizontal errors in different locations.

account as Equation 25:

$$X\begin{bmatrix}\gamma+\Delta\gamma\\ \beta+\Delta\beta\end{bmatrix}=y+n+\Delta p \tag{25}$$

From the previous Newtonian iterative process, it can be deduced that the relationship between the elevation angle and azimuth angle of the two satellites directly related to the user's position and the power calculation error is as Equation 26:

$$\begin{bmatrix}\Delta\gamma\\ \Delta\beta\end{bmatrix}=\left(X^{T}X\right)^{-1}X^{T}\Delta p \tag{26}$$

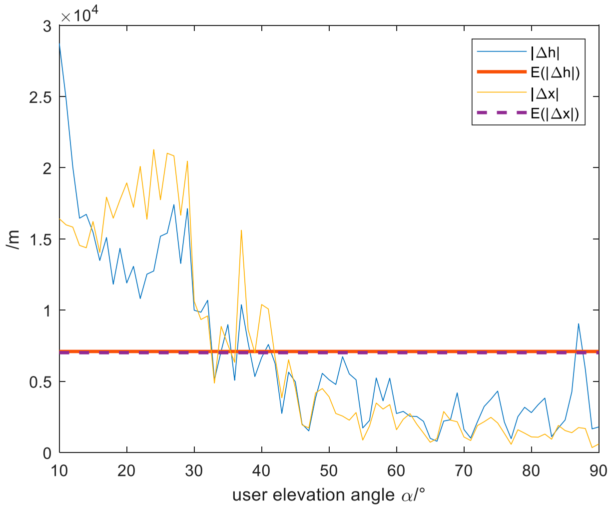

FIGURE 8
Vertical and horizontal bias of different user elevation angles.

Assuming that the parameters remain unchanged during the receiver receiving the satellite signal, and each observation value is independent of each other, the observation error $\Delta p$ obeys the standard normal distribution, the mean value is 0, and the variance is $\sigma^2$. So the covariance of $\begin{bmatrix}\Delta\gamma \\ \Delta\beta\end{bmatrix}$ can be expressed as Equation 27:

$$Cov\left(\begin{bmatrix}\Delta\gamma \\ \Delta\beta\end{bmatrix}\right) = \left(X^T X\right)^{-1}\sigma^2 \tag{27}$$

Taking the user's elevation angle of 60° (converted to a satellite elevation angle of 24.882°), the satellite azimuth angle of 30°, and the geodetic height of 0 m as an example, the receiver sensitivity is set to −160 dB W, and the results of multiple Monte Carlo simulations are as follows.

As can be seen from the Figure 5, the satellite tension angle and azimuth results of multiple Monte Carlo simulations are around the true value, and their statistical mean values can converge to within the range of 0.5° of the true value. The vertical and horizontal error of a single Monte Carlo simulation is less than 40 km, and its statistical average value can converge to within the range of 50 km of the true value, and the power positioning algorithm tends to converge, so the user can use the power positioning timing method to perform multiple positioning solutions to achieve better positioning performance. The results of 1,000 Monte Carlo simulations are statistically analyzed, and the probability distribution functions of each parameter are fitted as follows in Figure 6.

The normal fitting of satellite azimuth angle $\beta$, user vertical difference $\Delta h$, and horizontal difference $\Delta x$ is good. The solved satellite azimuth angle $\beta$ is approximately normally distributed as $N(30.05, 0.1426)$, and the elevation angle $\gamma$ is approximately normally distributed as $N(24.90, 0.0976)$, with deviations of 0.03° and 0.038°, respectively. The user vertical difference $\Delta h$ is approximately normally distributed as $N(595.18, 1.25 \times 10^8)$, and the horizontal difference $\Delta x$ is approximately normally distributed as $N(93.86, 6.57 \times 10^7)$. The power positioning accuracy of the user at this point is at the kilometer level.

## 4 Discussion

### 4.1 Different user locations

From Section 3.1, it is known that when the initial value of the least squares solution is taken to be less than 2° from the true value, it is difficult for some users to obtain a convergent solution. For such cases, the solution diverges, and the result should be taken as the uncertainty of the initial value. Furthermore, since the convergence of the least squares is defined as $\begin{bmatrix}\gamma_r \pm 0.5^\circ \\ \beta_r \pm 0.5^\circ\end{bmatrix}$, when the solution angle error deviation is greater than 0.5°, the deviation should be 1°, and when the solution angle error deviation is less than −0.5°, the deviation should be −1°. Similarly, for user vertical and horizontal information, when the solution distance error deviation is greater than 50 km, the deviation should be 100 km, and when the solution distance error deviation is less than −50 km, the deviation should be −100 km.

According to the above definition and the initial value limit of the algorithm, the user elevation angle $\alpha\epsilon[10^\circ, 90^\circ]$ (converted to the satellite elevation angle is $\gamma\epsilon[0, 55.8^\circ]$) and azimuth angle are traversed $\beta\epsilon[1^\circ, 360^\circ]$, while the receiver sensitivity is set to −160 dB W. The effects of different user elevation angles and satellite azimuth angles on user vertical errors and horizontal errors are discussed as follows in Figure 7.

It is not difficult to see that when the user is at a low elevation angle, the vertical and horizontal errors deviation of the users are generally large, and the convergence is not good. When the user is at a higher elevation angle, the horizontal and vertical errors of the user significantly decrease.

The following results in Figure 8 are obtained from the statistical analysis of user errors at different user elevation angles.

The numerical results of the aforementioned image can be further analyzed. First, by discussing the situation for all users, i.e., users with elevation angles $\alpha\epsilon[10^\circ, 90^\circ]$, the overall performance of power positioning can be obtained. Then, by separately discussing the two major parts of low user elevation angles $\alpha\epsilon[10^\circ, 30^\circ]$ and high user elevation angles $\alpha\epsilon[30^\circ, 90^\circ]$, the positioning and timing performance of users in different elevation angle regions can be obtained as follows in Table 2.

According to Equation 23, timing errors of the power positioning can be calculated by the difference between the true value and solution value. The timing errors affected by different user locations as follows in Figure 9.

The maximum timing error is 10.1 ms, and the statistical mean is 123 μs. When the user's elevation angle is below 30°, the average timing error is 305.8 μs; when the user's elevation angle is above 30°, the average timing error is 62.3 μs. Therefore, power positioning can provide users with microsecond-level timing accuracy.

When the user's horizontal or vertical difference exceeds the convergence condition of 50 km, the algorithm is judged to diverge, and the availability of power positioning is poor. By statistically analyzing the results for different user elevation angles, the positioning availability can be obtained as shown in Figure 10.

**TABLE 2** Satellite and user error table when receiver sensitivity is –160 dB W.

| User elevation angle range | Evaluation criteria | Elevation angle error $\Delta\gamma/°$ | Azimuth angle error $\Delta\beta/°$ | Vertical error $\Delta \boldsymbol{h}$/m | Horizontal error $\Delta \boldsymbol{x}$/m |
|---|---|---|---|---|---|
| [10°,90°] | Bias | 0.1038 | 0.1239 | 7,093.5 | 7,009.3 |
| | Standard deviation | 0.5016 | 1.1811 | 31,720 | 53,403 |
| [10°,30°] | Bias | 0.1683 | 0.0996 | 15,546 | 17,180 |
| | Standard deviation | 0.9562 | 1.9617 | 74,503 | 165,260 |
| [30°,90°] | Bias | 0.0817 | 0.1316 | 4,231.2 | 3,567.1 |
| | Standard deviation | 0.3455 | 0.8340 | 17,385 | 15,062 |

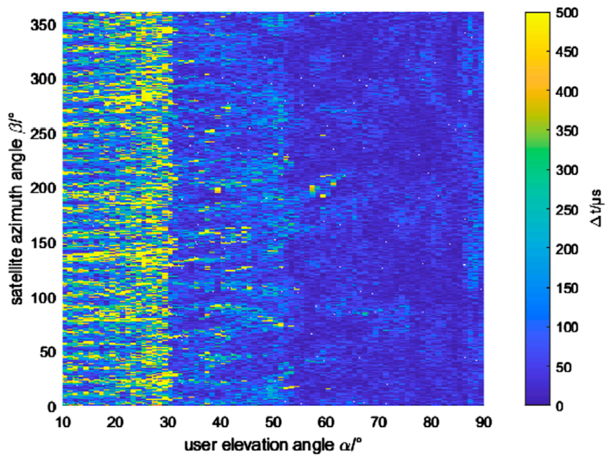

FIGURE 9
Timing errors of power positioning.

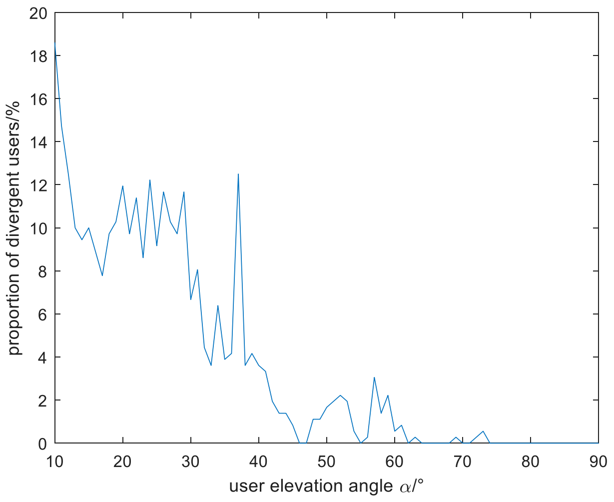

FIGURE 10
Availability of power positioning.

It can be seen that when the user's elevation angle is less than 40°, the proportion of divergent users is generally more than 10%, and the availability of power positioning is about 90%; when the elevation angle is higher than 40°, the proportion of divergent users is generally within 5%, and the availability of power positioning is above 95%. In summary, power positioning allows some users, especially those with high elevation angles, to have the potential to achieve better positioning and timing performance.

## 4.2 Different receiver sensitivity

The simulation is set with a certain receiving power sensitivity threshold. When the received power exceeds this threshold, the power measurements are processed; otherwise, the power value is considered to be significantly affected by noise and is not subjected to least squares iteration processing. Previous simulations were all conducted under the condition of a threshold of −160 dB W, which has high requirements for data quality. In this section, the receiver sensitivity is lowered to −190 dB W to explore the impact of receiving power sensitivity on power positioning.

As with section 4.1, the angle conditions are as the same. However, the receiver sensitivity is set to −190 dB W. Figure 11 illustrates the impact of the user's elevation angle and azimuth angle on the vertical and horizontal error biases in power positioning.

It can be observed that when the user's elevation angle is low, for example, below 30°, the receiver with −190 dB W sensitivity exhibits more divergence in power positioning compared to the receiver with −160 dB W sensitivity. This indicates that while increasing the receiver sensitivity makes it easier to receive signals from different beams, the power positioning algorithm becomes more challenging to converge due to noise interference. Therefore, to enable more users to achieve better performance with power positioning, it is necessary to reduce the receiver sensitivity to a certain extent, in order to mitigate the impact of noise on the solution. As with subsection 4.1, by statistically analyzing the error biases for users with different elevation angles, the following results can be obtained.

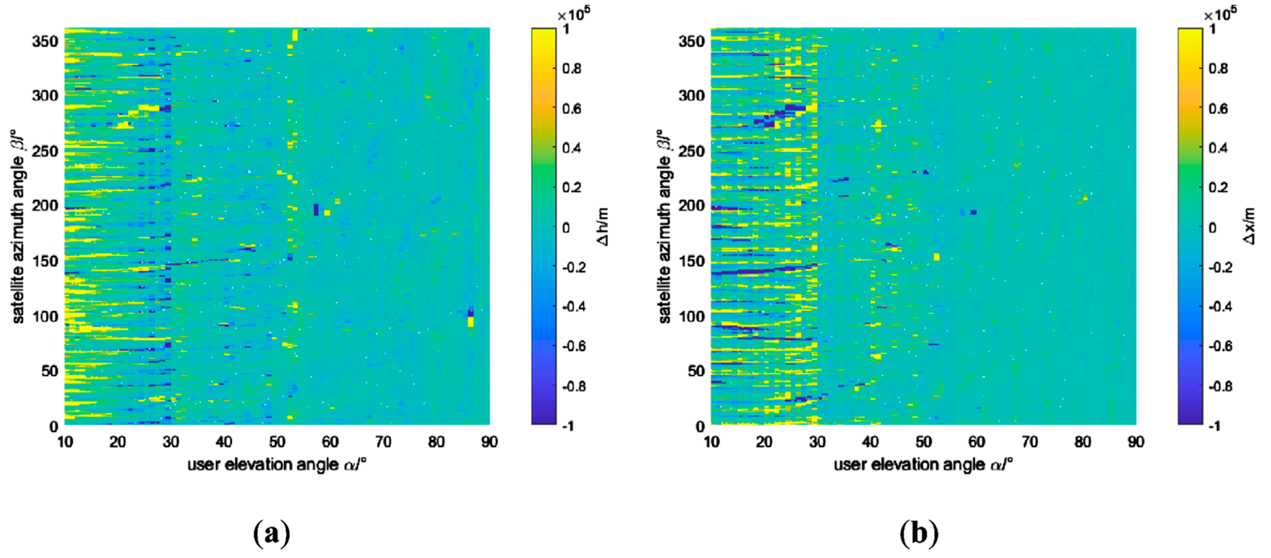

FIGURE 11
When receiver sensitivity is −190 dB W: **(A)**User vertical errors in different locations **(B)** User horizontal errors in different locations.

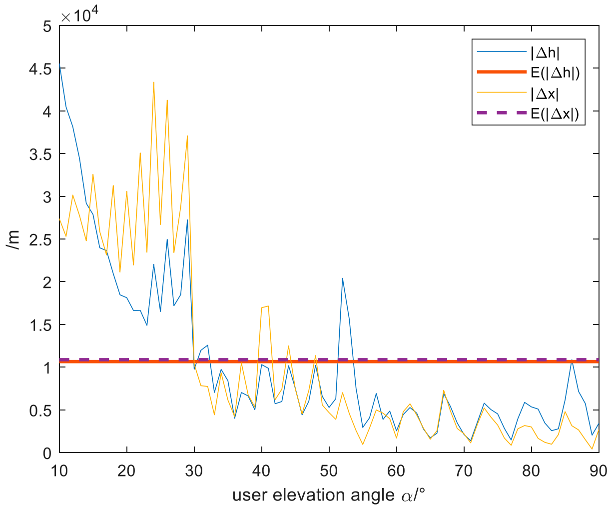

FIGURE 12
Vertical and horizontal deviations of different user elevation angles when receiver sensitivity is −190 dB W.

The resulting error table is as follows.

From Figure 12 and Table 3, it can be seen that the standard deviations of user vertical difference and horizontal difference obtained by the high-sensitivity receiver are comparable to those under low-sensitivity conditions. However, the error biases of satellite elevation angle and satellite azimuth angle have increased by 0.0311° and 0.0789°, respectively, and the biases of user vertical and horizontal errors have increased by 3,556.5 m and 3,859.7 m, respectively. Under low user elevation angles, the biases of vertical difference and horizontal difference have increased by 8,506 m and 10,975 m, respectively, while under high user elevation angles, the biases have increased by 1,790.9 m and 1,343.2 m, respectively. It is not difficult to find that high sensitivity has a very significant impact on users with low elevation angles, while the impact on users with high elevation angles is relatively small.

## 5 Conclusion

In scenarios where the number of LEO satellites in view is limited, pseudorange and carrier phase positioning are not available, and single-satellite Doppler positioning has poor applicability, ground users can utilize the received power measurements from different beams of LEO satellites to calculate their own position and time, thereby quickly obtaining positioning and timing results. Based on the multi-beam interrogation characteristics of LEO satellites, this paper employs the nearest neighbor algorithm for power matching to obtain convergent initial values and uses the least squares iteration to solve for the user's horizontal and vertical information. Experimental results show that the nearest neighbor algorithm can achieve initial values for satellite elevation and azimuth angles within 2° when the fingerprint library interval uncertainty is 5°; under the condition of initial values within 2°, the least squares solution can achieve convergence for the vast majority of users (94.5%, 93.2%).

For the least squares algorithm solution, multiple Monte Carlo simulation results indicate that the satellite elevation and azimuth angles, as well as user vertical and horizontal differences obtained from power positioning calculations, follow a normal distribution and have a good normal fitting relationship. There is a significant difference in power positioning results for users at different locations. For a receiver with −160 dB W sensitivity, the statistical error biases for horizontal and vertical positioning are approximately 7,000 m, and the average timing error is 123 μs. Users with low elevation angles (below 30°) generally have error biases

TABLE 3 Satellite and user error table when receiver sensitivity is –190 dB W.

| User elevation angle range | Evaluation criteria | Elevation angle error $\Delta\gamma/°$ | Azimuth angle error $\Delta\beta/°$ | Vertical error $\Delta h$/m | Horizontal error $\Delta x$/m |
|---|---|---|---|---|---|
| [10°,90°] | Bias | 0.1349 | 0.2028 | 10,650 | 10,869 |
| | Standard deviation | 0.3724 | 0.6374 | 28,955 | 33,410 |
| [10°,30°] | Bias | 0.1639 | 0.1556 | 24,052 | 28,155 |
| | Standard deviation | 0.5325 | 0.4881 | 65,283 | 90,783 |
| [30°,90°] | Bias | 0.1239 | 0.2177 | 6,022.1 | 4,910.3 |
| | Standard deviation | 0.3174 | 0.6847 | 16,740 | 13,961 |

higher than the average, at 1,5546 m and 17,180 m respectively, with a timing error of 305.8 μs, and power positioning availability of about 90%. In contrast, users with high elevation angles (above 30°) generally have error biases lower than the average, at 4,231.2 m and 3,567.1 m respectively, with a timing error of 62.3 μs, and availability about 95%. Under high receiver sensitivity at −190 dB W, affected by noise, the average error bias is about 10,000 m, with low elevation angle users being particularly affected, with an average bias worsening to over 20,000 m, and availability worsening to 70%. For high elevation angle users, the average bias only worsens to about 6,000 m, and power positioning availability is basically maintained above 90%.

In summary, the positioning accuracy of low Earth orbit multi-beam power positioning technology is at the kilometer level, and the timing accuracy is at the microsecond level, which can meet users' needs for real-time approximate position and time information.

As the technology of LEO power positioning evolves, future research will delve into the performance of the Least Squares algorithm and the K-Nearest Neighbors algorithm in this domain. By conducting a meticulous analysis of these two algorithms, we aim to uncover their respective advantages in various application scenarios, thereby providing theoretical foundations and technical support for achieving more accurate navigation and timing performance. In this process, our focus will extend beyond the mathematical properties and computational efficiency of the algorithms to encompass their adaptability and flexibility in practical applications. We are confident that through a comprehensive comparison and optimization of these algorithms, we can offer more reliable solutions for LEO power positioning technology in the complex and dynamic environments of its applications. Looking ahead, we anticipate that these research outcomes will propel the advancement of LEO power positioning technology and contribute new momentum to the development of LEO navigation systems.

## Data availability statement

The raw data supporting the conclusions of this article will be made available by the authors, without undue reservation.

## Author contributions

SG: Data curation, Formal Analysis, Software, Validation, Visualization, Writing–original draft, Writing–review and editing. CM: Data curation, Investigation, Methodology, Supervision, Writing–review and editing. XT: Methodology, Supervision, Writing–review and editing, Investigation, Resources. FW: Methodology, Supervision, Writing–review and editing, Funding acquisition, Software.

## Funding

The author(s) declare that financial support was received for the research, authorship, and/or publication of this article. National Natural Science Foundation of China, U20A20193.

## Conflict of interest

The authors declare that the research was conducted in the absence of any commercial or financial relationships that could be construed as a potential conflict of interest.

## Generative AI statement

The author(s) declare that no Generative AI was used in the creation of this manuscript.

## Publisher's note

# References

1. Yang Y, Yue M, Xia R, Xiaolin J, Bijiao S. Demand and key technology for a LEO constellation as augmentation of satellite navigation systems. *Satell Navig* (2024) 5(1):1–9. doi:10.1186/s43020-024-00133-w

2. Li X, Lu Z, Yuan M, Liu W, Wang F, Yu Y, et al. Tradeoff of code estimation error rate and terminal gain in SCER attack. *IEEE Trans Instrumentation Meas* (2024) 73:1–12. doi:10.1109/tim.2024.3406807

3. Tian R, Cui Z, Zhang S, et al. Overview of the development of navigation augmentation technology based on low-orbit communication constellation. *Navigation Positioning and Timing* (2021) 8(1):66–81.

4. Benzerrouk H, Nguyen Q, Fang X, et al. *26th saint petersburg international conference on integrated navigation systems (ICINS)*. St. Petersburg: IEEE (2019).

5. Min L, Tengda H, Wenwen L, Qile Z. A review of low earth orbit navigation enhancement technology development. *Surv Mapp Geomatics* (2024) 49(1):10–9.

6. Chen L, Kai L, Jin Y, Lin J, Shao H. Design of low earth orbit satellite constellation for regional navigation enhancement. *J Univ Electron Sci Technology China* (2022) 51(4):522–8.

7. Zhang X, Hu J, Ren X. New progress in PPP/PPP-RTK and comparison of BeiDou/GNSS PPP positioning performance. *Acta Geodaetica et Cartographica Sinica* (2020) 49(9):1084–100.

8. Li X, Zhao Y, Zhang K, Wu J, Zheng H, Zhang W. LEO real-time ambiguity-fixed precise orbit determination with onboard GPS/Galileo observations. *GPS Solutions* (2024) 28(4):188. doi:10.1007/s10291-024-01729-0

9. Hong J, Tu R, Zhang P, Zhang R, Han J, Fan L, et al. GNSS rapid precise point positioning enhanced by low Earth orbit satellites. *Satellite Navigation* (2023) 4(1):11–3. doi:10.1186/s43020-023-00100-x

10. Shi C, Zhang Y, Li Z. Revisiting Doppler positioning performance with LEO satellites. *GPS Solutions* (2023) 27(3):126. doi:10.1007/s10291-023-01466-w

11. Kershner RB, Newton RR. The transit system. *J Navigation.* (1962) 15(2):129–44. doi:10.1017/s0373463300035943

12. Kouba J. A review of geodetic and geodynamic satellite Doppler positioning. *Rev Geophys* (1983) 21(1):27–40. doi:10.1029/rg021i001p00027

13. Yi K, Yi L, Sun C, Chunguo N. Recent developments and prospects of satellite communication. *J Commun* (2015)(6) 161–76.

14. Bi J, Wang Y, Cao H, Shi T, Huang L. Supplementary open dataset for WiFi indoor localization based on received signal strength. *Satellite Navigation* (2022) 3(1):25–15. doi:10.1186/s43020-022-00086-y

15. Vincent H, Xiao Z, Semong T, Bai J, Chen H, Jiao L. Achieving reliable intervehicle positioning based on redheffer weighted least squares model under multi-GNSS outages. *IEEE Trans Cybernetics* (2023) 53(2):1039–50. doi:10.1109/TCYB.2021.3100080

16. Xiao Z, Chen Y, Alazab M, Chen H. Trajectory data acquisition via private car positioning based on tightly-coupled GPS/OBD integration in urban environments. *IEEE Trans Intell Transportation Syst* (2022) 23(7):9680–91. doi:10.1109/tits.2021.3105550

17. Kaemarungsi K, Krishnamurthy P. Modeling of indoor positioning systemsbased on location fingerprinting. *IEEE INFOCOM* (2004) 2:1012–22. doi:10.1109/ACCESS.2018.2817576

18. Li J, Gao X, Hu Z, Wang H, Cao T, Yu L. Indoor localization method based on regional division with IFCM. *Electronics* (2019) 8(5):559. doi:10.3390/electronics8050559

19. Kan C, Ding G, Wu Q, et al. Robust relative fingerprinting-based passive source localization via data cleansin. *IEEE Access* (2018) 6:19295–69.

20. Feng Y, Minghua J, Jing L, Xiao Q, Ming H, Tao P, et al. Improved AdaBoost-based fingerprint algorithm for WiFi indoor localization. In: *2014 IEEE 7th joint international information technology and artificial intelligence conference* (2014). p. 16–9.

21. Li Y, Zhuang Y, Hu X, Gao Z, Hu J, Chen L, et al. Toward location-enabled IoT (LE-IoT): IoT positioning techniques,error sources, and error mitigation. *IEEE Internet Things J* (2021) 8(6):4035–62. doi:10.1109/jiot.2020.3019199

22. Xie G. *Principles of GPS and receiver design*. Beijing: Publishing House of Electronics Industry (2022).

23. Xiao Z, Xiao D, Vincent H, Jiang H, Liu D, Wang D, et al. Toward accurate vehicle state estimation under non-Gaussian noises. *IEEE Internet Things J* (2019) 6(6):10652–64. doi:10.1109/JIOT.2019.2940412

24. GB/T 39399-2020. *General specification for BeiDou/global navigation satellite systems (GNSS) geodetic receivers* (2020). p. 11–9.

Frontiers in Physics

TYPE Review
PUBLISHED 06 February 2025
DOI 10.3389/fphy.2025.1487136

EDITED BY
Daniel Okoh,
The National Space Research and
Development Agency (NASRDA), Nigeria

REVIEWED BY
Lunlong Zhong,
Civil Aviation University of China, China
Yansong Meng,
China Academy of Space Technology, China

*CORRESPONDENCE
Zukun Lu,
luzukun@nudt.edu.cn
Shaojie Ni,
nishaojie@nudt.edu.cn

RECEIVED 27 August 2024
ACCEPTED 16 January 2025
PUBLISHED 06 February 2025

CITATION
Zeng Y, Lu Z, Xie Y, Ren B, Yu Y and Ni S (2025) Overview of development and challenges of attitude determination for rotary wing UAVs based on GNSS.
*Front. Phys.* 13:1487136.
doi: 10.3389/fphy.2025.1487136

# Overview of development and challenges of attitude determination for rotary wing UAVs based on GNSS

Yejia Zeng[1], Zukun Lu[1,2]*, Yuchen Xie[1,2], Binbin Ren[1,2], Yi Yu[3] and Shaojie Ni[1,2]*

[1]College of Electronic Science and Technology, National University of Defense Technology, Changsha, China, [2]National Key Laboratory for Positioning, Navigation and Timing Technology, Changsha, China, [3]Hunan Xinghe Electronics Co. LTD., Changsha, China

Attitude determination of rotary-wing unmanned aerial vehicles (RUAVs) is crucial for grasping their motion state and is a necessary condition to ensure the correct execution of flight missions. With the continuous development and the constant enhancement of measurement accuracy related to the Global Navigation Satellite System (GNSS), attitude determination based on GNSS have become the mainstream high-precision attitude measurement approach. This paper mainly discusses the relevant theories of using GNSS for RUAV's attitude determination, and introduces the relevent key aspects that determine attitude accuracy in the attitude resolution process, such as integer ambiguity fixing, attitude solution algorithms, and integrated attitude measurement. It especially elaborates on the challenges that faced to be solved for current RUAVs to use the GNSS system for real-time and guarded attitude measurement.

KEYWORDS

**satellite navigation, attitude determination, integer ambiguity, Kalman filtering, navigation interference**

## 1 Introduction

Unmanned Aerial Vehicles (UAVs), characterized by their high controllability, low production costs, and the separation of human operators from the vehicle, are widely used across various civilian and military domains. In the civilian sector, UAVs can be employed for applications such as topographic surveys, disaster detection, power line inspections, search and rescue operations, target tracking, and the establishment of wireless networks [1–4]. In the military sphere, their low cost, high mobility, compact size, and difficulty to detect make them ideal for battlefield reconnaissance, supply transportation, information confrontation, communication relay, and firepower engagement [5]. Conflicts such as those in Syria, the Nagorno-Karabakh region, and the Russia-Ukraine war have seen the emergence of various types of UAVs, including integrated reconnaissance-strike, surveillance, and suicide attack drones [6–8].

Rotor Unmanned Aerial Vehicles (RUAVs), a type of UAV, are relatively small in size and rely on the rotation of multiple wing propellers to lift and move. They possess the capability for vertical takeoff and landing and omnidirectional flight, exhibiting higher maneuverability and flexibility at a negligible cost compared to fixed-wing UAVs [9]. As

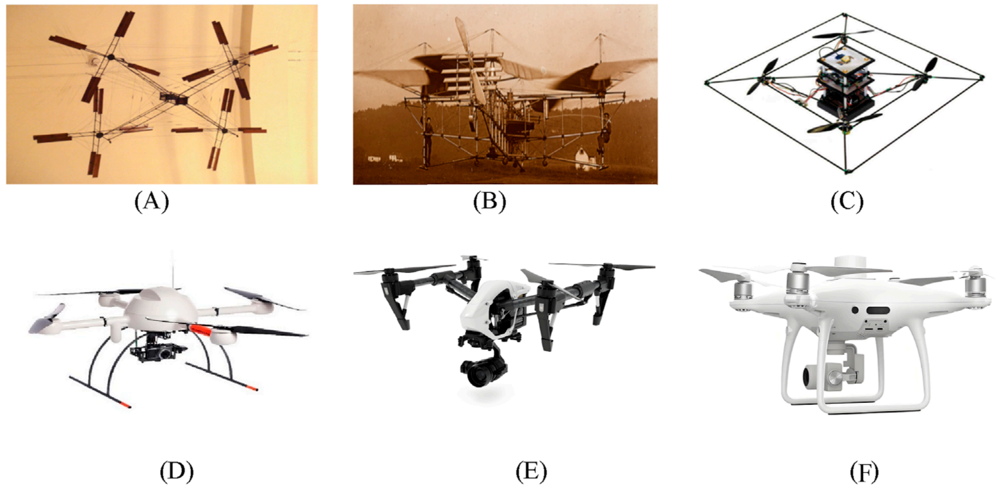

FIGURE 1
Classic drone. **(A)** “Gyroplane No.1”. **(B)** “Oehmichen No.2”. **(C)** “STARMAC-2”. **(D)** “MD4-1000”. **(E)** “Inspire 1”. **(F)** “Phantom 4”.

shown in Figure 1, the earliest RUAVs appeared in 1907 with the “Gyroplane No.1″designed by Professors Jacques Breguet and “Oehmichen No.2″invented by Etienne Oehmichen [10]. With the advent of the 21st century, the development level of rotor UAVs has been greatly enhanced by the invention of new controllers and sensors [11]. Stanford University designed the multi-autonomous platform control testbed STARMAC, capable of precise flight control and equipped with some obstacle avoidance capabilities [12, 13]. The German classic multi-rotor UAV, MD4-1000, equipped with a camera gimbal, can achieve autonomous navigation using image capture. In recent years, Dajiang UAV has rapidly occupied the RUAV Market, typical products like the Inspire 1, Mavic 2, and Phantom 4 can enhance obstacle avoidance capabilities using a visual processing unit [14].

The flight attitude information of a RUAV is a crucial parameter for describing its motion state, equally important as its position and velocity information. Attitude angles can provide data support for attitude control in the flight control system, assist the flight control system in making adjustments, ensuring that the drone maintains balance during flight, which is crucial for flight safety [15]; In the context of multi-drone systems or collaborative missions, accurate attitude measurement is crucial for maintaining formation flight and coordinated operations [16]; Attitude also helps drones avoid collisions and obstacles, especially when visual obstacle avoidance systems are combined with data from attitude sensors. The angular information obtained from attitude measurements assists the flight control system in calculating the necessary adjustments for obstacle avoidance [17]; The heading and attitude information of a UAV, is also a powerful basis for the UAV to counteract directional interference [18].

Initially, the attitude determination of the carrier relied on the Inertial Navigation System (INS), which, as a navigation system capable of independently outputting positioning and attitude, has the characteristics of working independently without the need for external equipment. It can effectively resist external interference, offering good autonomy, concealment, and continuity [19]. However, as the working time of INS increases, the measurement errors caused by mechanical devices will accumulate over time, leading to a decrease in measurement accuracy [20]. High-precision inertial navigation equipment is usually bulky and costly, making it unsuitable for small and low-cost RUAVs.

The Global Navigation Satellite System (GNSS), is fully applied in the fields of navigation, timekeeping, positioning, and attitude determination due to its all-weather, global, high-precision, and high-real-time characteristics. It has the advantages of low cost, small size, low power consumption, short initialization time, and no error accumulation effect [21]. Small RUAVs widely adopt satellite navigation to obtain state information such as position, velocity, and attitude [22]. The carrier phase differential as an observation method helps to minimize the impact of clock differences and atmospheric delays under short baselines, and when obtaining the right integer ambiguity, the phase observation is two orders of magnitude more accurate than pseudo-range observation, which helps UAVs achieve high-precision attitude determination [23]. Attitude measurement uses the changes in the short baseline in different coordinate systems to obtain the attitude angle, involving a series of key issues such as the flight integer ambiguity and attitude angle solution algorithm [24, 25].

The attitude determination of RUAVs is a critical step in grasping their motion state information and a necessary condition to ensure their own safety. Therefore, focusing on the UAV attitude determination based on GNSS, this paper elaborates on the relevant theories of attitude determination in recent years, concentrating on key technologies in the attitude determination process, such as the determination of integer ambiguity and attitude resolution algorithms. At the same time, it analyzes the security challenges faced when using GNSS for UAV attitude determination in complex electromagnetic environments.

# 2 Current research status of RUAV attitude measurement based on GNSS

## 2.1 Existing GNSS attitude measurement products

The application of GNSS was initially for precise positioning and navigation. As the navigation system evolved and the use of carrier phase differential observation became more mature, its high-precision measurement capabilities gradually extended to the field of attitude measurement [26, 27]. In 1978, Coumselma [28] proposed the use of GPS carrier phase differential measurement for attitude determination, designing a full link attitude measurement system from the satellite to the receiver. Hermann [29] tested the software receiver TI-AGR for attitude measurement, proving that GPS signals can achieve millimeter-level attitude measurement on long baselines. Trimble Navigation Limited used a three-antenna two-baseline attitude determination device on a U.S. Navy cruiser for dynamic determination experiments, verifying that GPS can provide attitude information for low-dynamic motion carriers [30]. Entering the 21st century, more mature GNSS-based attitude measurement systems have emerged abroad, such as the 3DF system by Ashtech [31], the Tans Vector system by Trimble [32], and the JNSGyro-2T and JNSGyro-4T systems by Javad [33]; the Beeline system by NovAtel [34].

Currently, the ZH6000A, developed by Zihang Electronic Technology, is a three-antenna GNSS full-attitude measurement and positioning GNSS-INS combined system, capable of precisely calculating attitude angles with an accuracy of 0.05° (4-meter baseline); meanwhile, the built-in IMU can perform real-time high-precision GNSS/INS combined solutions [35]. The SIN-INS3000 system, developed by Xi’an Sine Wave Measurement and Control Technology, utilizes a combination of GNSS and fiber optic inertial navigation to achieve a roll and pitch accuracy of 0.02° [36]. The GNSS/INS integrated navigation system, developed by Airic Co. Inertial Technology, provides continuous and high-precision information. Employing a dual-antenna GNSS module in conjunction with an INS system, the system offers combined attitude determination with roll and pitch accuracies of 0.01° and 0.004° post-processing, respectively. The heading accuracy can reach 0.05°, with post-processing accuracy achievable up to 0.01° [37].

There are also products that use multiple satellite navigation system signals for attitude measurement, such as the MTi-G-710 sensor, developed by Xsens [38], aided by INS and utilizing signals from navigation systems such as GLONASS and Beidou. It outputs GNSS-enhanced 3D orientation and is capable of achieving pitch, roll, and yaw angle accuracies of 0.2°, 0.3°, and 1.0°, respectively. The 3DM-GX5-GNSS/INS system, developed by MicroStrain Sensing Systems, utilizes global navigation satellite systems such as GPS and GLONASS to provide precise 3D attitude determination. By integrating GNSS data with INS data through an Extended Kalman Filter and a Complementary Kalman Filter, the system achieves roll and pitch angle accuracies of 0.25°, with a heading accuracy of 0.8° [39].

## 2.2 Unique aspects of RUAVs attitude determination

RUAVs, due to limitations of their own platform, are equipped with a limited number of receiver antennas, and the baseline length formed by the antennas is of the short-baseline type, which is different from the medium to long-baseline issues present in platforms like vehicles and ships (greater than 1 m) [40]. Attitude determination often benefits from longer baseline lengths. Therefore, the attitude determination of RUAVs differs from conventional circumstances, it is conducted under short-baseline conditions [41]. Besides, the limitation on the number of baselines due to the size constraints of their own platform is also a special issue that needs to be considered.

Secondly, during the flight of rotary-wing unmanned aerial vehicles, especially in swarm operations, when directional changes are flexible and diverse, and angular velocity changes are rapid, the refresh rate of satellite navigation measurements is low and cannot match the high-dynamic angle change requirements of the RUAVs. Therefore, it is common to combine the attitude determination with the inertial navigation system. However, due to the low-cost requirements of the UAVs themselves, the accuracy of low-cost inertial navigation devices is low, and there is an accumulation of errors that require correction by the satellite navigation system [15]. In addition to relying on satellite navigation signals for determination, it is also necessary to study the fusion data algorithms in integrated navigation to complement the advantages of satellite navigation and inertial navigation, thereby improving the precision of the measurements.

Since UAVs are often in complex electromagnetic environments, when using satellite navigation for positioning and attitude determination, the satellite navigation signals are relatively weak when reaching the ground, generally at −160dBW, and the navigation signal system is often semi-public. The rotary-wing unmanned aerial vehicle has a relatively low speed of movement, making it susceptible to jamming and spoofing interference [42]. At the same time, due to the load restrictions of rotary-wing UAVs, with limited anti-interference capabilities without the support of facilities such as null steering antenna, the accuracy of positioning and attitude determination results is seriously affected by interference, and the UAV’s own motion state faces safety issues. For example, during UAV swarm performances, unknown interference can lead to loss of control of the swarm [43]; To ensure the normal flight of UAVs in complex electromagnetic environments and ensure their survivability, it is necessary to considering the UAV’s anti-interference capabilities, which is the particularity of RUAV attitude measurement [44].

# 3 Knowledge of UAV attitude measurement

Using satellite navigation for attitude measurement, the accuracy of the attitude angles depends on factors such as observation quality, antenna configuration, and solving methods [39]. The attitude determination process using GNSS often involves two steps: coordinate conversion and baseline solution. Research is often conducted to improve the accuracy and reliability of

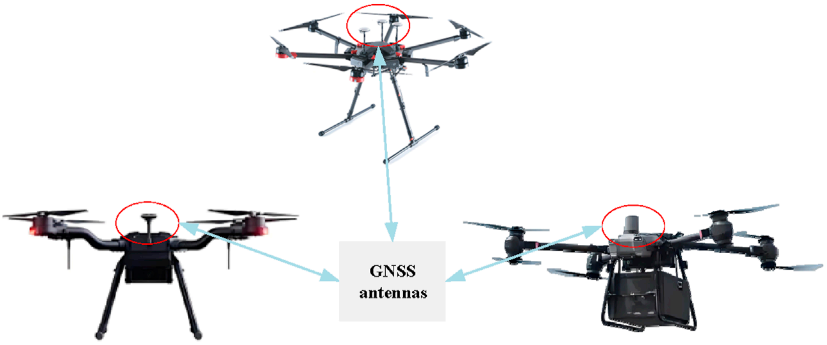

FIGURE 2
Common RUAV and navigation receiver antenna.

**TABLE 1 Common description methods for attitude angles.**

| Description method | Features | Usage scenarios |
|---|---|---|
| Euler Angles | Intuitively reflect the direction angles; have singularity issues | GNSS measurement systems |
| Quaternions | No singularity issues; have more parameters; not intuitive | INS measurement systems |
| Direction Cosines | Meet orthogonality constraint conditions; complex construction; large computational load | GNSS measurement systems; INS measurement systems; Optical Measurement System |

attitude calculation [45]. Key points of which integer ambiguity determination and attitude angle solution attract numerous researchers to study [46–48].

## 3.1 Basic principles of attitude determination

During the flight of an RUAV, the flight control system continuously receives real-time position and heading information from sensors such as GNSS receivers and gyroscopes. It then calculates the yaw distance and heading control quantities based on remote control commands, causing the aircraft wings to rotate to varying degrees, thereby steering the UAV in the correct direction [1]. As shown in Figure 2, attitude determination using satellite navigation generally involves the relative changes in the positions of multiple antennas fixed on the carrier in different coordinate systems. Key points related to the carrier's attitude include the description method of attitude angles, coordinate systems, and the transformation matrices between coordinate systems.

As shown in Table 1, there are three common ways to describe attitude angles: Euler angles, quaternions, and direction cosines, which can be converted from one to another [49, 50]. In UAV attitude measurement, the Euler angle method is often used, that is, heading angle, pitch angle, and roll angle, which can intuitively reflect the attitude information of the carrier.

In addition, attitude measurement often involves three coordinate systems, as shown in Figure 3, namely the Earth-centered Earth-fixed coordinate system (ECEF), the local horizontal coordinate system (LHCS), and the vehicle coordinate system (VCS). The ECEF coordinate system, as shown in Figure 3A, rotates with the Earth and is used to describe the position calculated according to navigation messages; the local horizontal coordinate system in Figure 3B, has its origin at the center of the carrier and describes the coordinates of a point in space relative to a selected reference point, also known as the East North Up (ENU) coordinate system; the vehicle coordinate system is fixed on the carrier and changes with the carrier's motion and attitude, which is shown in Figure 3C. The $Y$-axis generally points in the direction of the carrier's heading, the $Z$-axis points towards the zenith direction, and the $X$-axis, together with the $X$-axis and $Z$-axis, forms a right-handed coordinate system.

In Figure 3D, taking a single baseline formed by dual antennas as an example, antennas u and r fixed on the carrier constuct a baseline, whose coordinates in VCS are determined when the antennas are installed, that is $\boldsymbol{x}_b = [x_b \quad y_b \quad z_b]^{\mathrm{T}}$. Their positions in the LHCS are $\boldsymbol{x}_l = [x_l \quad y_l \quad z_l]^{\mathrm{T}}$, and in the ECEF, the positions are $\boldsymbol{x}_e = [x_e \quad y_e \quad z_e]^{\mathrm{T}}$. By performing coordinate transformations of this baseline in different coordinate systems, primarily from the local horizontal coordinate system to the carrier coordinate system, the attitude angles can be obtained.

A. From ECEF to LHCS:

$$\boldsymbol{x}_l = R_e^l \cdot \boldsymbol{x}_e \Leftrightarrow \begin{bmatrix} x_l \\ y_l \\ z_l \end{bmatrix} = \begin{bmatrix} -\sin\alpha & \cos\alpha & 0 \\ -\cos\alpha\sin\beta & -\sin\alpha\sin\beta & \cos\beta \\ \cos\alpha\cos\beta & \sin\alpha\cos\beta & \sin\beta \end{bmatrix} \cdot \boldsymbol{x}_{ur} \tag{1}$$

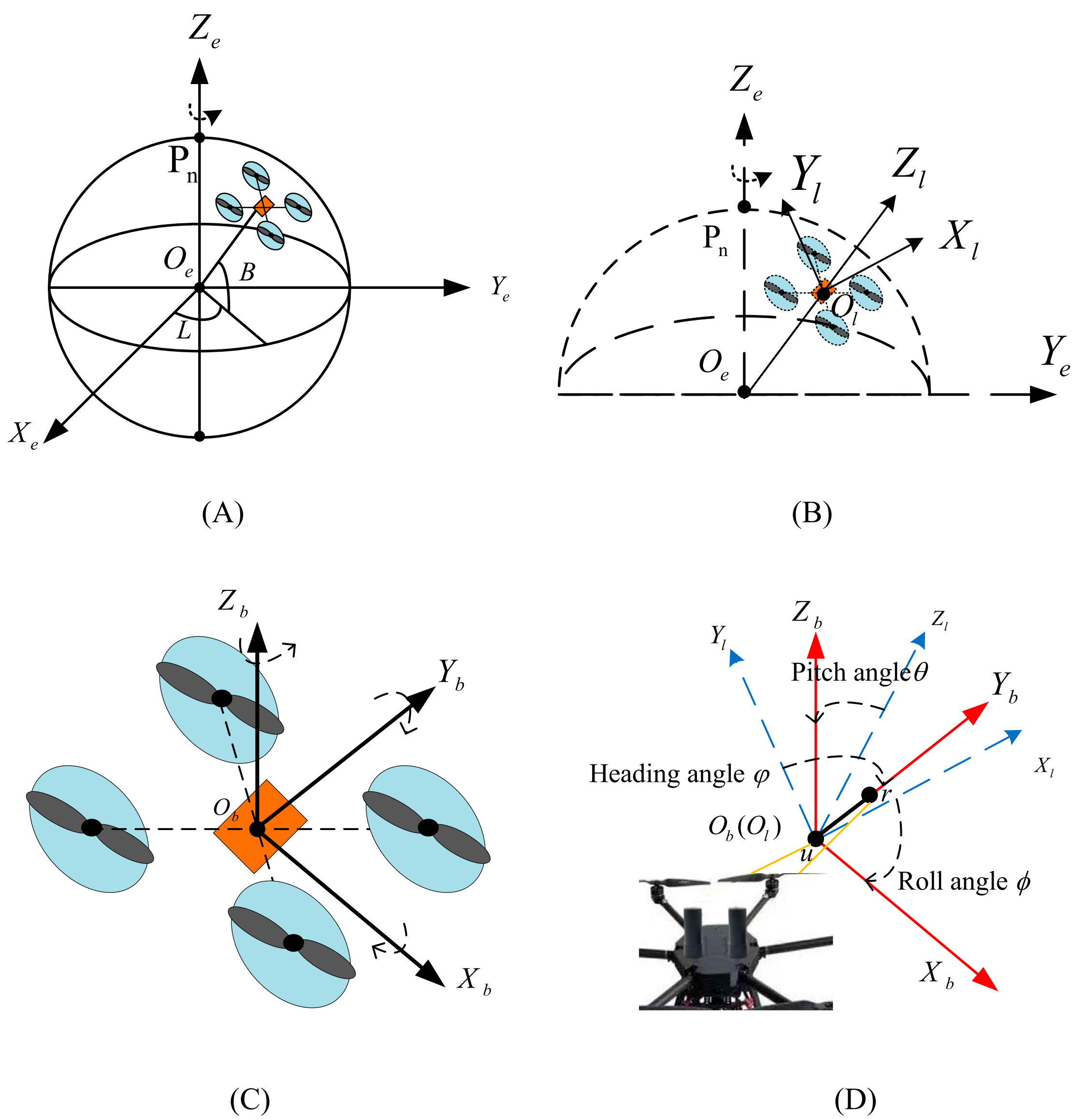

(A) (B)

(C) (D)

FIGURE 3
Coordinate system used for attitude determination. **(A)** Earth-centered earth-fixed coordinate system. **(B)** Local coordinate system. **(C)** Body coordinate system. **(D)** Rotation diagram.

where $\alpha$ and $\beta$ are respectively the longitude and latitude of antenna u in Figure 3D after positioning calculation; $\boldsymbol{x}_{ur}$ is the baseline vector composed of antenna u and antenna r, also denoted as $\boldsymbol{x}_e$.

B. From LHCS to VCS:

The common rotation sequence of the coordinate systems, according to the right-hand rule, involves rotating the local horizontal coordinate system successively around the $Z$-axis by angle $\psi$, around the $X$-axis by angle $\theta$, and around the $Y$-axis by angle $\phi$, to align with the vehicle coordinate system. $\psi$, $\theta$, $\phi$, correspond to the heading angle, pitch angle, and roll angle, respectively, as shown in Figure 3D. The corresponding rotation matrix is shown in Equation 2:

$$\boldsymbol{R}_l^b = \boldsymbol{R}_Y(\phi)\cdot\boldsymbol{R}_X(\theta)\cdot\boldsymbol{R}_Z(\psi) \tag{2}$$

where $R_Z(\psi)$, $R_X(\theta)$, and $R_Y(\phi)$ are the rotation matrices for rotations about the $Z$-axis, $X$-axis, and $Y$-axis, respectively. These rotation matrices can be defined individually as:

$$\boldsymbol{R}_Z = \begin{bmatrix} 0 & 0 & 1 \\ \cos\psi & \sin\psi & 0 \\ -\sin\psi & \cos\psi & 0 \end{bmatrix}, \boldsymbol{R}_X = \begin{bmatrix} 1 & 0 & 0 \\ 0 & \cos\theta & \sin\theta \\ 0 & -\sin\theta & \cos\theta \end{bmatrix},$$

$$\boldsymbol{R}_Y = \begin{bmatrix} \cos\phi & 0 & -\sin\phi \\ 0 & 1 & 0 \\ \sin\phi & 0 & \cos\phi \end{bmatrix} \tag{3}$$

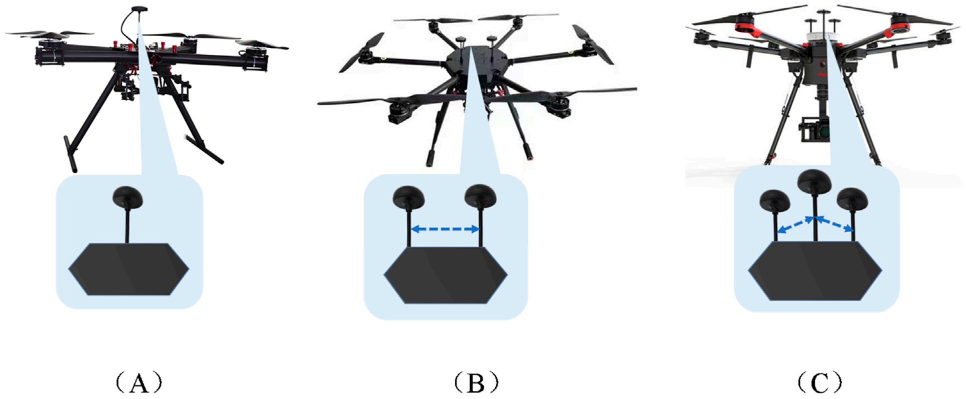

FIGURE 4
Schematic diagram of UAV navigation antenna and baseline. **(A)** Single-antenna. **(B)** Dual-antenna. **(C)** Multi-antenna.

Equation 4 represents the transformation of the baseline using Equation 3.

$$\boldsymbol{x}_b = \boldsymbol{R}_l^b \cdot \boldsymbol{x}_l \Leftrightarrow \begin{bmatrix} x_b \\ y_b \\ z_b \end{bmatrix} = \boldsymbol{R}_Y \cdot \boldsymbol{R}_X \cdot \boldsymbol{R}_Z \cdot \begin{bmatrix} x_l \\ y_l \\ z_l \end{bmatrix} \tag{4}$$

In Equation 3, the attitude angle information is contained in the rotation matrix. By solving Equation 4, the rotation matrix is obtained, and then the attitude angle is obtained. At least two non-collinear baselines are required to solve for the complete set of angles $\psi$, $\theta$, $\phi$,. The more baselines used, the higher the measurement redundancy, and consequently, the higher the measurement accuracy.

## 3.2 GNSS-based observation model

GNSS attitude measurement systems can be categorized based on the number of antennas deployed into single-antenna measurement, single-baseline (dual-antenna) measurement, and multi-baseline measurement [51, 52], as shown in Figure 4.

As shown in Figure 4A, single-antenna attitude measurement refers to an unmanned aerial vehicle (UAV) equipped with a single satellite navigation receiver antenna. The single antenna primarily relies on received signal strength for measurement, which has low precision. Multi-antenna attitude measurement refers to a UAV using two or more satellite navigation receiver antennas. Due to the size constraints of the UAV, the baseline length formed by the receiving antennas is generally less than 1 meter, belonging to the short-baseline category, which is different from the medium to long-baseline types formed by antenna arrangements on vehicles, where lengths typically range from 1.5 to 2 m [40]. The dual antenna constitutes a single baseline, as depicted in Figure 4B, which can only obtain limited attitude angle information [41], while three or more antennas form multiple baselines in Figure 4C. Table 2 lists the GNSS based attitude determination methods divided by the number of antennas or baselines, the principles and characteristics of each method, and typical application scenarios.

In Table 2, it can be observed that while single-antenna measurement is simple to deploy and has the lowest cost, it relies on signal strength and thus has low and unreliable accuracy, especially considering the inherently low power of navigation signals upon ground reception. Multi-baseline measurement can provide redundant information and obtain complete attitude angle data, but it requires a larger number of antennas, leading to higher hardware costs [53]. For low-cost RUAVs, which already equipped with gyroscopes and other inertial navigation devices, dual-antenna systems although not providing complete attitude angle information, can be integrated with inertial navigation devices, achieving complete information acquisition while balancing hardware costs and information retrieval capabilities. Additionally, dual-antenna systems can implement RTK, enabling precise positioning of UAVs [54]. Therefore, current RUAVs primarily carry dual antennas for positioning and attitude determination under short-baseline conditions.

Regarding the selection of the observation model, since the precision of carrier phase observation is more than two orders of magnitude higher than that of pseudo-range observation, carrier phase differential methods are commonly used for attitude determination [55]. For the short baseline measurement of UAVs, the use of carrier phase differential technology can largely eliminate satellite and receiver clock differences and mitigate the propagation delays caused by the ionosphere and troposphere.

The carrier observation equation of the receiver for the satellite is shown in Equation 5

$$\varphi_u^i = \rho_u^i + c\delta t_u - c\delta t^i - I_u^i + T_u^i - \lambda N_u^i + \varepsilon_u^i \tag{5}$$

Where $\varphi_u^i$ is the carrier phase observation value of the receiver $u$ for the satellite $i$; $\rho_u^i$ is the pseudo-range observation value from the receiver $u$ to the satellite $i$; $\delta t_u$ is the clock error of the receiver $u$ with $c$ being the speed of light; $\delta t^i$ is the clock error of the satellite $i$; $I_u^i$ is the ionospheric delay along the propagation path; $T_u^i$ is the tropospheric delay along the propagation path; $N_u^i$ is the integer ambiguity in the phase observation, representing the unknown number of whole cycles; $\varepsilon_u^i$ is the sum of all other errors in the observation.

The carrier phase differential method, based on the number of receivers and observed satellites, as shown in Figure 4, can be

TABLE 2 GNSS attitude determination model.

| Measurement basis | | Measurement basis | Features | Applicable scenarios |
|---|---|---|---|---|
| Single antenna | | Derive the direction and angle of acceleration from the signal strength | Lower accuracy, simple layout | Spacecraft system |
| Multiple Antennas | Single Baseline | Reflect the change in attitude angle by the change in the position of the baseline vector | Failed to obtain full attitude angle | Small-sized aircraft |
| | Multiple Baselines | | Measure complete attitude angles | Large-sized aircraft |

divided into single difference (SD), double difference (DD), and triple difference (TD), which can eliminate satellite clock differences, receiver clock differences, and integer ambiguities [56, 57].

In the three differential observation schematics shown in Figure 5, SD involves taking the difference between measurements of the same satellite by two receivers at the same observation time [58]. DD makes difference between two receivers for single difference observation of different satellites; TD involves differencing the double differences at two different times. Table 3 shows mathematical model of the common differential methods, which illustrates the observation equations, main error terms, ambiguities, and differential observation noise corresponding to the three types of differential methods [21].

Where, $\varphi_{ur}^{i}$ represents the difference between the carrier phase measurements of receiver *u* to satellite *i* and receiver *r* to satellite *i*; $\rho_{ur}^{i}$ represents the difference between the pseudo-range measurements of receiver *u* to satellite *i* and receiver *r* to satellite *i*; $\delta t_{ur}$ represents the difference in clock biases between receiver *u* and receiver *r*; $I_{ur}^{i}$ represents the difference in ionospheric errors between receiver *u* and receiver *r* receiving signals from satellite *i*; $T_{ur}^{i}$ represents the difference in tropospheric errors between receiver *u* and receiver *r* receiving signals from satellite *i*; $N_{ur}^{i}$ represents the difference in integer ambiguities between receiver *u* and receiver *r* relative to satellite *i*, and $\varepsilon_{ur}^{i}$ represents the difference in observation noise between receiver *u* and receiver *r* relative to satellite *i*; $\varphi_{ur}^{ij}$, $\rho_{ur}^{ij}$, $I_{ur}^{ij}$, $T_{ur}^{ij}$, $N_{ur}^{ij}$, $\varepsilon_{ur}^{ij}$ represent the differences in single-differences of the corresponding observations from receiver *u* and receiver *r* relative to satellite *i* and satellite *j*; $\Delta\varphi_{ur,n}^{ij}$, $\Delta\rho_{ur,n}^{ij}$, $\Delta I_{ur,n}^{ij}$, $\Delta T_{ur,n}^{ij}$, $\Delta\varepsilon_{ur,n}^{ij}$ represent the differences in double-differences of the corresponding observations from receiver *u* and receiver *r* relative to satellite *i* and satellite *j* at the $n+1$-th epoch and the *n*-th epoch.

From Table 3, it can be observed that SD completely eliminates satellite clock errors and approximately eliminates ionospheric and tropospheric delays when the two receivers are in close proximity. However, after single-differencing, receiver clock biases $\delta t_{ur}$, integer ambiguities $N_{ur}^{i}$, and phase observation noise $\varepsilon_{ur}^{i}$ still persist, even increasing to the original $\varepsilon_{u}^{i}$ $\sqrt{2}$ times. DD further eliminates receiver clock errors and reduces ionospheric and tropospheric delays, but integer ambiguities still exist, and the phase observation noise is doubled. TD not only eliminates satellite and receiver clock errors but also the integer ambiguities, but the phase observation noise is increased to the original $\varepsilon_{u}^{i}$ $2\sqrt{2}$ times.

As it is shown, although each time of differencing can further reduce the clock bias and other errors, the root mean square of the measurement noise will also increase to the $\sqrt{2}$ times the original, which is about 0.05 of the carrier for L1, that is, 1 cm [21]. Therefore double difference measurements are the most common observation method. Because it can both reduce certain errors and avoid excessively large measurement variance, and only needs to solve for the carrier integer ambiguity.

## 3.3 Analysis of influence factors of attitude determination

Based on the content of the previous two sections, attitude determination using satellite navigation involves coordinate transformations and the solution of navigation signal observations. From Equations 1, 4, it can be seen that to solve for the attitude angles, the essence is to solve for the baseline vector. Since the UAV's receiving antennas form a short baseline, the ionospheric delay errors and tropospheric delay errors have already been differentially eliminated in the single-difference process. The observation equations shown in Table 3 are then converted to be represented by the baseline vector, as shown in Table 4.

Where $\boldsymbol{I}_{r}^{i}$ indicates the observation direction of the receiver *r* to the satellite *i*; $\boldsymbol{I}_{r}^{j}$ indicates the observation direction of the receiver *r* to the satellite *j*; $\Delta\boldsymbol{I}_{r,n}^{i}$ indicates the difference between the direction of observation of satellite *i* by receiver *u* at *n*-th epoch and the direction of observation at $n+1$-th epoch; and $\Delta\boldsymbol{I}_{r,n}^{j}$ indicates the difference between the direction of observation of satellite *j* by receiver *u* at *n*-th epoch and the direction of observation at $n+1$-th epoch.

In the attitude determination of RUAVs, as discussed in the previous sections, attitude solutions can be divided into observation solutions and coordinate solutions. When using carrier phase observations for solving, the choice of observation method will affect the factors influencing the baseline vector solution process differently. SD observations are affected by receiver clock biases, integer ambiguities, and observation noise; DD observations are affected by integer ambiguities and observation noise; TD observations are only affected by observation noise. Receiver clock biases can cause phase misalignment, integer ambiguities can lead to errors in the distance measurement between the receiver and the satellite, directly affecting the reliability of the baseline vector; observation noise affects the accuracy of the baseline vector.

In coordinate calculation, it can be observed that the coordinate transformation in Equation 1 requires the longitude and latitude obtained from the receiver's positioning solution, meaning that the accuracy of positioning affects the accuracy of the baseline coordinate transformation. Additionally, in Table 4, the direction of the receiver's observations to the satellites also affects the accuracy

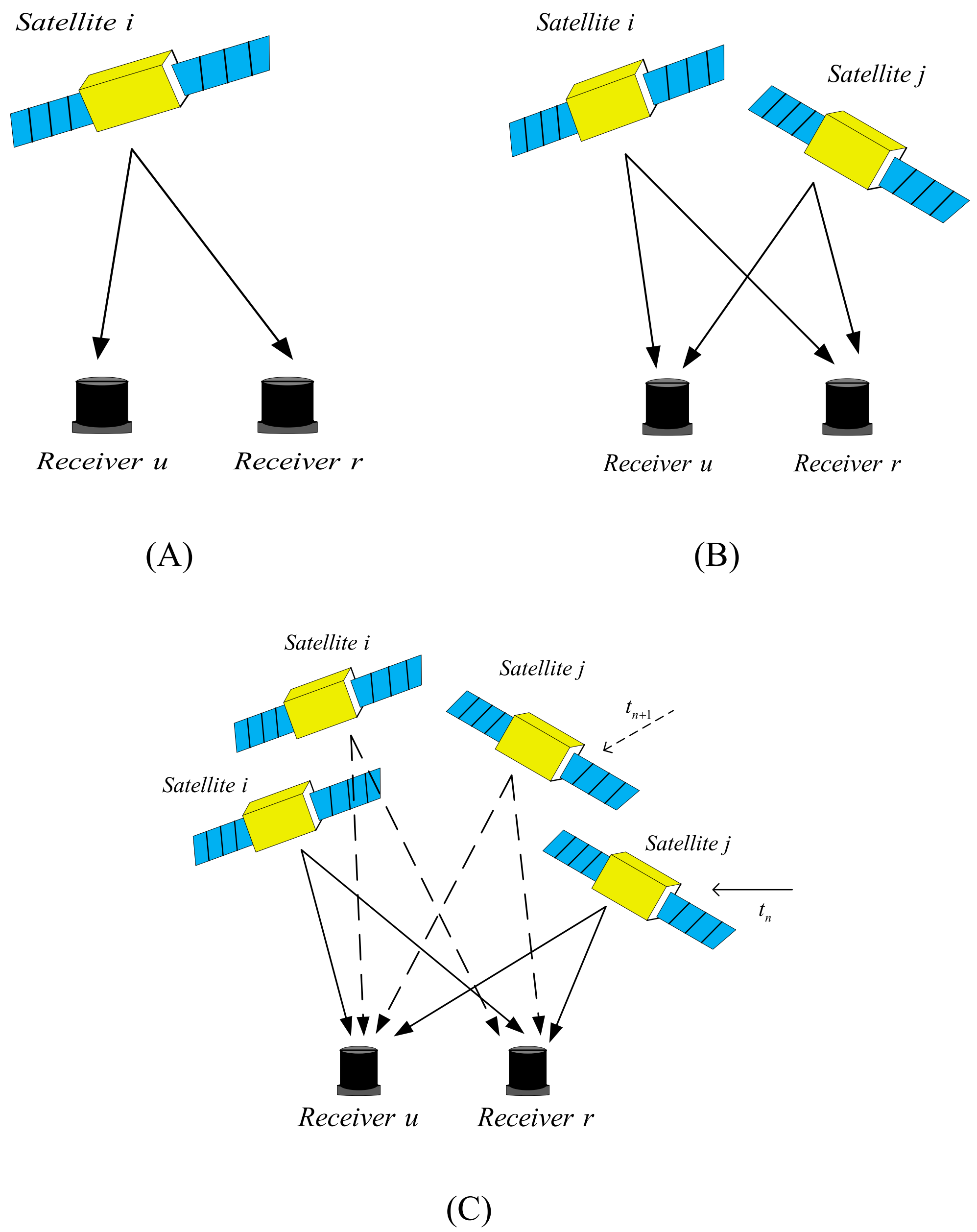

FIGURE 5
Schematic diagram of three differential observations. **(A)** Single difference observation. **(B)** Double difference observation. **(C)** Triple difference observation.

TABLE 3 Common differential methods.

| Differential observation | Equation | Error | Ambiguity $N_r^i$ | Observation noise |
|---|---|---|---|---|
| Single differenced | $\varphi_{ur}^i = \rho_{ur}^i + c\delta t_{ur} - I_{ur}^i + T_{ur}^i - \lambda N_{ur}^i + \varepsilon_{ur}^i$ | $\delta t_r$ | ✓ | $\sqrt{2}\sigma_\varphi$ |
| Double differenced | $\varphi_{ur}^{ij} = \rho_{ur}^{ij} - I_{ur}^{ij} + T_{ur}^{ij} - \lambda N_{ur}^{ij} + \varepsilon_{ur}^{ij}$ | – | ✓ | $2\sigma_\varphi$ |
| Triple difference | $\Delta\varphi_{ur,n}^{ij} = \Delta\rho_{ur,n}^{ij} - \Delta I_{ur,n}^{ij} + \Delta T_{ur,n}^{ij} + \Delta\varepsilon_{ur,n}^{ij}$ | – | – | $2\sqrt{2}\sigma_\varphi$ |

TABLE 4 Observation equation expressed by baseline.

| Differential observation | Equation |
|---|---|
| Single differenced | $\varphi_{ur}^{i} = -\boldsymbol{I}_r^i \cdot \boldsymbol{x}_{ur} + c\delta t_{ur} - \lambda N_{ur}^i + \varepsilon_{ur}^i$ |
| Double differenced | $\varphi_{ur}^{ij} = -\left(\boldsymbol{I}_r^i - \boldsymbol{I}_r^j\right) \cdot \boldsymbol{x}_{ur} + \lambda N_{ur}^{ij} + \boldsymbol{\varepsilon}_{ur}^{ij}$ |
| Triple differenced | $\Delta\varphi_{ur,n}^{ij} = -\Delta\left(\boldsymbol{I}_{r,n}^i - \boldsymbol{I}_{r,n}^j\right) \cdot \boldsymbol{x}_{ur} + \Delta\boldsymbol{\varepsilon}_{ur,n}^{ij}$ |

of the baseline vector solution. Furthermore, since it is necessary to solve the rotation matrix in Equation 4, when using Euler angles, singularity issues arise during high-dynamic complex motions of the UAV, making solutions unattainable. In such cases, quaternions must be used for representation, but this increases computational complexity. Therefore, the method of attitude representation also affects the solution of attitude angles [59].

The redundancy of baselines also affects measurement accuracy. When the number of baselines increases, the amount of observational information increases, which enhances the precision of baseline solutions. Additionally, redundancy is beneficial for adding prior constraints to the baselines, which in turn improves the success rate of ambiguity resolution, thereby affecting the precision of baseline measurements.

Since satellite navigation measurements rely on signals emitted by satellites in space, the geometric configuration of the satellite constellation also affects observation accuracy [60]; moreover, due to the inherent vulnerability of satellite navigation, when a UAV encounters navigation interference, it cannot receive navigation signals, and thus cannot measure the carrier phase, which means it cannot complete baseline solutions [61].

## 4 Key technologies for GNSS-Based UAV attitude measurement

Figure 6 illustrates the common solution steps for attitude determination of UAVs using the GNSS system. According to the fixed method of ambiguity, it can be divided into solution based on location domain and solution based on observation domain. When necessary, attitude determination should also be combined with an inertial navigation system.

The positioning domain solution requires the fixing of integer ambiguities first to obtain accurate baseline vectors, and then to determine the attitude angles, which is straightforward to implement, and obtaining accurate baseline vectors is a prerequisite for obtaining high-accuracy attitude angles. The accuracy of the baseline vectors directly determines the precision of the attitude angle solution [62], while the baseline vector accuracy, in turn, depends heavily on the accuracy with the fixed ambiguity [63]. This method solves sequentially and ignores the correlation between each baseline, reducing the redundancy of the attitude solution, especially when the integer ambiguities are difficult to fix successfully, leading to the affection to the determining performance. The observation domain solution solves for the integer ambiguities and the attitude angles simultaneously [64]. It is more complex to implement, although it can solve the integer ambiguities and attitude angles simultaneously, it ignores the correlation between ambiguity resolution and attitude calculation, which can also affect the reliability of the attitude [65].

Whether it is a positioning domain or observation domain solution, the key lies in the solution of integer ambiguities and the attitude calculation algorithm. The determination of integer ambiguities is essential to ensure the accuracy of the baseline vector position solution for UAVs. Given the limited number and length of baselines on RUAVs, the search space for integer ambiguities is large, leading to low search efficiency. The search space is also constrained by the length of the baselines. Therefore, how to achieve fast and effective fixing of ambiguities under the constraints of the UAV's own conditions is one of the important issues in the attitude determination of RUAVs.

Attitude determination algorithms, after obtaining observational values, use these values to calculate the attitude angle information. The accuracy of the determined attitude angles is often affected by the inherent accuracy of the observational values and observational noise. How to improve the calculation accuracy is also a key issue in attitude determination.

Furthermore, for low-cost RUAVs, dual antennas and low-cost inertial navigation devices are commonly used to achieve the integrity of attitude determination. This not only assists in determining integer ambiguities in GNSS observation solutions but also allows the INS to continue navigation when GNSS fails. The error accumulation phenomenon in the inertial navigation system can also be periodically corrected by GNSS measurement values [66]. In integrated navigation, data fusion processing is crucial. Rotary-wing UAVs are highly dynamic, inertial navigation devices have large measurement noise, and the precision of output measurement values is low. Moreover, the update rate of satellite navigation measurement values is much lower than that of inertial navigation. How to fuse measurement values of different rates is also a key issue that needs to be addressed. A high success rate of ambiguity fixing and efficient attitude calculation are necessary conditions for obtaining real-time high-precision attitude angles [67].

### 4.1 Integer ambiguity resolution algorithms

The challenge of fixing integer ambiguities lies in the planning of the search space. While reducing the search space and improving search efficiency, it is essential to ensure the correctness of the ambiguity fixing. Faced with the continuous change of the UAV's spatial position between epochs, a robust On The Fly (OTF) integer ambiguity determination algorithm is required. Based on different ambiguity search spaces, they can be categorized into observation domain-based, coordinate domain-based, and ambiguity domain-based ambiguity resolution [68], with common integer ambiguity resolution methods shown in Table 5.

Table 5 shows that among the three types of integer ambiguity resolution, the observation domain-based method is the simplest to implement. It relies on the linear combination of carrier frequencies of different wavelengths to obtain a shorter wavelength, thereby reducing the ambiguity fixing error. The TCAR method, based on wide and narrow lanes, uses pseudo-range to assist in ambiguity determination. Since there is no ambiguity search problem, the

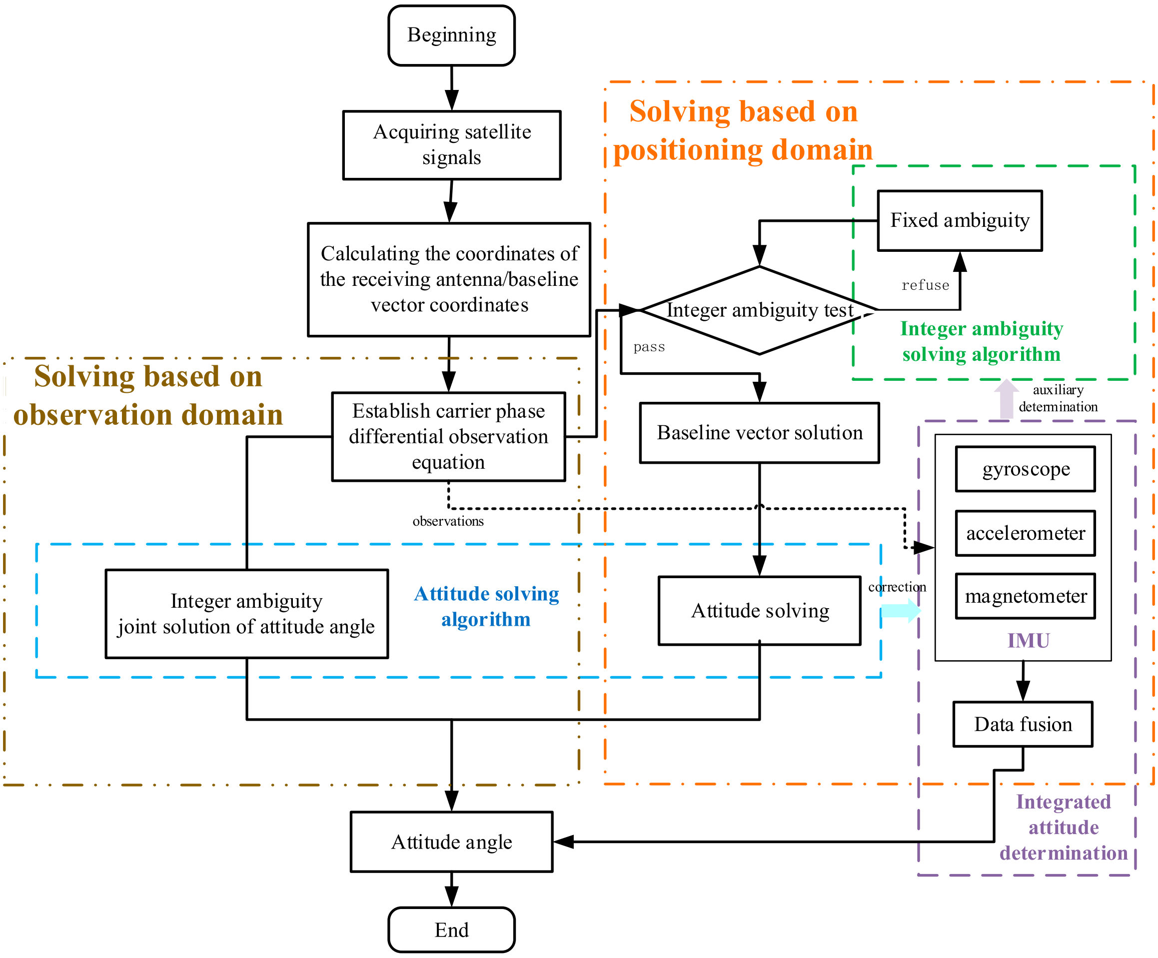

FIGURE 6
Drone attitude solution flowchart.

TABLE 5 Common algorithms for solving integer ambiguity.

| Classification | Typical algorithm | Features |
|---|---|---|
| Based on observation domain | Combinatorial Solution for Broad-Narrow Lane Configuration [21] | Improving stability while enhancing resolution, but the large wavelength variation is not conducive to real-time processing |
| | Three-carrier Ambiguity Resolution (TCAR) [69, 70] | Incrementally fixing the variables allows for a rapid resolution of ambiguities, which enhances the real-time performance |
| Based on positioning domain | Ambiguity function method (AFM) [71] | Insensitive to cycle slips, yet the search time is prolonged and there is the issue of multiple peak values |
| Based on the fuzzy domain | Least-squares ambiguity decorrelation adjustment (LAMBDA) [72] | Strong applicability, determination can be made with short time series |

calculation speed is fast. However, in a dynamic environment, the measurement accuracy decreases due to the influence of receiver performance and observation conditions [69]. Auxiliary information can be used to improve the calculation accuracy in a high-dynamic environment, such as the geometry-free and ionospheric-free TCAR (GIF-TCAR) [70] and the TCAR method assisted by INS (iTCAR) [71].

The positioning domain-based solution method first obtains the initial coordinate position, constructs an ambiguity function around the initial coordinate position, and traverses the global space to get the optimal estimate of the ambiguity function. In response to the long search time and multi-peak problem of AFM, there are also different solutions. For example, Han [73] uses multi-frequency combinations to determine the search step in AFM, reducing the search time; Zhao [74] uses multi-baseline constraints to solve the multi-peak problem of AFM; Wang [75] proposes the AFM under the initial pitch angle constraint (Pitch-constrained Ambiguity Function Method, PCAFM), which can reduce the search range but is very sensitive to the search step size. Since it takes the positioning coordinates as the search basis, the accuracy of the final fixed integer ambiguity is largely limited by the initial positioning accuracy.

The ambiguity domain-based solution is a more commonly used method in practice. The LAMBDA method proposed by Professor Teunissen [76] is the most widely used and effective method in engineering practice. It can solve the integer ambiguity in observation methods such as single-frequency, dual-frequency, non-differential, and single-dual differences. By continuously observing over a short period, the ambiguity can be fixed [77, 78]. The core of the algorithm is based on the Integer Least-Squares principle (ILS) shown in Equation 6 [79]. The integer solution of the ambiguity is the integer least-squares solution of Equation 7. By using the Z-transform in Equation 8, the search space is decorrelated, and finally, a sequential search method is used to obtain the integer solution, and then the inverse transformation is used to obtain the expected solution [72].

$$\min_{a,b} \|y - Aa - Bb\|^2_{Q_y} \text{ with } a \in \mathbb{Z}^n, b \in \mathbb{R}^3 \tag{6}$$

$$\min_{a \in Z^n} (a - \hat{a})^T Q_{\hat{a}}^{-1} (a - \hat{a}) \tag{7}$$

$$z = Z^T a, \quad \hat{z} = Z^T \hat{a}, \quad Q_{\hat{z}} = Z^T Q_{\hat{a}} Z \text{ with } Z \in \mathbb{Z}^{n\times n} \tag{8}$$

Where $y$ represents the phase observations; $a$ denotes the float solution of the ambiguities, $b$ denote the baseline vector; $\|\cdot\|^2_{Q_y} = (\cdot)^* Q_y^{-1}(\cdot)$; $Q_y$ is the covariance matrix of the carrier phase observations; $\mathbb{Z}^n$ represents the n-dimensional integer space; $\mathbb{R}^n$ denotes the n-dimensional real number space; $\hat{a}$ is the expected integer solution to be obtained; $Q_{\hat{a}}$ is the covariance matrix of $\hat{a}$; $Z^{n\times n}$ is the transformation matrix for the n-dimensional space; $\hat{z}$ and $z$ are the transformed integer solution and float solution obtained from the search, respectively.

The traditional LAMBDA algorithm has high computational complexity and wastes a lot of time during the variance reordering process. The generated search space is inappropriate, leading to low search efficiency, and it cannot utilize the known prior conditions of the baseline to reduce the search space. To address the shortcomings of the traditional LAMBDA algorithm, many scholars have proposed improvements in the decorrelation processing of the covariance matrix, the determination of the integer solution search space, and the search method for the integer solution in the general LAMBDA algorithm. This has led to the evolution of various improved LAMBDA algorithms, continuously enhancing the search efficiency and fixing success rate of the integer ambiguities, as shown in Table 6.

In Table 6, introducing constraint conditions is the main direction for the improvement of the LAMBDA method. Especially when the floating-point solution and the covariance matrix are not accurate enough, constraint conditions can improve the search efficiency and the success rate of fixing [81]. Common constraint methods include baseline constraints [82], triangular constraints [83], affine constraints [84], and so on. Teunissen used the LAMBDA method with constraint conditions to calculate the integer ambiguities and verified the advantages of the algorithm in terms of calculation stability and success rate through on-board dynamic experiments [85]. Shao [86] combines the M-LAMBDA algorithm with the C-LAMBDA algorithm, improving the success rate while reducing computational complexity and ensuring computational efficiency.

In response to the challenge of ambiguity fixing in low satellite visibility environments, there has been considerable research. Chen [87] adopts a spherical constraint on the ambiguity space to improve the success rate of integer ambiguity fixing, while also employing a joint search strategy in both the coordinate domain and ambiguity domain to achieve attitude determination under low satellite visibility. Giorgi [88] proposes an attitude solution method based on multivariate constraints in the observation domain (multivariate-constrained LAMBDA, MC-LAMBDA), which is not limited by the number of antennas, GNSS system combination methods, or kinematic prior information, and can solve for integer ambiguities and attitude angles simultaneously, significantly improving the success rate of ambiguity fixing. However, due to the consideration of multiple constraint conditions, the computational complexity increases. Liu [89] and Douik [90] improve MC-LAMBDA by using Riemannian optimization to solve nonlinear least squares constraints, reducing computational complexity while ensuring the reliability of ambiguities and the accuracy of attitude.

## 4.2 Attitude determination algorithms

The attitude determination algorithms are another significant factor affecting the accuracy of attitude angles. The challenge in calculation lies in achieving a solution with low time complexity while ensuring the accuracy of the solution. Additionally, for scenarios with multiple baselines, how to utilize redundant information to enhance the calculation accuracy is also a hot topic commonly researched by scholars.

Table 7 presents several common attitude determination algorithms. The TRIAD algorithm directly solves for the attitude angles based on the observation matrix without the need for iterative optimization, making it simple to implement with low computational complexity. However, it is limited by the baseline layout, cannot utilize redundant information, and thus has lower solution accuracy.

The least squares method solves for the attitude angles or attitude matrix using the classical principle of least squares. It is computationally efficient and can accurately approximate actual data. The least squares method can significantly improve the accuracy of the heading angle, but its improvement on the pitch and roll angles is not significant [94]. Liu [95] uses antenna arrays and the integer property of ambiguities to constrain the least squares solution, allowing for direct calculation of attitude angles, especially in challenging environments with single-system, single-frequency, and single-epoch conditions, further enhancing computational efficiency. Due to the constant state vector, the least squares method

TABLE 6 Least-squares ambiguity decorrelation adjustment.

| Algorithm | Principles | Algorithm features |
|---|---|---|
| Moddified-LAMBDA [80] | Introducing symmetric permutation and adopting greedy search strategy during covariance decomposition | Improved computational efficiency without affecting the success rate of fixing ambiguity |
| Constrained-LAMBDA [81] | Adjust the search space using constraint conditions | Improve the success rate of fuzzy search or enhance search efficiency |

TABLE 7 Common pose solving methods.

| Method | Representative algorithm | Features |
|---|---|---|
| Direct method | Triple vector attitude determination (TRIAD) [91] | Simple and fast, without prior conditions for baseline length, low accuracy |
| Least square method | Attitude matrix (attitude angle) least squares method; constraint least squares method | Good accuracy, high computational efficiency, and good precision in static positioning |
| Optimal estimation method | Quaternion estimation method [92]; rotation matrix method [93] | The calculation accuracy is good, but the time cost is high |

is suitable for static or low-dynamic attitude determination but performs poorly in high-dynamic conditions typical of UAVs.

The optimal estimation method transforms the attitude angle solution into a Wahba problem [96], taking into account the noise and uncertainty of the observational data, and adopts an iterative strategy to find the optimal solution or a non-iterative method to find a suboptimal solution. It establishes a cost function based on a large amount of observational data to achieve the estimation of attitude elements. Among them, the quaternion estimation (QUEST) algorithm, proposed by Shuster, uses quaternions to transform the process of solving the rotation matrix into the process of minimizing the cost function. This algorithm does not require initial values and is flexible in processing, but can only estimate the optimal value based on the current state. To address the limitations of the QUEST method, Bar-Itzha [97] proposed the REQUST algorithm, which uses historical state information for recursive solution, further improving the accuracy and robustness of the estimated values.

## 4.3 GNSS/INS integrated attitude determination

Utilizing GNSS for attitude determination can yield high-precision, cost-effective measurement outcomes. However, in complex environments where signals may be obstructed or interfered with, relying solely on the GNSS system for attitude determination becomes challenging. RUAVs, which are limited by the number of equipped antennas, use a two-antenna single-baseline setup allows for the measurement of only two attitude angles: the heading and pitch angles. Therefore, to ensure the integrity of the attitude determination system under various conditions and to obtain complete attitude information, multi-sensor fusion for attitude determination is an effective approach to achieving cost-effective and high-precision measurement [98].

As depicted in Figure 7, the combination of satellite navigation and inertial navigation for attitude determination leverages the inertial navigation system to assist the GNSS system, providing backup navigation for a short period during GNSS signal interruptions [99]. The Inertial Measurement Unit (IMU), which includes accelerometers and gyroscopes, provides raw measurement data [100]. The measurement values or states output by the GNSS component and the INS component are fused to varying degrees through a composite filter to jointly obtain the vehicle's attitude information. The IMU can detect the drone's attitude and balance status in real-time during flight and feedback to the control center, making up for the low rate of GNSS output measurement [101].

Integrated navigation is generally divided into three categories based on the degree of data fusion: loose integration, tight integration, and ultra-tight integration [102]. Loose integration fuses the output results of the GNSS system (position, velocity, attitude angles) with the output of the INS system, where the two systems work independently, making it simple to implement with good redundancy [103]. Tight integration fuses the GNSS observations such as pseudo-range and carrier phase with the state values of the INS system's gyroscopes and accelerometers, achieving better measurement accuracy under low signal-to-noise ratios [104]. Ultra-tight integration deeply integrates the GNSS receiver with the components of the INS system, starting the fusion from the satellite tracking loop [105], using the INS system information to adjust the GNSS tracking loop bandwidth, and improving the signal-to-noise ratio, which has superior calculation accuracy and robustness under interference conditions. The high cost of implementing ultra-tight integration does not meet the low-cost requirements of UAVs, so UAVs often adopt loose or tight integration of gyroscopes, accelerometers with the GNSS system.

The key to combination navigation is the data fusion model and the filtering update algorithm, which combines and smooths the output values of the two systems to reduce measurement errors. Common filtering fusion algorithms are shown in Table 8.

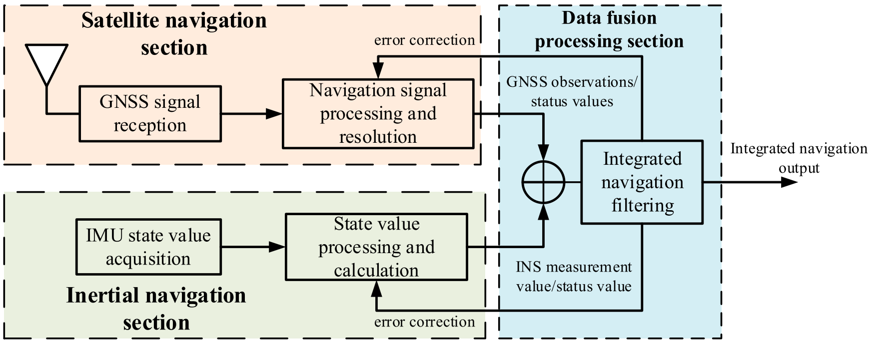

FIGURE 7
GPS/INS integrated navigation structure.

**TABLE 8** Typical filtering algorithm.

| Types | Principles | Advantages | Shortcomings |
|---|---|---|---|
| Kalman filter (KF) | Predicts the value of the next epoch based on the existing observations | Real time update state estimation;<br>Dynamic adjustment of parameters to adapt to system variation | Linear system model only;<br>Sensitive to initial state |
| Extended Kalman filter (EKF) | Nonlinear observation equation and state of the system | Simple algorithm implementation | Covariance tends to diverge under high nonlinearity;<br>Accuracy depends too much on initial error |
| Unscented Kalman filter (UKF) | Uses a selected set of minimum sample points to approximate the true model probability distribution | Accurately capture the statistical characteristics of nonlinear functions | Higher computational complexity;<br>Highly sensitive to noise, and the generation of sigma points may introduce additional noise |
| Particle filter (PF) | Use weighted random samples to statistically calculate the posterior probability | Applicable to nonlinear and non Gaussian problems | Particle degradation |
| Complementary filter (CF) | Weighted average of different sensor data | Balance short-term noise and long-term drift | High requirements for rationality of weight factor |

As shown in Table 8, the KF is an optimal regression data processing method that reasonably and has been applied in various fields such as multi-system data processing and fusion, space orbit prediction, and wireless positioning [106, 107]. However, the Kalman filter is only suitable for linear systems. To apply it to the baseline solution of GNSS nonlinear observation equations, the Kalman filter needs to be improved, resulting in the Extended Kalman Filter (EKF) [108], Unscented Kalman Filtering (UKF) [109], Particle Filter (PF) [110], Complementary Kalman Filter (CKF) [111], and so on. The Extended Kalman Filter (EKF) is the simplest to implement, but its accuracy depends on the initial error and the degree of approximation to the true model [112]. The Unscented Kalman Filter (UKF) uses a set of sigma points to approximate the true model, while the Particle Filter (PF) weights these sampling points to further enhance accuracy and eliminate the impact of multipath errors in the signal [110]. However, the Particle Filter suffers from the problem of particle degradation, and it is common to combine the Particle Filter with other types of nonlinear Kalman filters to improve particle distribution [112–114]. Complementary filtering can leverage the short-term accuracy of the gyroscope and the long-term stability of the accelerometer to achieve accurate attitude estimation.

The filtering algorithm in integrated navigation can effectively reduce the data error of attitude measurement between different sensors, reduce the impact of measurement noise on the final measured value, and use different sensor data to complement each other to improve the accuracy and reliability of attitude angle. Jwo [25] uses EKF for filtering the attitude estimation represented by quaternions, which can eliminate the noise of the quaternion itself and improve the attitude accuracy. The baseline can also be used to assist the Kalman filter using high-precision baseline prior length information to constrain the Kalman filter iteration process, thereby improving accuracy and robustness [115],. Dong [116] uses sequential adaptive Unscented Kalman filtering, estimating the measurement noise covariance matrix of the heading angle change in real-time, mitigating the problem of drastic noise changes in integrated attitude determination caused by object movement, and providing a stable and accurate heading angle.

In the loose or tight integration navigation of RUAV, different filtering algorithms are used to achieve different degrees of data fusion to obtain reliable and accurate attitude angle For loose integration, Ding [117] constructs an Error State Kalman (ESKF) filter, fusing inertial navigation sensors and GNSS data, continuously integrating the gyroscopic measured angular rate to propagate attitude, and compensating for cumulative errors through measurement updates, achieving combined attitude determination of MEMS systems and low-cost GNSS receivers. For tight integration, Wang [101] combines dual-antenna GNSS and MEMS, verifying that the inertial navigation device can stably measure the heading angle under brief GNSS signal loss. Yan [118] uses dual-rate filtering based on EKF, fusing high-rate high-noise observations and low-rate low-noise observations into an optimal estimation system, achieving real-time attitude determination in complex noise environments.

In addition to filtering out noise through combination, combined navigation attitude determination also helps to fix the integer ambiguity. Xiao [119] proposes a three-frequency differential GNSS/INS tight integration, using three-frequency solutions to improve the speed of measurement values and integer ambiguity fixing, and using tight integration to weaken the impact of TCAR algorithm instability on the results. Gao [120] proposes a new tight integration GNSS/MEMS model, using a single filter to achieve optimal estimation of attitude drift, gyro zero bias, and ambiguity, effectively improving the ambiguity fixing rate and reducing attitude error compared to a single GNSS system.

The integration of satellite navigation and inertial navigation can combine the advantages of the two systems to achieve complementary performance. The high-precision measurement values provided by the satellite navigation system help to reduce the cumulative error of the inertial navigation system, while the inertial navigation system does not require external signal input and can act as a backup navigation in the event of GNSS signal occlusion or interference, taking over the navigation task for a short period [121, 122].

# 5 Challenges

## 5.1 Real-time attitude determination under high dynamics

Currently, the use of GNSS for attitude determination is often aimed at the attitude determination of vehicle platforms, where the main change in the vehicle's attitude angles is in the heading angle, and the change is relatively slow. In contrast, rotary-wing UAVs have high dynamics, and during complex motion processes, multiple attitude angles change within a short period of time. Existing research is better for the attitude determination of vehicles or low-dynamic aircraft, but there is less research on the high dynamics of rotary-wing UAVs. However, the attitude determination of UAVs under high dynamics is crucial, as only by accurately grasping the real-time motion state of the UAV can the safe execution of tasks be ensured.

The high-dynamic flight of UAVs will lead to rapid changes in the baseline vectors formed by the receiving machinery, posing certain difficulties for baseline calculation. Since the premise of accurate baseline calculation is the determination of integer ambiguities, most existing ambiguity determination methods rely on searching in the ambiguity domain. Under high dynamics, the ambiguity space range is large, so how to constrain the ambiguity space, reduce the size of the search space, and thereby improve the fixing rate is a challenge [123]. The relatively effective MC-LAMBDA method, described in Section 4.1, can effectively reduce the search space by relying on multiple variables for constraints, but due to the consideration of multiple constraint conditions at the same time, it leads to increased algorithm complexity and to some extent, reduced search efficiency. Therefore, how to consider the accuracy of baseline calculation under high dynamics, especially the rapid determination of integer ambiguities under high dynamics, is a current major challenge.

High-precision attitude determination under high dynamics requires not only the method of solution but also the reliability of the solution results. Since the fixing of integer ambiguities is a key link affecting attitude determination, existing inspection methods mainly inspect the accuracy and stability of ambiguity fixing, thereby reflecting the reliability of attitude determination. Commonly used methods are based on positioning domain judgment, and under the premise of baseline constraints, the selected judgment threshold is largely related to the length of the baseline [124, 125]. For the attitude determination of RUAVs with short baselines, the requirements for the judgment threshold may be more stringent. Therefore, whether a method for attitude determination integrity inspection suitable for UAVs with short baseline systems can be developed, which can make judgments on attitude determination integrity without the need for prior conditions of baseline length, or relying on a small amount of baseline redundancy information, is a challenge.

## 5.2 Effective response to navigation interferences

Using GNSS signals for UAV attitude determination often faces the issue of navigation interference, where jamming and spoofing are the most common types of satellite navigation interference. The integrity of navigation services determines whether the UAV can work properly [126]. Especially for UAVs that require high-precision positioning and attitude determination equipment, once they encounter navigation interference, as depicted in Section 3.3, they will obtain incorrect position and attitude information, lose control of the UAV's motion state, and thus affect its operational effectiveness.

Jamming interference is low-cost, reliable, easy to implement, has a wide coverage range, and is widely used in various scenarios. A 1W jamming interference source can interfere with the maximum distance of about 16.96 km under ideal conditions [42]. Although the probability of successful implementation of jamming interference has been reduced with the application of frequency domain filtering technology, anti-jamming antenna technology, pseudo-satellite technology, and integrated navigation, etc., for small aircraft such as rotary-wing UAVs, it is still difficult to effectively resist jamming interference without external assistance. Although small inertial navigation devices can be equipped to take over the satellite navigation equipment and continue navigation in the face of interference, due to the serious accumulation of errors and low accuracy of small inertial navigation devices, the overall system navigation error increases without the error correction of the satellite navigation system, which still reduces the operational effectiveness of the UAV.

Compared to jamming interference, spoofing interference is characterized by its strong concealment, high threat, and low cost, and can deceive the UAV into flying along a specified trajectory [127]. With a low-cost spoofing device, a certain spoofing effect can be achieved [128, 129]. Generally, when the deceptive signal power is 3dB higher than the real signal power, the jammer can be deceived. The interferer fuses and calculates high-precision spoofing signals based on the UAV's position, speed, and other status information, making the spoofing signals highly similar to the real signals, thereby completing covert deception [130]. Especially for UAVs using public service navigation signals, due to the openness of the signal system and the use of less encryption and authentication, they are more susceptible to spoofing [131]. From random position spoofing [132], fixed-point position spoofing [133], delayed message spoofing [134], to state estimation value spoofing [135], different types of spoofing interference can severely affect the normal flight of UAVs. The implementation approaches also vary, such as adding interference to the receiver's phase-locked loop [136], and gradually guiding with trajectories of different Doppler shifts and delays [137], etc.

Addressing the diverse and complex satellite navigation interference methods of today, designing anti-satellite navigation interference systems suitable for rotary-wing UAVs is an urgent problem that needs to be solved. When facing jamming interference, the challenge is to ensure the normal operation of the UAV navigation receiver and to mitigate the effects of jamming signals. When facing spoofing interference, the system should be able to autonomously and effectively detect spoofing according to the abnormal receiving phenomena without adding extra weight or hardware requirements to the UAV. Compared with the mature deception detection without too many hardware requirements, the existing UAV is more difficult to suppress the suppression interference. Improving the survival rate of UAV under suppression jamming is the key problem to be solved. Existing anti-jamming methods often employ array antennas, but these can introduce significant phase pattern changes that affect the quality of observations [138]. Moreover, array antennas can only counteract interference from a limited number of directions, and their anti-jamming performance is limited in complex environments with multi-directional interference. At the same time, the use of array antenna will increase the hardware overhead and load. Therefore, achieving low-cost navigation anti-jamming in complex environments while ensuring the UAV's positioning and attitude determination is a significant challenge for rotary-wing UAVs.

## 5.3 Intelligent response to Multi-GNSS system integration

The current GNSS systems have been developed and refined, with each navigation system capable of independently performing positioning, navigation, and timing tasks. Utilizing multi-system GNSS can significantly increase the number of observable satellites, improve the geometric configuration of the satellite constellation, as depicted in Section 3.3, reduce reception costs, and obtain higher quality observational data, thereby enhancing measurement accuracy. Especially in challenging environments where satellite access is limited, when one system fails or is unavailable, another system can provide operational redundancy [139].

FIGURE 8
Beidou Satellite Communication System's receiving antennas specially used for small unmanned aerial vehicle. **(A)** HX-CH3602A. **(B)** HX-CH5601A.

Due to the low cost of current navigation equipment, multiple satellite navigation systems can be implemented on small-sized devices. As shown in Figure 8, the HX-CH3602A and HX-CH6601A from Beidou Xingtong are two receiver antennas specifically designed for small UAVs. They can respectively achieve triple-system tri-frequency reception for GPS L1, BDS B1, and GLONASS L1, and triple-system six-frequency reception for GPS L1/L2, GLONASS L1/L2, and BDS B1/B2.

The current attitude determination using multi-system GNSS is mainly focused on the combination of different systems on a single frequency. Teunissen [139] conducted simulation studies on the attitude determination of Galileo and GPS single-frequency combined data, obtaining relatively stable expected results, which verified the ability to use backup satellite data for instantaneous attitude determination in a disturbed environment. Zamanpardaz [140, 141] compared and analyzed the Indian Regional Navigation Satellite System (IRNSS) and GPS Block IIF on the L5 frequency point. When the two systems were combined for attitude determination, the ambiguity dilution of precision (ADOP) was significantly improved, and both the integer ambiguity fixing success rate and attitude accuracy were significantly enhanced [142]. Zhao [143] confirmed the improvement in attitude determination performance when GPS/BDS/GALILEO were used in a tight combination, with the percentages of pitch error, yaw error, and roll error within 2° in a complex environment increasing by 6.1%, 8.07%, and 13.43%, respectively, and the ambiguity fixing rate increased by 14.78%. Shu [144] conducted attitude determination with the combination of GPS, BDS, Galileo, and GLONASS, confirming that the combined attitude determination can significantly improve attitude accuracy on a moving vehicle platform. Yang [145] propose GPS/BDS dual-antenna attitude determination model which obviously improve the fixing rates, such as 16.0% improved in the static experiment and 23.6% in dynamic experiment. Although the aforementioned research can enhance the attitude measurement performance by utilizing GNSS signals at the same frequency point, they did not focus on attitude determination using different frequency point signal combinations under multi-GNSS systems.

In addition, common jamming and spoofing interferences are usually targeted at a specific system within the GNSS, making it difficult to interfere with the entire GNSS system simultaneously. By leveraging the mutual backup among navigation systems, it is possible to continue navigation using another system when faced with interference targeting a particular satellite navigation system. Therefore, under the current conditions where GNSS systems are increasingly refined, how to better utilize multiple GNSS systems to complete integrated attitude determination, mutual integration, and backup to enhance attitude determination accuracy in complex environments and resist navigation interference is a challenge.

Several factors need to be considered, such as the performance comparison of different navigation systems in UAV positioning and attitude determination applications; the basis for selecting signal combinations from different navigation system frequency points; the selection of integer ambiguity fixing methods and attitude determination algorithms under multi-system GNSS integrated attitude determination; the ability of different navigation systems to counteract jamming and spoofing interference; ensuring the continuity and accuracy of positioning and attitude determination results during system switching, etc. Moreover, when performing integrated attitude determination with multiple GNSS systems, the issue of inter-system bias (ISB) between systems also needs to be addressed [139, 146].

## 6 Conclusion

The article primarily discusses the current state and challenges of attitude determination for rotary-wing UAVs based on the GNSS. Attitude information is a necessary condition for the safe flight of UAVs. The article focuses on three main aspects of UAV attitude determination: integer ambiguity resolution, attitude calculation, and integrated navigation. The determination of integer ambiguities is a key factor affecting the accuracy of UAV carrier phase differential measurements. Only by obtaining accurate and reliable ambiguities can the precise baseline be calculated, which in turn determines the attitude angles. While integer ambiguity resolution has been proven to be reliable and accurate when searching within the ambiguity domain constrained by baselines, further constraints are needed for the high-dynamic mobile carrier. The attitude calculation method requires further improvement in computational complexity to meet the real-time attitude acquisition requirements of UAVs. Integrated navigation is the current development trend for achieving low-cost attitude measurement, and the integration of data from integrated navigation is an important direction for research. Filtering different navigation systems' data to reduce the impact of observation noise on attitude calculation and enhance the performance of integrated navigation is essential.

At the same time, due to the vulnerability of satellite navigation, using GNSS for attitude measurement is susceptible to common navigation interferences. Once interference occurs, UAVs may lose directional control, posing a significant safety risk. Therefore, further research is needed to enhance the anti-interference capabilities of rotary-wing UAV navigation. Given that current GNSS systems have matured and various satellite navigation systems can be used for attitude measurement, integrating multiple systems could be a potential approach to improving anti-interference capabilities. This not only enhances the accuracy of UAV attitude measurement but also improves the UAV's ability to continue navigation when encountering interference.

## Author contributions

YZ: Investigation, Writing–original draft. ZL: Methodology, Writing–original draft. YX: Formal Analysis, Writing–original draft. BR: Methodology, Writing–original draft. YY: Supervision, Writing–original draft. SN: Validation, Visualization, Writing–original draft.

## Funding

The author(s) declare that financial support was received for the research, authorship, and/or publication of this article. (1) National Nature Science Foundation of China under Grant (U20A0193). (2) The science and technology innovation Program of Hunan Province (2021RC3073).

## Conflict of interest

Author YY was employed by Hunan Xinghe Electronics Co. LTD.

The remaining authors declare that the research was conducted in the absence of any commercial or financial relationships that could be construed as a potential conflict of interest.

## Publisher's note

## References

1. Sonugür G. A Review of quadrotor UAV: control and SLAM methodologies ranging from conventional to innovative approaches. *Robot Auton Syst* (2023) 161:104342. doi:10.1016/j.robot.2022.104342

2. Gupta L, Jain R, Vaszkun G. Survey of important issues in UAV communication networks. *IEEE Commun Surv Tutorials* (2016) 18(2):1123–52. doi:10.1109/comst.2015.2495297

3. Mozaffari M, Saad W, Bennis M, Nam YH, Debbah M. A tutorial on UAVs for wireless networks: applications, challenges, and open problems. *IEEE Commun Surv Tutorials* (2019) 21(3):2334–60. doi:10.1109/comst.2019.2902862

4. Xiaoqian T, Feicheng Z, Zhengbing T, Hongying W. Nonlinear extended kalman filter for attitude estimation of the fixed-wing UAV. *Int J Opt* (2022) 2022:1–9. doi:10.1155/2022/7883851

5. Fan HB, Guo JL, Luo GW. Application of drones in modern warfare. *Light Weapons* (2022) 9:32–4. doi:10.3969/j.issn.1000-8810.2022.09.007

6. Jin Y, Gu QX. Overview of foreign military UAV equipment technology development in 2023. *Tactical Missile Tech* (2024) 1:33–47. doi:10.16358/j.issn.1009-1300.20240501

7. Yu W, Hou XL. Analyzing the application of drone operations from the Nagorno-Karabakh conflict. *Ship Mar Elect Eng* (2022) 42(10):8–12. doi:10.3969/j.issn.1672-9730.2022.10.003

8. Su RC, Xiang WH, Miao GC, Wang D. Operational application and analysis of drones in the Nagorno-Karabakh Conflict. *Missile J* (2021) 1:65–70. doi:10.16338/j.issn.1009-1319.20200330

9. Liao KN. *Research on attitude calculation and control method of quadrotor unmanned aerial vehicle*. Mianyang: Southwest University of Science and Technology (2023). dissertation/master's thesis.

10. Leishman JG. Etienne oehmichen: scientist, engineer and helicopter pioneer. In: *AHS international 62nd annual forum proceedings vol3:vertical flight:leading through innovation* (2006).

11. Fan BK, Li Y, Zhang RY, Fu QQ. Review on the technological development and application of UAV systems. *Chin J Elect* (2020) 29(2):199–207. doi:10.1049/cje.2019.12.006

12. Hoffmann GM, Huang HM, Waslander SL, Tomlin CJ. Quadrotor helicopter flight dynamics and control: theory and experiment. In: *AIAA guidance, navigation, and control conference proceedings* (2007).

13. Hoffmann GM, Waslander SL, Vitus MP, Huang H, Gillula J, Pradeep V, et al. Stanford testbed of autonomous rotorcraft for multi-agent control. In: *2009 IEEE/RSJ international conference on intelligent robots and systems* (2009). p. 404–5.

14. DJI. Technical support for mavic air 2 (2024). Available from: https://www.dji.com/cn/support/product/mavic-air-2 (Accessed April 20, 2024).

15. Ebeid E, Skriver M, Jin J. A survey on open-source flight control platforms of unmanned aerial vehicle. In: *2017 euromicro conference on digital system design (DSD)* (2017). p. 396–402.

16. Cetinsaya B, Reiners D, Cruz-Neira C. From PID to swarms: a decade of advancements in drone control and path planning - a systematic review (2013–2023). *Swarm Evol Comput* (2024) 89:101626. doi:10.1016/j.swevo.2024.101626

17. Rezaee MR, Hamid NAWA, Hussin M, Zukarnain ZA. Comprehensive review of drones collision avoidance schemes: challenges and open issues. *IEEE Trans Intell Transportation Syst* (2024) 25(7):6397–426. doi:10.1109/tits.2024.3375893

18. Zhang QL, Wang YM, Cheng EW, Chen YZ. Assessment method for electromagnetic interference situation of UAV satellite navigation system. *J Natl Univ Defense Tech* (2022). doi:10.11887/j.cn.202206014

19. Kim S-G, Lee E, Hong I-P, Yook J-G. Review of intentional electromagnetic interference on UAV sensor modules and experimental study. *Sensors (Basel, Switzerland)* (2022) 22(6):2384. doi:10.3390/s22062384

20. Xiao K. *Research on theory and method of multi-frequency GNSS/INS integrated precise positioning and attitude determination*. Zhengzhou, China: Information Engineering University of Strategic Support Force (2020). dissertation/master's thesis.

21. Xie G. *GPS principles and receiver design*. Beijing: Publishing House of Electronics Industry (2017).

22. Chen XG, Wang ES, Ren X, Shu WS, Wu LY, Xu S. Design of UAV system based on Beidou navigation. *Electron Devices* (2021) 44(5):1248–53. doi:10.3969/j.issn.1005-9490.2021.05.037

23. Giorgi G, Teunissen JGP. *GNSS carrier phase-based attitude determination*. London: Intech Open (2012).

24. Gong A, Zhao XB, Pang C, Duan R, Wang Y. GNSS single frequency, single epoch reliable attitude determination method with baseline vector constraint. *Sensors* (2015) 15(12):30093–103. doi:10.3390/s151229774

25. Jwo DJ. Estimation of quaternion motion for GPS-based attitude determination using the extended Kalman filter. *Comput Mater Continua* (2020) 66(2):2105–26. doi:10.32604/cmc.2020.014241

26. Shu TG, Kay SL. Survey of global-positioning-system-based attitude determination algorithms. *J Guidance, Control Dyn* (2017) 40(6):1321–35. doi:10.2514/1.G002504

27. Sabatini R, Salazar LR, Rodriguez L, Kaharkar A, Bartel C, Shaid T Carrier-phase GNSS attitude determination and control system for unmanned aerial vehicle applications. *ARPN J Syst Softw* (2012) 297–322. doi:10.4172/2168-9792.1000115

28. Xu JN, Zhu T, Bian HW. Overview of GPS attitude measurement technology. *J Naval Univ Eng* (2003) 3:17–22. doi:10.3969/j.issn.1009-3486.2003.03.005

29. Hermann RB. A simulation of the navigation and orientation potential of the Ti-Agr. *Mar Geodesy* (1985) 9(2):133–43. doi:10.1080/15210608509379522

30. Kruczynski LR, Li PC, Evans AG, Hermann BR *Using GPS to determine vehicle attitude: USS Yorktown test results* (1989).

31. Zheng GZ. Discussion on Ashtech GPS 3DF attitude measurement system. *Geology Mining Surv Mapp* (1994) 1994(2). doi:10.16864/j.cnki.dkch.1994.02.001

32. Wilson GJ, Tonnemacher JD. A GPS attitude determination system. *The J Navigation* (1992) 45(2):192–204. doi:10.1017/s0373463300010699

33. Guo WL, Pan YC, Zhai ZR. A method for heading and attitude measurement based on dual-antenna GPS receiver. *Radio Eng* (2012) 42(5):49–52. doi:10.3969/j.issn.1003-3106.2012.05.016

34. Tang JM, Wang Q, Ye S. Data acquisition and processing method of GPS-Beeline attitude measurement system. *Navigation* (2004) (1) 46–50.

35. GNSS-INS. *Three-antenna full-attitude measurement and positioning integrated system ZH6000A*. Shanghai, China: Shanghai Zihang Electronic Technology Co., Ltd (2024). Available from: https://www.zeenav.com/product-detail/gins-th.html (Accessed December 26, 2024).

36. GNSS-INS. *Fiber optic GNSS/INS combined inertial navigation system SIN-INS3000 - integrated navigation products*. Xi'an, China: Xi'an Sine Wave Measurement and Control Technology Co., Ltd (2024). Available from: http://www.fog-ins.com/content/?150.html (Accessed December 26, 2024).

37. Ericcotech. High-precision GNSS+INS integrated navigation: mastering speed, Position, Attitude Inertial Tech Supplier. (2024). Available from: https://www.ericcotech.com/?article/187.html (Accessed December 26, 2024).

38. MTI710 GNSS/INS. *Xi'an precision measurement and control Co., ltd* (2024). Available from: https://www.siliconmems.com/dproduct_detail/id-165.html (Accessed December 26, 2024).

39. MicroStrain 3DM-GX5-GNSS/INS. MicroStrain by HBK (2024). Available from: https://www.microstrain.com/inertial-sensors/3DM-GX5-4.5 (Accessed December 26, 2024).

40. Ding W, Sun W, Yan H, Li W, Jiang Y, Gao Y. Low-cost dual-antenna GNSS-based heading and pitch angles estimation considering baseline length constraint. *Measurement* (2025) 239:115492. doi:10.1016/j.measurement.2024.115492

41. Wu Y, Sun C. Dual-antenna GPS-based UAV attitude determination method and accuracy analysis. *J Phys Conf Ser* (2023) 2489:012035. doi:10.1088/1742-6596/2489/1/012035

42. Jiao B, Cong DW. Prospects of navigation jamming technology application in UAV defense. *Radio Eng* (2021) 51(10):1019–24. doi:10.3969/j.issn.1003-3106.2021.10.001

43. Xinhua News Agency. Drone show in xi'an goes wrong with "garbled code". Possibly Due to Signal Interference (2024). Available from: https://baijiahao.baidu.com/s?id=1599489299738948292&wfr=spider&for=pc (Accessed April 20, 2024).

44. Wu YW. Battlefield applications of unmanned aerial vehicles in complex electromagnetic environments. *Cruise Missiles* (2011) 1:30–5. doi:10.3969/j.issn.1006-141X.2013.02.001

45. Wang XZ, Yao YB, Xu CQ, Zhao Y, Zhang H. An improved single-epoch attitude determination method for low-cost single-frequency GNSS receivers. *Remote Sensing* (2021) 13(14):2746. doi:10.3390/rs13142746

46. Liang X, Huang ZG, Qin HL. A new rapid integer ambiguity resolution of GNSS phase-only dynamic differential positioning. *IEEE Geosci Remote Sensing Lett* (2022) 19:1–5. doi:10.1109/lgrs.2021.3117093

47. Wu HT, Zhao XB, Pang CL, Zhang L, Feng B. Multivariate constrained GNSS real-time full attitude determination based on attitude domain search. *J Navigation* (2019) 72(2):483–502. doi:10.1017/s0373463318000784

48. Zamanpardaz S, Teunissen PJG, Nadarajah N. IRNSS/NavIC L5 attitude determination. *SENSORS* (2017) 17(2):274. doi:10.3390/s17020274

49. Shuster MD. A survey of attitude representations. *J Astronautical Sci* (1993) 41(4):439–517. doi:10.1109/7.259548

50. Diebel J. Representing attitude: euler angles, unit quaternions, and rotation vectors. *Matrix* (2006) 58(15-16):1–35.

51. Axelrad P, Behre CP. Satellite attitude determination based on GPS signal-to-noise ratio. *Proc IEEE* (1999) 87(1):133–44. doi:10.1109/5.736346

52. Wang C, Walker RA, Moody MP. Single antenna attitude algorithm for nonuniform antenna gain patterns. *J Spacecraft Rockets* (2007) 44(1):221–9. doi:10.2514/1.19428

53. Medina D, Vilà-Valls J, Hesselbarth A, Ziebold R, García J. On the recursive joint position and attitude determination in multi-antenna GNSS platforms. *Remote Sensing* (2020) 12(12):1955. doi:10.3390/rs12121955

54. Henkel P, Lamm M, Mittmann U, Fritzel T, Strauß R, Steinert H-J, et al. Verification of RTK positioning of UAVs with high-precision laser tracker. In: *2022 16th European conference on antennas and propagation (EuCAP)* (2022). p. 1–5.

55. Ding W, Sun W, Gao Y, Wu J Carrier phase-based precise heading and pitch estimation using a low-cost GNSS Receiver. *Remote Sensing* (2021) 13(18):3642. doi:10.3390/rs13183642

56. Li ZH, Huang JS. *GPS measurement and data processing*. Wuhan: Wuhan University Press (2016).

57. Blewitt G. Basics of the GPS technique: observation equations. *Geodetic Appl GPS* (1997) 1:46.

58. Wu M, Luo S, Li JH, Liu W. Characterization of GNSS line bias and BDS-3 attitude determination with single-differenced observations from common-clock receiver. *IEEE Sensors J* (2023) 23(18):21842–52. doi:10.1109/jsen.2023.3300148

59. Nie B, Cai Z, Zhao J, Wang Y. Motion transformation solutions based on Euler angle perturbation model. *Measurement* (2025) 240:115631. doi:10.1016/j.measurement.2024.115631

60. An X, Meng X, Jiang W. Multi-constellation GNSS precise point positioning with multi-frequency raw observations and dual-frequency observations of ionospheric-free linear combination. *Satellite Navigation* (2020) 1(1):7. doi:10.1186/s43020-020-0009-x

61. Liu Y, Wang S, Hu L, Han C, Chai D. Analysis of the effect of GNSS interference on high-precision positioning applications of satellite navigation systems. In: *2021 IEEE international geoscience and remote sensing symposium IGARSS* (2021). p. 8554–7.

62. OliaZadeh N, Landry R, Yeste-Ojeda OA, Gagnon E, Wong F. GPS-based attitude determination using RLS and LAMBDA methods. In: *2015 international conference on localization and GNSS (ICL-GNSS)* (2015). p. 1–7.

63. Odolinski R, Teunissen PJG. Best integer equivariant estimation: performance analysis using real data collected by low-cost, single- and dual-frequency, multi-GNSS receivers for short-to long-baseline RTK positioning. *J Geodesy* (2020) 94(9):91–17. doi:10.1007/s00190-020-01423-2

64. Chen BW, Chang GB, Li SQ, Deng K. Analytical and iterative solutions to GNSS attitude determination problem in measurement domain. *Math Probl Eng* (2019). doi:10.1155/2019/7908675

65. Zhao L, Li N, Li L, Zhang Y, Cheng C. Real-time GNSS-based attitude determination in the measurement domain. *Sensors* (2017) 17(2):296. doi:10.3390/s17020296

66. Zhu F, Hu Z, Liu W, Zhang X. Dual-antenna GNSS integrated with MEMS for reliable and continuous attitude determination in challenged environments. *IEEE Sensors J* (2019) 19(9):3449–61. doi:10.1109/jsen.2019.2891783

67. Giorgi G, Teunissen PJG. Carrier phase GNSS attitude determination with the multivariate constrained LAMBDA method. In: *2010 IEEE aerospace conference* (2010). p. 1–12.

68. Zhang JY. *Research on theory and method of GNSS integer ambiguity estimation and testing*. Changsha, China: National University of Defense Technology (2019).

69. Forssell B, Martin-Neira M, Harrisz RA. Carrier phase ambiguity resolution in GNSS-2. In: *Proceedings of the 10th international technical meeting of the satellite division of the Institute of navigation (ION GPS 1997)* (1997). p. 1727–36.

70. Vollath U, Birnbach S, Landau L, Fraile-Ordoñez JM, Martí-Neira M. Analysis of three-carrier ambiguity resolution technique for precise relative positioning in GNSS-2. *Navigation* (1999) 46:13–23. doi:10.1002/j.2161-4296.1999.tb02392.x

71. Mader GL. Rapid static and kinematic global positioning system solutions using the ambiguity function technique. *J Geophys Res Solid Earth* (1992) 97(B3):3271–83. doi:10.1029/91jb02845

72. Teunissen PJG. The least-squares ambiguity decorrelation adjustment: a method for fast GPS integer ambiguity estimation. *J Geodesy* (1995) 70(1):65–82. doi:10.1007/bf00863419

73. Han SW, Rizos C. Improving the computational efficiency of the ambiguity function algorithm. *J Geodesy* (1996) 70(6):330–41. doi:10.1007/bf00868185

74. Zhao YZ, Zou JG, Zhang P, Guo J, Wang X, Huang G. An optimization method of ambiguity function based on multi-antenna constrained and application in vehicle attitude determination. *Micromachines* (2021) 13(1):64. doi:10.3390/mi13010064

75. Wang Y, Zhao XB, Pang CL, Wang X, Wu S, Zhang C. Improved pitch-constrained ambiguity function method for integer ambiguity resolution in BDS/MIMU-integrated attitude determination. *J Geodesy* (2019) 93(4):561–72. doi:10.1007/s00190-018-1182-7

76. Teunissen PJG. Least-squares estimation of the integer GPS ambiguities. In: *Invited lecture, section IV theory and methodology, IAG general meeting*. Beijing, China (1993). p. 1–16.

77. Teunissen PJG. A canonical theory for short GPS baselines. Part IV: precision versus reliability. *J Geodesy* (1997) 71(9):513–25. doi:10.1007/s001900050119

78. Verhagen S, Teunissen PJG. New global navigation satellite system ambiguity resolution method compared to existing approaches. *J Guidance, Control Dyn* (2006) 29(4):981–91. doi:10.2514/1.15905

79. Teunissen PJG. Integer least-squares theory for the GNSS compass. *J Geodesy* (2010) 84(7):433–47. doi:10.1007/s00190-010-0380-8

80. Chang XW, Yang X, Zhou T. MLAMBDA: a modified LAMBDA method for integer least-squares estimation. *J Geodesy* (2005) 79(9):552–65. doi:10.1007/s00190-005-0004-x

81. Zhang CL, Dong DN, Kubo N, Kobayashi K, Wu J, Chen W. Evaluation of different constrained LAMBDAs for low-cost GNSS attitude determination in an urban environment. *GPS Solutions* (2024) 28(1):42–16. doi:10.1007/s10291-023-01584-5

82. Ma LY, Zhu F, Liu WK, Lu L, Lou Y, Zhang X. VC-LAMBDA: a baseline vector constrained LAMBDA method for integer least-squares estimation. *J Geodesy* (2022) 96(9):59–14. doi:10.1007/s00190-022-01644-7

83. Wang B, Miao LJ, Wang ST, Shen J. A constrained LAMBDA method for GPS attitude determination. *GPS Solutions* (2009) 13(2):97–107. doi:10.1007/s10291-008-0103-2

84. Teunissen PJG. The affine constrained GNSS attitude model and its multivariate integer least-squares solution. *J Geodesy* (2012) 86(7):547–63. doi:10.1007/s00190-011-0538-z

85. Teunissen PJG, Buist PJ. Testing of a new single-frequency GNSS carrier phase attitude determination method: land, ship and aircraft experiments. *GPS Solutions* (2011) 15(1):15–28. doi:10.1007/s10291-010-0164-x

86. Shao K. *Research on GNSS attitude measurement algorithm and software development*. Beijing, China: Tsinghua University (2016).

87. Chen WT, Sun XL. Performance improvement of GPS single frequency, single epoch attitude determination with poor satellite visibility. *Meas Sci Tech* (2016) 27(7):075104. doi:10.1088/0957-0233/27/7/075104

88. Giorgi G, Teunissen PJG, Verhagen S, Buist PJ. Testing a new multivariate GNSS carrier phase attitude determination method for remote sensing platforms. *Adv Space Res* (2010) 46(2):118–29. doi:10.1016/j.asr.2010.02.023

89. Liu X, Ballal T, Ahmed M, Al-Naffouri TY. Instantaneous GNSS ambiguity resolution and attitude determination via Riemannian manifold optimization. *IEEE Trans Aerospace Electron Syst* (2023) 59(3):3296–312. doi:10.1109/taes.2022.3223330

90. Douik A, Liu X, Ballal T, Al-Naffouri TY, Hassibi B. Precise 3-D GNSS attitude determination based on Riemannian manifold optimization algorithms. *IEEE Trans Signal Process* (2020) 68:284–99. doi:10.1109/tsp.2019.2959226

91. Shuster MD. The optimization of TRIAD. *J Astronautical Sci* (2007) 55(2):245–57. doi:10.1007/bf03256523

92. Shuster M. Approximate algorithms for fast optimal attitude computation. In: *Guidance and control conference* (1978). p. 1249.

93. Markey FL. Attitude determination using vector observations - a fast optimal matrix algorithm. *J Astronautical Sciences* (1993) 41(2):261–80. doi:10.1109/7.210101

94. Zhang FZ, Chai YJ, Chai H, Ding LX. Precision analysis of two multi-antenna GNSS attitude determination methods. *J Chin Inertial Tech* (2016) 24(1):30–5. doi:10.13695/j.cnki.12-1222/o3.2016.01.007

95. Liu X, Ballal T, Chen H, Al-Naffouri TY. Constrained wrapped least squares: a Tool for high-accuracy GNSS attitude determination. *IEEE Trans Instrumentation Meas* (2022) 71:1–15. doi:10.1109/tim.2022.3193412

96. Wahba G. A least squares estimate of satellite attitude. *SIAM Rev* (1965) 7(3):409. doi:10.1137/1007077

97. Bar-Itzhak IY. REQUEST - a recursive QUEST algorithm for sequential attitude determination. *J Guidance, Control Dyn* (1996) 19(5):1034–8. doi:10.2514/3.21742

98. Li W, Fan P, Cui X, Zhao S, Ma T, Lu M. A low-cost INS-integratable GNSS ultra-short baseline attitude determination system. *Sensors* (2018) 18(7):2114. doi:10.3390/s18072114

99. De Celis R, Cadarso L. An estimator for UAV attitude determination based on accelerometers, GNSS sensors, and aerodynamic coefficients. *Navigation: J Inst Navigation.* (2018) 65(3):319–34. doi:10.1002/navi.256

100. Olivart I, Lop JM, Moreno-Salinas D, Sanchez J. Full real-time positioning and attitude system based on GNSS-RTK Technology. *Sustainability* (2020) 12(23):9796. doi:10.3390/su12239796

101. Wang H, Liu N, Su Z, Li Q. Research on low-cost attitude estimation for MINS/dual-antenna GNSS integrated navigation method. *Micromachines* (2019) 10(6):362. doi:10.3390/mi10060362

102. Grove (USA). *Principles of GNSS and inertial and multi-sensor integrated navigation systems*. Beijing: National Defense Industry Press (2015).

103. Cai XB, Hsu H, Chai H, Ding L, Wang Y. Multi-antenna GNSS and INS integrated position and attitude determination without base station for land vehicles. *J Navigation* (2019) 72(2):342–58. doi:10.1017/s0373463318000681

104. Perov A, Shatilo A. Deeply integrated GNSS/gyro attitude determination system. *Sensors* (2020) 20(8):2203. doi:10.3390/s20082203

105. Yan GM, Wu J. *Strapdown inertial navigation algorithm and integrated navigation principle*. Xi'an: Northwest Industrial University Press (2019).

106. Kalman RE. A new approach to linear filtering and prediction problems. *J Basic Eng* (1960) 82(1):35–45. doi:10.1115/1.3662552

107. Wang HN. *GPS navigation principles and applications*. Beijing: Science Press (2003).

108. Madhukar PS, Prasad LB. State estimation using extended kalman filter and unscented kalman filter. In: *2020 international conference on emerging trends in communication, control and computing (ICONC3)* (2020). p. 1–4.

109. Yang Y, Li Y, Chen P. Improved float ambiguities for real-time GNSS attitude determination via UKF. In: *2016 8th international conference on wireless communications and signal processing (WCSP)* (2016). p. 1–5.

110. Djuric PM, Kotecha JH, Zhang J, Huang Y, Ghirmai T, Bugallo M, et al. Particle filtering. *IEEE Signal Processing Magazine* (2003) 20(5):19–38. doi:10.1109/msp.2003.1236770

111. Jwo D. Complementary kalman filter as a baseline vector estimator for GPS-based attitude determination. *Comput Mater and Continua* (2020) 65(2):993–1014. doi:10.32604/cmc.2020.011592

112. Wan EA, van der Merwe R. The unscented Kalman filter for nonlinear estimation. In: *Proceedings of the IEEE 2000 adaptive systems for signal processing, communications, and control symposium (cat. No.00EX373)*. Lake Louise, Alta., Canada: IEEE (2000). p. 153–8.

113. Xi YH, Peng H. Iterative extended kalman aided particle filter and its performance analysis. *J Syst Eng* (2012) 27(5):593–9. doi:10.3969/j.issn.1000-5781.2012.05.003

114. Xu Y, Xu K, Wan J, Xiong Z, Li Y Research on particle filter tracking method based on kalman filter. In: *2018 2nd IEEE advanced information management, communicates, electronic and automation control conference (IMCEC)* (2018). p. 1564–8.

115. Wang SH, Liu YK, Sun XY, Ji YF. Dual-antenna attitude determination algorithm based on low-cost receivers. *J Comp Appl* (2019) 39(8):2381–5. doi:10.11772/j.issn.1001-9081.2018122554

116. Dong P, Cheng J, Liu L, Sun X, Fan S. A heading angle estimation approach for MEMS-INS/GNSS integration based on ZHVC and SAUKF. *IEEE Access* (2019) 7:154084–95. doi:10.1109/access.2019.2948368

117. Ding W, Jiang Y, Lyu Z, Liu B, Gao Y. Improved attitude estimation accuracy by data fusion of a MEMS MARG sensor and a low-cost GNSS receiver. *Measurement* (2022) 194:111019. doi:10.1016/j.measurement.2022.111019

118. Yan W, Wang L, Jin Y, Shi G High accuracy navigation system using GPS and INS system integration strategy. In: *2016 IEEE international conference on cyber technology in automation, control, and intelligent systems (CYBER)* (2016). p. 365–9.

119. Xiao K, Sun FP, Wang HY. Tightly coupled model of triple-frequency differential GNSS/INS. *J Chin Inertial Tech* (2018) 26(2):180–6. doi:10.13695/j.cnki.12-1222/o3.2018.02.007

120. Gao M, Liu G, Wang S, Xiao G, Zhao W, Lv D. Research on tightly coupled multi-antenna GNSS/MEMS single-frequency single-epoch attitude determination in urban environment. *Remote Sensing* (2021) 13(14):2710. doi:10.3390/rs13142710

121. Sun W, Sun P, Wu J. An adaptive fusion attitude and heading measurement method of MEMS/GNSS based on covariance matching. *Micromachines* (2022) 13(10):1787. doi:10.3390/mi13101787

122. Wend J, Meister O, Schlaile C, Trommer GF An integrated GPS/MEMS-IMU navigation system for an autonomous helicopter. *Aerospace Sci Tech* (2006) 10(6):527–33. doi:10.1016/j.ast.2006.04.002

123. Xu K, Tao J, Lei X, Zhang J, Liu C, Chen L. An improved low-cost dual-antenna GNSS dynamic attitude determination method in complex environments. *Remote Sensing* (2024) 16(21):4026. doi:10.3390/rs16214026

124. Na L. *Research on high-precision attitude measurement and integrity monitoring methods for GNSS*. Harbin, China: Harbin Engineering University (2020).

125. Kim D, Lee J. Kalman-filter-based integrity evaluation considering fault duration: application to GNSS-based attitude determination. *GPS Solutions* (2022) 26(2):51–13. doi:10.1007/s10291-022-01234-2

126. Guo L, Yu X, Zhang X, Zhang YM. Technology of unmanned aerial vehicle safety control system: progress and prospects. *Sci China Inf Sci* (2020) 50(2):184–94.

127. Li XJ, Lu ZK, Yuan MZ, Liu WX, Wang FX, Yu Y. Tradeoff of Code Estimation Error Rate and Terminal Gain in SCER Attack. *IEEE Transactions on Instrumentation and Measurement* (2024) 73:1–12. doi:10.1109/TIM.2024.3406807

128. Kerns AJ, Shepard DP, Bhatti JA, Humphreys TE. Unmanned aircraft capture and control via GPS spoofing. *J Field Robotics* (2014) 31(4):617–36. doi:10.1002/rob.21513

129. BaziAR AR, Moazedi M, Mosavi MR. Analysis of single frequency GPS receiver under delay and combining spoofing algorithm. *Wireless Personal Commun* (2015) 83(3):1955–70. doi:10.1007/s11277-015-2497-9

130. Shi PL, Wang XY, Xue R. Strategies for inducing position spoofing of unmanned aerial vehicles. *J Natl Univ Defense Tech* (2021) 43(2):40–6. doi:10.11887/j.cn.202102006

131. Seo SH, Lee BH, Im SH, Jee GI. Effect of spoofing on unmanned aerial vehicle using counterfeited GPS signal. *J Positioning, Navigation, Timing* (2015) 2(2):57–65. doi:10.11003/jpnt.2015.4.2.057

132. Mends D, IvakI N, Madeira H. Effects of GPS spoofing on unmanned aerial vehicles. In: *2018 IEEE 23rd pacific rim international symposium on dependable computing (PRDC)* (2018). p. 155–60.

133. Zhang L, Zhou JH, Qiao HD, Ma XD, Liu XG, Zhang GN. Satellite navigation signal spoofing interference method based on rotorcraft unmanned aerial vehicle's disturbed protection strategy. In: *14th China satellite navigation conference*. Jinan, Shandong, China (2024). p. 7.

134. Li HB, Zhang Y, Tang CK, Ma LJ. Method of satellite navigation spoofing interference for unmanned aerial vehicle swarms. In: *13th China satellite navigation conference*. Beijing, China (2022). p. 5.

135. Li C, Wang XD. Interference technology for GPS/INS integrated navigation system of unmanned aerial vehicles based on trajectory spoofing. *J Nanjing Univ Aeronautics Astronautics* (2017) 49(3):420–7. doi:10.16356/j.1005-2615.2017.03.016

136. Ma C, Yang J, Chen J, Qu Z, Zhou C. Effects of a navigation spoofing signal on a receiver loop and a UAV spoofing approach. *GPS Solutions* (2020) 24(3):76–13. doi:10.1007/s10291-020-00986-z

137. Zhang HS, Gao GG, Kou L, Gu G. Research on GPS spoofing interference technology based on trajectory induction. *J Projectiles, Rockets, Missiles Guidance* (2013) 33(3):149–52. doi:10.3969/j.issn.1673-9728.2013.03.041

138. Jin W, Gong W, Hou T, Sun X, Ma H. A dual-antenna heading determination method for single-frequency GNSS antennas with large phase pattern variations. *GPS Solutions* (2023) 27(2):96. doi:10.1007/s10291-023-01429-1

139. Nadarajah N, Teunissen PJG. Instantaneous GPS/Galileo/QZSS/SBAS attitude determination: a single-frequency (L1/E1) robustness analysis under constrained environments. *Navigation (Wiley-Blackwell)* (2014) 61(1):65–75. doi:10.1002/navi.51

140. Zamanpardaz S, Teunissen PJG, Nadarajah N. Single-frequency L5 attitude determination from IRNSS/NavIC and GPS: a single- and dual-system analysis. *J Geodesy* (2017) 91(12):1415–33. doi:10.1007/s00190-017-1033-y

141. Zamanpardaz S, Teunissen PJG, Nadarajah N. IRNSS/NavIC and GPS: a single- and dual-system L5 analysis. *J Geodesy* (2017) 91(8):915–31. doi:10.1007/s00190-016-0996-4

142. Xiao K, Sun F, Zhu X, Zhou P, Ma Y, Wang Y. Assessment of overlapping triple-frequency BDS-3/BDS-2/INS tightly coupled integration model in kinematic surveying. *GPS Solut* (2024) 28(2):85. doi:10.1007/s10291-024-01637-3

143. Zhao W, Liu G, Gao M, Hu S. Multi-antenna GNSS tight combination attitude determination in the urban environment. *Meas Sci Tech* (2022) 33(6):065109. doi:10.1088/1361-6501/ac55a9

144. Shu Y, Xu P, Niu X, Chen Q, Qiao L, Liu J. High-rate attitude determination of moving vehicles with GNSS: GPS, BDS, GLONASS, and Galileo. *IEEE Trans Instrumentation Meas* (2022) 71:1–13. doi:10.1109/tim.2022.3168896

145. Yang H, Shu Y, Fang R, Qiao L, Ding D, Li G. GPS/BDS dual-antenna attitude determination with baseline-length constrained ambiguity resolution: method and performance evaluation. *IEEE Trans Instrum Meas* (2024) 73:1–14. doi:10.1109/tim.2024.3374423

146. Wu MK, Li JH, Luo S, Liu W. Attitude determination with GPS L1/Galileo E1 observations from common-clock receiver: a comparison of four different models. *Remote Sensing* (2022) 14(21):5438. doi:10.3390/rs14215438

Frontiers in Astronomy and Space Sciences

TYPE Original Research
PUBLISHED 20 February 2025
DOI 10.3389/fspas.2025.1436270

OPEN ACCESS

EDITED BY
Zhu Xiao,
Hunan University, China

REVIEWED BY
Mohammad AlShabi,
University of Sharjah, United Arab Emirates
Atanu Panda,
Institute of Engineering and Management (IEM), India

*CORRESPONDENCE
Shao-Yong Han,
✉ hanshaoyong@zuaa.zju.edu.cn

RECEIVED 21 May 2024
ACCEPTED 23 January 2025
PUBLISHED 20 February 2025

CITATION
Dai Q, Wan R, Han S-Y and Xiao G-R (2025) A novel adaptive Gaussian sum cubature Kalman filter with time-varying non-Gaussian noise for GNSS/SINS tightly coupled integrated navigation system.
*Front. Astron. Space Sci.* 12:1436270.
doi: 10.3389/fspas.2025.1436270

# A novel adaptive Gaussian sum cubature Kalman filter with time-varying non-Gaussian noise for GNSS/SINS tightly coupled integrated navigation system

Qing Dai[1,2], Ru Wan[1], Shao-Yong Han[3,4]* and Guo-Rui Xiao[2]

[1]College of Urban Construction, Luoyang Polytechnic, Luoyang, China, [2]Institute of Geospatial Information, Information Engineering University, Zhengzhou, China, [3]School of Mathematics and Computer Science, Tongling University, Tongling, China, [4]College of Electrical Engineering, Zhejiang University, Hangzhou, China

The Gaussian sum cubature Kalman filter (GSCKF) based on Gaussian mixture model (GMM) is a critical nonlinear non-Gaussian filter for data fusion of global navigation satellite system/strapdown inertial navigation systems (GNSS/SINS) tightly coupled integrated navigation system. However, the stochastic model of non-Gaussian noise in practical operating environments is not static, but rather time-varying. So if the GMM of GSCKF cannot be adjusted adaptively, it will lead to a decrease in estimation accuracy. To address this issue, we propose a novel adaptive GSCKF (AGSCKF) based on the dynamic adjustment of GMM. By analyzing the impact of GMM displacement parameter on the fitting accuracy of non-Gaussian noise, a novel algorithm for GMM displacement parameter adaptive adjustment is proposed using a cost function. Then this novel algorithm is applied to overcome the limitations of GSCKF under time-varying non-Gaussian noise environment, thereby improving the filtering performance. The simulation and experimental results indicate that the proposed AGSCKF exhibits significant advantage in changeable environments affected by time-varying non-Gaussian noise, which is applied to GNSS/SINS tightly coupled integrated navigation system data fusion can improve estimation accuracy and adaptability without sacrificing significant computational complexity.

KEYWORDS

**GNSS/SINS tightly coupled integrated navigation system, adaptive filter (ADF), cubature Kalman filter (CKF), Gaussian mixture model (GMM), non-Gaussian noise, time-varying noise**

## 1 Introduction

The global navigation satellite system and strapdown inertial navigation system (GNSS/SINS) tightly coupled integrated navigation system data fusion is one of the key technologies in many fields, including unmanned aerial vehicles (UAVs), which enables precise navigation, guidance, and control capabilities (Grewal et al., 2020; Gyagenda et al., 2022; Boguspayev et al., 2023). The mathematical model for GNSS/SINS tightly coupled integrated navigation system data fusion is inherently nonlinear, and despite advances in navigation technology, its nonlinear characteristics cannot be eliminated. Therefore, the nonlinear filter remains a crucial technique in the field of GNSS/SINS tightly coupled integrated navigation system data fusion for UAVs (Groves, 2008; Li and Chen, 2022; Xiao et al., 2024).

## 1.1 Nonlinear filter

Extended Kalman filter (EKF) is a widely used nonlinear filter for GNSS/SINS tightly coupled integrated navigation systems data fusion, but its engineering application is limited by linearization errors and complex updating processes of Jacobian matrix (Wang et al., 2018). Thus, Unscented Kalman filter (UKF) is proposed to approximate the state estimation and its covariance through a set of sampling points by unscented transforms (UT). Compared to EKF, UKF does not require updating Jacobian matrix, and its accuracy can reach second-order Taylor series expansion or even higher. However, the parameters of UKF do not have deterministic values, and the computation increases dramatically with the increase of the dimension of state estimation (Rhudy et al., 2011; Hu et al., 2020). Quadrature Kalman filter (QKF) using Gaussian Hermitian quadrature rule can achieve high estimation accuracy. But as the number of state parameters increases, the required quadrature points will exponentially increase, resulting in that the computational complexity of QKF is higher than that of EKF and UKF (Monfort et al., 2015). To address the dimensionality curse in QKF, researchers have devised cubature Kalman Filter (CKF). Within the CKF framework, the utilization of the third-order spherical cubature rule not only possesses a more rigorous mathematical foundation compared to the UT employed in UKF, but also demonstrates a reduction in computational resources and an increase in computational efficiency during state estimation under comparable conditions, as compared to both UKF and QKF. Additionally, by integrating a square-root filtering approach, CKF exhibits superior numerical stability when confronted with nonlinear challenges, in contrast to the UKF. Currently, CKF has been widely used in fields such as navigation positioning, target tracking, and guidance and control system due to its advantages of superior estimation accuracy, remarkable numerical stability, and minimal computational requirements (Arasaratnam and Haykin, 2009; Sindhuja et al., 2023). And yet CKF assumes that the random model in the filter is white Gaussian noise. In practical application, it is common for the random model to deviate from the assumption of white Gaussian noise, which inevitably affects the accuracy of filtering estimation (Sun et al., 2022; Tang et al., 2023; Wang et al., 2023). Therefore, mitigating the impact of non-Gaussian noise on the estimation accuracy of CKF has been a prominent research topic in the field of GNSS/SINS tightly coupled integrated navigation data fusion.

## 1.2 Mproved cubature Kalman filter

In recent years, various optimized algorithms for CKF have been proposed to address the issue of non-Gaussian noise in states estimation. A strong tracking CKF with multiple sub-optimal fading factor is introduced to tackle the discrepancy between theoretical and practical models of measurement noise in GNSS/SINS tightly coupled integrated navigation systems, which significantly enhances the accuracy of navigation estimation (Huang et al., 2016). Furthermore, a robust CKF based on M-estimation is presented, which can reduce the impact of non-Gaussian measurement noise interference. This filter redefines the innovation sequence using the M-estimate of Huber's equivalent weight function, enhancing the robustness of the GNSS/SINS tightly coupled integrated navigation system data fusion (Wang et al., 2020). Additionally, an adaptive CKF based on Mahalanobis distance is designed to address the unknown noise statistics. By employing the Mahalanobis distance of innovations to determine the random model of filter, this filter improves the positioning accuracy of GNSS/SINS tightly coupled integrated navigation systems (Zhang et al., 2021). However, these above optimized algorithms for CKF approximate the true distribution of non-Gaussian through the Gaussian distribution approximation method with a larger variance, which may result in inaccurate estimated variance for state estimation (Legin et al., 2023; Dong et al., 2023).

Lately, the Gaussian mixture model (GMM) derived from the multimodal approximation method has emerged as a promising approach to solve non-Gaussian noise problems. Compared to the Gaussian distribution approximation method with a larger variance, the GMM offers higher accuracy in this regard (Alspach and Sorenson, 1972; George et al., 2022). By decomposing the probability density function (PDF) of non-Gaussian noise into multiple Gaussian components using GMM, Gauss-Hermite sum filter can be derived. Combining GMM with CKF yields the Gaussian sum CKF (GSCKF), which has been applied to GNSS/SINS tightly coupled integrated navigation data fusion, thereby contributing to improved navigation positioning accuracy (Bai et al., 2022). Since 2023, numerous improved algorithms for GSCKF have emerged in rapid succession, finding their applications within the domain of non-Gaussian nonlinear systems. These refined algorithms encompass: Credible GSCKF, Observability-Based GSCKF, quaternion constrained GSCKF, and so on (Ge et al., 2024; Jiang et al., 2024; Dai et al., 2024; Li et al., 2020). However, due to the non-stationary nature of practical operation environments of GNSS/SINS tightly coupled integrated navigation systems, the statistical characteristics of non-Gaussian noise also change over time (Zhou et al., 2024; Lin et al., 2023; Chen et al., 2023). Although the above research has to some extent improved the estimation accuracy of GNSS/SINS tightly coupled integrated navigation systems data fusion using GSCKF affected by non-Gaussian noises, the GMM modeling parameters in GSCKF cannot change with the statistical characteristics of non-Gaussian noise, and this limitation will lead to a decrease in estimation accuracy, which may seriously cause divergence.

## 1.3 Motivation and contributions

The motivation for this study stems from the intricate and dynamic nature of practical operating environments in GNSS/SINS tightly coupled integrated navigation system. These environments introduce time-varying non-Gaussian noise characteristics that exhibit stochastic behavior. Consequently, the inability of the GMM employed within GSCKF to adapt dynamically results in a degradation of estimation accuracy. Addressing the challenges posed by such time-varying non-Gaussian noise is crucial for maintaining the performance of GSCKF. Therefore, inspired by the research in reference (George et al., 2022; Dai et al., 2024; Lin et al., 2023; Panda et al., 2024a; Panda et al., 2024b), we propose a novel Adaptive GSCKF(AGSCKF), specifically designed to mitigate the adverse effects of time-varying non-Gaussian noise, thereby enhancing the performance of GNSS/SINS tightly coupled integrated navigation system.

The contributions of this work are concisely summarized as follows.

1) A novel AGSCKF is proposed, building upon the framework of GSCKF. This filter specifically targets the statistical properties of time-varying non-Gaussian noise, mitigating the adverse effects on the estimation accuracy of GSCKF.
2) The innovation of AGSCKF lies in its integration of a cost function-based adaptation algorithm. This algorithm dynamically optimizes the displacement parameter of GMM in real-time, ensuring precise tracking of the statistical characteristics of time-varying non-Gaussian noise.
3) Simulation and experimental analyses have been conducted to demonstrate the superior performance of AGSCKF, particularly in enhancing the estimation accuracy and adaptability of the GNSS/SINS tightly coupled integrated navigation system in time-varying non-Gaussian noise scenarios.

Collectively, these contributions highlight the superior performance of AGSCKF compared to CKF and GSCKF in addressing data fusion for GNSS/SINS tightly coupled integrated navigation systems in challenging environments.

# 2 Background and problem formulation

## 2.1 Mathematical models for GNSS/SINS tightly coupled integrated navigation system

The GNSS/SINS tightly coupled integrated navigation system exhibits excellent navigation accuracy and robustness against interference. Nevertheless, in the presence of high maneuvering, conventional linearized models tend to compromise the accuracy of estimation, necessitating the nonlinear mathematical model (Groves, 2008). The nonlinear mathematical model for GNSS/SINS tightly coupled integrated navigation system includes the state-space model and the measurement model.

The state estimation $\boldsymbol{x}_{k-1|k-1}$ at epoch k-1 encompasses attitude, velocity, position, gyroscope drift, accelerometer drift, GNSS clock bias, and GNSS clock drift. The state-space model can be mathematically expressed by Equation 1.

$$\boldsymbol{x}_{k|k-1} = f\left(\boldsymbol{x}_{k-1|k-1}\right) + \boldsymbol{g}_k \boldsymbol{w}_k \tag{1}$$

where $f(\cdot)$ is a nonlinear function, $\boldsymbol{g}_k$ is the noise coefficient matrix, $\boldsymbol{w}_k$ is the process noise, Assuming that $\boldsymbol{w}_k$ is characterized as white Gaussian noise, it can be represented mathematically as $\boldsymbol{w}_k \sim (0, \boldsymbol{Q}_k)$.

The measurement model is expressed by Equation 2.

$$\boldsymbol{z}_k = h\left(\boldsymbol{x}_{k|k-1}\right) + \boldsymbol{v}_k \tag{2}$$

where $\boldsymbol{z}_k$ is the measurement composed of pseud-orange and pseud-orange rate corrected by satellite clock bias, ionospheric delay, and tropospheric delay. $h(\cdot)$ is a nonlinear function. $\boldsymbol{v}_k$ is the measurement noise caused by GNSS receiver, multipath effects, and orbit prediction residuals. Since $\boldsymbol{v}_k$ does not conform to white Gaussian noise, it is classified as non-Gaussian noise. Its distribution can be closely approximated by two Gaussian components (Bai et al., 2022).

$$\boldsymbol{P}\left(\boldsymbol{v}_k\right) = (1-\varepsilon)\mathrm{N}\left(\boldsymbol{v}_k^A; \boldsymbol{\mu}_k^A, \boldsymbol{R}_k^A\right) + \varepsilon \mathrm{N}\left(\boldsymbol{v}_k^B; \boldsymbol{\mu}_k^B, \boldsymbol{R}_k^B\right) \tag{3}$$

where $\mathrm{N}\left(\boldsymbol{v}_k^A; \boldsymbol{\mu}_k^A, \boldsymbol{R}_k^A\right)$ is the Gaussian component of mean $\boldsymbol{\mu}_k^A$ and variance $\boldsymbol{R}_k^A$ at epoch $k$, $\mathrm{N}\left(\boldsymbol{v}_k^B; \boldsymbol{\mu}_k^B, \boldsymbol{R}_k^B\right)$ denotes the Gaussian component of mean $\boldsymbol{\mu}_k^B$ and variance $\boldsymbol{R}_k^B$, and $\varepsilon$ represents a factor with unmeasurable and time-varying characteristics, setting $\varepsilon \in [0, 1]$.

## 2.2 Cubature Kalman filter

CKF is a Gaussian filter that enables the approximation of the PDF of nonlinear functions through a set of cubature points. This approach avoids the need for linearization of the nonlinear function, thereby enhancing the accuracy and reliability of states estimation. By utilizing this method, the CKF offers significant advantages over traditional linearized filters in terms of its ability to handle non-linear systems with high dimensional states estimation. The specific implementation steps of CKF are as follows.

Step 1: Initialization.

Set $\boldsymbol{x}_{0|0} \sim \mathrm{N}\left(\boldsymbol{x}_{0|0}, \boldsymbol{P}_{0|0}\right)$, $\boldsymbol{x}_{0|0} = \mathrm{E}\left(\boldsymbol{x}_{0|0}\right)$ and $\boldsymbol{S}_{0|0} = \mathrm{chol}\left(\boldsymbol{P}_{0|0}\right)$, where $\mathrm{E}(\cdot)$ is the expected value, $\mathrm{chol}(\cdot)$ represents the Cholesky decomposition, and $\boldsymbol{P}_{0|0} = \boldsymbol{S}_{0|0}\boldsymbol{S}_{0|0}^{\mathrm{T}}$.

Step 2: Calculate the sampling points.

Let state estimation at epoch $k-1$ expressed as $\boldsymbol{x}_{k-1|k-1}$, and its covariance is computed as

$$\boldsymbol{P}_{k-1|k-1} = \boldsymbol{S}_{k-1|k-1}\boldsymbol{S}_{k-1|k-1}^{\mathrm{T}} \tag{4}$$

The third-order spherical phase diameter cubature rule is employed to generate a set of cubature points $\boldsymbol{\xi}_c$

$$\xi_c = \sqrt{\frac{m}{2}}\left\{\begin{pmatrix}1\\ \vdots\\ 0\end{pmatrix}, \cdots, \begin{pmatrix}0\\ \vdots\\ 1\end{pmatrix}, \begin{pmatrix}-1\\ \vdots\\ 0\end{pmatrix}, \cdots, \begin{pmatrix}0\\ \vdots\\ -1\end{pmatrix}\right\}_c \tag{5}$$

In Equation 5, $\boldsymbol{x}_{c,k-1|k-1}$ denotes the total number of cubature points, $c = 1, 2, \cdots m$, $m = 2n$. $\boldsymbol{x}_{c,k-1|k-1}$ is the dimension of the state estimation. In other words, the total number of cubature points is twice the dimension $\boldsymbol{x}_{c,k-1|k-1}$ of the state estimation.

Step 3: Prediction.

The estimation of cubature points $\boldsymbol{\chi}_{c,k-1|k-1}$ and propagation cubature points $\boldsymbol{x}^*_{c,k-1|k-1}$ are calculated separately.

$$\boldsymbol{\chi}_{c,k-1|k-1} = \boldsymbol{S}_{k-1|k-1}\boldsymbol{\xi}_c + \boldsymbol{x}_{k-1|k-1} \tag{6}$$

$$\boldsymbol{x}^*_{c,k|k-1} = f\left(\boldsymbol{\chi}_{c,k-1|k-1}\right) \tag{7}$$

Calculate the state prediction $\boldsymbol{x}_{k|k-1}$ and its covariance $\boldsymbol{P}_{k|k-1}$

$$\boldsymbol{x}_{k|k-1} = \frac{1}{m}\sum_{c=1}^{m}\boldsymbol{x}^*_{c,k|k-1} \tag{8}$$

$$P_{k|k-1}=\frac{1}{m}\sum_{c=1}^{m}\left(x^{*}_{c,k|k-1}-\chi_{c,k-1|k-1}\right)\left(x^{*}_{c,k|k-1}-\chi_{c,k-1|k-1}\right)^{\mathrm{T}}+Q_{k-1} \tag{9}$$

where $Q_{k-1}$ is the covariance of process noise.

Step 4: Update.

Calculate measurement prediction $z_{k|k-1}$, its corresponding covariance $P_{zz,k|k-1}$, and cross-covariance $P_{xz,k|k-1}$, respectively.

$$z_{k|k-1}=\frac{1}{m}\sum_{c=1}^{m}z^{*}_{c,k|k-1} \tag{10}$$

$$P_{zz,k|k-1}=\frac{1}{m}\sum_{c=1}^{m}\left(z^{*}_{c,k|k-1}-z_{k|k-1}\right)\left(z^{*}_{c,k|k-1}-z_{k|k-1}\right)^{\mathrm{T}}+R_{k} \tag{11}$$

$$P_{xz,k|k-1}=\frac{1}{m}\sum_{c=1}^{m}\left(x^{*}_{c,k|k-1}-\chi_{c,k-1|k-1}\right)\left(z^{*}_{c,k|k-1}-z_{k|k-1}\right)^{\mathrm{T}} \tag{12}$$

where $z^{*}_{c,k|k-1}=h\left(x_{c,k|k-1}\right)$, $x_{c,k|k-1}=S_{k|k-1}\chi_{c}+x_{k|k-1}$, $P_{k|k-1}=S_{k|k-1}S^{\mathrm{T}}_{k|k-1}$.

Update the filter gain $K_k$, state estimation $x_{k|k}$, and its covariance $P_{k|k}$ separately.

$$K_{k}=P_{xz,k|k-1}P^{-1}_{zz,k|k-1} \tag{13}$$

$$x_{k|k}=x_{k|k-1}+K_{k}\left(z_{k}-z_{k|k-1}\right) \tag{14}$$

$$P_{k|k}=P_{k|k-1}-K_{k}P_{zz,k|k-1}K^{\mathrm{T}}_{k} \tag{15}$$

## 2.3 Gaussian sum cubature Kalman filter

CKF is a nonlinear filter that assumes the random model is white Gaussian noise. However, in practical operating environments, the measurement noise encountered in GNSS/SINS tightly coupled integrated navigation systems exhibits non-Gaussian characteristics. Consequently, it becomes imperative to combine CKF with GMM to develop states estimation of the GSCKF. The GSCKF enables CKF to effectively address the challenges posed by non-Gaussian noise, thereby enhancing the accuracy and reliability of state estimation for GNSS/SINS tightly coupled integrated navigation systems data fusion.

The distribution of measurement noise is depicted as non-Gaussian noise in Equation 3. However, due to the unmeasurable and time-varying characteristics of the factor $\varepsilon$, $P(v_k)$ is often decomposed into two Gaussian distributions with equidistant distributions as illustrated below:

$$P(v_{k})\approx 0.5\mathrm{N}\left(v^{1}_{k};\mu^{1}_{k},R^{1}_{k}\right)+0.5\mathrm{N}\left(v^{2}_{k};\mu^{2}_{k},R^{2}_{k}\right) \tag{16}$$

where $\mathrm{N}\left(v^{1}_{k};\mu^{1}_{k},R^{1}_{k}\right)$ represents a Gaussian component characterized by its mean $\mu^{1}_{k}$ and variance $R^{1}_{k}$. Similarly, $\mathrm{N}\left(v^{2}_{k};\mu^{2}_{k},R^{2}_{k}\right)$ denotes another Gaussian component defined by its mean $\mu^{2}_{k}$ and variance $R^{2}_{k}$.

$$\begin{cases}\mu^{1}_{k}=\mu_{k}+d\sqrt{\lambda}u\\ \mu^{2}_{k}=\mu_{k}-d\sqrt{\lambda}u\\ R^{1}_{k}=R^{2}_{k}=R_{k}-d^{2}\lambda uu^{\mathrm{T}}\end{cases} \tag{17}$$

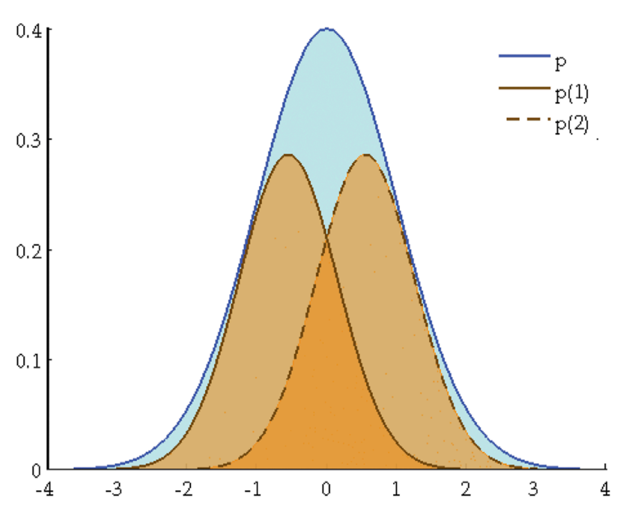

FIGURE 1
The decomposition process of GMM.

where $\lambda$ and $u$ correspond to the maximum eigenvalue and the corresponding eigenvector of $R_k$, respectively. $d$ is the GMM displacement parameter that influences the mean distance between the two Gaussian components, $d\in[0,1]$. In practical computations, $d$ is typically set to 0.5 (Sun et al., 2020; Yu et al., 2023). As depicted in Figure 1, the decomposition process of GMM is illustrated as below.

In Figure 1, the blue solid line $p$ represents the PDF of non-Gaussian noise, while the brown solid lines $p(1)$ and brown dotted lines $p(2)$ represent the two Gaussian components obtained through GMM decomposition respectively, with displacement parameter $d=0.5$. It can be seen that the probability density distribution after decomposition by GMM is close to the non-Gaussian noise in Equation 3. Therefore, GSCKF has better filtering performance than CKF owing to its accuracy random model under non-Gaussian noises scenarios.

The general implementation procedures of GSCKF can be described as follows. Firstly, based on GMM, the decomposition of non-Gaussian noise is performed using Equations 16, 17. Then, CKF is performed by employing Equations 4–15, and the state estimation of two components at the next epoch can be gotten separately. Finally, based on the weights of different components, a weighted combination is carried out to obtain the final state estimation and its covariance as outputs.

## 2.4 Flaws and shortcomings

The Allan variance analysis reveals that the measurement noise of GNSS/SINS tightly coupled integrated navigation systems is non-Gaussian in nature, rather than white Gaussian noise. Additionally, the mathematical statistical characteristics of non-Gaussian noise exhibit time-varying behavior due to changes in the practical operation environment over time (Tang et al., 2023; Zhang et al., 2020; Elmezayen and El-Rabbany, 2021; Taghizadeh and Safabakhsh, 2023). Although non-Gaussian noise can be approximated by Equation 17, the dynamic nature of the practical operation environment of GNSS/SINS tightly coupled integrated navigation systems introduces uncertainties in the factor, which makes the time-varying characteristics of $\boldsymbol{P}(\boldsymbol{v})$. Therefore, it limits the optimality of the GMM displacement parameter when setting, as shown in Equation 17. In other words, if the GSCKF based on GMM with a fixed GMM displacement parameter is directly applied to GNSS/SINS tightly coupled integrated navigation systems data fusion, it may not effectively cope with time-varying non-Gaussian noise, resulting in random model mismatches, reduced estimation accuracy, and even divergence in severe cases.

## 3 Gaussian sum cubature Kalman filter with time-varying Non-Gaussian noise

To address the challenge of deteriorating estimation accuracy of GSCKF, where in the measurement noise is time-varying non-Gaussian noise, this section proposes a novel adaptive GSCKF (AGSCKF) based on the adaptively adjustment of the GMM displacement parameter. According to the impact analysis of GMM displacement parameter on the accuracy of GMM modeling, the AGSCKF employs an adaptive algorithm to select the optimal GMM displacement parameter between two Gaussian components to track changes in the statistical characteristics of non-Gaussian noise. As a result, the derivation of the AGSCKF for GNSS/SINS tightly coupled navigation system data fusion is achieved when measurement noise becomes time-varying non-Gaussian noise.

### 3.1 Analysis of the GMM displacement parameter on the accuracy of GMM modeling

The GSCKF decomposes non-Gaussian noise through GMM to obtain an approximate model by Equation 17, which makes the decomposed mixed model close to the non-Gaussian noise model in Equation 3. However, the time-varying $\varepsilon$ in Equation 3 also introduces uncertainty for $\boldsymbol{P}(\boldsymbol{v}_k)$ in Equation 17. And in the decomposition process of GMM, Equation 17 typically determines the GMM displacement parameter as $d = 0.5$, which is not optimal. If $d > 0.5$, the effect of $\varepsilon\mathrm{N}\left(\boldsymbol{v}_k^B;\boldsymbol{\mu}_k^B,\boldsymbol{R}_k^B\right)$ is stronger than that of $(1-\varepsilon)\mathrm{N}\left(\boldsymbol{v}_k^A;\boldsymbol{\mu}_k^A,\boldsymbol{R}_k^A\right)$; while $d > 0.5$, the effect of $\varepsilon\mathrm{N}\left(\boldsymbol{v}_k^B;\boldsymbol{\mu}_k^B,\boldsymbol{R}_k^B\right)$ is smaller than that of $(1-\varepsilon)\mathrm{N}\left(\boldsymbol{v}_k^A;\boldsymbol{\mu}_k^A,\boldsymbol{R}_k^A\right)$. So, it is required that when non-Gaussian noise varies, the GMM displacement parameter can be adjusted adaptively.

In Figure 2, $p$ represents non-Gaussian noise in Equation 3, while $p(A)$ and $p(B)$ represent the two components in Equation 3. As shown in Figure 2A, when $d < 0.5$, the GMM modeling result of Equation 17 is represented by the area enclosed by $p(1)$, $p(2)$ and the $x$-axis. The overlap between this area and the area enclosed by $p(A)$, $p(B)$ and the $x$-axis is the actual estimation result, denoted as M. The higher the overlap, the higher the estimation accuracy. On the other hand, when $d > 0.5$, the actual estimation result, denoted as N in Figure 2A. Comparing M and N, it can be observed that the degree of overlap of M is lower than that of N, indicating that the estimation result shown in Figure 3D is better than that shown in Figure 3A.

Further, as the effect of $\varepsilon\mathrm{N}(\boldsymbol{v}_\mathrm{B};\boldsymbol{\mu}_\mathrm{B},\boldsymbol{\Sigma}_\mathrm{B})$ weakens ($\varepsilon$ changes from 0.20 to 0.10), the mean centers of $p(A)$ and $p(B)$ shift towards each other. The estimation result repressed as $\mathrm{M}'$ when $d < 0.5$ in Figure 3C, and the estimation result repressed as $\mathrm{N}'$ when $d > 0.5$ in Figure 3F. It is observed that the overlap degree of $\mathrm{M}'$ is higher than that of $\mathrm{N}'$, indicating that the estimation accuracy in Figure 3C is superior to that in Figure 3F when $d < 0.5$.

This demonstrates that when non-Gaussian noise varies, adaptive adjustments in the GMM displacement parameter $d$ can effectively track the time-varying nature of non-Gaussian noise, resulting in a more reasonable GMM decomposition process and a closer fit to the actual non-Gaussian noise. By incorporating this approach into the GSCKF, more accurate stochastic models can be obtained, thereby enhancing the accuracy of GSCKF estimation.

### 3.2 Adaptive algorithm for the GMM displacement parameter

An adaptive algorithm is devised to address the real-time estimation challenge of the GMM displacement parameter under time-varying non-Gaussian noise condition. This algorithm employs the maximum value of the cost function as the optimal criterion and adaptively selects the optimal parameter within a specified range. The cost function is defined as follows:

$$p(\boldsymbol{z}_k|\boldsymbol{z}_{k-1},d) = \frac{1}{\sqrt{2\pi\sigma^2}}\exp\left(-\frac{1}{2}\left(\frac{\boldsymbol{z}_k-\boldsymbol{z}_{k|k-1}}{\sigma}\right)^2\right) \qquad (18)$$

Subsequently, the corresponding value of the GMM displacement parameter $d$ within its range of variation $[d_{\min},d_{\max}]$ can be calculated. The GMM displacement parameter that corresponds to the maximum value $p(z_k|z_{k-1},d)$ is identified as the optimal parameter value $\hat{d}$ by Equation 19.

$$\hat{d} = \arg\max \hat{p}(z_k|z_{k-1},d) \qquad (19)$$

where $d \in [d_{\min},d_{\max}]$.

### 3.3 The process of AGSCKF

The proposed AGSCKF is derived by incorporating the adaptive algorithm for the GMM displacement into GSCKF. The specific implementation steps of the AGSCKF are as follows.

Step 1: Set the step size of displacement parameter's changes $sl = 0.1$ and displacement parameter's range of variation $[d_{\min},d_{\max}]$.

The choice of step size has a significant impact on the accuracy of proposed AGSCKF. A smaller step size generally leads to higher accuracy, albeit at the cost of increased computational complexity.

Step 2: Let $d = d_{\min}$, and the maximum likelihood function is given by $\max \quad LH = 0$.

Step 3: The state prediction $\boldsymbol{x}_{k|k-1,d}$, measurement prediction $\boldsymbol{z}_{k|k-1,d}$, and its corresponding covariance $\boldsymbol{P}_{k|k-1,d}$, cross-covariance $\boldsymbol{P}_{zz,k|k-1,d}$ are computed utilizing Equations 4–12.

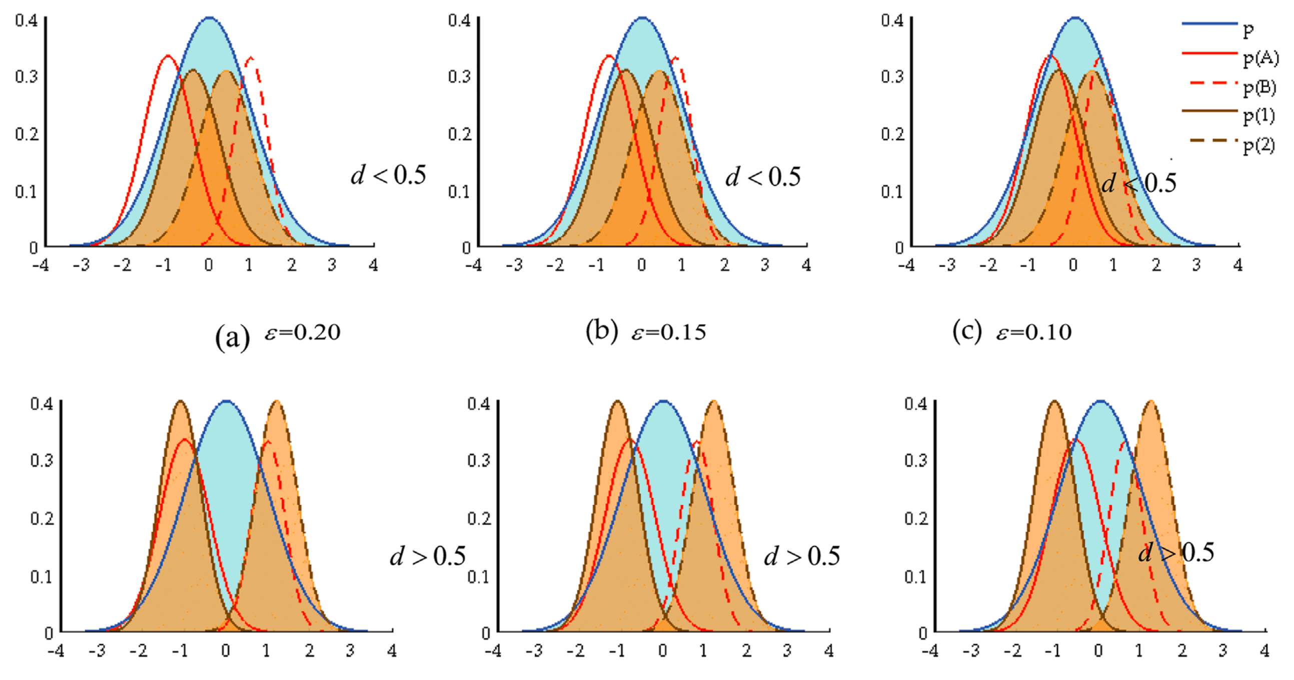

(a) $\varepsilon$=0.20 (b) $\varepsilon$=0.15 (c) $\varepsilon$=0.10

(b) $\varepsilon$=0.20 (e) $\varepsilon$=0.15 (f) $\varepsilon$=0.10

FIGURE 2
Relationship between the GMM displacement parameter and GMM modeling. **(A)** $\varepsilon = 0.20$ **(B)** $\varepsilon = 0.15$ **(C)** $\varepsilon = 0.10$. **(D)** $\varepsilon = 0.20$ **(E)** $\varepsilon = 0.15$ **(F)** $\varepsilon = 0.10$.

Step 4: To determine whether GMM decomposition is necessary, the nonlinearity $\eta$ is calculated by Equation 20.

$$\eta = \frac{1}{2n}\sum_{c=1}^{2n}\eta_c \tag{20}$$

where $\eta_c = \frac{1}{2}\left\| z^{*}_{c,k|k-1} - h\left(\boldsymbol{x}_{k|k-1}\right)\right\|^2$. Set $\gamma$ is threshold. If $\eta_c > \gamma$, it is hypothesized that the high nonlinearity is exhibited in the presence of non-Gaussian noise, necessitating GMM decomposition. Consequently, the algorithm proceeds to the iteration of step 5. In contrast, if $\eta_c < \gamma$, GMM decomposition is not performed, the state estimation $\boldsymbol{x}_{k|k}$ and its corresponding covariance $\boldsymbol{P}_{k|k}$ at the subsequent epoch can be obtained using Equations 13–15.

Step 5: The following iteration (sub-step 1 to sub-step 5) is executed until $d > d_{\max}$.

Sub-step 1: The state prediction $\boldsymbol{x}^1_{k|k-1,d}$, the measurement prediction $\boldsymbol{z}^1_{k|k-1,d}$, and its corresponding covariance $\boldsymbol{P}^1_{k|k-1,d}$ and $\boldsymbol{P}^1_{zz,k|k-1,d}$ are calculated by Equations 4–15.

Sub-step 2: The state prediction $\boldsymbol{x}^2_{k|k-1,d}$, the measurement prediction $\boldsymbol{z}^2_{k|k-1,d}$, and its corresponding covariance $\boldsymbol{P}^2_{k|k-1,d}$ and $\boldsymbol{P}^2_{zz,k|k-1,d}$ are obtained by Equations 4–15.

Sub-step 3: In the presence of two Gaussian components, the cost function in Equation 18 is modified by Equation 21.

$$\begin{aligned} p_g(\boldsymbol{z}_k|\boldsymbol{z}_{k-1},d) = {} & w^1\frac{1}{\sqrt{2\pi\sigma_1^2}}\exp\left(-\frac{1}{2}\left(\frac{\boldsymbol{z}_k-\hat{\boldsymbol{z}}^1_{k|k-1}}{\sigma_1}\right)^2\right) \\ & + w^2\frac{1}{\sqrt{2\pi\sigma_2^2}}\exp\left(-\frac{1}{2}\left(\frac{\boldsymbol{z}_k-\hat{\boldsymbol{z}}^2_{k|k-1}}{\sigma_2}\right)^2\right) \end{aligned} \tag{21}$$

where $w$ is the weight of components, and $\sigma$ is the covariance of measurement noise, superscript represent different components.

Sub-step 4: If $p_g(\boldsymbol{z}_k|\boldsymbol{z}_{k-1},d) \geq \max \ LH$, reset $\max \ LH = p_g(\boldsymbol{z}_k|\boldsymbol{z}_{k-1},d)$, and $\hat{d} = d$.

Sub-step 5: Update the GMM displacement parameter $d$ by Equation 22.

$$d = d + ST \tag{22}$$

Step 6: Based on the weights of components, calculate the state estimation $\boldsymbol{x}_{k|k}$ and its covariance $\boldsymbol{P}_{k|k}$ by Equations 23–26.

$$\boldsymbol{x}_{k|k} = \boldsymbol{x}_{k|k,\hat{d}} = \sum_{g=1}^{2} w_k^{g,\hat{d}}\boldsymbol{x}^g_{k|k} \tag{23}$$

$$\boldsymbol{P}_{k|k} = \boldsymbol{P}_{k|k,\hat{d}} = \sum_{g=1}^{2} w_k^{g,\hat{d}}\left[\boldsymbol{P}^g_{k|k} + \left(\boldsymbol{x}^g_{k|k}-\boldsymbol{x}_{k|k}\right)\left(\boldsymbol{x}^g_{k|k}-\boldsymbol{x}_{k|k}\right)^{\mathrm{T}}\right] \tag{24}$$

$$\omega_k^i = \omega_{k-1}^i\beta_k^i \Big/ \sum_{i=1}^{2}\omega_{k-1}^i\beta_k^i \tag{25}$$

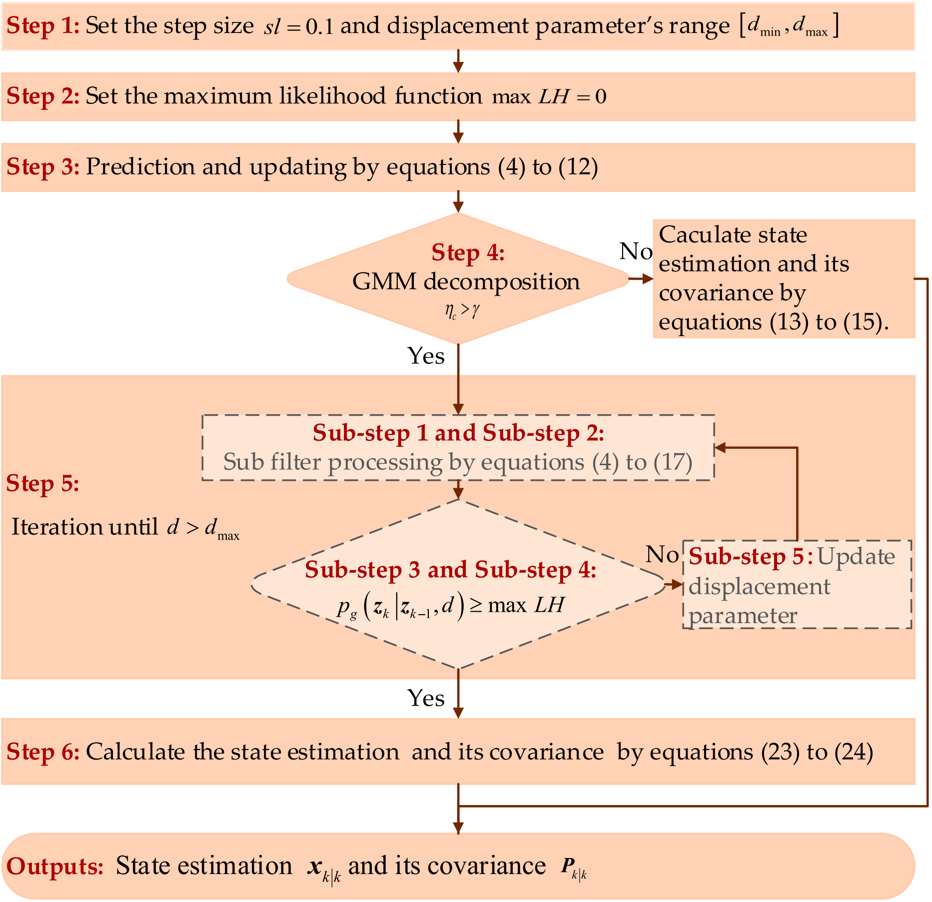

FIGURE 3
The flowchart of the proposed AGSCKF.

$$\beta_k^i \approx \mathrm{N}\left(L_k - A_k \overline{X}_k, A_k \Sigma_{\overline{X}_k} A_k^{\mathrm{T}} + \Sigma_k^i\right) \tag{26}$$

Through the aforementioned calculation procedures, it becomes evident that the GMM displacement parameter can be adaptively adjusted, thereby bringing the non-Gaussian noise model shown in Equation 17 closer to that shown in Equation 3. This approach effectively addresses the limitations of GMM modeling inherent in the GSCKF. Consequently, the AGSCKF proposed in this section is theoretically expected to exhibit superior estimation accuracy compared to the GSCKF. The flowchart for the proposed AGSCKF is illustrated in Figure 3.

# 4 Performance evaluation and discussions

The proposed AGSCKF has been thoroughly assessed through simulations and experiments for GNSS/SINS tightly coupled integrated navigation system data fusion. In this section, the comparison and analysis of the proposed AGSCKF with CKF and GSCKF are discussed.

## 4.1 Simulations and analysis

The proposed AGSCKF is assessed for the data fusion of an UAV utilizing a GNSS/SINS tightly coupled integrated navigation system. The simulate trajectory of UAV flight, which includes various maneuvering states such as climbing, level flight, turning, and descending, is depicted in Figure 4. The initial attitude of UAV is all 0° in pitch, row and yaw respectively; the initial velocities are set as 0 m/s, 120 m/s and 0 m/s in the east, north and up respectively; the initial position is set as 110.20°, 34.00° and 2,000 m in longitude, latitude and altitude respectively. The simulated sensor's parameters for the GNSS/SINS tightly coupled integrated navigation system are listed in Table 1. The GNSS measurement utilized in the simulation was derived from satellite constellations and epoch information obtained on 28 July 2023. Simulation duration is 1,000 s. Computer utilized in simulations encompasses an Intel Core i7-12700 CPU, 128 GB DDR4 memory, and Matlab R2020b software.

The initial parameters for three different algorithms (CKF, GSCKF and AGSCKF) are given in Table 2. The measurement non-Gaussian noise is generated by Equation 27.

$$p(\nu_k) \approx 0.9N(0, \Sigma_{\mathrm{A}}) + 0.1N(0.5, \Sigma_{\mathrm{B}}) \tag{27}$$

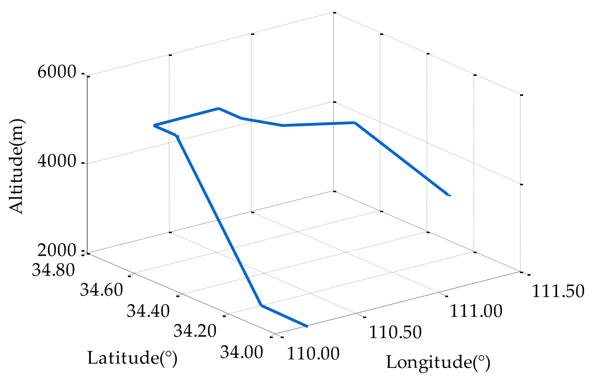

FIGURE 4
UAV flight trajectory.

TABLE 1 Sensor's parameters.

| Parameter | | Value |
|---|---|---|
| Gyroscope | Constant drift | 0.1°/h |
| | Random walk coefficient | 0.01°/h |
| Accelerometers | Zero bias | 0.001 g |
| | Random walk coefficient | $0.001\,\mathrm{g}\cdot\sqrt{s}$ |
| | Sampling frequency | 50 Hz |
| GNSS receiver | Pseudo range observation error | 15 m |
| | Sampling frequency | 1 Hz |

where $\boldsymbol{\Sigma}_{\mathrm{A}} = 3\boldsymbol{\Sigma}_{\mathrm{B}} = \mathrm{diag}(0.3^2\cdots0.3^2)$. In order to evaluate the performance of three different algorithms in terms of time-varying non-Gaussian noise, two different changes were implemented to the measurement non-Gaussian noise, respectively. During the epoch period from 401 s to 500 s and the epoch period from 601 s to 800 s, the measurement non-Gaussian noise is generated by Equation 28.

$$p(\boldsymbol{v}_k) \approx 0.7N(0,\boldsymbol{\Sigma}_{\mathrm{A}}) + 0.3N(0.5,\boldsymbol{\Sigma}_{\mathrm{B}}) \tag{28}$$

where $\boldsymbol{\Sigma}_{\mathrm{A}} = 3\boldsymbol{\Sigma}_{\mathrm{B}} = \mathrm{diag}(0.5^2\cdots0.5^2)$.

The attitude error curves and positioning error curves of various algorithms (CKF, GSCKF, and AGSCKF) are illustrated in Figure 5. As can be observed from it, prior to the occurrence of changes for non-Gaussian noise statistical properties (0 s–400 s), the estimation error of CKF is highest of the three, while the estimation accuracies of GSCKF and AGSCKF are nearly equal and superior to that of CKF. This phenomenon can be attributed to the fact that GSCKF and AGSCKF employ GMM to model non-Gaussian noise, thereby mitigating its impact on estimation accuracy and ensuring enhanced attitude and positioning accuracy of GNSS/SINS tightly coupled integrated navigation systems operating in non-Gaussian noise environments.

However, upon the occurrence of changes for non-Gaussian noise statistical properties (401 s–500 s, and 601 s–

TABLE 2 Initial parameters for the algorithms.

| Parameter | | Value |
|---|---|---|
| Attitude error | Yaw | 1.5′ |
| | Pitch | 1′ |
| | Roll | 1′ |
| Velocity error | East | 0.5 m/s |
| | North | 0.5 m/s |
| | Up | 0.5 m/s |
| Position error | Longitude | 10 m |
| | Latitude | 10 m |
| | Altitude | 15 m |

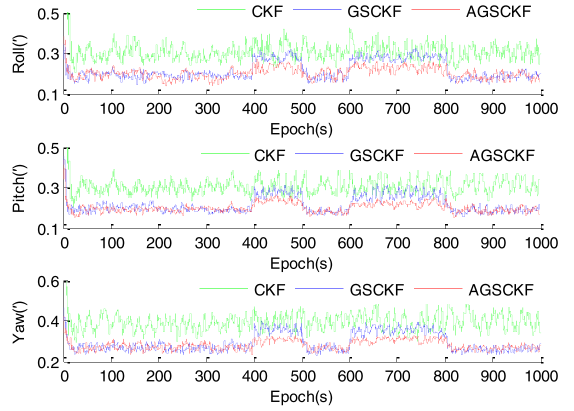

(a) Attitude

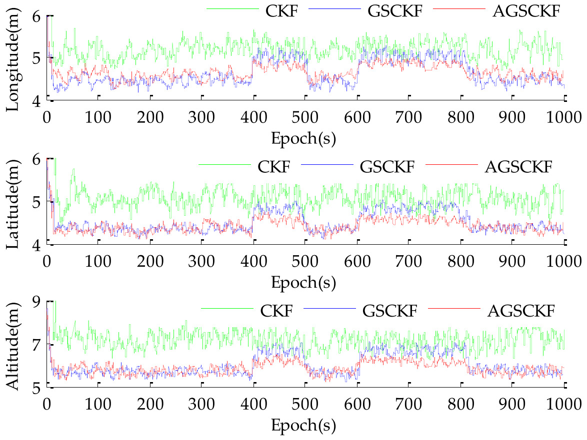

(b) Position

FIGURE 5
Estimation errors by the CKF, GSCKF and proposed AGSCKF for simulations. **(A)** Attitude **(B)** Position.

TABLE 3 (a): RMSEs of attitude errors (′). (b) RMSEs of position errors (′).

| Algorithm | Attitude | 0 s–400 s | 401 s–500 s | 601 s–800 s | 801 s–1,000 s |
|---|---|---|---|---|---|
| CKF | Roll | 0.292 | 0.318 | 0.313 | 0.297 |
| | Pitch | 0.288 | 0.294 | 0.304 | 0.286 |
| | Yaw | 0.365 | 0.388 | 0.389 | 0.365 |
| GSCKF | Roll | 0.223 | 0.258 | 0.253 | 0.222 |
| | Pitch | 0.218 | 0.244 | 0.244 | 0.212 |
| | Yaw | 0.317 | 0.343 | 0.342 | 0.311 |
| AGSCKF | Roll | 0.218 | 0.235 | 0.238 | 0.213 |
| | Pitch | 0.213 | 0.228 | 0.224 | 0.200 |
| | Yaw | 0.298 | 0.308 | 0.308 | 0.298 |
| **Algorithm** | **Position** | **0 s–400 s** | **401 s–500 s** | **601 s–800 s** | **801 s–1,000 s** |
| CKF | Longitude | 5.589 | 5.787 | 5.782 | 5.585 |
| | Latitude | 5.591 | 5.634 | 5.739 | 5.593 |
| | Altitude | 7.998 | 8.102 | 8.103 | 7.993 |
| GSCKF | Longitude | 4.521 | 4.872 | 4.875 | 4.522 |
| | Latitude | 4.519 | 4.611 | 4.612 | 4.514 |
| | Altitude | 5.654 | 6.361 | 6.366 | 5.658 |
| AGSCKF | Longitude | 4.327 | 4.623 | 4.625 | 4.326 |
| | Latitude | 4.340 | 4.467 | 4.467 | 4.337 |
| | Altitude | 5.537 | 5.793 | 5.866 | 5.493 |

TABLE 4 The average time spent per epoch (ms).

| Algorithm | 0 s–400 s | 401 s–500 s | 601 s–800 s | 801 s–1,000 s |
|---|---|---|---|---|
| CKF | 5.79 | 5.65 | 5.84 | 5.92 |
| GSCKF | 8.28 | 8.32 | 7.92 | 8.52 |
| AGSCKF | 13.73 | 16.73 | 16.61 | 13.68 |

800 s), a significant increase in estimation error is observed for GSCKF as compared to AGSCKF. The discrepancy is caused by the change of non-Gaussian noise and the inability of the GMM displacement parameter of GSCKF to adapt accordingly, which leads to deterioration of estimation accuracy due to inaccurate GMM modeling for GSCKF. In contrast, the AGSCKF employs adaptive corrected GMM displacement parameter to achieve real-time tracking of time-varying non-Gaussian noise, thereby achieving more stable estimation performance than GSCKF.

In order to exemplify the impartiality of algorithm comparison, the root mean square error (RMSE) with 100 Monte-Carlo simulations is used to quantify the estimation accuracy of all the algorithms, which is defined by Equation 29.

$$\mathrm{RMSE} = \sqrt{\frac{1}{N}\sum_{i=1}^{I}\left(\overline{\boldsymbol{X}}_i - \boldsymbol{X}_i\right)^2} \tag{29}$$

where $N$ is the total number of Monte Carlo simulations; $\boldsymbol{X}_i$ is the reference; $\overline{\boldsymbol{X}}_i$ is the state estimation. And the time consumption

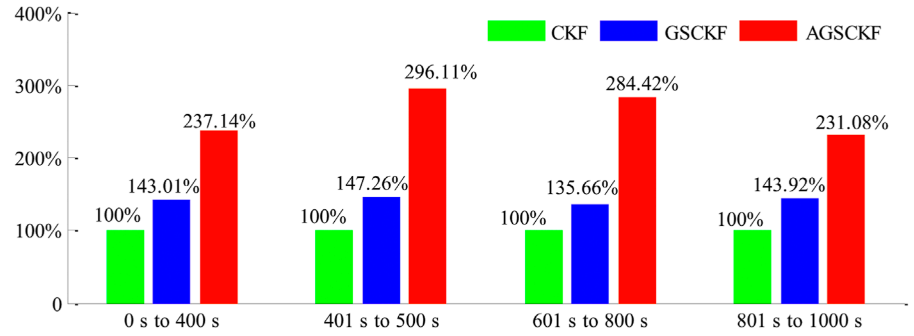

FIGURE 6
Relative computational complexity of the three different algorithms.

**TABLE 5** Parameters of GNSS/SINS tightly coupled navigation system.

| Sensors | Parameter | Value |
|---|---|---|
| SINS | Gyroscope constant drift | $10^{\circ}/h$ |
| | Gyroscope random walk coefficient | $0.6^{\circ}/\sqrt{h}$ |
| | Accelerometer zero bias | 40 $\mu g$ |
| | Accelerometer random walk coefficient | 80 $\mu g\cdot\sqrt{h}$ |
| | Sampling rate | 100/Hz |
| GNSS | Positioning errors | 15/m |
| | Sampling rate | 10/Hz |

**TABLE 6** Statistical characteristics analysis of G22 pseudo-range noise.

| Epoch periods | Pseudo-range noise | | |
|---|---|---|---|
| | Mean/(m) | Covariance/(m) | Kurtosis |
| [201 s, 300 s] | 0.997 | 0.881 | 0.90 |
| [801 s, 900 s] | 0.156 | 0.225 | 3.06 |
| [1,101 s, 1,200 s] | 0.178 | 0.264 | 2.89 |
| [1,301 s, 1,400 s] | 0.823 | 0.732 | 1.34 |

per epoch is calculated for the quantitative comparison of the computational complexity of various algorithms.

As shown in Table 3, the yaw is taken as an example. Prior to the occurrence of changes for non-Gaussian noise statistical properties (0 s–400 s), the estimation accuracy of GSCKF and AGSCKF are relatively close ($0.317'$ and $0.298'$), both of which are higher than that of CKF ($0.365'$). When the first occurrence of changes for non-Gaussian noise statistical properties (401 s–500 s), AGSCKF achieves higher estimation accuracy due to real-time correction of GMM displacement parameter by AGSCKF. Compared to GSCKF and CKF, it has increased by $0.035'$ and $0.080'$, respectively. When the second occurrence of changes (601 s–800 s), the accuracy advantage of AGSCKF estimation is significant, with AGSCKF improving $0.034'$ and $0.081'$ compared to GSCKF and CKF, respectively.

As depicted in Table 4 and Figure 6, it reveals that the changes of computation time for all three algorithms are relatively similar in all different epoch periods. Take epochs 601 s–800 s as example, the analysis of the average time spent per epoch reveals that CKF has the shortest computational time (5.84 ms) among all the algorithms. In contrast, the computational time of GSEKF is significantly larger than that of CKF by at least 135.66% times (7.92 ms). This is due to the complex computational process of GSCKF involved in distributed filtering and global point estimation at each epoch. Furthermore, the computational time of AGSCKF is at least 284.42% longer (16.61 ms) than that of CKF because AGSCKF needs to update the GMM displacement parameter by iteration.

## 4.2 Experiments and analysis

This section presents the analysis and verification of the performance of the proposed AGSCKF through experiments. The experimental data was collected from a GNSS/SINS tightly coupled integrated navigation system mounted on UAVs. The experiment was conducted on 18 Oct 2023, at Zhengzhou, China. Table 5 shows the parameters of the SINS device and GNSS receiver in the GNSS/SINS tightly coupled integrated navigation system.

The initial position of the UAV was at latitude 34.654°, longitude 109.193°, and altitude 3,783 m, with initial velocities of 180 m/s, 60 m/s, and 40 m/s in the east, north, and up directions, respectively. The other initial parameters were consistent with those utilized in the simulations. A continuous data collection was conducted for a duration of 3,000 s, encompassing various maneuvering states such as climbing, level flight, turning, and descending. To ensure accurate results, a GNSS reference station was placed on the ground within a maximum distance of 20 km from the UAV. The differential data calculation result between the GNSS receiver on the UAV and the GNSS reference station served as the reference value. Subsequent post-processing yielded a differential positioning result with an accuracy better than 0.1 m. Three different algorithms

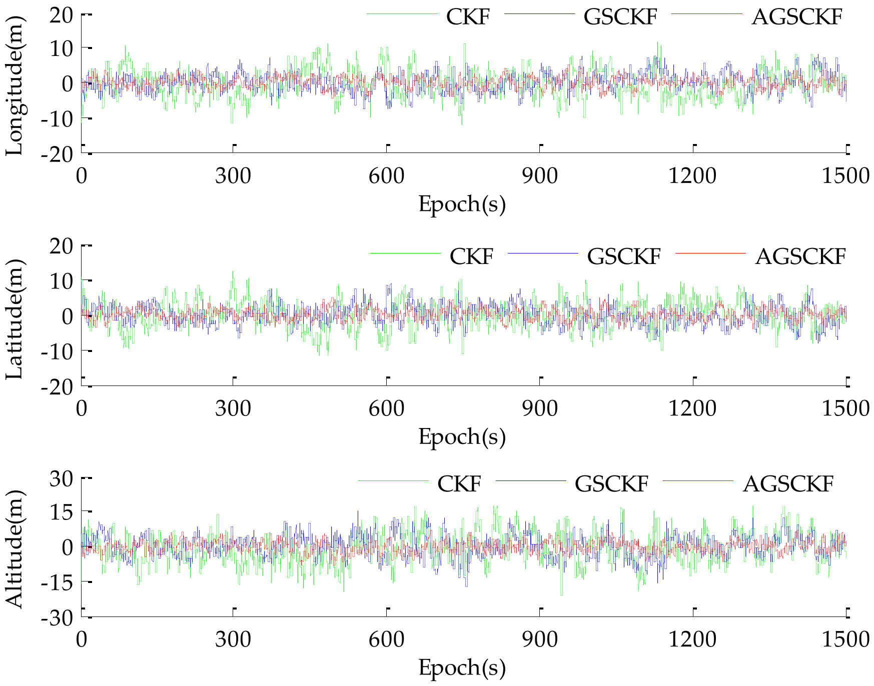

FIGURE 7
Position errors by CKF, GSCKF and proposed AGSCKF for experiment case.

**TABLE 7** Comparison of estimation results with different datasets.

| Algorithms | 1,500 sets data | | | 3,000 sets data | | | The average time spent per epoch (ms) |
|---|---|---|---|---|---|---|---|
| | Longitude (m) | Latitude (m) | Altitude (m) | Longitude (m) | Latitude (m) | Altitude (m) | |
| CKF | 3.835 | 3.945 | 7.043 | 4.067 | 4.186 | 7.557 | 8.7 |
| GSCKF | 3.245 | 3.294 | 4.154 | 3.384 | 3.433 | 4.366 | 13.4 |
| AGSCKF | 2.854 | 2.975 | 3.583 | 2.953 | 3.076 | 3.735 | 16.9 |

same with simulation were employed for data fusion (CKF, GSCKF, and AGSCKF).

To assess the non-Gaussian and time-varying nature of GNSS measurement noise in experimental data, the statistical analysis was conducted on the pseudo-range noise of GNSS. The non-Gaussian nature of noise was measured using kurtosis. When $K = 3$, the noise follows a Gaussian distribution; otherwise, it can be concluded that the noise does not follow a Gaussian distribution. When $K > 3$, the noise obeys a super-Gaussian distribution or a thick-tailed distribution; when $K < 3$, the noise obeys a sub-Gaussian distribution (Celikoglu and Tirnakli, 2018; Hatem et al., 2022). Table 6 presents the statistical characteristics of pseudo-range noise for the G22 satellite during different epoch periods.

As depicted in Table 6, the kurtosis of the pseudo-range noise generated by the G22 satellite is noticeably less than 3 within the epoch intervals of [201,300] (s) and [1,301, 1,400] (s), indicating a negative kurtosis. This suggests that the G22 pseudo-range noise exhibits significant non-Gaussian characteristics. Conversely, the kurtosis of satellite's pseudo-range noise within the epoch intervals of [801, 900] (s) and [1,101, 1,200] (s) are close to 3. As such, the G22 pseudo-range noise exhibits relatively weak non-Gaussian characteristics. This observation highlights the temporal variation in the statistical characteristics of non-Gaussian noise from measurement, which can be characterized as time-varying non-Gaussian noise.

The positioning error curves of different algorithms (CKF, GSCKF, and AGSCKF) during the epoch period of [0, 1,500] (s) are depicted in Figure 7. As observed from it, the range of changes for the CKF positioning error curve is significantly higher than that of GSCKF and AGSCKF. This can be attributed to the fact that CKF is unable to effectively counteract the influence of non-Gaussian noise, resulting in a larger positioning error. However, due to the use of GMM in GSCKF to accurately process the random model, the impact of non-Gaussian noise is mitigated. Consequently, the positioning accuracy of GSCKF has been enhanced. Furthermore, the maximum value of the positioning error curve variation range of AGSCKF is smaller than that of GSCKF. The main reason is that AGSCKF takes into account the time-varying non-Gaussian noise and employs the adaptive algorithm of GMM displacement parameter to improve the accuracy of GMM modeling, thereby minimizing the positioning error of AGSCKF.

To further validate the performance of the proposed AGSCKF, Table 7 presents a quantitative comparison of the RMSEs of different algorithms (CKF, GSCKF, and AGSCKF) for both 1,500 sets data and 3,000 sets data. As observed from it, an increase in navigation duration leads to a decrease in estimation accuracy for all algorithms. Specifically, when considering longitude positioning error as an example, CKF exhibits a reduction from 3.835 m to 4.067 m (about 5.70%), GSCKF shows a reduction from 3.245 m to 3.384 m (about 4.10%), and AGSCKF experiences a reduction from 2.854 m to 2.953 m (about 3.35%). It is evident that the estimation accuracy of AGSCKF consistently surpasses that of CKF and GSCKF. This highlights that AGSCKF not only possesses robust processing capabilities for time-varying non-Gaussian noise but also significantly enhances the GNSS/SINS tightly coupled integrated navigation positioning accuracy of UAVs in challenge environments. Furthermore, it maintains excellent stability of GNSS/SINS tightly coupled integrated positioning in long-sailing missions.

The computational complexity of AGSCKF is analyzed. It is observed that AGSCKF slightly increases the computation time per epoch, but does not result in a significant decrease in computational efficiency. This can be attributed to the fact that although AGSCKF requires iterative calculation of the GMM displacement parameter, relatively high-accuracy estimation can reduce the initial sensitivity of GMM and accelerate the convergence speed of GMM displacement parameter estimation.

In conclusion, the experiment confirms the same conclusion as the simulations, namely, that AGSCKF outperforms the other two algorithms (CKF and GSCKF) in terms of estimation accuracy and adaptability of GNSS/SINS tightly coupled integrated navigation data fusion.

## 5 Conclusion

The limitations of the GSCKF in the context of time-varying non-Gaussian noise of GNSS/SINS tightly coupled integrated navigation systems is analyzed theoretically. It is revealed that the GMM displacement parameter between Gaussian components significantly impact the accuracy of GMM fitting. To address this issue, a novel adaptive adjustment method for GMM displacement parameter is presented, which dynamically modifies this parameter through the cost function, thereby enhancing the rationality of the GMM decomposition process. This approach is incorporated into GSCKF to improve filtering accuracy, and effectively addresses the challenges posed by time-varying non-Gaussian noise, providing a viable solution to achieve high-accuracy estimation for GNSS/SINS tightly coupled integrated navigation systems operating in maneuvering states within challenging environments. Simulations and experiments demonstrate that the proposed AGSCKF enhances the estimation accuracy and adaptability of GSCKF in non-Gaussian noise condition, and exhibits superior stability in long-sailing missions. The research findings have significant implications for both nonlinear non-Gaussian filtering theory and GNSS/SINS tightly coupled integrated navigation systems data fusion algorithms for engineering applications.

While the proposed AGSCKF proves to be effective in modeling time-varying non-Gaussian noise in GNSS/SINS tightly coupled integrated navigation systems, it disregards the undefined noise scenarios, rendering the random model unable to adapt to the statistical characteristics of undefined noise. This limitation impairs the ability of AGSCKF proposed in this paper to effectively address undefined noise, potentially leading to a decline in estimation accuracy under severe conditions. So, the real-time dynamic GMM modeling techniques for undefined noise are very meaningful research points in the future.

## Data availability statement

The raw data supporting the conclusions of this article will be made available by the authors, without undue reservation.

## Author contributions

QD: Writing–original draft, Writing–review and editing. RW: Writing–review and editing. S-YH: Writing–review and editing. G-RX: Writing–original draft.

## Funding

The author(s) declare that financial support was received for the research, authorship, and/or publication of this article. This research was funded by the following projects: The National Natural Science Foundation of China, grant number 42274045; the Henan Province Science and Technology Research Projects, grant number 242102241067; The Key Research Funding Projects for Higher Education Institutions in Henan Province, grant number 24A420003.

## Conflict of interest

The authors declare that the research was conducted in the absence of any commercial or financial relationships that could be construed as a potential conflict of interest.

## Publisher's note

# References

Alspach, D., and Sorenson, H. (1972). Nonlinear bayesian estimation using Gaussian sum approximations. *IEEE Trans. Automatic Control* 17, 439–448. doi:10.1109/TAC.1972.1100034

Arasaratnam, I., and Haykin, S. (2009). Cubature kalman filters. *IEEE Trans. automatic control* 54, 1254–1269. doi:10.1109/TAC.2009.2019800

Bai, J. G., Ge, Q. B., Li, H., Xiao, J. M., and Wang, Y. L. (2022). Aircraft trajectory filtering method based on Gaussian-sum and maximum correntropy square-root cubature kalman filter. *Cognitive Comput. Syst.* 4, 205–217. doi:10.1049/ccs2.12049

Boguspayev, N., Akhmedov, D., Raskaliyev, A., Kim, A., and Sukhenko, A. (2023). A comprehensive review of GNSS/INS integration techniques for land and air vehicle applications. *Appl. Sci.* 13 (8), 4819. doi:10.3390/APP13084819

Celikoglu, A., and Tirnakli, U. (2018). Skewness and kurtosis analysis for non-Gaussian distributions. *Phys. A Stat. Mech. its Appl.* 499, 325–334. doi:10.1016/j.physa.2018.02.035

Chen, H. K., Lu, T. D., Huang, J. H., He, X. X., Yu, K. G., Sun, X. W., et al. (2023). An improved VMD-LSTM model for time-varying GNSS time series prediction with temporally correlated noise. *Remote Sens.* 15 (14), 3694. doi:10.3390/RS15143694

Dai, Q., Xiao, G. R., Zhou, G. H., Ye, Q., and Han, S. Y. (2024). A novel Gaussian sum quaternion constrained cubature Kalman filter algorithm for GNSS/SINS integrated attitude determination and positioning system. *Front. Neurorobotics* 18, 1374531. doi:10.3389/fnbot.2024.1374531

Dong, J. Q., Lian, Z. Z., Xu, J. C., and Yue, Z. (2023). UWB localization based on improved robust adaptive cubature kalman filter. *Sensors* 23 (5), 2669. doi:10.3390/S23052669

Elmezayen, A., and El-Rabbany, A. (2021). Real-time GNSS precise point positioning using improved robust adaptive kalman filter. *Surv. Rev.* 53, 528–542. doi:10.1080/00396265.2020.1846361

Ge, Q. B., Cheng, Y., Yao, G., Chen, S., and Zhu, Y. (2024). Credible Gaussian sum cubature Kalman filter based on non-Gaussian characteristic analysis. *Neurocomputing* 565, 126922. doi:10.1016/J.NEUCOM.2023.126922

George, S. M., Selvi, S. S., and Raol, J. R. (2022). Aircraft parameter estimation using Gaussian sum extended information filter with lyapunov stability analysis. *Int. J. Veh. Struct. and Syst.* 14, 540–545. doi:10.4273/IJVSS.14.4.23

Grewal, M. S., Andrews, A. P., and Bartone, C. G. (2020). *Global navigation satellite systems, inertial navigation, and integration*. Hoboken, NJ, USA: John Wiley and Sons. doi:10.1002/9781119547860

Groves, D. P. (2008). *Principles of GNSS, inertial, and multisensor integrated navigation systems*. London, England: Artech House, 7–20. doi:10.1017/s0373463313000672_1

Gyagenda, N., Hatilima, J. V., Roth, H., and Zhmud, V. (2022). A review of GNSS-independent UAV navigation techniques. *Robotics Aut. Syst.* 152, 104069. doi:10.1016/J.ROBOT.2022.104069

Hatem, G., Zeidan, J., Goossens, M., and Moreira, C. (2022). Normality testing methods and the importance of skewness and kurtosis in statistical analysis. *BAU Journal-Science Technol.* 3 (2), 7. doi:10.54729/KTPE9512

Hu, G. G., Gao, B. B., Zhong, Y. M., and Gu, C. F. (2020). Unscented kalman filter with process noise covariance estimation for vehicular ins/gps integration system. *Inf. Fusion* 64, 194–204. doi:10.1016/j.inffus.2020.08.005

Huang, W., Xie, H. S., Shen, C., and Li, J. P. (2016). A robust strong tracking cubature kalman filter for spacecraft attitude estimation with quaternion constraint. *Acta Astronaut.* 121, 153–163. doi:10.1016/j.actaastro.2016.01.009

Jiang, H., Zhang, Y., Wang, X., and Cai, Y. (2024). Observability-based Gaussian sum cubature Kalman filter for three-dimensional target tracking using a single two-dimensional radar. *Remote Sens.* 16 (22), 4172. doi:10.3390/rs16224172

Legin, R., Adam, A., Hezaveh, Y., and Perreault-Levasseur, L. (2023). Beyond Gaussian noise: a generalized approach to likelihood analysis with non-Gaussian noise. *Astrophysical J. Lett.* 949 (2), L41. doi:10.3847/2041-8213/ACD645

Li, B. F., and Chen, G. E. (2022). Improving the combined GNSS/INS positioning by using tightly integrated RTK. *GPS Solutions* 26 (4), 144. doi:10.1007/S10291-022-01331-2

Li, D. G., Wu, Y. Q., and Zhao, J. M. (2020). Novel hybrid algorithm of improved CKF and GRU for GPS/INS. *IEEE Access* 8, 202836–202847. doi:10.1109/ACCESS.2020.3035653

Lin, X. Y., Liu, L. L., Dong, Y. Y., Chen, X. G., and Yang, H. L. (2023). Improved adaptive filtering algorithm for GNSS/SINS integrated navigation system. *Geomatics Inf. Sci. Wuhan Univ.* 48, 127–134. doi:10.13203/j.whugis20200436

Monfort, A., Renne, J. P., and Roussellet, G. (2015). A quadratic Kalman filter. *J. Econ.* 187, 43–56. doi:10.1016/j.jeconom.2015.01.003

Panda, A., Mahapatra, S., Ag, K. R., and Panda, R. C. (2024b). Lowering carbon emissions from a zinc oxide rotary kiln using event-scheduling observer-based economic model predictive controller. *Chem. Eng. Res. Des.* 207, 420–438. doi:10.1016/j.cherd.2024.06.017

Panda, A., Thirunavukarasu, N., and Panda, R. C. (2024a). Predictive control scheme by integrating event-triggered mechanism and disturbance observer under actuator failure and sensor fault. *Proc. Institution Mech. Eng. Part I J. Syst. Control Eng.* 238 (4), 621–647. doi:10.1177/09596518231204725

Rhudy, M., Gu, Y., Gross, J., and Napolitano, M. R. (2011). *Sensitivity analysis of EKF and UKF in GPS/INS sensor fusion. AIAA guidance navigation and control conference*. Portland, Oregon, USA. doi:10.2514/6.2011-6491

Sindhuja, P. P., Panda, A., Velappan, V., and Panda, R. C. (2023). Disturbance-observer-based finite time sliding mode controller with unmatched uncertainties utilizing improved cubature Kalman filter. *Trans. Inst. Meas. Control* 45 (9), 1795–1812. doi:10.1177/01423312221140507

Sun, B., Zhang, Z. W., Liu, S. C., Yan, X. B., and Yang, C. X. (2022). Integrated navigation algorithm based on multiple fading factors kalman filter. *Sensors* 22, 5081. doi:10.3390/S22145081

Sun, L. L., Cao, Y. H., Wu, W. H., and Liu, Y. T. (2020). A multi-target tracking algorithm based on Gaussian mixture model. *J. Syst. Eng. Electron.* 31, 482–487. doi:10.23919/jsee.2020.000020

Taghizadeh, S., and Safabakhsh, R. (2023). Low-cost integrated INS/GNSS using adaptive H∞ cubature kalman filter. *J. Navigation* 76, 1–19. doi:10.1017/S0373463322000583

Tang, J., Bian, H. W., Ma, H., and Wang, R. Y. (2023). Initialization of SINS/GNSS error covariance matrix based on error states correlation. *IEEE Access* 11, 94911–94917. doi:10.1109/ACCESS.2023.3293158

Wang, G. C., Xu, X. S., and Zhang, T. (2020). M-M estimation-based robust cubature kalman filter for INS/GPS integrated navigation system. *IEEE Trans. Instrum. Meas.* 70, 1–11. doi:10.1109/TIM.2020.3021224

Wang, J. W., Chen, X. Y., and Shi, C. F. (2023). A novel robust iterated CKF for GNSS/SINS integrated navigation applications. *Eurasip J. Adv. Signal Process.* 1, 83. doi:10.1186/S13634-023-01044-9

Wang, M. S., Wu, W. Q., Zhou, P. Y., and He, X. F. (2018). State transformation extended Kalman filter for GPS/SINS tightly coupled integration. *GPS Solutions* 22, 112–12. doi:10.1007/s10291-018-0773-3

Xiao, G. R., Yang, C., Wei, H. P., Xiao, Z. Y., Zhou, P. Y., Li, P. G., et al. (2024). PPP ambiguity resolution based on factor graph optimization. *GPS solutions* 28 (4), 178. doi:10.1007/s10291-024-01715-6

Yu, B., Zhang, Y. Z., Xie, W. S., Zuo, W. J., Zhao, Y. M., and Wei, Y. L. (2023). A network traffic anomaly detection method based on Gaussian mixture model. *Electronics* 12 (6), 1397. doi:10.3390/ELECTRONICS12061397

Zhang, B., Wang, X. D., Lu, H., Hao, Z. J., and Gu, C. C. (2021). Application of adaptive robust CKF in SINS/GPS initial alignment with large azimuth misalignment angle. *Math. Problems Eng.* 2021, 1–6. doi:10.1155/2021/7398706

Zhang, Q., Niu, X. J., and Shi, C. (2020). Impact assessment of various IMU error sources on the relative accuracy of the GNSS/INS systems. *IEEE Sensors J.* 20, 5026–5038. doi:10.1109/jsen.2020.2966379

Zhou, P., Xiao, G., and Du, L. (2024). Initial performance assessment of galileo high accuracy service with software-defined receiver. *GPS solutions* 28 (1), 2. doi:10.1007/s10291-023-01540-3

Frontiers in Physics

TYPE Original Research
PUBLISHED 09 April 2025
DOI 10.3389/fphy.2025.1557330

Check for updates

OPEN ACCESS

EDITED BY
Zhu Xiao,
Hunan University, China

REVIEWED BY
Lixun Li,
Air Force Engineering University, China
Kai Li,
Chinese Academy of Sciences (CAS), China

*CORRESPONDENCE
Bin Fan,
fb540623907@163.com

RECEIVED 08 January 2025
ACCEPTED 11 March 2025
PUBLISHED 09 April 2025

CITATION
Yao L, Fan B, Qin H, Xian D, Gu B, Sha H, Guan G, Liu Z, He D and Zhang L (2025) A research on low-earth-orbit signal-of-opportunity interference suppression algorithm based on adaptive signal iterative subspace projection technique. *Front. Phys.* 13:1557330.
doi: 10.3389/fphy.2025.1557330

# A research on low-earth-orbit signal-of-opportunity interference suppression algorithm based on adaptive signal iterative subspace projection technique

Lihao Yao[1,2], Bin Fan[3]*, Honglei Qin[2], Deyong Xian[1], Boyun Gu[4], Hai Sha[1], Gangqiang Guan[1], Zhijun Liu[1], Donghan He[1] and Liwei Zhang[1]

[1]Beijing Satellite Navigation Center, Beijing, China, [2]School of Electronics and Information Engineering, Beihang University, Beijing, China, [3]PLA Army Academy of Artillery and Air Defense, Hefei, China, [4]Beijing Institute of Technology, Beijing, China

Signal-of-Opportunity (SOP) positioning based on Low-Earth-Orbit (LEO) constellations has gradually become a research hotspot. LEO satellite SOP positioning possess strong anti-jamming capabilities due to their large quantity, wide spectral coverage, and high signal power. However, few studies have deeply investigated their anti-jamming performance, particularly regarding the most common interference type faced by ground receivers - Periodic Frequency Modulation (PFM) interference. The downlink signals of LEO satellites differ significantly from those of Global Navigation Satellite Systems (GNSS) based on Medium-Earth-Orbit (MEO) or Geostationary-Earth-Orbit (GEO) satellites, making traditional interference suppression methods inapplicable. In this paper, we utilize the generalized periodicity of PFM interference signals and the characteristics of LEO constellation signals to propose an Adaptive Signal Iterative Projection and Interference Suppression (ASIPIS) algorithm. This algorithm concentrates the energy of PFM interference, which is dispersed over a wide bandwidth, into a few frequency points, enhancing the concentration of the interference and its separation from the LEO satellite signals. This effectively reduces the overlap between LEO satellite signals and interference. The algorithm then uses subspace projection to map the interference and the desired signal into different subspaces, eliminating the interference components and thus reducing the damage to the desired signal during the interference suppression process. Simulations and experiments demonstrate that compared to conventional methods, ASIPIS effectively eliminates single/multi-component PFM interference, improves suppression performance under narrow-bandwidth/high-power conditions, and overcomes limitations of traditional PFM interference suppression approaches for single-antenna LEO signal reception. The significant performance improvement in LEO anti-jamming scenarios against PFM interference confirms the algorithm's value.

KEYWORDS

**signal of Opportunity, low-earth-orbit satellite, PFM, anti-jamming, adaptive signal iterative, subspace projection**

## 1 Introduction

With the development of the Global Navigation Satellite System (GNSS), GNSS has become an important infrastructure for a country's information construction. It provides Positioning, Navigation, and Timing (PNT) services for a wide range of applications [1–5]. However, with the deepening of GNSS applications, its own shortcomings have gradually become apparent. These drawbacks primarily include: low signal power at the ground, limited frequency points, high construction and maintenance costs, and vulnerability to malicious interference, which can lead to service unavailability, especially in times of conflict or crisis [6–8]. Overcoming and addressing these GNSS shortcomings, particularly the ability to independently provide reliable and high-precision PNT services in environments where GNSS services are unavailable, has become a key focus for future development [9, 10].

Currently, nations are actively developing resilient PNT systems to ensure that military equipment can achieve accurate positioning even when GNSS performance is degraded or denied. Notably, the U.S. Department of Defense's 2020 PNT technology development roadmap highlighted the use of Signals of Opportunity (SOP) for absolute positioning, thereby supplementing GPS functionality and enhancing its availability and robustness. SOP positioning is a technology that utilizes any detectable non-navigation signals, such as acoustic, optical, electrical, magnetic, and force-based information, for positioning purposes. Given the abundance of radio signals from various applications in space, current research primarily focuses on radio-based SOP. SOP typically includes terrestrial and space-based radio signals of opportunity. However, terrestrial SOP has limited coverage and struggles to achieve seamless global coverage in areas such as deserts, oceans, and polar regions. Space-based SOP mainly refers to signals transmitted by non-navigation/non-cooperative satellites. With the recent significant development and deployment of Low-Earth-Orbit (LEO) satellites by various countries, space-based LEO satellite SOP (LEO-SOP) has emerged as a primary space-based SOP and is increasingly being applied in navigation and positioning [11, 12]. Compared to traditional GNSS-based navigation, SOP positioning using LEO satellites mainly relies on the downlink signals from communication satellites as the radiation source for positioning ground terminals. The positioning methods include instantaneous Doppler, instantaneous Doppler combined with pseudorange, and carrier phase differential techniques [13–15]. Additionally, with the rapid development of emerging satellite constellations such as Starlink and OneWeb, the large number of LEO satellites provides abundant radiation sources for space-based SOP positioning [16]. Against this backdrop, exploring SOP positioning based on LEO constellations has become a current research hotspot. Numerous studies have introduced cases where various research teams have used LEO satellites for positioning, and the research outcomes generally achieve positioning accuracy on the order of tens of meters [17–25].

At present, there is limited research on anti-jamming technologies for positioning using LEO satellite SOP. To date, only one study has been conducted on anti-narrowband interference for Iridium satellite SOP under single-antenna reception conditions [35]. Particularly for Periodic Frequency Modulation (PFM) interference, such as Periodic Linear Frequency Modulation (PLFM) and Periodic Sinusoidal Frequency Modulation (PSFM) interference signals. Currently, there has been limited in-depth research on these types of interference both domestically and internationally. PFM interference is one of the most common types of interference faced by LEO satellites SOP positioning receivers. PFM interference signals are a typical dynamic interference pattern characterized by concentrated energy, wide bandwidth, ease of implementation, and high interference efficiency. This type of interference is highly effective and relies on mature technology, making it widely used. Such interference is typically generated by malicious jammers, radar systems, or civilian radio stations and is commonly distributed across the frequency bands used by LEO satellites SOP signals [26–28]. According to surveys, over 80% of commercially available jammers utilize PFM signals as their interference source [39]. Previous research on suppressing PFM interference has primarily focused on GNSS and similar areas, with the general approach being to utilize the differences between GNSS signals and interference in the time-frequency (TF) domain, spatial domain, or spatiotemporal domain, and to propose corresponding interference suppression methods [29, 30]. Among these, using the spatial resolution of the receiver's antenna array for spatiotemporal joint processing can effectively suppress various types of interference. However, considering the high cost and complexity of terminal hardware, this method has limited applicability. In contrast, single-antenna systems, due to their small size, low cost, and low power consumption, are widely used. Therefore, detection and suppression methods for PFM interference suitable for single-antenna receivers remain a research hotspot. Currently, the most effective method is to transform the received signal into the TF domain for interference detection. Based on the different energy distribution characteristics of the received signal and interference after transformation into the TF domain, typical TF analysis methods include Short-Time Fourier Transform (STFT) [31], Wavelet Packet Transform (WPT) [32], Wigner-Ville Distribution (WVD) [33], and Fractional Fourier Transform (FrFT) [34], among others. However, STFT cannot effectively accumulate signal energy and suffers from insufficient resolution due to the fixed window width; discrete WPT is prone to spectral aliasing and amplitude distortion; WVD and other nonlinear transforms generate cross-terms that affect the parameter estimation accuracy of multi-component interference; and the non-orthogonality of discrete FrFT distorts the desired signal, with better performance only for linear frequency modulation interference. Most importantly, while these methods offer some suppression capabilities for frequency modulation (FM) interference, due to the significant overlap between the interference and the desired signal in the TF or FrFT domains, the desired signal inevitably suffers considerable damage when the interference is eliminated. This issue is further exacerbated by recent advancements in electronics, as modern small jammers can generate interference containing multiple FM components, which increases the damage to the desired signal during interference elimination.

This type of interference suppression process can be tolerated when processing downlink GNSS signals with bandwidths generally on the order of tens of MHz. However, due to the relatively narrow downlink bandwidth of LEO satellite signals (the Iridium system has a bandwidth of 500 kHz, and the Orbcomm system only 25 kHz), the signal quality degradation caused by interference suppression can severely impact the subsequent positioning accuracy. Therefore, directly applying traditional TF analysis-based interference suppression methods to PFM interference suppression in LEO satellite systems is not very effective.

This paper proposes an Adaptive Signal Iterative Projection and Interference Suppression (ASIPIS) algorithm, utilizing the characteristics of PFM interference signals and LEO constellation signals. The algorithm concentrates the energy of PFM interference, which is spread over a wide bandwidth, into a few frequency points, thereby enhancing the interference's concentration and its separation from the LEO satellite signals. This effectively reduces the overlap between the LEO satellite signals and interference. The algorithm then uses subspace projection to map the interference and desired signals into different projection subspaces, eliminating the interference components and minimizing the damage to the desired signal during the interference suppression process. Finally, simulations and experiment results validate the enhanced performance of the proposed algorithm. The results demonstrate that the method can effectively eliminate single/multiple-component PFM interference, causing minimal damage to SOP signals, and is applicable to high-precision positioning receivers.

## 2 LEO satellite signal and PFM interference signal model

In an interference environment, the signal model at the input of the LEO satellite downlink receiver can be represented as:

$$x(t) = \sum_{i}^{N} s_i(t) + \sum_{m}^{M} j_m(t) + n(t) \tag{1}$$

Where $s_i(t)$ represents the signal received from the i-th LEO satellite (i = 1,2,3,…N), N represents the number of LEO satellites visible during the signal reception period, and $j_m(t)$ represents the interference signal of the $m$th component received by the receiver (m = 1,2,3,…,M). M represents the number of interferences received, and n(t) denotes the Additive White Gaussian Noise (AWGN) with a mean of zero.

When considering the received signal of a single LEO satellite, the reception signal of the i-th satellite can be expressed as Equation 2 [40]:

$$s_i(t) = AD(t)\cos\left(\omega_0 t + \varphi\right) \tag{2}$$

Where A is the signal amplitude, D(t) is the data code level value broadcasted by the satellite, $\omega_0$ is the signal broadcast frequency, and $\varphi$ is the broadcast phase.

$j_m(t)$ is PFM interference, and its instantaneous frequency $f(t)$ varies periodically over time, represented as:

$$f(t) = f_{0m} + \Delta f_m \cdot \sin\left(\frac{2\pi t}{T_m}\right) \tag{3}$$

Where $f_{0m}$ is the carrier frequency of the PFM interference signal, $\Delta f_m$ is the modulation amplitude of its frequency, $T_m$ is the modulation period (MP) of the interference, $\sin\left(\frac{2\pi t}{T_m}\right)$ is the periodic modulation function, and the instantaneous frequency $f(t)$ of the interference oscillates periodically within the range of $[f_{0m} - \Delta f_m, f_{0m} + \Delta f_m)$.

Then, the phase function $\phi(t)$ can be expressed by Equation 3 as Equation 4:

$$\begin{aligned}\phi(t) &= 2\pi\int_0^t f(\tau)d\tau = 2\pi\int_0^t \left(f_{0m} + \Delta f_m \cdot \sin\left(\frac{2\pi\tau}{T_m}\right)\right)d\tau \\ &= 2\pi f_{0m}t - \frac{\Delta f_m T_m}{2}\cdot\cos\left(\frac{2\pi t}{T_m}\right)\end{aligned} \tag{4}$$

So, the PFM interference signal $j_m(t)$ can be expressed as:

$$j_m(t) = A_m \exp\left[2\pi f_{0m}t - \frac{\Delta f_m T_m}{2}\cdot\cos\left(\frac{2\pi t}{T_m}\right) + \varphi_m\right] \tag{5}$$

Where $A_m$ is the carrier amplitude of the PFM interference signal, $\varphi_m$ represents the initial carrier phase of the PFM interference, which is a random variable uniformly distributed within the range of $[-\pi, +\pi)$. $2\pi f_{0m}t$ is the linear phase term of the interference, which determines the central frequency of the signal; $\frac{\Delta f_m T_m}{2}\cdot\cos\left(\frac{2\pi t}{T_m}\right)$ is the nonlinear phase term, representing the periodic variation of the frequency with time, with a period of $T_m$.

## 3 The adaptive signal iterative projection and interference suppression (ASIPIS) algorithm

This section proposes the ASIPIS algorithm based on the characteristics of PFM interference signals and LEO constellation signals. The algorithm eliminates the influence of LEO satellite signals in the input signal, isolates the PFM interference signal, and reconstructs the observation matrix by the modulation period of the interference. It concentrates the energy, originally spread over a wide bandwidth, into a single frequency point in the rearranged data, thereby enhancing the interference's concentration. Furthermore, a spatial projection method is used to construct the interference subspace and the noise subspace. Finally, the LEO satellite signals and PFM interference signals in the original observation matrix are mapped into the newly constructed subspaces to eliminate the interference components. This algorithm effectively overcomes the challenges that traditional anti-PFM interference algorithms based on single-antenna reception of LEO satellite signals cannot resolve.

## 3.1 Signal adaptive iterative cancellation

Due to the high signal-to-noise ratio (SNR) of LEO satellite signals on the ground (typically 15–30 dB), directly performing subspace decomposition would cause serious impacts and misjudgments in the division of the interference space. Therefore, before performing subspace decomposition, high-power LEO satellite signals need to be eliminated, and PFM interference should be isolated, to facilitate the subsequent division of the interference space. The ASIPIS algorithm eliminates the LEO satellite signals using the approach proposed in Ref. [35], which utilizes the SCCI algorithm. This method adaptively iterates to approximate and fit the power spectrum of the LEO satellite signals, thereby eliminating the impact of the LEO satellite signal power from the input signal.

Through analysis, it is found that the power spectrum of the input signal (signal and noise) in the LEO satellite signal reception scenario follows a chi-square distribution [41]. Based on this, a first-order expression for the relationship between the input signal power spectrum and the signal power spectral density is derived, and an approximation model is constructed.

$$Y_e(f) = aG_s(f) + b \tag{6}$$

Where $Y_e(f)$ is the estimated value of the input signal power spectrum, and $G_s(f)$ is the signal power spectrum.

Let the error between the input signal power spectrum $P(f)$ and the model estimate $Y_e(f)$ be Equation 7:

$$e(a,b) = \sum_{f=1}^{N} \left(aGs(f) + b - P(f)\right) \tag{7}$$

Where N is the number of FFT points, the mean square error (MSE) is Equation 8:

$$\begin{aligned} e(a,b)^2 = \sum_{f=1}^{N} (aGs(f) + b - P(f))^2 = a^2 \sum_{f=1}^{N} Gs^2(f) + Nb^2 + 2ab \sum_{f=1}^{N} Gs(f) \\ + \sum_{f=1}^{N} P^2(f) - 2a \sum_{f=1}^{N} Gs(f)P(f) - 2b \sum_{f=1}^{N} P(f) \end{aligned} \tag{8}$$

Using the gradient descent method, the criterion of minimizing MSE between $P(f)$ and the model estimate $Y_e(f)$ is adopted. Through multiple rounds of adaptive iterations, in each iteration, the portion of interference higher than the model power spectrum estimate in that round is eliminated, thereby achieving the goal where the final estimated signal power spectrum in the iterative process is nearly identical to the true value. The parameter estimates a and b in Equation 6 are obtained, and then the input signal power spectrum mean $Y_e(f)$ is derived. The next step is to subtract the estimated power spectrum mean $Y_e(f)$ from the input signal power spectrum $P(f)$. This subtraction can be considered as removing the power spectrum value of the LEO satellite signal contained in the input signal, leaving approximately only the noise and PFM interference signals. At this point, the next step is to construct the interference subspace.

## 3.2 Construct subspace

After the previous step of adaptive iterative cancellation of the signal, the input signal approximately only contains noise and PFM interference signals, which can be derived from Equation 1:

$$\hat{x}(t) \doteq \sum_{m}^{M} j_m(t) + n(t) \tag{9}$$

For the multi-component PFM interference in Equation 9, let the periods of the m PFM interference signals be $T_1, T_2, \ldots, T_m$, then their least common multiple is $T_M$, that is Equation 10:

$$T_M = n_1 T_1 = n_2 T_2 = \cdots n_m T_m \tag{10}$$

Where $n_1, n_2, \ldots, n_m$ are positive integer.

Using $nT_M$ (n as a positive integer) as the interval to truncate the input signal data in Equation 9, forming the observation data matrix:

$$\begin{aligned} \hat{X} &= \begin{bmatrix} \hat{x}(1) & \hat{x}(2) & \cdots & \hat{x}(c) & \cdots & \hat{x}(nT_M) \\ \hat{x}(nT_M+1) & \hat{x}(nT_M+2) & \cdots & \hat{x}(nT_M+c) & \cdots & \hat{x}(2nT_M) \\ \vdots & \vdots & \ddots & \vdots & \ddots & \vdots \\ \hat{x}((R-1)nT_M+1) & \hat{x}((R-1)nT_M+2) & \cdots & \hat{x}((R-1)nT_M+c) & \cdots & \hat{x}(RnT_M) \end{bmatrix} \\ &= \begin{bmatrix} \hat{x}_{1,1} & \hat{x}_{1,2} & \cdots & \hat{x}_{1,c} & \cdots & \hat{x}_{1,nT_M} \\ \hat{x}_{2,1} & \hat{x}_{2,2} & \cdots & \hat{x}_{2,c} & \cdots & \hat{x}_{2,nT_M} \\ \vdots & \vdots & \ddots & \vdots & \ddots & \vdots \\ \hat{x}_{R,1} & \hat{x}_{R,2} & \cdots & \hat{x}_{R,c} & \cdots & \hat{x}_{R,nT_M} \end{bmatrix} \\ &= \begin{bmatrix} \hat{x}_1 & \hat{x}_2 & \cdots & \hat{x}_c & \cdots & \hat{x}_{nT_M} \end{bmatrix} \end{aligned} \tag{11}$$

Where $R = \lfloor L_s / nT_M \rfloor$, $\lfloor \cdot \rfloor$ denotes the integer floor, $L_s$ is the total length of the sampled data, $\hat{x}_c$ is a column vector, $\hat{x}_c = \left[\hat{x}_{1,c} \quad \hat{x}_{2,c} \quad \cdots \quad \hat{x}_{R,c}\right]^T$, $\hat{x}_{r,c} = \hat{x}((r-1)nT_M + c) = j((r-1)nT_M + c) + n((r-1)nT_M + c)$, r represents the number of rows of the matrix, $r = 1, 2, \ldots, R$, and c represents the number of columns of the matrix, $c = 1, 2, \ldots, nT_M$. For PFM interference $j_m(t)$, from Equation 5, the expression at time $t + nT_M$ can be written as Equation 12:

$$\begin{aligned} j_m(t+nT_M) &= A_m \exp\left[2\pi f_{0m}(t+nT_M) - \frac{\Delta f_m T_M}{2} \cdot \cos\left(\frac{2\pi}{T_M}(t+nT_M)\right) + \varphi_m\right] \\ &= A_m \exp\left[2\pi f_{0m} t + 2\pi f_{0m} nT_M - \frac{\Delta f_m T_M}{2} \cdot \cos\left(\frac{2\pi}{T_M} t\right) + \varphi_m\right] \\ &= A_m \exp\left[2\pi f_{0m} t - \frac{\Delta f_m T_M}{2} \cdot \cos\left(\frac{2\pi}{T_M} t\right) + \varphi_m\right] \exp\left(2\pi f_{0m} nT_M\right) \\ &= j_m(t) \exp\left(2\pi f_{0m} nT_M\right) \end{aligned} \tag{12}$$

As can be seen from the above equation, when the time interval is $nT_M$, the PFM interference data differ only by a scaling factor. Therefore, the observation matrix of the PFM interference signal can be expressed as:

$$\begin{aligned} J &= \begin{bmatrix} j(1) & j(2) & \cdots & j(nT_M) \\ j(nT_M+1) & j(nT_M+2) & \cdots & j(2nT_M) \\ \vdots & \vdots & \ddots & \vdots \\ j((R-1)nT_M+1) & j((R-1)nT_M+2) & \cdots & j(RnT_M) \end{bmatrix} \\ &= \begin{bmatrix} j(1) & j(2) & \cdots & j(nT_M) \\ j(1)\exp\left(2\pi f_0 nT_M\right) & j(2)\exp\left(2\pi f_0 nT_M\right) & \cdots & j(nT_M)\exp\left(2\pi f_0 nT_M\right) \\ \vdots & \vdots & \ddots & \vdots \\ j(1)\exp\left(2\pi f_0 (R-1) nT_M\right) & j(2)\exp\left(2\pi f_0 (R-1) nT_M\right) & \cdots & j(nT_M)\exp\left(2\pi f_0 (R-1) nT_M\right) \end{bmatrix} \end{aligned} \tag{13}$$

From Equation 13, it can be seen that each element in the observation matrix is obtained by multiplying the corresponding element in the first row by a constant. Therefore, by multiplying each element of the first row by $-\exp\left(2\pi f_0 (r-1) nT_M\right)$ and adding it to the $r$th row, and performing elementary row transformations, the interference signal observation matrix in Equation 13 can be transformed into:

$$J = \begin{bmatrix} j(1)\ j(2) & \cdots & j(c) & \cdots & j(nT_M) \\ 0 \quad 0 & \cdots & 0 & \cdots & 0 \\ \vdots \quad \vdots & \ddots & \vdots & \ddots & \vdots \\ 0 \quad 0 & \cdots & 0 & \cdots & 0 \end{bmatrix}_{R\times nT_M} = \left[j_1\ j_2\ \cdots\ j_c\ \cdots\ j_{nT_M}\right]_{1\times nT_M} \tag{14}$$

Where $j_c$ is a column vector, represented as: $j_c = \left[j(c) \quad 0 \quad \cdots \quad 0\right]^T$

Through matrix calculations, the eigenvalue matrix of matrix $J \cdot J^H$ is obtained as Equation 15:

$$\Lambda = diag\left(j(1)\times\overline{j(1)} + j(2)\times\overline{j(2)} + \cdots + j(nT_M)\times\overline{j(nT_M)}, 0, \cdots, 0\right) \tag{15}$$

The singular value matrix of matrix $J$ is Equation 16:

$$\Sigma_J = diag\left(\sqrt{j(1)\times\overline{j(1)} + j(2)\times\overline{j(2)} + \cdots + j(nT_M)\times\overline{j(nT_M)}}, 0, \cdots, 0\right) \tag{16}$$

That is, perform subspace decomposition on the data matrix truncated with a period of $nT_M$, and the interference is concentrated in the subspace corresponding to the first singular value.

Therefore, the periodic truncated data matrix $\hat{X}$ of Equation 11 can be subjected to subspace decomposition, that is:

$$\hat{X} = U\Sigma V^T = \left[U_1 \quad U_2 \quad \cdots\right] \begin{bmatrix} \lambda_1 & 0 & 0 \\ 0 & \lambda_2 & 0 \\ 0 & 0 & \ddots \end{bmatrix} \begin{bmatrix} V_1 \\ V_2 \\ \vdots \end{bmatrix} \tag{17}$$

Where $U = \left[U_1 \quad U_2 \quad \cdots\right]$ and $V = \left[V_1 \quad V_2 \quad \cdots\right]$ represent the left singular matrix and the right singular matrix, respectively, $\Sigma$ represents the singular value matrix, and the subscript $\lambda$ indicates the order of the main diagonal, with $\lambda_1 \geq \lambda_2 \geq \ldots \geq 0$.

From Equations 13, 14, it can be seen that the interference components in each column of the matrix have the same frequency, which corresponds to a single-frequency interference. According to Ref. [36], if the data in each column only differ in phase, the rank of the corresponding matrix is 1. If there is only PFM interference, the rank of matrix $\hat{X}$ is 1, i.e., $\lambda = 0$. In other words, by performing subspace decomposition on the data matrix formed by truncating with a period of $nT_M$, the PFM interference can be concentrated in the subspace corresponding to the first singular value. When there are other signal components (such as desired signals and noise) unrelated to the interference, the above conclusion still holds, and the desired signals and noise will be spread across the entire space, thus enabling the construction of the interference subspace.

Equation 17 can be rewritten as Equation 18:

$$\hat{X} = U\Sigma V^T = \left[U_j \quad U_n\right] \begin{bmatrix} \Sigma_j & 0 \\ 0 & \Sigma_n \end{bmatrix} \begin{bmatrix} V_j \\ V_n \end{bmatrix} \tag{18}$$

Where $\Sigma_j$ corresponds to $\lambda_1$, $\Sigma_n$ corresponds to $diag\{\lambda_2 \quad \lambda_3 \quad \cdots\}$, the right singular vector corresponding to $\Sigma_j$ is $V_j$, $V_j = V_1$, and the corresponding left singular vector is $U_j$, $U_j = U_1$; $\Sigma_n$ corresponds to the right singular vector $V_n$, $V_n = \left[V_2 \quad V_3 \quad \cdots\right]$, and the corresponding left singular vector is $U_n$, $U_n = \left[U_2 \quad U_3 \quad \cdots\right]$. The interference subspace $P_{A_J}$ and noise subspace $P_{A_J}^{\perp}$ are constructed separately as follows by Equations 19, 20:

$$P_{A_J} = V_j V_j^{\ T} \tag{19}$$

$$P_{A_J}^{\perp} = V_n V_n^{\ T} \tag{20}$$

Truncate the original input signal data of Equation 1 (including LEO satellite signals) with $nT_M$ as the interval, forming the observed data matrix X. Then, project X onto the subspaces constructed in the previous step as Equation 21.

$$U^{-1}X\left(V^{-1}\right)^T = X' \tag{21}$$

Extract the corresponding part $\Sigma_n$ from the newly obtained data matrix $X'$, i.e., remove the data corresponding to the first row and first column of matrix $X'$ to obtain the data matrix $X''$. Multiply matrix $X''$ by the corresponding left and right singular vectors $V_n$ and $U_n$, respectively, and then the data matrix with the interference components eliminated can be restored as Equation 22.

$$X_{after\_AJ} = U_n X'' V_n^{\ T} \tag{22}$$

Unfold the data in matrix $X_{after\_AJ}$ sequentially to obtain the interference-suppressed signal y(t).

## 3.3 Estimation of modulation period (MP)

The next step is to discuss the estimation of the PFM interference modulation period when forming the data matrix in the previous step. Since the interference and noise components in the received signal are statistically uncorrelated, their cross-correlation function theoretically approaches zero and can be ignored. Therefore, the following will estimate the period of the periodic component in the received signal through autocorrelation processing.

From Equation 9, the autocorrelation function of $\hat{x}(t)$ can be expressed as:

$$R_x(\tau) = \sum_{m=1}^{M} R_{j_m}(\tau) + R_n(\tau) = R_j(\tau) + R_n(\tau) \tag{23}$$

Where $R_{j_m}(\tau)$ and $R_n(\tau)$ are the autocorrelation functions of $j_m(t)$ and $n(t)$, respectively. Then,

$$\begin{aligned} \left|R_j(\tau)\right| &= \left|\sum_{m=1}^{M} R_{j_m}(\tau)\right| \\ &= \left|\sum_{m=1}^{M} \frac{A_m^2}{2} \exp\left(2\pi f_{0m}\tau\right) \lim_{T\to\infty} \frac{1}{T} \int_{-T}^{T} \exp\left\{\frac{\Delta f_m T_m}{2}\cos\left(\frac{2\pi}{T_m}t\right) - \frac{\Delta f_m T_m}{2}\cos\left[\frac{2\pi}{T_m}(t-\tau)\right]\right\} dt\right| \end{aligned} \tag{24}$$

From Equation 24, it can be seen that:

$$\left|R_j(\tau)\right| \leq \sum_{m=1}^{M} \frac{A_m^2}{2} \tag{25}$$

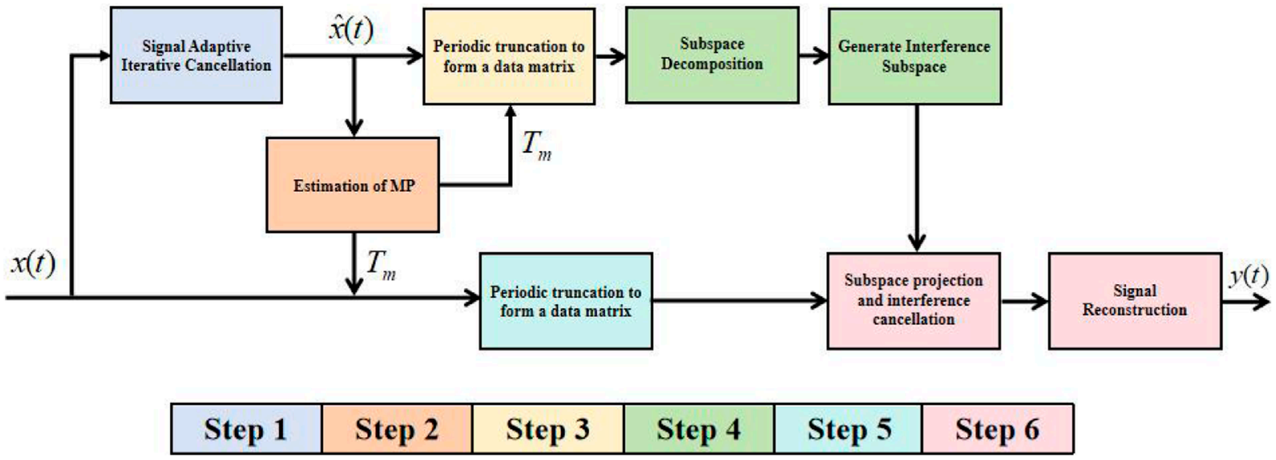

FIGURE 1
ASIPIS algorithm flowchart.

TABLE 1 Step of ASIPIS algorithm.

| ASIPIS algorithm specific steps |
|---|
| Step 1: Start signal adaptive iterative cancellation on the original received signal to eliminate the power spectral value of LEO satellite signals, obtaining noise and interference signals |
| Step 2: Perform autocorrelation processing on the noise and interference signals obtained in the first step to obtain the modulation period estimate $T_m$ |
| Step 3: Using the obtained modulation period to perform periodic truncation on the noise and interference mixed signal obtained in the first step, forming the observation matrix $\hat{X}$ |
| Step 4: Perform subspace decomposition on the observation matrix $\hat{X}$ to construct the interference subspace |
| Step 5: Periodically truncate the original received signal using the modulation period to form the observation matrix X |
| Step 6: Project X onto the subspace constructed in Step 4, eliminate the interference components, and obtain the interference-suppressed signal |

$\frac{\Delta f_m T_m}{2}\cdot\cos\left(\frac{2\pi t}{T_m}\right)$ is a periodic function with $T_m$ as its modulation period, so Equation 25 holds true if and only if $t = nT_m$. That is, $\left|R_j(\tau)\right|$ reaches a maximum at $nT_m$. Therefore, by detecting the peaks of $\left|R_x(\tau)\right|$, the estimated value of the PFM interference modulation period $T_m$ can be obtained.

At this point, the ASIPIS algorithm process can be summarized as shown in Figure 1:

The specific steps of the ASIPIS algorithm can be summarized as shown in Table 1.

## 4 Simulation and test verification

To verify the effectiveness of the proposed algorithm, relevant simulations and experiments were conducted. Without loss of generality, the Iridium system, a LEO constellation, was selected as the signal radiation source. The Iridium system consists of Polar-Earth-Orbit satellites at an altitude of 780 km, evenly distributed across six orbits in approximately the north-south direction. Each orbit contains 12 satellites (including one backup satellite), with an orbital inclination of 86.4° and an orbital period of 100.13 min, enabling global coverage. The user link adopts FDMA/TDMA/SDMA/TDD multiple access methods, grouping 12 adjacent beams from the 48-point beams of each satellite into a set for frequency reuse (SDMA) of the total available frequency band. Within each beam, the frequency band is divided into multiple TDMA channels by FDMA. In each TDMA channel, time division duplex (TDD) is applied for the uplink and downlink of the same user, meaning the uplink and downlink share the same TDMA carrier and frame but occupy different time slots. The total bandwidth allocated to Iridium is 1,616.0 MHz–1,626.5 MHz, with 1,616.0 MHz–1,626.0 MHz used for duplex channels as business channels, and 1,626.0 MHz–1,626.5 MHz used for downlink simplex channels as signaling channels [37, 38].

### 4.1 Simulation test

In the simulation experiment, the signal used was a downconverted Iridium intermediate frequency (IF) simulated signal with a center frequency of 270,833 Hz. The interference signal was set with a modulation type of Gaussian band-limited, having a mean of zero and a variance of one.

To validate the performance of the proposed algorithm, its anti-jamming capability was compared with other algorithms under different interference scenarios. In the interference scenario settings, multi-component PFM interference can be divided into two cases based on whether the carrier frequencies are consistent. The single-component PFM interference scenario can be considered a special case of multi-component PFM interference where the carrier frequencies are identical. Therefore, two interference scenarios were designed, with parameter settings as shown

TABLE 2 Interference scenarios parameter settings.

| Interference scenario | Carrier frequency (kHz) | Modulation period (μs) | Bandwidth (kHZ) |
|---|---|---|---|
| Dual-component PFM interference scenario 1 | 270 | 360; 420 | 400; 250 |
| Dual-component PFM interference scenario 2 | 270; 280 | 360; 420 | 400; 250 |

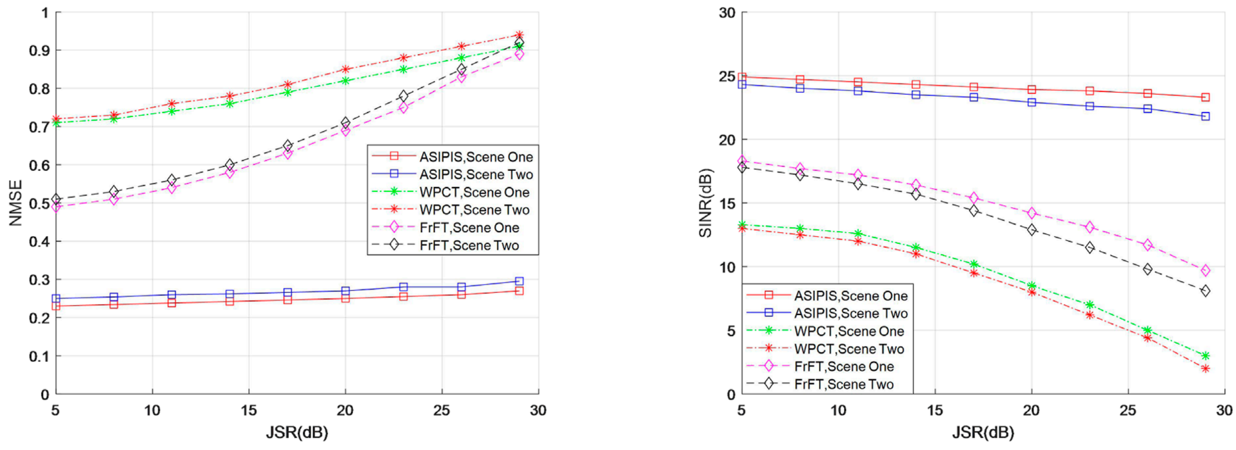

(a) NMSE of the Iridium signal after interference suppression

(b) the output SINR after interference suppression

FIGURE 2
Verification of interference performance of various algorithms under interference scenarios. **(a)** NMSE of the Iridium signal after interference suppression. **(b)** the output SINR after interference suppression.

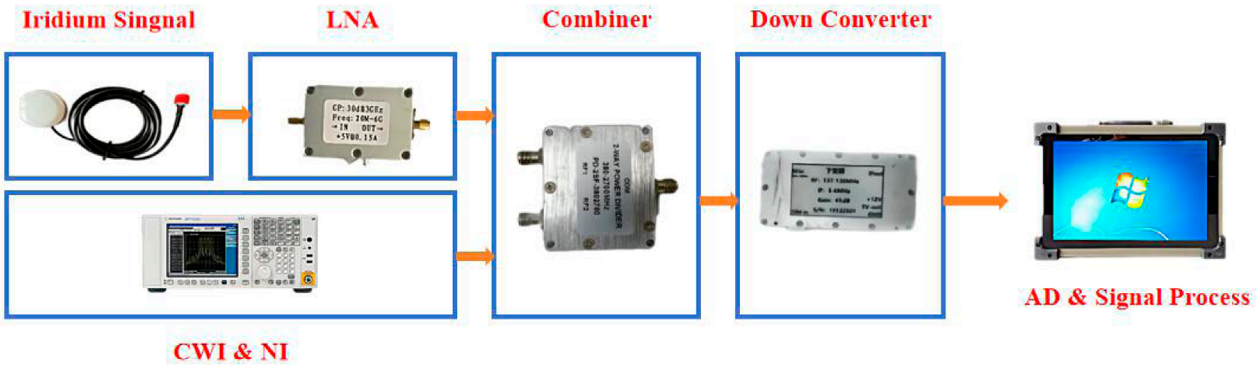

FIGURE 3
Hardware connection diagram.

in Table 2. The comparison algorithms include the Adaptive Wavelet Packet Coefficient Thresholding (WPCT) method [32] and the Time-Domain Combined Fractional Fourier Transform (FrFT) method [34]. For WPCT, the "Dmey" mother wavelet function was used, with five levels of wavelet decomposition, and soft thresholding was employed for interference detection and suppression. For FrFT, to search for the optimal order of the interference signal, the scanning points were set to 2000, and parameter estimation was performed only once for each batch of data.

When the input jamming-to-signal ratio (JSR) varies from 5 to 30 dB, Figures 2A, B respectively show the normalized mean square error (NMSE) of the Iridium signal after interference suppression processing and the output signal-to-interference-plus-noise ratio (SINR) under different interference scenarios, based on 50 Monte Carlo experiments.

(c) Experimental test scenarios

(b) Constellation map during the satellite visibility period

FIGURE 4
Actual experimental scenario. **(a)** Experimental test scenario. **(b)** Constellation map during the satellite visibility period.

**TABLE 3 Experiment scenarios parameter setting.**

| Interference scenario | Carrier frequency (MHz) | Modulation period (μs) | Bandwidth (kHZ) |
|---|---|---|---|
| Dual-component PFM interference scenario 1 | 1,626.25 | 360; 420 | 400; 250 |
| Dual-component PFM interference scenario 2 | 1,626.25; 1,626.26 | 360; 420 | 400; 250 |

As shown in Figure 2, the ASIPIS algorithm outperforms the other compared algorithms in terms of anti-jamming performance. Its output SINR and NMSE degrade only slightly as the input JSR increases, ensuring the successful acquisition of Iridium signals. The superior anti-jamming performance of the ASIPIS algorithm stems from its pre-subspace decomposition process, where high-power Iridium signals are removed to isolate PFM interference. This step eliminates the influence of Iridium signals on the interference detection process. Furthermore, the algorithm's performance is only marginally affected by increasing interference energy due to its periodic truncation and rearrangement method, which effectively concentrates the interference components into a single frequency. Subspace decomposition then projects the interference into a single subspace, achieving high interference concentration, reducing overlap between the desired signal and interference, and preventing the interference from spreading as its energy increases.

In contrast, the WPCT and FrFT algorithms show overall inferior anti-jamming performance. This is because, in the LEO satellite anti-jamming scenarios, the presence of high-power LEO signals significantly affects interference detection and suppression, leading to severe misjudgments. Traditional time-frequency-based interference suppression methods applied directly to these scenarios yield poor results. Their anti-jamming performance deteriorates rapidly with an increasing JSR due to the growing overlap between the desired signal and interference in the TF domain or FrFT domain as the number or energy of interference signals increases. This overlap results in damage to the desired signal during interference suppression, with more severe overlap causing greater signal loss. Specifically, the WPCT algorithm suffers from limited TF resolution, and higher interference energy leads to greater energy diffusion in the TF domain, negatively affecting the desired signal. While the FrFT algorithm improves the energy concentration of PFM interference to some extent, it is affected by spectral leakage inherent in digital FrFT implementations. Consequently, its interference suppression performance also degrades with increasing interference energy, though it remains superior to the WPCT algorithm.

## 4.2 Actual experimental verification

In the above simulation experiments, the ASIPIS algorithm's improved interference suppression performance has been verified. To further evaluate the effectiveness of proposed algorithm, a hardware platform was set up on the roof of the New Main Building at Beihang University, and real-signal anti-jamming experiments were conducted. The hardware platform is shown in Figure 3. This system uses a dedicated Iridium antenna to capture its signals. Gaussian interference signals generated by a signal source are combined with Iridium signals using a combiner. The combined signals are then frequency-shifted to IF through a down-converter. The system captures the signals at a sampling rate of 25 MHz, after which the signal reception and processing platform applies the anti-jamming algorithm for performance comparison. The experimental test scenario is shown in Figure 4A. During the test period, a total of four Iridium satellites were visible. The constellation map corresponding to the visible epoch of the Iridium satellites is shown in Figure 4B.

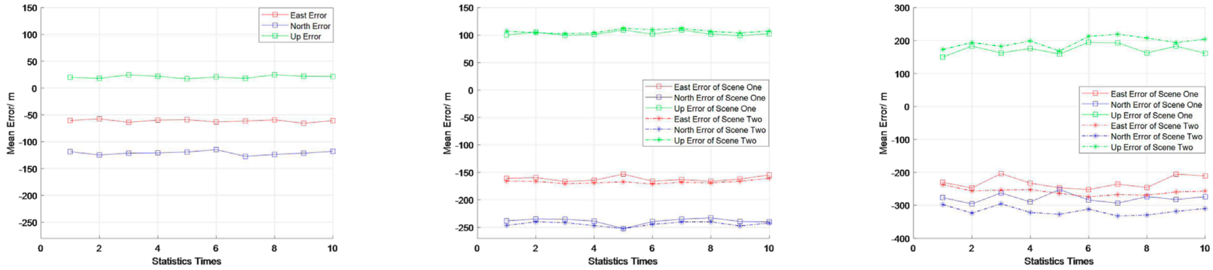

(a) Positioning result without interference

(b) Positioning result after anti-jamming (JSR is 15dB)

(c) Positioning result without anti-jamming algorithm (JSR is 15dB)

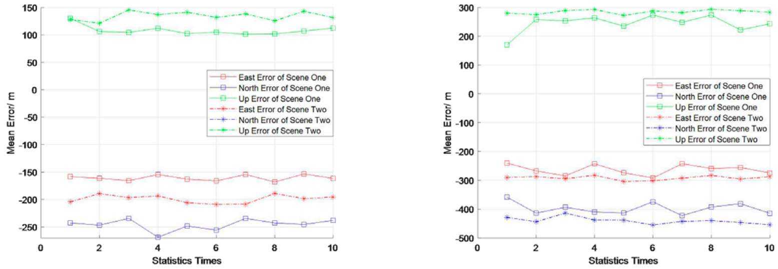

(d) Positioning result after anti-jamming (JSR is 30dB)

(e) Positioning result without anti-jamming algorithm (JSR is 30dB)

FIGURE 5
Comparison of positioning results in different scenarios. **(a)** Positioning result without interference. **(b)** Positioning result after anti-jamming (JSR is 15dB). **(c)** Positioning result without anti-jamming algorithm (JSR is 15dB). **(d)** Positioning result after anti-jamming (JSR is 30dB). **(e)** Positioning result without anti-jamming algorithm (JSR is 30dB)

Similarly, by configuring the signal source to generate interference scenarios of different intensities (with JSR of 15 dB and 30 dB, respectively), the ASIPIS algorithm was applied for anti-jamming processing. The positioning results after anti-jamming were compared with those obtained without activating the anti-jamming algorithm and under interference-free conditions. The interference scenario parameters are shown in Table 3.

The positioning results are statistically analyzed in the East-North-Up (ENU) coordinate system, comparing the positioning errors in the East-West, North-South, and Upward directions with the reference point coordinates. During the result analysis, the average of 50 positioning results is considered as one trial, and a total of 10 trials are conducted. The obtained results are shown in Figure 5.

The positioning results indicate that, compared to the positioning results under interference-free conditions, the positioning accuracy after interference suppression in interference scenarios shows a certain degree of decline. However, it still successfully retrieves Doppler information and achieves effective positioning. In contrast to interference scenarios where the interference suppression algorithm is not applied, activating the ASIPIS algorithm significantly improves positioning accuracy. The experimental results further validate the effectiveness of the ASIPIS algorithm and its interference suppression performance in LEO satellite PFM interference scenarios.

## 5 Conclusion

This paper proposes the ASIPIS algorithm, addressing the characteristics of narrow downlink bandwidth, high ground SNR in LEO constellation signals, and the generalized periodicity of PFM interference signals. The algorithm concentrates the dispersed PFM interference energy over a wide bandwidth into a few frequency points, enhancing the clustering of interference and its separation from LEO satellite signals. This effectively reduces the overlap between LEO satellite signals and interference. Additionally, subspace projection is employed to map the interference and desired signals into different subspaces, eliminating interference components and minimizing damage to the desired signal during anti-jamming processing. The algorithm comprehensively considers the effects of parameters such as PFM interference bandwidth, carrier frequency, modulation period, and intensity. Simulation and real data tests were conducted using Iridium signals from LEO systems for anti-jamming verification. Results show that, compared to traditional algorithms, this method effectively suppresses single/multi-component PFM interference, improving interference suppression performance under conditions such as narrow bandwidth and high power. It demonstrates significant enhancements in mitigating PFM interference in LEO satellite anti-jamming scenarios.

## Data availability statement

The raw data supporting the conclusions of this article will be made available by the authors, without undue reservation.

## Author contributions

LY: Writing – review and editing, Writing – original draft, Software. BF: Writing – review and editing, Supervision, Resources, Formal Analysis, Investigation, Funding acquisition, Methodology, Data curation, Project administration. HQ: Writing – review and editing, Writing – original draft, Methodology, Conceptualization. DX: Writing – review and editing. BG: Writing – review and editing, Supervision, Resources, Investigation. HS: Writing – review and editing, Methodology, Investigation, Conceptualization. GG: Writing – review and editing, Supervision, Investigation. ZL: Writing – review and editing, Supervision, Formal Analysis, Data curation. DH: Writing – review and editing, Visualization, Supervision, Software. LZ: Writing – review and editing, Supervision, Resources.

## Funding

The author(s) declare that financial support was received for the research and/or publication of this article. This research was funded from the Army Academy of Artillery and Air Defense under Grant 220214003.

## Acknowledgments

The authors would like to thank the editors and reviewers for their efforts to help the publication of this paper.

## Conflict of interest

The authors declare that the research was conducted in the absence of any commercial or financial relationships that could be construed as a potential conflict of interest.

## Generative AI statement

The author(s) declare that no Generative AI was used in the creation of this manuscript.

## Publisher's note

## References

1. Jia Q, Zukun L, Baojun L, Jie S, Zhibin X, Zhi W A survey of GNSS interference monitoring technologies. *Front Phys* (2023) 11:11–2023. Sec. Interdisciplinary Physics. doi:10.3389/fphy.2023.1133316

2. Danning Z, Yu L. Effects of ionosphere dispersion on wideband GNSS signals. *Front Phys* (2023) 11:11–2023. Sec. Space Physics. doi:10.3389/fphy.2023.1103159

3. Shaojie N, Binbin R, Feiqiang C, Zukun L, Jie W, Pengcheng M, et al. GNSS spoofing suppression based on multi-satellite and multi-channel array processing. *Front Phys* (2022) 10:10–2022. Sec. Space Physics. doi:10.3389/fphy.2022.905918

4. Takeshi I, Motoyuki K, Yusaku O, Tatsuya F, Fumiaki T, Iwao U. GNSS-acoustic observations of seafloor crustal deformation using a wave glider. *Front Earth Sci.* (2021) 9–2021. doi:10.3389/feart.2021.600946

5. Ting Y, Nan C. A preliminary view of the CYGNSS soil moisture-vegetation activity linkage. *Front. For. Glob.* (2023) 6–2023. doi:10.3389/ffgc.2023.1320432

6. Binbin R, Feiqiang C, Shaojie N, Chunyang H, Zukun L, Shujian H. Performance analysis of repeater spoofing suppression based on GNSS multi-beam receiver. *Front Phys* (2022) 10:10–2022. Sec. Space Physics. doi:10.3389/fphy.2022.970132

7. Lei W, Lei C, Baiyu L, Zhe L, Zongnan L, Zukun L. Development status and challenges of anti-spoofing technology of GNSS/INS integrated navigation. *Front Phys* (2024) 12:12–2024. Sec. Space Physics. doi:10.3389/fphy.2024.1425084

8. Xiangjun L, Zukun L, Muzi Y, Wenxiang L, Feixue W, Yi Y, et al. Tradeoff of code estimation error rate and terminal gain in SCER attack. *IEEE Transactions Instrumentation Measurement* (2024) 73:1–12. doi:10.1109/tim.2024.3406807

9. Alexander M, Laurie B, Robert C, Walterio M, Jianing C, Colin G, et al. Visual odometry using pixel processor arrays for unmanned aerial systems in GPS denied environments. *Front. Robot.* 7–2020. doi:10.3389/frobt.2020.00126

10. Matteo F, Riccardo B, Matteo M On the precision of 6 DoF IMU-LiDAR based localization in GNSS-denied scenarios. *Front. Robot.* (2023). 10:2023. doi:10.3389/frobt.2023.1064930

11. Kassas ZM, Khalife J, Abdallah AA, Lee CI. I Am not afraid of the GPS jammer: resilient navigation via signals of opportunity in GPS-denied environments. *IEEE Aerosp Electron Syst Mag* (2022) 37:4–19. doi:10.1109/maes.2022.3154110

12. Zhang Y, Ho KC. Localization by signals of opportunity in the absence of transmitter position. *IEEE Trans Signal Process* (2022) 70:4602–17. doi:10.1109/tsp.2022.3198182

13. Hu Z, Li S, Xiang Y. Time information transmission based on FM broadcast signal. *IEEE Access* (2021) 9:16360–4. doi:10.1109/access.2021.3050410

14. Han K, Yu SM, Kim S-L, Ko S-W. Exploiting user mobility for WiFi rtt positioning: a geometric approach. *IEEE Internet Things J* (2021) 8:14589–606. doi:10.1109/jiot.2021.3070367

15. Zhao C, Qin H, Li Z. Doppler measurements from multiconstellations in opportunistic navigation. *IEEE Trans Instrum Meas* (2022) 71:1–9. doi:10.1109/tim.2022.3147315

16. Zhao C, Qin H, Wu N, Wang D. Analysis of baseline impact on differential Doppler positioning and performance improvement method for LEO opportunistic navigation. *IEEE Trans Instrum Meas* (2023) 72:1–10. doi:10.1109/tim.2023.3235456

17. Duran MAC, D'Amico AA, Dardari D, Rydström M, Sottile F, Ström EG, et al. Chapter 3—terrestrial network-based positioning and navigation. In: D Dardari, E Falletti, M Luise, editors. *Satellite and terrestrial radio positioning techniques*. Oxford, UK: Academic Press (2012). p. 75–153.

18. Tan Z, Qin H, Cong L, Zhao C. New method for positioning using IRIDIUM satellite signals of opportunity. *IEEE Access* (2019) 7:83412–23. doi:10.1109/access.2019.2924470

19. Neinavaie M, Khalife J, Kassas ZM. Acquisition, Doppler tracking, and positioning with starlink LEO satellites: first results. *IEEE Trans Aerosp Electron Syst* (2022) 58:2606–10. doi:10.1109/taes.2021.3127488

20. Morales J, Khalife J, Kassas ZM. Simultaneous tracking of Orbcomm LEO satellites and inertial navigation system aiding using Doppler measurements. In: *Proceedings of the 2019 IEEE 89th vehicular technology conference (VTC2019-Spring)*. Malaysia: Kuala Lumpur (2019). p. 1–6.

21. Khairallah N, Kassas ZM. Ephemeris closed-loop tracking of LEO satellites with pseudorange and Doppler measurements. In: *Proceedings of the 34th international*

*technical meeting of the satellite division of the institute of navigation (ION GNSS+ 2021)*. St. Louis, MO, USA (2021). p. 2544–55.

22. Morales-Ferre R, Lohan ES, Falco G, Falletti E. GDOP-based analysis of suitability of LEO constellations for future satellite-based positioning. In: *Proceedings of the 2020 IEEE international conference on wireless for space and extreme environments (WiSEE)* (2020). p. 147–52. Vicenza, Italy.

23. Leng M, Razul SG, See CMS, Tay WP, Cheng C, Quitin F. Joint navigation and synchronization using SOOP in GPS-denied environments: algorithm and empirical study. In: *Proceedings of the 2015 sensor signal processing for defence (SSPD), Edinburgh, UK*. New York, NY, USA: IEEE (2015). p. 9–10. September 2015.

24. Parkinson BW, Spliker JJ. *Global positioning system: theory and application*. Cambrige, MA, USA: American Insitute of Aeronautics and Astronautics Inc. (1996).

25. Qin H, Zhang Y. Positioning technology based on starlink signal of opportunity. *J Navig Position* (2023) 11:67–73. doi:10.16547/j.cnki.10-1096.20230110

26. Mitch R, Dougherty R, Psiaki M, Powell S, et al. Signal characteristics of civil GPS Jammers. *Proc.24th ION GNSS* (2011) 1907–19. Portland, OR, USA.

27. Ryan M., Ryan D., Mark P, Steven D., Brady O., Jahshan B., et al. Signal characteristics of civil GPS Jammers. Proceedings of the 24th International Technical Meeting of the Satellite Division of the Institute of Navigation (ION GNSS 2011), Portland, OR, (2011), 1907–1919.

28. Dovis F. *GNSS interference threats and countermeasures*. Norwood,MA, USA: Artech House (2015).

29. Ioannides R, Pany T, Gibbons G. Known vulnerabilities of global navigation satellite systems, status, and potential mitigation techniques. *Proc IEEE* (2016) 104(6):1174–94. doi:10.1109/jproc.2016.2535898

30. Gao G, Sgammini M, Lu M, Kubo N. Protecting GNSS receivers from jamming and interference. *Proc IEEE* (2016) 104(6):1327–38. doi:10.1109/jproc.2016.2525938

31. Rezaei M, Mosavi M, Abedi M. New GPS anti-jamming system based on multiple short-time Fourier transform. *IET Radar,Sonar Navigat* (2016) 10(4):807–15. doi:10.1049/iet-rsn.2015.0417

32. Mosavi M, Pashaian M, Rezaei M, Mohammadi K. Jamming mitigation in global positioning system receivers using wavelet packet coefficients thresholding. *IET Signal Process* (2015) 9(5):457–64. doi:10.1049/iet-spr.2014.0280

33. Sun K, Jin T, Yang D. An improved time-frequency analysis method in interference detection for GNSS receivers. *Sensors* (2015) 15(4):9404–26. doi:10.3390/s150409404

34. Huang K, Tao R, Wu K, Wang Y. Study on interference suppression based on joint fractional Fourier domain and time domain. *Sci China Technol Sci* (2011) 54(10):2674–86. doi:10.1007/s11431-011-4533-7

35. Yao L, Qin H, Gu B, Shi G, Sha H, Wang M A study on anti-jamming algorithms in low-earth-orbit satellite signal-of-opportunity positioning systems for unmanned aerial vehicles. *Drones* (2024) 8(4):164. doi:10.3390/drones8040164

36. Kanjilal PP, Palit S. On multiple patternextraction using singular value decomposition. *IEEETransactions Signal Process.* (1995) 43(6):1536–40. doi:10.1109/78.388873

37. *Iridium burst detector and demodulator*. (2019) GNU Radio Iridium Out of Tree Module. Available online at: https://github.com/muccc/gr-iridium. Accessed July 4, 2023.

38. Iridium NEXT engineering statement. FCC File Number 1031348.

39. Mitch R, Dougherty R, Psiaki M., Powell S., OHanlon B., Bhatti J., et al. *Know your enemy: signal characteristics of civilGPS jammers[J]. GPS* (2012) 25:64–71.

40. Zhao C. *Research on fusion and differential positioning technology of iridium/orbcomm dual constellation signals of opportunity[D]*. Beihang University (2024).

41. Li J. *Strong interference supression for satellite navigation receiver with single antenna[D]*. National University of Defense Technology (2017).

frontiers | Frontiers in Physics

TYPE Review
PUBLISHED 20 May 2025
DOI 10.3389/fphy.2025.1592447

OPEN ACCESS

EDITED BY
Zhu Xiao,
Hunan University, China

REVIEWED BY
Yq Hei,
Xidian University, China
Laiding Zhao,
Nanjing University of Posts and Telecommunications, China
Jing Bai,
Xidian University, China

*CORRESPONDENCE
Zhibin Xiao,
✉ xiaozb1986@163.com

RECEIVED 12 March 2025
ACCEPTED 30 April 2025
PUBLISHED 20 May 2025
CORRECTED 04 July 2025

CITATION
He J, Ni S, Lin H, Liu Z and Xiao Z (2025) Survey on positioning technology based on signal of opportunity from low earth orbit. *Front. Phys.* 13:1592447.
doi: 10.3389/fphy.2025.1592447

# Survey on positioning technology based on signal of opportunity from low earth orbit

Jiawei He[1,2], Shaojie Ni[1,2], Honglei Lin[1,2], Zhe Liu[1,2] and Zhibin Xiao[1,2]*

[1]College of Electronic Science and Technology, National University of Defense Technology, Changsha, China, [2]National Key Laboratory for Positioning, Navigation and Timing Technology, Changsha, China

Positioning, Navigation, and Timing (PNT) services are essential for supporting various aspects of modern society. Fields such as communications, transportation, and military operations heavily rely on accurate and reliable PNT services, with this dependence expected to grow. However, the limitations of the predominant Global Navigation Satellite System (GNSS) in complex environments have become increasingly apparent. As an effective supplementary approach, space-based signals of opportunity (SOPs) from Low Earth Orbit (LEO) have garnered significant attention. This paper begins by introducing the principle of Doppler location and analyzing its error sources. It then discusses in detail the methods of observation extraction, including cognitive-based and blind-based methods. Focusing on major domestic and international LEO constellations (such as Iridium, Orbcomm, Globalstar, Starlink, OneWeb, etc.), this paper summarizes their signal characteristics and the current status of positioning research, and discusses the latest advancements in observable estimation algorithms. Finally, the paper proposes key research directions for the future, including breakthroughs in satellite recognition technology, optimization of positioning algorithms, development of multi-source fusion positioning technology, and observation extraction in complex environments.

KEYWORDS

**LEO, PNT, signal of opportunity, doppler positioning, observational estimation**

## 1 Introduction

Since the advent of the Global Navigation Satellite System (GNSS), it has played a pivotal role in both military and civilian domains, making irreplaceable contributions to national defense and economic construction. As its application scope continues to expand, the demands on GNSS have far exceeded the initial design specifications. The most prominent issue is the inability of traditional satellite navigation receivers to meet positioning requirements in complex environments [1]. Firstly, the signal strength of satellite signals diminishes with increasing propagation distance during space transmission, resulting in weak signal power reaching the ground and limiting its application in urban areas and canyons. Secondly, GNSS operates on a single, transparent frequency point, making it vulnerable to malicious interference and deception, which can lead to service unavailability. The limitations of Global Navigation Satellite Systems have been significantly exacerbated in recent battlefield scenarios observed during the Russia-Ukraine conflict, where such systems have demonstrated critical vulnerabilities and operational unreliability in combat environments. In stark contrast, LEO satellite constellations exemplified by Starlink have emerged as resilient alternatives. These advanced LEO systems not only maintain robust communication capabilities but also demonstrate enhanced positioning potential in complex battlefield conditions, presenting a paradigm shift in tactical navigation solutions. Over the past decade, an increasing number of researchers have demonstrated the potential of signals of Opportunity (SOPs) in Positioning, Navigation, and Timing (PNT), which can effectively compensate for the shortcomings of GNSS.

SOPs positioning technology offers a viable alternative for positioning services when GNSS signals are unavailable or denied. SOPs encompass all potential radio signals in the environment from which location and time information can be extracted for navigation purposes. These signals are categorized into land-based and space-based SOPs. Ground-based SOPs, such as radio, mobile communication, and WIFI signals, primarily cover urban areas but lack coverage in deserts, oceans, and remote regions. In contrast, space-based SOPs utilize Earth-orbiting satellites as radiation sources, including non-cooperative/non-navigation satellite signals, non-cooperative navigation satellite signals, and cooperative non-navigation signals. Compared to ground-based SOPs, space-based signals offer the advantage of extensive coverage, enabling seamless global positioning. Among these, Low Earth Orbit (LEO) satellite signals are a typical example of space-based SOPs emitters. Compared with GNSS satellites in Medium Earth Orbit (MEO), LEO satellites exhibit significant advantages, such as rapid geometric changes, stronger received signal strength, and larger Doppler frequency shifts [2]. Additionally, many LEO constellations possess rich spectral resources and strong anti-interference capabilities. Moreover, Two-Line Element (TLE) data for LEO satellites is readily available, allowing for precise satellite position calculations through models like the Simplified General Perturbations No. 4 (SGP4). These advantageous properties ensure the PNT capabilities of LEO satellites in GNSS-denied environments. Consequently, LEO constellations are considered a promising alternative for PNT services. Currently, numerous countries are planning or have already launched a large number of LEO satellites, providing abundant radiation sources for space-based SOPs [2–4]. Table 1 lists the main LEO satellite constellations that have been deployed or are planned both domestically and internationally.

The first satellite navigation system was the U.S. Navy's Meridian Satellite Navigation System (TRANSIT), which was the first positioning system based on satellite Doppler. It was introduced for military applications in 1964 and then disclosed for positioning and navigation services in 1968. The TRANSIT system used the Doppler frequency shift of LEO satellite signals to achieve a positioning accuracy of about 70 m [5, 6]. This system demonstrated the method of using LEO satellites for positioning within the framework of SOPs navigation. The advantages of opportunistic LEO positioning technology are evident [7]:

1. A large number of satellites can provide signals globally, making opportunistic LEO satellites a potential global PNT system.
2. Almost no additional infrastructure is required, and positioning can be achieved using existing receivers.
3. The satellite system does not need to be adjusted, and it can be used without special navigation functions for LEO satellites.
4. User-side positioning can be realized, and the user's location will not be disclosed to constellation operators, thus protecting user privacy.

Despite the many advantages of opportunistic LEO positioning technology, it also faces several challenges. Most of these challenges stem from the fact that satellite systems or transmitted signals are not designed for PNT purposes. This leads to two main issues [8]:

1. Non-navigation signals may lack broadband pseudo-random codes for satellite identification and pseudo-range measurement. The modulation format of the signal is unknown or partially unknown, making it difficult to extract navigation observations from satellite signals.
2. Weak space-time reference: Most LEO satellites are not equipped with high-precision atomic clocks like those in traditional GNSS systems. Therefore, they lack precise clocks, making it difficult to meet the requirements for high-precision pseudo-range measurement. Additionally, there is a lack of strict clock synchronization between satellites, and most broadcast ephemeris data are not available. The published TLE data and the Simplified General Perturbations No. 4 (SGP4) model can be used, but this introduces significant system errors into the positioning algorithm.

The solutions to these problems will be described in the main part of the article.

Given the challenges associated with space-based LEO signals of opportunity, this paper reviews the development process of space-based SOPs positioning, focusing on the extraction of mesoscopic measurements and the correction of systematic errors. We first describe the principle of Doppler positioning. Then, we analyze the Doppler positioning performance and main error sources of LEO satellites, summarize the existing LEO-based navigation systems, their observation extraction methods, and determine the future research direction in this field.

# 2 Doppler positioning

## 2.1 Positioning principle

Benefiting from the rapid movement of LEO satellites, there is a significant difference in relative motion speeds between satellites and the ground, resulting in an obvious Doppler effect. Therefore, LEO satellites generally use Doppler frequency shift information for positioning, typically employing integrated Doppler and instantaneous Doppler as observation measurements [9, 10]. Generally, the integrated Doppler measurement value is used as the navigation observation value and then converted into a range difference bi-curve. Through the accumulation of measurements at multiple different times, the intersection of multiple hyperboloids determines the position. When there are many visible satellites, instantaneous Doppler positioning, i.e., single epoch positioning, can be used. Generally, at least four satellites are required for instantaneous Doppler positioning, and instantaneous Doppler measurement information can be used to achieve real-time positioning.

TABLE 1 Major domestic and international LEO constellations.

| Constellation | Country | Plan | Downlink frequency/bandwidth |
|---|---|---|---|
| Iridium | United States | 66 | L: 1626–1626.5 MHz |
| Orbcomm | United States | 36 | VHF: 137–138 MHz |
| Globalstar | United States | 48 | S: 2483.5–2500 MHz |
| Starlink | United States | 42,000 | Ku: 10.7–12.7 GHz, Ka/V/Q: 37.5–42.5 GHz |
| OneWeb | United States, United Kingdom | 720 | Ku: 10.7–12.7 GHz |
| Kuiper | United States | 3,236 | X/Ku: 10.7–12.7 GHz |
| Telesat | Canada | 298 | Ka: 17.8–20.2 GHz |
| LeoSat | United States | 108 | Ka: 17.7–20.2 GHz |
| Tianqi | China | 38 | UHF: 318–320 MHz |
| Xingwang | China | 12,992 | K: 17.7–20.2 GHz, Ka/V/Q: 37.5–42.5 GHz |
| Xiaozhizhuwang | China | 650 | K: 17.7–20.2 GHz |

The Doppler frequency is a function of satellite speed and position, which can be obtained through auxiliary information. According to the satellite's velocity and position, and the measured Doppler shift, a circular conical surface with equal Doppler can be determined. For static receivers, since the receiver's coordinates remain constant over time, Doppler measurements from the same or different satellites at different times can be used for positioning. When a user receives a satellite signal, the Doppler shift value of the signal can be measured, and the user must be on the equivalent Doppler circular conical surface (EDCCS) with the satellite as the apex. The Doppler shift value is the same for all points on this surface and equals the measured Doppler shift value. When signals from multiple satellites are received, multiple equivalent Doppler circular conical surfaces are formed. These surfaces intersect at a point, which is calculated as the user's position. Figure 1 illustrates the principle of Doppler positioning.

## 2.2 Measurement equation

The Doppler effect, caused by the relative motion between the satellite signal transmitter and the ground receiver, can be expressed as:

$$f_d = f_R - f_T = \frac{v_{rv}}{c} . f_T = \frac{v_{rv}}{\lambda_{f_T}} \tag{1}$$

In the Equation 1, $f_d$ represents the Doppler frequency shift, $f_R$ denotes the received carrier wave frequency, $f_T$ is the transmitted carrier frequency, $c$ is the speed of light, $\lambda_{f_T}$ is the wavelength of the transmitted signal, and $v_{rv}$ is the relative speed in the line-of-sight direction between the receiver and transmitter. If the transmitter and receiver are approaching each other, the Doppler frequency shift is positive; if they are moving away from each other, the Doppler shift is negative. Additionally, $v_{rv}$ is also referred to as the pseudo-range rate, which can be expressed as:

$$v_{rv} = \left(\boldsymbol{v}_r - \boldsymbol{v}^s\right) . \frac{\boldsymbol{x}^s - \boldsymbol{x}_r}{\| \boldsymbol{x}^s - \boldsymbol{x}_r \|} = \dot{\rho} \tag{2}$$

In the Equation 2, $\boldsymbol{v}^s = \left[v_x^s \quad v_y^s \quad v_z^s\right]$ and $\boldsymbol{v}_r = \left[v_{r_x} \quad v_{r_y} \quad v_{r_z}\right]$ are the velocity vectors of the satellite and the receiver, respectively. Similarly, $\boldsymbol{x}^s = \left[x^s \quad y^s \quad z^s\right]^T$ and $\boldsymbol{x}_r = \left[x_r \quad y_r \quad z_r\right]^T$ are their respective position vectors in 3-dimensional space. The term $\dot{\rho}$ represents the pseudo-range rate, which is the first derivative of the pseudo-range with respect to time. The measurement equation for the pseudo-range can be expressed as [11]:

$$\rho = \|\boldsymbol{x}^s - \boldsymbol{x}_r\| + c \cdot \left(\delta t_r - \delta t^s\right) + c \cdot dR_r^s + T_r^s + I_{r,f}^s + dE_r^s + \varepsilon_\rho \tag{3}$$

In the Equation 3, $\rho$ represents the pseudo-range, $\delta t_r$ and $\delta t^s$ respectively represent clock bias of receiver and satellite, $T_r^s$ and $I_{r,f}^s$ are tropospheric and ionospheric delay, $dR_r^s$ is the satellite clock offset correction due to the relativistic effect, $dE_r^s$ is the error caused by the Sagnac effect due to Earth rotation, and $\varepsilon_\rho$ represents other modeling errors. The measurement equation for pseudo-range rate can be expressed as:

$$f_d \cdot \lambda_{f_r} = \dot{\rho} = \left(\boldsymbol{v}_r - \boldsymbol{v}^s\right) . \frac{\boldsymbol{x}^s - \boldsymbol{x}_r}{\| \boldsymbol{x}^s - \boldsymbol{x}_r \|} + c \cdot \left(\delta \dot{t}_r - \delta \dot{t}^s\right) + c \cdot d\dot{R}_r^s + \dot{T}_r^s + \dot{I}_{r,f}^s + d\dot{E}_r^s + \varepsilon_{\dot{\rho}} \tag{4}$$

In the Equation 4, $\delta \dot{t}_r$ and $\delta \dot{t}^s$ represent the clock drift of the receiver and satellite, respectively. $\dot{T}_r^s$ and $\dot{I}_{r,f}^s$ represent the delay rates caused by the troposphere and ionosphere, respectively. $\varepsilon_{\dot{\rho}}$ represents measurement noise errors and other unmodeled noise errors. $d\dot{R}_r^s$ is the clock drift correction caused by relativistic effects, and $d\dot{E}_r^s$ is the rate of distance change caused by the Sagnac effect due to Earth's rotation. They can be obtained from literature [12]:

$$d\dot{R}_r^s = \frac{-2}{c^2} \left(\dot{\boldsymbol{x}}^s \cdot \boldsymbol{v}^s + \boldsymbol{x}^s \cdot \dot{\boldsymbol{v}}^s\right) \tag{5}$$

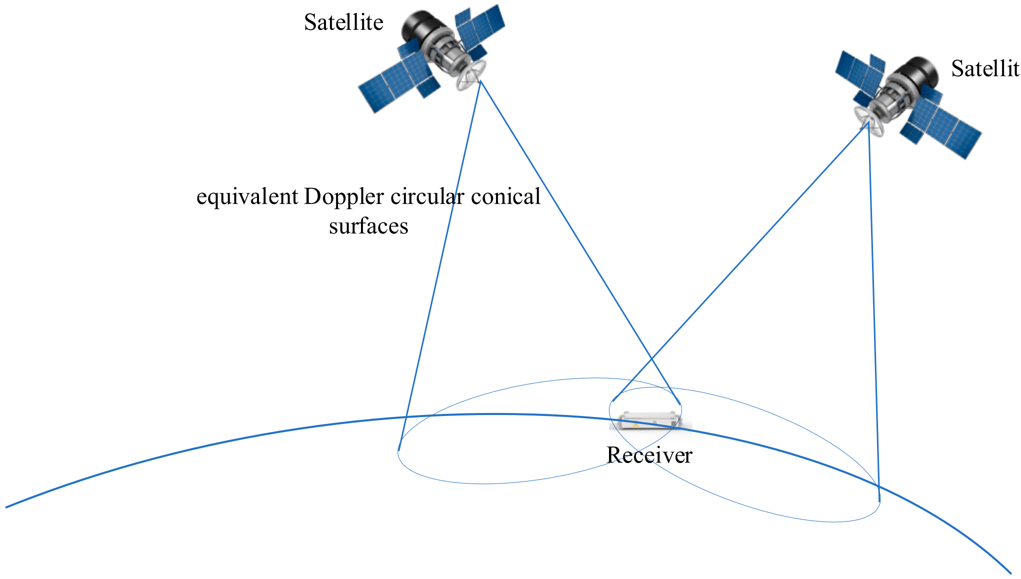

FIGURE 1
Schematic diagram of Doppler positioning.

$$d\dot{E}_r^s = \frac{\omega_e}{c}\left(v_x^s \cdot y_r + v_{r_y} \cdot x^s - v_y^s \cdot x_r - v_{r_x} \cdot y^s\right) \tag{6}$$

In the Equation 6, $\omega_e$ is the angular velocity of rotation.

## 2.3 Location model

In traditional GNSS pseud-orange positioning, an initial estimate is typically provided to the user, and the Newton iteration method is employed for iterative calculation. The final convergence value is utilized as the positioning result. Doppler-based positioning systems generally utilize two models. One is a positioning model based on the least squares method, and the other is a positioning model based on the extended Kalman filter. In the currently published literature, the least squares method is suitable for static receivers, while the extended Kalman filter (EKF) is suitable for both static and dynamic receivers. Both methods require an initial estimated solution $\mathbf{X}_0 = \left[x_r^0, y_r^0, z_r^0, v_{r_x}^0, v_{r_y}^0, v_{r_z}^0, \delta\dot{t}_{r,0}\right]^T$ for the receiver, and then linearize the pseudo-range rate observation equation:

$$\begin{aligned}\dot{\rho}_i \approx \dot{\rho}_i^0 &+ \frac{\partial\dot{\rho}_i}{\partial x_r}\bigg\|_{x_r=x_r^0} \cdot \Delta x_r + \frac{\partial\dot{\rho}_i}{\partial y_r}\bigg\|_{y_r=y_r^0} \cdot \Delta y_r + \frac{\partial\dot{\rho}_i}{\partial z_r}\bigg\|_{z_r=z_r^0} \cdot \Delta z_r \\ &+ \frac{\partial\dot{\rho}_i}{\partial v_{r_x}}\bigg\|_{v_{r_x}=v_{r_x}^0} \cdot \Delta v_{r_x} + \frac{\partial\dot{\rho}_i}{\partial v_{r_y}}\bigg\|_{v_{r_y}=v_{r_y}^0} \cdot \Delta v_{r_y} + \frac{\partial\dot{\rho}_i}{\partial v_{r_z}}\bigg\|_{v_{r_z}=v_{r_z}^0} \cdot \Delta v_{r_z} \\ &+ \frac{\partial\dot{\rho}_i}{\partial\delta\dot{t}_r}\bigg\|_{\delta\dot{t}_r=\delta\dot{t}_{r,0}} \cdot \Delta\delta\dot{t}_r + \varepsilon_{\dot{\rho}_i}\end{aligned} \tag{7}$$

$$\begin{aligned}\frac{\partial\dot{\rho}_i}{\partial x_r}\bigg\|_{x_r=x_r^0} &= \left[\frac{v_{s_x}^i - v_{r_x}^0}{\|\boldsymbol{p}_s^i - \boldsymbol{p}_r^0\|} + (x_r^0 - x_s^i)(\boldsymbol{v}_s^i - \boldsymbol{v}_r^0).\frac{\boldsymbol{p}_s^i - \boldsymbol{p}_r^0}{\|\boldsymbol{p}_s^i - \boldsymbol{p}_r^0\|^3}\right] \\ \frac{\partial\dot{\rho}_i}{\partial y_r}\bigg\|_{y_r=y_r^0} &= \left[\frac{v_{s_y}^i - v_{r_y}^0}{\|\boldsymbol{p}_s^i - \boldsymbol{p}_r^0\|} + (y_r^0 - y_s^i)(\boldsymbol{v}_s^i - \boldsymbol{v}_r^0).\frac{\boldsymbol{p}_s^i - \boldsymbol{p}_r^0}{\|\boldsymbol{p}_s^i - \boldsymbol{p}_r^0\|^3}\right] \\ \frac{\partial\dot{\rho}_i}{\partial z_r}\bigg\|_{z_r=z_r^0} &= \left[\frac{v_{s_z}^i - v_{r_z}^0}{\|\boldsymbol{p}_s^i - \boldsymbol{p}_r^0\|} + (z_r^0 - z_s^i)(\boldsymbol{v}_s^i - \boldsymbol{v}_r^0).\frac{\boldsymbol{p}_s^i - \boldsymbol{p}_r^0}{\|\boldsymbol{p}_s^i - \boldsymbol{p}_r^0\|^3}\right] \\ \frac{\partial\dot{\rho}_i}{\partial v_{r_x}}\bigg\|_{v_{r_x}=v_{r_x}^0} &= \frac{(x_s^i - x_r^0)}{\|\boldsymbol{p}_s^i - \boldsymbol{p}_r^0\|} \\ \frac{\partial\dot{\rho}_i}{\partial v_{r_y}}\bigg\|_{v_{r_y}=v_{r_y}^0} &= \frac{(y_s^i - y_r^0)}{\|\boldsymbol{p}_s^i - \boldsymbol{p}_r^0\|} \\ \frac{\partial\dot{\rho}_i}{\partial v_{r_z}}\bigg\|_{v_{r_z}=v_{r_z}^0} &= \frac{(z_s^i - z_r^0)}{\|\boldsymbol{p}_s^i - \boldsymbol{p}_r^0\|} \\ \frac{\partial\dot{\rho}_i}{\partial\delta\dot{t}_r}\bigg\|_{\delta\dot{t}_r=\delta\dot{t}_{r,0}} &= c\end{aligned} \tag{8}$$

In the Equations 7, 8, $\boldsymbol{p}_s^i = [x_s^i, y_s^i, z_s^i]^T$ and $\boldsymbol{v}_s^i = \left[v_{s_x}^i, v_{s_y}^i, v_{s_x}^i\right]^T$ represent the satellite position and velocity at that moment, respectively. $\boldsymbol{p}_r^0 = [x_r^0, y_r^0, z_r^0]^T$ and $\boldsymbol{v}_r^0 = \left[v_{r_x}^0, v_{r_y}^0, v_{r_z}^0\right]^T$ represent the receiver position and velocity at the initial moment. $\Delta\mathbf{X}_r = \left[\Delta x_r, \Delta y_r, \Delta z_r, \Delta v_{r_x}, \Delta v_{r_y}, \Delta v_{r_x}, \Delta\delta t_r\right]^T$ is a correction to the initial value. For the positioning model based on the least squares method, when the receiver receives signals of opportunity from N satellites, the least squares iterative equation can be obtained from multiple observation equations:

$$\Delta\dot{\boldsymbol{\rho}} = \mathbf{G}\cdot\Delta\mathbf{X}_r + \boldsymbol{\varepsilon}$$

$$\mathbf{G} = \begin{bmatrix} \frac{\partial\dot{\rho}_1}{\partial x_r} & \frac{\partial\dot{\rho}_1}{\partial y_r} & \frac{\partial\dot{\rho}_1}{\partial z_r} & \frac{\partial\dot{\rho}_1}{\partial v_{r_x}} & \frac{\partial\dot{\rho}_1}{\partial v_{r_y}} & \frac{\partial\dot{\rho}_1}{\partial v_{r_z}} & c \\ \frac{\partial\dot{\rho}_2}{\partial x_r} & \frac{\partial\dot{\rho}_2}{\partial y_r} & \frac{\partial\dot{\rho}_2}{\partial z_r} & \frac{\partial\dot{\rho}_2}{\partial v_{r_x}} & \frac{\partial\dot{\rho}_2}{\partial v_{r_y}} & \frac{\partial\dot{\rho}_2}{\partial v_{r_z}} & c \\ \vdots & \vdots & \vdots & \vdots & \vdots & \vdots & \vdots \\ \frac{\partial\dot{\rho}_n}{\partial x_r} & \frac{\partial\dot{\rho}_n}{\partial y_r} & \frac{\partial\dot{\rho}_n}{\partial z_r} & \frac{\partial\dot{\rho}_n}{\partial v_{r_x}} & \frac{\partial\dot{\rho}_n}{\partial v_{r_y}} & \frac{\partial\dot{\rho}_n}{\partial v_{r_z}} & c \end{bmatrix}_{N\times 7} \tag{9}$$

In the Equation 9, $\Delta\dot{\boldsymbol{\rho}}$ represents the difference vector between the observed and predicted values of the Doppler frequency shift of the satellite signal received by the receiver, and $\boldsymbol{\varepsilon}$ denotes the observed noise vector. According to the principle of least squares, the solution can be determined as follows:

$$\Delta\mathbf{X}_r = \left(\mathbf{G}^T\cdot\mathbf{W}\cdot\mathbf{G}\right)^{-1}\mathbf{G}^T\cdot\mathbf{W}\cdot\Delta\dot{\rho} \tag{10}$$

In the Equation 10, $\mathbf{W}$ represents the weight matrix, typically the inverse of the Doppler measurement error covariance matrix. If the errors of different measurement values are uncorrelated, $\mathbf{W}$ becomes a diagonal matrix. By correcting the initial value $\mathbf{X}_0$ with the calculated $\Delta\mathbf{X}_r$, the updated estimated solution is obtained as $\mathbf{X}_0 + \Delta\mathbf{X}_r$. This updated solution is then carried over to the next iteration. The process continues until $\Delta\mathbf{X}_r$ converges to a predefined threshold. At this point, the iteration stops, and the final estimated value is obtained as $\mathbf{X}_k = \mathbf{X}_{k-1} + \Delta\mathbf{X}_r$.

The positioning models based on the least squares method are not robust to erroneous data, but they are simple and offer high computational efficiency [31]. Psiaki et al. [33] demonstrated single epoch positioning simulations using the Doppler frequency shift from eight or more measurements through least squares fitting. Khalife et al. [34] employed the weighted least squares method to achieve multi-epoch positioning using the Doppler frequency shift of Starlink satellites. For positioning models based on the extended Kalman filter (EKF), in addition to utilizing the aforementioned linearized observation model, the state model of the receiver is also required. The accuracy of the state model directly impacts the positioning performance of the receiver. Singh et al. [35] introduced the use of the EKF to fuse information from multiple satellites for positioning and evaluated the algorithm's performance. In addition to the initial state, an initial error covariance matrix must be provided when using the EKF. Currently, there is no explanation in the published literature on how to determine the initial covariance matrix. Beyond its application in positioning models, the EKF is also frequently used in observation extraction. Stock et al. [7] summarized examples of EKF usage in existing literature and explained its feasibility with the navigation system.

# 3 Error source analysis

The measurement errors can be categorized into three types based on their sources: satellite-related errors, signal propagation-related errors, and receiver-related errors. Satellite-related errors primarily consist of satellite clock errors and satellite ephemeris errors. These errors are caused by the inability of the satellite ground monitoring system to make absolutely accurate measurements and predictions of the satellite orbit and the frequency drift of the satellite clock. Signal propagation-related errors refer to the atmospheric delay caused by the impact of satellite signals as they pass through the atmosphere. Receiver-related errors are caused by the multipath effect and the clock error of the receiver. The following sections analyze the impacts on Doppler-based positioning in LEO systems and present corresponding mitigation strategies. Table 2 provides a fundamental overview of error sources and their associated mitigation techniques, with generalized indications of each error source's relative significance. However, when considering specific opportunistic LEO-PNT implementations, the actual relevance of these error sources may diverge substantially from the tabular representations. This discrepancy arises because error source impacts are fundamentally contingent upon multiple system-specific parameters including (but not limited to) constellation size, signal frequency allocation, observation duration characteristics, and orbital data provenance.

TABLE 2 Major error sources in opportunistic LEO-PNT.

| Error source | Significance | Mitigation techniques |
|---|---|---|
| Orbital Errors | Highly Significant | - Enhanced precision orbit determination<br>- Differential positioning |
| Clock Errors | Significant | - Highly stable receiver clocks<br>- Receiver clock state estimation |
| Atmospheric error | Significant | - Applying atmospheric models<br>- Dual-frequency observations<br>- Signals with higher frequencies |

## 3.1 Satellite orbit error

The rapid movement of LEO satellites results in frequent changes in their position and elevation, making LEO-based positioning more sensitive to satellite-related errors, such as satellite position and velocity errors. The orbit determination of GNSS satellites has been extensively studied, achieving accuracy at the centimeter level or higher. However, for LEO satellites without GNSS receivers and atomic clocks, this poses a challenging problem [12]. A precise Positioning, Navigation, and Timing (PNT) receiver needs to know the position and velocity of the satellite at the time of signal transmission. Typically, this information is obtained using a set of parameter data called ephemeris, such as the TLE file format published online by Celestrak [13]. TLE files are published once or twice a day, including the status of satellites at specific past times, and then the SGP4 propagation algorithm is used to predict the satellite's position and velocity during signal transmission [14, 15]. Since the estimated orbit observation data and model contain errors, and the orbit recurrence method also introduces errors, the assumed satellite state of the receiver differs from the actual state, resulting in positioning errors of the receiver.

The accuracy of satellite orbits has always been a focal point for space-based signals of opportunity (SOP). Currently, the only available online resource is the Two-Line Element (TLE) file released by the North American Aerospace Defense Command (NORAD). However, the accuracy of these orbits at the epoch time is approximately 3 km [16], and the accuracy is further reduced due to the recurrence of orbits. In this context, satellite orbit error is typically considered the primary error source for space-based SOP positioning. Qinhonglei et al. [17] used a geometric analysis method to analyze the impact of orbit error on Doppler positioning error from a geometric perspective. For a stationary ground receiver, the relative operating speed between the transmitter and the receiver is primarily caused by the satellite's speed, which can be expressed as:

$$v_{rv} = v_{sat} \cos\theta \tag{11}$$

In the Equation 11, $v_{sat}$ represents the speed of the satellite, and $\theta$ is the angle between the direction of satellite motion and the line-of-sight direction, also known as the field-of-view angle

When an error exists in the satellite speed, the field-of-view angle will change accordingly. This relationship can be expressed as:

$$\theta_{obs} = \theta + \Delta\theta = \arccos\left(\frac{f_{d\mathrm{Real}}}{v_{sat} + \Delta v_{sat}} \cdot \lambda_{f_T}\right) \tag{12}$$

In the Equation 12, $f_{d\mathrm{Real}}$ represents the true Doppler frequency shift, and $\Delta v_{sat}$ represents the satellite speed error.

The impact of velocity error on positioning is shown in Figure 2A. The effect of satellite velocity error on the equivalent Doppler circular conical surface is to alter the field-of-view angle. When the receiver uses this satellite and other satellites for positioning, due to the presence of satellite velocity error, the actual intersection should be located on the inaccurate equivalent Doppler circular conical surface, rather than the true equivalent Doppler circular conical surface. Consequently, the positioning solution is at point B rather than the true position A. In reality, $\Delta\theta$ is not a constant. Assuming that the equal Doppler circular conical surface 2 and the equal Doppler circular conical surface 1 correspond to the boundary value of velocity error, the equal Doppler circular conical surface obtained by the receiver lies between the equal Doppler circular conical surface 1 and the Doppler circular conical surface 2, sharing the same vertex. Therefore, the influence of velocity error transforms the equal Doppler circular conical surface into a special geometric shape, with its base forming a ring.

When considering the influence of satellite motion direction error, let $\Delta\beta$ denote the deviation of satellite motion direction. The impact of this error on positioning is depicted in Figure 2B. The equivalent Doppler circular conical surface with error deviates from the real equivalent Doppler circular conical surface by $\Delta\beta$. Consequently, the position solution should be at point B, rather than point A. Given that the error is random, its magnitude and corresponding direction are uncertain. Assuming that the equivalent Doppler circular conical surface with velocity direction error rotates around the real line of sight direction while the field angle $\Delta\beta$ remains unchanged, the equivalent Doppler circular conical surface transforms into a special geometric shape. It can be observed that the influence of the direction error of satellite velocity on the equivalent Doppler circular conical surface is analogous to that of satellite velocity error.

For the satellite position error, the field angle of the equivalent Doppler conical surface is independent of the satellite's position. The impact of this error on positioning is depicted in Figure 2C. The satellite position with error is located inside or on the surface of a sphere centered at the true satellite position, with a radius equal to the maximum error $L_{max}$.

Therefore, the satellite position error transforms the normal equivalent Doppler circular conical surface into an irregular geometry. Generally, the sensitivity of Doppler positioning to satellite position error is less than that to satellite velocity error. This is because the former only changes the position of the equivalent Doppler circular conical surface, while the latter changes the field angle, and the positioning error is related to the line of sight. For a specific satellite, the influence of orbit error on the equivalent Doppler circular conical surface is the combination of all effects of satellite positioning error, satellite velocity error, and velocity direction error. When the orbit error exists, the satellite velocity error will change the contour of the equivalent Doppler circular conical surface, while the satellite position error will change the position of the equivalent Doppler circular conical surface, resulting in an irregular geometry of the equivalent Doppler circular conical surface.

Shi et al. [10] conducted a simulation analysis by adding random errors of varying magnitudes to the satellite position or velocity. The results indicate that the positioning results are less sensitive to satellite position errors than to satellite velocity errors. The positioning accuracy will be reduced if the satellite position error is at the meter level and the velocity error is at the centimeter level per second. When the satellite orbit error increases by one order of magnitude, the positioning error will also increase by one order of magnitude. The positioning results are presented in Table 3, where RMS, N, E, and U represent the root mean square, north, east, and up directions, respectively.

In order to address the impact of satellite orbit errors, Ardito et al. [18] proposed a Simultaneous Tracking and Navigation (STAN) framework, which solves this issue by tightly integrating an Inertial Navigation System (INS) with Doppler and pseudo-range measurements. Khalife et al. [19] proposed a differential framework to tackle this problem. Qinhonglei et al. [20] targeted the traditional long baseline model, arguing that the assumption of parallel sight vectors between the two receivers in the basic differential positioning model is untenable. They proposed a Doppler differential positioning algorithm based on sight vector correction. By determining the sight vectors, the projection of the baseline in this direction becomes a pseudorange difference, thereby reducing positioning errors under long baselines. Zhao et al. [21] analyzed the error elimination method in the differential Doppler positioning system based on the differential framework and proposed a signal transmission time algorithm based on Maximum Likelihood Estimation (MLE) to mitigate the impact of orbit errors. In addition to the differential method requiring additional reference stations, Wang et al. [22] reduced the impact of satellite position errors by introducing a coarse time compensation term. Although this compensates for errors along the satellite motion direction, it cannot compensate for radial direction errors. Furthermore, positioning accuracy can also be improved by obtaining high-precision tracking data. Khairallah and Kassas et al. [16] conducted experiments on Doppler and carrier phase

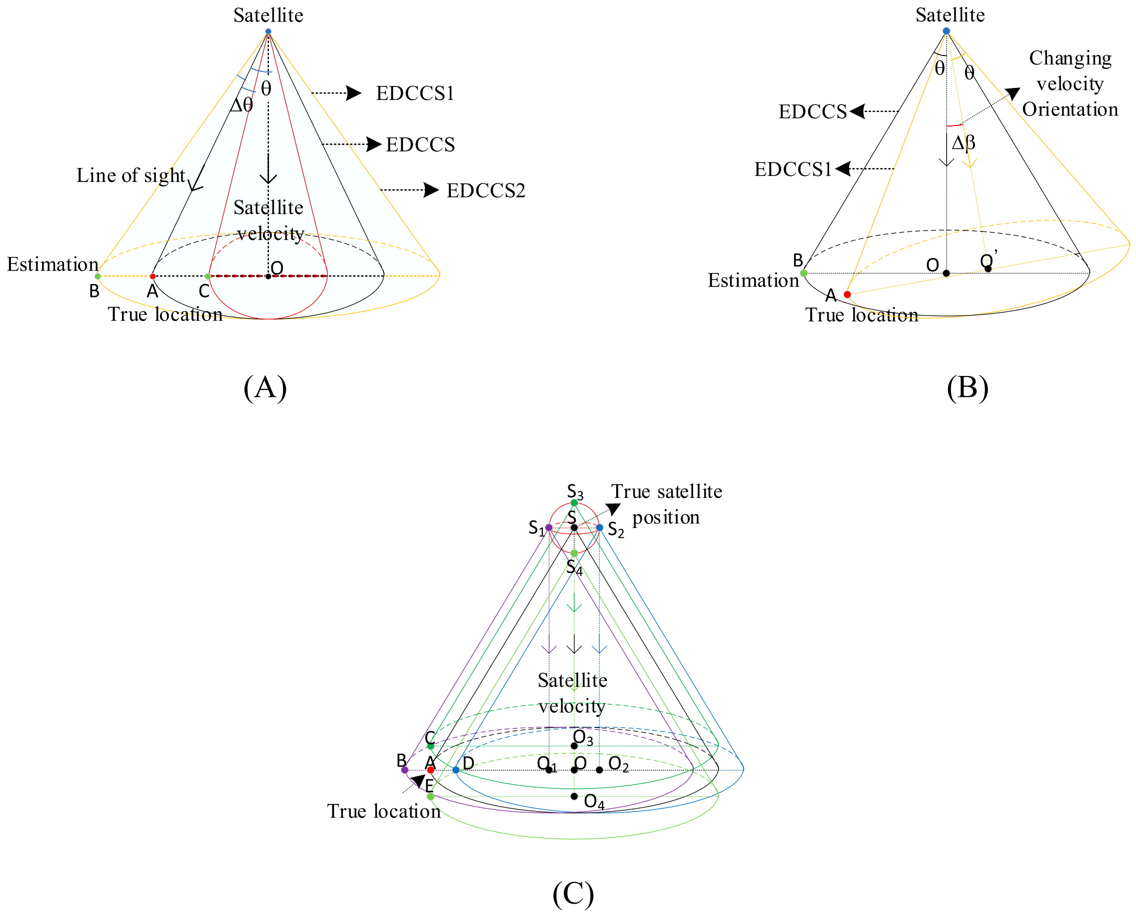

FIGURE 2
Impact analysis of orbital errors [16]. **(A)** Velocity errors **(B)** velocity direction errors **(C)** Position errors.

ephemeris tracking, providing precise ephemeris for positioning another static receiver. To address the challenge that traditional orbit determination methods are difficult to apply to non-cooperative LEO satellites, Deng et al. [23] proposed a multi-receiver Doppler orbit determination scheme and introduced a Search Least Squares (SLS) algorithm for initial orbit determination, offering a reliable initial value method for accurate orbit determination. However, this method is overly dependent on prior orbit parameters. With the advancement of artificial intelligence, machine learning methods are gradually being applied to the orbit determination of LEO satellites.

## 3.2 Clock error

Because most LEO satellites are not designed for navigation purposes, the on-board clock of LEO satellites is not necessarily an atomic clock, nor is it necessarily precisely synchronized. In addition, the receiver typically uses a lower-quality oscillator. Therefore, the offset and drift of the satellite and receiver clocks may be quite significant. Although LEO opportunistic signal positioning is not affected by the clock offset between the satellite and the receiver as in the pseudorange positioning of the GNSS system, the clock drift between the satellite and the receiver will seriously impact the measured Doppler frequency shift.

Mortlock et al. [24] conducted a simulation-based comparative analysis through two controlled experimental scenarios:1. Fixed receiver clock with variable satellite clock parameters; 2. Fixed satellite clock with variable receiver clock specifications. Their investigation systematically quantified how positioning performance responds to receiver clock quality variations and transmitter clock imperfections in LEO constellations. Notably, the study revealed that positioning accuracy exhibits remarkable insensitivity to LEO transmitter clock quality regardless of constellation size. In a complementary approach, Cassel et al. [25] implemented synchronized clock variation simulations where both transmitters and receivers employed identical clock architectures. Their results demonstrated that simultaneous adoption of next-generation atomic clocks at both ends enhances Doppler-based positioning precision by approximately an order of magnitude compared to conventional oscillators. These findings collectively establish that receiver clock characteristics exert critical influence on LEO-PNT performance–while transmitter clock quality shows limited impact, receiver clock advancements yield substantial system-level improvements.

To mitigate the impact of clock errors, several methods have been proposed. Wang et al. [26] addressed the impact of receiver clock errors on LEO positioning performance by proposing a mutual feedback positioning algorithm based on the LSTM model and the error state Kalman filter (ESKF) model, which can compensate for clock errors and reduce their impact on positioning accuracy. To enhance the accuracy of the receiver clock model, Cassel et al. [25] utilized a more complex three-state model instead of the conventional dual-state model, thereby improving positioning accuracy. In addition to reducing the impact of receiver clock errors, this approach can also enhance the accuracy of LEO clocks. Yang et al. [27] proposed a real-time estimation method for low Earth orbit (LEO) satellite clock errors based on ground tracking stations, and the feasibility of this method was verified through simulations. Wang et al. [28] investigated two typical types of satellite clocks and proposed a LEO satellite clock prediction model based on GNSS accurate clock estimation. The model considered systematic effects and was compared with a simple polynomial fitting model. Khairallah et al. [29] proposed a method for adaptive estimation of satellite clock state noise covariance for positioning filtering. Compared with the Kalman filter with mismatched measurement covariance, this method can improve positioning accuracy.

## 3.3 Atmospheric error

Atmospheric errors can be categorized into ionospheric and tropospheric errors. Ionospheric delay is inversely proportional to the square of the frequency and directly proportional to the total number of free electrons in the signal path. Small-scale irregularities in electron density lead to rapid fluctuations in amplitude (fading) and carrier phase (scintillation). Due to the group delay effect of the ionosphere, pseudo-range and phase measurements deviate, and since frequency is the rate of phase change over time, Doppler measurements are also affected. The impact of ionospheric delay on positioning accuracy is highly dependent on the signal frequency. For Doppler-based positioning systems, the ionospheric effect is primarily reflected in the change of delay rate. The ionospheric delay rate for VHF/L-band signals cannot be ignored in LEO positioning, as it is inversely proportional to the square of the frequency. In the VHF band, ionospheric delay rate can cause positioning errors based on Doppler frequency shift of up to several kilometers [30]; in the L-band, the error is tens of meters [10]; in the K-band, the error is far less than 1 m and can be neglected [10]. For dual-frequency receivers, ionospheric delay rate can be eliminated by using ionosphere-free combinations of pseudo-range rate measurements. However, this method is not suitable for space-based LEO opportunistic signals. Nonetheless, the ionospheric effect can be mitigated by using signals with higher carrier frequencies.

In addition to the ionospheric effect, the tropospheric effect must also be considered. Since the troposphere is non-dispersive, it introduces a non-frequency-selective delay to the signal, which depends on factors such as temperature, atmospheric pressure, humidity, water vapor, and elevation [31]. Similar to the ionosphere, the troposphere also introduces a delay rate. For Doppler positioning, a high delay rate may lead to Doppler positioning errors as large as tens of meters [10]. If the tropospheric error is not corrected, the positioning accuracy will deteriorate significantly. Tropospheric error can be corrected through modeling. Khalife et al. [32] studied the impact of tropospheric delay on carrier phase and differential measurements using the typical Hopfield model and concluded that the longer the baseline length, the greater the residual delay, and the greater the impact on positioning accuracy.

# 4 Advances in observable extraction and positioning using LEO opportunistic signals

At present, the number of LEO satellites in orbit is the largest, and tens of thousands of LEO satellites will be launched in the next few years, providing a large number of radiation sources for space-based signals of opportunity positioning. In recent years, low Earth orbit satellite systems (such as Orbcomm, Starlink, OneWeb, etc.) have developed rapidly. Many scholars regard them as signals of opportunity sources to study and explore the possibility of their positioning. Table 4 summarizes the information of the five LEO constellations that have been widely studied at present. In this paper, the LEO constellations in the following table will be introduced in detail, and their current research status will be summarized.

## 4.1 Location based on iridium opportunistic signal

The Iridium system, proposed by Motorola, is a global satellite mobile communication system. It comprises 66 LEO satellites, distributed across 6 orbital planes, with each plane consisting of 11 operational satellites and 1 backup satellite. The orbital inclination is 86.4°, and the altitude is approximately 780 km, enabling global coverage. After undergoing bankruptcy and reorganization, the system was redesigned as the second-generation Iridium Next to provide Satellite Timing and Location (STL) services. These services are intended to serve as a backup to the Global Positioning System (GPS) and represent a dedicated low Earth orbit positioning system. Iridium Next employs Time Division Multiple Access (TDMA) for signal transmission. The downlink frequency band allocated to Iridium is 1616–1626.5 MHz, of which 1616–1626 MHz are duplex channels used as traffic channels, divided into 30 sub-bands. Each sub-band is further divided into 8 channels, resulting in a bandwidth of 41.67 kHz per channel. The 1626–1626.5 MHz band is a simplex channel, divided into 12 subchannels, each with a bandwidth of 41.67 kHz. This bandwidth is further divided into a working bandwidth of 31.50 kHz and a protection bandwidth of 10.17 kHz [36]. Five simplex downlink channels are utilized, including Ring Alert signal and four other signals. The Medium Quaternary Message Channel is also used for the Satellite Time and Location service, which is only accessible to authorized users. The remaining seven simplex downlink channels serve as protection bands [37]. The downlink frequency band distribution of the system is illustrated in Figure 3.

The frame length of Iridium Next is 90 ms, and the Ring Alert signal has high availability and wide coverage, which meets the

TABLE 3 Impact of different orbital errors on Doppler positioning accuracy [9].

| Satellite position error (m) | Satellite velocity error (cm/s) | RMS-N (m) | RMS-E (m) | RMS-U (m) | RMS-3D (m) |
|---|---|---|---|---|---|
| 0 | 0 | 1.379 | 2.920 | 4.070 | 5.195 |
| 0 | 0 | 1.379 | 2.920 | 4.070 | 5.195 |
| 0.03 | 0 | 1.378 | 2.921 | 4.070 | 5.196 |
| 0 | 0.3 | 1.384 | 2.950 | 4.091 | 5.230 |
| 3 | 0 | 1.602 | 3.516 | 4.364 | 5.829 |
| 0 | 3 | 1.749 | 3.934 | 5.109 | 6.681 |
| 30 | 0 | 8.196 | 18.773 | 18.261 | 27.444 |
| 0 | 30 | 10.953 | 25.828 | 29.017 | 40.361 |
| 300 | 0 | 80.279 | 178.167 | 183.805 | 268.277 |
| 0 | 300 | 108.827 | 255.685 | 286.723 | 399.285 |
| 3000 | 0 | 790.073 | 1865.394 | 1773.159 | 2692.212 |
| 0 | 3000 | 1085.340 | 2561.022 | 2842.690 | 3977.145 |

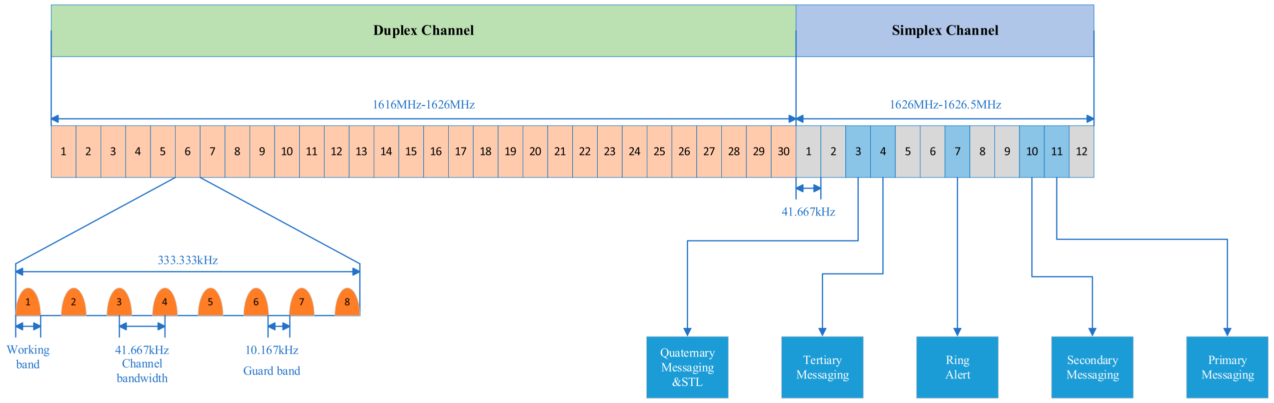

FIGURE 3
Iridium system user link frequency band allocation [43].

requirements for positioning. Users can receive the Ring Alert signal in simplex channel 7 every 4.32 s, with a time slot length of 20.32 ms for the simplex channel. Each Ring Alert signal consists of three parts: an unmodulated single-tone signal; a unique word modulated using Binary Phase Shift Keying (BPSK), whose modulation information is a 12-bit baseband data represented as “789” in hexadecimal; and data information modulated using Differential Quadrature Phase Shift Keying (DQPSK) [38]. The structure of the Iridium Next burst signal is shown in Figure 4. The single-tone signal is located at the front of the signal with a duration of 2.6 ms; the unique word has a duration of 0.48 ms; the data information is located at the end of the signal and has a duration of 3.42–17.24 ms [39], depending on the duration of the transmitted data. The duration of the Iridium Next signal ranges from 6.5 ms to 20.32 ms, with most signals lasting approximately 7 ms, and its spectrum is shown in Figure 5.

The Iridium Next signal is a discontinuous signal with a burst structure. Currently, most methods for its localization are based on the burst signal. A clear single-tone signal is transmitted at the front of each burst signal to facilitate signal acquisition, enabling the estimation of the Doppler frequency shift. The traditional Doppler measurement method for Iridium Next signals is typically implemented in the frequency domain. Khalife et al. [40] proposed a method that involves raising the signal to the Mth power to eliminate the influence of modulation information, then performing a Fast Fourier Transform (FFT) on the Mth power signal, and searching for the FFT peak as the Doppler measurement value to obtain the Doppler frequency shift of Iridium Next. Based

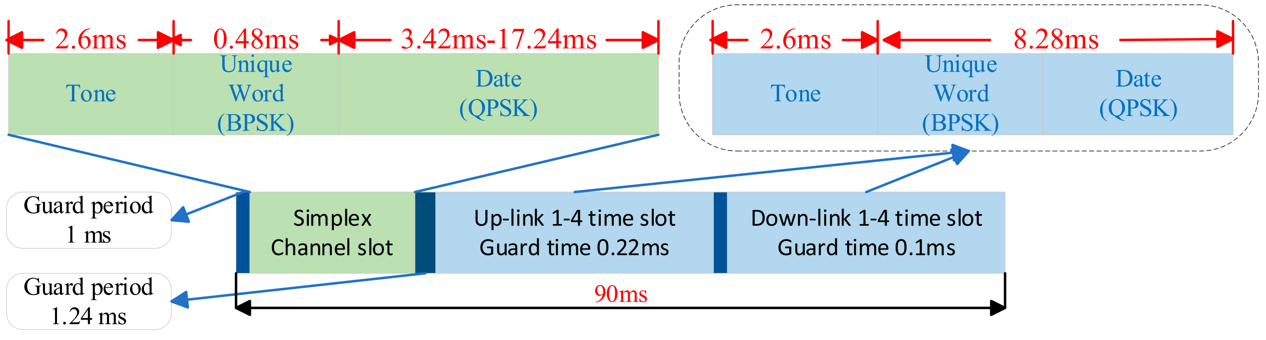

FIGURE 4
Iridium next burst signal structure.

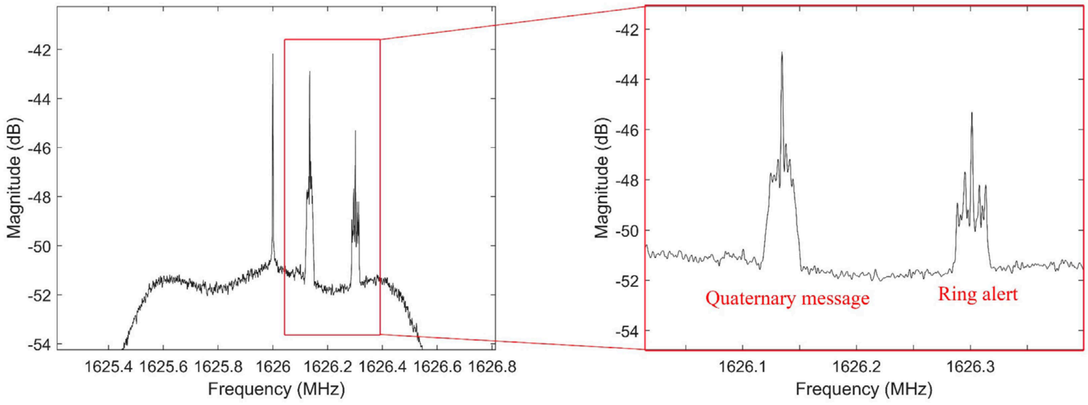

FIGURE 5
Power spectrum of Iridium-next [67].

on the unique structure of the Iridium Next signal, the existing Doppler measurement methods can be summarized as follows: first, coarse Doppler estimation is obtained by FFT for the single-tone (pilot) signal in the burst signal. Then, precise Doppler measurement is achieved through frequency-domain maximum likelihood estimation [17, 41]. Although the frequency-domain Doppler measurement algorithm is effective and relatively simple, its performance is limited by the frequency resolution. The traditional time-domain Doppler measurement method is generated by carrier phase difference. However, since the Iridium Next signal is modulated by QPSK and the modulation information is unknown, it is difficult to estimate the carrier phase, and this method is affected by noise in baseband signal processing. Wei et al. [42] proposed a method of fitting the phase of explicit and implicit pilots to obtain Doppler measurements. This method is limited to the simulation phase and is only applicable to signals with known implicit pilots. For signals without known implicit pilots, this method cannot further improve Doppler accuracy. Huang et al. [39] proposed the phase time method, which can utilize the complete Iridium Next signal, including pilot and modulation signals, without requiring prior information. This method can obtain more accurate Doppler measurements in static receivers and improve the stability and reliability of positioning, but it lacks verification in dynamic scenarios. To address the localization accuracy limitations of the Doppler-based method, Liang et al. [43] proposed a localization method based on Doppler-compensated pseudorange by decoding the Iridium signal. This method obtains the pseudorange and pseudorange rate by jointly estimating the time delay and Doppler, and uses this information for positioning. This method solves the problem of inconsistency between the epoch time of the Iridium signal and the assumed signal time. By estimating the epoch time error and compensating the pseudorange, the positioning error is significantly reduced. However, this method has the issue of high complexity and difficulty in adapting to rapidly changing signal environments. Tan et al. [44] studied the positioning method using Iridium signals in weak signal environments, analyzed the signal characteristics of Iridium in detail, and proposed a QSA-IDE algorithm to estimate its Doppler frequency shift in weak signal environments. This novel approach enhances weak-signal Doppler estimation through two-stage processing:1. Quadratic square accumulation processing boosts signal-to-noise ratio (SNR); 2. Full-duration Iridium signals are utilized for maximum likelihood estimation (MLE) to achieve precise Doppler frequency shift estimation.

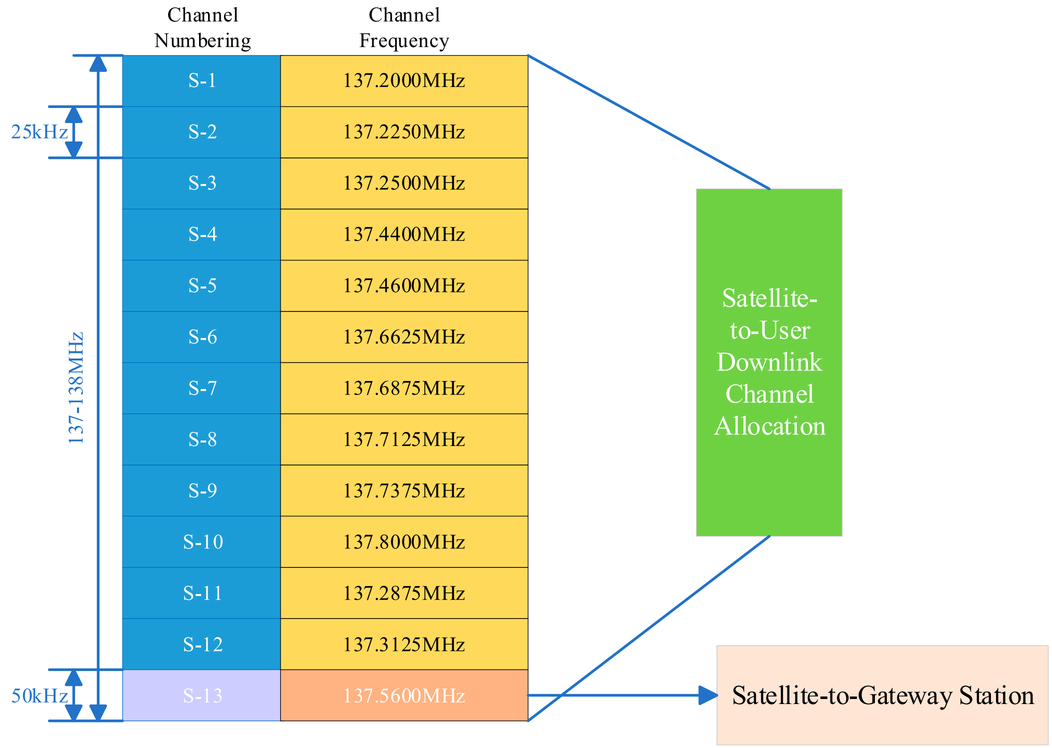

FIGURE 6
Orbcomm satellite downlink frequency band allocation [46].

## 4.2 Location based on Orbcomm opportunistic signals

The Orbcomm system is a two-way communication system that utilizes a low Earth orbit satellite constellation to provide global geographic coverage. There are 42 satellites distributed across 7 orbital planes labeled a through g [45]. Each of the a, b, c, and d planes contains 8 satellites, with an inclination of 45° and an orbital altitude of approximately 815 km. Plane e has an inclination of 0°, includes 6 satellites, and has an orbital altitude of 975 km. Plane f has an inclination of 70° and contains two satellites in a near-polar circular orbit at an altitude of 740 km. Plane g has an inclination of 108° and contains two satellites in a near-polar elliptical orbit, with the orbital altitude varying from 785 km to 875 km. Orbcomm completed the deployment of the second-generation satellite (OG2) constellation in 2014. The OG2 constellation is a Walker constellation, with its satellites evenly distributed across four orbital planes at an inclination of 47°. The orbital altitude and period of the OG2 satellite are approximately 710 km and 97 min, respectively. Currently, positioning research based on the Orbcomm satellite is conducted using the OG2 satellite.

The Orbcomm system employs Frequency Division Multiple Access (FDMA) to transmit downlink signals, which occupy the Very High Frequency (VHF) band of 137–138 MHz, as illustrated in Figure 6 [46].

The downlink channel of the Orbcomm system includes 12 channels designated for user transmission and one gateway channel for ground station transmission. Each satellite broadcasts signals in two specific channels through spectrum sharing, employing symmetric differential quadrature phase shift keying (SD-QPSK) modulation, with a symbol rate of 4,800 bps. Currently, only the VHF signal of the downlink channel is utilized for opportunistic localization.

The expression of SD-QPSK modulation signal is:

$$s(t) = \sum_{i=-\infty}^{\infty} g\left(t - iT_{sym}\right) \exp\left[j\left(2\pi f_r t + \varphi_r + \varphi_i\right)\right] \tag{13}$$

In the Equation 13, $g(t)$ represents the pulse function, where $t > 0$ denotes the time elapsed since the signal was received, $f_r$ is the carrier frequency of the received signal, $\varphi_r$ is the initial phase of reception, $T_{sym}$ is the symbol period, and $\varphi_i$ is the phase of the $i$-th symbol, which can be expressed as:

$$\begin{cases} \varphi_i = \varphi_{i-1} + \dfrac{\pi}{2} b_i \\ \varphi_0 = 0, i = \lceil (t + \tau_r)/T_{sym} \rceil \end{cases} \tag{14}$$

In the Equation 14, $b_i = \pm 1$ represents unknown baseband data, and $\tau_r \in \left(0, T_{sym}\right)$ is an unkown symbol delay. The spectrum diagram of the received signal is shown in Figure 7.

The power of the Orbcomm satellite signal reaching the ground is generally higher than that of the noise. Due to its SD-QPSK modulation, it is unable to directly obtain the Doppler measurement value through its spectrum. When using the Maximum Likelihood Estimation (MLE) method for accurate Doppler measurement, the correlation between the local carrier generated by the Doppler rough measurement value and the Orbcomm signal affects the relevant peak, which is influenced by the data bits. Qinhonglei et al. [46]

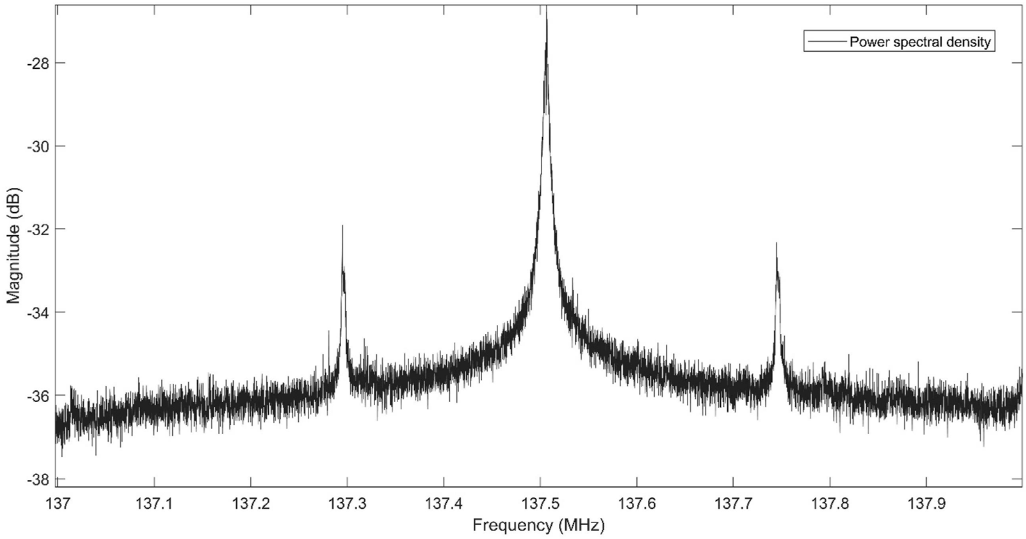

FIGURE 7
Power spectrum of Orbcomm [67].

found that after square processing of their signals, peak spectral lines appeared symmetrically on the left and right sides of the center frequency of the signal spectrum. Zhao et al. [41] detected the Orbcomm signal according to the spectral characteristics and estimated the coarse Doppler by calculating the center frequency of the bispectral line. Khalife et al. [47] used a phase-locked loop to achieve positioning of the Orbcomm opportunity signal and employed a Costas loop based on the maximum likelihood phase discriminator. However, the symbol period limits the coherent integration time, which reduces the input signal-to-noise ratio of the ML phase detector and makes the ML Costas loop unstable. Xie et al. [48] designed a carrier tracking loop based on square sum code phase assistance, which eliminates the disadvantage of the symbol period limiting the coherent integration time and obtains accurate carrier phase measurement under a low carrier-to-noise ratio.

## 4.3 Location based on Globalstar opportunistic signals

The Globalstar second-generation constellation, operational since 2013, consists of 32 satellites distributed in 8 orbital planes (4 satellites per plane) at an altitude of 1,414 km. This system employs Wideband Code Division Multiple Access (WCDMA) technology with QPSK modulation for its communication signals, as specified in. The user link facilitates bidirectional ground-to-satellite communication through a transparent payload architecture: user terminals receive signals relayed from ground stations via satellites, defined as the forward link. Specifically, the downlink operates in the S-band at 2,483.5–2,500 MHz, which constitutes the forward link's frequency allocation. To date, all published studies exclusively utilize the forward link's pilot signal for positioning purposes, whose modulation structure (including chip rate, symbol mapping, and pseudorandom noise sequence design) is analytically illustrated in Figure 8.

Each pilot signal employs three distinct pseudo-random noise (PN) sequences for QPSK modulation, namely, the short PN sequence, inner PN sequence, and outer PN sequence. These sequences are used to distinguish between satellites, orbits, and beams. In summary, the Globalstar downlink pilot signal can be expressed as:

$$\begin{aligned} s(t) &= AP(t)O(t)I(t)\cos\left(2\pi\left(f_0+f_d\right)t+\varphi\right) \\ &\quad + AP(t)O(t)Q(t)\sin\left(2\pi\left(f_0+f_d\right)t+\varphi\right)+n(t) \end{aligned} \tag{15}$$

In the Equation 15, $A$ represents the signal amplitude; $P(t)$ is short PN sequence; $O(t)$ is the outer PN sequence; $I(t)$ is the inner PN sequence used by QPSK modulation in the in-phase branch; $Q(t)$ is the inner PN sequence used by QPSK modulation in the quadrature branch; $f_0$ is the carrier fundamental frequency; $f_d$ is Doppler shift; $\varphi$ is the initial phase of the carrier; $n(t)$ is the noise.

Doppler compensation is the most challenging issue in opportunistic positioning using Globalstar satellites. In the Globalstar system, Doppler is compensated to a nominal value at the satellite or ground station [49]. When Doppler compensation is applied, the Doppler measured by the ground receiver differs from the true Doppler, making the measured Doppler unsuitable for opportunistic localization. Neinavaie et al. [50] confirmed the presence of Doppler compensation through experiments and found discrepancies between the received Doppler and theoretical calculations. They proposed a method to recover the Doppler frequency by exploiting spectral distortion, enabling the retrieval of the true Doppler frequency even when compensation is applied. Zhang et al. [51] analyzed the modulation process of Globalstar signals, processed the Quadrature Phase Shift Keying (QPSK) pilot signal to the fourth power, selected an appropriate Fast Fourier Transform (FFT) time, extracted the Doppler observation value, and discovered that the pilot signal of the Globalstar forward link

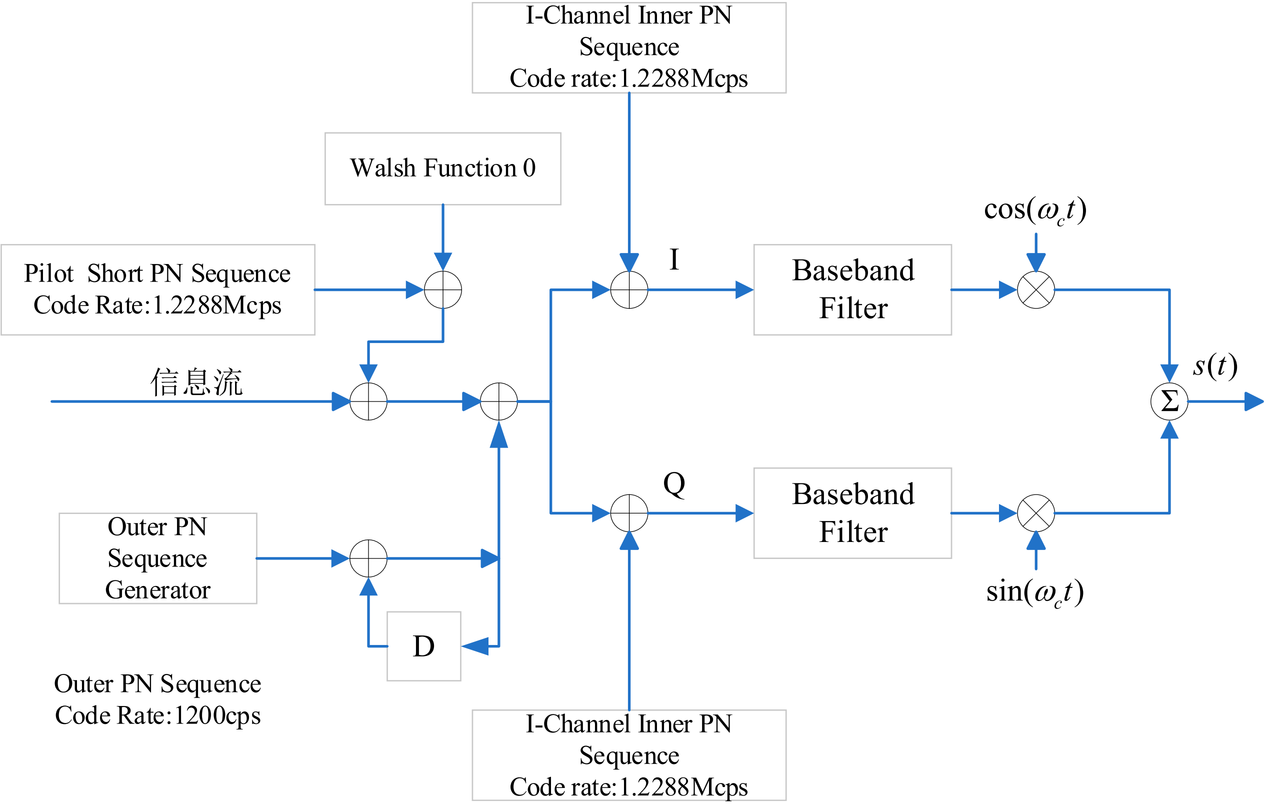

FIGURE 8
Forward link QPSK spread spectrum modulation.

in Beijing did not pre-compensate for Doppler. Due to the low signal-to-noise ratio of the Globalstar signal, traditional quartic despreading severely degrades the signal-to-noise ratio, leading to the failure of Doppler frequency extraction. Qinhonglei et al. [52] proposed that the acquisition of the Globalstar pilot signal is achieved by decoding the square cross-harmonic term and conducting parallel code phase frequency searches. The decoded local spread spectrum sequence is not affected by the degradation of the signal-to-noise ratio, thereby overcoming the challenge of low signal-to-noise ratio to a certain extent.

## 4.4 Location based on Starlink opportunistic signals

Starlink, a low Earth orbit (LEO) satellite constellation launched by SpaceX, aims to provide high-speed Internet services globally [53]. The system comprises thousands of satellites operating at different altitudes, with the majority located in LEO at an altitude of 550 km. To date, over 7,000 satellites have been launched, with 4,748 currently in service, primarily distributed across five distinct orbital shells to achieve global coverage. The detailed format of Starlink's downlink signals is not publicly available. The only known information about these signals is their carrier frequency and bandwidth. The downlink signals occupy a 250 MHz bandwidth in the Ku band to provide high-speed broadband connections. Nine single-tone signals are broadcast at the center of this bandwidth, spaced approximately 43.9 kHz apart [4].

Neinavaie et al. [54] analyzed the spectrum of the received Starlink signal after Doppler compensation and found that, in addition to the central single-tone signal, the Starlink downlink signal spectrum contains subcarriers similar to those used in Orthogonal Frequency Division Multiplexing (OFDM), as shown in Figure 9. Humphreys et al. provided a blind identification technology for the downlink signal of the satellite link in the 10.7–12.7 GHz band, given its OFDM format. This technology is an extension of the existing blind orthogonal frequency division multiplexing signal recognition method [55]. Using this method, the structure of the Starlink downlink signal in the 10.7–12.7 GHz band is described in detail, and the parameters within the signal are estimated and identified, as shown in Table 5. Currently, the published literature indicates that Starlink is primarily used to extract observations by utilizing its beacon signals located at the center of the user's downlink signal channel, i.e., a single-tone signal or by assuming that there is a periodic reference sequence in the frame of the OFDM signal.

For the single-tone signal in the spectrum, Khalife et al. [56] observed the beacon signal at 11.325 GHz of the Starlink satellite and used a carrier phase tracking algorithm based on the Adaptive Kalman filter to extract the Doppler frequency shift, achieving a three-dimensional positioning error of 33.5 m and a horizontal positioning error of 25.9 m. Jardak et al. [57] explored the feasibility

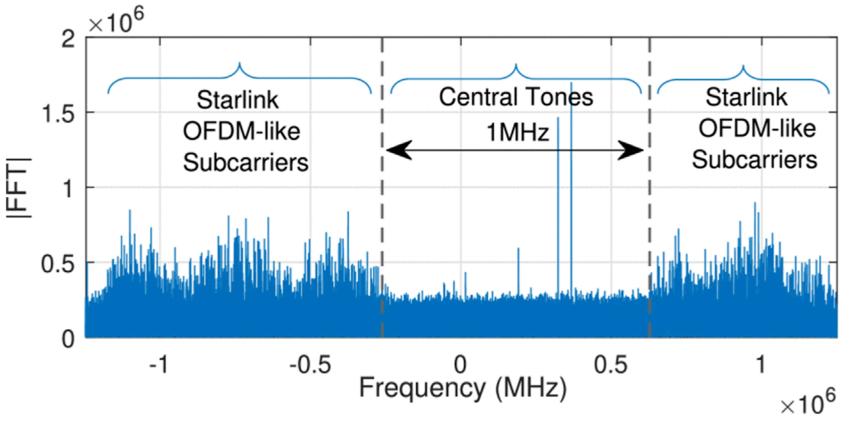

FIGURE 9
Spectrum of Starlink downlink signals after Doppler rate wipe-off [54].

TABLE 4 Comparison of LEO constellation parameters.

| Parameter | Iridium | Orbcomm | Globalstar | Starlink | OneWeb |
|---|---|---|---|---|---|
| Bandwidth | 31.5 kHz | 25 kHz | 1.23 MHz | 240 MHz | 230 MHz |
| Beacon Length | 90 ms | 1s | 0.24s | 4/3 ms | 10 ms |
| Modulation Type | DE-QPSK | SD-QPSK | QPSK | OFDM | OFDM |
| Frequency Band | L | VHF | S | Ku, Ka | Ku |
| Downlink Frequency | 1.616–1.626 GHz | 137–138 MHz | 2483.5MHz–2500 MHz | 10.7–12.7 GHz | 10.7–12.7 GHz |
| Number of Channels | 240 | 13 | 13 | 8 | 8 |
| Number of Beams | 48 | Unkown | 16 | 48 | 16 |
| Orbital Height | 780 km | 750 km | 1414 km | 550 km | 1200 km |

of receiving Starlink downlink signals for positioning without using a parabolic reflector and proposed a signal detection and tracking method using a general low noise block down converter and software-defined radio, which aggregated the Doppler frequency shift of multiple subcarriers of the beacon signal, reducing the impact of measurement noise. Yang et al. [58] proposed a baseband signal processing scheme without prior information of receiver position and time. Through a two-step method, it is challenging to determine the signal source of the Starlink signal in the presence of multiple satellites, and simple single-tone tracking cannot accurately estimate the carrier center frequency, which introduces ambiguity to Doppler estimation. Nonetheless, this method realizes the effective utilization of the Starlink signal and accurate Doppler and Doppler rate estimation. Qinhonglei et al. [59] used the beacon signals located at 11.325 GHz and 11.575 GHz simultaneously for positioning, employed the short-time Fourier transform for coarse Doppler extraction, and then used maximum likelihood estimation for accurate measurement. With the aid of elevation data, the horizontal positioning error of the results was 15 m. Yuanyiping et al. [60] designed a lightweight modular universal receiving device and observed the beacon signal (11.95 GHz/12.45 GHz) at the interval center between the downlink signal channels of the satellite link for the first time. Based on the beacon signal, a frequency-domain sliding window estimation algorithm was proposed, which successfully realized the estimation of Doppler frequency shift.

In addition to utilizing existing beacon signals, some scholars assume that the downlink signals of satellite link users contain periodic reference signals and use the characteristics of these periodic signals to extract the Doppler frequency shift. Khalife et al. [61] hypothesized that the downlink signal of the satellite link user contains periodic reference signals. Based on this assumption, they constructed a matching subspace detection method to detect the unknown reference signal of Starlink and estimate the unknown period and Doppler frequency. They also proposed a linear frequency modulation parameter estimator to track the Doppler frequency of the unknown Starlink signal by using the Wigner distribution to estimate the parameters of the linear frequency modulation signal. Building on this, the team developed an algorithm based on the Kalman filter to track the Doppler frequency of the unknown Starlink signal [34]. Neinavaie et al. [54] combined the beacon-based method with the OFDM-based reference signal method to significantly reduce the positioning error,

**TABLE 5** Starlink downlink signal parameters [55].

| Name | Parameter | Value | Unit |
|---|---|---|---|
| Channel Bandwidth | $F_s$ | 240 | MHz |
| Number of Subcarriers in bandwidth | $N$ | 1,024 | |
| Number of cyclic prefic intervals | $N_g$ | 32 | |
| Frame Period | $T_f$ | 1/750 | s |
| Frame guard interval | $T_{fg}$ | $68/15 = 4.5\overline{33}$ | μs |
| Number of non-zero symbols in a frame | $N_{sf}$ | 302 | |
| Number of data symbols in a frame | $N_{sfd}$ | 298 | |
| Useful OFDM symbol interval | $T = N/F_s$ | $64/15 = 4.2\overline{66}$ | $\mu s$ |
| Symbol guard interval | $T_g = N_g/F_s$ | $2/15 = 0.1\overline{33}$ | $\mu s$ |
| OFDM symbol duration | $T_{sym} = T + T_g$ | 4.4 | $\mu s$ |
| Subcarrier spacing | $F = F_s/N$ | 234,375 | Hz |
| Center frequency of $i$ th channel | $F_{ci}$ | $10.7+F/2+0.25\ (i\text{-}1/2)$ | GHz |
| Channel spacing | $F_\delta$ | 250 | MHz |
| Width of guard band between channels | $F_g$ | 10 | MHz |

decreasing the horizontal positioning error from 10 m to 6.5 m and thereby improving positioning accuracy. Shadram et al. [62] proposed a sequential method based on the classical linear model to estimate the number of Starlink satellites and their corresponding reference signals. This method uses the generalized likelihood ratio detector to design the Doppler tracking algorithm, establishes the equivalence between the generalized linear model and the matched subspace detector for the first time, and employs differential Doppler positioning technology to simultaneously receive satellite link beacon signals through two receivers separated by 1 km. The horizontal positioning error of the result is 5.6 m. Kozhaya et al. [63] proposed a blind Doppler spectrum method from the perspective of the frequency domain. This method uses a blind Doppler discriminator based on the frequency domain and a Doppler tracking algorithm based on the Kalman filter to achieve Doppler tracking accuracy at the Hertz level and a 2-D positioning error of 4.3 m.

## 4.5 Location based on OneWeb opportunistic signals

One of the goals of the OneWeb constellation is to create a navigation system independent of the Galileo system. The constellation plans to have 720 satellites, distributed across 18 orbital planes, with an orbital altitude of approximately 1,200 km and an orbital inclination of 87.9°. Satellites are evenly distributed within each plane and travel along the north-south direction. Satellites in adjacent planes are offset by half a satellite in latitude. OneWeb users' downlink signals are transmitted in the Ku band (10.7–12.7 GHz), and the downlink band is divided into eight consecutive 250 MHz channels [64]. The OneWeb constellation typically provides users with one of the 16 downlink beams at any given time, and each beam transmits on only one of the eight channels. Therefore, each OneWeb satellite multiplexes multiple users through frequency division (8 × 250 MHz channels) and spatial division (16 beams), as illustrated in Figure 10.

At present, the public literature indicates that research on positioning using the OneWeb constellation is limited. Kozhaya et al. [65] conducted the first study on OneWeb LEO satellite signals. Given the acquisition challenges such as high Doppler frequency and large search grid, they proposed a Doppler search algorithm based on two-step sampling to reduce computational complexity. A Kalman filter tracking loop combined with a phase-locked loop and delay locked loop was utilized to track satellite signals, generate code phase and carrier phase observations, and achieve positioning based on nine OneWeb satellites. Additionally, no other literature on OneWeb constellation positioning has been found.

## 4.6 Observation estimation algorithm

Before opportunistic low Earth orbit (LEO) positioning, navigation, and timing (PNT) processing, observations must be estimated as accurately as possible. However, the acquisition and frequency estimation of LEO signals are very challenging. Firstly, due to the high and rapidly changing relative speed between the transmitter and receiver, the transmission channel imposes a significant Doppler frequency shift on the signal. In addition, if the exact signal structure is not known, signal acquisition and frequency estimation

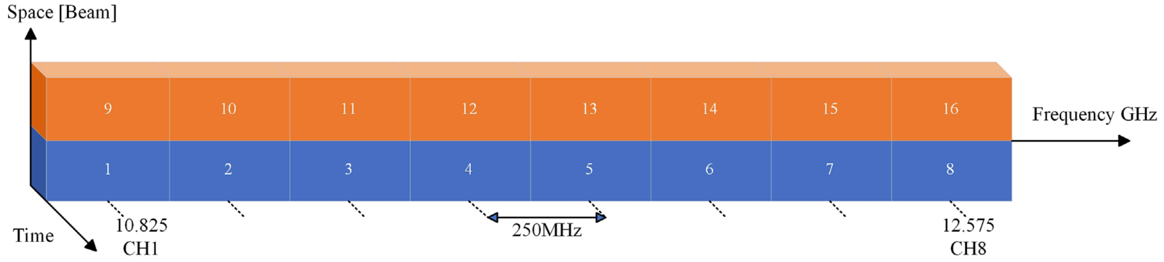

FIGURE 10
Diagram showing OneWeb's Ku-band downlink signal allocation [65].

TABLE 6 Comparative analysis of positioning performance across satellite constellations.

| Constellation | Receiver state | Observation | Positioning Error(m) | Ref |
|---|---|---|---|---|
| Iridium | Static | Doppler | 22 m (2D) | [16] |
| Orbcomm | Static | Carrier Phase | 77.5 m (3D) | [47] |
| Globalstar | Static | Doppler | ≤100 m (2D) | [51] |
| Starlink | Static | Doppler | 4.3 m (2D)<br>19.4 m (3D) | [62] |
| OneWeb | Static | Carrier Phase | 30.4 m (2D)<br>30.4 m (2D) | [64] |

will be hindered, requiring more complex algorithms. While the aforementioned challenges pose significant difficulties in observable extraction, thereby adversely affecting positioning accuracy. The current positioning results derived from major constellations have yielded surprisingly encouraging outcomes. A comparative analysis of these results is presented in Table 6, as detailed below. As illustrated in the table, opportunistic signals typically rely on either Doppler frequency shift measurements or carrier phase observations as primary observables. Currently, the published signal acquisition and observation estimation algorithms can be divided into two categories: one is a cognitive-based method, which uses the least available prior information about the LEO satellite signal structure; the other is the blind method, which does not assume that the Doppler frequency, modulation type, length, and symbol of the beacon signal are known, but only knows its bandwidth, and uses a cognitive decoding method to obtain this information [66].

### 4.6.1 Cognitive based approach

These methodologies typically necessitate prior knowledge of the satellite signal architecture, including modulation schemes, timing characteristics, and protocol-specific features, to enable effective observable extraction and parameter estimation.

#### 4.6.1.1 Mth-power algorithm

The Mth-power algorithm is specifically designed for M-ary Phase Shift Keying (MPSK) modulated satellite signals. This method operates by raising the received signal to the Mth power to eliminate modulation symbol effects, followed by spectral analysis via Fast Fourier Transform (FFT). In reference [47], it is deduced that the carrier phase or Doppler frequency shift of multiple different carrier frequency multiplexed signals is used. An independent Phase-Locked Loop (PLL) is employed to track the LEO satellite signal of each channel, and a maximum likelihood phase discriminator is used to obtain the phase error. Reference [40] proposed a receiver architecture suitable for processing Time Division Multiple Access (TDMA) and Frequency Division Multiple Access (FDMA) signals from Orbcomm and Iridium next-generation satellites. The received signals are down-converted and partitioned to generate Doppler frequency measurements of multi-constellation LEO satellites. However, when processing TDMA signals, it is necessary to use an energy detector to obtain the burst start time during its initialization phase and assume that the initial Doppler frequency is known. Reference [67] designed a multi-constellation software-defined receiver capable of processing QPSK modulated signals from Orbcomm and Iridium next satellites. The received signals are processed to the fourth power, the power spectral density (PSD) is analyzed using the Welch method, the PSD peak is found through a search window to determine the Doppler frequency, and the Doppler frequency shift of the detected signals is tracked using the classic Costas loop. Literature [41, 68] proposed a Doppler fusion positioning model based on the Helmert variance component estimation (HVCE) algorithm, analyzing the above Doppler frequency shift extraction methods of Orbcomm and Iridium signals, which improved positioning accuracy.

#### 4.6.1.2 Code phase search acquisition algorithm

The Code Phase Search Acquisition Algorithm can be employed to extract Doppler observables from opportunistic signals. Its fundamental principle lies in extracting the PN code sequences utilized in LEO satellite pilot signals or exploiting known pilot sequences, followed by correlation processing with the intermediate frequency signals acquired by receivers to estimate observation parameters. As demonstrated in literature [51], this methodology has been successfully applied to extract Doppler observables from GlobalStar downlink pilot signals, achieving horizontal positioning accuracy better than 100 m. The implementation procedure involves: Firstly, obtaining squared cross-harmonic terms through squaring processing. Owing to the strict orthogonality between the quadrature-phase and in-phase PN code sequences embedded in pilot signals, their coupled sequences maintain orthogonal characteristics while preserving identical code period and chip rate as the original PN sequences [51]. This inherent property facilitates periodic superposition operations, thereby enabling effective estimation of spread spectrum codes. Reference [69] studies the problem of joint synchronization and positioning using signals with known pulse shapes and modulation schemes and proposes a bandwidth-efficient algorithm for estimating the time difference of arrival (TDOA) and frequency difference (FDOA) between two receivers without exchanging original signals. Reference [71] proposed a Doppler frequency shift estimation algorithm based on correlation, but this algorithm assumes that the synchronization sequence is known.

#### 4.6.1.3 Matched subspace detector

The matched subspace algorithm constitutes a Doppler observable extraction methodology rooted in binary hypothesis testing and maximum likelihood estimation principles. The matched subspace detector has been widely used to address the detection problem of signal sources with unknown parameters in the presence of other interference sources [72, 73]. In the Starlink satellite, there are always-on and on-demand OFDM signals [70]. Certain LEO satellite synchronization signals exhibit inherent periodicity in their transmission characteristics, as exemplified by the Starlink constellation's synchronization signal architecture. In OFDM-based transmission, each OFDM frame contains periodic signals that are always-on and on-demand, which are used for synchronization and channel estimation. The period of these signals is typically equal to the frame length of the OFDM signals. However, in most cases, the synchronization sequence and its length are unknown. References [34, 61, 62] utilize the matched subspace algorithm to detect received opportunistic signals to provide initial estimates of unknown parameters. These parameters include: 1. The unknown number of satellites, 2. The corresponding periodic signal, and 3. Linear frequency modulation parameters (Doppler and Doppler rate). This method detects satellite signals in the environment by solving hypothesis testing problems at different stages. Compared with reference [90], a constant Doppler subspace is used to distinguish different satellites, and the matched subspace is defined based on the LFM parameters of each satellite. At each stage, a hypothesis test is conducted to detect the strongest satellite signal, and the LFM subspace of the previously detected satellite periodic signal is set to zero. A generalized likelihood ratio detector is used in each stage of the sequential detection algorithm. In the first stage of the sequential algorithm, it detects whether there is the strongest satellite signal. If the null hypothesis is accepted, it means that no satellite signal is detected in the received signal. If the null hypothesis is rejected, it indicates that there is at least one satellite signal, and if the detected satellite signal exists, hypothesis testing is carried out to detect the presence of other satellite signals, and the unknown LFM parameters and periodic sequence of each satellite signal are estimated at each stage.

### 4.6.2 Blind based approach

The core capability of a blind receiver lies in its ability to cognitively decode partially transmitted signals, estimate and track them, and ultimately generate navigation observables.

#### 4.6.2.1 Blind beacon estimation algorithm

This algorithm postulates the existence of periodically transmitted beacon signals and performs blind estimation through coherent integration of subsequent signal transmissions. The methodology proves applicable during online navigation operations or pre-navigation calibration phases, enabling subsequent utilization in formal navigation processes. As beacon signals become *a priori* known (or estimated) during navigation phases, such receiver architectures typically achieve concurrent estimation of carrier phase, Doppler shift, and code phase parameters through adaptive tracking loops. Currently, most communication systems incorporate periodic reference signals, which can thus be leveraged for opportunistic navigation [74, 75]. Reference [76] proposed a blind opportunistic navigation (BON) framework, which can decode and utilize signals of opportunity for navigation without fully understanding the prior knowledge of the signals. The framework primarily comprises three key steps: blind Doppler frequency estimation, coherent integration, and beacon signal decoding. The blind Doppler frequency estimation algorithm is employed to estimate the Doppler frequency of the opportunity signal, thereby mitigating the impact of high dynamic effects on the coherent integration time. Building on this foundation, reference [77] introduced a blind channel equalization step to compensate for channel distortion, focusing on the blind detection and tracking of M-PSK modulated signals. A chirp parameter estimation algorithm based on the Wigner distribution was proposed to estimate and track the time-varying Doppler frequency, achieving long-term coherent integration of the signal and enhancing the signal-to-noise ratio. Drawing on the aforementioned two articles, reference [78] presented a navigation framework with high computational efficiency, concentrating on the detection of constrained unknown beacon signals. Low-complexity beacon detection and blind Doppler frequency shift estimation algorithms were proposed, addressing detection challenges under conditions of unknown beacon signals and low SNR. Literatures [79–81] concentrate on extracting navigation information from orthogonal frequency division multiplexing (OFDM) signals with unknown signal structures. Particularly for OFDM signals transmitted by low Earth orbit (LEO) satellites, the importance of blind signal processing at the receiver end is emphasized. That is, without knowledge of the specific signal structure, navigation information within the signal is detected, tracked, and utilized through cognitive decoding techniques. Reference [79] proposed a computationally efficient blind Doppler frequency estimation algorithm and discussed solving the ambiguity problem in Doppler estimation using polynomial curve fitting. Reference [80] also proposed a blind Doppler estimation algorithm, focusing more on reducing the impact of Doppler frequency through preprocessing and employing a difference framework to resolve the ambiguity problem in Doppler estimation, thereby obtaining more accurate navigation observations. The aforementioned algorithms are all designed for a single signal source. Literature [81] proposed a receiver architecture for signal detection and tracking in both static and high dynamic Doppler rate scenarios, capable of jointly estimating the unknown reference signals of multiple signal sources. This architecture can detect and track the "always-on" and "on-demand" signals of 5G NR and Starlink satellites. Reference [82] do not assume any specific modulation scheme but only assume the presence of a periodic reference signal in the received signal and proposed a general receiver architecture, highligh ting the versatility and adaptability of the receiver to different signals.

#### 4.6.2.2 Frequency-domain estimation methodology

This approach initiates analysis through spectral decomposition of received signals, leveraging distinctive spectral signatures to construct optimized estimator configurations. References [83, 84] both employ blind Doppler discriminators based on spectral cross-correlation and Kalman filter (KF) for Doppler tracking. However, literature [83] focuses on the design of a three-stage blind receiver, while literature [84] focuses on the estimation framework of blind periodic sequences, estimating LEO satellite repeat sequences without knowledge of the signal structure and proposing a solution to the ambiguity of Doppler estimation. As demonstrated in literature [59], spectral analysis of Starlink beacon signals revealed three critical subcarrier characteristics: (1) an approximate linear correlation between spectral bandwidth and integration time, (2) constant signal power characteristics, and (3) individual subcarriers exhibiting frequency-modulated (FM) signal behavior. This fundamental insight enables the transformation of Doppler extraction challenges into parameter estimation problems for short-duration linear frequency-modulated (LFM) signals. Based on this framework, the authors developed a frequency-domain sliding-window estimation algorithm that successfully achieved Doppler shift estimation through adaptive spectral tracking and phase continuity maintenance across consecutive window intervals.

In observable extraction, cognitive-based and blind-based approaches leverage the characteristics of opportunistic signals in the time and frequency domains, respectively. Table 7 summarizes the advantages and disadvantages of these algorithms. Cognitive-based methods are more suitable for scenarios with known signal structures, such as commercial satellites, offering high accuracy but limited flexibility. In contrast, blind-based approaches are ideal for unknown or dynamic signals, like emerging LEO constellations, providing robustness but requiring solutions for ambiguity and computational complexity issues.

## 5 Future research directions

The preceding research has demonstrated that LEO opportunistic positioning can function effectively in GNSS-denied environments. However, most of these achievements have been realized through data post-processing, which is still far from practical application. In addition to the error sources that impact the opportunistic positioning system, there are still several issues that require further investigation to facilitate the eventual application of the opportunistic positioning system. The following section summarizes the key issues that warrant further exploration.

### 5.1 Satellite identification

The receiver in both GNSS systems and opportunistic positioning systems must know the satellite's position and velocity of the transmitted signal, which is essential for the receiver to achieve positioning. It is relatively easy for GNSS systems to obtain such information, but it is challenging for opportunistic positioning systems. For existing opportunistic signal receivers, it is common to track a specific satellite and receive signals from only one satellite at a time. In practical positioning tasks, the opportunistic receiver often does not know which satellite the received signal is from. It must match the observed signal with one of the thousands of candidate satellites to identify and obtain its orbital information. This can be achieved by searching for the most matching satellite from all possible satellite ephemerides using the measured Doppler curve and the receiver's prior position information [58]. However, when the receiver's prior position information is unavailable or the satellite orbits are very close, this method may fail. Therefore, it is urgent to find a new technology that allows the receiver to recognize satellites through satellite signals.

### 5.2 Optimization of location algorithm

For receivers in both GNSS and opportunistic positioning systems, receiver initialization is required when performing a positioning solution, meaning an initial solution must be provided. In GNSS positioning, each coordinate component of the receiver's initial position can be simply set to zero. By using the Newton iteration method, a convergent solution can be obtained within just a few iteration cycles. In Doppler-based LEO positioning, an appropriate initial value must be given. When using a least squares-based positioning solution, the epoch solution will fail if the initial value error exceeds 200 km [10]. In the Extended Kalman Filter (EKF) method, a larger error in the initial iteration value will lead to a larger velocity error [85]. In low dynamic scenarios, this issue can be resolved by introducing a Tikhonov regularization term [86]. However, this method fails in high dynamic scenarios. Therefore, it is of great significance to study the sensitivity of initial values in LEO Doppler positioning and to obtain accurate initial values without relying on additional prior information.

### 5.3 Multi source fusion location

For positioning in GNSS-denied environments, multi-sensor data fusion can compensate for PNT services by utilizing other navigation sources when GNSS is unavailable. Currently, the multi-source fusion of LEO opportunistic signals includes: multi-constellation fusion [84], fusion with inertial navigation systems [87], or fusion with altimeters [88]. Additionally, fusion with other sensors, such as LiDAR or ground-based opportunistic

TABLE 7 Comparison of different extraction methods.

| Approach | Algorithm | Advantages | Disadvantages |
|---|---|---|---|
| Cognitive-based | Mth-power | Computationally efficient, suitable for MPSK signals | Limited to specific modulations, requires initial frequency offset assumptions |
| | Code phase search | High precision, strong noise resistance | Depends on PN code orthogonality, high computational load |
| | Matching subspace | Multi-satellite joint detection, high dynamic parameter estimation | High complexity, assumes periodic signals |
| Blind-based | Blind beacon estimation | No prior knowledge required, adaptable to low SNR | Depends on periodicity, limited integration time |
| | Frequency-Domain Estimation | Robust performance | Low spectral resolution, Doppler ambiguity requires resolution |

PNT, may also be beneficial [82]. In general, sensor fusion enhances the positioning accuracy and availability of opportunistic systems by incorporating additional information. Although multi-source fusion offers numerous advantages, the complexity of the receiver increases due to the fusion processing of multi-source data. Moreover, under multi-source fusion, each data source is interconnected and influences the others. If one of them is erroneous, it will also impact the final positioning result. Therefore, it is necessary to study localization algorithms with low complexity and various fusion strategies that can identify and eliminate abnormal data, leveraging the benefits of multi-source data.

### 5.4 Observation extraction in complex environment

At present, most of the published experiments on low Earth orbit (LEO) opportunistic positioning are conducted in simple scenarios, where there is an absence of obstructions from surrounding buildings or trees. The received signals in these experiments typically have a high signal-to-noise ratio (SNR) and are less affected by multipath effects. To date, only a limited number of studies have specifically considered signals with low SNR in complex environments [44, 57, 89]. Low-cost or small antennas are unable to provide significant antenna gain, and interference and occlusion in complex environments further reduce the SNR of the signals. A low SNR makes signal detection more challenging, leading to difficulties in observation extraction and reducing the accuracy and availability of the estimated observations. Therefore, it is urgent to investigate observation extraction methods in complex environments, with a focus on the performance of observable signal estimation algorithms.

## 6 Conclusion

This paper reviews the current state, key technologies, and future research directions in positioning using terrestrial low-orbit opportunistic signals. As the limitations of Global Navigation Satellite Systems (GNSS) in complex environments become increasingly evident, terrestrial low-orbit opportunistic signal positioning has emerged as a promising complementary approach. We delve into the principles of Doppler positioning, analyze error sources, and explore observable extraction methods while summarizing major technological advancements to date. The accuracy and reliability of observable extraction are critical to positioning performance. Existing methods are introduced and compared, and challenges in positioning algorithms—such as sensitivity to initial values and the complexity of multi-source data fusion—are highlighted. Cognitive-based methods rely on prior signal knowledge, while blind approaches offer greater adaptability; both face accuracy challenges from multipath effects and low signal-to-noise ratios in complex environments.

Future development in terrestrial low-orbit opportunistic signal positioning is likely to focus on several key areas: 1) Advancing satellite recognition technology and developing efficient signal feature extraction and matching algorithms; 2) Refining positioning algorithms to create robust methods that minimize dependence on prior information; 3) Promoting multi-source fusion positioning technology to enhance accuracy and availability; 4) Designing signal processing algorithms for complex environments to improve the availability and reliability of observables.

In conclusion, terrestrial low-orbit opportunistic signal positioning holds significant potential. However, breakthroughs are still needed in observable extraction, algorithm optimization, multi-source fusion, and adaptability to complex environments. These advancements will pave the way for practical applications and provide reliable PNT services in GNSS-denied environments.

## Author contributions

JH: Writing – original draft, Writing – review and editing. SN: Methodology, Writing – original draft, Writing – review and editing.

HL: Methodology, Writing – original draft, Writing – review and editing. ZL: Writing – original draft, Writing – review and editing, Supervision. ZX: Conceptualization, Investigation, Methodology, Supervision, Writing – original draft, Writing – review and editing.

## Funding

The author(s) declare that financial support was received for the research and/or publication of this article. National Natural Science Foundation of China under Grant U20A0193.

## Conflict of interest

The authors declare that the research was conducted in the absence of any commercial or financial relationships that could be construed as a potential conflict of interest.

## Correction note

A correction has been made to this article. Details can be found at: 10.3389/fphy.2025.1653131.

## Generative AI statement

The author(s) declare that no Generative AI was used in the creation of this manuscript.

## Publisher's note

## References

1. Li X, Lu Z, Yuan M, Liu W, Wang F, Yu Y, et al. Tradeoff of code estimation error rate and terminal gain in SCER attack. *IEEE Trans Instrumentation Meas* (2024) 73:1–12. doi:10.1109/TIM.2024.3406807

2. Reid TG, Neish AM, Walter T, Enge PK. Broadband LEO constellations for navigation. *NAVIGATION: J Inst Navigation* (2018) 65(2):205–20. doi:10.1002/navi.234

3. Reid TG, Neish AM, Walter TF, Enge PK. Leveraging commercial broadband leo constellations for navigating. In: *29th international technical meeting of the satellite division of the institute of navigation (ion Gnss+ 2016)*, 12 (2016). p. 2016–6. doi:10.33012/2016.14729

4. Del PI, Cameron BG, Crawley EF. A technical comparison of three low earth orbit satellite constellation systems to provide global broadband. *Acta astronautica* (2019) 159:123–35. doi:10.1016/j.actaastro.2019.03.040

5. Danchik RJL. Lee pryor the navy navigation satellite system (transit) (1984). Available online at: https://secwww.jhuapl.edu/techdigest/Content/techdigest/pdf/V05-N04/05-04-Danchik.pdf (Accessed February 15, 2025).

6. Danchik RJ. An overview of transit development. *Johns Hopkins APL Tech Dig* (1998) 19(1):19.

7. Stock W, Schwarz RT, Hofmann CA, Knopp A. Survey on opportunistic PNT with signals from LEO communication satellites. *IEEE Commun Surv and Tutorials* (2024) 30:77–107. doi:10.1109/COMST.2024.3406990

8. Kassas Z, Neinavaie M, Khalife J, Khairallah N, Kozhaya S, Haidar-Ahmad J, et al. Enter LEO on the GNSS stage. *Inside GNSS* (2021)(6):16.

9. Benzerrouk H, Nguyen Q, Xiaoxing F, Rasaee H, Landry RJ. LEO satellites based Doppler positioning using distributed nonlinear estimation. *IFAC-PapersOnLine* (2019) 52(12):496–501. doi:10.1016/j.ifacol.2019.11.292

10. Shi C, Zhang Y, Li Z. Revisiting Doppler positioning performance with LEO satellites. *GPS Solutions* (2023) 27(3):126. doi:10.1007/s10291-023-01466-w

11. Li ZH, Huang JS. *GPS measurement and data processing*. 3rd Edition. Wuhan: Wuhan University Press (2016).

12. Morales JJ, Khalife J, Cruz US, Kassas ZM. Orbit modeling for simultaneous tracking and navigation using LEO satellite signals. In: *InProceedings of the 32nd international technical meeting of the satellite division of the institute of navigation (ION GNSS+ 2019)* (2019). p. 2090–9. doi:10.33012/2019.17029

13. CelesTrak. Two-line element sets (2023). Available online at: http://celestrak.org/publications (Accessed July 25, 2023).

14. Vallado D, Crawford P, Hujsak R, Kelso TS. Revisiting spacetrack report# 3. In: *AIAA/AAS astrodynamics specialist conference and exhibit*. (2006). p 6753. doi:10.2514/6.2006-6753

15. Vallado D, Crawford P. SGP4 orbit determination. In: *InAIAA/AAS astrodynamics specialist conference and exhibit* (2008). p. 6770. doi:10.2514/6.2008-6770

16. Khairallah N, Kassas ZM. Ephemeris closed-loop tracking of LEO satellites with pseudorange and Doppler measurements. *InProceedings 34th Int Tech Meet satellite division Inst Navigation (ION GNSS+ 2021)* (2021) 2544–55. doi:10.33012/2021.18114

17. Tan Z, Qin H, Cong L, Zhao C. New method for positioning using IRIDIUM satellite signals of opportunity. *IEEE access* (2019) 7:83412–23. doi:10.1109/ACCESS.2019.2924470

18. Ardito CT, Morales JJ, Khalife J, Abdallah A, Kassas ZM. Performance evaluation of navigation using LEO satellite signals with periodically transmitted satellite positions. *InProceedings 2019 Int Tech Meet The Inst Navigation* (2019) 306–18. doi:10.33012/2019.16743

19. Khalife J, Neinavaie M, Kassas ZM. Navigation with differential carrier phase measurements from megaconstellation LEO satellites. *In2020 IEEE/ION Position, Location Navigation Symp (Plans)* (2020) 1393–404. doi:10.1109/PLANS46316.2020.9110199

20. Qin H, Wu N, Zhao C. Differential positioning with Doppler measurements from Iridium satellite signals of opportunity based on lines of sight correction. *J Beijing Univ Aeronautics Astronautics* (2022) 50(3):748–56. doi:10.13700/j.bh.1001-5965.2022.0378

21. Zhao C, Qin H, Wu N, Wang D. Analysis of baseline impact on differential Doppler positioning and performance improvement method for LEO opportunistic navigation. *IEEE Trans Instrumentation Meas* (2023) 72:1–10. doi:10.1109/TIM.2023.3235456

22. Wang D, Qin H, Huang Z. Doppler positioning of LEO satellites based on orbit error compensation and weighting. *IEEE Trans Instrumentation Meas* (2023) 72:1–11. doi:10.1109/TIM.2023.3286001

23. Deng R, Qin H, Li H, Wang D, Lv H. Noncooperative LEO satellite orbit determination based on single pass Doppler measurements. *IEEE Trans Aerospace Electron Syst* (2022) 59(2):1–12. doi:10.1109/TAES.2022.3194977

24. Mortlock TR, Kassas ZM. Performance analysis of simultaneous tracking and navigation with LEO satellites. *InProceedings 33rd Int Tech Meet Satellite Division The Inst Navigation (ION GNSS+ 2020)* (2020) 2416–29. doi:10.33012/2020.17658

25. Cassel RS, Scherer DR, Wilburne DR, Hirschauer JE, Burke JH. Impact of improved oscillator stability on LEO-based satellite navigation. *InProceedings 2022 Int Tech Meet Inst navigation* (2022) 893–905. doi:10.33012/2022.18258

26. Wang D, Qin H, Liang H, Zhang Y. Clock error analysis and compensation for LEO signal of opportunity positioning. *IEEE Sensors J* (2024) 4:12716–27. doi:10.1109/JSEN.2024.3370249

27. Yang Z, Liu H, Qian C, Shu B, Zhang L, Xu X, et al. Real-time estimation of low Earth orbit (LEO) satellite clock based on ground tracking stations. *Remote Sensing* (2020) 12(12):2050. doi:10.3390/rs12122050

28. Wang K, El-Mowafy A. LEO satellite clock analysis and prediction for positioning applications. *Geo-spatial Inf Sci* (2022) 25(1):14–33. doi:10.1080/10095020.2021.1917310

29. Khairallah N, Kassas ZM. An interacting multiple model estimator of LEO satellite clocks for improved positioning. In: In2022 IEEE 95th Vehicular Technology Conference. IEEE (2022). p. 1–5.

30. Kassas ZZ. Navigation from low-earth orbit Part 2: models, implementation, and performance zaher (zak) M. Kassas university of California irvine, United States. Position, navigation, and timing technologies in the 21st century: integrated satellite navigation. *Sensor Syst Civil Appl* (2020) 2:1381–412. doi:10.1002/9781119458555.ch43b

31. Prol FS, Ferre RM, Saleem Z, Välisuo P, Pinell C, Lohan ES, et al. Position, navigation, and timing (PNT) through low earth orbit (LEO) satellites: a survey on current status, challenges, and opportunities. *IEEE access* (2022) 10:83971–4002. doi:10.1109/ACCESS.2022.3194050

32. Khalife J, Kassas ZZ. Performance-driven design of carrier phase differential navigation frameworks with megaconstellation LEO satellites. *IEEE Trans Aerospace Electron Syst* (2023) 59(3):2947–66. doi:10.1109/TAES.2023.3234521

33. Psiaki ML. Navigation using carrier Doppler shift from a LEO constellation: TRANSIT on steroids. *Navigation* (2021) 68(3):621–41. doi:10.1002/navi.438

34. Neinavaie M, Khalife J, Kassas ZM. Acquisition, Doppler tracking, and positioning with Starlink LEO satellites: first results. *IEEE Trans Aerospace Electron Syst* (2021) 58(3):2606–10. doi:10.1109/TAES.2021.3127488

35. Singh UK, Shankar MB, Ottersten B. Opportunistic localization using LEO signals. In: In2022 56th Asilomar Conference on Signals, Systems, and Computers 2022 Oct, 31. IEEE (2022). p. 894–9. doi:10.1109/ieeeconf56349.2022.10051941

36. ICAO. *Manual for ICAO aeronautical mobile satellite(ROUTE) service. Part2-Iridium. Draft v4.0 [Z]*. Montreal: ICAO (2007). p. 9–12.

37. FCC. Iridium NEXT engineering statement No.1031348. Available online at: https://fcc.report/IBFS/SAT-MOD-20131227-00148/1031348.pdf (Accessed February 20, 2025).

38. Shahriar CM. A scheme to mitigate interference from iridium Satellite's downlink signal captured by omnidirectional antenna array. In: In2008 IEEE Antennas and Propagation Society International Symposium. IEEE (2008). p. 1–4. doi:10.1109/APS.2008.4619788

39. Huang C, Qin H, Zhao C, Liang H. Phase-time method: accurate Doppler measurement for Iridium NEXT signals. *IEEE Trans Aerospace Electron Syst* (2022) 58(6):5954–62. doi:10.1109/TAES.2022.3180702

40. Orabi M, Khalife J, Kassas ZM. Opportunistic navigation with Doppler measurements from iridium next and Orbcomm LEO satellites. In: In2021 IEEE Aerospace conference. IEEE (2021). p. 1–9.

41. Zhao C, Qin H, Li Z. Doppler measurements from multiconstellations in opportunistic navigation. *IEEE Trans Instrumentation Meas* (2022) 71:1–9. doi:10.1109/TIM.2022.3147315

42. Wei Q, Chen X, Zhan YF. Exploring implicit pilots for precise estimation of LEO satellite downlink Doppler frequency. *IEEE Commun Lett* (2020) 24(10):2270–4. doi:10.1109/LCOMM.2020.3003791

43. Liang H, Qin H, Li H. Doppler compensated pseudorange based signal-of-opportunity positioning using iridium satellite. *IEEE Trans Aerospace Electron Syst* (2024) 60:8605–18. doi:10.1109/TAES.2024.3432645

44. Tan Z, Qin H, Cong L, Zhao C. Positioning using IRIDIUM satellite signals of opportunity in weak signal environment. *Electronics* (2019) 9(1):37. doi:10.3390/electronics9010037

45. Ilcev SD. Orbcomm space segment for mobile satellite system (MSS). In: In2011 10th International Conference on Telecommunication in Modern Satellite Cable and Broadcasting Services (TELSIKS); 2011 Oct 5, 2. IEEE (2011). p. 689–92. doi:10.1109/telsks.2011.6143205

46. Qin H, Tan Z, Cong L, Zhao C. Positioning technology based on ORBCOMM signals of opportunity. *J Beijing Univ Aeronautics Astronautics* (2020) 46(11):1999–2006. doi:10.13700/j.bh.1001-5965.2019.0565

47. Khalife JJ, Kassas ZM. Receiver design for Doppler positioning with LEO satellites. In: InICASSP 2019-2019 IEEE International Conference on Acoustics, Speech and Signal Processing (ICASSP); 2019 May 12. IEEE (2019). p. 5506–10.

48. Xie Y, Li G, Qin H, Zhao C, Chen M, Zhou W. Carrier phase tracking and positioning algorithm with additional system parameters based on Orbcomm signals. *GPS Solutions* (2024) 28(4):184. doi:10.1007/s10291-024-01721-8

49. Schiff L, Chockalingam A. Signal design and system operation of Globalstar TM versus IS-95 CDMA–similarities and differences. *Wireless Networks* (2000) 6:47–57. doi:10.1023/A:1019164909332

50. Neinavaie M, Khalife J, Kassas ZM. Doppler stretch estimation with application to tracking Globalstar satellite signals. In: InMILCOM 2021-2021 IEEE Military Communications Conference (MILCOM). IEEE (2021). p. 647–51.

51. Zhang Y, Qin H, Shi G. Doppler positioning based on globalstar signals of opportunity. In: In2023 5th International Conference on Electronic Engineering and Informatics (EEI). IEEE (2023). p. 666–9.

52. Qin H, Zhang Y, Shi G, Wang D. Doppler positioning technology based on Globalstar signals of opportunity. *J Beijing Univ Aeronautics Astronautics* (2023). doi:10.13700/j.bh.1001-5965.2023.0013

53. Luo S, Mao J. Overview of Starlink satellite system technology. *Aerospace Electron Warfare* (2020) 36(5):51–6. doi:10.16328/j.htdz8511.2020.05.011

54. Neinavaie M, Kassas ZM. Unveiling Starlink LEO satellite OFDM-like signal structure enabling precise positioning. *IEEE Trans Aerospace Electron Syst* (2023) 10:2486–9. doi:10.1109/TAES.2023.3265951

55. Humphreys TE, Iannucci PA, Komodromos ZM, Graff AM. Signal structure of the starlink ku-band downlink. *IEEE Trans Aerospace Electron Syst* (2023) 59(5):1–16. doi:10.1109/TAES.2023.3268610

56. Khalife J, Neinavaie M, Kassas ZM. The first carrier phase tracking and positioning results with Starlink LEO satellite signals. *IEEE Trans Aerospace Electron Syst* (2021) 58(2):1487–91. doi:10.1109/TAES.2021.3113880

57. Jardak N, Adam R. Practical use of Starlink downlink tones for positioning. *Sensors* (2023) 23(6):3234. doi:10.3390/s23063234

58. Yang C, Soloviev A. Starlink Doppler and Doppler rate estimation via coherent combining of multiple tones for opportunistic positioning. In: In2023 IEEE/ION Position, Location and Navigation Symposium (PLANS). IEEE (2023). p. 1143–53.

59. Qin H, Zhang Y. Positioning technology based on starlink signal of opportunity. *J Navig Position* (2023) 11:67–73. doi:10.16547/j.cnki.10-1096.20230110

60. Yuan Y, Yi J, Wan X, Hao C. Doppler positioning method and experiment based on starlink beacon signal. *Syst Eng Electron* (2024) 46:2535–45. doi:10.12305/j.issn.1001506X.2024.08.01

61. Neinavaie M, Khalife J, Kassas ZM. Exploiting starlink signals for navigation: first results. *InProceedings 34th Int Tech Meet Satellite Division The Inst Navigation (ION GNSS+ 2021)* (2021) 2766–73. doi:10.33012/2021.18122

62. Neinavaie M, Shadram Z, Kozhaya S, Kassas ZM. First results of differential Doppler positioning with unknown Starlink satellite signals. In: *In2022 IEEE Aerospace conference (AERO)*. IEEE (2022). p. 1–14. doi:10.1109/AERO53065.2022.9843493

63. Kozhaya SE, Kassas ZM. Positioning with Starlink LEO satellites: a blind Doppler spectral approach. In: In2023 IEEE 97th Vehicular Technology Conference (VTC2023-Spring). IEEE (2023). p. 1–5.

64. Blázquez-García R, Cristallini D, Ummenhofer M, Seidel V, Heckenbach J, O'Hagan D. Experimental comparison of Starlink and OneWeb signals for passive radar. In: *In2023 IEEE radar conference (RadarConf23)*. IEEE (2023). p. 1–6. doi:10.1109/RadarConf2351548.2023.10149580

65. Kozhaya S, Kassas ZM. A first look at the OneWeb LEO constellation: beacons, beams, and positioning. *IEEE Trans Aerospace Electron Syst* (2024) 60:7528–34. doi:10.1109/TAES.2024.3410252

66. Kassas ZM, Kozhaya S, Kanj H, Saroufim J, Hayek SW, Neinavaie M, et al. Navigation with multi-constellation LEO satellite signals of opportunity: starlink, oneweb, Orbcomm, and iridium. In: *In2023 IEEE/ION position, location and navigation symposium (PLANS)*. IEEE (2023). p. 338–43. doi:10.1109/PLANS53410.2023.10140066

67. Farhangian F, Landry JR. Multi-constellation software-defined receiver for Doppler positioning with LEO satellites. *Sensors* (2020) 20(20):5866. doi:10.3390/s20205866

68. Qin H, Li Z, Zhao C. Fusion positioning based on Iridium/ORBCOMM signals of opportunity. *J Beijing Univ Aeronautics Astronautics* (2021) 48(10):1845–53. doi:10.13700/j.bh.1001-5965.2021.0041

69. Leng M, Lei L, Razul SG, See CM. Joint synchronization and localization using Iridium ring alert signal. In: In2015 10th International Conference on Information, Communications and Signal Processing (ICICS). IEEE (2015). p. 1–5.

70. Neinavaie M, Kassas ZM. Signal mode transition detection in starlink LEO satellite downlink signals. In2023 IEEE/ION Position. *Location Navigation Symp (Plans)* (2023) 24:360–4. doi:10.1109/PLANS53410.2023.10139993

71. Stock W, Hofmann CA, Knopp A. LEO-PNT with Starlink: development of a burst detection algorithm based on signal measurements. In: InWSA and SCC 2023; 26th International ITG Workshop on Smart Antennas and 13th Conference on Systems, Communications, and Coding, 27. VDE (2023). p. 1–6. doi:10.48550/arXiv.2304.09535

72. Scharf LL, Friedlander B. Matched subspace detectors. *IEEE Trans signal Process* (1994) 42(8):2146–57. doi:10.1109/78.301849

73. Kraut S, Scharf LL, McWhorter LT. Adaptive subspace detectors. *IEEE Trans signal Process* (2001) 49(1):1–16. doi:10.1109/78.890324

74. Yang C, Arizabaleta-Diez M, Weitkemper P, Pany T. An experimental analysis of cyclic and reference signals of 4G LTE for TOA estimation and positioning in mobile fading environments. *IEEE Aerospace Electron Syst Mag* (2022) 37(9):16–41. doi:10.1109/MAES.2022.3186650

75. Shamaei K, Kassas ZM. Receiver design and time of arrival estimation for opportunistic localization with 5G signals. *IEEE Trans Wireless Commun* (2021) 20(7):4716–31. doi:10.1109/TWC.2021.3061985

76. Neinavaie M, Khalife J, Kassas ZM. Blind opportunistic navigation: cognitive deciphering of partially known signals of opportunity. *InProceedings 33rd Int Tech Meet Satellite Division The Inst Navigation (ION GNSS+ 2020)* (2020) 2748–57. doi:10.33012/2020.17592

77. Neinavaie M, Khalife J, Kassas ZM. Blind Doppler tracking and beacon detection for opportunistic navigation with LEO satellite signals. In: *In2021 IEEE Aerospace conference*. IEEE (2021). p. 1–8. doi:10.1109/AERO50100.2021.9438258

78. Neinavaie M, Khalife J, Kassas ZM. Detection of constrained unknown beacon signals of terrestrial transmitters and LEO satellites with application to navigation. In: *In2022 IEEE 96th vehicular technology conference (VTC2022-Fall)*. IEEE (2022). p. 1–5. doi:10.1109/VTC2022-Fall57202.2022.10012987

79. Khalife J, Neinavaie M, Kassas ZM. Blind Doppler estimation from LEO satellite signals: a case study with real 5G signals. *InProceedings 33rd Int Tech Meet Satellite Division The Inst Navigation (ION GNSS+ 2020)* (2020) 3046–54. doi:10.33012/2020.17668

80. Khalife J, Neinavaie M, Kassas ZM. Blind Doppler tracking from OFDM signals transmitted by broadband LEO satellites. In: *In2021 IEEE 93rd vehicular technology conference (VTC2021-Spring)*, 25. IEEE (2021). p. 1–5. doi:10.1109/VTC2021-Spring51267.2021.9448678

81. Neinavaie M, Kassas ZM. Cognitive sensing and navigation with unknown OFDM signals with application to terrestrial 5G and Starlink LEO satellites. *IEEE J Selected Areas Commun* (2023) 42(1):146–60. doi:10.1109/JSAC.2023.3322811

82. Khalife J, Neinavaie M, Kassas ZM. Universal Receiver architecture for blind navigation with partially known terrestrial and extraterrestrial signals of opportunity. *InProceedings 34th Int Tech Meet Satellite Division The Inst Navigation (ION GNSS+ 2021)* (2021) 2201–11. doi:10.33012/2021.18065

83. Kozhaya SE, Kassas ZM. Blind receiver for LEO beacon estimation with application to UAV carrier phase differential navigation. *InProceedings 35th Int Tech Meet Satellite Division The Inst Navigation (ION GNSS+ 2022)* (2022) 2385–97. doi:10.33012/2022.18582

84. Kozhaya S, Kanj H, Kassas ZM. Multi-constellation blind beacon estimation, Doppler tracking, and opportunistic positioning with OneWeb, Starlink, Iridium NEXT, and Orbcomm LEO satellites. In2023 IEEE/ION Position. In: *Location and navigation symposium (PLANS)*, 24. IEEE (2023). p. 1184–95. doi:10.1109/PLANS53410.2023.10139969

85. Guo F, Yang Y, Ma F, Zhu Y, Liu H, Zhang X. Instantaneous velocity determination and positioning using Doppler shift from a LEO constellation. *Satellite Navigation* (2023) 4(1):9. doi:10.1186/s43020-023-00098-2

86. Xu Z, Li Z, Liu X, Ji Z, Wu Q, Liu H, et al. Doppler positioning with LEO mega-constellation: equation properties and improved algorithm. *Remote Sensing* (2024) 16(16):2958. doi:10.3390/rs16162958

87. Du Y, Qin H, Zhao C. LEO satellites/INS integrated positioning framework considering orbit errors based on FKF. *IEEE Trans Instrumentation Meas* (2024) 26:1–14. doi:10.1109/TIM.2024.3369693

88. Hayek S, Saroufim J, Neinavaie M, Kozhaya S, Kassas ZM. Assessment of differential Doppler navigation with Starlink LEO satellite signals of opportunity. *InProceedings 2023 Int Tech Meet The Inst navigation* (2023) 1021–31. doi:10.33012/2023.18669

89. Kanj H, Kozhaya S, Kassas ZM. Acquisition and tracking of Starlink LEO satellite signals in low SNR regime. *InProceedings 36th Int Tech Meet Satellite Division The Inst Navigation (ION GNSS+ 2023)* (2023) 3420–31. doi:10.33012/2023.19451

90. Neinavaie M, Khalife J, Kassas ZM. Cognitive opportunistic navigation in private networks with 5G signals and beyond. *IEEE J Selected Top Signal Process* (2021) 16(1):129–43. doi:10.1109/JSTSP.2021.3119929

TYPE Correction
PUBLISHED 04 July 2025
DOI 10.3389/fphy.2025.1653131

OPEN ACCESS

APPROVED BY
Frontiers Editorial Office,
Frontiers Media SA, Switzerland

*CORRESPONDENCE
Zhibin Xiao,
✉ xiaozb1986@163.com

RECEIVED 24 June 2025
ACCEPTED 27 June 2025
PUBLISHED 04 July 2025

CITATION
He J, Ni S, Lin H, Liu Z and Xiao Z (2025) Correction: Survey on positioning technology based on signal of opportunity from low earth orbit.
*Front. Phys.* 13:1653131.
doi: 10.3389/fphy.2025.1653131

# Correction: Survey on positioning technology based on signal of opportunity from low earth orbit

Jiawei He[1,2], Shaojie Ni[1,2], Honglei Lin[1,2], Zhe Liu[1,2] and Zhibin Xiao[1,2]*

[1]College of Electronic Science and Technology, National University of Defense Technology, Changsha, China, [2]National Key Laboratory for Positioning, Navigation and Timing Technology, Changsha, China

KEYWORDS

**LEO, PNT, signal of opportunity, doppler positioning, observational estimation**

A Correction on
Survey on positioning technology based on signal of opportunity from low earth orbit

by He J, Ni S, Lin H, Liu Z and Xiao Z (2025). Front. Phys. 13:1592447. doi: 10.3389/fphy.2025.1592447

Author **Zhibin Xiao** was erroneously spelled as Zhibing Xiao.

The original version of this article has been updated.

## Publisher’s note

frontiers | Frontiers in Physics

TYPE Review
PUBLISHED 25 June 2025
DOI 10.3389/fphy.2025.1567301

OPEN ACCESS

EDITED BY
Zhu Xiao,
Hunan University, China

REVIEWED BY
Gaosheng Li,
Hunan University, China
Yq Hei,
Xidian University, China

*CORRESPONDENCE
Weihua Mou,
✉ drmou@163.com

RECEIVED 27 January 2025
ACCEPTED 02 June 2025
PUBLISHED 25 June 2025

CITATION
Huang Z, Mou W, Wang R, Li P, Lyu Z and Ou G (2025) A survey of GNSS receiver autonomous integrity monitoring: Research status and opportunities.
*Front. Phys.* 13:1567301.
doi: 10.3389/fphy.2025.1567301

# A survey of GNSS receiver autonomous integrity monitoring: Research status and opportunities

Zhen Huang[1,2], Weihua Mou[1,2]*, Rui Wang[3], Pengpeng Li[1,2], Zhicheng Lyu[1,2] and Gang Ou[1,2]

[1]College of Electronic Science and Technology, National University of Defense Technology, Changsha, China, [2]National Key Laboratory for Positioning, Navigation and Timing Technology, Changsha, China, [3]Chongqing Academy of Metrology and Quality Inspection, Chongqing, China

Integrity monitoring is crucial in applications closely related to the safety of human life and property, such as aviation, maritime navigation, autonomous driving, and rail transportation. Receiver autonomous integrity monitoring (RAIM) has attracted significant attention due to its comprehensive monitoring coverage and fast alerting capability. The paper provides a comprehensive review of RAIM algorithms for global navigation satellite system (GNSS) positioning applications. The parameters related to integrity assessment and typical fault detection and exclusion methods are reviewed, and RAIM is categorized into three types of methods: error probability distribution model-based, set representation-based, and machine learning-based. The latest state-of-the-art research, along with the strengths and shortcomings of each type of method, is presented for each type. The opportunities for the future development of RAIM are analyzed in the light of current challenges and existing results, aiming to promote further research and provide effective assurance for GNSS integrity.

KEYWORDS

**global navigation satellite system, integrity, receiver autonomous integrity monitoring, fault detection and exclusion, protection level**

## 1 Introduction

The global navigation satellite system (GNSS) offers many advantages, such as all-weather, all-time, and global coverage, providing accurate and extensive positioning, navigation, and timing services for aviation [1], maritime navigation [2], railway transport [3], and autonomous driving [4]. Among these, integrity is one of the key criteria for evaluating GNSS performance. It is used to assess the trustworthiness of the navigation system, and its concept originally came from the field of aviation, aiming to provide highly reliable navigation and positioning information for civil aviation users. With the widespread application of GNSS in fields closely related to the safety of human lives and property, the concept of integrity has been expanded to other areas and has attracted much attention.

Integrity is defined as the ability to alert the user in a timely manner when the performance of the navigation information provided by GNSS fails to meet specified requirements [5, 6]. In January 2024, two ship groundings occurred in the Israeli ports of Haifa and Ashdod, as a result of excessive global positioning system (GPS) positioning

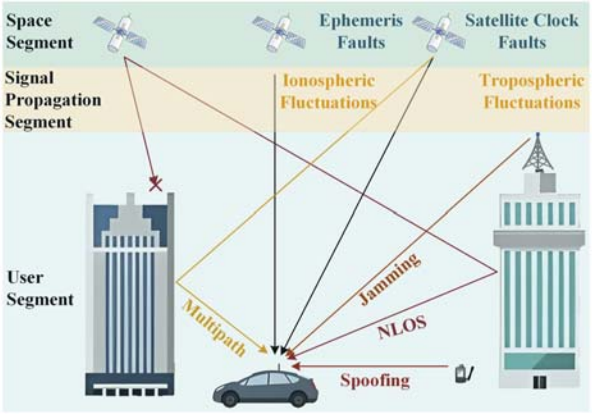

FIGURE 1
Faults or anomalies that may threaten integrity.

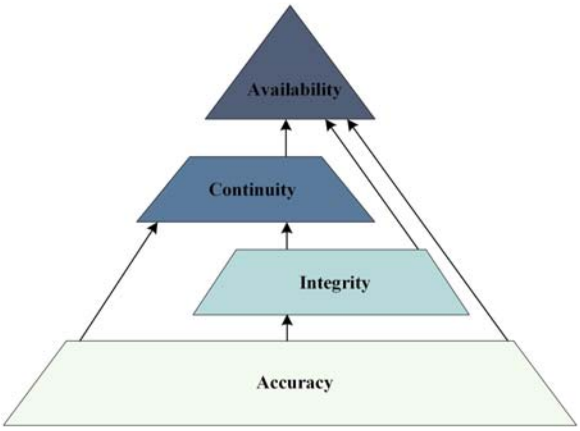

FIGURE 2
Navigation performance pyramid [6].

deviation but the receivers did not warn the crews in time [7], which shows that safeguarding GNSS integrity is crucial for the safety of human lives and property. On the other hand, due to the vulnerability of the GNSS signals themselves, they are highly susceptible to jamming and spoofing. On 6 September 2024, OPSGROUP, an organization of aviation practitioners, compiled statistics on GPS spoofing in civil aviation, and the data showed that in the first three-quarters of 2024, an average of up to 1,500 flights were subjected to GPS spoofing every day [8]. The frequent occurrence of jamming and spoofing events will seriously weaken GNSS integrity, at the same time, ephemeris and clock failures, ionospheric and tropospheric fluctuations, and common multipath and non-line-of-sight (NLOS) signals in urban canyons may pose a threat to GNSS integrity, leading users to incorrectly believe and adopt navigation information with excessive errors, which can jeopardize the safety of human life and property. Therefore, providing accurate and reliable integrity services for GNSS users is an urgent issue, and integrity monitoring of GNSS is crucial and irreplaceable.

Depending on the stage of implementation of integrity monitoring, it can be divided into system-level and user-level methods. System-level methods rely on integrity information broadcast by satellite-based or ground-based monitoring stations. User-level methods, on the other hand, do not rely on external information or facilities, but only utilize their own redundant measurement information for integrity monitoring [9], and their main means of implementation is receiver autonomous integrity monitoring (RAIM). As shown in Figure 1, RAIM is theoretically able to monitor faults and abnormalities in the space segment, signal propagation segment, and user segment, with a comprehensive monitoring scope. Additionally, because RAIM is directly deployed at the user terminal, it can respond quickly to all kinds of faults and alert the user in time, and the response speed is usually much better than that of system-level integrity monitoring methods.

Several review works have summarized the research progress of RAIM. For instance [5], focuses on the advancements of RAIM in aviation [6], summarizes the integrity detection algorithms used in urban canyon environments [9], systematically reviews the integrity monitoring methods in GNSS and inertial navigation system (INS) integrated navigation for autonomous driving applications, and [10] highlights the progress in autonomous integrity monitoring within multi-source fusion navigation. However, these works do not provide a systematic overview of the more novel machine learning (ML)-based and set representation-based RAIM algorithms. Furthermore, many innovative developments in traditional RAIM have emerged, which are not covered in the existing reviews.

Therefore, this paper systematically describes the state-of-the-art RAIM algorithms for GNSS positioning applications. The remaining chapters are organized as follows: Section 2 reviews the parameters related to integrity assessment and typical fault detection and exclusion (FDE) methods. Section 3 introduces the state-of-the-art of three types of RAIMs: those based on the error probability distribution models, set representation, and ML, respectively, and analyzes the strengths and weaknesses of each. Section 4 examines the future development opportunities for RAIM by considering current challenges and existing research results. Finally, Section 5 provides conclusions and future outlooks.

## 2 Basic definition and theory

### 2.1 Integrity performance evaluation and related parameters

Four metrics—accuracy, integrity, continuity, and availability—are usually used to evaluate GNSS navigation performance, and the relationship between them can be represented by the navigation performance pyramid [6], as shown in Figure 2.

Among them, integrity is used to assess the trustworthiness of GNSS, which is measured by a series of parameters such as alert limit (AL), time to alert (TTA), integrity risk (IR), protection level (PL), etc. [6, 11], taking the positioning application as an example, these parameters are defined as follows:

AL: The maximum tolerable position error (PE), usually preset according to user requirements. Different requirements often exist in the horizontal and vertical directions, so it can be further divided into horizontal alert limit (HAL) and vertical alert limit (VAL).

TTA: The maximum tolerable time from when the PE exceeds the AL to when the user receives an alert.

IR: The maximum tolerable probability that the PE exceeds the AL but the user is not alerted within the TTA. This is usually given in terms of per hour or per mile [9]. Alternatively, IR can be defined as the maximum tolerable probability that RAIM fails to alert the user in time in case of a position failure.

PL: Since PE is often difficult to calculate directly, PL is used to represent the statistical bounds of PE. PL should fulfill the following condition: when PE exceeds AL, the probability that PL is less than AL should not exceed the specified IR, as shown in Equation 1.

$$P(\mathrm{PE} > \mathrm{AL} \,\&\, \mathrm{PL} < \mathrm{AL}) \leq \mathrm{IR} \tag{1}$$

PL is usually calculated by the user to determine the availability of the navigation system, declaring the navigation system available when PL < AL, and declaring the navigation system unavailable and alerting the user when PL ≥ AL. Similar to AL, PL can be further classified into horizontal protection level (HPL) and vertical protection level (VPL) [6].

The relationship between the integrity parameters can be more intuitively understood by using the Stanford Diagram [12], as shown in Figure 3. When the system is working normally, PE < PL < AL, corresponding to region ① in the figure. When PL ≥ AL, RAIM will declare the navigation system unavailable and issue an alert that the user should not trust the current navigation system, corresponding to regions ③, ④, and ⑤ in the figure, where the events in region ③ unnecessarily declares the navigation system unavailable and reduces the availability. When the actual PE exceeds PL, the navigation system provides misleading information to the user, and the probability of its occurrence is called the probability of misleading information $P_{\mathrm{MI}}$, corresponding to regions ②, ⑤, and ⑥ in the figure. The events in regions ② and ⑤, only provide misleading information and the system is not in a dangerous state, but the events in region ⑥, in which the PE still exceeds AL despite the declaration of the navigation system's availability, results in the user mistakenly trusting the wrong navigation information and is in a dangerous state, and its occurrence probability is called the hazardous misinformation probability $P_{\mathrm{HMI}}$.

The RAIM algorithm should minimize the probability of events in region ③ to improve system availability; and minimize $P_{\mathrm{MI}}$ and $P_{\mathrm{HMI}}$ so that they do not exceed at least the preset IR to guarantee integrity.

## 2.2 Typical fault detection and exclusion method

RAIM usually requires fault detection, identification, and exclusion based on redundant measurement information. This subsection introduces several typical FDE methods to set the stage for the subsequent introduction of RAIM algorithms.

### 2.2.1 $\chi^2$ test

The $\chi^2$ test [13], which is the most typical fault detection method, constructs the residual in the least squares (LS) algorithm or the innovation in the Kalman filter (KF) as a test statistic $t_k$, as shown in Equation 2:

$$t_k = \boldsymbol{r}_k^T \boldsymbol{S}_k^{-1} \boldsymbol{r}_k \tag{2}$$

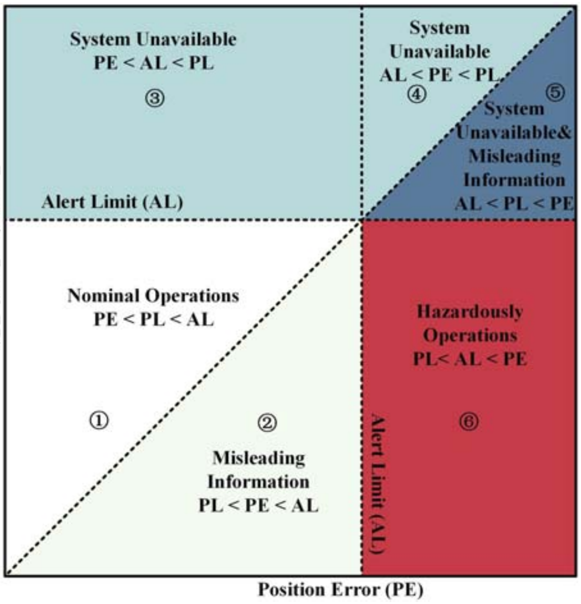

FIGURE 3
Stanford Diagram [12].

In the equation, $\boldsymbol{r}_k$ is the residual or innovation, $\boldsymbol{S}_k$ is its covariance matrix, and $k$ is the index of the measurement epoch, assuming that the measurement noise follows a zero-mean Gaussian distribution, $t_k$ will obey a central $\chi^2$ distribution under the fault-free hypothesis $\mathcal{H}_0$ (fault-free case), and a non-central $\chi^2$ distribution under the fault hypothesis $\mathcal{H}_1$ (faulty case), as shown in Equation 3:

$$t_k \sim \begin{cases} \chi^2(df) & \mathcal{H}_0 \\ \chi^2(df,\lambda) & \mathcal{H}_1 \end{cases} \tag{3}$$

where $df$ is the degree of freedom of the $\chi^2$ distribution, depending on the number of visible satellites, and $\lambda$ is the non-centrality parameter.

When $t_k$ is greater than the detection threshold $T_k$, the fault hypothesis $\mathcal{H}_1$ is accepted to alert the user, and *vice versa*, the fault-free hypothesis $\mathcal{H}_0$ is accepted. The false alarm rate $P_{\mathrm{FA}}$ and the missed detection rate $P_{\mathrm{MD}}$ are usually set according to the application requirements, and their relationship with $T_k$ is shown in Figure 4.

After a fault is detected by the $\chi^2$ test, the fault can be further identified by the subset $\chi^2$ test [14], a method that recalculates the test statistic by removing one satellite measurements in turn, and ultimately selects the set of satellite measurements that passes the $\chi^2$ test with the smallest test statistic.

### 2.2.2 W-test

The w-test [15, 16] implements the FDE by performing a mean-shifted Gaussian test on each component of the normalized residual or innovation, and its test statistic is calculated

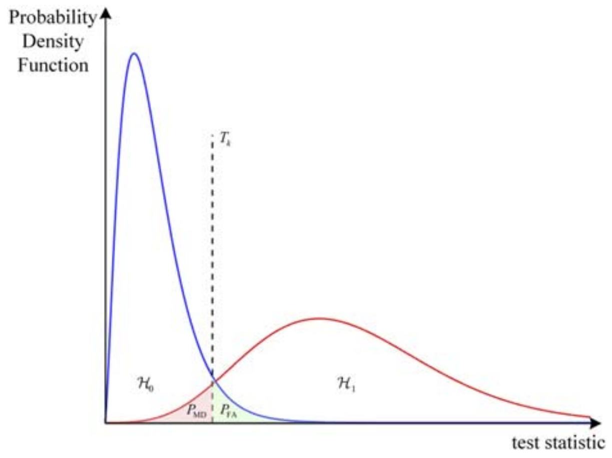

FIGURE 4
Principle of the $\chi^2$ test.

as shown in Equation 4:

$$w_k^{(i)} = \left| \frac{r_k^{(i)}}{\sqrt{\boldsymbol{S}_k^{(i,i)}}} \right| \tag{4}$$

where $r_k^{(i)}$ is the $i$-th component in the residual or innovation $\boldsymbol{r}_k$, and $S_k^{(i,i)}$ is the $i$-th diagonal element in its covariance matrix $\boldsymbol{S}_k$. If $w_k^{(i)}$ exceeds the detection threshold $N_{1-P_{\rm FA}/2}(0,1)$, the $i$-th satellite measurement is considered to be possibly faulty, and after completing the test for all satellite measurements, the maximum value exceeding the detection threshold is usually considered faulty and excluded, after which the w-test is re-run to verify that no other faulty measurements still exist. Typically, the w-test is used for fault identification and exclusion when a fault is detected in the $\chi^2$ test.

### 2.2.3 Solution separation

The solution separation (SS) [17, 18] method is no longer carried out in the range domain but directly implements fault detection on the position domain and is able to synchronize fault identification and exclusion. The computation process of its test statistics is shown in Figure 5, It accepts the fault hypothesis $\mathcal{H}_i$ and excludes the corresponding fault measurement when the test statistic $d_k^{(i)}$ exceeds the corresponding detection threshold $D_k^{(i)}$.

### 2.2.4 Likelihood ratio test

The likelihood ratio test [11] is able to give the optimal result for hypothesis testing, using the ratio of the likelihood function of the measurement vector under opposing hypotheses to construct the test statistic, as shown in Equation 5:

$$l_k = ln\left( \frac{p(\boldsymbol{y}_k \mid \mathcal{H}_m)}{p(\boldsymbol{y}_k \mid \mathcal{H}_0)} \right) \tag{5}$$

In the equation, $p(\boldsymbol{y}_k \mid \mathcal{H}_0)$ is the likelihood function under the fault-free hypothesis $\mathcal{H}_0$, and $p(\boldsymbol{y}_k \mid \mathcal{H}_m)$ is the likelihood function under the fault hypothesis $\mathcal{H}_m$. In practical RAIM applications, $p(\boldsymbol{y}_k \mid \mathcal{H}_m)$ is usually computed after excluding the measurement under the corresponding fault hypothesis [19, 20], and this approach is similar to the SS method, which can also be synchronized to achieve FDE.

## 3 RAIM algorithms

RAIM algorithm usually consists of two modules: the FDE module and the error bounding module. The FDE module detects, identifies and excludes faulty measurements based on the consistency checking principle using redundant measurement information. For a single-constellation receiver, at least five visible satellites are required to perform fault detection, and at least six visible satellites are required to perform fault exclusion [6]. The error bounding module is usually realized by calculating the PL, which is calculated by the user according to the requirements of the IR and other parameters, and compared with the preset al to discriminate the availability of the navigation system in real time. Currently, there are two main ways of calculating PL, one is to quantify the PE caused by undetected faults in the FDE module, and the other is to try to directly characterize the PE and then calculate its statistical bounds. Figure 6 provides a typical flow of RAIM, and it should be noted that not all RAIM algorithms strictly follow this general flow, and some algorithms may include additional steps or omit specific steps.

Initially, traditional RAIM algorithms relied on prior modeling of the probability distribution of measurement errors or state estimation errors, which in turn led to the derivation of the probability distribution model of the test statistic for constructing hypothesis tests and calculating PL. However, since error probability distribution models are often difficult to build and validate accurately, the performance of RAIM based on these models is limited by the accuracy of the models, while RAIM based on set representation sidesteps this challenge by no longer treating errors as random quantities, but as unknown deterministic values. In addition, the data-driven ML approach provides another way of thinking for integrity monitoring, showing great potential and advantages in complex scenarios that are difficult to handle with traditional RAIM.

## 3.1 RAIM based on error probability distribution model

RAIM based on the error probability distribution model is the most widely used, which has the advantages of clear mathematical expression and the detection threshold can be calculated by the preset $P_{\rm FA}$. Many studies have further divided the RAIM into snapshot scheme and filtering scheme, according to the number of measurement epochs used. The snapshot scheme is based on the current single-epoch measurement data only, and usually employs the LS algorithm for navigation solution calculation; The filtering scheme is based on current and historical measurement data, and usually employs the filtering methods such as the KF, extended KF (EKF), unscented KF (UKF) and the particle filter (PF), among other estimation methods for navigation solution calculation.

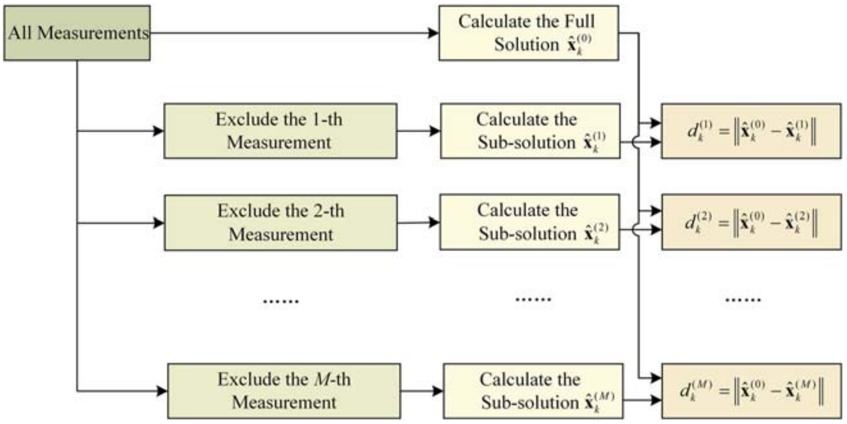

FIGURE 5
Calculation flowchart of the SS method.

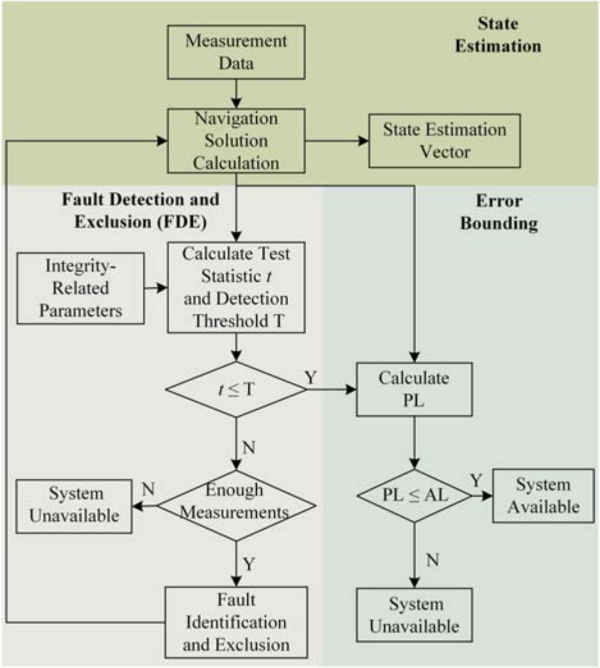

FIGURE 6
General RAIM algorithm flow [10].

### 3.1.1 Classic LS RAIM

The classic LS RAIM is one of the most typical snapshot schemes. It models the pseudo-range error as a zero-mean Gaussian distribution in the fault-free case, introduces a mean deviation for the error distribution in the faulty case, and considers only the single fault case. The classic LS RAIM includes the pseudo-range comparison method [21], the least squares residual method [22], and the parity vector method [23]. The equivalence of these methods was theoretically demonstrated by [24], where the parity vector method employs an orthogonal transformation to convert residual vectors into parity vectors, providing computational simplicity and high efficiency in calculating test statistics [25].

In the FDE module, the classic LS RAIM employs the $\chi^2$ test for fault detection, which constructs the normalized sum of squares of the pseudo-range residual vectors as a test statistic as shown in Equation 2; after a fault has been detected, the w-test is usually used to further identify and exclude fault.

In the error bounding module, Brown et al [26] pioneered the approximated radial protection (ARP) algorithm for calculating the PL, whose computational principle is shown in Figure 7 [13]; if the measurement noise is ignored, there is a linear relationship between the test statistic $t$ and the horizontal PE (HPE), and different satellites $i$ have their own characteristic slope SLOPE$_i$ [27], assuming that the HPE caused by the failure of a single satellite is certain, the corresponding test statistic t is the smallest when the failure occurs on the satellite with the largest characteristic slope SLOPE$_{\text{MAX}}$, making the failure most difficult to be detected. Based on this assumption, the calculation method of HPL is given as shown in Equations 6, 7:

$$\text{HPL} = \text{SLOPE}_{\text{MAX}} \cdot \sqrt{\lambda_{min}} \cdot \sigma \tag{6}$$

$$P_{\text{MD}} = \int_0^{T_k} f_{\chi^2(n-4,\lambda_{min})}(x)dx \tag{7}$$

In the equation, $\sigma$ is the standard deviation of the measurement noise, and $\lambda_{min}$ is the minimum non-centrality parameter required to satisfy the specified $P_{\text{FA}}$ and $P_{\text{MD}}$. This parameter can be can be calculated according to Equation 7, where $n$ is the number of visible satellites.

Since the ARP algorithm ignores the effect of measurement noise, in this regard, Sang and Kubik [28] proposed an improved ARP algorithm by incorporating a term related to measurement noise to the PL calculation. The calculation principle is also shown in Figure 7 [13], when the measurement noise is ignored, the minimum detectable fault corresponds to point A in the figure, when the measurement noise is taken into account, the distribution of the test statistic t and the HPE will be elliptical, and the center of the ellipse corresponds to point B in the figure. The HPL is thus divided

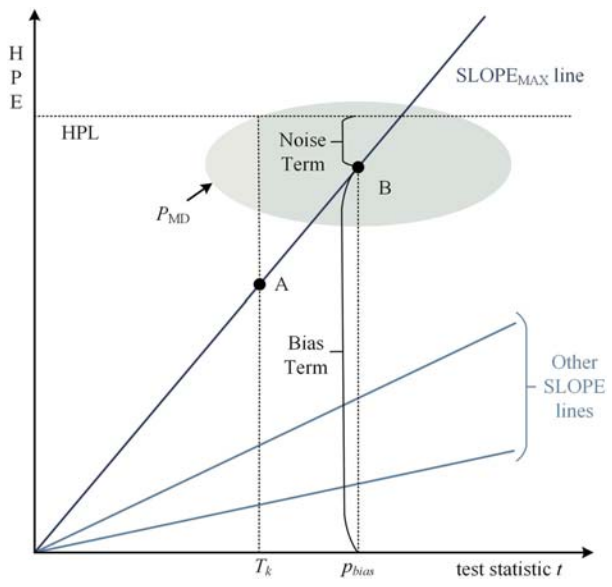

FIGURE 7
Principle of PL calculation in classic LS RAIM [13].

into bias term and noise term, as shown in Equations 8, 9. The bias term is calculated using the typical ARP algorithm, and the noise term is calculated by multiplying the expansion factor $k$ and the standard deviation $\sigma_H$ of the HPE, which is borrowed from the kSigma algorithm commonly used in the monitoring of system-level integrity [29].

$$\mathrm{HPL} = \mathrm{SLOPE}_{\mathrm{MAX}} \cdot p_{bias} + k \cdot \sigma_H \tag{8}$$

$$p_{bias} = \sqrt{\lambda}_{min} \cdot \sigma \tag{9}$$

In the equation, $k$ is the expansion factor related to $P_{\mathrm{MD}}$, and $\sigma$ is the standard deviation of the measurement noise.

### 3.1.2 Advanced RAIM and relative RAIM

Classic LS RAIM is unable to meet the high integrity requirements of the precision approach phase of civil aviation. In response, the GNSS Evolutionary Architecture Study (GEAS) Panel developed advanced RAIM (ARAIM) algorithm [30–34]. Compared with the classic LS RAIM algorithm, ARAIM has several advantages, including the ability to detect and recognize multi-faults, applicability to multi-constellation GNSS, the ability to monitor integrity in the vertical direction, and the capability to eliminate the first-order ionospheric delay using dual-frequency measurements.

ARAIM employs the Multiple Hypothesis Solution Separation (MHSS) [35, 36] algorithm for FDE, which allows for multi-faults detection by additionally considering multi-faults scenarios on top of the traditional SS method. In addition, ARAIM assigns a specific $P_{\mathrm{FA}}$ and $P_{\mathrm{HMI}}$ values to each fault hypothesis, performs independent hypothesis testing and PL computation, and assigns a specific $P_{\mathrm{HMI}}$ to the fault-free hypothesis $\mathcal{H}_0$ for the computation of PL in the case of fault-free. Ultimately, it takes the maximum value as the final PL. The detailed algorithm of ARAIM can be found in [37].

The ARAIM algorithm relies on periodically received integrity support messages (ISM) [38]. To guarantee integrity over longer reception intervals, relative RAIM (RRAIM) has been proposed [30, 39]. The RRAIM algorithm employs a time-differenced carrier phase measurement, defining the epoch of the received ISM as the initial time, and defines the interval from the current epoch back to the initial time as the coasting time. The algorithm combines the pseudo-range of the initial time and the variation of the carrier phase within the coasting time to construct a new measurement model, which employs a residual-based $\chi^2$ test for fault detection. Similar to ARAIM, PL is calculated under each hypothesis separately, and the maximum of all results is taken as the final PL [40]. pointed out that system availability is closely related to the length of the coasting time, with the best availability achieved when the coasting time is around 1 min; after this, availability gradually decreases with the extension of the coasting time.

So far, there are still ongoing research efforts aimed at improving to the ARAIM algorithm to improve its performance, and these improvements are mainly focused on the following four aspects:

1) When the number of visible satellites is large and the maximum number of faults (the hypothesis that the number of faults is greater than this value is ignored) is large, the computational burden of ARAIM increases significantly, so there are researches aiming to improve its computational efficiency.
2) The traditional ARAIM algorithm assigns $P_{\mathrm{FA}}$ and $P_{\mathrm{HMI}}$ fixed to each fault hypothesis $\mathcal{H}_i$, and simply averages them for the same type of fault hypotheses, in this regard, some studies have proposed to optimize the allocation of $P_{\mathrm{FA}}$ and $P_{\mathrm{HMI}}$ to improve the availability.
3) ARAIM also models the measurement errors as Gaussian distributions and obtains parameters such as the mean and variance of the error model based on the ISM parameters, and some studies aim to improve the performance of ARAIM by accurately calculating the model parameters or improving the error model.
4) The traditional ARAIM is based on pseudo-range only, in view of the high accuracy advantage of carrier phase, some studies have adopted carrier phase measurement on the basis of ARAIM framework.

This paper summarizes the latest ARAIM improvement studies in the above four aspects as shown in Table 1.

### 3.1.3 KF-based RAIM

The above two types of methods belong to the category of snapshot scheme, which only uses single-epoch measurements, and can quickly detect step errors, but the detection ability of slowly growing errors (SGEs) is seriously insufficient; in addition, they are only applicable to receivers that use the LS algorithm for navigation solving, and can not be applied to the real time kinematic (RTK) or precise point positioning (PPP) receivers that have to use filtering methods such as KF. The KF-based RAIM (KF-RAIM) algorithm introduced next can well solve the above problems. Traditional KF-RAIM borrows from the classic LS RAIM and employs residuals or innovations for FDE, such as autonomous integrity monitoring by extrapolation (AIME) [52, 53], extended RAIM (ERAIM) [54, 55],

TABLE 1 Status of ARAIM improvement research.

| Category of improvement | Overview of the approach | Comment | References |
|---|---|---|---|
| Improve computational efficiency | Since satellites in the same orbital plane are subject to similar disturbing force, using the orbital plane as a unit instead of satellites in MHSS can effectively reduce the number of subsets | Since measurement errors are not only related to the orbital plane, they can affect the FDE capability | [41] |
| | A feedback structure with probability Accumulation scheme is proposed to synchronize hypothesis testing and error bounding so as to avoid redundant subset computation | Reduced computation time by nearly 40% and was able to increase system availability somewhat | [42] |
| | By solving for the subset error covariance matrices upper bounds, it avoids the need to compute each subset one by one | Reduce computation by more than 95% | [43] |
| | Propose a fault grouping strategy to merge a larger number of double fault subsets into a constellation fault subset. | Reduce computation by more than 90% | [44] |
| Optimize $P_{FA}$ and $P_{HMI}$ allocation | The problem is transformed into an optimization problem under constraints, and a search algorithm for the optimal configuration is provided based on sequential quadratic programming | Availability is effectively improved, at some computational cost | [45] |
| | Solving optimal allocation configurations using dynamic particle swarm optimization algorithm | Availability is effectively improved, but computationally expensive | [46] |
| | Assign larger $P_{HMI}$ directly to fault hypotheses with suboptimal satellite geometry | Availability is improved with little or no computational cost | [47] |
| Optimization error model | The non-Gaussian and correlation components of the measurement errors are taken into account, and the position-domain Gaussian overbounding method is used to model the PE. | Availability is improved | [48] |
| | Calculation of residual tropospheric delay variance using the general extreme value (GEV) analysis method for accurate calculation of pseudo-range variance parameters in the ISM. | Availability is improved | [49] |
| | Estimating receiver noise variance using least square variance component estimation (LS-VCE) method | Availability is improved, but results in increased $P_{MI}$ | [50] |
| Introducing carrier phase | Applying ARAIM algorithm in single-epoch precise point positioning based on real-time kinematic networks (PPP-RTK) framework | PL reach meter and even sub-meter level, with significant increase in availability | [51] |

and other typical algorithms. AIME constructs the normalized sum of squares of the innovations $\boldsymbol{r}_k$ as the test statistic $s_k^2$, and to improve the detection of SGEs, performs a weighted average within a sliding time window, as shown in Equations 10–12:

$$s_k^2 = \left(\boldsymbol{r}_{avg}^T\right)\left(\boldsymbol{S}_{avg}^{-1}\right)\left(\boldsymbol{r}_{avg}\right) \tag{10}$$

$$\boldsymbol{r}_{avg} = \left(\boldsymbol{S}_{avg}^{-1}\right)^{-1} \sum_{j=k-\tau+1}^{k} \boldsymbol{S}_j^{-1}\boldsymbol{r}_j \tag{11}$$

$$\boldsymbol{S}_{avg}^{-1} = \sum_{j=k-\tau+1}^{k} \boldsymbol{S}_j^{-1} \tag{12}$$

where $\tau$ is the time window length, $\boldsymbol{r}_j$ is the innovation, and $\boldsymbol{S}_j$ is its covariance matrix. The detection delay of the AIME algorithm for the SGEs is inversely proportional to its growth rate, in order to further reduce the detection delay, Bhatti and Ochieng [56] proposed a rate detection method, which adds a KF based on the AIME algorithm to monitor the rate of change of $s_k^2$, reducing the SGEs detection delay by more than 33%.The ERAIM algorithm [54, 55], on the other hand, combines the predicted state vectors and measurement vectors in the KF, constructs a new measurement model and calculates the residuals, which in turn is used for the FDE using the $\chi^2$ test and the w-test. In addition, the correlation coefficients between the test statistics are also calculated by ERAIM, which is used to analyze the separability of the faults.

Carrier phase measurements are usually several orders of magnitude more accurate and more robust to noise compared to code measurements. Therefore, Feng et al. [57] developed carrier phase-based RAIM (CRAIM) using innovations to guarantee the integrity of relative positioning, and Schuster et al. [58] further utilized CRAIM for RTK positioning. The CRAIM algorithm uses the double difference of pseudo-range, wide lane, and carrier phase measurements as the EKF measurements, estimating the ambiguity of whole cycles as states to assist in ambiguity resolution. In addition, CRAIM can use the carrier phase measurements to construct a specialized test statistic for detecting cycle slip faults. Addressing the lack of fault identification capability in the CRAIM algorithm, Liu et al. [59] further proposed an extended w-test method with multi-fault detection and identification capability.

In addition to the KF-RAIM based on residuals or innovations, the KF-RAIM based on SS is also widely used [17]. Its test statistics are computed as shown in Figure 4, featuring the unique capability of using both main filter and sub-filters to compute the full solution $\hat{\boldsymbol{x}}_k^{(0)}$ and sub-solution $\hat{\boldsymbol{x}}_k^{(i)}$ in parallel. However, the method proposed in [17] lacks multi-fault detection capability and cannot detect INS fault in GNSS/INS integrated navigation. To address this problem, Bhatti et al. [60] proposed a FDE method using a multi-stage parallel subset filter based on the MHSS, which can detect and identify double faults, including INS fault. Zhang et al. [61] further improved the filter bank scheme so that it can be applied to carrier phases for integrity monitoring in PPP, and noting that periodic initialization of the filters can reduce the maximum number of faults that need to be considered, thereby effectively reducing the computational burden. Meng et al. [62], instead of adopting the filter bank scheme, consider the new measurement model constructed in ERAIM as a "pseudo-snapshot" model, and then use the least squares form of the SS method to compute the full solution $\hat{\boldsymbol{x}}_k^{(0)}$ and the sub-solution $\hat{\boldsymbol{x}}_k^{(i)}$, which reduces the computational burden to some extent. Gao et al [63] further applied this method to integrity monitoring in RTK positioning and used it to detect fault ambiguity solution.

In terms of error bounding, the innovation or residual-based KF-RAIM divides the PL into a noise term and a bias term [64], where the noise term represents the upper bound of the PE caused by the noise, and the bias term represents the upper bound of the PE caused by measurement bias. In contrast, the SS-based KF-RAIM directly takes the detection threshold $D_k^{(i)}$ in each fault hypothesis $\mathcal{H}_i$ as a bias term, as shown in Equation 13:

$$PL_k = \max_i \left\{ a_k^{(i)} + D_k^{(i)} \right\} \tag{13}$$

where the noise term $a_k^{(i)}$ can be solved based on $P_{\text{MD}}$ and the state covariance matrix of each sub-filter. Tanil et al. [65] compared the above two types of methods in GNSS/INS integrated navigation in an urban environment, and the results showed that when the number of visible satellites is more than four, the KF-RAIM based on the SS method has a smaller $P_{\text{HMI}}$, but the computational burden is heavier.

In view of the high accuracy of carrier phase measurements, the PL calculated by KF-RAIM with the introduction of carrier phase is significantly smaller, reaching meter or even sub-meter level. This improvement enhances the availability of the system, and the experimental results of Schuster et al. [58] show that the HPL calculated by the CRAIM algorithm is in the range of 0.5 m in the case of fault-free. In addition, since carrier phase measurements usually require a ratio test [66] to verify whether the ambiguity of whole cycles is correctly fixed, Li et al. [67] introduced the concept of completeness to the ambiguity validation by defining an ambiguity protection level. When the ambiguity protection level exceeds the ambiguity alarm threshold, the ambiguity validation is considered to have failed, and an alarm is generated.

Since KF and EKF are always limited by Gaussian error models, the actual measurement error and state estimation error are affected by various factors such as receiver motion, linearization modeling errors of nonlinear models, and residual tropospheric and ionospheric errors. As a result, the Gaussian assumption is not appropriate, leading to inherent limitations in KF-RAIM [68]. In response to this challenge, some studies have begun to explore KF-RAIM based on non-Gaussian error models.

Madrid et al. [69] proposed an integrity monitoring scheme called Kalman integrated protection level (KIPL) based on the isotropy assumption (the residual vector points in any direction with equal probability over the measurement space) [70]. The approach models the measurement error as a Student's t-distribution, which in turn leads to the derivation of a Student's t-distribution model for the state estimation error, which ultimately allows for the computation of the PL based on the preset IR. Validation results from Gottschalg et al. [71] show that the HPL calculated by KIPL is smaller compared to that calculated by traditional KF-RAIM under the same IR requirement. Wang et al. [72] further extended this algorithm for application in PPP. Similarly, Shao et al. [68] used a robust KF based on the Student's t distribution [73] for state estimation, which models both measurement and process noises as student's t-distributions. This method uses a variational Bayesian approach to approximate the state estimation error as a Gaussian distribution for calculating the PL [68]. also discusses multi-faults detection and identification schemes accordingly.

### 3.1.4 PF-based RAIM

PF allows better state estimation in nonlinear systems and non-Gaussian noise conditions, eliminating the Gaussian noise assumption restriction found in traditional KF-RAIM. Moreover, the posteriori particle ensemble of PF provides a new approach for error bounding.

Li and Kadirkamanathan [74] were the first to propose the introduction of the likelihood ratio test in PF to achieve fault detection. Based on this, some studies [20, 75, 76] borrowed the concept of the SS method and used the likelihood ratio test for integrity monitoring by constructing a parallel filter bank. They calculated the cumulative log-likelihood ratio $LLR_k^{(i)}$ in the time window under different fault hypothesis $\mathcal{H}_i$ as a test statistic, as shown in Equation 14:

$$LLR_k^{(i)} = \sum_{j=k-\tau+1}^{k} ln\left(\frac{\sum_{r=1}^{N} p\left(\boldsymbol{z}_j|\boldsymbol{x}_j^{(i)}(r)\right)}{\sum_{r=1}^{N} p\left(\boldsymbol{z}_j|\boldsymbol{x}_j^{(0)}(r)\right)}\right) \tag{14}$$

where $\tau$ is the time window length, $k$ denotes the current epoch, $i$ is the fault hypothesis index, $r$ is the particle index, $N$ is the total number of particles, $p\left(\boldsymbol{z}_j|\boldsymbol{x}_j^{(i)}(r)\right)$ and $p\left(\boldsymbol{z}_j|\boldsymbol{x}_j^{(0)}(r)\right)$ are the likelihood functions under the fault hypothesis $\mathcal{H}_i$ and the fault-free hypothesis $\mathcal{H}_0$, respectively. The maximum value of $LLR_k^{(i)}$ is usually taken as the test statistic. The fault detection threshold of this method typically needs to be selected empirically, for this problem, He et al [77] proposed to optimize the computation of the detection threshold using a genetic algorithm.

The above fault detection methods require several parallel PFs, which can impose a significant computational burden in the case of a large number of visible satellites. To address this, Han et al. [78] proposed constructing the test statistic using the measurement residuals vector corresponding to the particle of maximum weight, pointing out that the correlation between the residual vector and the satellite projection vector can be used to identify faulty satellites. Hafez et al. [79] proposed constructing the test statistic using the weighted average measurement predicted value of the particle ensemble.

The error bounding method of PF-RAIM is more special, evaluating the actual IR based on the *a posteriori* set of particles to achieve error bounding, known as Bayesian RAIM (BRAIM) [80]. BRAIM calculates the error of each particle state with respect to the *a posteriori* estimation and accumulates the weights of the particles whose errors exceed the AL to obtain the estimated integrity risk. This risk is then compared with the preset IR to determine availability, as illustrated in Figure 8 [81]. Gabela et al. [82, 83] further improved this scheme by introducing spatial feature constraint information to assist the weight update step in PF. Empirical results show that with the HAL set to 5 m and the IR requirement specified, the navigation system's availability exceeds 99%, regardless of whether the measurement noise is modeled as a Gaussian model or a three-component Gaussian mixture model (GMM).

However, the integrity risk estimated by BRAIM is only the empirical risk based on the set of particles, which has limitations. Because the number of particles in the PF is always limited, it does not fully reflect the state posterior distribution, leading to some underestimation of the estimated integrity risk. Regarding this problem, Gupta et al [81, 84] proposed an improved BRAIM algorithm based on probably approximately correct- Bayesian (PAC-Bayesian) theory, which introduces the divergence risk to quantify the uncertainty caused by the above problem, and derives a method for calculating the upper bound on IR, which is also schematically shown in Figure 8 [81]. Additionally, this study models the measurement noise as a GMM while employing the expectation-maximization (EM) algorithm to determine the model parameters, thereby reducing the difficulty of model parameter estimation.

On the other hand, the particle impoverishment problem, i.e., reduced particle diversity, arises from the resampling operation in PF, which affects the performance of PF-RAIM. In this regard, several studies have proposed improvements to address particle impoverishment, including: introducing a Markov chain Monte Carlo (MCMC) moving step for each particle [75, 85], utilizing selection, crossover, and mutation operations in genetic algorithms to replace the traditional resampling method [86], employing backpropagation neural network (BPNN) to adjust the particle weights [87], and using chaotic particle swarm optimization algorithms to increase particle diversity [20].

### 3.1.5 Brief summary

Table 2 provides a comparative analysis of different RAIM algorithms based on the error probability distribution model. Among them, the snapshot scheme can quickly detect step errors; however, due to its reliance on only a single epoch measurement, its detection capability is seriously insufficient for SGEs caused by aging satellite equipment or clock drift. In this regard, some studies [88, 89] have improved the snapshot scheme by averaging the test statistics within a sliding time window to enhance SGEs detection capability. Additionally, the filtering scheme can be easily integrated with the INS, and the additional redundant information provided by the INS can effectively improve the system's availability. However, the introduction of the INS also brings an additional source of integrity risk.

## 3.2 RAIM based on set representation

Traditional RAIM always assumes that the error probability distribution model is known, but in practice, there are significant challenges in the accurate construction and validation of the error probability distribution model. RAIM based on set representation is able to get rid of the limitation of traditional statistical distribution models, and this type of approach treats the error as an unknown deterministic value, aiming to construct the set characterizing the state estimation error by determining the uncertainty intervals of the error, which is used for further FDE and error bounding.

### 3.2.1 FDE module

In the FDE module [90], proposes an innovative fault detection strategy based on set representation theory, converts the navigation problem into a convex polytope solving problem by applying the uncertainty interval $[-\boldsymbol{e}, \boldsymbol{e}]$ of the observation error to the observed-minus-computed values (OMC) vector $\boldsymbol{y}$ as shown in Equation 15.

$$\boldsymbol{y} - \boldsymbol{e} \leq \boldsymbol{A}\delta\boldsymbol{x} \leq \boldsymbol{y} + \boldsymbol{e} \tag{15}$$

In the above equation, $\boldsymbol{A}$ is the design matrix and $\delta\boldsymbol{x}$ is the state estimation vector. It has been shown that the volume of the polytope is negatively correlated with the degree of consistency of the measurements, therefore, a decrease in the volume predicts an increase in the probability of the existence of fault measurements, which in turn leads to the proposal of a new inconsistency metric that warns the user when it exceeds a threshold value. In addition, when the fault value is large, the polytope will be the empty set, so some studies also directly achieve fault detection by determining whether the set of polytope characterizing the state estimation error is empty [91, 92], it is worth noting that [91] compares this method with the traditional classical LS RAIM and ARAIM algorithms based

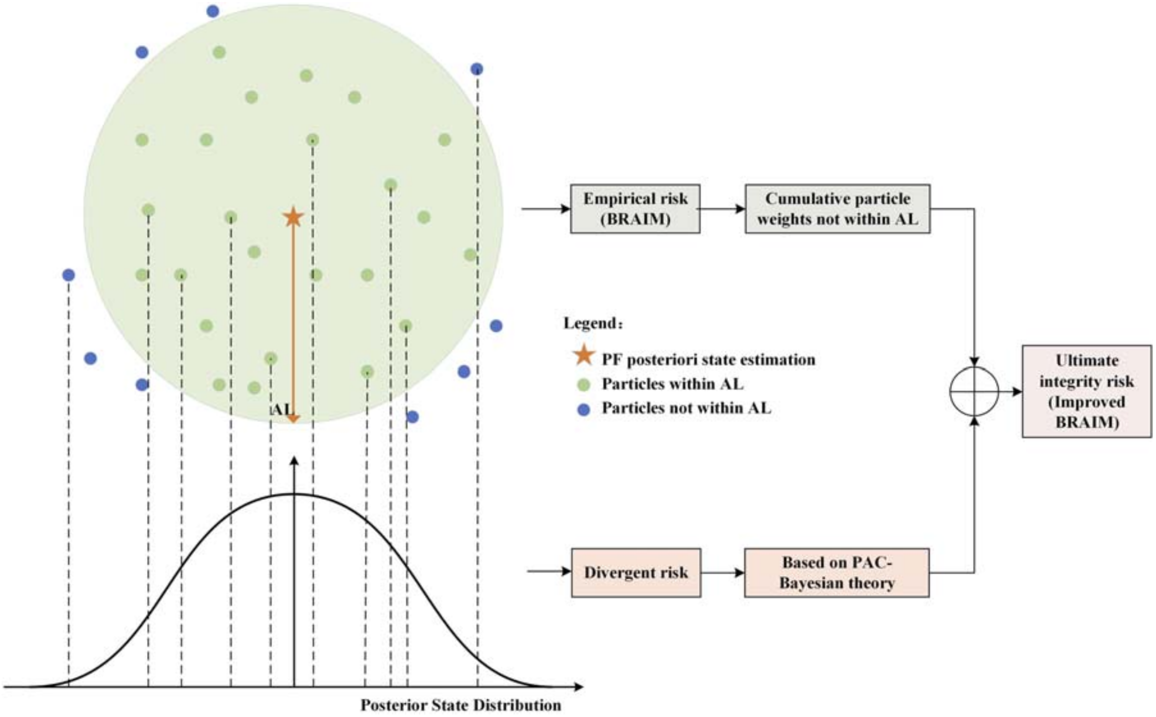

FIGURE 8
Braim and improved BRAIM Schematics [81].

on the SS method, under the assumption of Gaussian noise were compared, but found to be inferior to the traditional methods in terms of fault detection rate and $P_{\mathrm{HMI}}$ metrics [92]. further proposed a corresponding fault identification and exclusion scheme based on the SS idea on the basis of this method.

### 3.2.2 Error bounding module

The advantage of RAIM based on set representation is reflected in the error bounding module, which can compute the set characterizing the state estimation errors in real time. Among many studies, a special polytope, namely, the zonotope, has been widely chosen as a set representation of the state estimation errors due to its favorable mathematical properties (e.g., Minkowski sum, linear transformation) [93]. The zonotope $\mathbb{Z}$ was first used by Combastel [94] to characterize the state estimation errors $\delta\mathbf{x}$, which is defined as:

$$\mathbb{Z} =< \mathbf{c}, \mathbf{H} >= \left\{\delta\mathbf{x} \in \mathbb{R}^n \mid \delta\mathbf{x} = \mathbf{c} + \mathrm{Hb} \|\|\mathbf{b}\|_\infty \leq 1\right\} \tag{16}$$

in Equation 16, $\mathbf{c} \in \mathbb{R}^n$ is called the center vector, $\mathbf{H} \in \mathbb{R}^{n\times m}$ is called the generation matrix, and $m$ is the order of the zonotope $\mathbb{Z}$. By adjusting the order $m$, the number of faces and the shape of $\mathbb{Z}$ can be changed, making it more flexible in characterizing the state estimation errors. Usually, zonotope is used in combination with filter estimation methods. Liu et al. [93] used zonotope for error bounding and PL calculation in tightly coupled GNSS/INS navigation systems, and pioneered the use of the extended H-infinity filter (EHF), which treats the noise as an unknown deterministic quantity instead of a random quantity, to replace the traditional EKF for state estimation. And the validation results show that the proposed method has higher system availability and lower $P_{\mathrm{MI}}$ than the traditional KF-RAIM.

Referring to the [93, 95], this paper summarizes the generalized flowchart of error bounding based on zonotope set representation at the $k$-th epoch in Figure 9. It is worth noting that, as epoch $k$ advances, the order of the zonotope set characterizing the state estimation error will increase, which will generate a huge computational burden and affect the real-time performance of the algorithm, in this regard [93], proposes an order limitation scheme based on the zonotope reduction method, with the upper limit of the order being customized by the user, and experimentally explores the effect of the order on the computational time and PL.

In addition to the above studies using the standard zonotope set, there have been some studies using variants of the zonotope for error bounding. Ashraf et al. [95] proposed to use constrained zonotope to characterize the state estimation error, which makes the geometry of the set more closely match the actual state space and further reduces the conservatism of error bounding. Shetty et al. [96], on the other hand, chose to adopt probabilistic zonotopes as a set representation tool while still assuming that the measurement errors and process errors follow a Gaussian distribution. This allows the state estimation error set to be solved according to the preset confidence level; however, there are some limitations, as the Gaussian distribution assumption is not strictly valid. Additionally [96], employs urban 3D maps and ray-tracing to determine multipath errors uncertainty intervals, in turn, the uncertainty interval of the measurement errors is determined. Su et al [92, 97], on the other hand, proposed an extended point confidence region for characterizing the state-domain error set, which uses a zonotope set to quantify the impact

TABLE 2 Comparative Analysis of RAIM based on error probability distribution model.

| Category | Algorithm | Input data | FDE method | Advantages | Disadvantages | Ref. |
|---|---|---|---|---|---|---|
| Snapshot Scheme | Classic LS RAIM | GNSS Code | $\chi^2$-test, w-test | Low computational burden | Single-constellation only; no multi-fault detection and identification capability | [21–23, 26, 28] |
| | ARAIM | GNSS Code<br>ISM | MHSS | Suitable for multi-constellation, can detect and identify multi-fault | High computational burden when the maximum number of faults is large | [30–34] |
| | RRAIM | GNSS Code, Time-Differenced Carrier Phase | $\chi^2$-test | Can ensuring the integrity of ARAIM in the ISM reception interval | Performance is limited by the length of coasting time | [30, 39] |
| Filtering Scheme | AIME | GNSS Code | $\chi^2$-test, rate detection method, w-test | Strong detection capability for SGEs | Performance is strongly correlated with the length of the time window | [52, 53] |
| | ERAIM | GNSS Code, INS | $\chi^2$-test, w-test | Can detect and identify multi-fault | INS measurements must be required | [54, 55] |
| | CRAIM | GNSS Code, Carrier Phase | $\chi^2$-test, extended w-test | System availability is very high | Need to consider the ambiguity of whole cycles | [57, 58] |
| | SS KF-RAIM | GNSS Code (optional: Carrier Phase, INS) | MHSS | Can detect and identify multi-fault | Multiple parallel filters are often required, high computational burden | [17, 60–63] |
| | KIPL | GNSS Code (optional: Carrier Phase, INS) | N/A | Error probability distribution is modeled as Student's t-distribution, high availability | No ability to detect and identify fault | [69, 71, 72] |
| | PF-RAIM | GNSS Code (optional: INS) | likelihood ratio test | Can escape the limitation of the Gaussian noise assumption | Performance is limited by the number of particles, high computational burden | [20, 75, 76, 80–83] |

caused by systematic errors, and at the same time uses the traditional confidence ellipsoid or ellipsoid set to quantify the impact caused by stochastic errors, and finally take the Minkowski sum of the two sets as the final set of state estimation errors.

### 3.2.3 Brief summary

At present, there are not many studies on RAIM based on set representation. Theoretically, this approach does not rely on the error probability distribution model; however, many studies still use the traditional Gaussian distribution assumption to determine the error uncertainty interval based on the preset confidence level. Only some studies have discussed the determination of measurement error intervals, such as those for multipath errors [92, 96] and residual tropospheric and ionospheric errors [98]. These studies cover only part of the measurement errors and lack the determination of process error intervals. There have been studies using ML methods to estimate pseudo-range errors [99, 100], suggesting that attempts could be made to predict the uncertainty intervals of pseudo-range errors with the help of ML, which may be a direction for further research in the future.

## 3.3 ML-based RAIM

ML-based RAIM (ML-RAIM) has great potential and advantages, as it can effectively address the challenges posed by nonlinear systems and non-Gaussian noise, and it supports integrity monitoring in complex scenarios where it is difficult to model error probability distributions in traditional RAIM (e.g., urban canyon). In addition, since ML-RAIM mostly follow the idea of characterizing

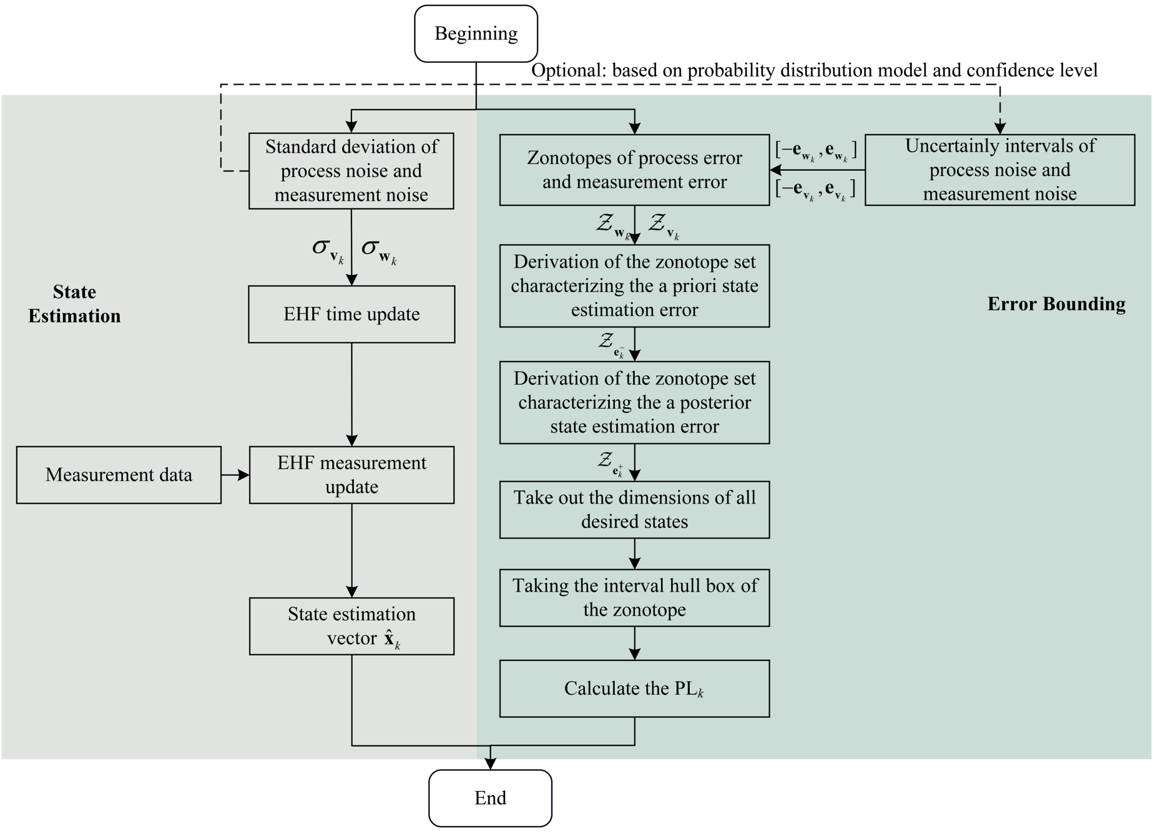

FIGURE 9
Generalized flowchart of error bounding based on zonotope set representation.

the PE in calculating the PL, it makes the two modules of FDE and error bounding relatively independent of the study.

### 3.3.1 FDE module

According to whether the training data need labels, ML algorithms can be classified into two main categories: supervised learning and unsupervised learning. Supervised learning relies on labeled datasets for training, while unsupervised learning does not require data labels.

In terms of supervised learning research, it can be categorized as traditional pattern recognition, traditional neural networks, and deep learning based on the ML algorithms employed in the research. Traditional pattern recognition methods with inherent advantages such as high interpretability and fast training speed are widely used to detect and identify faulty measurements, especially for NLOS signals [101]. used support vector machine (SVM) algorithm to classify LOS signals and NLOS signals, and six commonly used features were analyzed, and it was found that the feature of pseudo-range residuals had no significant contribution [102]. systematically evaluated the detection effectiveness of various ML algorithms under different fault thresholds and found that the k-nearest neighbor (KNN) algorithm exhibits an optimal fault detection rate.

Compared to single models, ensemble learning has good robustness and stability by combining the prediction results of multiple base learners. Comparative studies in [103] have shown that boosting and bagging ensemble learning algorithms exhibit better performance in NLOS signal detection compared to single models such as support vector regression (SVR), KNN and gradient boosting decision tree (GBDT). Among them, the random forest (RF) algorithm with Bagging strategy performs most prominently. Based on RF algorithm [104], used factor analysis to aggregate the original features into three more interpretable common factors, which improved computational efficiency by about 30%. While the base learner of the above two types of ensemble learning is limited to the same class of models [105], innovatively detects NLOS signals based on the stacking ensemble learning (SEL) algorithm, which supports the use of different classes of models as the base learner. It achieves better generalization ability in different scenarios such as static, low-speed, and high-speed dynamic.

Many studies have also used traditional neural network (NN) algorithms with relatively simple structures for FDE [106]. directly predicts the receiver fault rate based on multi-layer perceptron (MLP) algorithm and alerts the user when the prediction exceeds a specified threshold [107], proposes a NLOS signal detection scheme based on the MLP algorithm, which effectively improves the PPP-RTK positioning accuracy.

Among the traditional NN algorithms, radial basis function neural network (RBFNN) has received a lot of attention from researchers due to its fast training speed and applicability to small sample datasets. Zheng et al. [108] used probabilistic neural network (PNN), which is an RBFNN integrated with Bayesian theory, to propose a fault detection scheme that employs a particle swarm optimization algorithm to compute a specific fitness function, ensuring the preset $P_{\mathrm{FA}}$ and $P_{\mathrm{MD}}$ [108]. also proposed a novel dataset acquisition method to generate training data by sampling the position error distribution in fault and fault-free modes according to the variance inflation model. Huang et al. [109] also used a similar method to acquire training data, employing nonparametric estimation-based neural network (NE-NN) for fault detection and combining it with the SS method for fault identification. Wu et al. [110] similarly proposed a PNN-based fault detection and identification method characterized by the use of single-satellite multi-epoch pseudo-range residuals as feature vectors, which has higher sensitivity compared to classic LS RAIM.

Deep learning algorithms consist of multi-layer NNs that can automatically learn and extract higher-order features from the data and have high generalization ability. Zhu et al [111] enriched and enhanced one-dimensional features within a time window into two-dimensional features and proposed an NLOS signal detection scheme based on convolutional neural network (CNN). Sun et al [112] used a long short-term memory (LSTM) for fault detection, and specially designed a loss function to synthesize the advantages of the snapshot scheme and the filtering scheme, thus improving the detection performance for small magnitude step errors and SGEs [113]. used Hopfield network for NLOS signals detection, and the experimental results show that accuracy is effectively improved compared with traditional SVM and gradient boost machine (GBM) algorithms.

In addition, it has been found that the emergence of NLOS signals has obvious spatiotemporal correlation [114–116], and the self-attention mechanism is able to capture long-range dependence and global contextual information by calculating the relational weights between any two elements in the sequence. Therefore [116], proposed a dual self-attention mechanism (DSN) model to construct two self-attention channels to extract spatial environment features and signal time features, respectively; the former inputs the feature data of all measurements, while the latter inputs the historical feature data of the target measurement, which significantly improves the detection effect of NLOS signals.

On the other hand, in order to cope with the difficulty of adapting the trained model to new environments, and to further improve the model generalization ability [115], further introduced the Siamese neural network architecture based on DSN model, so that the model can be quickly adapted to new environments under the condition of few-shot labeled data. Similarly, Sun et al [117, 118] also proposed a continuous learning-based NLOS detection scheme based on LSTM model, and the experimental results show that the proposed method improves the NLOS signal detection rate by 5%–12% in new environments compared with the traditional model fine-tuning scheme. Table 3 summarizes the above supervised learning-based FDE studies for comparison.

Compared to supervised learning, FDE methods based on unsupervised learning do not rely on acquiring difficult labeled data and are able to cope with fault types that do not occur during training. The current research can be divided into two categories, one method is based on traditional clustering or single classification algorithms, and the other method is based on deep learning reconstructed models.

In the field of research based on traditional clustering or one-class classification algorithms, Xia et al [119] used the hierarchical density-based spatial clustering of applications with noise (HDBSCAN) algorithm to cluster and identify fault [120, 121]. compared three clustering algorithms, k-means, Gaussian mixed clustering and fuzzy c-means, and found that the k-means algorithm has the optimal performance in identifying NLOS signals. Wang et al. [122] proposed a fault detection scheme based on the one-class support vector machine (OCSVM) algorithm, which uses only the data from the fault-free case as the training dataset. A fault is detected when the similarity measure of the OCSVM outputs is less than a specified threshold.

Another type of fault detection principle based on deep learning reconstruction model is: using the data in the fault-free case to train the model with data reconstruction ability, when the difference between the model output and the real sample is too large, it indicates that there is a fault. Kim et al. [123] utilized a time-delayed neural network (TDNN) to make predictions based on historical test statistics and compared them with the current test statistics for fault detection. Gogliettino et al. [106] proposed an autoencoder-based fault detection scheme by calculating the difference between the input data and the reconstruction results from the autoencoder, determining that it is a faulty case when the difference exceeds a specified threshold. Shen et al. [124] proposed a combination of a generative adversarial network (GAN) and a recurrent neural network (RNN) for GNSS/INS integrated navigation integrity monitoring. The verification results show that the detection performance for small magnitude step errors and SGEs is improved compared to traditional KF-RAIM; however, this method assumes that the INS is always fault-free and ignores the potential fault risk of the INS. Table 4 summarizes the above unsupervised learning-based FDE studies for comparison.

### 3.3.2 Error bounding module

In terms of error bounding studies [109], borrowed the idea of PL calculation from the classical LS RAIM algorithm, i.e., to quantify the effect of undetected faults on PE, and proposed to calculate the maximum PE caused by undetected faults in the FDE module based on the search strategy, and then obtain the PL.

In addition, some studies have chosen to use ML algorithms to directly predict PL. Mendonca et al [125] proposed to use decision tree (DT) and NN algorithms to directly predict PL respectively, both of which have smaller $P_{\mathrm{HMI}}$ compared to the traditional KF-RAIM. The conformal regression algorithm has the ability to output the confidence interval of the prediction result under the specified confidence level. Kuratomi et al [126] combined conformal regression with RF algorithm and proposed conformal regression forests (CRF) for predicting PE intervals at specified confidence levels, which provides insights for PL calculation. The confidence level was set to 99.999% in the paper, and the prediction is considered successful if the actual PE falls within the prediction interval. Unfortunately, the optimal set of experimental results in the paper only achieved a 99.99% prediction success rate, which requires further research.

Probabilistic regression ML algorithms provide the credibility or probability distribution model of the prediction results along with the output of the prediction results, so some researchers have tried to use probabilistic regression ML algorithms to predict

TABLE 3 FDE based on supervised learning.

| Category | Advantages | Disadvantages | ML model | Dataset type and labeling | Ref |
|---|---|---|---|---|---|
| Traditional pattern recognition | High interpretability; support small-scale data; fast training speed; real-time FDE ability | Poor generalization ability; reliance on artificially designed normative features | SVM | Real measurement, UrbanLoco open source dataset, labeling based on fisheye camera | [101] |
| | | | KNN | Real measurement, labeling inferred from actual pseudo-range error and fault threshold | [102] |
| | | | RF | Real measurement, open dataset from Chemnitz University of Technology, labeling inferred from actual pseudo-range error | [103] |
| | | | SEL | Real measurement, labeling based on fisheye camera and 3D map | [105] |
| Traditional neural network | Fast training speed, especially for RBFNN algorithm; real-time FDE ability | Poor generalization ability; poor interpretability; medium data scale requirement | MLP | Real measurement, open source dataset, labeling based on fisheye camera | [107] |
| | | | NE-NN, PNN | Simulation, dynamically sampling the position error distribution and get labels | [108, 109] |
| | | | PNN | Simulation, add simulated fault and obtain labels | [110] |
| Deep learning | Support continuous learning; high generalization ability; can automatically extract higher-order features from data | Very poor interpretability; require large-scale data; low training speed; poor real-time performance | CNN | Real measurement, labeling based on 3D map | [111] |
| | | | LSTM | Real measurement, add simulated faults and obtain label | [112] |
| | | | Hopfield network | Real measurement, labeling based on fisheye camera | [113] |
| | | | DSN, Siamese neural network | Real measurement, labeling based on fisheye camera | [115, 116] |
| | | | LSTM, continual learning | Real measurement, UrbanNav open source dataset, labeling based on 3D map | [117, 118] |

the statistical characteristics of PE, thus realizing error bounding. Geragersian et al. [127] proposed the use of a Bayesian-LSTM algorithm to predict PE, and since the parameters of the Bayesian neural network are random quantities, the PE standard deviation can be estimated using Monte Carlo methods, and then obtain the PL. Isik et al. [128] proposed a scheme for PL calculation based on natural gradient boosting (NGBoost). The NGBoost algorithm is capable of predicting a probability distribution model that matches the input samples, but it requires pre-determination of the type of the probability distribution model. In this study, PE is assumed to be Gaussian distributed, and the mean and variance are predicted separately, which can be combined with a predefined confidence level to calculate the PL. The experimental results show that system availability is significantly improved in simulated

TABLE 4 FDE based on unsupervised learning.

| Category | Advantages | Disadvantages | ML model | Dataset type | Ref |
|---|---|---|---|---|---|
| Traditional clustering or single classification | High interpretability; support small-scale data; fast training speed; real-time FDE ability | Poor generalization ability | k-means | Real measurement | [119] |
| | | | HDBSCAN | Real measurement | [120, 121] |
| | | | OCSVM | Simulation, add simulated faults | [122] |
| Reconstruction models based on deep learning | High generalization ability; can handle fault situations that have not been encountered during the training process | Poor interpretability; require large-scale data; low training speed; poor real-time performance | TDNN | Combination of simulated and real data | [123] |
| | | | Autoencoder | Simulation, add simulated faults | [106] |
| | | | GAN, RNN | Real measurement, add simulated faults | [124] |

TABLE 5 ML-based error bounding studies.

| Category | Characteristic | ML model | Dataset type and labeling | Ref. |
|---|---|---|---|---|
| Quantifying the effect of undetected faults on PE | Based on Gaussian distribution; search for the minimum detectable fault variance expansion factor and fault deviation value, respectively | NE-NN | Simulation, dynamically sampling the position error distribution and get labels | [109] |
| Direct predicting PL based on ML algorithm | no need to predetermine the type of probability distribution model | DT, NN | Real measurement, labeling based on RTK high-precision positioning results | [125] |
| | | CRF | 132 land-vehicle challenging urban kinematic GNSS datasets | [126] |
| Based on probabilistic regression ML algorithm | predicting the probability distribution of PE; need to predetermine the type of the probability distribution model | Bayesian -LSTM | Simulation, the actual PE is known | [127] |
| | | NGBoost | Simulation, the actual PE is known | [128] |

suburban, urban, and urban canyon environments compared to classic LS RAIM. Table 5 summarizes and compares the above availability discriminative studies in ML-RAIM.

### 3.3.3 Brief summary

Currently, there have been many ML-based GNSS jamming and spoofing detection studies [129–131], but relatively few studies have been applied to integrity monitoring. Although there are similarities between the two, the additional IR requirements of RAIM itself, along have made ML-RAIM studies relatively challenging. Firstly, the datasets used in existing studies are usually limited to a single scenario, failing to comprehensively reflect multiple factors such as satellite faults, ionospheric fluctuations, multipath effects, spoofing, and jamming. This results in flaws in the generalization ability of the trained models. Secondly, most current ML-based FDE strategies lack corresponding error bounding module studies, and in the few studies of error bounding, it is still limited to the traditional Gaussian distribution assumption. Thirdly, there is a lack of relevant research dedicated to feature extraction and selection.

## 3.4 Comparison and summary

The advantages and disadvantages of the above three types of RAIM algorithms are shown in Table 6.

# 4 Challenges and opportunities of RAIM research

With the wide application of GNSS, existing RAIM research faces the following challenges: Firstly, due to the vulnerability of

TABLE 6 Characteristics of the three types of RAIM.

| Category | Advantage | Disadvantage |
|---|---|---|
| RAIM based on error probability distribution model | Mathematical expression is clear, IR and $P_{MD}$ can be estimated analytically | Commonly used Gaussian models have limitations, it is often difficult to establish and validate error probability distribution models in complex scenarios |
| RAIM based on set representation | Avoiding the difficult task of modeling error probability distributions, the set of state estimation errors that can be characterized | Performance is limited by the accuracy of determining the measurement and process error uncertainty intervals |
| ML-RAIM | Better cope with non-linear systems, non-Gaussian noise environment, support for integrity monitoring in complex scenarios | Dependence on reliable datasets, poor generalization ability, insufficient research on the error bounding module |

the GNSS signals themselves, it is very susceptible to jamming and spoofing [132]. Additionally, for the vast number of urban users, multipath and even NLOS signals are very common, which leads RAIM to operate in a more complex and harsh electromagnetic environment. Secondly, in key applications such as assisted driving, autonomous driving, and low-altitude unmanned aerial vehicles (UAVs), the required PL is usually small, often in the meter or even sub-meter level [9]. However, the PL calculated by existing RAIM is often overly conservative (reaching up to tens of meters or even hundreds of meters), resulting in seriously inadequate system availability. Thirdly, most existing RAIM algorithms are based on the Gaussian error model, but the study by [133] have shown that actual measurement and position error often exhibit characteristics of heavy-tailed distributions, making the Gaussian assumption that do not hold strictly. In addition to considering the multipath effects, jamming and spoofing, etc., it is even more difficult for the actual error to follow the assumption of the Gaussian distribution, and at this time, if the Gaussian distribution is still used for modeling errors, an excessively large variance is required to ensure that the estimation of the error is conservative enough, thus seriously reducing the system availability [134].

Considering the current challenges and existing results, future opportunities for RAIM development lie in the following areas: the development and application of adaptive non-Gaussian error probability distributions; the application of more flexible and tight error bounding techniques; and the improvement of the ML-RAIM methods' generalization ability.

## 4.1 Adaptive non-Gaussian error probability distributions

Firstly, there have been studies using student's t-distribution [68] and GMM [84, 135] for modeling measurement or process errors and for integrity monitoring, with experimental results showing superior performance compared to traditional Gaussian model-based approaches. In addition, several other models have been employed to discuss error modeling, including the Rayleigh distribution and the generalized Pareto distribution (GPD) [136], the Dirichlet process mixture (DPM) model [137, 138], and the generalized extreme value (GEV) distribution [133]. Among these, the GPD and GEV distribution are based on extreme value theory and are specifically designed to analyze rare but potentially severe extreme events, focusing on the tail distribution properties of random variables. This aligns well with the needs of integrity studies and has been used for integrity risk assessment and validation [139]. The use of these non-Gaussian error models in conjunction with non-Gaussian noise estimators, such as PF, is expected to effectively improve integrity monitoring performance.

Secondly, almost all existing RAIM systems ignore the temporal correlation of measurement noise. However, colored noise is unavoidable and cannot be overlooked due to hardware noise, multipath effects, and unmodeled errors [140]. Gao et al. [141, 142] exploited the temporal correlation of colored noise by modeling it as a first-order Gaussian-Markov process. The proposed colored Kalman filter outperforms the traditional KF-RAIM in integrity monitoring. Therefore, studying and utilizing the temporal correlation of errors for error modeling will be an important opportunity for the future development of RAIM.

Finally, the error model will change with time, electromagnetic environment, and receiver type, making it a challenge to adaptively select the appropriate error model. This challenge can be improved or even solved by using artificial intelligence (AI) methods to automatically recognize receiver electromagnetic environment [143] (e.g., suburban, urban, and urban canyon) and then automatically and intelligently select the appropriate types and parameters of error models.

## 4.2 More flexible and tight error bounding

In terms of error bounding module, most RAIM algorithms are usually given in the scalar form of HPL and VPL. It is assumed that the maximum PE in the horizontal plane and vertical line does not exceed the HPL and VPL in each direction, respectively, with the properties of isotropy and symmetry about the origin. However, in complex applications, users often have different AL requirements in different directions, e.g., autonomous driving usually has different AL requirements in the longitudinal and lateral directions [144], and the traditional HPL discriminative method instead constrains the system availability. In view of the above limitations of the traditional scalar form of PL, opening up and applying more flexible error bounding techniques such as ellipsoid or ellipsoid models constructed based on matrix quadratic [145], zonotope sets [93], and extended point confidence region [92, 97] can help to improve navigation system availability.

On the other hand, existing error bounding techniques have the problem of being too conservative, constructing error bounds that are much larger than the actual PEs, leading to a significant increase in the number of events that unnecessarily declare the system unavailable, which seriously reduces the availability. In this regard, the nominal information metric proposed by [125] based on the quantity of information theory, and the average bound gap (ABG) metric proposed by [128] can better assess this issue. The former nominal information metric quantifies the reference value of the information provided by the error bounds, and its larger value implies the stronger ability of the error bounds to envelope the actual PE. The latter ABG is defined as:

$$\mathrm{ABG} = \frac{1}{N_{ALL}}\sum_{k}\left(PL_k - PE_k\right) \text{When } PL_k > PE_k \tag{17}$$

in Equation 17, where $N_{ALL}$ is the total number of epochs, and $PL_k$ and $PE_k$ are the PL and actual PE for the $k$-th epoch. Minimizing the ABG of the RAIM algorithm while ensuring that it does not increase the $P_{\mathrm{MI}}$ can further improve the availability of the navigation system. By developing a more appropriate error probability distribution model, applying a more flexible error bounding form, and integrating advanced AI algorithms, a tighter error bounding technique can be developed with the goal of optimizing nominal information and ABG, under the premise of guaranteeing that the core integrity related indexes of $P_{\mathrm{MI}}$ and $P_{\mathrm{HMI}}$ meet the standards. This will be another development opportunity for RAIM algorithm in the future.

## 4.3 Improvement of ML-RAIM generalization ability

The current ML-RAIM research generally overly relies on training data from specific regions or scenarios, and performs poorly in the face of changes in the region as well as brand new measurement anomalies, and the generalization ability is still insufficient. For this problem, comprehensive and reliable datasets should be constructed first. Current datasets for integrity monitoring often rely on simulated faults and lack realistic anomalies such as satellite failures, ionospheric and tropospheric fluctuations, spoofing and jamming. Therefore, efforts should be made to collect data under various application scenarios (e.g., civil aviation, automobiles, personal cell phones, etc.) and to incorporate various types of anomalous conditions. And the dataset should be expanded and enhanced by combining it with AI methods, such as GANs. In addition, the dataset features should be rich enough to cover pre-correlation domain features (e.g., radio frequency fingerprint), spatial domain features (e.g., angle of arrival), and correlation domain features (e.g., carrier to noise density) prior to the navigation solving phase, in addition to the widely used measurement domain features. The constructed dataset is also important for error probability distribution modeling and validation, RAIM algorithm testing and validation, in addition to effectively improving the generalization ability of ML-RAIM.

On the other hand, by introducing advanced training strategies such as incremental learning [117], continuous learning [118], and transfer learning [143], ML-RAIM is able to quickly adapt to data in brand new regions and scenarios, and improve the model generalization ability. Meanwhile, automatic identification of receiver electromagnetic environment based on AI technology [143, 146], so as to target the selection of appropriate trained models, may be a further development opportunity for ML-RAIM algorithm in the future.

## 5 Conclusion

Integrity monitoring is crucial to safeguard the lives and properties of GNSS users, and RAIM has always attracted significant attention due to its advantages of comprehensive monitoring range and fast alerting. With the wide application of GNSS, existing RAIM algorithms are facing a more complex electromagnetic environment and higher demands for integrity. To assist scholars in related fields in exploring and developing more advanced RAIM algorithms, this paper systematically describes the basic principles of RAIM algorithms and the current status of research in GNSS. The advantages and shortcomings of three types of methods are analyzed: RAIM based on error probability distribution model, RAIM based on set representation, and ML-RAIM. Additionally, the paper discusses the opportunities for future development in light of the latest research on RAIM and the challenges faced.

Finally, although the research on RAIM algorithms in the field of GNSS has made great progress, there are still deficiencies in integrity standard, hardware implementation and algorithm testing, which are outlooked in this paper:

1) At present, the GNSS integrity standard in the civil aviation field has been relatively mature, but for ground applications such as autonomous driving and low-altitude UAVs, the formulation of the corresponding GNSS integrity standard is still an urgent problem to be solved.
2) Almost all RAIM algorithms are developed based on software platforms and offline datasets, and how to implement these RAIM algorithms in hardware while taking into account computational efficiency and real-time performance still needs to be explored in depth.
3) Integrity monitoring strategies usually require performance testing and evaluation, but given the extremely low probability of integrity event, it remains a challenge to effectively, quickly and cost-effectively verify that the performance meets the standard.

## Author contributions

ZH: Writing – original draft, Writing – review and editing. WM: Writing – review and editing. RW: Writing – review and editing. PL: Writing – review and editing. ZL: Writing – review and editing. GO: Writing – review and editing.

## Funding

The author(s) declare that financial support was received for the research and/or publication of this article. (1) National Nature Science Foundation of China under Grant (U20A0193).

## Conflict of interest

The authors declare that the research was conducted in the absence of any commercial or financial relationships that could be construed as a potential conflict of interest.

## Generative AI statement

The author(s) declare that no Generative AI was used in the creation of this manuscript.

## Publisher's note

## References

1. Sabatini R, Moore T, Ramasamy S. Global navigation satellite systems performance analysis and augmentation strategies in aviation. *Prog aerospace Sci* (2017) 95:45–98. doi:10.1016/j.paerosci.2017.10.002

2. Giorgi G, Teunissen PJ, Gourlay TP. Instantaneous global navigation satellite system (GNSS)-based attitude determination for maritime applications. *IEEE J oceanic Eng* (2012) 37:348–62. doi:10.1109/JOE.2012.2191996

3. Mikhaylov D, Amatetti C, Polonelli T, Masina E, Campana R, Berszin K, et al. Toward the future generation of railway localization exploiting RTK and GNSS. *IEEE Trans Instrumentation Meas* (2023) 72:1–10. doi:10.1109/TIM.2023.3272048

4. Tahir M, Afzal SS, Chughtai MS, Ali K. On the accuracy of inter-vehicular range measurements using GNSS observables in a cooperative framework. *IEEE Trans Intell Transportation Syst* (2018) 20:682–91. doi:10.1109/TITS.2018.2833438

5. Xu X, Yang C, Liu R. Review and prospect of GNSS receiver autonomous integrity monitoring. *Acta Aeronautica et Astronautica Sinica* (2013) 34:451–63. doi:10.7527/S1000-6893.2013.0081

6. Zhu N, Marais J, Betaille D, Berbineau M. GNSS position integrity in urban environments: a review of literature. *Ieee T Intell Transp* (2018) 19:2762–78. doi:10.1109/TITS.2017.2766768

7. China Shipowners Mutual Assurance Association. LP 06/2024 GPS boat positions not to be overly trusted or gently doubted (2024). Available online at: https://www.chinapandi.com/index.php/cn/loss-prevention-menu-cn/loss-prevention-content-cn/5897-lp-06-2024-gps (Accessed April 25, 2025).

8. OPS GROUP. GPS spoofing: final report published by WorkGroup (2024). Available online at: https://ops.group/blog/gps-spoofing-final-report/(Accessed April 25, 2025).

9. Jing H, Gao Y, Shahbeigi S, Dianati M. Integrity monitoring of GNSS/INS based positioning systems for autonomous vehicles: state-of-the-art and open challenges. *IEEE Trans Intell Transportation Syst* (2022) 23:14166–87. doi:10.1109/TITS.2022.3149373

10. Fan Z, Zhao L. Autonomous integrity of multi-source information resilient fusion navigation system: state-of-the-art and open challenges. *IEEE Trans Instrumentation Meas* (2024) 73:1–17. doi:10.1109/TIM.2024.3427865

11. Costa de Oliveira FA, Torres FS, García-Ortiz A. Recent advances in sensor integrity monitoring methods—a review. *IEEE Sensors J* (2022) 22:10256–79. doi:10.1109/JSEN.2022.3169659

12. The Stanford The Stanford – ESA integrity Diagram: focusing on SBAS integrity - navipedia. (2006). Available online at: https://gssc.esa.int/navipedia/index.php/The_Stanford_%E2%80%93_ESA_Integrity_Diagram:_Focusing_on_SBAS_Integrity#The_Stanford-ESA_Modified_Integrity_Diagram[Accessed January 21, 2025].

13. Zabalegui P, De Miguel G, Perez A, Mendizabal J, Goya J, Adin I. A review of the evolution of the integrity methods applied in GNSS. *Ieee Access* (2020) 8:45813–24. doi:10.1109/ACCESS.2020.2977455

14. Zhu N, Marais J, Bétaille D, Berbineau M. Evaluation and comparison of GNSS navigation algorithms including FDE for urban transport applications. In: *Proceedings of the 2017 international technical meeting of the institute of navigation*. California: Monterey (2017). p. 51–69. doi:10.33012/2017.14962

15. Ni J, Zhu Y, Guo W. An improved RAIM scheme for processing multiple outliers in GNSS. In: *21st international conference on advanced information networking and applications workshops*. ON, Canada: Niagara Falls (2007). p. 840–5. doi:10.1109/AINAW.2007.86

16. Jiang Y. RAIM fault detection and exclusion with spatial correlation for integrity monitoring. *Remote Sensing* (2022) 15:176. doi:10.3390/rs15010176

17. Da R, Lin C-F. A new failure detection approach and its application GPS to autonomous integrity monitoring. *IEEE Trans Aerospace & Electron Syst* (1995) 31:499–506. doi:10.1109/7.366336

18. Blanch J, Ene A, Walter T, Enge P. An optimized multiple hypothesis RAIM algorithm for vertical guidance. In: *Proceedings of the 20th international technical meeting of the satellite division of the institute of navigation* (2007). p. 2924–33.

19. Siegert G, Banyś P, Martínez CS, Heymann F. EKF based trajectory tracking and integrity monitoring of AIS data. In: *2016 IEEE/ION position, location and navigation symposium (PLANS)*. Savannah, GA, USA (2016). p. 887–97. doi:10.1109/PLANS.2016.7479784

20. Wang E, Jia C, Tong G, Qu P, Lan X, Pang T. Fault detection and isolation in GPS receiver autonomous integrity monitoring based on chaos particle swarm optimization-particle filter algorithm. *Adv Space Res* (2018) 61:1260–72. doi:10.1016/j.asr.2017.12.016

21. Lee YC. Analysis of range and position comparison methods as a means to provide GPS integrity in the user receiver. In: *Proceedings of the 42nd annual meeting of the institute of navigation*. Washington, USA: Seattle (1986). p. 1–4.

22. Parkinson BW, Axelrad P. Autonomous GPS integrity monitoring using the pseudorange residual. *Navigation* (1988) 35:255–74. doi:10.1002/j.2161-4296.1988.tb00955.x

23. Sturza MA. Navigation system integrity monitoring using redundant measurements. *Navigation* (1988) 35:483–501. doi:10.1002/j.2161-4296.1988.tb00975.x

24. Brown RG. A baseline GPS RAIM scheme and a note on the equivalence of three RAIM algorithms. *Navigation* (1992) 39:301–16. doi:10.1002/j.2161-4296.1992.tb02278.x

25. Mi J, Li Y. Research on RAIM algorithm. In: *Bulletin of surveying and mapping* (2001). p. 7–9.

26. Brown RG, Chin GY, Kraemer JH. Update on GPS integrity requirements of the RTCA MOPS. In: *Proceedings of the 4th international technical meeting of the satellite division of the institute of navigation*. Albuquerque, NM (1991). p. 761–72.

27. Zhan X, Su X. *Integrity monitoring and assisted performance enhancement technology*. Beijing: Science Press (2016). p. 145.

28. Sang J, Kubik K. A probabilistic approach to derivation of geometrical criteria for evaluating GPS RAIM detection availability. In: *Proceedings of the 1997 national technical meeting of the institute of navigation*. Santa Monica, CA (1997). p. 511–7.

29. Santa J, Ubeda B, Toledo RG, Skarmeta AF. Monitoring the position integrity in road transport localization based services. In: *IEEE vehicular technology conference*. Montreal, QC, Canada (2019). p. 1–5. doi:10.1109/VTCF.2006.575

30. Geas P. GNSS evolutionary architecture study. Phase I - Panel report. *Fed Aviation Adm* (2008). Available online at: https://libproxy.libyc.nudt.edu.cn/http/80/cn/com/sunwayinfo/bg/yitlink/report_detail?id=EC23CC4F-FD61-4937-9358-3C67B455B381 (Accessed January 22, 2025).

31. Geas P. GNSS evolutionary architecture study: phase II-Panel report. *Fed Aviation Adm* (2010). Available online at: https://www.faa.gov/sites/faa.gov/files/about/office_org/headquarters_offices/ato/GEASPhaseII_Final.pdf (Accessed January 22, 2025).

32. EU-U.S. Cooperation on satellite navigation working group C (2012). Available online at: https://www.gps.gov/policy/cooperation/europe/2013/working-group-c/ARAIM-report-1.0.pdf [Accessed January 22, 2025]

33. EU-U.S. Cooperation on satellite navigation working group C-ARAIM technical sub-group: milestone 2 report (2015). Available online at: https://www.gps.gov/policy/cooperation/europe/2015/working-group-c/ARAIM-milestone-2-report.pdf (Accessed January 22, 2025).

34. EU-U.S. Cooperation on satellite navigation working group C-ARAIM technical subgroup: milestone 3 report (2016). Available online at: https://www.gps.gov/policy/cooperation/europe/2016/working-group-c/ARAIM-milestone-3-report.pdf (Accessed January 22, 2025).

35. Pervan BS, Pullen SP, Christie JR. A multiple hypothesis approach to satellite navigation integrity. *Navigation* (1998) 45:61–71. doi:10.1002/j.2161-4296.1998.tb02372.x

36. Blanch J, Walter T, Enge P, Wallner S, Fernandez FA, Dellago R, et al. A proposal for multi-constellation advanced RAIM for vertical guidance. In: *Proceedings of the 24th international technical meeting of the satellite division of the institute of navigation*. Portland, OR (2011). p. 2665–80.

37. Blanch J, Walter T, Enge P, Lee Y, Pervan B, Rippl M, et al. Advanced RAIM user algorithm description: integrity support message processing, fault detection, exclusion, and protection level calculation. In: *Proceedings of the 25th international technical meeting of the satellite division of the institute of navigation*. Nashville, TN (2012). p. 2828–49.

38. Walter T, Blanch J, Enge P. Evaluation of signal in space error bounds to support aviation integrity. *Navigation* (2010) 57:101–13. doi:10.1002/j.2161-4296.2010.tb01770.x

39. Walter T, Enge P, Blanch J, Pervan B. Worldwide vertical guidance of aircraft based on modernized GPS and new integrity augmentations. *Proc IEEE* (2008) 96:1918–35. doi:10.1109/JPROC.2008.2006099

40. Jiang Y, Wang J. A-RAIM and R-RAIM performance using the classic and MHSS methods. *J Navigation* (2014) 67:49–61. doi:10.1017/s0373463313000507

41. Ge Y, Wang Z, Zhu Y. Reduced ARAIM monitoring subset method based on satellites in different orbital planes. *GPS Solut* (2017) 21:1443–56. doi:10.1007/s10291-017-0658-x

42. Meng Q, Liu J, Zeng Q, Feng S, Xu R. Improved ARAIM fault modes determination scheme based on feedback structure with probability accumulation. *GPS Solut* (2019) 23:16. doi:10.1007/s10291-018-0809-8

43. Blanch J, Walter T. Fast protection levels for fault detection with an application to advanced RAIM. *IEEE Trans Aerosp Electron Syst* (2021) 57:55–65. doi:10.1109/TAES.2020.3011997

44. Wang S, Zhai Y, Chi C, Zhan X, Jiang Y. Implementation and analysis of fault grouping for multi-constellation advanced RAIM. *Adv Space Res* (2023) 71:4765–86. doi:10.1016/j.asr.2023.01.020

45. Blanch J, Walter T, Enge P. RAIM with optimal integrity and continuity allocations under multiple failures. *IEEE Trans Aerosp Electron Syst* (2010) 46:1235–47. doi:10.1109/TAES.2010.5545186

46. Wang E, Sun X, Qu P, Zeng H, Xu S, Pang T. ARAIM availability optimization method based on dynamic particle swarm optimization algorithm. *Acta Geodætica et Cartographica Sinica* (2024) 53:137–45. doi:10.11947/j.AGCS.2024.20230101

47. Zhao H, Wu Y, Liu M. Performance analysis of GNSS ARAIM protection level calculation methods. *J Navigation Positioning* (2023) 11:133–42. doi:10.16547/j.cnki.10-1096.20230517

48. Zhao L, Zhang J, Li L, Yang F, Liu X. Position-domain non-Gaussian error overbounding for ARAIM. *Remote Sensing* (2020) 12:1992. doi:10.3390/rs12121992

49. Yang L, Sun N, Rizos C, Jiang Y. ARAIM stochastic model refinements for GNSS positioning applications in support of critical vehicle applications. *Sensors* (2022) 22:9797. doi:10.3390/s22249797

50. Yang L, Zhu J, Sun N. Stochastic model refinement of GNSS advanced receiver autonomous integrity monitoring. *Acta Geodætica et Cartographica Sinica* (2024) 53:286–95. doi:10.11947/j.AGCS.2024.20210665

51. Zhang W, Wang J. Integrity monitoring scheme for single-epoch GNSS PPP-RTK positioning. *Satell Navig* (2023) 4:10. doi:10.1186/s43020-023-00099-1

52. Diesel J, Dunn G. GPS/IRS AIME: certification for sole means and solution to RF interference. In: *Proceedings of the 9th International Technical Meeting of the Satellite Division of The Institute of Navigation*. Kansas City, MO (1996). p. 1599–606.

53. Diesel J, King J. Integration of navigation systems for fault detection, exclusion, and integrity determination-Without WAAS. In: *Proceedings of the 1995 national technical meeting of the institute of navigation*. CA: Anaheim (1995). p. 683–92.

54. Hewitson S, Wang J. GNSS receiver autonomous integrity monitoring with a dynamic model. *J Navigation* (2007) 60:247–63. doi:10.1017/S0373463307004134

55. Hewitson S, Wang J. Extended receiver autonomous integrity monitoring (eRAIM) for GNSS/INS integration. *J Surv Eng* (2010) 136:13–22. doi:10.1061/(ASCE)0733-9453(2010)136:1(13)

56. Bhatti UI, Ochieng WY, Feng S. Integrity of an integrated GPS/INS system in the presence of slowly growing errors. Part II: analysis. *GPS Solut* (2007) 11:183–92. doi:10.1007/s10291-006-0049-1

57. Feng S, Ochieng W, Moore T, Hill C, Hide C. Carrier phase-based integrity monitoring for high-accuracy positioning. *GPS Solut* (2009) 13:13–22. doi:10.1007/s10291-008-0093-0

58. Schuster W, Bai J, Feng S, Ochieng W. Integrity monitoring algorithms for airport surface movement. *GPS Solut* (2012) 16:65–75. doi:10.1007/s10291-011-0209-9

59. Liu H, Meng X, Chen Z, Stephenson S, Peltola P. A closed-loop EKF and multi-failure diagnosis approach for cooperative GNSS positioning. *GPS Solut* (2016) 20:795–805. doi:10.1007/s10291-015-0489-6

60. Bhatti UI, Ochieng WY. Detecting multiple failures in GPS/INS integrated system: a novel architecture for integrity monitoring. *J Glob Positioning Syst* (2009) 8:26–42. doi:10.5081/jgps.8.1.26

61. Zhang W, Wang J, El-Mowafy A, Rizos C. Integrity monitoring scheme for undifferenced and uncombined multi-frequency multi-constellation PPP-RTK. *GPS Solut* (2023) 27:68. doi:10.1007/s10291-022-01391-4

62. Meng Q, Hsu L-T. Integrity monitoring for all-source navigation enhanced by Kalman filter-based solution separation. *IEEE Sensors J* (2020) 21:15469–84. doi:10.1109/JSEN.2020.3026081

63. Gao Y, Jiang Y, Gao Y, Huang G, Yue Z. Solution separation-based integrity monitoring for RTK positioning with faulty ambiguity detection and protection level. *GPS Solut* (2023) 27:140. doi:10.1007/s10291-023-01472-y

64. Bhatti UI, Ochieng WY, Feng S. Integrity of an integrated GPS/INS system in the presence of slowly growing errors. Part I: a critical review. *GPS Solut* (2007) 11:173–81. doi:10.1007/s10291-006-0048-2

65. Tanil C, Khanafseh S, Joerger M, Kujur B, Kruger B, de Groot L, et al. Optimal INS/GNSS coupling for autonomous car positioning integrity. In: *Proceedings of the 32nd international technical meeting of the satellite division of the institute of navigation* (2019). p. 3123–40.

66. Teunissen PJ, Verhagen S. The GNSS ambiguity ratio-test revisited: a better way of using it. *Surv Rev* (2009) 41:138–51. doi:10.1179/003962609X390058

67. Li L, Li Z, Yuan H, Wang L, Hou Y. Integrity monitoring-based ratio test for GNSS integer ambiguity validation. *GPS Solut* (2016) 20:573–85. doi:10.1007/s10291-015-0468-y

68. Shao J, Yu F, Zhang Y, Sun Q, Wang Y, Chen W. Robust sequential integrity monitoring for positioning safety in GNSS/INS integration. *IEEE Sensors J* (2024) 24:15145–55. doi:10.1109/JSEN.2024.3379578

69. Madrid PFN, Saenz MA, Varo CM, Schortmann JC. Computing meaningful integrity bounds of a low-cost Kalman-filtered navigation solution in urban environments. In: *Proceedings of the 28th international technical meeting of the satellite division of the institute of navigation*. Florida: Tampa (2015). p. 2914–25.

70. Azaola-Saenz M, Cosmen-Schort-mann J. Autonomous integrity – an error isotropy based approach for multiple fault conditions. In: *Inside GNSS* (2009). p. 28–36.

71. Gottschalg G, Gottschalg G, Leinen S, Leinen S. Comparison and evaluation of integrity algorithms for vehicle dynamic state estimation in different scenarios for an application in automated driving. *Sensors* (2021) 21:1458. doi:10.3390/s21041458

72. Wang C-W, Jan S-S. Kalman filter-based integrity monitoring for MADOCA-PPP in terrestrial applications. In: *2023 IEEE/ION position, location and navigation symposium (PLANS)*. Monterey, CA, USA (2023). p. 436–45.

73. Huang Y, Zhang Y, Zhao Y, Chambers JA. A novel robust Gaussian–student's t mixture distribution based kalman filter. *IEEE Trans Signal Process* (2019) 67:3606–20. doi:10.1109/TSP.2019.2916755

74. Li P, Kadirkamanathan V. Particle filtering based likelihood ratio approach to fault diagnosis in nonlinear stochastic systems. *IEEE Trans Syst Man, Cybernetics, C (Applications Reviews)* (2001) 31:337–43. doi:10.1109/5326.971661

75. Yang C. *Monitoring theory in global nav satellite system*. Nanjing: Nanjing University of Aeronautics and Astronautics (2013).

76. Ahn J-S, Rosihan R, Won D-H, Lee Y-J, Nam G-W, Heo M-B, et al. GPS integrity monitoring method using auxiliary nonlinear filters with log likelihood ratio test approach. *J Electr Eng Technology* (2011) 6:563–72. doi:10.5370/JEET.2011.6.4.563

77. He P, Liu G, Tan C, Lu Y. Nonlinear fault detection threshold optimization method for RAIM algorithm using a heuristic approach. *GPS Solut* (2016) 20:863–75. doi:10.1007/s10291-015-0494-9

78. Han S, Luo D, Meng W, Li C. Antispoofing RAIM for dual-recursion particle filter of GNSS calculation. *Ieee T Aero Elec Sys* (2016) 52:836–51. doi:10.1109/TAES.2015.140297

79. Hafez OA, Joerger M, Spenko M. How safe is particle filtering-based localization for mobile robots? An integrity monitoring approach. *IEEE Trans Robotics* (2024) 40:3372–87. doi:10.1109/TRO.2024.3420798

80. Pesonen H. A framework for Bayesian receiver autonomous integrity monitoring in urban navigation. *Navigation* (2011) 58:229–40. doi:10.1002/j.2161-4296.2011.tb02583.x

81. Gupta S, Gao GX. Particle RAIM for integrity monitoring. In: *Proceedings of the 32nd international technical meeting of the satellite division of the institute of navigation*. Miami, Florida (2019). p. 811–26.

82. Gabela J, Majic I, Kealy A, Hedley M, Li S. Robust vehicle localization and integrity monitoring based on spatial feature constrained PF. In: *2020 IEEE/ION position, location and navigation symposium (PLANS)*. Portland, OR, USA (2020). p. 661–9. doi:10.1109/PLANS46316.2020.9110189

83. Gabela J, Kealy A, Hedley M, Moran B. Case study of bayesian RAIM algorithm integrated with spatial feature constraint and fault detection and exclusion algorithms for multi-sensor positioning. *Navigation* (2021) 68:333–51. doi:10.1002/navi.433

84. Mohanty A, Gupta S, Gao GX. A particle-filtering framework for integrity risk of GNSS-camera sensor fusion. *Navigation* (2021). 68(4). p. 709–26. doi:10.1002/navi.455

85. Wang E, Zhang S, Hu Q. Research on GPS receiver autonomous integrity monitoring algorithm based on MCMC particle filtering. *Chin J Scientific Instrument* (2009) 30:2208–12. doi:10.19650/j.cnki.cjsi.2009.10.035

86. Wang E, Zhang S, Cai M, Pang T. GPS receiver autonomous integrity monitoring algorithm using the genetic particle filter. *J Xidian Univ* (2015) 42:136–41. doi:10.3969/j.issn.1001-2400.2015.01.022

87. Wang E, Pang T, Cai M, Zhang Z. Application of neural network aided particle filter in GPS receiver autonomous integrity monitoring. In: *China satellite navigation conference (CSNC) 2014 proceedings: volume II*, 304. Berlin, Heidelberg (2014). p. 147–57. doi:10.1007/978-3-642-54743-0_13

88. Liu W, Li Z, Wang F. A new RAIM algorithm for detecting and correcting weak pseudo-range bias under gradual change. *J Astronautics* (2010) 31:1024–9. doi:10.3873/j.issn.1000-1328.2010.04.014

89. Sun R, Xu C, Huang G, Lan X, Wu M. Multiple epochs solution separation RAIM algorithm considering alarm time. *Syst Eng Electronics* (2023) 45:1469–75. doi:10.12305/j.issn.1001-506X.2023.05.23

90. Dbouk H, Schön S. Reliable bounding zones and inconsistency measures for GPS positioning using geometrical constraints. *Acta Cybern* (2020) 24:573–91. doi:10.14232/actacyb.24.3.2020.16

91. Su J, Schön S, Joerger M. Towards a set-based detector for GNSS integrity monitoring. In: *2023 IEEE/ION position, location and navigation symposium (PLANS)*. Monterey, CA, USA (2023). p. 421–9. doi:10.1109/PLANS53410.2023.10139987

92. Su J, Schön S. Advances in deterministic approaches for bounding uncertainty and integrity monitoring of autonomous navigation. In: *Proceedings of the 35th international technical meeting of the satellite division of the institute of navigation*. Denver, Colorado (2022). p. 1442–54. doi:10.33012/2022.18418

93. Liu S, Wang K, Abel D. Robust state and protection-level estimation within tightly coupled GNSS/INS navigation system. *GPS Solut* (2023) 27:111. doi:10.1007/s10291-023-01447-z

94. Combastel C. A state bounding observer based on zonotopes. In: *2003 European control conference (ECC)* (2003). p. 2589–94. doi:10.23919/ECC.2003.7085991

95. Ashraf FF. An application of a set-valued state estimator based on constrained zonotopes in GNSS-INS integration. In: *2023 9th international conference on control, automation and robotics (ICCAR)*. Beijing, China (2023). p. 49–54. doi:10.1109/ICCAR57134.2023.10151757

96. Shetty A, Gao GX. Predicting state uncertainty bounds using non-linear stochastic reachability analysis for urban GNSS-based UAS navigation. *IEEE Trans Intell Transportation Syst* (2020) 22:5952–61. doi:10.1109/TITS.2020.3040517

97. Su J, Schön S. Deterministic approaches for bounding GNSS uncertainty: a comparative analysis. In: *2022 10th workshop on satellite navigation technology (NAVITEC)* (2022). p. 1–8.

98. Su J, Schön S. Improved observation interval bounding for multi-GNSS integrity monitoring in urban navigation. In: *Proceedings of the 34th international technical meeting of the satellite division of the institute of navigation* (2021). p. 4141–56. doi:10.33012/2021.18078

99. Sun R, Fu L, Cheng Q, Chiang K-W, Chen W. Resilient pseudorange error prediction and correction for GNSS positioning in urban areas. *IEEE Internet Things J* (2023) 10:9979–88. doi:10.1109/JIOT.2023.3235483

100. Zhang T, Zhou L, Feng X, Shi J, Zhang Q, Niu X. INS aided GNSS pseudo-range error prediction using machine learning for urban vehicle navigation. *IEEE Sensors J* (2024) 24:9135–47. doi:10.1109/JSEN.2024.3355705

101. Yin N, He D, Xiang Y, Yu W, Zhu F, Xiao Z. Features effectiveness verification using machine-learning-based GNSS NLOS signal detection in urban canyon environment. In: *Proceedings of the 36th international technical meeting of the satellite division of the institute of navigation (ION GNSS+ 2023)*. Colorado: Denver (2023). p. 3035–48. doi:10.33012/2023.19363

102. Alghananim MS, Feng C, Feng Y, Ochieng WY. Machine learning-based fault detection and exclusion for global navigation satellite system pseudorange in the measurement domain. *Sensors* (2025) 25:817. doi:10.3390/s25030817

103. Li L, Elhajj M, Feng Y, Ochieng WY. Machine learning based GNSS signal classification and weighting scheme design in the built environment: a comparative experiment. *Satell Navig* (2023) 4:12. doi:10.1186/s43020-023-00101-w

104. Li L, Xu Z, Jia Z, Lai L, Shen Y. An efficient GNSS NLOS signal identification and processing method using random forest and factor analysis with visual labels. *GPS Solut* (2024) 28:77. doi:10.1007/s10291-024-01624-8

105. Zheng F, Li Q, Wang J, Gong X, Jia H, Zhang C, et al. GNSS NLOS detection method based on stacking ensemble learning and applications in smartphones. *GPS Solut* (2024) 28:129. doi:10.1007/s10291-024-01665-z

106. Gogliettino G, Renna M, Pisoni F, Di Grazia D, Pau D. A machine learning approach to GNSS functional safety. In: *Proceedings of the 32nd international technical meeting of the satellite division of the institute of navigation*. Miami, Florida (2019). p. 1738–52. doi:10.33012/2019.17001

107. Li X, Xu Q, Li X, Xin H, Yuan Y, Shen Z, et al. Improving PPP-RTK-based vehicle navigation in urban environments via multilayer perceptron-based NLOS signal detection. *GPS Solut* (2024) 28:29. doi:10.1007/s10291-023-01567-6

108. Zheng X, Xu C, Wang Y, Zou H, Lv X, Zhao S, et al. A dynamic-data-driven method for improving the performance of receiver autonomous integrity monitoring. *IEEE access* (2021) 9:55833–43. doi:10.1109/ACCESS.2021.3070658

109. Huang G, Xu C, Zheng X. Nonparametric estimation-based five-layer neural network RAIM with improved availability. *Meas Sci Technology* (2022) 34:035009. doi:10.1088/1361-6501/aca555

110. Wu M, Xu C, Huang G, Sun R, Lu Z. Probabilistic neural network multi epoch residual RAIM algorithm. *Syst Eng Electronics* (2023) 45:3967–74. doi:10.12305/j.issn.1001-506X.2023.12.27

111. Zhu N, He R, Wang Z. CarNet: a generative convolutional neural network-based line-of-sight/non-line-of-sight classifier for global navigation satellite systems by transforming multivariate time-series data into images. *Eng Appl Artif Intelligence* (2025) 145:110160. doi:10.1016/j.engappai.2025.110160

112. Sun Y. RAIM-NET: a deep neural network for receiver autonomous integrity monitoring. *Remote Sensing* (2020) 12:1503. doi:10.3390/rs12091503

113. Zhou Z, Stefanakis D, Liu B, Yang H. Hopular-based GNSS signal reception classification method for LOS/NLOS detection in urban environments. In: *Proceedings of the 36th international technical meeting of the satellite division of the institute of navigation (ION GNSS+ 2023)*. Colorado: Denver (2023). p. 2990–3004. doi:10.33012/2023.19358

114. Zeng K, Li Z, Zhao H, Xie K, Xie S, Niyato D, et al. A spatiotemporal information-driven cross-attention model with sparse representation for GNSS NLOS signal classification. *IEEE Internet Things J* (2024) 11:31892–908. doi:10.1109/JIOT.2024.3423016

115. Zeng K, Li Z, Xie S, Wang Q, Chen W, Zheng Z. A few-shot learning-based semi-supervised method to enhance NLOS recognition accuracy across multiple locations by cross-spatiotemporal information. *IEEE Trans Instrum Meas* (2024) 73:1–14. doi:10.1109/TIM.2024.3440416

116. Zeng K, Wang Q, Tang J, Li Z, Xie K, Xie S. Mitigating NLOS interference in GNSS single-point positioning based on dual self-attention networks. *IEEE Internet Things J* (2025) 12:4318–30. doi:10.1109/JIOT.2024.3485099

117. Sun Y, Li S, Deng Z. Incremental learning for LOS/NLOS classification of global navigation satellite system. In: *Proceedings of the 36th international technical meeting of the satellite division of the institute of navigation (ION GNSS+ 2023)*. Colorado: Denver (2023). p. 231–44. doi:10.33012/2023.19314

118. Sun Y, Li S, Fu L, Yin L, Deng Z. NICL: non-line-of-sight identification in global navigation satellite systems with continual learning. *IEEE Trans Veh Technol* (2025) 74:2480–90. doi:10.1109/TVT.2024.3482452

119. Xia Y, Pan S, Meng X, Gao W, Ye F, Zhao Q, et al. Anomaly detection for urban vehicle GNSS observation with a hybrid machine learning system. *Remote Sensing* (2020) 12:971. doi:10.3390/rs12060971

120. Zhu B, Yang C, Liu Y. Analysis and comparison of three unsupervised learning clustering methods for GNSS multipath signals. *Acta Geodaetica et Cartographica Sinica* (2021) 50(12):1762–71. doi:10.11947/j.AGCS.20210233

121. Hu Z, Xu S, Guo J, Li Z. Non-line-of-sight GNSS signal classification for urban navigation based on machine learning: comparison and validation. *Adv Space Res* (2025) 75:7817–34. doi:10.1016/j.asr.2025.03.018

122. Wang Y, Masoud N, Khojandi A. Real-time sensor anomaly detection and recovery in connected automated vehicle sensors. *IEEE Trans Intell transportation Syst* (2020) 22:1411–21. doi:10.1109/TITS.2020.2970295

123. Kim D, Cho J. Improvement of anomalous behavior detection of GNSS signal based on TDNN for augmentation systems. *Sensors* (2018) 18:3800. doi:10.3390/s18113800

124. Shen Z, Zhao X, Pang C, Zhang L. GAN-FDSR: GAN-based fault detection and system reconfiguration method. *Sensors* (2022) 22:5313. doi:10.3390/s22145313

125. Mendonca M, Jokinen A, Yang R, Hau G, Tseng Y-F. Improving integrity and information output on a low-cost GNSS platform using machine-learning algorithms. In: *Proceedings of the 35th international technical meeting of the satellite division of the institute of navigation*. Denver, Colorado (2022). p. 2694–700. doi:10.33012/2022.18513

126. Kuratomi A, Lindgren T, Papapetrou P. Prediction of global navigation satellite system positioning errors with guarantees. In: *Machine learning and knowledge discovery in databases: applied data science track*. Cham, Switzerland (2021). p. 562–78. doi:10.1007/978-3-030-67667-4_34

127. Geragersian P, Petrunin I, Guo W, Grech R. A hybrid deep learning approach for robust multi-sensor GNSS/INS/VO fusion in urban canyons. In: *Proceedings of the*

*36th international technical meeting of the satellite division of the institute of navigation*. Denver, Colorado (2023). p. 2624–43. doi:10.33012/2023.19271

128. Isik OK, Petrunin I, Tsourdos A. Machine learning-based environment-aware GNSS integrity monitoring for urban air mobility. *DRONES* (2024) 8:690. doi:10.3390/drones8110690

129. Brkić M, Begušić D. Recent advances on jamming and spoofing detection in GNSS. *Sensors (Basel, Switzerland)* (2024) 24:4210. doi:10.3390/s24134210

130. Zhong W, Xiong H, Hua Y, Shah DH, Liao Z, Xu Y. TSFANet: temporal-spatial feature aggregation network for GNSS jamming recognition. *IEEE Trans Instrumentation Meas* (2024) 73:1–13. doi:10.1109/TIM.2024.3375975

131. Li J, Chen Z, Yuan X, Xie T, Xu Y, Zheng Z, et al. A real-time GNSS time spoofing detection framework based on feature processing. *GPS Solut* (2025) 29:45. doi:10.1007/s10291-024-01802-8

132. Li X, Lu Z, Yuan M, Liu W, Wang F, Yu Y, et al. Tradeoff of code estimation error rate and terminal gain in SCER attack. *IEEE Trans Instrum Meas* (2024) 73:1–12. doi:10.1109/TIM.2024.3406807

133. Panagiotakopoulos D, Majumdar A, Ochieng WY. Extreme value theory-based integrity monitoring of global navigation satellite systems. *GPS Solut* (2014) 18:133–45. doi:10.1007/s10291-013-0317-9

134. Kbayer N, Sahmoudi M. 3D-mapping-aided gnss localization for integrity monitoring in urban environments. In: *2017 14th international multi-conference on systems, signals & devices (SSD)*. Marrakech, Morocco (2017). p. 591–6. doi:10.1109/SSD.2017.8167014

135. Fang X, Song D, Shi C, Fan L, Hu Z. Multipath error modeling methodology for GNSS integrity monitoring using a global optimization strategy. *Remote Sensing* (2022) 14:2130. doi:10.3390/rs14092130

136. Ahmad KAB, Sahmoudi M, Macabiau C. Characterization of GNSS receiver position errors for user integrity monitoring in urban environments. In: *ENC-GNSS 2014, European navigation conference. Rotterdam,Pays-Bas* (2014).

137. Rabaoui A, Viandier N, Marais J, Duflos E. On the use of Dirichlet process mixtures for the modelling of pseudorange errors in multi-constellation based localisation. In: *2009 9th international conference on intelligent transport systems telecommunications,(ITST)*. Lille, France (2009). p. 465–70.

138. Rabaoui A, Viandier N, Marais J, Duflos E. Using Dirichlet Process Mixtures for the modelling of GNSS pseudorange errors in urban canyon. In: *Proceedings of the 22nd international technical meeting of the satellite division of the institute of navigation*. Savannah, GA (2009). p. 2391–9.

139. Li L, Li R, Wang L, Wang R, Li M, Li M. GNSS integrity risk evaluation in the position domain based on the generalized Pareto distribution. *Meas Sci Technol* (2023) 34:095010. doi:10.1088/1361-6501/acd137

140. Li B, Zhang Z, Shen Y, Yang L. A procedure for the significance testing of unmodeled errors in GNSS observations. *J Geod* (2018) 92:1171–86. doi:10.1007/s00190-018-1111-9

141. Gao Y, Gao Y, Liu B, Jiang Y. Enhanced fault detection and exclusion based on Kalman filter with colored measurement noise and application to RTK. *GPS Solut* (2021) 25:82. doi:10.1007/s10291-021-01119-w

142. Gao Y, Jiang Y, Gao Y, Huang G. A linear Kalman filter-based integrity monitoring considering colored measurement noise. *GPS Solut* (2021) 25:59–13. doi:10.1007/s10291-021-01086-2

143. Zhu F, Luo K, Tao X, Zhang X. Deep learning based vehicle-mounted environmental context awareness via GNSS signal. *IEEE Trans Intell Transport Syst* (2024) 25:9498–511. doi:10.1109/TITS.2024.3350874

144. Bijjahalli S, Sabatini R. A high-integrity and low-cost navigation system for autonomous vehicles. *IEEE Trans Intell Transportation Syst* (2019) 22:356–69. doi:10.1109/TITS.2019.2957876

145. Bruckner D, Van Graas F, Skidmore T. Statistical characterization of composite protection levels for GPS. *GPS Solut* (2011) 15:263–73. doi:10.1007/s10291-010-0188-2

146. Yaqoob S, Cafiso S, Morabito G, Pappalardo G. Deep transfer learning-based anomaly detection for cycling safety. *J Saf Res* (2023) 87:122–31. doi:10.1016/j.jsr.2023.09.010

frontiers | Frontiers in Physics

TYPE Review
PUBLISHED 09 October 2025
DOI 10.3389/fphy.2025.1569385

OPEN ACCESS

EDITED BY
Zhu Xiao,
Hunan University, China

REVIEWED BY
Yq Hei,
Xidian University, China
Chonghui Li,
Information Engineering University, China
Kun Wu,
PLA Army Academy of Artillery and Air Defense, China

*CORRESPONDENCE
Bin Fan,
✉ fb540623907@163.com

RECEIVED 31 January 2025
ACCEPTED 30 June 2025
PUBLISHED 09 October 2025

CITATION
Yao L, Fan B, Qin H, Xian D, Wang M, Gu B, Chen S, Wang C, Wang X, Shen J, Jiang D, Wei H, Yu H, Liu B and Shao S (2025) Overview of the system-level anti-jamming capability and developmental challenges of low-earth-orbit signal-of-opportunity. *Front. Phys.* 13:1569385.
doi: 10.3389/fphy.2025.1569385

# Overview of the system-level anti-jamming capability and developmental challenges of low-earth-orbit signal-of-opportunity

Lihao Yao[1,2], Bin Fan[3]*, Honglei Qin[1], Deyong Xian[2], Mengli Wang[2], Boyun Gu[4], Sumin Chen[1,5], Changhong Wang[1,2], Xuyu Wang[2], Jiemin Shen[2], Dongfang Jiang[2], Heng Wei[2], Haoyuan Yu[2], Bingjie Liu[2] and Shuai Shao[6]

[1]School of Electronics and Information Engineering, Beihang University, Beijing, China, [2]Beijing Satellite Navigation Center, Beijing, China, [3]Department of Information Engineering, Army Academy of Artillery and Air Defense, Hefei, China, [4]Beijing Institute of Technology, Beijing, China, [5]COMAC Shanghai Aircraft Design and Research Institute, Shanghai, China, [6]Shaanxi Datang Gas Safety Technology Co., LTD, Beijing, China

Signal-of-Opportunity (SOP) navigation based on Low-Earth-Orbit (LEO) satellite constellations has increasingly become a research hotspot. Due to the large number of LEO satellites, wide spectrum coverage, and strong signal power, LEO satellite Signal-of-Opportunity (LEO-SOP) inherently possess strong anti-jamming capabilities. However, there has been limited in-depth research on the overall system-level anti-jamming capability of LEO-SOP. This paper reviews the current state of research on LEO-SOP and anti-jamming technologies, introduces the principles of LEO-SOP Doppler-based positioning and receiver operation, and analyzes the system-level anti-jamming capability of LEO-SOP. Additionally, it explores the key challenges in the development of LEO-SOP anti-jamming technologies and discusses future research directions. This study aims to provide insights into the development prospects of LEO-SOP anti-jamming technologies, promote further research and development efforts, and establish a solid technical foundation for the secure application of LEO-SOP. Ultimately, ensuring the integrity and resilience of LEO-SOP systems against complex threats.

KEYWORDS

**signal of opportunity, low-Earth-orbit satellite, system-level anti-jamming capability, anti-jamming, GNSS, PNT**

## 1 Introduction

The acquisition of location information based on satellite navigation plays an extremely important role in today's technological development and social progress. Among these, positioning technology based on the Global Navigation Satellite System (GNSS) is the primary method for obtaining location information via satellite navigation. The current major GNSS systems include the United States' Global Positioning System (GPS), Russia's GLONASS, Europe's Galileo, and China's BeiDou Navigation Satellite System (BDS).

With the development of GNSS, it is becoming a crucial infrastructure for national informatization construction, providing Positioning, Navigation, and Timing (PNT) service information for a variety of applications [1–5]. It plays a significant role in daily life, scientific research, and military applications. However, as the use of GNSS deepens, its inherent shortcomings have gradually become apparent, including low signal power upon reaching the ground, single frequency points, high construction and maintenance costs, and significant risks such as susceptibility to malicious interference leading to service unavailability during peacetime or tense situations [6–8]. How to overcome and compensate for these GNSS shortcomings, especially in environments where GNSS services fail, and still independently provide reliable and high-precision PNT services has become a focus of future development [9, 10]. Currently, countries are actively building resilient PNT systems to ensure that military equipment can still achieve accurate positioning when GNSS performance is degraded or denied. In the PNT technology development roadmap released by the U.S. Department of Defense in 2020, it mentioned the use of Signal-of-Opportunity (SOP) for absolute positioning, thereby supplementing GPS positioning functions and enhancing GPS availability and robustness.

SOP positioning refers to a technology that utilizes all perceivable non-navigation and non-positioning application information such as sound, light, electricity, magnetism, and force for positioning. Due to the abundant presence of various radio signals in space, the current research primarily focuses on radio SOP. SOP typically includes terrestrial and space-based radio Signal-of-Opportunity. Terrestrial SOP has limited coverage and struggles to achieve global seamless coverage in areas such as deserts, oceans, and polar regions [11–13]. Space-based SOP mainly refers to signals transmitted by non-navigation/non-cooperative satellites. With the recent vigorous development and construction of Low-Earth-Orbit (LEO) satellites by various countries, space-based LEO satellite SOP (LEO-SOP) has gradually been applied in navigation and positioning as a primary space-based SOP [14]. Unlike GNSS, LEO satellites orbit at altitudes between 500 km and 2,000 km, resulting in higher signal power upon reaching the ground [15]. Additionally, the large number of LEO satellites means their signals cover a wide range of frequencies, with many available frequency points. Currently, the published satellite signal frequency bands can cover from 100 MHz to 40 GHz [16]. These characteristics ensure that LEO satellite signals have stronger anti-jamming capabilities compared to GNSS. Finally, using LEO-SOP for positioning does not require additional construction, resulting in lower costs. Therefore, positioning technology based on LEO-SOP leverages existing satellite resources and requires only minimal financial investment to meet positioning service needs, providing an effective backup to GNSS.

Currently, LEO constellations can be categorized into three types based on their construction maturity: ① Traditional LEO constellations that have been completed and networked, primarily consisting of narrowband communication satellite constellations. Examples include the United States' Iridium, Globalstar, Swarm SpaceBEE, France's Argos, and the jointly constructed Orbcomm satellites by the United States and Canada. These operate in frequency ranges from VHF to L-band and mainly provide narrowband communication services to the ground [17–19]. ② LEO constellations that have been planned and have undergone significant satellite launches, primarily broadband internet satellite systems, mainly using Ku-band and higher frequency signals. The main goal is to provide broadband internet access services to the ground through large-scale LEO constellations, achieving global seamless coverage through satellite networking. Currently under construction are the UK's OneWeb and the United States' Starlink constellations. OneWeb has completed the launch and networking of its first-generation internet constellation, with 618 satellites in orbit at an operational altitude of 1,200 km. As of March 2025, Starlink has successfully launched over 6,000 satellites, with 5,614 still operational in orbit, making it the largest LEO internet constellation currently in service. These satellites are primarily deployed to build a global LEO satellite internet network, providing coverage for fixed, mobile, maritime, and aeronautical users. By the end of 2024, the system had delivered satellite internet services to over 4 million users across nearly 100 countries. SpaceX is accelerating Starlink satellite deployment through its Starship program. On 6 March 2025, the eighth test flight of Starship was completed, successfully validating its payload deployment capability, including the release of four Starlink satellite simulators. The test also demonstrated upgraded atmospheric re-entry technology and propulsion systems, laying the groundwork for future large-scale satellite deployment [20]. ③ Constellations that have been planned but have only launched a small number of satellites, with functions and frequency bands similar to the aforementioned broadband internet constellations. These include Canada's Telesat and China's StarNet, Xingyun Project, Tianqi Satellites, and Galaxy Aerospace, among others. Additionally, some independent LEO satellite navigation and timing systems are being constructed to enhance the anti-jamming capabilities of traditional GNSS, including China's Weili Space and the United States' Pulsar. According to the UCS satellite database, LEO satellites account for nearly 90% of all operational satellites in orbit. In the coming years, the number of global LEO satellites in orbit is expected to exceed 22,000, providing a vast number of radiation sources for LEO satellite positioning, making it a key research subject for signal of opportunity positioning [21]. The current major LEO satellite constellations domestically are shown in Table 1.

This paper reviews the research on LEO-SOP and anti-jamming technologies and analyzes the system-level anti-jamming capability of LEO-SOP while exploring its future development challenges. The remainder of this paper is structured as follows: Section 2 reviews the current research status of LEO-SOP and anti-jamming technologies. Section 3 introduces the Doppler-based positioning principle of LEO-SOP and the receiver operation process. Section 4 analyzes the system-level anti-jamming capability of LEO-SOP. Section 5 discusses the challenges and prospects of LEO-SOP anti-jamming development. Finally, Section 6 summarizes the discussions above.

To facilitate the reader's understanding, Table 2 lists some important abbreviations involved in this paper, with specific explanations provided in Table 2.

## 2 Current research status of related technologies in domestic and international contexts

This section reviews and summarizes national-level plans for space-based SOP positioning, the development of LEO-SOP

**TABLE 1** Current status and future plans of LEO satellite development (as of January 2025).

| Constellation name | Country/Company | Planning/Current quantity | Downlink frequency/Bandwidth |
|---|---|---|---|
| Starlink | USA/SpaceX | 40,000+/7,516 | 10.7~12.7 GHz<br>37.5~42.5 GHz |
| OneWeb | Bharti Global | 6,372/648 | 10.7~12.7 GHz |
| Kuiper | USA/Amazon | 3,236/2 | 10.7~12.7 GHz |
| Telesat | Canada/Telesat | 298/6 | 17.8~20.2 GHz |
| Globalstar | USA/Loral& Qualcomm, etc. | 24/33 (Including Spare) | 2.4835~2.5 GHz |
| Iridium | USA/mortorola | 66/75 (Including Spare) | 1.626~1.6265 GHz |
| Orbcomm | USA/Orbcomm | 40/36 (Including Failure) | 0.137~0.138 GHz |
| GW | China | 12992/10 | — |
| Spacesail Constellation | China | 15000+/54 | Ku, Q/V |

**TABLE 2** Abbreviations table.

| Abbreviation | Meaning |
|---|---|
| GNSS | Global Navigation Satellite System |
| GPS | Global Positioning System |
| BDS | BeiDou Satellite Navigation Sytem |
| PNT | Positioning, Navigation and Timing |
| SOP | Signals of Opportunity |
| LEO | Low Earth Orbit |
| VHF | Very high frequency |
| INS | Inertial Navigation System |
| SGP4 | Simplified General Perturbations 4 |
| TLE | Two-Line Elements |
| CNR | Carrier to Noise Ratio |
| STL | Satellites Time and Location |
| EKF | Extended Kalman Filter |
| VLEO | Very Low Earth Orbit |
| GDOP | Geometric Dilution of Precision |

positioning technology, and the current state of anti-jamming research. This provides a theoretical foundation for the subsequent analysis of anti-jamming capabilities.

## 2.1 National PNT strategy

The current national plans that have been announced for positioning using SOP mainly include the United States' All Source Positioning and Navigation (ASPN) project, the United Kingdom's Navigation Signal of Opportunity (NavSOP) system, the European Space Agency's Navigation Innovation Support Program (NAVISP), and the Future Navigation (FutureNAV) plan.

①ASPN Project: In 2010, the Defense Advanced Research Projects Agency (DARPA) of the United States proposed a research plan to combine inertial navigation systems (INS) with non-navigation SOP from satellites, broadcasts, and other sources to achieve positioning. This project has achieved significant results in both military and civilian fields. In 2021, the United States released its Space Policy Directive-7 (SPD-7), also known as the U.S. National Space-Based Positioning, Navigation, and Timing (PNT) Policy. The policy focuses on improving GPS performance while reiterating concerns about over-reliance on PNT data systems. It emphasizes the need for multi-source PNT that can supplement or replace GPS when necessary. The policy also highlights the future development of LEO communication constellations, which will be integrated into the PNT system to enhance the robustness and reliability of GNSS signals, contributing to the establishment of an integrated PNT system. In April and November 2021, the U.S. Air Force, in collaboration with the Naval Surface Warfare Center, successfully completed flight tests of a new type of PNT "agile pod." The signal sources included SOP, which validated the ability to provide PNT capabilities in GPS-denied environments. In June 2021, the U.S. Army signed a contract with Iridium to develop payloads that can be hosted on LEO satellites for broadcasting timing or positioning signals. This initiative is considered a backup solution for the GPS system.

②NavSOP System: In 2012, BAE Systems developed a new type of positioning system that does not rely on GNSS, aiming to provide an alternative solution for positioning in complex environments. The core of this system is to utilize SOP such as mobile phone signals, Wi-Fi, broadcast signals, and TV tower signals to achieve a positioning system that is highly resistant to interference, low-cost, and flexible in application. In October 2020, the UK Space Agency proposed the Space-Based Positioning, Navigation, and Timing Program (SBPP). This program is based on a space-based PNT system composed of multiple satellites, aiming to build a system with independent PNT capabilities. It provides high-precision and highly reliable positioning and timing services for various fields such as defense, infrastructure, intelligent transportation, and emergency rescue, reducing dependence on existing GNSS.

③NAVISP Plan: In 2016, the European Space Agency (ESA) introduced the NAVISP plan, aiming to provide better solutions for Europe's PNT systems by supporting new technologies, research, and applications. The plan includes enhancing the satellite navigation services of the Galileo system using LEO satellites. In October 2021, an ESA-funded project known as "Next-Generation Network-Aided PNT Assurance" utilized encrypted signals from Iridium, LTE/5G, and GNSS as potential SOPs to enhance PNT functionality. In February 2024, a machine learning-based SOP navigation plan was proposed. This plan integrates terrestrial SOP signals such as 5G or Wi-Fi with space-based SOP signals from LEO satellites and GNSS signals to overcome the limitations of traditional GNSS.

④FutureNAV Plan: In 2022, ESA introduced the FutureNAV plan, building on the foundation of the NAVISP program. The FutureNAV plan aims to address the increasingly complex needs for PNT and to enhance Europe's independence and technological innovation capabilities in the global navigation domain. The plan promotes advancements in PNT systems through the application of LEO satellites, innovative navigation signal design, and enhanced anti-jamming and security features, providing support for applications across multiple industries.

All of the aforementioned national plans have incorporated space-based SOP based on LEO satellites into the research of new-generation PNT systems. Corresponding experiments with weapons and equipment have been conducted, as well as performance validation in typical environmental scenarios. These efforts have demonstrated the viability and feasibility of positioning technology using space-based LEO satellite SOP. After several years of research by relevant institutions both domestically and internationally, a large number of phased achievements have been made in the field of LEO-SOP positioning. The following section will summarize the current research status in this field both domestically and internationally.

## 2.2 Current research status of LEO-SOP positioning technology

The signals from LEO satellites are generally non-navigation/non-cooperative signals, which either do not contain or make it difficult to extract navigation information. Therefore, the current research on LEO-SOP positioning technology mainly focuses on analyzing the signal structure of LEO satellites to extract Doppler measurements for positioning.

The earliest research on positioning using LEO satellites appeared in 1998. This study used one or two Globalstar satellites to determine the location of a user terminal, achieving instantaneous user positioning with a horizontal position accuracy better than 10 km [22]. In 1999, Levanon N from Tel Aviv University in Israel proposed an instantaneous positioning method using a single LEO satellite. This method measured the distance between the satellite and the user terminal, as well as the Doppler frequency, and assumed that the user terminal was on the Earth's surface to achieve instantaneous user positioning [23]. The concept of SOP positioning and related research began after 2000. The term SOP first appeared in a 2005 graduate thesis from the Air Force Institute of Technology at the United States Air Force University. This thesis primarily focused on the study of ground-based SOP for positioning, such as AM, FM, WiFi, and OFDM [24].

Traditional LEO-SOP positioning primarily relies on single-constellation LEO-SOP positioning technology. Since LEO satellites are not designed for navigation purposes, their visibility and constellation configurations are generally poor. In recent years, to further enhance positioning accuracy and system availability, various positioning technologies developed based on single-constellation LEO-SOP positioning have been extensively studied. These newly developed technologies reduce errors generated during the positioning process through different approaches, such as: multi-constellation LEO-SOP positioning technology, which integrates multiple constellations to overcome the limitations of single-constellation satellite selection; LEO-SOP differential positioning technology, which eliminates orbital errors caused by extrapolation using the Simplified General Perturbations 4 (SGP4) model and Two-Line Elements (TLE) in traditional techniques through differential methods; and LEO-SOP/INS integrated positioning technology, which combines LEO-SOP with INS to ensure real-time dynamic positioning, as the low output rate of LEO-SOP navigation measurements makes it difficult to meet real-time dynamic positioning requirements. Below, we will summarize the research status at home and abroad from four aspects: single-constellation LEO-SOP positioning technology, multi-constellation LEO-SOP joint positioning technology, LEO-SOP differential positioning technology, and LEO-SOP/INS integrated positioning technology.

### 2.2.1 Single-constellation LEO-SOP positioning technology

In the field of single-constellation LEO-SOP positioning technology, the main research institutions include the team of Qin H from Beihang University in China and the team of Kassas Z from the University of California in the United States. In the early stages of research, the focus was primarily on the Iridium and Orbcomm constellations, which are typical LEO constellations. In recent years, with the development of the Starlink and Globalstar constellations, research on these systems has also garnered widespread attention.

In 2019, the team of Qin H from Beihang University first established a receiving and positioning system based on Iridium satellite signals. By combining TLE orbital information with Doppler measurements, the system achieved positioning. The experimental results showed that after accumulating Doppler measurements from 7 Iridium satellites over 30 min, the positioning accuracy was better than 200 m with the aid of elevation information

[25]. In 2020, building on their previous research, the team further developed positioning technology for Iridium signals in weak signal environments. They proposed a secondary square cumulative instantaneous Doppler estimation algorithm to enhance the Doppler estimation capability of weak Iridium signals. The experimental results indicated that the proposed method could improve positioning performance in weak signal environments, thereby enhancing the environmental adaptability of Iridium positioning [26]. In 2023, the team of Qin H established an orbital error equivalent Doppler measurement error model for LEO satellites. Based on the model analysis, they proposed a two-step improved positioning method using orbital error compensation and weighting to suppress the impact of orbital errors. The method was validated using real signals from Iridium and Orbcomm satellites, and the results showed that the positioning accuracy of the proposed method was significantly higher than that of existing methods [27]. In the same year, the team analyzed the pilot signal structure of Globalstar and obtained Doppler measurements through fourth-order processing for despreading. The experiments demonstrated that static positioning with a horizontal error of less than 300 m could be achieved using signals from two Globalstar satellites [28]. In 2024, addressing the issue of receiver hardware limitations that prevent the full utilization of all visible satellite information, the team proposed a fast clustering satellite selection algorithm. This algorithm aims to achieve higher performance positioning results with a limited number of satellites. The method was validated using real Starlink signals, and the results showed that compared to traditional methods, the positioning error was stably reduced by more than 45% [29].

In 2019, the Kassas Z team at the University of California, USA, developed a positioning system based on Orbcomm satellites and proposed a receiver architecture for acquisition and tracking using an Extended Kalman Filter (EKF). Experimental results demonstrated that the static positioning accuracy, utilizing Doppler measurements from two Orbcomm satellites, could reach 360 m [30]. In 2021, the team established a Starlink signal model and introduced an adaptive carrier phase tracking algorithm to track Starlink signals. The experiment successfully extracted carrier phase measurements from six Starlink satellites, achieving a static positioning accuracy of 33.5 m [31]. In 2023, the Kassas Z team proposed a blind receiver architecture that captures satellite measurements through sequential generalized likelihood ratio testing. The experiment tracked six Starlink satellites, with three transmitting single-tone signals and the other three transmitting OFDM-like signals. The results showed a static positioning horizontal error of 6.5 m [32].

### 2.2.2 Multi-constellation LEO-SOP positioning technology

When using a single LEO satellite constellation for positioning, issues such as insufficient visible satellites and poor satellite geometry may arise. These problems can be effectively addressed through multi-constellation LEO-SOP joint positioning. In the field of multi-constellation LEO-SOP joint positioning technology, the main research institutions include the Farhangian F team at the University of Quebec in Canada, the Kassas Z team at the University of California in the United States, and the Qin H team at Beihang University in China. Current practical testing has primarily focused on Iridium/Orbcomm joint positioning. Figure 1 illustrates the schematic diagram of multi-constellation LEO-SOP integrated positioning.

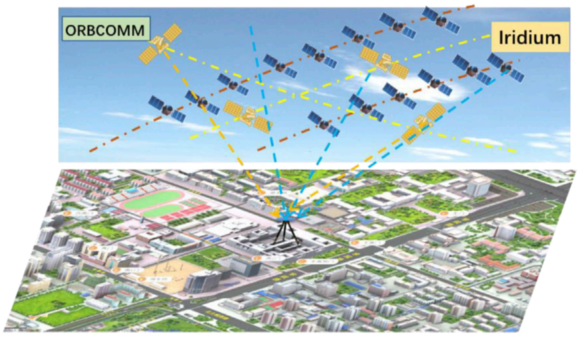

FIGURE 1
Schematic diagram of multi-constellation LEO-SOP integrated positioning.

In 2020, the Farhangian F team at the University of Quebec in Canada pioneered the design of a multi-constellation software receiver to extract Doppler measurements from LEO satellites. By tracking and collecting Doppler data from one Iridium satellite and two Orbcomm satellites, and utilizing EKF for positioning, the results demonstrated that the dual-constellation positioning accuracy reached 132 m. This represented a 72% improvement compared to single-constellation positioning accuracy [33].

In 2021, the Kassas Z team at the University of California, USA, proposed a receiver architecture suitable for processing signals from Orbcomm and Iridium satellites. By collecting data from one Orbcomm satellite and four Iridium satellites over a period of 7 min and using EKF for positioning, they achieved a horizontal positioning accuracy of 22.7 m [34]. In 2023, the team introduced a novel blind spectral estimation method for blind beacon estimation, Doppler tracking, and SOP positioning. Utilizing signals from two OneWeb satellites, four Starlink satellites, one Iridium satellite, and one Orbcomm satellite, they achieved a three-dimensional positioning error of 5.8 m and a two-dimensional positioning error of 5.1 m within 560 s [35, 36].

In the aforementioned multi-constellation joint positioning studies, the differences in measurement noise between different constellations were not taken into account, which could potentially degrade positioning performance to some extent. To address this issue, in 2022, the Qin H team at Beihang University proposed an Iridium/Orbcomm dual-constellation fusion positioning scheme based on the Helmert variance component weight estimation algorithm. This approach effectively improves the accuracy of weight allocation between different constellations. Experimental results demonstrate that the proposed method significantly enhances the performance of multi-constellation fusion positioning [37].

### 2.2.3 LEO-SOP differential positioning technology

LEO satellites face challenges in obtaining precise orbital parameter information, and atmospheric delay errors also significantly impact LEO satellite positioning. Differential positioning technology can mitigate the effects of orbital errors and

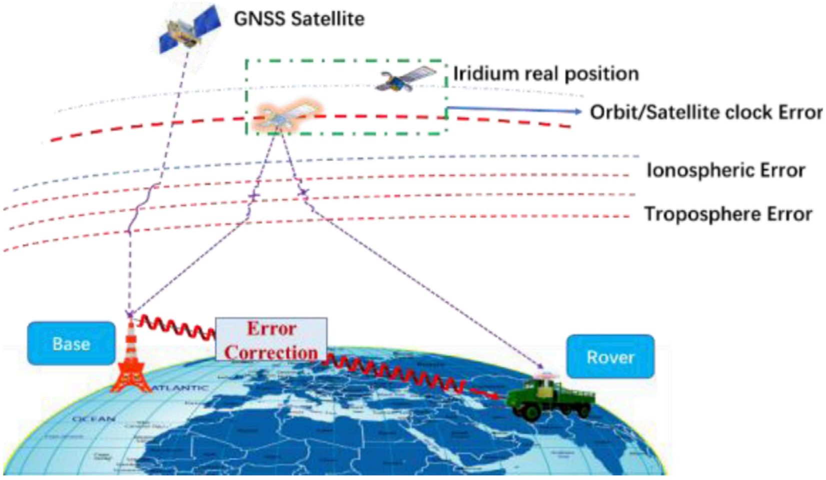

FIGURE 2
Schematic diagram of LEO-SOP differential positioning process.

atmospheric delay errors on positioning, thereby further enhancing the accuracy of LEO satellite SOP positioning. Figure 2 illustrates the schematic diagram of the LEO-SOP differential positioning process.

In 2019, the Kassas Z team at the University of California proposed a differential positioning framework based on carrier phase and validated it using Orbcomm signals. The results showed a positioning accuracy of 11.93 m, representing a significant improvement over single-point positioning [38]. In 2020, the team further introduced a differential carrier phase navigation framework utilizing signals from massive LEO satellite constellations. They derived the joint probability density function of LEO satellite azimuth and elevation angles to enhance navigation performance. Experimental results demonstrated that the Root Mean Square Error (RMSE) reached 14.8 m within 2 min [39, 40]. By 2022, the team developed a receiver capable of capturing and tracking the Doppler frequency of Starlink satellites. They designed a Kalman filter-based chirp parameter tracking algorithm and performed differential positioning using Doppler frequency. With baselines of 1 km and 9 m, the positioning errors were 5.6 m and 2.6 m, respectively [41].

In 2022, the Qin H team at Beihang University proposed a LEO-SOP Doppler differential positioning framework. To address the issue of reduced positioning accuracy caused by inconsistent spatiotemporal references in long-baseline differential positioning, the team introduced a signal transmission time estimation algorithm based on Maximum Likelihood Estimation (MLE), which further improved the accuracy of static differential positioning [42]. In 2023, to enhance the performance of long-baseline differential positioning, the team proposed a space-based SOP long-baseline differential positioning algorithm based on baseline projection vector geometric model correction. This algorithm mitigates the impact of baseline length on positioning performance and significantly improves the accuracy of long-baseline differential positioning. Experimental results demonstrate that, with a baseline length of 20 km, a positioning accuracy of 30 m can be achieved using 20 min of Iridium satellite signals, representing an improvement of over 70% compared to non-differential positioning accuracy [43]. In 2024, the team addressed the issue of significant errors in traditional Doppler differential positioning under long baselines by proposing a Doppler differential positioning algorithm based on line-of-sight vector correction. Experimental results show that, with a baseline length of 50 km, the positioning accuracy using Iridium satellite signals is better than 10 m [44].

### 2.2.4 LEO-SOP/INS integrated positioning technology

The output rate of LEO satellite SOP navigation measurements is relatively low, making it difficult to meet the requirements for real-time dynamic positioning. Additionally, the limited number of mature LEO satellite constellations available for navigation results in insufficient instantaneous visibility for the carrier, preventing instantaneous positioning. Therefore, integrating LEO-SOP with INS is necessary to ensure the real-time performance of dynamic positioning, thereby enhancing the system's availability.

In 2019, the Kassas Z team at the University of California utilized Orbcomm Doppler measurements to assist INS for positioning. Experimental results showed that, when using two Orbcomm satellites for positioning, the final positioning error after 30 s of GNSS unavailability was reduced from 31.7 m to 8.9 m [45]. In the same year, the Benzerrouk team in Canada proposed a multivariate orthogonal Kalman filtering method to integrate Iridium Doppler measurements with INS and tested it using airborne data. The experimental results indicated that the dynamic positioning accuracy ranged between 200 m and 1,000 m [46].

In 2022, researchers at the University of Quebec in Canada combined LEO satellite measurements with INS using a second-order EKF. They conducted vehicle-based experiments using actual Iridium and Orbcomm signals, as well as simulated Globalstar Doppler measurements, integrated with an INS with a drift rate of 10°/h. The results demonstrated that the positioning accuracy was better than 10 m within 150 s [47].

In 2023, the Qin H team at Beihang University proposed an Iridium/INS integrated positioning method based on adaptive robust filtering, validated using actual vehicle data. When using low-precision Micro Electro Mechanical Systems (MEMS), the positioning accuracy was better than 300 m over 15 min. In 2024, the same team addressed the issue of significant tangential errors in LEO satellite orbits by proposing a Doppler measurement model based on equivalent transmission time, effectively reducing the impact of orbital errors. They also developed an integrated positioning framework for LEO satellite SOP and INS based on adaptive federated Kalman filtering. Real-world vehicle data demonstrated that the positioning accuracy could reach 200 m [48].

## 2.3 Development of anti-jamming technology

Currently, there is no research on anti-jamming technology specifically targeting LEO-SOP positioning, either domestically or internationally. Previous achievements in anti-jamming technology have primarily focused on GNSS and similar systems. Based on the number of receiver array elements, anti-jamming technologies can be classified into two categories: single-antenna anti-jamming technology and antenna array anti-jamming technology [49, 50]. The former, due to having only a single array element, lacks spatial resolution capabilities and mainly relies on time-domain, frequency-domain, and other transform-domain interference suppression techniques. Its interference suppression capability is limited, making it suitable for navigation receivers operating in general non-malicious electromagnetic interference environments with high positioning accuracy requirements [50–53]. The latter, by incorporating spatial domain information, can distinguish between interference sources and useful signals arriving from different directions. It primarily employs spatial domain interference suppression techniques and is less sensitive to the type of interference. The maximum interference suppression capability depends on the number of array elements and the specific interference scenario, offering stronger interference suppression capabilities [54–58]. Below, we will summarize the research status at home and abroad from four aspects: time-domain, frequency-domain, transform-domain, and spatial-domain anti-jamming technologies.

### 2.3.1 Time-domain anti-jamming

In single-antenna receivers, time-domain and frequency-domain anti-jamming algorithms are the most widely used. Among these, the primary approach of time-domain anti-jamming technology is to analyze the time-domain characteristics of the signal and process it under specific constraints to reduce or eliminate the impact of interference on the signal.

Since the spectra of narrowband interference, continuous wave interference, and strong out-of-band interference differ significantly from that of navigation signals, they can be filtered using FIR or IIR bandpass filters to selectively process signals in the frequency domain. Narrowband interference signals exhibit high correlation between sampled values, making them predictable and estimable. In contrast, desired signals are typically broadband with low correlation, making them difficult to predict. Therefore, the difference in predictability between these signals can be exploited to suppress interference [59].

Currently, pulse blanking technology and time-domain adaptive filtering technology are the most commonly used time-domain anti-jamming techniques. Pulse blanking technology can effectively eliminate pulsed interference, but this method can lead to distortion of the desired signal and is only applicable to anti-pulsed interference [60]. Time-domain adaptive filtering technology involves designing a filter in the time domain that meets user requirements. By using adaptive algorithms to perform real-time weighting on data at the current moment, this technology can predict the desired signal to achieve the goal of countering narrowband interference [61]. This technology has been commonly used in GPS terminal applications since the late 20th century. For example, the adaptive time-domain filter chip developed by Mayflower Communications Company can enhance the GPS terminal's narrowband interference resistance by 30 dB [62]. In recent years, many scholars have conducted further research on time-domain adaptive filtering technology. In 2017, the team led by Chien Y R from National Ilan University in Taiwan proposed a time-domain adaptive filter composed of multiple sub-filters in parallel, which can process input data in parallel. By properly designing the starting frequencies and convergence ranges of each filter, this filter can detect and suppress multiple continuous wave interferences (CWI). However, its performance is reduced in mixed interference scenarios, and it has a certain attenuation effect on GNSS signals [63]. In 2020, the team led by Qin H from Beihang University proposed a cascaded second-order direct-form IIR notch filter, which can provide better anti-jamming capabilities in mixed scenarios where CWI and narrowband interference coexist. However, it performs poorly in suppressing broadband interference and has a higher computational complexity for the system [64]. In 2016, the team led by Mosavi M R from Iran University of Science and Technology combined neural networks with adaptive notch filters. By leveraging the parallel processing and strong adaptability of neural network technology, they reduced the computational complexity during interference suppression and improved the output performance of the notch filter [65]. However, the aforementioned time-domain anti-jamming techniques, although effective in suppressing narrowband mixed interference, perform poorly in suppressing broadband interference and can attenuate the desired signal to some extent [66].

### 2.3.2 Frequency-domain anti-jamming

Compared with time-domain anti-jamming algorithms, frequency-domain anti-jamming algorithms have the following advantages: they can simultaneously suppress multiple single-frequency interferences; when the interference bandwidth is greater than 5%, the performance of frequency-domain anti-jamming algorithms is better; with sufficient quantization word length, they have a larger dynamic range; the principle is simple and can take advantage of the well-established Fast Fourier Transform (FFT) algorithm, making it easy to implement in engineering; they have good adaptability for segmenting data processing. Therefore, frequency-domain anti-jamming algorithms are the most commonly used anti-jamming algorithms in engineering [66, 67].

Davidovici et al. proposed an implementation method for frequency-domain anti-jamming algorithms using windowing and overlap-add techniques, and they conducted a detailed analysis of the signal-to-noise ratio (SNR) loss associated with the algorithm [67–69]. In 2000, the team led by Li C from Shanghai Jiao Tong University improved the overlapping transform-domain algorithm,

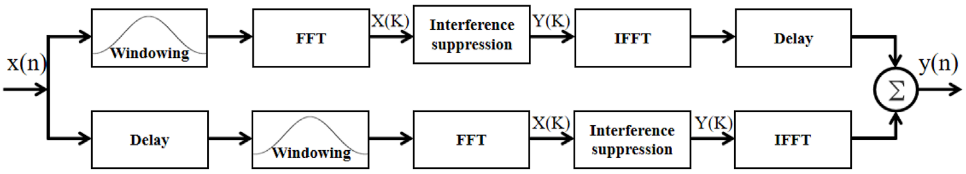

FIGURE 3
Flowchart of frequency-domain anti-jamming implementation.

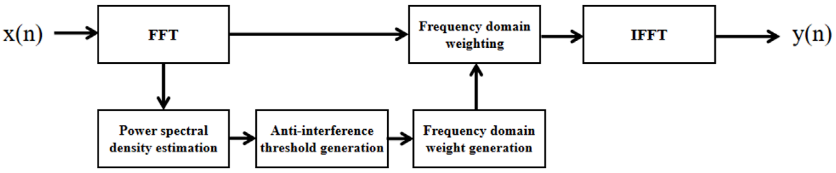

FIGURE 4
Interference suppression process flowchart.

decoupling the system performance from the interference frequency and thereby enhancing the system's robustness [70]. In 2005, Sun Z from Harbin Engineering University summarized the advantages and disadvantages of traditional adaptive time-domain and frequency-domain algorithms and proposed improvements based on this analysis [71]. In 2004, the team led by Zeng X from the National University of Defense Technology derived in detail the time-domain windowing effects on the overlap-add frequency-domain anti-jamming algorithm and analyzed the carrier-to-noise ratio (CNR) loss caused by time-domain windowing [72]. Through continuous exploration, the implementation of frequency-domain anti-jamming in engineering has evolved into a windowing overlap-add approach, the specific process of which is shown in Figure 3.

The detailed implementation process of interference suppression in Figure 3 is illustrated in Figure 4. The interference suppression component is the core of frequency-domain anti-jamming, which is divided into FFT-based power spectral density estimation, anti-jamming threshold generation, frequency-domain weight generation, and weighting. Among these, threshold generation is the key to interference suppression. In other words, a reasonable interference detection threshold is crucial for frequency-domain anti-jamming, and whether the threshold is set appropriately largely determines the performance of the frequency-domain anti-jamming algorithm.

In recent years, many scholars have further investigated frequency-domain adaptive filtering techniques. In 2016, the Rezaei M J team at Iran University of Science and Technology employed a frequency-domain transformation method based on multi-scale short-time Fourier transform (STFT), enhancing the signal's aggregation in the frequency domain and improving the filter's anti-jamming capability. However, this method came at the cost of increased computational complexity [73]. In the same year, the Chang C L team at National Pingtung University of Science and Technology in Taiwan combined compressed sensing with frequency-domain processing techniques, reducing the system sampling rate and thereby decreasing the computational complexity of anti-jamming processing. Nevertheless, the performance in suppressing wideband interference remained suboptimal [74]. In 2017, the Chien Y R team utilized wavelet packet transform (WPT), which offers higher time-frequency resolution than wavelet transform (WT), to detect interference parameters and estimate the current waveform of the interference, thereby suppressing it. This further enhanced the signal's aggregation in the frequency domain, but the method still struggled when dealing with a large number of wideband interferences [75]. In 2024, the Ding M team at Hong Kong Polytechnic University introduced a Signal Prediction-Assisted Reference Spectrum Model (SPRSM) to mitigate the loss of desired signals during frequency-domain filtering. The introduced SPRSM equalizer leverages GNSS signal prediction to compensate for distortion, reducing signal degradation and quality loss caused by signal distortion during frequency-domain filtering [76].

In summary, frequency-domain anti-jamming techniques are only suitable for dealing with multiple narrowband interferences and broadband interferences that have certain spectral energy aggregation. When it comes to broadband interferences with poor energy distribution aggregation or a large number of broadband interferences, the interference suppression capability of frequency-domain anti-jamming techniques still falls short.

### 2.3.3 Transformation-domain anti-jamming

Transformation-domain anti-jamming technology involves mapping the received signal into a transformation domain (such as the frequency domain or time-frequency domain). By exploiting the differences in characteristics between the interference and the desired signal in the transformation domain, interference detection algorithms are used to estimate the parameters of the interference. The interference signal can then be removed using pulse blanking methods or filters. The processed signal is subsequently inverse-transformed back to the time domain. Alternatively, the interference signal waveform can be reconstructed based on the estimated parameters and then eliminated from the received signal [75, 77].

The choice of transform domain or transformation method can lead to differences in the obtained interference distribution characteristics. Therefore, the transform domain and method need to be selected or optimized based on the types of interference in the receiving environment. The frequency domain is the earliest and most commonly used transform domain. Stationary narrowband interference signals exhibit high aggregation in the frequency domain, and frequency-domain data can be quickly obtained through FFT, offering strong practicality [75]. With the continuous development of interference technology, non-stationary time-varying interference has become increasingly prominent in adversarial environments. As a result, cyclic spectrum analysis and time-frequency (TF) analysis methods have been introduced into the field of anti-jamming. Typical TF transformation methods include Short-Time Fourier Transform (STFT), Wavelet Transform (WT), Wigner-Ville Distribution (WVD), and Fractional Fourier Transform (FrFT), among others. To further enhance the aggregation of interference signals in the transform domain and achieve more accurate detection results, several new transformation methods have been proposed and applied in the field of GNSS interference detection and suppression. In 2015, the Sun K team at Hefei University of Technology combined reassignment techniques with the Smoothed Pseudo Wigner-Ville Distribution (SPWVD) to propose the Reassigned Smoothed Pseudo Wigner-Ville Distribution (RSPWVD). This method enhanced the aggregation of interference signals in the TF domain, improved TF resolution, and reduced cross-term interference [78]. In 2016, the Rezaei M J team at Iran University of Science and Technology employed multi-scale STFT, achieving improved TF aggregation of interference signals at the cost of a slight increase in computational complexity [73]. In the same year, the Li J team at Tianjin University of Technology used Time-Modulated Windowed All-Phase Discrete Fourier Transform (TMWAP-DFT) to detect the frequency parameters of pulse signals emitted by Distance Measurement Equipment (DME) [77]. In 2017, the Chien Y R team utilized WPT to detect the TF parameters of fast-varying interference signals and predict their waveforms [75]. Also in 2017, the Mosavi M R team at Iran University of Science and Technology demonstrated that WPT could suppress narrowband and chirp interference with a capability of up to 55 dB [79]. With the gradual maturation of compressed sensing theory, in 2016, the Chang C L team at National Pingtung University of Science and Technology in Taiwan introduced compressed sensing theory into the field of GNSS anti-jamming to reduce the sampling rate and the computational complexity of interference detection and suppression [74]. In 2024, the Sun K team at Hefei University of Technology proposed a Generalized Time-Fractional Bandwidth Product (GTFrBP) search model based on FrFT combined with a notch filter. Experimental results demonstrated that this model achieved high precision in detecting the optimal FrFT order [80].

The efficiency of transformation-domain anti-jamming techniques is independent of the number of interferences and is suitable for scenarios with multiple narrowband interferences. Moreover, these techniques can effectively handle non-stationary broadband interference signals such as linear frequency-modulated (LFM) signals. Therefore, they are considered a very promising anti-jamming strategy. However, these algorithms are only applicable to narrowband interferences and broadband interferences with strong TF energy distribution aggregation. They are powerless in the case of complex forms of broadband interferences or a large number of broadband interferences.

### 2.3.4 Spatial anti-jamming

Spatial filtering is one of the most effective methods for suppressing spatial interference signals. It employs adaptive null-steering antennas to achieve adaptive filtering functions. The working principle involves using adaptive weighting coefficients to control the antenna pattern, thereby filtering out interference signals in the spatial domain without degrading the gain of the desired signal [81]. The structure is shown in Figure 5.

Classic spatial anti-jamming algorithms include the Power-Inversion (PI) method [82], Minimum Variance Distortionless Response (MVDR) method [83, 84], and Minimum Power Distortionless Response (MPDR) method [85]. The PI algorithm does not require prior information about the jamming and desired signals; it can form nulls in the direction of strong jamming to suppress it. This method has low computational complexity and is easy to implement. However, its suppression performance against weak jamming (JNR <20 dB) is not satisfactory [86], and it lacks constraints on the desired signal, making it unable to guarantee the gain of the desired signal. The MVDR and MPDR algorithms impose constraints on the beam response in the direction of the desired signal, enabling the spatial filter to have a distortionless response to the desired signal while suppressing jamming from other directions. However, the MVDR algorithm requires estimating the covariance of interference and noise without the desired signal, whereas the MPDR leverages the characteristic that the GNSS signal power at the navigation receiver is significantly lower than that of the jammer noise, directly using the covariance of the received signal to solve for the spatial filter weights. Since these methods were introduced into the field of GNSS receiver anti-jamming in the 1990s, they have been successfully applied in practical equipment. For example, Boeing developed a four-element antenna array anti-jamming receiver that can adaptively adjust the nulls in the antenna beam pattern, enhancing the anti-jamming capability of satellite navigation equipment on Joint Direct Attack Munitions (JDAM) [87]. Similarly, NovAtel developed a miniaturized GNSS Anti-Jam Technology (GAJT) antenna, employing a seven-element antenna array, capable of countering up to six strong jamming sources [88].

To enhance the capability of spatial filters to counter complex jamming environments, multi-antenna-based spatial anti-jamming technologies have been further researched. Regarding the selection of reference elements in the PI algorithm, in 2016, Chen F's team from the National University of Defense Technology analyzed the impact of the relative position of reference elements on anti-jamming performance under different interference conditions [89]. In the same year, the team proposed an optimal element selection method based on joint acquisition results, adaptively selecting reference elements based on optimal acquisition outcomes [90, 91]. In 2017, Lu Z's team from the National University of Defense Technology suggested that selecting appropriate reference elements can reduce the impact of channel mismatch and proposed choosing

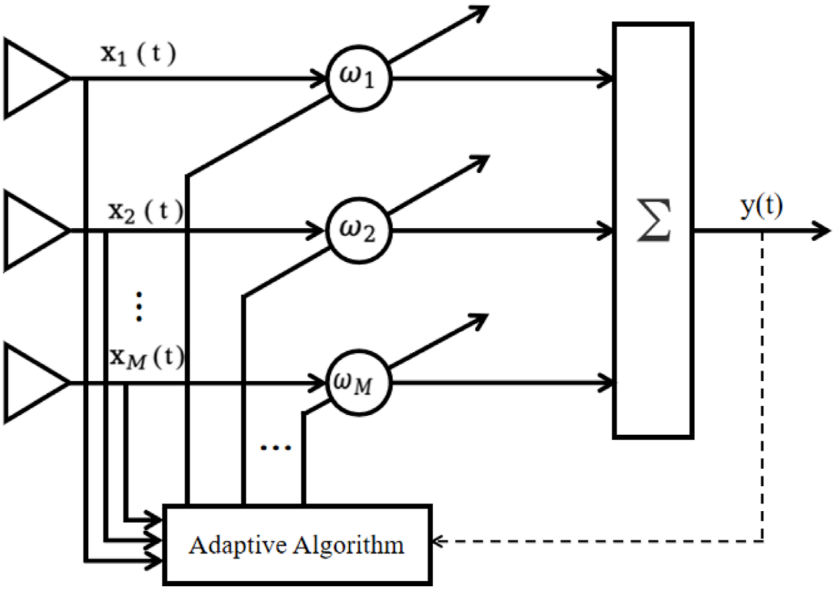

FIGURE 5
Spatial anti-jamming structure.

the optimal reference element based on output power to improve interference suppression performance [92]. Addressing the issue where blind adaptive beamforming algorithms (such as the PI algorithm) do not constrain the desired signal, leading to distortion in satellite navigation signals, in 2012, Zhang Y D's team from Villanova University proposed a method to estimate the steering vector based on the autocorrelation characteristics of navigation signals, thereby estimating the carrier error introduced by blind adaptive beamforming and compensating for it [93]. In 2016, Daneshmand S's team from the University of Calgary utilized the symmetry in symmetric arrays to estimate the signal distortion parameters introduced by adaptive filters, subsequently calculating compensation weight vectors [94]. In high-dynamic application scenarios, where rapid changes in interference direction over short periods lead to performance degradation in conventional algorithms, besides typical null broadening strategies [95], in 2016, Chen L W's team from Wuhan University proposed using a Hidden Markov Process to detect interference characteristics within sub-bands, then employing a multi-constraint PI algorithm to eliminate interference, thereby enhancing the efficiency of processing rapidly changing interference [96]. In 2014, Wang W's team from the Civil Aviation University of China proposed leveraging the sparsity of the spatial spectrum of interference signals, using short snapshot (single snapshot) Direction of Arrival (DOA) estimation methods to estimate interference directions, quickly constructing interference subspaces, and then suppressing interference through orthogonal subspace projection algorithms. This method can rapidly update spatial filter weights based on the instantaneous DOA information of interference sources, thus exhibiting high robustness in high-dynamic environments [97]. Regarding spatially proximal interference (interference incident within the main beam) causing a decrease in the output SNR of spatial filters, in 2017, Gong Y's team from Northwestern Polytechnical University proposed a covariance matrix reconstruction method. This approach first eliminates spatially proximal interference from the covariance matrix to achieve the suppression of other interferences, and then uses an eigenvalue protection matrix to eliminate spatially proximal interference [98]. Addressing the drawback of uniform linear arrays being unable to distinguish between desired and interference signals located on the same ambiguity cone, in 2013, Wang X's team from the University of New South Wales analyzed the relationship between spatial correlation coefficients [99] among signals and array orientation, proposing to rotate the linear array to obtain optimal anti-jamming performance by optimizing the spatial correlation coefficient [100]. In certain jamming scenarios, where high spatial correlation between interference and desired signals leads to reduced interference suppression effectiveness in fixed-array-based spatial filtering algorithms, in 2016, Wang X's team from the University of New South Wales and Amin M G's team from Villanova University respectively researched reconfigurable array technologies. These methods improve anti-jamming performance without increasing RF channels by selecting appropriate elements in redundant antenna arrays to reduce the correlation between interference and desired signals [101, 102].

## 3 Principle of LEO-SOP positioning

LEO satellites signals are generally non-navigation/non-cooperative signals, which either do not contain or make it difficult to extract navigation information. Therefore, it is challenging to obtain pseudorange measurements, and positioning is usually achieved by extracting Doppler shifts. This section introduces the principle model of LEO-SOP Doppler positioning and the working process of the receiver. The details are as follows.

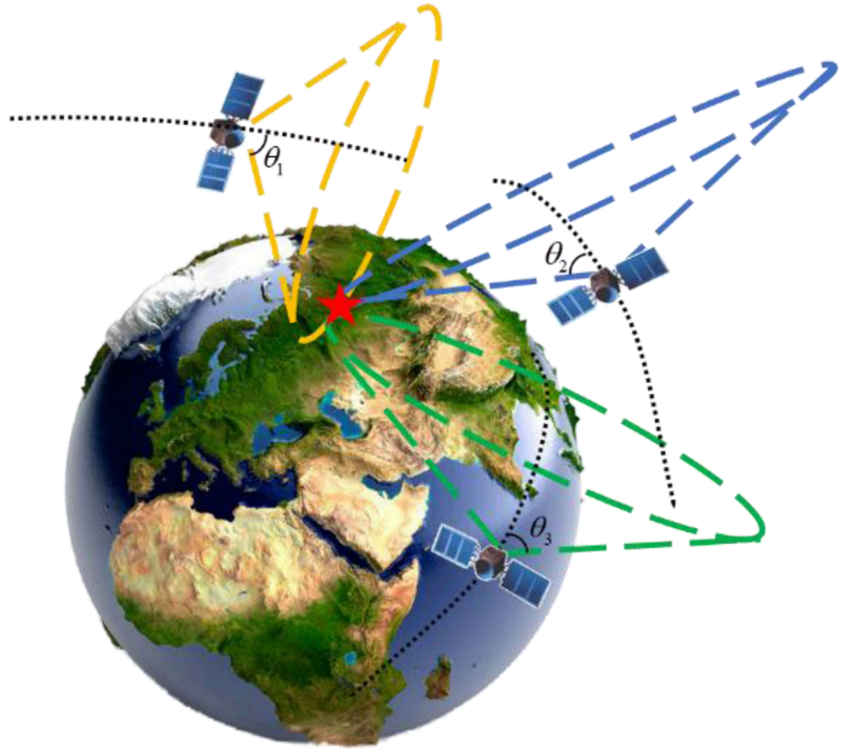

FIGURE 6
Schematic diagram of multi-satellites doppler positioning algorithm principle.

## 3.1 LEO-SOP Doppler positioning principle model

By measuring the instantaneous Doppler frequency of LEO satellites, positioning can be achieved. The principle is based on the Doppler effect caused by the high-speed motion of satellites relative to the ground. The change in Doppler frequency reflects the relationship between the satellite's position and the navigation terminal's position. The relative velocity between the receiver and the satellite can be obtained using the carrier Doppler measurements of the satellite signal and its wavelength. This constrains the receiver's position to the surface of a cone with the satellite's position as the origin, the satellite's velocity direction as the axis, and the opening angle determined by the relative velocity. When a sufficient number of LEO satellites are received, the receiver's position can be determined by the intersection of multiple conical surfaces calculated from the measurements. A schematic diagram of the multi-satellites Doppler positioning principle is shown in Figure 6. When LEO satellite visibility is insufficient, multiple measurements from a single satellite can also be used. Similarly, the intersection of multiple conical surfaces calculated from these measurements can determine the receiver's position. The basic principle is the same as that of multi-satellites Doppler positioning. A schematic diagram of the single-satellite Doppler positioning principle is shown in Figure 7.

Below, the Doppler positioning equation is derived from the pseudorange positioning equation. Taking a single satellite as an example, the traditional pseudorange positioning equation is:

$$\delta\rho = H\delta X + \varepsilon \tag{1}$$

In the equation, $\delta\rho$ represents the residual between the measured pseudorange and the back-calculated pseudorange; $\delta X = \left[\delta r_x, \delta r_y, \delta r_z, \delta(\partial t_c)\right]^T$, where $\delta r_x$, $\delta r_y$ and $\delta r_z$ are position errors; $\delta(\partial t_c)$ is the receiver clock bias error; $\varepsilon$ is the measurement error; $H$ is the measurement equation, which takes the form of Equation 2:

$$H = \begin{bmatrix} -e^{(1)} & 1 & \nu^{(1)} \\ \vdots & \vdots & \vdots \\ -e^{(K)} & 1 & \nu^{(K)} \end{bmatrix} \tag{2}$$

In the equation, K represents the Kth satellite received, $e^{(K)}$ is the unit line-of-sight vector from the receiver to satellite K, and $\nu^{(K)}$ is the pseudorange rate.

Taking the derivative of both sides of Equation 1 yields:

$$\delta\dot{\rho} = \frac{\partial\delta\rho}{\partial t} = \frac{\partial(HX)}{\partial t} + \dot{\varepsilon} = H\frac{\partial(X)}{\partial t} + \frac{\partial(H)}{\partial t}X + \dot{\varepsilon} \tag{3}$$

In the Equation 3, $\delta\dot{\rho}$ represents the residual between the measured Doppler shift and the back-calculated Doppler shift. The polynomial on the right-hand side of the equation can be calculated using the following formula. Specifically, the first polynomial $H\frac{\partial(X)}{\partial t}$ can be obtained from the classical linear equation of the receiver's velocity:

$$H\frac{\partial(X)}{\partial t} = H\frac{\partial}{\partial t}\left[\delta r_x, \delta r_y, \delta r_z, \delta(\partial t_c)\right]^T = H\left[\delta\dot{r}_x, \delta\dot{r}_y, \delta\dot{r}_z, \delta(\partial f_c)\right]^T \tag{4}$$

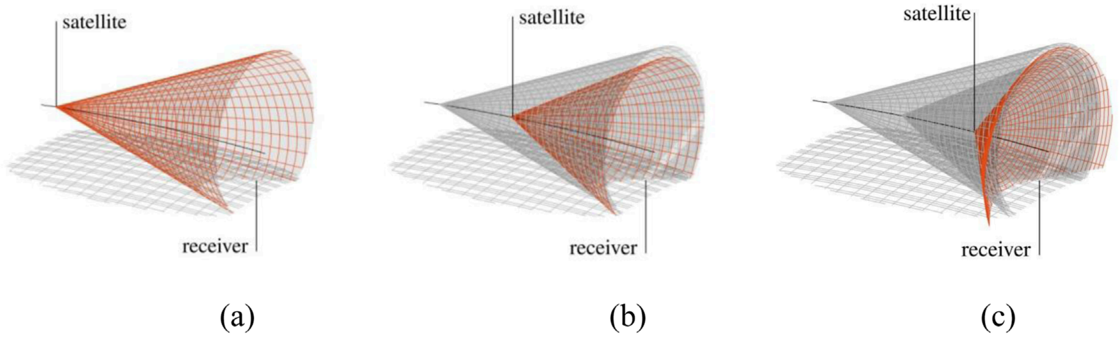

FIGURE 7
Schematic Diagram of Single-Satellite Doppler Positioning Principle. **(a)** First measurement, **(b)** Second measurement, **(c)** Third measurement.

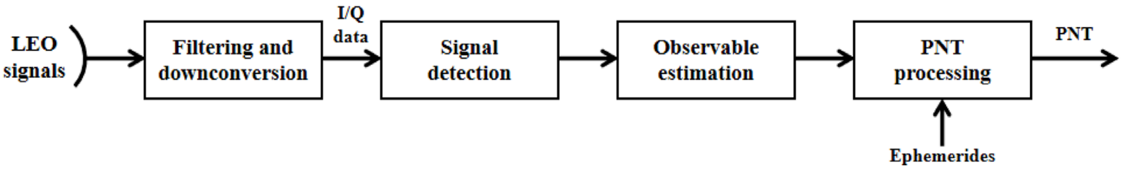

FIGURE 8
Flowchart of LEO-SOP receiver operation.

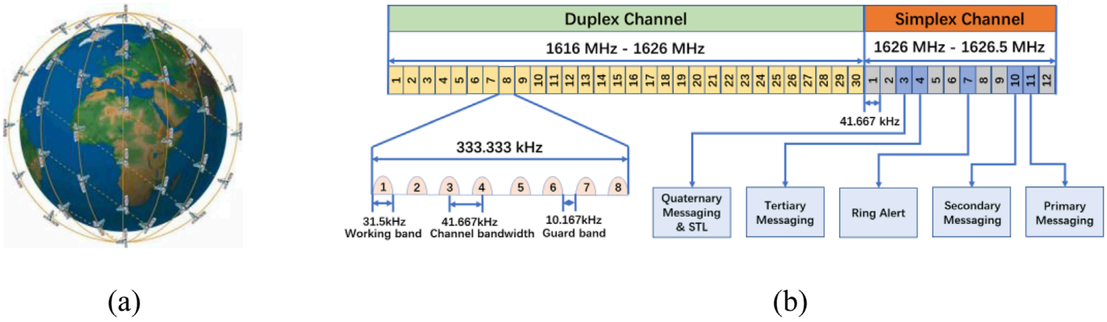

FIGURE 9
Basic satellite orbit distribution and signal system of the iridium system. **(a)** Constellation orbit, **(b)** L-band frequency allocation.

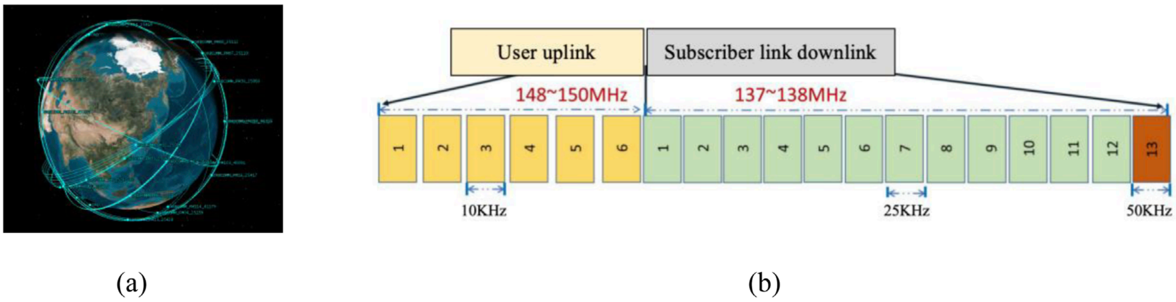

FIGURE 10
Orbcomm Satellite orbital distribution and signal System. **(a)** Constellation orbit, **(b)** downlink allocation.

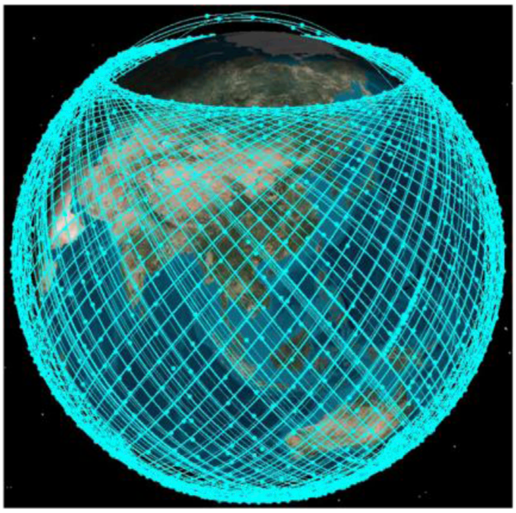

FIGURE 11
Schematic diagram of starlink constellation deployment.

Where, $\delta\dot{r}_x$, $\delta\dot{r}_y$ and $\delta\dot{r}_z$ represent the velocity errors, while $\delta(\partial f_c)$ denotes the receiver frequency bias.

The second term $\frac{\partial(H)}{\partial t}X$ represents the relationship between the Doppler measurement and the position:

$$\begin{aligned}\frac{\partial(H)}{\partial t}X &= \frac{\partial}{\partial t}\begin{bmatrix}-e^{(1)} & 1\\ \vdots & \vdots\\ -e^{(K)} & 1\end{bmatrix}\left[\delta r_x, \delta r_y, \delta r_z, \delta(\partial t_c)\right]^T\\ &= \begin{bmatrix}-\partial e^{(1)}/\partial t & 0\\ \vdots & \vdots\\ -\partial e^{(K)}/\partial t & 0\end{bmatrix}\left[\delta r_x, \delta r_y, \delta r_z, \delta(\partial t_c)\right]^T\end{aligned} \tag{5}$$

By combining Equations 4, 5, we obtain:

$$\delta\dot{\rho} = H\left[\delta\dot{r}_x, \delta\dot{r}_y, \delta\dot{r}_z, \delta(\partial f_c)\right]^T + \begin{bmatrix}-\partial e^{(1)}/\partial t\\ \vdots\\ -\partial e^{(K)}/\partial t\end{bmatrix}\left[\delta r_x, \delta r_y, \delta r_z\right] + \dot{\varepsilon} \tag{6}$$

The above equation is the Doppler positioning equation, which establishes a linear relationship between seven states (receiver position, velocity, and frequency bias) and the instantaneous Doppler shift. If the receiver is stationary, the number of unknowns in the equation reduces to four, namely, $\left[\delta r_x, \delta r_y, \delta r_z, \delta(\partial f_c)\right]^T$. In this case, positioning can be directly performed using the instantaneous Doppler measurements from four satellites. Equation 6 then becomes:

$$\delta\dot{\rho} = \begin{bmatrix}-\partial e^{(1)}/\partial t & 1\\ \vdots & \vdots\\ -\partial e^{(K)}/\partial t & 1\end{bmatrix}\left[\delta r_x, \delta r_y, \delta r_z, \delta(\partial f_c)\right]^T + \dot{\varepsilon} \tag{7}$$

Before solving the navigation Equation 7, the expression for the three-dimensional vector $-\partial e^{(k)}/\partial t$ must be derived, which is:

$$\frac{\partial e^{(k)}}{\partial t} = \frac{\partial}{\partial t}\left(\frac{x^{(k)} - x_{xyz0}}{\left|x^{(k)} - x_{xyz0}\right|}\right) \tag{8}$$

Where, $x^{(k)}$ represents the position of satellite k, and $x_{xyz0}$ is the prior position information of the receiver. For the sake of simplifying the description below, the superscript (k) can be omitted, and the variable r can be used to represent the distance from the satellite to the receiver, that is Equation 9:

$$r = \left|x^{(k)} - x_{xyz0}\right| \tag{9}$$

Therefore, Equation 8 can be written as:

$$\begin{aligned}\frac{\partial e}{\partial t} &= \frac{\partial}{\partial t}\left(\frac{x - x_{xyz0}}{r}\right)\\ &= \left(\frac{\partial\left(x - x_{xyz0}\right)}{\partial t}\cdot r - \left(x - x_{xyz0}\right)\cdot\frac{\partial r}{\partial t}\right)\frac{1}{r^2}\\ &= \left(\frac{\partial x}{\partial t}\cdot r - \left(x - x_{xyz0}\right)\cdot(e\cdot v)\right)\frac{1}{r^2}\\ &= \left(\frac{\partial x}{\partial t}\cdot r - (r\cdot e)\cdot(e\cdot v)\right)\frac{1}{r^2}\\ &= \left(\frac{\partial x}{\partial t} - e\cdot(e\cdot v)\right)\frac{1}{r}\end{aligned} \tag{10}$$

From Equation 10, the physical meaning of the three-dimensional vector expression $-\partial e^{(k)}/\partial t$ in Equation 7 can be understood, which is: the ratio of the difference between the satellite's velocity and its velocity component in the line-of-sight direction to the distance.

## 3.2 LEO-SOP receiver operation process

Since LEO satellites are generally not designed for navigation purposes, it is difficult to obtain traditional navigation observation information such as pseudoranges. Therefore, LEO-SOP receivers typically need to analyze the characteristics of LEO satellite signals, such as signal structure and signal power, to extract navigation observation information. Additionally, they rely on external ephemeris data to assist in obtaining satellite position and velocity parameters. These steps are essential for the receiver to complete its own positioning and obtain PNT status. By substituting TLE parameters into the SGP4 model, the satellite's position and velocity at a specific moment can be calculated.

Generally, after the antenna of a LEO-SOP receiver completes the acquisition of the SOP signal, it uses a down-conversion device to shift the frequency of the collected signal to an intermediate frequency. Subsequently, the SOP signal is detected, and navigation observation information is analyzed and extracted. Finally, the receiver estimates its own PNT status using the observation information and external ephemeris data. The operation process of the LEO-SOP receiver is shown in Figure 8.

# 4 Analysis of the system-level anti-jamming capability of LEO-SOP

This section analyzes the system-level anti-jamming capability of the LEO-SOP. It first provides a detailed introduction to the constellation characteristics of the Iridium, Orbcomm, and Starlink satellites within the LEO system. The analysis of system-level anti-jamming capabilities is then conducted from several aspects,

TABLE 3 Configuration of the first phase of the starlink constellation.

| Constellation type | Orbital altitude/km | Orbital inclination/(°) | Number of orbital planes | Number of satellites in the orbital plane | Total number of satellites |
|---|---|---|---|---|---|
| LEO | 550 | 53 | 72 | 22 | 1,584 |
| | 540 | 53.2 | 72 | 22 | 1,584 |
| | 570 | 70 | 36 | 20 | 720 |
| | 560 | 97.6 | 6 | 58 | 348 |
| | 560 | 97.6 | 4 | 43 | 172 |
| VLEO | 345.6 | 53 | | | 2,547 |
| | 340.8 | 48 | | | 2,748 |
| | 335.9 | 42 | | | 2,493 |

TABLE 4 Frequency bands of the starlink system.

| Uplink/Downlink | Ku | Ka | V |
|---|---|---|---|
| DownlinkUplink | 10.7~12.7 | — | 37.5~42.5 |
| | 14.0~14.5 | — | 47.2~50.2 |
| | | | 50.4~52.4 |

including GDOP (Geometric Dilution of Precision) values, satellite visibility, SNR at the receiver, and downlink user frequencies. Without loss of generality, the GPS system from the GNSS is selected as a representative for comparative analysis with the LEO system.

## 4.1 Characteristics of LEO constellations

This subsection selects the relatively mature Iridium and Obrcomm satellites, as well as the rapidly developing Starlink satellites, as representatives of the LEO system. It provides a detailed introduction to the constellation characteristics of each representative satellite, laying the theoretical foundation and technical support for subsequent analysis of anti-jamming capabilities. The details are as follows.

### 4.1.1 Iridium system

The Iridium system is a global satellite mobile communication network developed by Motorola and others, consisting of 66 LEO satellites. In January 2017, the first batch of 10 Iridium NEXT satellites was successfully launched. On 20 May 2023, an additional five backup satellites were launched aboard SpaceX's Falcon 9 rocket [103–105]. Currently, the Iridium NEXT constellation has 80 satellites in orbit (66 of which are actively transmitting signals, with the remaining 14 serving as backups). A schematic diagram of the Iridium NEXT system constellation is shown in Figure 9a.

The Iridium system's satellites have an orbital inclination of 86.4° and an orbital period of 100.13 min, enabling global coverage. The user link employs a combination of FDMA/TDMA/SDMA/TDD multiple access techniques. The 48 spot beams of each satellite are grouped into sets of 12 adjacent beams, which spatially reuse the total available frequency band (SDMA). Within each beam, the frequency band is further divided into multiple TDMA channels using FDMA. For the same user, the uplink and downlink within each TDMA channel are time-division multiplexed (TDD), meaning the uplink and downlink occupy different time slots within the same frame of the same TDMA carrier [106–110].

The total bandwidth allocated to Iridium is 1,616.0 MHz–1,626.5 MHz. Specifically, 1,616.0 MHz - 1,626.0 MHz is used for full-duplex channels as the service channels, while 1,626.0 MHz - 1,626.5 MHz is designated for the downlink simplex channel, used as the signaling channel. The 0.5 MHz bandwidth of the downlink channel is divided into 12 channels, each with a bandwidth of 41.67 kHz. The FDMA frequency allocation for the user links of the Iridium system is shown in Figure 9b; [111–114].

### 4.1.2 Orbcomm system

Orbcomm satellites are a joint project between Orbital Sciences Corporation of the United States and Teleglobe of Canada. This satellite system offers several advantages, including low investment, short development cycles, dual capabilities in communication and positioning, lightweight satellites, mobile phone user terminals, high levels of system automation, and strong autonomous functionality. Utilizing the Orbcomm system, users can engage in applications such as remote data collection, system monitoring, tracking of vehicles, vessels, and mobile facilities, as well as sending and receiving emails. In 2008, Orbcomm announced the deployment of its second-generation satellite (OG2) constellation. Currently, there are 12 OG2 satellites in orbit, evenly distributed across four primary orbital planes. The OG2 satellites operate at an altitude of 620 km with an orbital inclination of 47° and an orbital period of 97 min. A schematic diagram of the Orbcomm constellation is shown in Figure 10a; [115–118].

The downlink of Orbcomm satellites occupies the frequency band of 137–138 MHz, which includes 13 channels. Twelve channels, each with a bandwidth of 25 kHz, are used for communication with user terminals (employing FDMA multiple

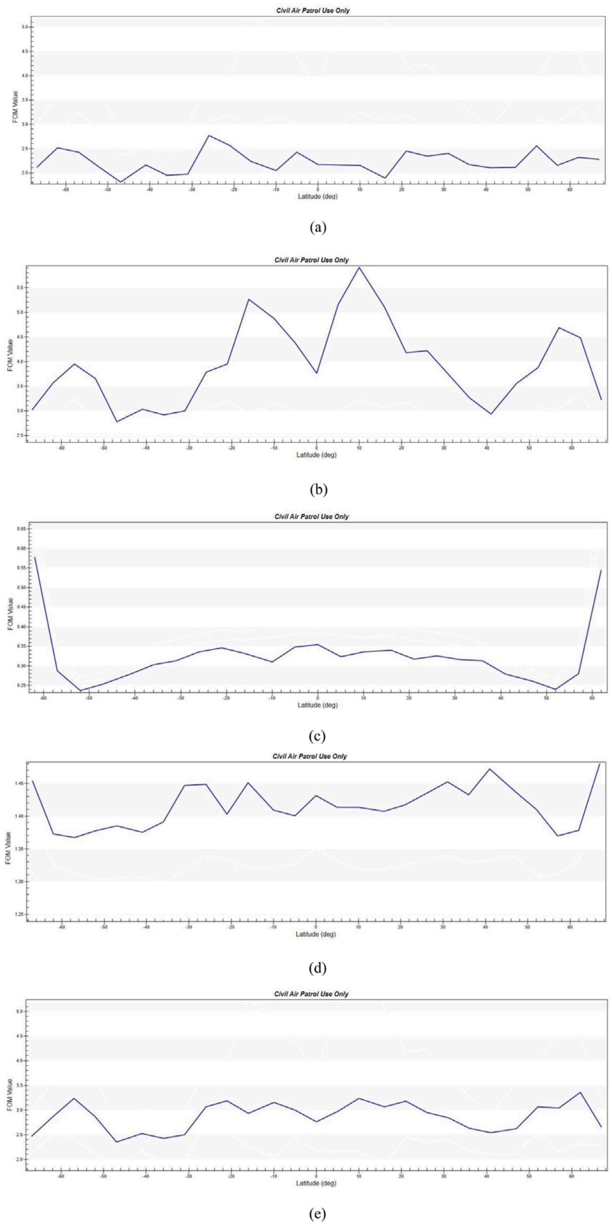

(a)

(b)

(c)

(d)

(e)

FIGURE 12
Gdop values of various constellations. **(a)** Iridium single constellation, **(b)** orbcomm single constellation, **(c)** Starlink single constellation, **(d)** Iridium/orbcomm dual constellation, **(e)** GPS satellites.

access), while the remaining channel, with a bandwidth of 50 kHz, is used for communication with gateway stations. All Orbcomm satellites share the 12 user downlink channels. The user downlink employs SDPSK modulation. The downlink allocation of the Orbcomm constellation is illustrated in Figure 10b; [119, 120].

### 4.1.3 Starlink system

Starlink is a Non-Geostationary Orbit (NGSO) satellite system being developed by SpaceX, an American space services company. It boasts numerous advantages, including extensive coverage, high signal strength, and a large number of satellites. The system consists of two sub-constellations: a LEO constellation at an altitude of 550 km and a Very Low Earth Orbit (VLEO) constellation at an altitude of 340 km. Although the Starlink constellation is not yet fully deployed, the number of satellites already in orbit far surpasses that of other LEO constellations. By November 2024, the number of Starlink satellites in orbit had exceeded 6,000, significantly more than any other existing LEO constellation. The system is projected to grow into a mega-constellation of nearly 12,000 satellites to provide satellite internet services. Figure 11 illustrates the schematic diagram of the deployed constellation [121–123].

The constellation design of Starlink has gone through two phases. As early as April 2020, SpaceX adjusted the orbital altitudes of all satellites in the LEO constellation from 1,150 km to 550 km to a range of 540–570 km in the first phase configuration. The modified configuration of the first phase of the Starlink constellation is shown in Table 3; [124, 125].

In May 2020, SpaceX submitted the constellation design for its second-generation Starlink system (Gen2), which includes 30,000 satellites.

The Starlink system features inter-satellite communication capabilities. Network users will utilize the V and Ku bands, while the V and Ka bands will primarily be used for connecting gateways and for tracking, telemetry, and control. The LEO sub-constellation satellites will operate in the Ku, Ka, and V bands, with the Ku band used for downlink operations. The VLEO sub-constellation satellites will only use the V band. The frequency bands used by the Starlink system are shown in Table 4.

## 4.2 Analysis of the system-level anti-jamming capability

LEO-SOP demonstrates a significant improvement in the system-level anti-jamming capability due to the numerous inherent advantages of LEO constellations compared to traditional GNSS navigation constellations. The following analysis will focus on GDOP values, satellite visibility, SNR at the receiver, and downlink user frequency. During the analysis, four currently well-established LEO-SOP positioning scenarios will be considered: Iridium single-constellation positioning, Orbcomm single-constellation positioning, Starlink single-constellation positioning, Iridium/Orbcomm dual constellation joint positioning, as well as a comparative scenario with GPS positioning.

### 4.2.1 GDOP value

Using STK software, the GDOP values of various constellations under five scenarios in the Asia-Pacific region over a 24-h period were simulated. The horizontal axis represents the latitude values, while the vertical axis represents the corresponding GDOP values. The results are shown in Figure 12.

As can be seen from Figure 12, the GDOP value of the Orbcomm single-constellation performs relatively the worst. This is because Orbcomm is a Walker constellation with only 12 available satellites. In contrast, the GDOP value of the Iridium single constellation is better than that of GPS satellites. Although Iridium has a polar orbit type, its constellation consists of 66 satellites, which is a

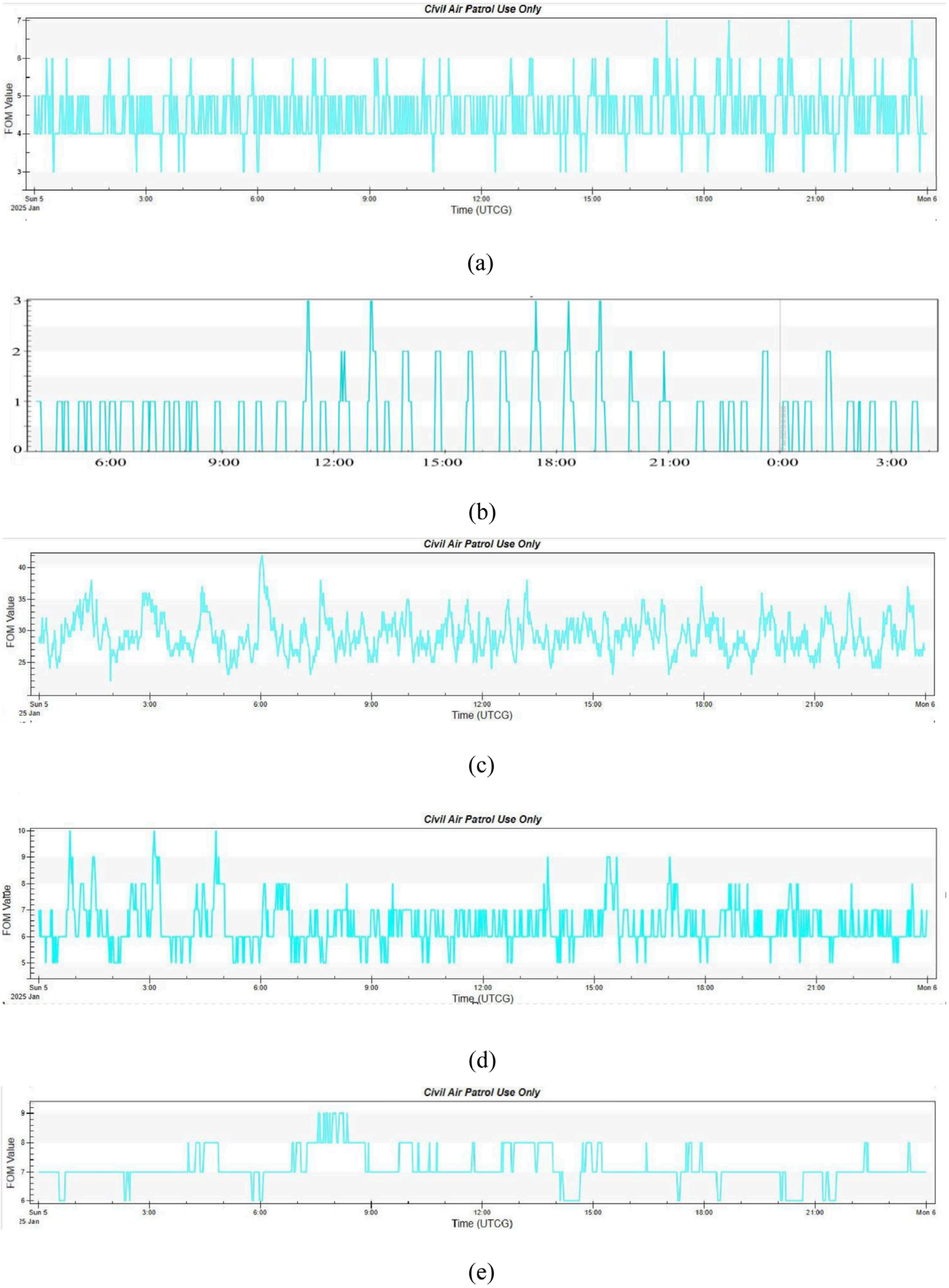

FIGURE 13
Satellite visibility of various constellations. **(a)** Iridium single constellation, **(b)** orbcomm single constellation, **(c)** Starlink single constellation, **(d)** Iridium/orbcomm dual constellation, **(e)** GPS satellites.

relatively large number, resulting in better GDOP performance. Moreover, when combined with Orbcomm to form a dual constellation, the GDOP value improves significantly, effectively enhancing the satellite geometry. The Starlink constellation, with the largest number of satellites, exhibits the best GDOP performance.

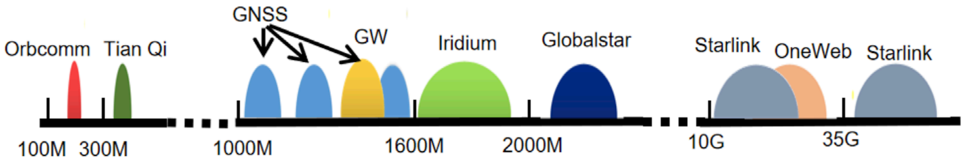

FIGURE 14
Spectrum range illustration of LEO satellites and GNSS satellites.

### 4.2.2 Satellite visibility

Similarly, using STK software to simulate the satellite visibility of each constellation in the five scenarios in Beijing area over a 24-h period, the results are shown in Figure 13.

It can be observed that the satellite visibility of each constellation follows a similar trend to their GDOP performance. The Starlink constellation boasts the best visibility. Although the Iridium constellation has a relatively large number of satellites, its orbital configuration is suboptimal, while the Orbcomm constellation suffers from a limited number of available satellites. However, in the case of dual-constellation combinations, the satellite geometry can be effectively improved.

### 4.2.3 Received signal power

The GPS constellation employs satellites in Medium-Earth-Orbit (MEO). The high orbital altitude results in significant signal attenuation during the transmission of navigation signals, leading to low received power (typically between −160 dBW and −155 dBW). The signals are often submerged in noise, resulting in a low SNR, generally ranging from −20 dB to −30 dB.In contrast, LEO satellites, with their lower orbital altitudes (typically between 700 km and 900 km), experience less signal attenuation during propagation. This results in a higher received SNR (commonly between 15 dB and 30 dB). In terms of received signal power, LEO satellite signals have a significant advantage over GPS signals in terms of anti-jamming capability.

### 4.2.4 Downlink user frequency

Compared with the user downlink spectrum of GNSS applications, which are mostly concentrated in the L-band, LEO satellites have a wide range of available frequency bands due to the numerous applications from various LEO systems. These bands (100 MHz - 42.5 GHz) provide extensive coverage and greater flexibility in terms of anti-jamming capabilities. Unlike current GNSS systems, most LEO satellites operate at very high frequencies, which also enhances their resilience to interference. Detailed parameters of the downlink frequencies and bandwidths of major domestic and international LEO satellites, refer to Table 1. Figure 14 illustrates the downlink spectrum of GNSS navigation systems and selected LEO systems, including Orbcomm, Tianqi, StarNet, Iridium, Globalstar, Starlink, and OneWeb constellations.

In summary, LEO-SOP systems have significant advantages over GNSS systems in terms of received signal power and downlink user frequencies, which contribute to better anti-jamming capability. Regarding GDOP values and satellite visibility, LEO-SOP systems also show clear advantages over GNSS, except for some constellations with fewer satellites and less favorable orbital configurations. Moreover, adopting a dual-constellation system can greatly mitigate potential deficiencies in satellite numbers and orbital configurations that may exist in a single constellation.

## 5 Future challenges

Although LEO-SOP systems have significant advantages over GNSS systems in terms of anti-jamming capability, in everyday positioning scenarios, they are still often affected by various adverse electromagnetic environments, such as urban multipath interference and malicious human-made interference. Therefore, researching anti-jamming algorithms specifically for LEO-SOP positioning holds extremely high application value. In addition, there are still several anti-jamming-related challenges that deserve attention.

### 5.1 Anti-broadband interference under single-antenna reception and mitigation of desired signal loss

Due to the relatively narrow downlink signal bandwidth of LEO satellites (e.g., the Iridium system has a bandwidth of 500 kHz, while the Orbcomm system has only 25 kHz), and the fact that single-antenna receivers remain the preferred choice for most LEO satellite receptions, the available anti-jamming measures are limited when facing wideband or severe interference environments. Moreover, the signal quality degradation caused by anti-jamming measures is more severe given the already narrow signal bandwidth. To address this challenge, future research on single-antenna anti-jamming will focus on how to counteract the effects of wideband interference and mitigate the loss of desired signals during the anti-jamming process, thereby reducing signal distortion and quality degradation caused by signal distortion.

### 5.2 Measurement estimation in low SNR environments

Currently, the majority of research on LEO-SOP positioning is based on the calculation and estimation of observations under relatively high SNR conditions. However, in most usage scenarios, various factors can lead to a lower SNR of the received LEO-SOP signals. For example, low-cost or small-sized antennas inherently cannot provide high antenna gain; rain fade or other path losses particularly affect the energy of high-frequency band signals, resulting in a lower SNR of the received signals; and harsh interference environments can further reduce the signal SNR. A low SNR makes signal detection more challenging and decreases the accuracy of observation estimation. Therefore, future research needs to further explore how to achieve precise estimation of observations in low SNR environments.

### 5.3 Interference scenarios from other satellites

With the construction and deployment of mega-constellations represented by Starlink, interference among different satellites within the same system will become increasingly common. Under such conditions, the receiving environment will be more challenging, as the receiving end often faces signals from other satellites that have similar frequencies and power levels. Therefore, future research needs to further explore how to accurately receive and estimate the target signals in scenarios with interference from other satellites.

## 6 Conclusion

This paper provides a comprehensive review of LEO-SOP and anti-jamming technology research, and analyzes the anti-jamming capability of the LEO-SOP system. Firstly, the current research status of LEO-SOP and anti-jamming technologies is summarized, including the Doppler positioning principle model of LEO-SOP and the workflow of the receiver. Secondly, the anti-jamming capabilities of the LEO-SOP system are analyzed. Finally, the challenges and future development directions of LEO-SOP anti-jamming technologies are discussed, aiming to provide a solid technical foundation for the secure application of LEO-SOP.

## Author contributions

LY: Software, Writing – original draft, Writing – review and editing. BF: Investigation, Resources, Supervision, Formal analysis, Funding Acquisition, Writing – review and editing. HQ: Conceptualization, Methodology, Writing – original draft, Writing – review and editing. DX: Writing – review and editing. MW: Writing – review and editing. BG: Investigation, Resources, Supervision, Writing – review and editing. SC: Investigation, Supervision, Writing – review and editing. CW: Data curation, Formal Analysis, Supervision, Writing – review and editing. XW: Project administration, Resources, Supervision, Writing – review and editing. JS: Investigation, Resources, Supervision, Writing – review and editing. DJ: Investigation, Resources, Supervision, Writing – review and editing. HW: Investigation, Resources, Supervision, Writing – review and editing. HY: Investigation, Resources, Supervision, Writing – review and editing. BL: Investigation, Resources, Supervision, Writing – review and editing. SS: Investigation, Resources, Supervision, Writing – review and editing.

## Funding

The author(s) declare that financial support was received for the research and/or publication of this article. This research was funded from the Army Academy of Artillery and Air Defense under Grant 220214003.

## Acknowledgments

The authors would like to thank the editors and reviewers for their efforts to help the publication of this paper.

## Conflict of interest

Author SS was employed by Shaanxi Datang Gas Safety Technology Co., LTD.

The remaining authors declare that the research was conducted in the absence of any commercial or financial relationships that could be construed as a potential conflict of interest.

The reviewer KW declared a shared affiliation with the author BF to the handling editor at time of review.

## Generative AI statement

The author(s) declare that no Generative AI was used in the creation of this manuscript.

## Publisher's note

## References

1. Jia Q, Zukun L, Baojun L, Jie S, Zhibin X, Zhi W, et al. A survey of GNSS interference monitoring technologies. *Front Phys* (2023) 11. doi:10.3389/fphy.2023.1133316

2. Danning Z, Yu L. Effects of ionosphere dispersion on wideband GNSS signals. *Front Phys* (2023) 11. doi:10.3389/fphy.2023.1103159

3. Shaojie N, Binbin R, Feiqiang C, Zukun L, Jie W, Pengcheng M, et al. GNSS spoofing suppression based on multi-satellite and multi-channel array processing. *Front Phys* (2022) 10. doi:10.3389/fphy.2022.905918

4. Takeshi I, Motoyuki K, Yusaku O, Tatsuya F, Fumiaki T, Iwao U. GNSS-acoustic observations of seafloor crustal deformation using a wave glider. *Front Earth Sci 11 March 2021 Sec Solid Earth Geophys* (2021) 9. doi:10.3389/feart.2021.600946

5. Ting Y, Nan C. A preliminary view of the CYGNSS soil moisture-vegetation activity linkage. Front. For. Glob. Change, 30 November 2023. *Sec For Management* (2023) 6. doi:10.3389/ffgc.2023.1320432

6. Haopeng W, Guorui X, Peiyuan Z, Peigong L, Zhengyang X, Baoxiang Z. Combining Galileo HAS and beidou PPP-B2b with Helmert coordinate transformation method. *GPS Solutions* (2025) 29:35. doi:10.1007/s10291-024-01789-2

7. Peiyuan Z, Guorui X, Lan D. Initial performance assessment of Galileo high accuracy service with software-defined receiver. *GPS Solutions* (2024) 28:2. doi:10.1007/s10291-023-01540-3

8. Xiangjun L, Zukun L, Muzi Y, Wenxiang L, Feixue W, Yi Y, et al. Tradeoff of code estimation error rate and terminal gain in SCER Attack. *Ieee Trans instrumentation Meas* (2024) 73:1–12. doi:10.1109/tim.2024.3406807

9. Alexander M, Laurie B, Robert C, Walterio M, Jianing C, Colin G, et al. Visual odometry using pixel processor arrays for unmanned aerial systems in GPS denied environments. *Front Robot Ai, 29 September 2020 Sec Robot Vis Artif Perception* (2020) 7:126. doi:10.3389/frobt.2020.00126

10. Matteo F, Riccardo B, Matteo M. On the precision of 6 DoF IMU-LiDAR based localization in GNSS-denied scenarios. *Front Robot Ai, 24 January 2023 Sec Field Robotics* (2023) 10:1064930. doi:10.3389/frobt.2023.1064930

11. Hu Z, Zhang L, Ji Y. Applications of differential barometric altimeter in ground cellular communication positioning network. *IET Sci Meas &Technology* (2020) 14(3):322–31. doi:10.1049/iet-smt.2018.5316

12. Sial M, Deng Y, Ahmed J, Nallanathan A, Dohler M. Modeling and analysis of cellular V2X communications over shared channels. *IEEE Trans Vehicular Technology* (2019) 68(12):12079–92. doi:10.1109/TVT.2019.2945481

13. Zhang J, Li Y, Su T, He X. Quadratic FM signal detection and parameter estimation using coherently integrated trilinear autocorrelation function. *IEEE Trans Signal Process* (2020) 68:621–33. doi:10.1109/tsp.2020.2965279

14. Shtark T, Gurfil P. Regional positioning using a low Earth orbit satellite constellation. *Celestial Mech Dynamical Astron* (2018) 130(2):14–28. doi:10.1007/s10569-017-9811-7

15. Reid TG, Neish AM, Walter TF, Enge PK. Leveraging commercial broadband leo constellations for navigating. In: Proceedings of the 29th International Technical Meeting of the Satellite Division of the Institute of Navigation (Ion Gnss+ 2016), (2016) 12. Portland, Oregon. 2016: 2016–6.09. doi:10.33012/2016.14729

16. Han Y, Wang L, Fu W, Zhou H, Li T, Xu B, et al. LEO navigation augmentation constellation design with the multiobjective optimization approaches. *Chin J Aeronaut* (2021) 34(4):265–78. doi:10.1016/j.cja.2020.09.005

17. Zhang Y, Liu A, Li P, Jiang S. Deep learning (DL)-Based channel prediction and hybrid beamforming for LEO satellite massive MIMO system. *IEEE Internet Things J* (2022) 9(23):23705–15. doi:10.1109/jiot.2022.3190412

18. Kodheli O, Maturo N, Chatzinotas S, Andrenacci S, Zimmer F. NB-IoT via LEO satellites: an efficient resource allocation strategy for uplink data transmission. *IEEE Internet Things J* (2022) 9(7):5094–107. doi:10.1109/jiot.2021.3109456

19. Gasparollo L, Bailey E. The globalstar system: a complement to terrestrial mobile networks. *Eur Workshop Mobile and Personal Satellite Commun* (1996) 10–5. doi:10.1109/EMPS.1996.864081

20. Di B, Song L, Li Y, Poor HV. Ultra-dense LEO: integration of satellite access networks into 5G and beyond. *IEEE Wireless Commun* (2019) 26(2):62–9. doi:10.1109/mwc.2019.1800301

21. Yao L, Qin H, Gu B, Shi G, Sha H, Wang M, et al. A study on anti-jamming algorithms in low-earth-orbit satellite signal-of-opportunity positioning systems for unmanned aerial vehicles. *Drones* (2024) 8(4):164. doi:10.3390/drones8040164

22. Levanon N. Quick position determination using 1 or 2 LEO satellites. *IEEE Trans Aerospace Electron Syst* (1998) 34(3):736–54. doi:10.1109/7.705883

23. Levanon N. Instant active positioning with one LEO satellite. *Navigation* (1999) 46(2):87–95. doi:10.1002/j.2161-4296.1999.tb02397.x

24. Fisher KA. *The navigation potential of signals of opportunity-based time difference of arrival measurements*. USA: Air Force Institute of Technology (2005).

25. Tan Z, Qin H, Cong L, Zhao C. New method for positioning using IRIDIUM satellite signals of opportunity. *IEEE access* (2019) 7:83412–23. doi:10.1109/access.2019.2924470

26. Tan Z, Qin H, Cong L, Zhao C. Positioning using IRIDIUM satellite signals of opportunity in weak signal environment. *Electronics* (2019) 9(1):37. doi:10.3390/electronics9010037

27. Wang D, Qin H, Huang Z. Doppler positioning of LEO satellites based on orbit error compensation and weighting. *IEEE Trans Instrumentation Meas* (2023) 72(1):1–11. doi:10.1109/tim.2023.3286001

28. Zhang Y, Qin H, Shi G. Doppler positioning based on globalstar signals of opportunity. In: 2023 5th International Conference on Electronic Engineering and Informatics (EEI). IEEE (2023). p. 666–9.

29. Qin H, Zhang Y, Yang Y, Lv H. Fast clustering satellite selection based on Doppler positioning GDOP lower bound for LEO constellation. *IEEE Trans Aerospace Electron Syst* (2024) 60(6):9401–10. doi:10.1109/taes.2024.3443021

30. Khalife J, Kassas ZM. Receiver design for Doppler positioning with LEO satellites. In: ICASSP 2019-2019 IEEE International Conference on Acoustics, Speech and Signal Processing (ICASSP). IEEE (2019). p. 5506–10.

31. Neinavaie M, Khalife J, Kassas ZM. Acquisition, Doppler tracking, and positioning with Starlink LEO satellites: first results. *IEEE Trans Aerospace Electron Syst* (2021) 58(3):2606–10. doi:10.1109/taes.2021.3127488

32. Neinavaie M, Kassas ZM. Unveiling Starlink LEO satellite OFDM-like signal structure enabling precise positioning. *IEEE Trans Aerospace Electron Syst* (2023) 60:2486–9. doi:10.1109/taes.2023.3265951

33. Farhangian F, Landry JR. Multi-constellation software-defined receiver for Doppler positioning with LEO satellites. *Sensors* (2020) 20(20):5866. doi:10.3390/s20205866

34. Orabi M, Khalife J, Kassas ZM. Opportunistic navigation with Doppler measurements from Iridium next and Orbcomm LEO satellites. In: 2021 IEEE Aerospace Conference (50100). IEEE (2021). p. 1–9.

35. Kozhaya S, Kanj H, Kassas ZM. Blind Doppler tracking and positioning with NOAA LEO satellite signals. In: Proceedings of the 36th International Technical Meeting of the Satellite Division of The Institute of Navigation (ION GNSS+ 2023) (2023). p. 363–72.

36. Kozhaya S, Kanj H, Kassas ZM. Multi-constellation blind beacon estimation, Doppler tracking, and opportunistic positioning with OneWeb, Starlink, Iridium NEXT, and Orbcomm LEO satellites[C]//2023 IEEE/ION Position. In: Location and Navigation Symposium (PLANS). IEEE (2023). p. 1184–95.

37. Zhao C, Qin H, Li Z. Doppler measurements from multiconstellations in opportunistic navigation. *IEEE Trans Instrumentation Meas* (2022) 71:1–9. doi:10.1109/tim.2022.3147315

38. Khalife J, Kassas ZM. Assessment of differential carrier phase measurements from Orbcomm LEO satellite signals for opportunistic navigation. In: Proceedings of the 32nd International Technical Meeting of the Satellite Division of The Institute of Navigation (ION GNSS+ 2019). Miami, Florida: ION (2019). p. 4053–63. doi:10.33012/2019.17031

39. Khalife J, Neinavaie M, Kassas ZM. Navigation with differential carrier phase measurements from megaconstellation LEO satellites[C]//2020 IEEE/ION Position. *Location Navigation Symp (Plans) IEEE* (2020) 1393–404. doi:10.1109/PLANS46316.2020.9110199

40. Khalife J, Kassas ZZM. Performance-driven design of carrier phase differential navigation frameworks with megaconstellation LEO satellites. *IEEE Trans Aerospace Electron Syst* (2023) 59(3):2947–66. doi:10.1109/taes.2023.3234521

41. Neinavaie M, Shadram Z, Kozhaya S, Zaher MK. First results of differential Doppler positioning with unknown Starlink satellite signals. In: 2022 IEEE Aerospace Conference (AERO). IEEE (2022). p. 1–14.

42. Zhao C, Qin H, Wu N, Wang D. Analysis of baseline impact on differential Doppler positioning and performance improvement method for LEO opportunistic navigation. *IEEE Trans Instrumentation Meas* (2023) 72:1–10. doi:10.1109/tim.2023.3235456

43. Wu N, Qin H, Zhao C. Long-baseline differential Doppler positioning using space-based SOP based on BPVGMM. *IEEE Trans Instrumentation Meas* (2023) 72:1–10. doi:10.1109/tim.2023.3276510

44. Qin H, Wu N, Zhao C. Differential positioning with Doppler measurements from Iridium satellite signals of opportunity based on linesof sight correction. *J Beijing Univ Aeronaut Astronaut* (2022) 50(03):748–756. doi:10.13700/j.bh.1001-5965.2022.0378

45. Morales J, Khalife J, Kassas ZM. Simultaneous tracking of Orbcomm LEO satellites and inertial navigation system aiding using Doppler measurements. In: 2019 IEEE 89th Vehicular Technology Conference (VTC2019-Spring). IEEE (2019). p. 1–6. doi:10.1109/VTCSpring.2019.8746485

46. Benzerrouk H, Nguyen Q, Xiaoxing F, Amrhar A, Nebylov AV, Landry R. Alternative PNT based on Iridium Next LEO satellites Doppler/INS integrated navigation system. In: 2019 26th Saint Petersburg international conference on integrated navigation systems (ICINS). IEEE (2019). p. 1–10.

47. Farhangian F, Landry RJ. High-order pseudorange rate measurement model for multi-constellation LEO/INS integration: case of Iridium-NEXT, Orbcomm, and Globalstar. *Proc Inst Mech Eng G: J Aerospace Eng* (2023) 237(4):925–39. doi:10.1177/09544100221113123

48. Du Y, Qin H, Zhao C. LEO satellites/INS integrated positioning framework considering orbit errors based on FKF. *IEEE Trans Instrumentation Meas* (2024) 73:1–14. doi:10.1109/tim.2024.3369693

49. Cheng J, Ren P, Deng T. A novel ranging and IMU-based method for relative positioning of two-MAV formation in GNSS-denied environments. *Sensors* (2023) 23(9):4366. doi:10.3390/s23094366

50. Dong P, Cheng J, Liu L. A novel anti-jamming technique for INS/GNSS integration based on black box variational inference. *Appl Sci* (2021) 11(8):3664. doi:10.3390/app11083664

51. Shao Y, Ma H, Zhou S, Wang X, Antoniou M, Liu H. Target localization based on bistatic T/R pair selection in GNSS-based multistatic radar system. *Remote Sens* (2021) 13(4):707. doi:10.3390/rs13040707

52. Łukasz L, Aleksandra R, Andrzej P, Dobryakova L, Ochin E. GNSS and LNSS positioning of unmanned transport systems: the brief classification of terrorist attacks on USVs and UUVs. *Electronics* (2021) 10(4):401. doi:10.3390/electronics10040401

53. Wang H, Chang Q, Xu Y. An anti-jamming null-steering control technique based on double projection in dynamic scenes for GNSS receivers. *Sensors* (2019) 19(7):1661. doi:10.3390/s19071661

54. Jiang Y, Fu J, Li B, Jiang P. Distributed sensitivity and critical interference power analysis of multi-degree-of-freedom navigation interference for global navigation satellite system array antennas. *Sensors* (2024) 24(2):650. doi:10.3390/s24020650

55. Sun Y, Chen F, Lu Z, Wang F. Anti-jamming method and implementation for GNSS receiver based on array antenna rotation. *Remote Sens* (2022) 14(19):4774. doi:10.3390/rs14194774

56. Lu Z, Chen F, Xie Y, Sun Y, Cai H. High precision pseudo-range measurement in GNSS anti-jamming antenna array processing. *Electronics* (2020) 9(3):412. doi:10.3390/electronics9030412

57. Zhang J, Cui X, Xu H, Lu M. A two-stage interference suppression scheme based on antenna array for GNSS jamming and spoofing. *Sensors* (2019) 19(18):3870. doi:10.3390/s19183870

58. Xu H, Cui X, Lu M. An SDR-based real-time testbed for GNSS adaptive array anti-jamming algorithms accelerated by GPU. *Sensors* (2016) 16(3):356. doi:10.3390/s16030356

59. Zhou C, Wang Y, Qiao C, Dai W. Anti-jamming method using complex ANF for GNSS receivers. *J Natl Univ defense Technol* (2016) 38(No.5).

60. Grabowski J, Hegarty C. Characterization of L5 receiver performance using DigitalPulse blanking. In: Proceedings of International Technical Meeting of the SatelliteDivision of the Institute of Navigation (ION GPS 2002) Portland, OR (2002). 1630–1635.

61. Song J, Lu Z, Liu Z. Review on the time-domain interference suppression of navigation receiver. *Syst Eng Electronics* (2023) 45(No.4).

62. Lv M. *Research and implementation of anti-jamming technology for satellite navigation receiver based on array antenna*. Harbin Engineering University (2019).

63. Chien YR. Design of GPS anti-jamming systems using adaptive notch filters. *IEEE Syst J* (2015) 9(2):451–460. doi:10.1109/jsyst.2013.2283753

64. Lv Q, Qin H. General method to mitigate the continuous wave interference andnarrowband interference for GNSS receivers. *IET radar, sonar and navigation* (2020) 14(9):1430–5. doi:10.1049/iet-rsn.2020.0115

65. Mosavi MR, Shafiee F. Narrowband interference suppression for GPS navigationusing neural networks. *GPS Solutions* (2016) 20(3):341–51. doi:10.1007/s10291-015-0442-8

66. Qi L. In: Research on Anti-jamming Methods for GNSS Signal Acquisition under Complex Interference Environment. Harbin Engineering University (2018).

67. DiPietro RC. An FFT based technique for suppressing narrow-band interferencein PN spreading spectrum communications systems. In: Proceedings of IEEEICASSP (1989). p. 1360–1363. doi:10.1109/ICASSP.1989.266690

68. Davidovici S, Kanterakis EG. Narrow-band interference rejection rejection usingreal-time Fourier transforms. *IEEE Trans Commun* (1989) 37(7):713–72.

69. Young JA, Lehnert JS. Analysis of DFT-based frequency excision algorithms fordirect-sequence spread-spectrum communications. *IEEE Trans On Commun* (1998) 46(8):1076–1087. doi:10.1109/26.705409

70. Li C, Hu G. A new lapped transform domain narrow-band interference excision technique. *Acta Elec Sinca* (2000) 28(1):117–119.

71. Sun Z. *Adaptive algorithms of suppression narrow-band interference in DSSS*. Harbin Engineering University (2005).

72. Zeng X, Li Z, Wang F. Study on windowing degradation of frequency-domain narrowband interference suppression algorithms in spread spectrum system. *J Electronics and Inf Technology* (2004) 26(8):1276–81.

73. Rezaei MJ, Abedi M, Mosavi MR. New GPS anti-jamming system based on multipleshort-time Fourier transform. *IET Radar Sonar and Navigation* (2016) 10(4):807–15. doi:10.1049/iet-rsn.2015.0417

74. Chang CL. Modified compressive sensing approach for GNSS signal reception in thepresence of interference. *GPS Solutions* (2016) 20:201–213. doi:10.1007/s10291-014-0429-x

75. Chien YR, Chen PY, Fang SH. Novel anti-jamming algorithm for GNSS ReceiversUsing wavelet-packet-transform-based adaptive predictors. *IEICE Transactionson Fundamentals Electronics Commun and Computer Sci* (2017) E100.A(2):602–10. doi:10.1587/transfun.e100.a.602

76. Ding M, Mi X, Chen W, Weng D, Ding W. Equalization of frequency domain adaptive filter(FDAF) using signal prediction aided ReferenceSpectrum model (SPRSM). *IEEE Trans instrumentation Meas* (2024) 73:1–16. doi:10.1109/tim.2024.3366269

77. Li J, Wu R, Hao Y, Wang X, Wang Y, Zhao A. DME interference suppression algorithm based on signal separation estimation theory for civil aviation system. *Eurasip J WirelessCommunications and Networking* (2016) (1):247. doi:10.1186/s13638-016-0736-8

78. Sun K, Jin T, Yang D. An improved time-frequency analysis method in InterferenceDetection for GNSS receivers. *Sensors* (2015) 15(4):9404–26. doi:10.3390/s150409404

79. Mosavi MR, Rezaei MJ, Pashaian M, Moghaddasi MS. A fast and accurate anti-jamming SystemBased on wavelet packet transform for GPS receivers. *GPS Solutions* (2017) 21(2):1–12.

80. Sun K, Yu B, Xu L, Elhajj M, Yotto Ochieng W. A novel GNSS anti-interference method usingFractional fourier transform and notch filtering. *IEEE Trans instrumentation Meas* (2024) 73:1–17. doi:10.1109/tim.2024.3451600

81. Wan Y, Chen F, Nie J, Sun G. Optimum reference element selection for GNSSPower-inversion adaptive arrays. *Electronics Lett* (2016) 52(20):1723–1725.

82. Moelker DJ, Pol EVD, Bar-Ness Y. *Adaptive antenna arrays for interferencecancellation in GPS and GLONASS receivers[C]//Position Location and Navigation Symposium*. IEEE (1996). p. 191–198. doi:10.1109/PLANS.1996.509077

83. VanTrees HL. *Optimum array processing: Part IV of Detection, estimation andmodulation theory*. Wiley-Interscience (2002).

84. Capon J. High-resolution frequency-wavenumber spectrum analysis. *Proc of the IEEE* (2005) 57(8):1408–1418. doi:10.1109/proc.1969.7278

85. Zoltowski MD, Gecan AS. Advanced adaptive null steering concepts for GPS Military Communications Conference. In: MILCOM '95 Conference Record, 3. San Diego, CA: IEEE (1995). p. 1214–1218. doi:10.1109/MILCOM.1995.483688

86. Zheng J, Chen L, Dai Y, Chen Z, Xu X. Performance estimates of GNSS receiver jamming with adaptive nulling technique. *Geomatics Inf Sci Wuhan Univ* (2015) 40(8):1006–11.

87. Cui Y. *Research on anti-jamming techniques forReceiver of satellite navigation system*. Tianjin University (2012).

88. Author anonymous (2024) Mtigating the threat of GPS jamming anti-jam technology. Available online at: https://www.novatel.com/solutions/anti-jamming-technology/ (Accessed April 2, 2024).

89. Chen F, Nie J, Zhu X, Sun G, Wang F. *Impact of reference element selection on performance of power inversion adaptive arrays[C]*. Savannah, GA: IEEE/ION Position, Location and Navigation Symposium (PLANS) (2016). doi:10.1109/PLANS.2016.7479756

90. Chen F, Nie J, Ni S, Li Z, Wang F. Combined algorithm for interference suppression and signalacquisition in GNSS receivers. *Electronics Lett* (2017) 53(4):274–275.

91. Wan Y, Chen F, Nie J, Sun G. Optimum reference element selection for GNSSpower-inversion adaptive arrays. *Electronics Lett* (2016) 52(20):1723–1725. doi:10.1049/el.2016.2360

92. Lu Z, Nie J, Wan Y, Ou G. Optimal reference element for interference suppression inGNSS antenna arrays under channel mismatch. *Iet Radar Sonar and Navigation* (2017) 11(7):1161–1169.

93. Zhang YD, Amin MG. Anti-jamming GPS receiver with reduced PhaseDistortions. *IEEE Signal Process. Lett* (2012) 19(10):635–8. doi:10.1109/lsp.2012.2209873

94. Daneshmand S, Marathe T, Lachapelle G. Millimetre level accuracy GNSSPositioning with the blind adaptive beamforming method in InterferenceEnvironments. *Sensors* (2016) 16(11):1824. doi:10.3390/s16111824

95. Wang L, Han Y. Moving jammer suppression with robust blind adaptive algorithms inGPS receiver. (2015).

96. Chen LW, Zheng JS, Su MK, Zhang J. A strong interference suppressor for SatelliteSignals in GNSS receivers. *Circuits Syst and Signal Process* (2016) 36(7):1–16.

97. Wang W, Du Q, Wu R. High dynamic interference suppression based on FewSnapshots for satellite navigation system. *J Electronics and Inf Technology* (2014) 36(10):2445–2449.

98. Gong Y, Wang L, Yao R, Zhang Z. A robust method to suppress jamming for GNSS ArrayAntenna based on reconstruction of sample covariance matrix. *InternationalJournal of Antennas and Propagation* (2017) 2017(3):1–12. doi:10.1155/2017/9764283

99. Lin HC. Spatial correlations in adaptive arrays. *IEEE Trans Antennas &Propagation* (2003) 30(2):212–23.

100. Wang X, Aboutanios E. Reconfigurable adaptive linear array signal processing inGNSS applications. In: IEEE International Conference on Acoustics, Speech andSignal Processing. IEEE (2013). p. 4154–8.

101. Wang X, Aboutanios E, Amin MG. Generalised array reconfiguration for adaptivebeamforming by antenna selection. In: IEEE International Conference on Acoustics,Speech and Signal Processing. IEEE (2015). p. 2479–83.

102. Amin MG, Wang X, Zhang YD, Ahmad F, Aboutanios E. Sparse arrays and sampling for InterferenceMitigation and DOA estimation in GNSS. *Proc IEEE* (2016) 104(6):1302–17. doi:10.1109/jproc.2016.2531582

103. Kassas ZM, Khairallah N, Kozhaya S. *Ad astra*: simultaneous tracking and navigation with megaconstellation LEO satellites. *IEEE Aerospace Electron Syst Mag* (2024) 39:46–71. doi:10.1109/maes.2023.3267440

104. Lemme PW, Glenister SM, Miller AW. Iridium (R) aeronautical satellite communications. *IEEE Aerospace Electron Syst Mag* (1999) 14(11):11–6. doi:10.1109/62.809197

105. Cobb S, Lawrence D, Gutt G, O'Connor M. Differential and rubidium disciplined test results from an Iridium-based secure timing solution. In: Proceedings of the 2017 International Technical Meeting of The Institute of Navigation (2017). p. 1111–1116.

106. Lawrence D, Cobb HS, Gutt G, Tremblay F, Laplante P, O'Connor M. Test results from a LEO-satellite-based assured time and location solution. In: *Proceedings of the 2016 international technical meeting of the Institute of navigation* (2016). p. 125–129.

107. Li B, Ge H, Ge M, Nie L, Shen Y, Schuh H. LEO enhanced Global Navigation Satellite System (LeGNSS) for real-time precise positioning services. *Adv Space Res* (2019) 63(1):73–93.

108. Leng M, Razul SG, See CMS, Tay W, Cheng C, Quitin F. *Joint navigation and synchronization using SOOP in GPS-denied environments: algorithm and empirical study 2015 sensor signal processing for defence (SSPD)*. Edinburgh, United Kingdom: IEEE (2015). p. 1–5.

109. Braun TM. *Satellite Communications payload and system*. John Wiley & Sons (2012). 552–559. Available online at: https://books.google.com.sg/books?hl=zh-CN&lr=&id=pSrcHzgCGyQC&oi=fnd&pg=PR19&ots=rvj81LkRny&sig=FQo9bw-fhN6mgKa_YillnCaSNKo&redir_esc=y#v=onepage&q&f=false (Accessed April 25, 2025).

110. Author anonymous. (2025) Iridium NEXT engineering statement. FCC File Number 1031348. Available online at: https://fcc.report/IBFS/SAT-MOD-20131227-00148/1031348.pdf (Accessed April 2, 2025).

111. Author anonymous. (2019) *Iridium burst detector and demodulator*. GNU Radio Iridium Out of Tree Module. Available online at: https://github.com/muccc/gr-iridium (Accessed April 02, 2024).

112. Hong Y, Viterbo E, Chockalingam A. (2019) *Orthogonal time frequency space (OTFS) modulation*. Shanghai, China: Proc. IEEE ICC Tutorial. Available online at: https://ecse.monash.edu/staff/eviterbo/OTFS-VTC18/TutorialICC2019OTFSmodulation.pdf (Accessed April 2, 2024).

113. Yatrakis CL. (2025) Computing the cross ambiguity function – a review.

114. Kiefer J. Sequential minimax search for a maximum. *Proc Am Math Soc* (1953) 4(3):502–506. doi:10.2307/2032161

115. HARAT. ORBCOMM low Earth orbit mobile satellite communication system. In: OTactical Communications Conference. Piscataway: IEEE Press (1994). 5050499

116. Wang M, Ma LH, Zhang L, Ji H, Shi H. Three-satellite positioning algorithm with altitude aiding for regional navigation satellite system. *J Shanghai Jiao Tong Univ* (2012) 46(10):1647–1652.

117. Orbcomm LLC. *ORBCOMM system overview: a80TD0008 Revision G*. Rochelle Park: ORBCOMM (2001).

118. Wang JG, Gopaul N, Scherzinger B. Simplified algorithms of variance component estimation for static and kinematic GPS SinglePoint positioning. *J Glob Positioning Syst* (2009) 8(1):43–52. doi:10.5081/jgps.8.1.43

119. Liu GL. *Theory and method of adjustment in modern measurement*. China University of Mining and Technology Press (2012). p. 64–8.

120. Benzerrouk H, Nguyen Q, Xiaoxing F, Amrhar A, Rasaee H, Landry R. LEO satellites based Doppler positioning using D istributed nonlinear estimation. *IFAC-Papers Online* (2019) 52(12):496–501.

121. Savin A, Cherniakov M, Antomiou M. Passive radar using Starlink transmissions: a theoretical study. In: The Institute of Electrical and Electronics Engineers(IEEE).2019 20th International Radar Symposium (IRS). Piscataway,NJ: IEEE Press (2019). p. 1–7.

122. Space Exploration Technologies. SpaceX non-geostationary satellite system attachment a:technical information to supplement schedules [EB/OL]. Available online at: https://www.fcc.report/IBFS/SAT-MOD-20181108-00083/1569860.pdf (Accessed April 2, 2024).

123. Kay SM. *Fundamentals of statistical signal processing: estimation theory*. Upper Saddle River: Prentice-Hall Inc (1993). p. 193–7.

124. Kassas ZM, Neinavaie M, Khalife J. Acquisition, Doppler tracking, and positioning with Starlink LEO satellites: first results. Available online at: https://ieeexplore.ieee.org/stamp/stamp.jsp?tp=&arnumber=9612022&tag=1 (Accessed April 2, 2024).

125. Neinavaie M, Khalife J, Kassas ZM. Exploiting Starlink signals for navigation: first results. In *Proceedings of the 34th internationl technical meeting of the satellite division of the Institute of navigation (ION GNSS+ 2021)*. St. Louis, Missouri: The Institute of Navigation, Inc. (2021). 2766–2773. doi:10.33012/2021.18122

126. Milstein LB, Das PK. An analysis of real-time transform domain filteringdigital communication system-Part I: narrow-band interference rejection. *IEEE trans Commun* (1980) 28 (6):816–824. doi:10.1109/TCOM.1980.1094725

127. Milstein LB, Das PK. Spread spectrum receiver using surface acoustic wavetechnology. *IEEE Trans Commun* (1977) 25:841–7. doi:10.1109/tcom.1977.1093905